



FRIEDRICH-SCHILLER- UNIVERSITÄT JENA

Aqueous Organic Redox-Flow-Batteries: From Electrolyte Development to Detailed Stability Studies

Dissertation

(kumulativ)

zur Erlangung des akademischen Grades

doctor rerum naturalium (Dr. rer. nat.)

vorgelegt dem Rat der Chemisch-Geowissenschaftlichen Fakultät
der Friedrich-Schiller-Universität Jena

von Philip Rohland, M. Sc.
geboren am 03.05.1990 in Zeitz

Gutachter:

1. Prof. Dr. U. S. Schubert
2. Prof. Dr. M. Oschatz

Tag der öffentlichen Verteidigung: 15.02.2023

Table of Contents

Documentation of Authorship	1
1 Introduction	1
2 Fundamentals of redox flow batteries: Material requirements and critical parameters	6
2.1. Material requirements	8
2.2. Critical battery parameters	9
3 Synthesis and stability investigation of active materials for redox flow batteries	11
3.1 In depth investigation of the TMA-TEMPO decay	13
3.2 Synthetic approaches towards a new more stable TEMPO derivative	19
3.3 Application of the advanced cycling protocol to negolytes.....	29
4 State of charge and state of health measurement methods for RFB electrolytes	32
4.1 Liquid chromatography analysis of TEMPO electrolytes	33
4.2 Low-cost amperometric determination for the combined SOC, SOH and capacity monitoring	38
4.3 Inexpensive microelectrodes for amperometric SOC, SOH, and capacity co-determination.....	48
5 Summary	54
6 Zusammenfassung	58
7 References	63
Abbreviations.....	68
Symbols	71
Curriculum vitae	72
Publication list	73
Acknowledgements	75
Declaration of authorship/Selbstständigkeitserklärung	77
Publications P1	78
Publications P2	79

Publications P3.....	80
Publications P4.....	81
Publications P5.....	82
Publications P6.....	83
Publications P7.....	84

Documentation of Authorship

This section contains a list of individual authors' contributions to the publications reprinted in this thesis.

P1: *Redox-active polymers: The magic key towards energy storage – A polymer design guideline*
P. Rohland,¹ E. Schröter,² O. Nolte,³ G. R. Newkome⁴, M. D. Hager,⁵ U. S. Schubert,⁶
Prog. Polym. Sci. **2022**, 125, 101474.
<https://doi.org/10.1016/j.progpolymsci.2021.101474>.

Author	1	2	3	4	5	6
Conceptual contribution	■	■	■	■		
Preparation of the manuscript	■	■		■		
Correction of the manuscript			■	■	■	■
Supervision of P. Rohland					■	■
Proposal for crediting publication equivalents	0.5	0.5				

E. Schröter and P. Rohland contributed equally to this review.

P2: *Stability of TMA-TEMPO-based aqueous electrolytes for redox-flow batteries*
P. Rohland,¹ O. Nolte,² N. Ueberschaar,³ M. D. Hager,⁴ U. S. Schubert,⁵ *J. Power Sources* **2022**, 525, 230996.
<https://doi.org/10.1016/j.jpowsour.2022.230996>.

Author	1	2	3	4	5
Conceptual contribution	■	■			
Electrochemical investigations	■	■			
Battery experiments	■	■			
Mass spectrometry measurements			■		
Preparation of the manuscript	■	■			
Correction of the manuscript			■	■	■
Supervision of P. Rohland				■	■
Proposal for crediting publication equivalents	0.75	0.75			

O. Nolte and P. Rohland contributed equally to this publication.

Documentation of Authorship

P3: *Structural alterations on the TEMPO scaffold and their impact on the performance as active materials for redox flow batteries*

P. Rohland,¹ O. Nolte,² K. Schreyer,³ H. Goerls⁴, M. D. Hager,⁵ U. S. Schubert,⁶ *Mater. Adv.* **2022**, 3, 4278-4288.

<https://doi.org/10.1039/D1MA00663K>.

Author	1	2	3	4	5	6
Conceptual contribution	■	■				
Electrochemical investigations	■					
Synthesis	■		■			
Battery experiments	■	■				
X-Ray crystallography				■		
Preparation of the manuscript	■					
Correction of the manuscript		■		■	■	■
Supervision of P. Rohland					■	■
Proposal for crediting publication equivalents	1.0					

P4: *Anthraquinone-2,6-disulfamidic acid: An anolyte with low decomposition rates at elevated temperatures*

P. Rohland,¹ K. Schreyer,² M. D. Hager,³ U. S. Schubert,⁴ *RSC Adv.* **2021**, 11, 38759-38764.

<https://doi.org/10.1039/D1RA05545C>.

Author	1	2	3	4
Conceptual contribution	■			
Electrochemical characterization	■			
Synthesis	■	■		
Battery experiments	■			
Preparation of the manuscript	■			
Correction of the manuscript		■	■	■
Supervision of P. Rohland			■	■
Proposal for crediting publication equivalents	1.0			

P5: *Liquid chromatography analysis of reactive oxoammonium cations*
P. Rohland¹, K. Schreyer,² R. Burges,³ N. Fritz,⁴ M. D. Hager,⁵ U. S. Schubert⁶,
Chromatographia **2021**, *84*, 999-1007.
<https://doi.org/10.1007/s10337-021-04084-1>.

Author	1	2	3	4	5	6
Conceptual contribution	■		■			
Analyte preparation	■	■				
HPLC protocol development	■	■	■			
HPLC measurements		■		■		
LC-MS measurements				■		
Preparation of the manuscript	■					
Correction of the manuscript			■	■	■	■
Supervision of P. Rohland					■	■
Proposal for crediting publication equivalents	1.0					

P6: *A low-cost amperometric sensor for the combined state-of-charge, capacity, and state-of-health monitoring of redox flow battery electrolytes*
C. Stolze¹, P. Rohland², K. Zub³, O. Nolte⁴, M. D. Hager⁵, U. S. Schubert⁶, *Energy Convers. Manag. X* **2022**, *14*, 100188.
<https://doi.org/10.1016/j.ecmx.2022.100188>.

Author	1	2	3	4	5	6
Conceptual contribution	■					
Electrochemical characterization	■	■				
Temperature investigations	■	■				
Microelectrode manufacturing	■			■		
Online state-of-charge monitoring experiments	■	■				
SEM & EDX Investigation			■			
Preparation of the manuscript	■					
Correction of the manuscript		■	■	■	■	■
Supervision of P. Rohland					■	■
Proposal for crediting publication equivalents		0.5				

Documentation of Authorship

P7: *Inkjet-printed microband electrodes for a cost-efficient state-of-charge monitoring in redox flow batteries*

K. Zub¹, C. Stolze², P. Rohland³, S. Stumpf⁴, S. Hoepfner⁵, M. D. Hager⁶, U. S. Schubert⁷, *Sens. Actuators B Chem.* **2022**, accepted.

<https://doi.org/10.1016/j.snb.2022.132291>.

Author	1	2	3	4	5	6	7
Conceptual contribution	■	■					
Preparation of microband electrodes	■						
Electrochemical characterization		■	■				
SEM & EDX Investigation	■			■			
Preparation of the manuscript	■	■					
Correction of the manuscript		■	■	■	■	■	■
Supervision of P. Rohland						■	■
Proposal for crediting publication equivalents			0.5				

Erklärung zu den Eigenanteilen des Promovenden/der Promovendin sowie der weiteren Doktoranden/Doktorandinnen als Koautoren an den Publikationen und Zweitpublikationsrechten bei einer kumulativen Dissertation

Für alle in dieser kumulativen Dissertation verwendeten Manuskripte liegen die notwendigen Genehmigungen der Verlage („Reprint permissions“) für die Zweitpublikation vor.

Die Co-Autorinnen/-Autoren der in dieser kumulativen Dissertation verwendeten Manuskripte sind sowohl über die Nutzung, als auch über die oben angegebenen Eigenanteile der weiteren Doktorandinnen/Doktoranden als Co-Autorinnen/Autoren an den Publikationen und Zweitpublikationsrechten bei einer kumulativen Dissertation informiert und stimmen dem zu.

Die Anteile des Promovenden sowie der weiteren Doktorandinnen/Doktoranden als Co-Autorinnen/Co-Autoren an den Publikationen und Zweitpublikationsrechten bei einer kumulativen Dissertation sind in der Anlage aufgeführt.

Philip Rohland		Jena	_____
Name des Promovenden	Datum	Ort	Unterschrift

Ich bin mit der Abfassung der Dissertation als publikationsbasierte Dissertation, d.h. kumulativ, einverstanden und bestätige die vorstehenden Angaben.

Prof. Dr. Ulrich S. Schubert		Jena	_____
Name Betreuer	Datum	Ort	Unterschrift

Dr. Martin D. Hager		Jena	_____
Name Betreuer	Datum	Ort	Unterschrift

1 Introduction

The global surface temperature in July 2022 was 0.87 °C above the 20th century temperature average, representing the fifth warmest July in 143 years of global climate records.^[1] Furthermore, it is the 46th consecutive July as well as the 451th consecutive month above the 20th century's average temperature.^[1] While the increase of the worldwide median temperatures is one of the most prominent indicators for global warming, the phenomenon is mainly based on the increasing amounts of man-made greenhouse gases (GHG). Over the last 170 years, the global atmospheric carbon dioxide concentration rose from 280 ppm in 1750 to 417 ppm in June 2022.^[2] The widely performed combustion of hydrocarbons like methane, oil, and coal for energy production or in the transport sector can be considered as the main reason for this enormous rise. To reduce the anthropogenic climate change, consequences must be drawn in our social life, economics, and energy production.^[3] Aware of their responsibility for further generations, the international community of states has put significant effort into the implementation of a global treaty to keep the global temperature increase “best-below” 2 °C – with the Kyoto Protocol and, subsequently, the Paris Agreement.^[4] The ratifying states agreed to reduce their GHG emission by 20% (relative to 2010) until 2030. To achieve this mission, a change from conventional fossil energy sources to renewable sources, for instance based on wind or solar energy, is inevitable. However, these new “green” approaches for energy production have the drawback of a discontinuous output, depending on the daytime and the weather conditions. The resulting fluctuations must be compensated by the electrical grid. Thus, a reorganization of the electricity infrastructure towards a “smart” grid with large scale energy storage capacities is required.

The nowadays most prominent storage technology, the lithium-ion battery (LIB), combines high power densities and low costs while delivering high voltages. This leads to their ubiquitous usage and the replacement of many other technologies, like lead-, cadmium-, or nickel-based batteries. The impact of LIBs has been and still is so high that their pioneers were even rewarded with the Nobel prize in 2019.^[5] The forerunner, however, also has its limitations. Many LIBs suffer from a high flammability when the active materials are exposed to oxygen or water. Furthermore, larger battery packs need a temperature control mechanism to prevent overheating and explosions.^[6] Another disadvantage lies in the used electrode materials, which often comprise toxic heavy metals like cobalt or nickel. In particular cobalt, which is required for

commercial lithium-nickel-manganese-cobalt batteries, is mined under unsustainable conditions, particularly involving child labor.^[7]

Since LIBs tend to be unfavored for large-scale application, especially grid stabilization and onsite storage, another battery technology is currently gaining a lot of interest for this purpose by scientists and companies alike. The redox flow battery (RFB) combines high storage capacities with an excellent scalability and is, thus, well-suited for smart grids.^[8] Invented by Kangro back in 1949, this battery concept comprises three components: Two tanks, one for each half cell, which serve as storage for the liquid active materials and an electrochemical cell, where the charging and discharging processes take place (cf. **Figure 1.1.**).^[9] Since the size of the tanks can be adjusted, the capacity of the battery is customizable to the intended application. In the electrochemical cell both half cells are separated by a semipermeable membrane. The membrane is used to hold back the active materials of the two electrolytes but enables the exchange of ions from the supporting electrolyte. The type of this membrane is adapted for the used storage materials. However, since the active material is mainly stored in the tanks, it must be actively transported into the electrochemical cell by pumps during charging/discharging processes. This might be a drawback because the battery is more complex and the pumps consume energy, lowering the overall efficiency. Nevertheless, since only a small amount of the active material remains in the electrochemical cell when the battery is not used, the self-discharge is drastically slowed down.

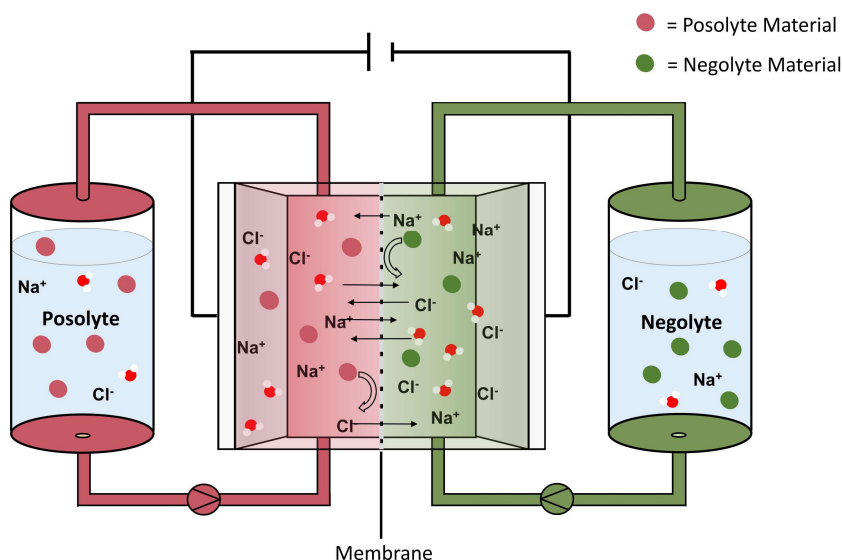


Figure 1.1: Schematic representation of an RFB in aqueous media with sodium chloride as supporting electrolyte. The battery consists of two tanks for the electrolytes (posolyte for the positive half-cell material, negolyte for the negative half-cell material) and the electrochemical cell with two compartments, which are separated by the membrane. The redox-active materials circulate between the tanks and the cell utilizing pumps.

One of the greatest advantages in comparison to LIBs is the independent scalability of the power output ability and the capacity of the battery. By adjusting the characteristics of the cell stack, in particular the active membrane area, the power output can be tailored and as previously mentioned the volume of the tanks defines the capacity of the battery.

The nowadays most advanced RFBs utilize vanadium species in high concentrated sulfuric acid as active material and, therefore, the electrolytes are highly toxic, corrosive, and expensive. Thus, it is not surprising that the vanadium redox flow battery (VRFB) gains only slowly a higher market share. The currently emerging organic redox flow batteries (ORFBs) target some the drawbacks of VRFBs. The used organic molecules contain earth-abundant elements, therefore lowering the electrolyte price. Some of the active materials do not need drastic pH conditions and can work under neutral conditions or are even bioinspired.^[10] Furthermore, the usage of organic molecules offers a wide selection of scaffolds for redox-active molecules to tailor the characteristics of the battery even further to the implied application. Among the most relevant redox-active molecule classes, alloxazines,^[11] flavines,^[10a] quinones,^[11a, 12] ferrocenes,^[13] stable organic radicals,^[10b, 14] and viologen derivatives^[10b, 15] have been applied in ORFBs. Despite the wide variety of utilizable molecules, only a few meet the requirements as active material for a future commercial ORFB. High achievable capacities, voltages, and current densities were demonstrated for many molecules, but they often exhibit low stabilities during long-time tests, at elevated temperatures, or when held in a vulnerable state of charge (SOC). In particular, the last two conditions are often not even investigated, despite the findings being crucial for a market-ready product.

In this thesis active materials for aqueous electrolytes in water based RFBs were investigated. Thus, in **Chapter 2** the fundamentals of RFBs are summarized and detailed information on the requirements for active materials are presented. The focus of the experimental work of this thesis is on 2,2,6,6-tetramethylpiperidine-*N*-oxyl (TEMPO) based electrolytes for aqueous RFBs. The TEMPO scaffold itself is among the most popular organic redox scaffolds for ORFBs. In particular, the *N,N,N*-2,2,6,6-heptamethylpiperidine-*N*-oxy-4-ammonium chloride (TMA-TEMPO) shows great potential for a “green” alternative to the VRFB and is on its way to market introduction.^[10b, 16] Nevertheless, only a limited number of publications deal with the temperature stability of TEMPOs. Murayama *et al.* investigated the decomposition products of 4-oxo-TEMPO under thermal stress and could show that the corresponding hydroxylamine and (poly)-unsaturated aldehydes and ketones are the main decomposition products.^[17] While the proposed mechanism of the TEMPO decay involves a deprotonation of the alpha-hydrogen atom adjacent to the keto group, Ma *et al.* could show that the corresponding TEMPO-

oxoammonium cations suffer from similar problems. When this thesis started, there were no studies known dealing with the stability of TEMPO materials in a redox flow battery and the reactions of the molecule during charging and discharging under elevated temperatures.

Thus, the focus of **Chapter 3** lies on the investigation of the thermal stability of TMA-TEMPO, the most promising TEMPO material for ORFBs so far (*cf.* **Figure 1.2**). Highly concentrated electrolyte solutions were charged in a RFB and afterwards heated up to 60 °C. The decomposition products were subsequently investigated *via* gas chromatography coupled mass spectrometry (GC-MS). While the findings confirmed the studies of Ma *et al.* and extended the insight of the decomposition pathways. In the subsequent investigations with a full cell, it could be shown that, a lot of the temperature induced decay of the battery capacity is linked to the formation of the corresponding hydroxylamines. These hydroxylamines can be electrochemically reoxidized to TMA-TEMPO which restores significant parts of the capacity fade. But since the process is relatively slow in comparison to the cycling speed, it is difficult to detect with the standard battery cycling protocols that were known from literature during the initial period of this PhD project. Thus, symmetrical cell tests to suppress influences of the other electrolyte or artefacts, caused by crossover through the membrane, were utilized. Furthermore, cycling at elevated temperatures and hold times at vulnerable SOC were included into the testing protocol to mimic unfavored but realistic conditions. In the next step, based on the three revealed possible decay mechanisms, five new and two known TEMPO derivatives were synthesized. It was investigated whether the introduction of a linker between the SPG and the TEMPO core could increase the material stability. Furthermore, the influence of an enhanced radical shielding and the exchange of counter ions or the solubility promoting group (SPG) was determined. To compare the synthesized TEMPO derivatives to each other the revised cycling protocol was applied. In the last step the enhanced cycling protocol was applied to a completely new anthraquinone (AQ) based electrolyte and it could be shown that the electrolyte exhibits a high stability at elevated temperatures.

However, the usage of symmetric cell tests, hold times and temperature tests can provide macroscopic hints on the stability of a new active material, nevertheless it lacks the possibility to gain a more in-depth view on the ongoing processes. Nevertheless, the half-cell wise addressable SOC and its influence on the measurement as well as the electrolyte stability was hardly determinable. For the development of a market ready ORFB it is necessary to have tools in hand capable of determining not only the electrolyte stability over a longer time scale, but also to measure the SOC and, maybe even more important, the state of health (SOH).

With these problems in mind, **Chapter 4** is discussing new alternative analyzing techniques. (*cf.* **Figure 1.2**). At first an *ex-situ* method based on high-pressure liquid chromatography (HPLC) for TEMPO was developed. It could be shown that the method is not limited to battery electrolytes, but can also be used to analyze drugs or reaction catalyst based on the TEMPO scaffold. This method is not only the first HPLC protocol for highly reactive oxoammonium cations reported so far, but it was also validated under the guidelines of the International Council for Harmonization (ICH) and United States Pharmacopeia (USP), enabling its utilization also in different application fields not related to the battery sector. Despite having great potential for analyzing TEMPO electrolytes the method is cost-intensive and takes a lot of preparation and measurement time. Thus, the next part of the chapter deals with the development of a low-cost and simple real-time method for SOC and SOH determination. The protocol presented by Stolze *et al.* offered a good starting point for this task.^[18] Therein, the mass transfer limited currents after application of positive and negative voltage to the electrolyte are obtained. The ratio between anodic and cathodic current corresponds to the SOC of the solution. From now on this measuring principle is referred to as the “amperometric SOC measurement”. Furthermore, it could be shown that after simplification of the measuring setup, the data could be also acquired by cheap Arduino micro controllers. The achievable precision is comparable to source meter units (SMU) 100-fold more expensive. Furthermore, the setup is capable of measuring the SOC continuously in real time in a running redox flow battery with higher accuracy compared to state-of-the-art techniques like open-circuit voltage (OCV) cells.^[19] Additionally, the SOH of the solution can be determined simultaneously in an easy way with high precision. One drawback of the method is the used expensive microelectrodes. These were exchanged with cheap inkjet-printed microelectrodes which show only slightly lower accuracy in comparison to commercial electrodes, as is demonstrated in the last part of the chapter.

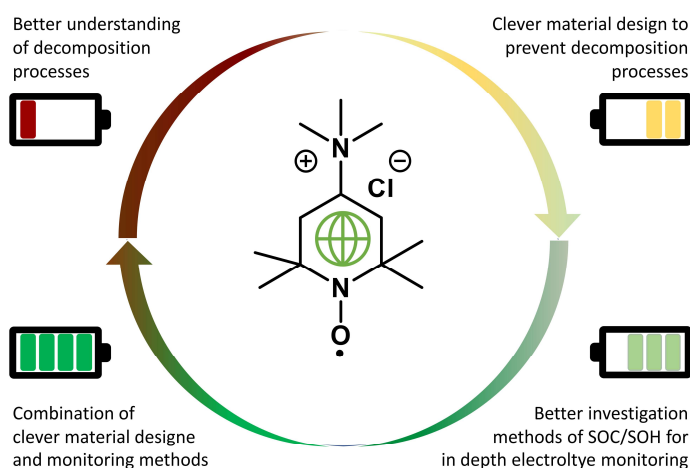


Figure 1.2: Schematic representation of the motivation of this thesis.

2 Fundamentals of redox flow batteries: Material requirements and critical parameters

Parts of this chapter have been published in *Redox-active polymers: The magic key towards energy storage – A polymer design guideline*, P. Rohland, E. Schröter, O. Nolte, G. R. Newkome, M. D. Hager, U. S. Schubert, *Prog. Polym. Sci.* **2022**, *125*, 101474.

Since the invention of RFBs, the design of the active material represents a crucial point for the battery's performance. The start of the materials' evolution was the initial concept from 1949 by Kangro.^[9] By using $\text{Cr}(\text{SO}_4)_2$ in 2 M sulfuric acid as posolyte and negolyte in a symmetrical cell setup, Kangro created the world's first RFB. The next big steps were the iron-chromium system patented by the NASA in the 1970s and the development of the VRFB in 1986.^[20] The technology itself is quite old and a lot of research effort has been made; nevertheless the market penetration of the batteries is still progressing slowly. The named highly corrosive, expensive, and toxic electrolytes of metal based RFBs are the main reasons. With the current upcoming organic RFBs and their ability of using cheap organic molecules in neutral electrolytes, this might change. ORFBs can be subdivided into two categories based on their material characteristics. One group comprises small molecules as redox-active materials, the other embeds these units into polymers. Both systems have their individual advantages and are currently existing side by side, but until to now it is not clear which one will prevail.

Nevertheless, both can use the same redox active scaffolds as storage site in the molecules. Therefore, investigations on the behavior of these moieties in flow batteries is a central part of the research for ORFBs. The history of redox-active molecules can be traced back to the beginning of organic chemistry and, over the years, many possible structures have been investigated. A summarized history of redox active moieties in polymers is shown **Figure 2.1**. Therefore, when choosing active materials, a wide range of possible options is available. Nevertheless, every new material must be critically evaluated under the material requirements (*cf.* **Chapter 2.1.**) aspect before being used in an RFB.

Fundamentals of redox flow batteries: Material requirements and critical parameters

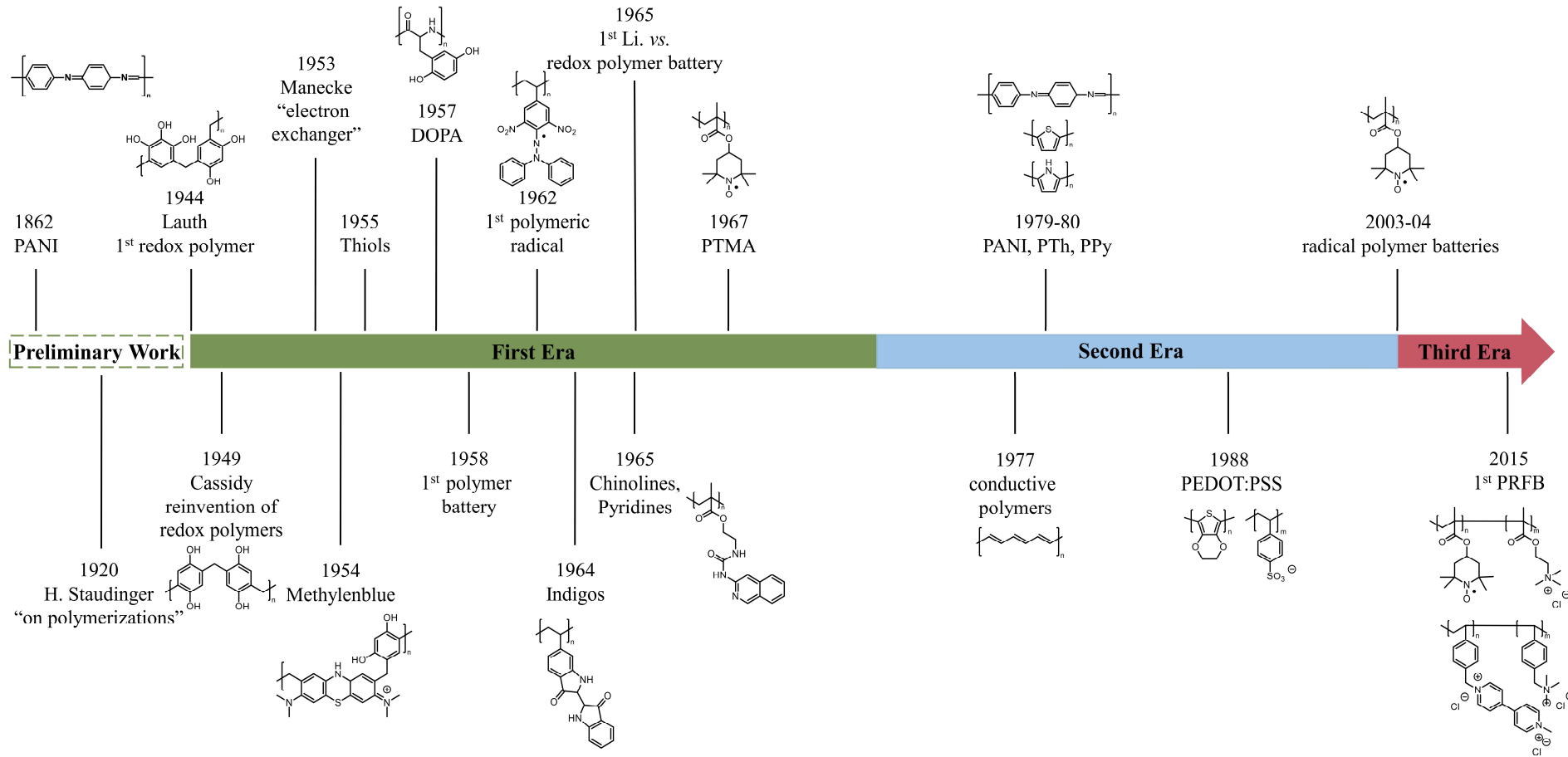


Figure 2.1: Timeline with the most noteworthy inventions and scientific milestones in the field of redox-active polymers. (The figure was taken from P1).^[21]

2.1. Material requirements

In general, every active material must be as stable as possible because this stability correlates directly with the lifespan of the battery. Thus, it is one of the most crucial points the electrolyte must fulfill. Under the preliminary evaluation of an active material, it is impossible to determine long-term stability and it can often only be investigated in cell tests. Thus, it is discussed more in detail in **Chapter 2.2**. When an active material is planned to be used in RFBs, the solubility is one of the most crucial points (*cf.* **Figure 2.2**). In contrast to other battery types like solid state-batteries, the solubility of the redox-active material in the electrolyte should be as high as possible as it directly influences the theoretical capacity. It is necessary to keep in mind that not only the uncharged state should be well dissolvable, but also the solubility of the charged molecule must be high. Since many organic molecules with a high molar mass show a low solubility in water, the molar mass of the molecule itself should be reasonably low. However, low solubilities can be mitigated by the introduction of charged groups or by the possibility of exchanging more than one electron per molecule. Thus, the molar mass is more or less a soft criterion during evaluation. Nevertheless, to keep the overall costs of the material low, it is important that the molecule is not too complex and does not require expensive or time-consuming synthetic procedures.

In contrast to other battery types, which are aiming for a maximum battery voltage, RFBs are limited by the electrochemical stability window of the used electrolyte. In aqueous RFBs, the electrochemical water window determines the edges of the possible material's redox potentials. Depending on the pH value of the solution, it lies between +1.23 V and 0 V at pH = 0 and 0.40 V and -0.83 V at a pH value of 14 (potentials vs. SHE).^[22]

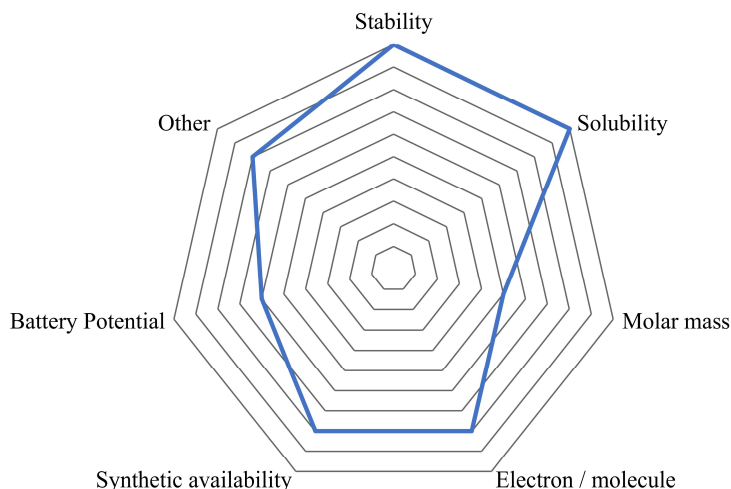


Figure 2.2: Spider web diagram of the most important material requirements for aq. redox flow batteries. Special requirements, like pH values or supporting electrolyte are subsumed by the point “others”. (The figure was taken from **P1**).^[21]

The water stability window describe the applicable voltage range which can be safely applied without causing water-splitting reactions. Thus, it is only hardly possible to achieve cell voltages of over 1.23 V. Beside that, the need for special requirements on aqueous electrolyte, like supporting electrolytes, is subsumed under the point “other” in **Figure 2.2**.

Considering only these criteria, many molecules can be dismissed even before using them in an RFB. Yet, the remaining ones are not necessarily the ideal active material. This often can only be revealed with battery cycling experiments.

2.2. Critical battery parameters

One of the most critical battery parameters is the overall capacity. It determines the application possibilities and is directly influenced by the material, like the redox species' solubility. Nevertheless, there is a difference between theoretical (determined by the amount of accessible active material) and experimentally achievable values. This is either linked to side reactions of the active material upon charging, like quinhydrone formation,^[23] and dimerizations^[24] or due to cell characteristics like overpotentials or inner resistance. However, only few active materials suffer from significant differences between theoretical and practical capacity.

Furthermore, the rate capacity of a battery can be considered an important material characteristic. It determines how fast a battery can be charged and discharged and is linked to the kinetics of the material's redox reactions. However, many organic molecules stand out due to their rapid electrochemistry, unlocking potential new application possibilities beside the classical grid stabilization on large time scales.

Since RFBs are meant to be operated on-site of, *e.g.*, at a wind power plant, so the influence of the weather must be kept in mind. Depending on the climatic situation and storage conditions, electrolyte temperatures of 50 °C or higher are imaginable. The elevated temperature facilitates unwanted side reactions, leading to accelerated material decomposition. Thus, stability investigations must always include high-temperature tests. However, flow batteries are currently meant to be applied in grid stabilization on a time scale of days to weeks and not for fast charging and discharging scenarios. This might result in long hold times in a vulnerable SOC, leading to facilitated side or decomposition reactions. The charged form of organic molecules is often more instable since electrons are “pushed” into or withdrawn from the scaffold. Thus, high SOC are considered as more crucial to the long term cyclability of an organic active material. This shows that, for more detailed information on ongoing processes during the cycling of the material, reliable SOC-data and SOH-data are required.

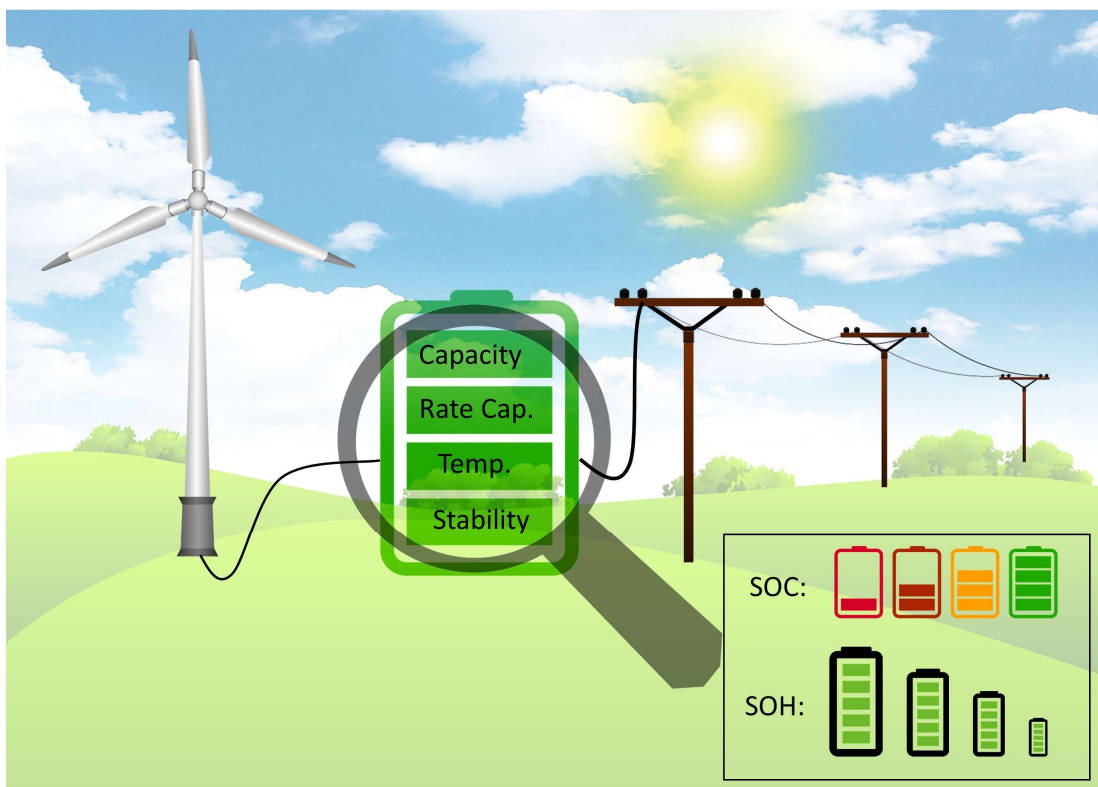


Figure 2.3: Schematic representation of the integration of a RFB in a smart grid and the enumeration as well as clarification of their critical parameters. SOC = State of charge, SOH = State of health.

Without sufficient individual SOC- and SOH monitoring of both half cells a stable and secure longtime operation of an RFB is hardly possible.^[25] Having information about the SOC of the electrolyte in correlation to possibly occurring decomposition reactions enables an enhanced battery management extending the lifespan of the battery. But despite the large variety of the available methods, like coulomb counting, they all struggle with at least one of the following challenges: Error accumulation over time, time consuming-recalibration, temperature, no half-cell resolution, no real-time monitoring capability, mathematic complexity, cost intensive instrumentation or limitation to certain electrolytes.^[18] A fast, cheap, temperature-independent, and calibration-free method for real-time SOC monitoring is, thus, needed. Still, SOH information would complement the SOC data, since they are correlated to the amount of cyclable active material (*cf.* **Figure 2.3**) and, thus, provide information about the overall capacity and stability/lifetime of the electrolyte. The link between certain cycling-conditions and the battery/electrolyte state could lead to tailored cycling procedures expanding the lifetime significantly. Furthermore, time-dependent investigations in combination with temperature and hold times would lead to a better understanding of the ongoing processes. But reliable determination methods for the electrolytes' SOH are even more complex than for SOC.

3 Synthesis and stability investigation of active materials for redox flow batteries

Parts of this chapter have been published in **P2**: *Stability of TMA-TEMPO-based aqueous electrolytes for redox-flow batteries*, P. Rohland, O. Nolte, N. Ueberschaar, M. D. Hager, U. S. Schubert, *J. Power Sources* **2022**, 525, 230996. **P3**: *Structural alterations on the TEMPO scaffold and their impact on the performance as active materials for redox flow batteries*, P. Rohland, O. Nolte, K. Schreyer, H. Goerls, M. D. Hager, U. S. Schubert, *Mater. Adv.* **2022**, 3, 4278-4288. **P4**: *Anthraquinone-2,6-disulfamic acid: An anolyte with low decomposition rates at elevated temperatures*, P. Rohland, K. Schreyer, M. D. Hager, U. S. Schubert, *RSC Adv.* **2021**, 11, 38759-38764.

Due to their stable and fast redox kinetics, their low costs, and the synthetic accessibility of TEMPO derivatives, they are among the most comprehensively investigated organic battery storage materials.^[10b, 26] The redox behavior of the aminoxyl radical **1** was the subject of many studies over the last decades. While oxidation leads to the respective oxoammonium cation **2**, reduction yields the hydroxylamine **3** (*cf.* **Figure 3.1**). Despite the amphoteric character of the material, in batteries, the radical- oxoammonium cation redox couple is favored due to its high redox potential and pH-independence.^[27] Nevertheless, the materials need sufficient stability in both used redox states for a successful implementation in a market ready battery. While the radical **1** is known to be thermally stable due to the steric shielding of the four methyl groups vicinal to the NO radical (*cf.* **Figure 3.1**), protecting it from attacking species or radical recombination reactions,^[28] the oxoammonium cation **2** may be subject to decomposition. In an in-depth investigation of TEMPO in acidic media, Ma *et al.* could demonstrate that the formation of the oxoammonium cation is the starting point of subsequent decomposition pathways.^[29] The findings suggest that the oxoammonium cation is the limiting factor regarding the stability for an application in RFBs.

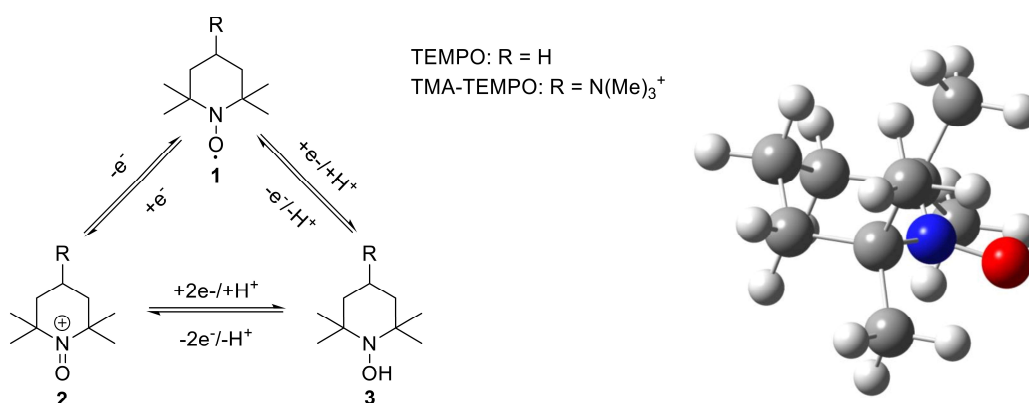
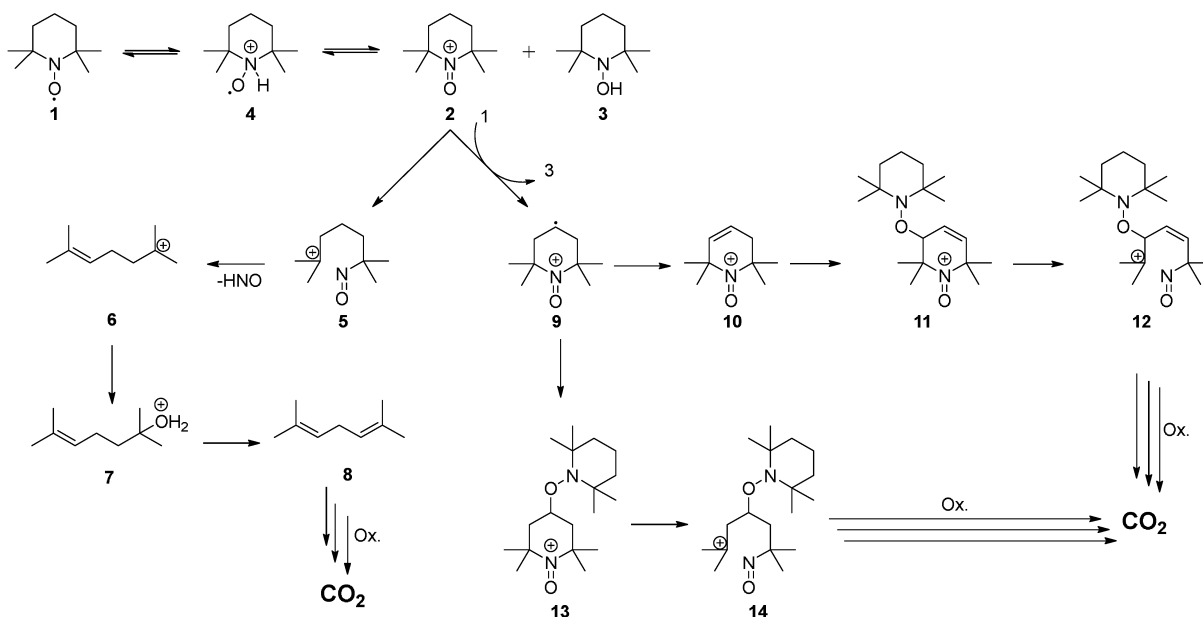


Figure 3.1: Left) Schematic representation of the redox chemistry of TEMPO-derivatives **1** to the oxoammonium cation **2** or the hydroxylamine **3**. Right) Demonstration of the shielding of the radical by the four methyl groups in TEMPO. Picture was prepared using Gaussian 09 and GaussView 5 (DFT-geometry optimization in vacuum, CAM-B3LYP 3-21G).

Interestingly, the decay starts with the nitrogen protonation of the aminoxyl radical **1** and a subsequent disproportionation (*cf.* **Scheme 3.1**). While the formed hydroxylamine **3** tends to be stable, the oxoammonium cation **2** is the subject of the ongoing decomposition. One pathway involves the ring opening to compound **5** with a subsequent loss of HNO and the formation of an unsaturated carbocation **6**. Addition of water to the intermediate can lead to phorone **8** and oxidation, finally yielding CO₂. The other pathway starts with a homolytic bond cleavage and abstraction of a hydrogen radical in the 4-position of the oxoammonium cation **2** by another TEMPO radical (**1**), which is reduced to the hydroxylamine **3**. The produced radical-cation **9** can then undergo further oxidation reactions with other TEMPO molecules (**1**) to form a piperidine with an endocyclic double bond **10**. The emerging strained ring performs an addition-elimination reaction under oxidative conditions with another oxoammonium cation **2** or TEMPO (**1**) to system **11**. A subsequent ring opening reaction with the loss of HNO and further oxidation finally leads to CO₂, according to pathway one. Another possible pathway would be a radical recombination reaction between the radical-cation **9** and a TEMPO (**1**) to the adduct **13**. The ring opening reaction to compound **14**, the loss of HNO, and further oxidations would also finally yield a CO₂ formation, like described for pathway one.

In summary, the study of Ma *et. al.* revealed that from every mol of decomposed TEMPO (**1**), 0.8 mol of hydroxylamine **3** is formed. Or in other words, the complete decomposition of one oxoammonium cation **2** to CO₂ reduces approximately four molecules of either the cation **2** or the radical **1** to the corresponding hydroxylamine **3**.



Scheme 3.1: Schematic representation of the proposed decomposition mechanism of TEMPO in acidic media according to Ma *et al.*^[29]

2.1 In depth investigation of the TMA-TEMPO decay

The findings of Ma *et al.* provide an in-depth understanding of the possible decomposition pathways of TEMPO. Transferred to TMA-TEMPO molecule for battery application, the findings from Ma *et al.* trigger the following questions:

1. How does the forced formation of an oxoammonium cation during charging influence the decomposition?
2. In consequence, is the hydroxylamine still the main decomposition product and is the subsequent formation of CO₂ maybe more pronounced or is maybe another gas formed? (A massive rise of gas side product would also lead to security issues since the battery is a closed system, where overpressures should always be prevented.)
3. If the hydroxylamine is still the main side product, can it be reoxidized to the radical during the charging process?
4. Can the substituent in 4-position in TMA-TEMPO block the second and third pathway?
5. How high is the decomposition rate of the active material?

To investigate the influence of the oxoammonium cation concentration on the decomposition, the gas phase over TMA-TEMPO samples were analyzed utilizing headspace-(HS)-GC-MS. If the mechanism proposed by Ma *et al.* also applies for TMA-TEMPO, the measurement of the carbon dioxide concentration, in particular, provides information about the decay rate of TMA-TEMPO. In a preliminary experiment, highly concentrated aq. TMA-TEMPO solutions (1.3 M) were transferred into a glove box to avoid atmospheric influences, splitted up, and stored under different conditions. Upon heating to 60 °C the CO₂ concentration increased by a factor of five and by one magnitude if the radical is charged to the oxoammonium cation (*cf.* **Figure 3.2**). Furthermore, the analysis of the gas phase revealed the formation of chloromethane upon oxidation of TMA-TEMPO. As demonstrated in this preliminary test, the temperature has a significant influence on the rate of the decomposition reaction – even on the allegedly “stable” radical. To further map its influence on the vulnerable oxoammonium cation, different samples of charged 1.3 M TMA-TEMPO were prepared and, subsequently, stored at different temperatures (room temperature to 50 °C) as well as for different durations (0 to 16 days) and the amounts of emerging carbon dioxide and chloromethane were analyzed. The data revealed an increased amount of volatile components over time and with increasing temperatures. While this experiment showed a basic connection between decay and the storage conditions, the source and possible generation mechanism of the chloromethane was still unclear.

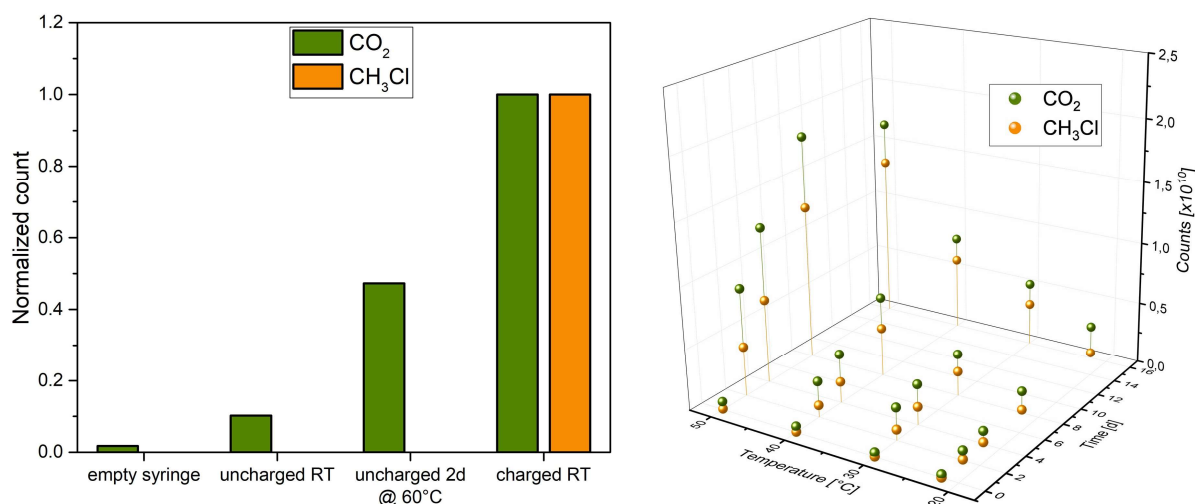
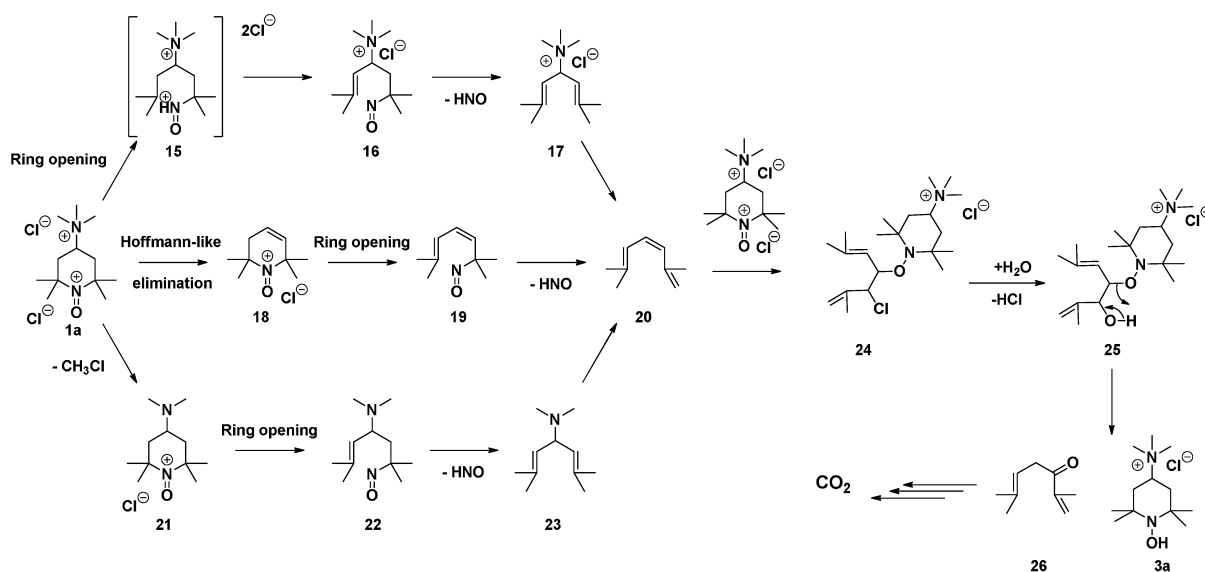


Figure 3.2: HS-GC-MS results: Left) Comparison of emerging carbon dioxide and chloromethane of charged and uncharged TMA-TEMPO-solutions after tempering. Right) Influence of temperature and time on the amount of emerging carbon dioxide and chloromethane of charged TMA-TEMPO solutions. (The figure was taken from **P2**).

To get more detailed information about the emerging volatile substances, a divinylbenzene/carboxen/polydimethylsiloxan fiber was placed in the gas phase over charged and uncharged samples that were stored under different conditions.

After the fiber remained in the gas phase for several minutes, it was placed in a headspace-GC-MS. The technique, also known as solid-phase micro extraction (SPME), is able to analyze low-volatile substances by accumulating them on the fiber. The detected decomposition intermediates revealed that one of the decomposition pathways starts with the ring-opening reaction of the piperidine core to compound **15** (*cf.* **Scheme 3.2**). A subsequent oxidation and elimination of nitroso and ammonium compounds leads to unsaturated hydrocarbon **20**. The second pathway (*cf.* **Scheme 3.2**) is initiated by a Hoffmann-like elimination of the trimethylamine group and the formation of a tetrahydropyridine derivative **18** with a follow-up ring-opening reaction and the loss of a nitroso compound. While the generation mechanisms and structures are a bit different, the pathways follow the mechanism proposed for TEMPO of Ma *et al.*^[29] In a third pathway, the TMA-TEMPO oxoammonium cation **2** loses chloromethane (*cf.* **Scheme 3.2**), in the first step producing a dimethyl amine compound **21**. The subsequent ring-opening, oxidation, and elimination reactions follow the known schemes. All three mechanisms generate an intermediate unsaturated hydrocarbon **20**, which is later oxidized to carbon dioxide. The mechanism of oxidation starts most likely with a 1,2-electrophilic addition of the oxoammonium cation to the olefine **24**. Takata and co-workers reported this behavior in 1999.^[30] Furthermore, the authors showed that the addition products undergo rapid substitution reactions with water to alcohol **25**. A subsequent bond break between the TEMPO moiety and

the hydrocarbon would result in a ketone **26** and a hydroxylamine **3**. In sum, the unsaturated hydrocarbon is oxidized by the oxoammonium cation to the ketone **26**. The assumption is confirmed by the detection of ketones in the SPME-HS-GC-MS chromatograms. Subsequent oxidation reactions following the same principle would explain the formation of carbon dioxide and the hydroxylamine as a main side product. To further prove the assumed mechanism of a 1,2-electrophilic addition finally leading to carbon dioxide, the decomposition of the TMA-TEMPO cation was studied in H_2^{18}O and D_2O . The intermediary substitution of chlorine with water would produce ^{18}O -marked ketones and C^{18}O_2 . Both proposed structures were found in the (SPME)-HS-GC-MS of the gas phase. Furthermore, it was observed that mostly isotopically labelled carbon dioxide is formed. The unmarked molecules are attributed to the remaining unlabelled water in the used 97% enriched H_2^{18}O . These findings confirm the assumption that water is the source of oxygen for the carbon dioxide, strengthening the proposed mechanism. However, no deuterated intermediates or products could be detected *via* (SPME)-HS-GC-MS indicating that the hydrogen atoms from the added water are transferred to the hydroxylamine (*cf.* **Scheme 3.2**). The detection of deuterated hydroxylamine would finally proof the mechanism, but it is not detectable *via* (SPME)-HS-GC-MS due to the missing volatility. A liquid chromatography (LC) method coupled to an MS would be necessary. But at the time of the investigations, no LC-MS method for TMA-TEMPO derivatives is available. In retrospect, three of the five initially stated questions could be answered so far. The concentration of the oxoammonium cation has a significant influence on the decomposition (Question 1). The hydroxylamine is still one major decomposition product, and the formation of carbon dioxide is more pronounced when the electrolyte is charged



Scheme 3.2: Schematic representation of the proposed decomposition pathways of TMA-TEMPO towards carbon dioxide.

Furthermore, toxic chloromethane is formed (Question 2). The introduction of a TMA group in 4-position of the ring does not prevent the second decay mechanism that Ma *et al.* proposed. The substituent is eliminated in a Hoffmann-like manner, generating one of the key intermediates of the second mechanism. It can be stated that the introduction of the SPG bypasses the initial steps, but the outcome is the same (Question 4). What remains to be answered is whether the generated hydroxylamine can be reoxidized (Question 3) and how fast the decomposition really takes place (Question 5).

For this purpose, charged 1.3 M TMA-TEMPO samples were stored at 40 °C for 0, 4, 8, and 16 days, respectively, and afterwards charged/discharged against methyl viologen (MV). In particular for the 16 d-storage time sample, only an 80% discharge of the initial charge was achieved which corresponds to a decay rate of around 1.25% d⁻¹. Nevertheless, during the consecutive cycle, the TEMPO electrolyte showed an overcharge of approx. 15% and a recovery of the initially accessible discharge capacity during the subsequent cycle. While during the first discharge only 80% of the initial charge can be accessed, the loss can be recovered to 96% of the initial capacity after three consecutive cycles, representing an overall decay rate of 0.22% d⁻¹. This is linked to the reoxidation of the formed hydroxylamine to the radical. This corresponds to a 4:1 ratio of hydroxylamine to decayed oxoammonium cation, which is in good agreement with the data Ma *et al.* reported. The other samples for 4 d and 8 d of storage revealed the same behavior. Nevertheless, the data demonstrated that the decomposition of the oxoammonium cation and the formation of hydroxylamine is a slow process and mostly invisible under elevated temperatures.

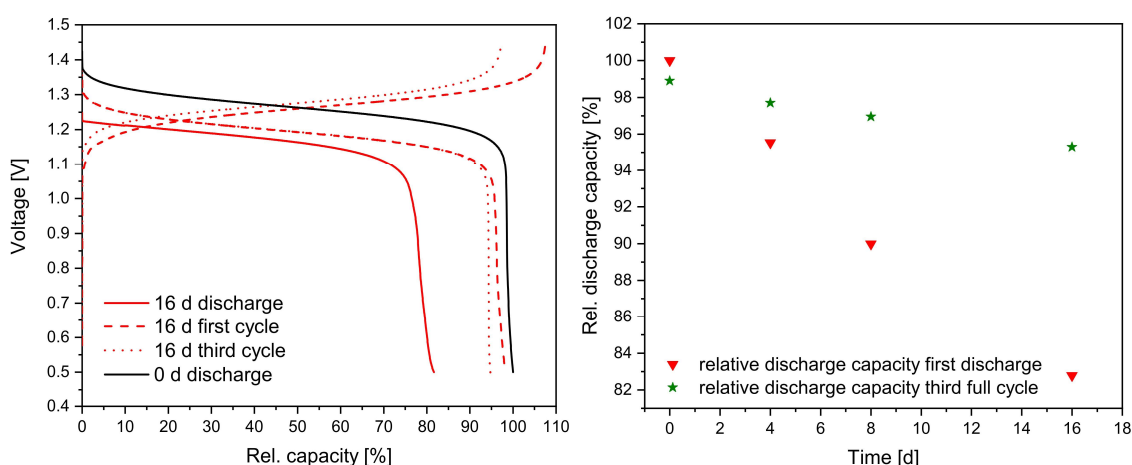


Figure 3.3: Left) representative charge/discharge curves after 0 d (black) and first discharge (red solid line), first full cycle (red dashed line) and third full cycle (red dotted line) after 16 d. Right) relative discharge capacity over time of the first discharge (red) and of the third full cycle (green). (Parts of the figure were taken from P2).^[31]

Most of the published investigation protocols rely only on charging/discharging the active materials at room temperature as often as possible at a maximum of viable redox couple concentration. While this gives first hints for long-term stabilities, the unravelled temperature-dependent and slow decay mechanism would barely be detectable. Thus, a new cycling protocol must be developed.

The starting point were the studies of Brushett *et al.* who introduced the concept of a symmetric cell cycling method for ORFB.^[32] The procedure enables an in-depth investigation of the ongoing decomposition of a single electrolyte under battery conditions by using the same electrolyte in both half cells with an SOC of approximately 50% and cycling the battery around 0 V. Because the same electrolyte with the same concentration and supporting electrolyte is used, artifacts due to crossover through the membrane can be mitigated (*cf.* Figure 3.4). Furthermore, the influence of an instable counter electrolyte, like the air-sensitive MV negolyte, can be omitted. The concept was further improved by Goulet and Aziz, who used this cycling method for an elaborated new protocol, comprising an unbalanced, compositionally symmetric flow battery setup (*cf.* Figure 3.4), hold times in different SOC's as well as potentiostatic cycling.^[33]

Consequently, in order to determine the temperature-dependent decay of TMA-TEMPO in this thesis, this protocol was used and extended by temperature test. To stress the active material and to mimic unfavorable but realistic conditions, the cell was cycled for 175 consecutive cycles in an unbalanced compositionally symmetric cell (*cf.* Figure 3.4 right). In each cycle, after a galvanostatic part, a potentiostatic part was also integrated to ensure that the maximum reachable SOC was achieved in the capacity-limiting side (CLS). After 50, 100, and 150 cycles, a hold time of 24 h in this maximum SOC was applied.

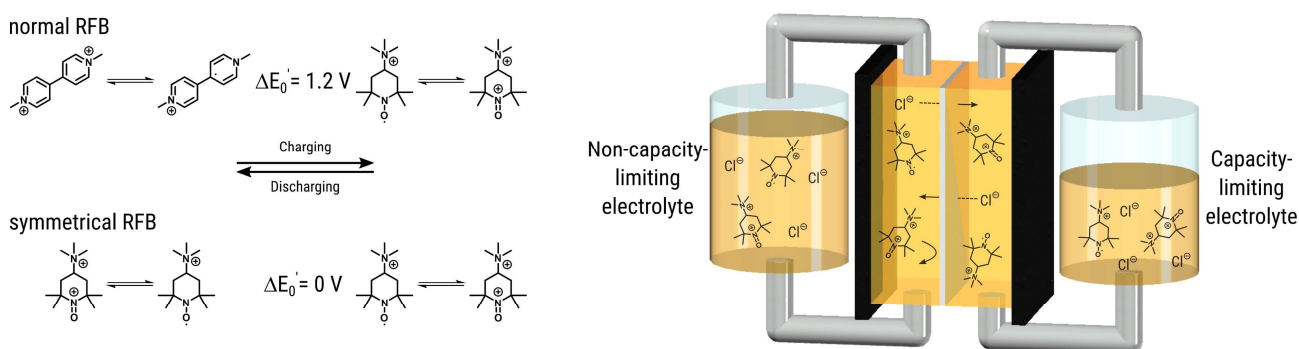


Figure 3.4: Left) Cell reactions of a “normal” (asymmetric) RFB represented by the MV/TMA-TEMPO system (top) and a symmetric TMA-TEMPO RFB (bottom). Right) Schematic illustration of an unbalanced, compositionally symmetric (UCS) RFB. (The figure was taken from **P2**).^[31]

The RFB was then discharged, the CLS tank was placed in an oil bath heated to 40 °C, and the protocol was repeated. The purpose of this cycling strategy was to determine the decomposition rate during cycling and, in comparison, during hold times as well as under temperature influence. In order to keep the experiment duration in a viable time frame, a comparably low concentration of 0.1 M TMA-TEMPO was used.

Figure 3.5 shows the results of the unbalanced, compositionally symmetric (UCS)-RFB experiment. While an initial rise with a subsequent stabilization of the accessible capacity is visible during the first cycling block, the first hold time in the maximum SOC leads to a capacity drop of 2%. However, the drop can be partially recovered to 99% of the initial capacity during the following two to three cycles which can be attributed presumably to the reoxidation of the hydroxylamine. Nevertheless, the cell needs two to three cycles to fully re-equilibrate, which is in good accordance with the previous findings. But the process is now visible during the cycling experiment by the application of the protocol in contrast to cycling with the standard settings. The process is also visible in the coulombic efficiency (CE) graph, where a 2% drop of the CE after the hold time is detectable.

The battery capacity decays after the first hold time with an average loss of 1.5% d⁻¹ in pure cycling mode, while the large drops during hold times continue to appear. The battery loses around 2.3% d⁻¹ during the hold times. A similar trend is visible when the CLS is warmed to 40 °C. However, with average decay rates of 1.09% d⁻¹ during cycling and 3.12% d⁻¹ during hold times the decay is comparable to room temperature values. The average decay rates for each mode (hold time yes/no, temperature RT/40 °C) are summarized in **Table 3.1**.

As evident from **Table 3.1**, a significant difference exists between the average capacity decay calculated per cycle and the average capacity decay calculated per day, confirming the need for a temporal fade rate measurement approach as discussed in detail by Goulet *et al.* earlier.^[33] Furthermore, the fade rates show a SOC influence on the TMA-TEMPO decomposition, since cycling and hold time fade rates are different. However, the SOC-dependent quantification of fade rates requires SOC determination tools that provide reliable outputs over days to weeks. But easy to implement, cheap, and reliable SOC measuring techniques were not available during this study. Thus, further research in the development of these methods were performed and the results are summarized in **Chapter 4**.

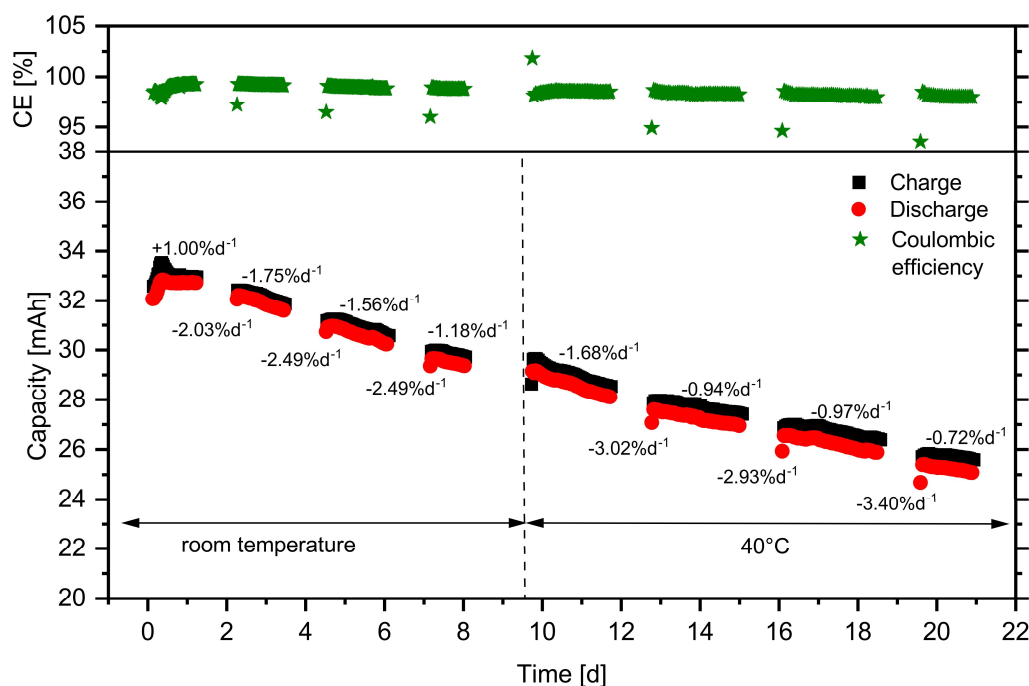


Figure 3.5: Charge and discharge capacities of an unbalanced compositionally symmetric cell as a function of time as obtained by potentiostatic cycling with hold times. The cell used 0.1 M solutions of TMA-TEMPO; 15 mL on the capacity-limiting side (CLS) and 25 mL on the non-capacity-limiting side (NCLS). Temperatures indicate the reservoir temperature. Temporal fade rates were determined by linear regression of the respective cycling sequences (for continuous cycling sequences, the initial capacity drop was omitted). (The figure was taken from **P2**).^[31]

Table 3.1: Experimentally obtained average capacity fade rates for the experiment of **Figure 3.5**. Fade rates were obtained by linear regression.

Entry	Average capacity fade rate		Average capacity fade rate	
	cycles per day	reservoir temperature	cyclic [%]	temporal [% d ⁻¹]
1	1	RT (23 °C)	2.34	2.34
2	32.3	RT (23 °C)	0.046	1.50
3	1	40 °C	3.12	3.12
4	21.1	40 °C	0.052	1.09

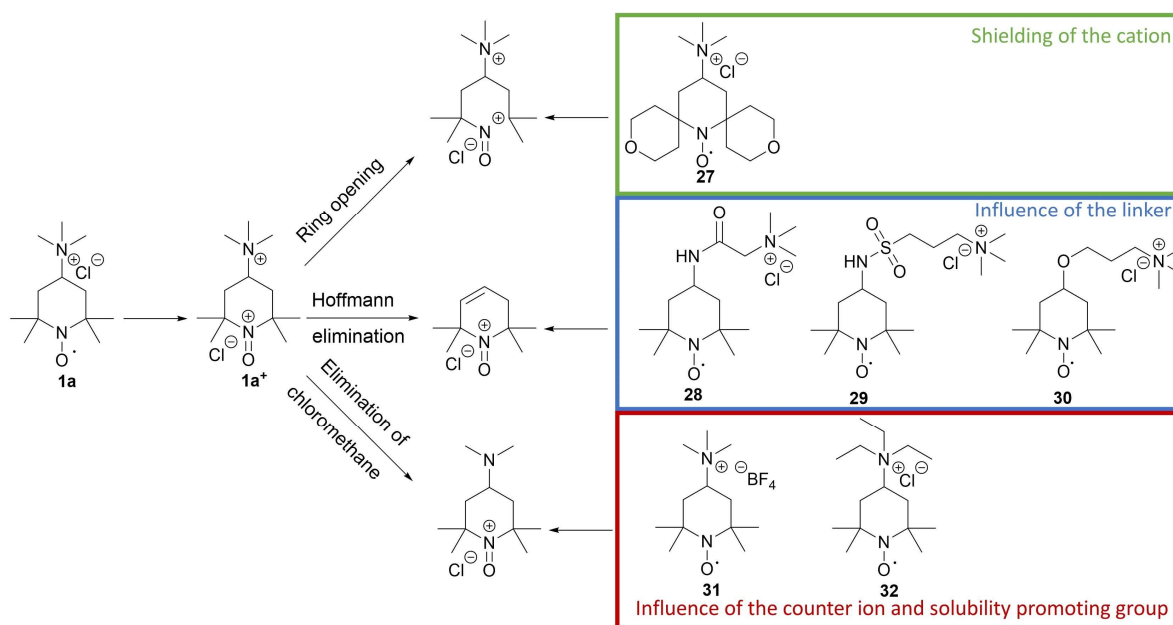
2.2 Synthetic approaches towards a new more stable TEMPO derivative

In the previous section the decay of TMA-TEMPO was investigated in detail and three different decomposition mechanisms were identified (*cf.* **Scheme 3.1**). It was demonstrated that the stability of TMA-TEMPO is insufficient for RFB applications at higher temperatures. This chapter describes the influence of TEMPO scaffold modifications to the active materials decay rate.

The first decomposition pathway originates from the ring opening reaction caused by the CN-bond break (*cf.* **Scheme 3.1**). Since the TMA-TEMPO and the corresponding oxoammonium

radical are stabilized by the shielding effect of the four vicinal methyl groups, the idea was to enhance this effect by the introduction of two spiro tetrahydropyran rings (*cf.* **Scheme 3.3**). The reactive site of the resulting Spiro-TEMPO **27** should be further protected and, thus, side reactions may be hindered.

The second decomposition pathway is caused by the elimination of the trimethylammonium SPG in a Hoffmann-like manner (*cf.* **Scheme 3.3**). To prevent this mechanism, a linker between the SPG and the piperidiny core was introduced in a second synthetic approach. Furthermore, the linker introduction should also affect the stability of the oxoammonium cation as Liu *et al.* demonstrated recently.^[26] The authors introduced a propyl ether between the core and the SPG, effectively enhancing the stability of the active material. They attributed this finding to the decoupling of the strongly electron-withdrawing trimethyl ammonium cation from the piperidyl core. The reduced inductive effects should decrease the CN bond polarization and, thus, enhance the overall stability. To investigate these possible effects in detail, the TEMPO-amide **27**, the TEMPO-sulfonamide **28**, and the TEMPO-ether **30** reported by Liu *et al.* were synthesized. The amide **27** and sulfonamide **28** were expected to show the same polarization reduction effects as the ether and prevent the Hoffmann like elimination. The linkers are known to be more stable towards possible pH changes caused by decomposition reactions, like HCl formation during the 1,2 bipolar addition.

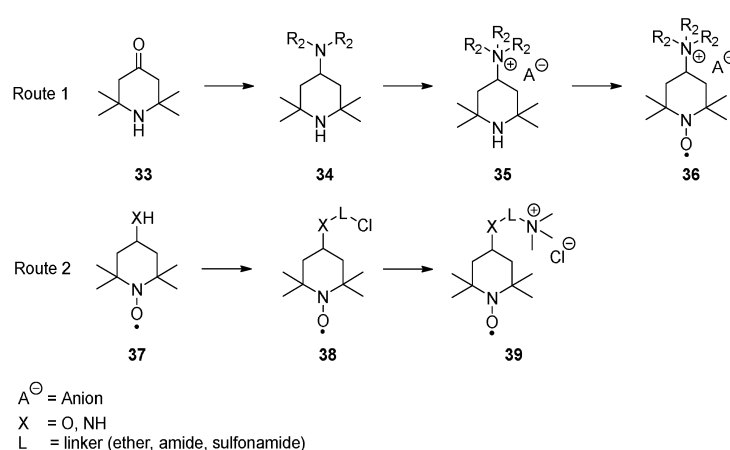


Scheme 3.3: Schematic representation of the three suggested decomposition pathways of TMA-TEMPO **1** and the planned TEMPO derivatives to hinder them. (The scheme was taken from **P3**).^[34]

The last pathway starts with the elimination of chloromethane. Herein, an influence of the nucleophilic character of the counterion of the trimethylammonium SPG is proposed (*cf.* **Scheme 3.1** and **Scheme 3.3**). The exchange of the chloride with the less nucleophilic BF₄ to the TMA-TEMPO BF₄ salt **31** might hinder the chloromethane formation. Furthermore, the effect of the three methyl groups was investigated. The switch to a triethylammonium (TEA)-TEMPO **32** might suppress the halogenoalkane formation and the Hoffmann-like elimination of pathway two.

In general, the syntheses of the desired new TEMPO-derivatives follow two main routes (*cf.* **Scheme 3.4**). Derivative **27**, **31**, **32** were received after reductive amination of the triacetone-amine precursor **33**, a subsequent quaternization to system **35** and final oxidation to the desired product **36**. In the second strategy, an already oxidized commercial TEMPO derivative **37** bearing an amino or hydroxy group in 4-position was used as starting material. After introduction of the linker with a terminal chlorine, the TMA-SPG was introduced by a nucleophilic substitution of the halogen with trimethylamine. After the successful synthesis of the new TEMPO derivatives, their suitability as active material for RFB was investigated.

One key point is the degree of oxidation (DoO), which describes how much of the piperidine is oxidized to the radical. Since the radical is the redox-active species, the DoO directly determines the achievable specific capacity of the active material. The DoO was determined by a new cerimetric redox titration method, which can be followed by measuring the potential of the titrated solution rather than the color change of indicators. When the added volume of cerium solution was plotted over the measured potential a sigmoidal curve is visible.



Scheme 3.4: Schematic representation of the general synthesis routes applied for the syntheses of the TEMPO derivatives investigated in this thesis. (The scheme was taken from **P3**).^[34]

To determine the equilibrium point the following adjusted equation after Levie^[35] was fitted to the data set.

$$V_t = a \frac{10^{(-f)}(10^{-fE} + 10^{-f})}{10^{(-f)}(10^{-fx+1} - f)} \quad (4.1)$$

(added volume of the titrant V_t , added volume of titrant at the equilibration point a , standard redox potential of the analyte b , standard redox potential of the titrant c , $f = \frac{F}{RT} \ln 10$, which describes the pre-factor in the Nernst equation and was set to a value of 17.2, measured equilibrium potential E)

A comparison between the DoO received from the optical titration and the potentiostatically determined DoO shows deviations of 2% with exception of the TEMPO ether (**30**) (5%) (*cf.* **Table 3.2**). Nevertheless, only the TMA-TEMPO (**1**) and the sulfonamide **29** derivatives revealed DoO values of around 100%. The amid **28** reveals a DoO of around 90%, the ether **30** and the BF₄-TEMPO **31** around 80% and the TEA-TEMPO (**32**) 60%. In contrast, the DoO of the Spiro-TEMPO is not determinable with this approach. Reduced radical content can be linked to radical loss because of side reactions, like disproportionation, during the purification processes. However, this non-ideal DoO only reduces the overall battery capacity and not the molecular stability as shown in previous publications.^[14, 36]

Since the fit of the titrations also delivers the redox potential of the analyte b (in this case the TEMPO derivative) and titrant c , the titration approach was additionally validated by measuring the standard potentials of the TEMPO derivatives utilizing cyclic voltammetry (CV). The redox potential is not only interesting for the validation of the method but also for the future cell potential since the maximum voltage of the battery is linked to the difference between the potentials of the used active materials. The comparison between the standard potential determined by CV and titration revealed only small deviations of around 10 mV (*cf.* **Table 3.2**), except for the Spiro- **27** and TEA-TEMPO **31**. The reasons are explained later in this section. The data indicates that the introduction of a linker shifts the redox potential by around 100 mV to a more negative value. This is a hint for the influence of the reduced inductive effects of the SPG. In a subsequent investigation, the kinetic parameters of the active materials were obtained *via* rotating disc electrode (RDE) experiments. The received values for the electron-transfer rates k^0 , diffusion coefficients D and transfer coefficients α (*cf.* **Table 3.2**) are in the range of previously published data for TMA-TEMPO in aqueous solutions or other small molecules, like quinones.^[10b, 37] Beside the influence on the inductive effect and the linked reduced redox potential, structural alterations on the TEMPO scaffold do not significantly affect the overall redox or kinetic properties. This is not surprising since the molecular orbitals of the oxoammonium cation and the radical are mainly located at the NO in the scaffold.^[38]

Synthesis and stability investigation of active materials for redox flow batteries

Table 3.2: Overview of the degrees of oxidation determined by optical ($DoO_{opt.}$) and potentiometric titration ($DoO_{pot.}$) as well as the redox potentials of different TEMPO derivatives determined by CV ($E_{CV}^{1/2}$) and by titration ($E_{tit}^{1/2}$) with the corresponding standard deviation. The electron-transfer rates k^0 , diffusion coefficients D , and transfer coefficients α of the different TEMPO-derivatives were measured utilizing RDE technique. Stated error intervals correspond to the standard-deviation of three repetitions.

Compound	$DoO_{opt.}$ [%]	$DoO_{pot.}$ [%]	$E_{CV}^{1/2}$ [V]	$E_{tit}^{1/2}$ [V]	$\Delta E^{1/2}$ [mV]	k^0 [10^{-3} cm s $^{-1}$]	D [10^{-6} cm 2 s $^{-1}$]	α
1b	99 ± 0.3	103 +/- 0.5	0.754 ± 1 mV	0.747 ± 1 mV	6	2.43	4.7	0.66
27	*	*	0.883 ± 7 mV	*	*	*	*	*
28	86 ± 0.1	88 ± 0.2	0.644 ± 1 mV	0.652 ± 1 mV	7	1.97	3.8	0.54
29	101 ± 0.1	100 ± 0.8	0.648 ± 1 mV	0.652 ± 1 mV	4	3.04	4.0	0.60
30	81 ± 0.1	74 ± 0.7	0.623 ± 2 mV	0.610 ± 2 mV	13	1.61	3.7	0.55
31	79 ± 0.2	78 ± 0.2	0.755 ± 1 mV	0.753 ± 1 mV	2	2.61	3.9	0.60
32	59 ± 0.6	58 ± 1	0.841 ± 6 mV	0.754 ± 1 mV	85	*	*	*

* Data could not be obtained.

In contrast, the Spiro- (**27**) or TEA-TEMPO (**31**) were barely measurable during this preliminary investigation. Regarding the Spiro-TEMPO **27**, this is most likely due to the very fast hydrolyzation of the ether in the tetrahydropyran rings because of their exposed location. The received terminal hydroxy groups are vulnerable towards oxidation either by the cerium (interference with titration) or by the oxoammonium cation itself (interference with RDE measurements). Although the TEA-TEMPO (**31**) was detectable *via* titration, significant deviations between the standard potentials determined by CV and the titration fit were observed. This is mainly linked to the species low DoO of below 60% showing the limits of the titration method. The low DoO might interfere with the RDE measurements, where the received data hinders a simple evaluation with the Levich equations. Because of the instability of the Spiro-TEMPO **27** and the low DoO of the TEA-TEMPO (**31**) as well as the time-consuming synthesis of both, the derivatives were omitted from future battery tests.

After the unsuitable derivatives were singled out, the others were tested with the same low-concentrated, unbalanced, compositionally symmetric RFB approach described in **Chapter 2.1**. The cell was charged/discharged 175 times at room temperature and a hold time of 24 h in the maximum SOC of the CLS was applied after every 50 cycles. The charging and discharging protocol included a galvanostatic and a potentiostatic part to ensure that the maximum amount of active material was used. After the 175 cycles, the protocol was repeated at 40 °C.

At first, the TMA-TEMPO **1a** was investigated to create a benchmark to which the other derivatives were compared. During the first 50 cycles TMA-TEMPO revealed at first relatively constant charge and discharge capacities. But after a small peak, the electrolyte capacity started to decay. This decay was even more pronounced when a hold time of 24 h was applied. This trend continued over the next 125 cycles, representing an average room temperature decay rate of 1.5% d⁻¹ during the hold times (average of the three hold times) in comparison to 0.9% d⁻¹ (average of the four cycling periods) (*cf.* **Table 3.3**). Increasing the temperature to 40 °C leads to increased average decay rates during hold times (2.0% d⁻¹). Interestingly, the average capacity fade during the cycling is with 0.8% d⁻¹ comparable to the results obtained at room temperature. Furthermore, the described healing mechanism, namely the hydroxylamine reoxidation, was visible after the hold times. However, after the test, 73.0% of the initial capacity could be recovered.

As mentioned before the linker may have a massive influence on the stability of the derivatives, and, thus, the TEMPO-amide **28** was investigated first. It exhibited a capacity decrease of 6.6% during the first 50 cycles which then equilibrates over the next 125 cycles. With average decay rates of 1.3% d⁻¹ at RT and 0.8% d⁻¹ at 40 °C the stability of **28** is comparable to TMA-TEMPO.

Furthermore, the amide **28** showed a comparable capacity retention of 71% at the end of the test (*cf.* **Figure 3.6**). During the hold times, a significant decay of over 10% is visible, which was recoverable at continued cycling. Since the observed capacity decrease is much more pronounced in comparison to TMA-TEMPO, either the ratio between the formed hydroxylamine and the decomposed oxoammonium cation is different or a secondary self-discharge mechanism is present. Up until now, a detailed evaluation of the ongoing processes is pending. In comparison to the amide **28** or TMA-TEMPO, the sulfonamide **29** and the ether **30** are much more prone to irreversible decomposition reactions. Both followed the same trend with a pronounced capacity decay during the first 50 cycles to a capacity of below 30% of the initial capacity as well as a capacity decrease of more than 10% during the applied hold times at the maximum SOC (*cf.* **Figure 3.6**). The accessible capacity stabilizes during the experiment; however, with an overall capacity retention of 20% after 350 cycles both molecules are not applicable as active materials in RFBs. Originally intended to be more stable compared to the TMA-TEMPO, the amide **28**, the sulfonamide **29**, and the ether **30** failed. While the amide **28** showed comparable decay rates, the sulfonamide **29**, and the ether **30** are decaying significantly faster than the benchmark molecule **1a**. This behavior is mainly attributed to the instability of the linker. The N-S-bond of the sulfonamide **29** is prone to oxidative cleave at a redox potential of 0.75 to 0.9 V *vs.* Ag/AgCl,^[39] which is in the redox potential range of the TEMPO derivatives. Furthermore, oxoammonium cations are known to cleave ether bonds.^[40] The decomposition products 4-amino- and 4-hydroxy-TEMPO derivatives are known to be much more instable than TMA-TEMPO, explaining the fast decomposition of the sulfonamide **28** and the ether **30**.^[41] In contrast to that, the N-C-bond of the amides is capable of withstanding oxidative cleavage to a redox potential of up to 1.25 V *vs.* Ag/AgCl, explaining its higher stability.^[42] It is noteworthy, that the findings and suggestions by Liu *et al.*,^[26] that the introduction of a linker between the piperidyl core and the SPG can increase the stability, could not be confirmed in the experiments of this thesis. This might be because Liu only cycled in galvanostatic mode without hold times and temperature test giving the TEMPO ethers **28** oxoammonium cation not enough time to decompose.

To investigate the influence of the nucleophilicity of the counter ion, a TMA-TEMPO derivate with less nucleophilic behavior, compared to halogen ions, BF₄ salt **31** was synthesized.^[43] As expected, the solubility of the compound was relatively low and the applied concentration of 0.1 M was at the edge of maximum solubility.

Furthermore, the accessible current densities were so low that the first block of 50 cycles took over eight days (two days for the other derivatives) (*cf.* **Figure 3.6**). Although the membrane

was pre-wetted, the ion transport through the membrane might have been hindered. At the beginning of the experiment, the capacity increased slightly from 50% of the theoretically accessible capacity to approx. 80% and stayed nearly constant thereafter. During the first hold time no capacity dip was visible in contrast to the other derivatives. This atypical behavior can be linked to a very low solubility and a possible participation-dissolution equilibrium. This would also explain the low accessible capacity. Nevertheless, the experiment could not be finished since the membrane was damaged. This might be linked to a possible penetration of the membrane by salt crystals or clogging of the cell with an associated pressure rise due to participate formation.

The failed improvement of the stability by the introduction of linkers and the comparable decay rates of the amides lead to the hypothesis that neither the Hoffmann elimination of the SPG nor the loss of chloromethane is the stability limiting pathway. The N-C-bound next to the radical or the oxoammonium cation is the weakest part in the scaffold. A stabilization *via* enhanced shielding or utilizing electronic or mesomeric effects by substituents vicinal to the NO-substructure might help preventing the bond cleavage. However, the decomposition data once again showed the influence of the SOC on the stability which again highlights the need for the development of simple and reliable SOC determination methods for RFB electrolytes. As the increased stability Liu *et al.*^[26] reported could not be reproduced with our setup and the applied stability assessment protocol. The main difference between the measuring protocols is that we added a potentiostatic part during the cycling period, hold times and tests at elevated temperatures. The findings empathizing the need of concentration and temperature dependent studies with hold times. Furthermore, the observed discrepancy between cycle-based and time-based decay rates also emphasize the importance of time-based decay rate measurements.

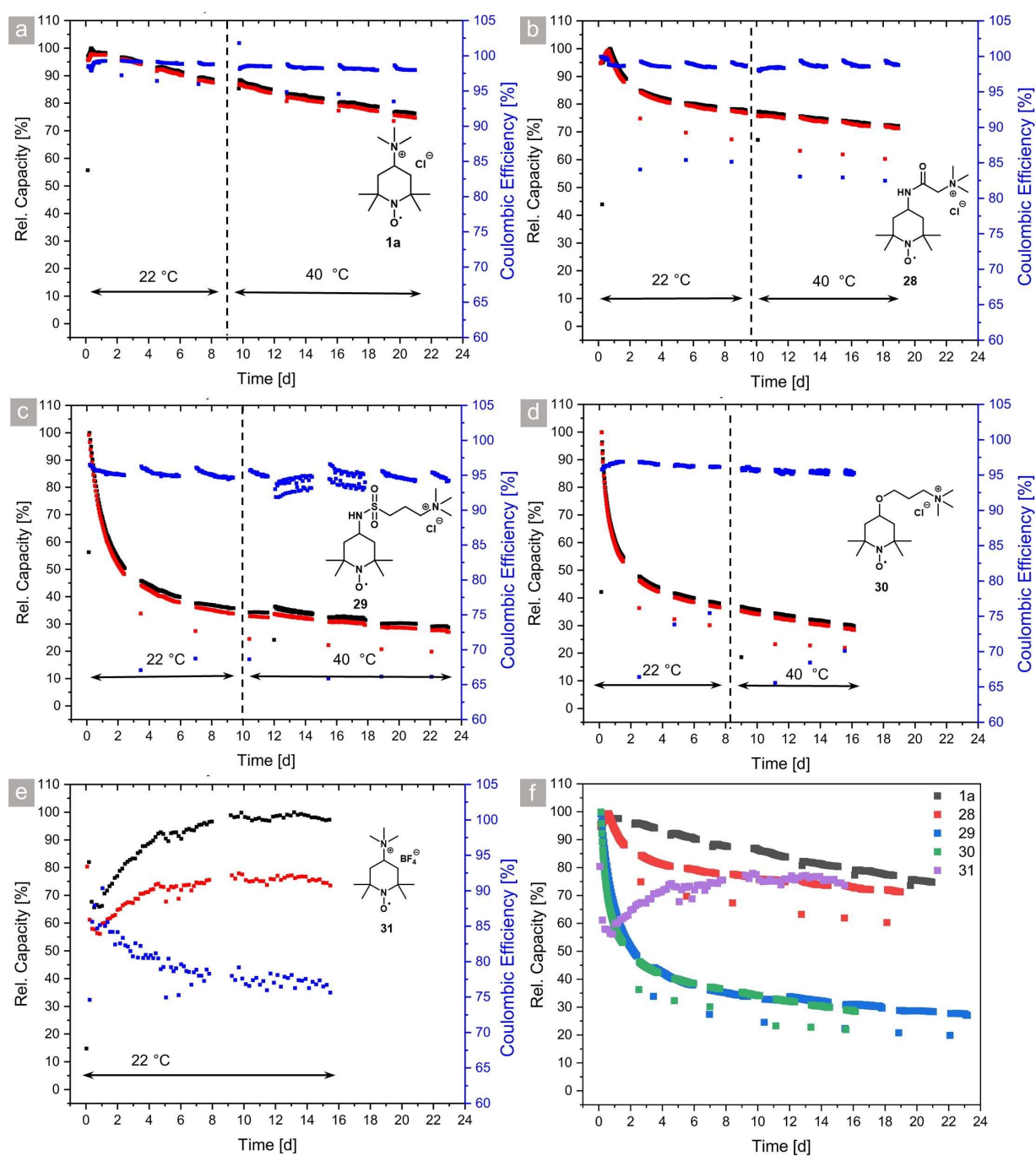


Figure 3.6: Overview of the battery performance of different TEMPO-derivatives in symmetrical redox flow battery tests cycled galvanostatic with 10 mA cm^{-2} with consecutively added a potentiostatically part with a current limitation of 0.5 mA cm^{-2} . The cells consist of 12 mL vs. 18 mL 0.1 M active material solution, except for TMA-TEMPO, where 15 mL vs. 20 mL solutions were used. All electrolytes consist of 1.5 M appropriate supporting salt in water. The charge capacity is represented in black, the discharge capacity in red and the coulombic efficiency in blue. a) TMA-TEMPO **1a**; b) Tempo-amide **28**; c) TEMPO-sulfonamide **29**; d) TEMPO-ether **30**; e) TMA-TEMPO BF₄ **31**. f) Comparison of the discharge capacity of the TEMPO-derivatives. (The figure was taken from **P3**).^[34]

Synthesis and stability investigation of active materials for redox flow batteries

Table 3.3: Overview of the capacity decay of different TEMPO derivatives during cell test for pure cycling (50 cycles 1-3 period, 25 cycles 4 period) and hold times of 24 h at room temperature and 40 °C.

Compound	Start rel. Discharge Capacity	decay 22 °C [% d ⁻¹]								Final rel. Discharge Capacity	decay 40 °C [% d ⁻¹]							
		1. Cycling period	1. Hold time	2. Cycling period	2. Hold time	3. Cycling period	3. Hold time	4. Cycling period	1. Cycling period		1. Hold time	2. Cycling period	2. Hold time	3. Cycling period	3. Hold time	4. Cycling period		
1a	95.62	+0.80	1.98	1.64	2.52	1.42	2.53	1.07	87.57	1.60	2.94	0.89	2.90	0.90	3.42	0.69	74.79	
28	94.74	6.79	12.80	2.10	10.36	1.01	10.18	0.84	76.84	0.45	11.32	0.92	11.35	0.97	11.44	0.97	71.33	
29	99.24	20.45	13.75	2.57	10.02	0.92	8.90	0.35	32.47	0.76	8.98	0.35	8.47	0.15	8.10	0.43	27.09	
30	99.95	28.31	16.35	3.30	9.77	1.52	8.15	1.11	36.59	1.16	10.60	0.87	9.00	0.60	8.80	0.97	28.47	
31	80.43	+1.98	+1.12	0.16			*		73.60					*				

* Data could not be obtained.

2.3 Application of the advanced cycling protocol to negolytes

Up to now, the cycling protocol featuring hold times and elevated temperatures was used to investigate the limitations of one electron exchanging TEMPO-based posolytes in symmetric RFBs. To further demonstrate the applicability of the protocol, negolytes were investigated as well. Therefore, a new 2,6-disubstituted anthraquinone derivative was synthesized. Anthraquinones (AQs) stand out due to their fast and reliable two electron redox chemistry, which made them one of the most thoroughly investigated negolyte active materials.^[41] Beside this, they exhibit extraordinarily high stabilities in comparison to other organic redox couples.^[44]

The new AQ derivative is synthesized from cheap raw materials in a straightforward manner without time consuming purification steps. As starting material, the 2,6-diamino-AQ was chosen, which is one order of magnitude cheaper than the often used 2,6-dihydroxy-AQ. To promote water solubility, it was reacted with chlorosulfuric acid and transferred to the corresponding metal salt by neutralization (*cf.* **Figure 3.7a**). The utilization of sulfamidic acids was inspired by the design strategy of new drugs, where the used functional group is often utilized to enhance the solubility in aqueous media.^[45] Furthermore, a lithium chloride based electrolyte was chosen to further increase the solubility by imposing polarization effects similar to the lithium chloride/*N,N*-dimethylacetamide system for cellulose.^[46] Since it is known that AQ undergo a proton-coupled electron transfer (PCET), their electrochemical properties – in particular the reversibility and the redox potential – are highly dependent on the pH value of the electrolyte.^[47]

As expected, the performance as active material is low between pH values of 7 to 11, as indicated by CV investigations (*cf.* **Figure 3.7b**). The curves give hints that the reoxidation from the hydroquinone to the quinone is hindered. This changes at pH value of 12, and at a pH value of 13 the AQ typical redox pattern can be observed. At a pH value of 14 the reduction to the hydroquinone produces sharp peaks even at high scan speeds of 2000 mVs⁻¹ (*cf.* **Figure 3.7c**) while the reoxidation broadens with the scanning speed which indicates slower redox kinetics (*cf.* **Figure 3.7d**). However, when the peak current is plotted over the square root of the scan speed the data points exhibit a linear behavior indicating a reversible redox behavior. From these preliminary investigations, an optimal pH value of the electrolyte between 13 and 14 was found and used for the following battery experiments.

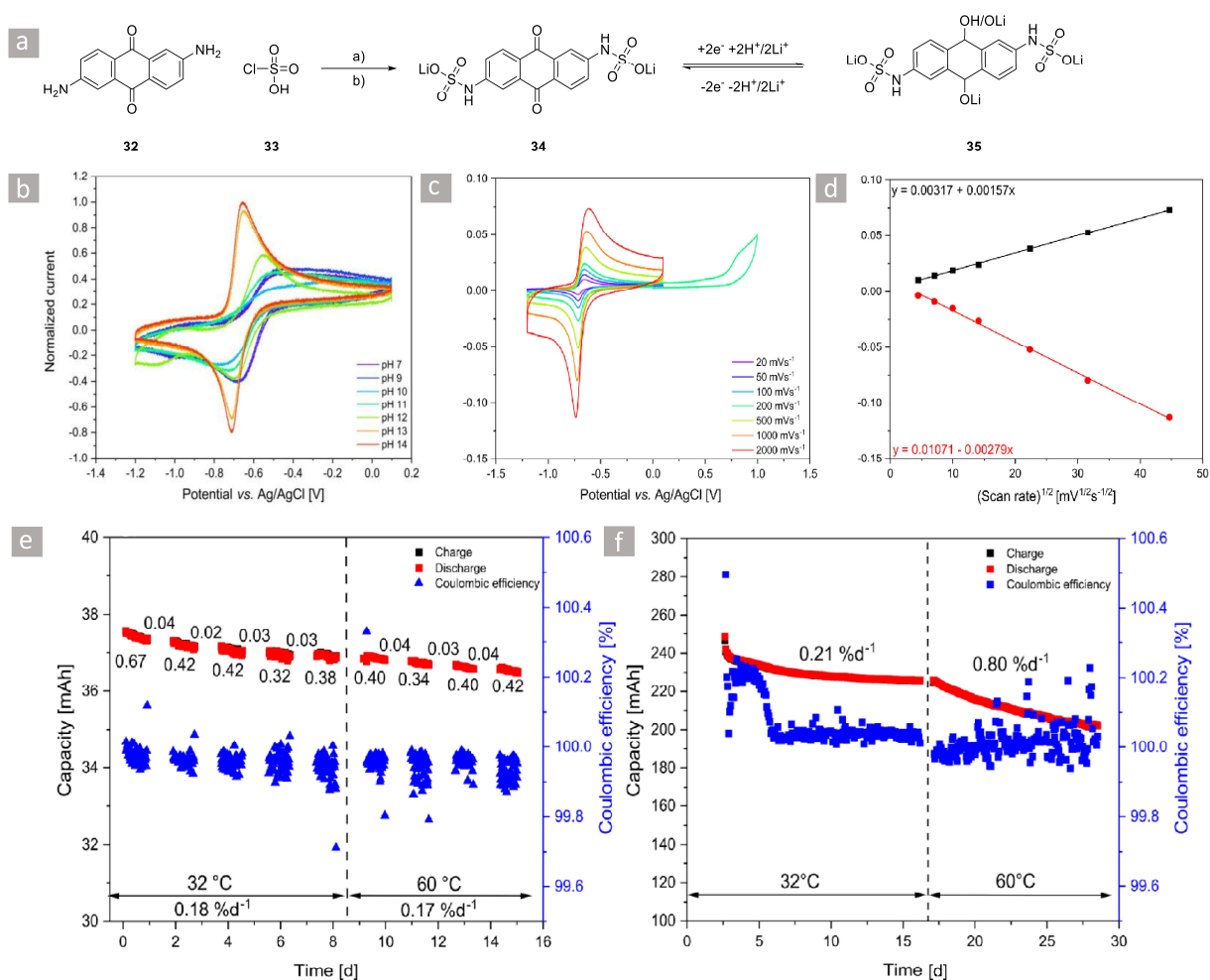


Figure 3.7: a): Schematic representation of the synthesis and redox chemistry of the LiAQS. a) Dichloromethane, Pyridine, 0 °C to room temperature 16 h. b) Water, Lithium hydroxide, room temperature, 30 min, 87%. Cyclovoltammetry of a 50 mM LiAQS solution in 0.1 M lithium chloride solution, b) pH dependent investigation utilizing lithium hydroxide for adjusting the pH value with a scan speed of 100 mVs⁻¹. c) CV at different scan speeds at a pH value of 14. d) Plot of the peak current for the oxidation (black) and reduction process. (red) vs. the square root of the scan speed at a pH value of 14. e) Longterm stability test of 15 mL of a 0.1 M LiAQS solution in 1 M LiCl and 0.25 M LiOH vs. 35 mL of the same solution. The values below the red and black squares indicate the decay rate during the representative 50 cycles in % d⁻¹. After every 50 cycles the electrolyte was kept for 24 h at maximum SOC and then cycled again. The values above the squares represent the decay rate during these hold times. After 250 cycles the temperature of the electrolyte was raised to 60 °C (indicated by the dashed line). The values below the temperature represent the decay rates during the whole temperature experiment. f) Longterm test of 10 mL of a 0.75 M LiAQS solution in 1 M LiCl and 0.25 M LiOH vs. 25 mL of the same solution. (The figure was taken from P4).^[48]

In contrast to the TEMPO-based electrolytes, the AQ derivatives revealed a constant average temperature independent decomposition rate when cycled with the advanced protocol (*cf.* Figure 3.7e). Even when an 0.1 M AQ solution was exposed to temperatures of up to 60 °C the fade rates do not differ much from the rates measured at 32 °C (room temperature in the glove box). However, when a pure cycling mode without hold times is applied, the decomposition is rather high with an average value of 0.4% d⁻¹. However, when hold times in the maximum SOC

are used, the fade reduces by one order of magnitude to a value of 0.04% d⁻¹. Compared to other AQ derivatives, the new lithium anthraquinone sulfamic acid (LiAQS) revealed the highest stability under elevated temperatures of 60 °C reported so far.^[37, 49] This trend is also recognizable during a long-term stability test (200 cycles at 32 °C and 60 °C, respectively) when electrolyte concentration is increased to its maximum of 0.75 M. While the electrolyte needs approximately 25 cycles to equilibrate (as judged from the fluctuating CE and the increased decomposition), the fade rate of 0.21% d⁻¹ is subsequently stable to the end of the 32 °C test. However, when elevated temperatures are used also the decomposition increased. Nevertheless, the 0.75 M LiAQS solution at 60 °C with 0.80% d⁻¹ also showed the lowest fade rate for AQ electrolytes so far. However, in both tests only 50% of the theoretical capacity is accessible, hinting at a one electron process. The most plausible explanation would be the formation of a formally one-time reduced quinhydrone complex from an uncharged and a fully charged AQ.^[23a, 50] The process might be enhanced by a complex formation caused by the oxophilicity of the used lithium salts and lithium enolates^[51] or by dimerization reactions amplified by hydrogen bonds between the sulfamidic functional groups.^[52]

Nevertheless, the LiAQS represents a promising active material for application in AORFBs due to its low fade rate of 0.17% d⁻¹ with 0.1M and 0.80% d⁻¹ with 0.75M at elevated temperatures of 60 °C. The stability may be further enhanced by the introduction of linkers between the SPG and the AQ core as shown by Aziz *et al.* for comparable derivatives.^[44, 53] However, the tests revealed the complex relationship between the decomposition and the concentration on the one hand and the SOC on the other hand. The enhanced cycling protocol has been shown to be capable of investigating both, but it can only reveal a small part of the stability properties of the material. It should always be used in combination with a long-term cycling stability test. Furthermore, it has its limitation by quantifying the SOC dependent decomposition rates showing once more the need of reliable SOC determination methods. Nevertheless, it is a helpful tool for quantifying temperature dependent fade rates and qualifying SOC dependent rates.

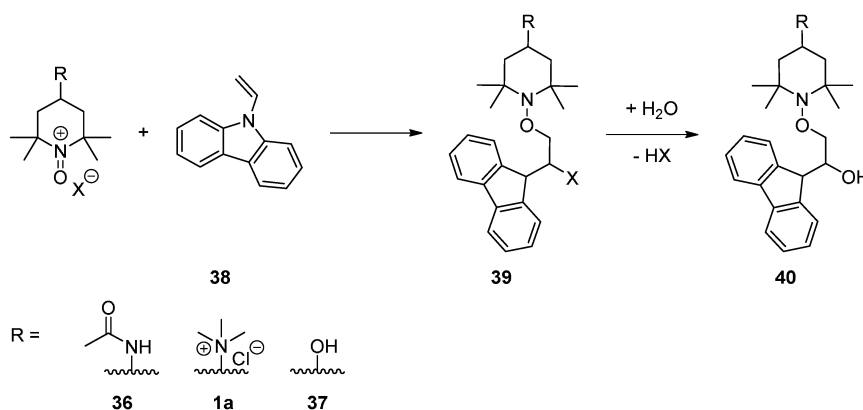
4 State of charge and state of health measurement methods for RFB electrolytes

During the stability investigations of TEMPO- and anthraquinone derivatives the switch from full cell test against another active material to symmetric cell test with hold times and temperature tests enabled a more in-depth investigation of the electrolyte's stability. However, the method cannot resolve SOC dependent decay rates. But the results of **Chapter 3** empathize the investigation of the SOC on the decomposition rate. For further insights on the active materials stability methods, a simultaneously SOC and SOH determination of the individual electrolytes in the cell would be highly advantageous. One approach would include the use of "classical" analytical methods, but most of the methods are quite limited in their applicabilities.^[54] While, *e.g.*, anthraquinones can be analyzed *via* NMR spectroscopy in the charged as well as the uncharged state, the radical character of the TEMPO ground state hinders such measurements.^[55] Furthermore, the discrimination between the charged and the uncharged state of battery materials, in general, might be difficult because the classical methods often cannot differentiate between them. A previous separation between the redox states, *e.g.*, by chromatographic methods is, thus, required. As mentioned in **Chapter 3**, the investigation of the partially decomposed TMA-TEMPO electrolytes utilizing MS-coupled liquid chromatography (LC) would be greatly beneficial for the detailed confirmation of the proposed decomposition mechanism. In addition to that, a LC method could be used to determine SOC and SOH in the battery. Furthermore, liquid chromatographic protocols can be very sensitive and even small changes in the SOC or small amounts of impurities can be detected and, depending on the used detector, identified. Besides the combination of "classical" analytical methods with preceding separation techniques, electrochemical protocols can be applied. They enable the *in-operando* monitoring without the need of sample extraction which is required for LC methods. However, the currently used methods suffer from several drawbacks like high measurement uncertainties, the need for (re)calibration, and the limitation to special active materials. A robust, precise, simple, cheap, and universal method is required. Here the amperometric SOC measurement technique introduced by Stolze *et al.* recently represents a good starting point.^[18] But the currently high SOC errors of the method of 3 to 7% and the need of cost intensive potentiostats are the main drawbacks. A simplification by a simultaneous increase of the measuring procedure accuracy is, thus, necessary. Both aforementioned approaches were investigated for this thesis and the obtained results are presented in this chapter.

4.1 Liquid chromatography analysis of TEMPO electrolytes

Parts of this chapter have been published in **P5**: *Liquid chromatography analysis of reactive oxoammonium cations*, P. Rohland, K. Schreyer, R. Burges, N. Fritz, M. D. Hager, U. S. Schubert, *Chromatographia* **2021**, *84*, 999-1007.

For reliable SOC and SOH data, the overall concentration and the ratio between charged and uncharged active material must be determined. As initially stated, many analytic methods like ESR, NMR, titration, and MS have issues with analyzing the amount and identity of oxoammonium cations and radicals.^[10b, 56] This is either caused by the short molecule lifetime due to decomposition reactions or method-specific limitations, like the restriction to paramagnetic species in the NMR. The UV/vis spectra of the two species are in many cases too similar for proper analysis.^[54] Small amounts of remaining radicals will disturb the NMR while ESR is not sensitive enough for radical impurity quantification in oxoammonium cations.^[55] MS is also insufficient, since the radical is oxidized under the measurement conditions.^[57] Since the common analytical techniques are often unable to analyze the identity and, simultaneously, the amounts of cation and radical, a preliminary separation between the radical and the cation is hardly inevitable. While most of the investigated compounds are not volatile, GC dropped out of the possible separation techniques, leaving only liquid chromatography as the remaining possible technique. But the steel parts in commonly used high pressure liquid chromatography systems can be corroded by the oxoammonium cation.^[10b] A derivatization reaction, which transforms the highly reactive oxoammonium cations in an analyzable species is thus needed. In 1999, Takata *et al.* showed that oxoammonium cation undergo 1,2-electrophilic additions to electron rich olefines with excellent yields (*cf.* **Scheme 4.1**).^[58] But the adducts are not stable – not even at low temperatures of around -20 °C. In this thesis, this reaction was so far used to explain the oxidative degradation of phorones to CO₂ in the TMA-TEMPO **1** decomposition mechanism. In this chapter, it is used to transfer oxoammonium cation into suitable and detectable candidates for HPLC separation. As model substances the Bobbitt salt (*N*-(2,2,6,6-tetramethyl-1-oxopiperidin-1-ium-4-yl)acetamide tetrafluoroborate) (**36**), the TMA-TEMPO oxoammonium cation (2,2,6,6-tetramethyl-1-oxo-4-(trimethylammonium)piperidin-1-ium dichloride) (**1a**), and the TEMPOL oxoammonium cation (4-hydroxy-2,2,6,6-tetramethyl-1-oxopiperidin-1-ium chloride) (**37**) were chosen to show the transferability of the method to a broad range of possible TEMPO derivatives. The Bobbitt salt **36** was selected to demonstrate that the protocol is not only interesting for the organic battery community but also for organic chemists or pharmacists, since this salt is often used as “green” catalyst in the oxidation of alcohols to their corresponding carbonyl or even carboxyl analogues.^[59] In addition to that, TEMPOL is currently investigated as antihypertensive or pro-oxidant.^[60]



Scheme 4.1: Schematic representation of the derivatization reaction of the Bobbitt salt (**36**), TMA-TEMPO oxoammonium cation (**1a**) and TEMPOL oxoammonium cation (**37**) to the corresponding HPLC detectable derivatives. (The scheme was taken from **P5**).^[61]

But before the derivatisation protocol can be used for HPLC determination of TEMPO derivatives, the stability of the adducts must be increased. As Takata *et al.* demonstrated, the derivatisation products do only have a limited lifetime even at low temperatures. This is probably due to the cleavage of the O-C bond between the former olefin and the oxoammonium cation resulting in a formal oxidation of the olefin to a carbonyl compound, which might be catalyzed by the intermediary formed acids (*cf.* **Chapter 2.1**, **Scheme 3.2** and **Scheme 4.1**).

With the usage of tetramethylurea (TMU) as solvent, not only the acid problem but also some solubility issues can be solved. As it is often used as solvent for the production of aromatic polyamides like Nomex[®], TMU stands out due to its dissolving capabilities, even for charged molecules and salts, and its intrinsic non-nucleophilic basicity.^[62] On the one hand the double positively charged TMA-TEMPO oxoammonium cation **1a** and the non-polar mesitylene, which is used as internal standard, are soluble in the derivatization solvent. On the other hand, intermediary formed acids can be bound. To validate the new solvent approach, three different samples for each of the three different concentrations (35, 28, 21 mmol L⁻¹) of the three model substances were prepared and kept in the auto-sampler of the HPLC at 5 °C for 12 days. During this long-term experiment, one measurement per day was carried out for each sample. The data revealed a massive increase in the stability of the analyte molecules. While Takata *et al.* stated that the adducts decompose completely within minutes to hours at -20 °C, the decay rate observed in the experiments of this thesis was approximately 0.5 to 1.0% d⁻¹ at +5 °C for the three different concentrations. Decomposition rates of 0.5 to 1.0% d⁻¹ at +5 °C were considered as suitable for HPLC analysis.

Subsequently, TMA-TEMPO was utilized to validate the proposed HPLC protocol. The international conference on harmonisation and the United States pharmacopeia prescribe a

precise protocol for method validation.^[63] Since the protocol was developed for a broad applicability in non-battery related research fields like life science and pharmacy, the strict ICH/USP guidelines were applied during the validation process.^[63]

At first a system suitability test (SST) as well as a linearity and range test were performed. In the SST, the validation parameters including resolution, plate count, capacity factor, tailing factor, and relative standard deviation (RSD) of the peak areas were determined for each analyte and compared to the USP guidelines.^[64] For this, the data of six replicate injections of samples with a concentration of 30 mmol L⁻¹ were used. Afterwards the linearity of the calibration as well as the range was determined using calibration samples with analyte concentrations of 14, 21, 24, 28, and 35 mmol L⁻¹. For each concentration, six replicates were produced and injected once into the chromatographic system. The calibration curves were calculated utilizing the least-squares linear regression analysis while the limits of detection (LOD) and the limits of quantification (LOQ) were calculated using the following formula:^[63b]

$$LOD = \frac{3.3 \sigma}{S} \quad (4-2)$$

$$LOQ = \frac{10 \sigma}{S} \quad (4-3)$$

(σ = standard deviation of y-intercept of regression lines, S = slope of the calibration curve).

Table 4.1: Above dashed line) Results of the system suitability test (n = 6). Below dashed line) Data of the linearity study (n = 6).

Parameter	Bobbitt salt	TMA-TEMPO oxo. cat.	TEMPOL oxo. cat.	Internal Standard	Required according to USP
Resolution (R_s)	1.87	24.52	2.64	6.25	> 2
Plate count (N)	130903	5773	127494	64575	> 2000
Capacity factor (k')	9.82	4.61	9.72	13.23	> 2
Tailing factor (T)	1.08	3.58	1.04	1.09	≤ 2
% RSD (peak area)	0.27	0.16	0.20	0.18	≤ 1
Range (mmol L ⁻¹)	14 to 35	14 to 35	14 to 35		
Determination coefficient (R^2)	0.9990	0.9985	0.9980		
Slope of the calibration curve (S) (mmol ⁻¹ L)	175.5695	142.7708	68.4183		
Intercept	-0.0068	-0.0973	-0.0299		
Standard deviation of the slope (σ)	4.6347	3.1944	1.7834		
Standard deviation of y-intercept (σ)	0.0075	0.0068	0.0037		
LOD (mmol L ⁻¹)	0.13	0.14	0.16		
LOQ (mmol L ⁻¹)	0.43	0.47	0.55		

The, in **Table 4.1** summarized, data show that in general the USP requirements are fulfilled. Exceptions are the resolution of the Bobbitt salt **36** with 1.87 (required to be higher than 2), and the too high tailing factor of TMA-TEMPO oxoammonium cation **1a**. Nevertheless, the peak overlap of the Bobbitt salt signal with the next analyte is below 5% and, as a consequence, resolution issues are considered to be negligible. Furthermore, the high tailing factor of the TMA-TEMPO oxoammonium cation **1a** is acceptable due to the high resolution of 24.52. In the linearity study, the data revealed a linear behavior over the measured range and the determination coefficient (R^2) as well as the LOD and LOQ showed HPLC analysis typical values that are suitable for further investigations. After the system suitability and the linearity as well as the range of the method was verified, the accuracy and precision as well as the suitability of the method for “real” probes were investigated in a final step. For the intra- and interday recovery experiments, samples of three concentrations (18, 23, and 30 mmol L⁻¹) within the calibrated range were used. For each probe, six replicant samples were produced, injected once into the chromatographic system, and the accuracy as well as the recovery rate were determined. The procedure was repeated twice on two consecutive days. Since the purpose of the method for this thesis was the determination of the overall concentration of oxidized TEMPO derivatives in solution, the influence of the corresponding radical was investigated by the analysis of “real” samples with SOC of 80, 65, and 50% with a total TEMPO derivative concentration of 35 mmol L⁻¹. The study was not designed to cover the full concentration range, since it should be investigated how the radical to oxoammonium cation ratio interferes with the measurement. Although the intraday RSD with values of 2 to 8% for all three derivatives are quite high, the intraday RSD of the Bobbitt salt **36** and TMA-TEMPO oxoammonium cation **1a** are below 3% (*cf.* **Table 4.2**), which are acceptable values for this newly developed HPLC method for the detection of highly reactive analytes. In contrast to that, the interday RSD of the TEMPOL oxoammonium cation **37** yielded values of over 16%, which is intolerable and suggests that the protocol is not suitable for this derivative. This conclusion is supported by the calculated recovery rate of >150%. The great deviation are most likely linked to possible side reactions of the 4-hydroxy group of the TEMPOL, which can be oxidized by the oxoammonium cation to its corresponding ketone.^[65] Also the TMA-TEMPO oxoammonium cation **1a** reveals greater deviations in the recovery data, but in this case an indirect linear dependency on the concentration was found. This is linked to the demanding calibration because of the lack of commercially available reference substances. The required oxoammonium cation preparation utilizing the electrochemical oxidation of the radical in a RFB suffers from technical problems like fluctuating concentrations caused by osmotic pressure differences.^[36, 66]

Table 4.2: Data of the intraday (day one) and interday recovery experiments for accuracy and precision determination ($n = 3$) as well as the data of the recovery studies for samples of the three different oxoammonium cations mixed with their corresponding radicals ($n = 6$).

	Concentration (mmol L ⁻¹)	Intraday		Interday		Concentration oxoammonium cation / radical [mmol L ⁻¹]	Recovery rate [%]	RSD [%]
		Recovery [%]	RSD [%]	Recovery [%]	RSD [%]			
Bobbitt salt	30	101	6	101	3	28 / 7	101.99	2.95
	23	104	6	105	1	22.75 / 12.25	109.50	2.54
	18	105	7	106	2	17.5 / 17.5	115.89	6.18
TMA- TEMPO oxoammo nium cation	30	121	8	122	2	28 / 7	113.24	11.25
	23	135	6	131	3	22.75 / 12.25	140.82	4.83
	18	142	8	143	3	17.5 / 17.5	152.72	5.82
TEMPOL oxoammo nium cation	30	192	11	165	14	28 / 7	202.93	2.97
	23	206	4	175	16	22.75 / 12.25	209.90	3.82
	18	207	7	175	16	17.5 / 17.5	225.15	1.79

Consequently, only the Bobbitt salt **36** satisfies the requirements on accuracy and precision. Nevertheless, also recovery experiments with “real” probes were performed in which oxoammonium cations of TMA-TEMPO and TEMPOL suffer from the same problems as discussed during the inter- and intraday experiments. In addition to that, the Bobbitt salt **36** reveals greater deviations when the radical content is elevated as well. A nitroxide mediated polymerization-like reaction of the radical with the olefine to alkoxyamines, with similar structures as the analyte, is the most plausible explanation of the increased over estimation during the experiments.^[67]

In summary, it is shown that the HPLC method can be used for the determination of oxoammonium cations even in the presence of high amounts of corresponding radicals (approximately up to 30%) but the suitability for a specific substance must be checked in advance. All in all, this is acceptable for pharmaceutical or life science application but not for the desired SOC determination of a RFB electrolyte where the method must tolerate radical contents between at least 5 to 95%. To overcome these drawbacks, the improvement of a recently reported electrochemical analysis method was investigated for this purpose.

4.2 Low-cost amperometric determination for the combined SOC, SOH and capacity monitoring

Parts of this chapter have been published in **P6**: *A low-cost amperometric sensor for the combined state-of-charge, capacity, and state-of-health monitoring of redox flow battery electrolytes*, C. Stolze, P. Rohland, K. Zub, O. Nolte, M. D. Hager, U S. Schubert, *Energy Convers. Manag. X* **2022**, *14*, 100188.

Currently most of the evaluated analysis methods suffer from at least one of the following issues: Error accumulation over time, time consuming (re)calibration, dependency on system parameters like temperature, no half-cell resolution, no real-time monitoring capability, mathematic complexity, cost intensive instrumentation, and limitation to certain electrolytes.^[18] Furthermore, most of the conventional approaches determine the SOC/SOH on the battery level and not on the electrolyte level.^[68] However, the separate monitoring of the individual electrolyte parameters would enable a more detailed overview about performance and, hence, simplifies the detection of, *e.g.*, safety and performance issues. Regarding this, Stolze *et al.* recently reported that the anodic and the cathodic mass transfer limited currents, $i_{l,a}$ and $i_{l,c}$, measured with a disk-shaped microelectrode, can be used to calculate the SOC by the following formulas:^[69]

$$i_{l,a} = 4nFrD_R c_R = 4nFrD_R c(1 - SOC) \quad \text{and} \quad i_{l,c} = -4nFrD_O c_O = -4nFrD_O c SOC \quad (4-4)$$

(F = the Faraday's constant, n = the number of transferred electrons, r = the radius of the disk, $D_{O/R}$ = the diffusion coefficients, $c_{O/R}$ = the bulk concentrations of the oxidized and the reduced form of the redox couple, and $c = c_O + c_R$ its total concentration).

By using the ratio of $i_{l,a}$ and $i_{l,c}$, the calculation of the SOC – defined as $SOC \equiv c_O c^{-1}$ for posolytes and $\overline{SOC} \equiv c_R c^{-1}$ for negolytes – according to:

$$SOC = \frac{1}{1 - \frac{i_{l,a} D_O}{i_{l,c} D_R}} \quad (\text{posolytes}), \quad \overline{SOC} = \frac{1}{1 - \frac{i_{l,c} D_R}{i_{l,a} D_O}} \quad (\text{negolytes}) \quad (4-5)$$

With this approach, the SOC of various aqueous electrolyte systems were determined with absolute root-mean-square deviations (RMSD) between 3% and 7%. This infers a wide applicability of the amperometric approach by Stolze *et al.* Nevertheless, it is limited to the SOC determination and a co-estimation of the electrolyte SOH and capacity would be highly favorable. In theory, both can be co-determined by the combination of coulomb counting and an absolute SOC measuring method.

Coulomb counting is based on the integration of the electrical charging or discharging current over time and is commonly applied to various battery types:

$$SOC(t_1) = SOC(t_0) + \frac{1}{Q_{max}} \int_{t_0}^{t_1} i(\tau) d\tau = SOC(t_0) + \frac{\Delta Q}{Q_{max}}. \quad (4-6)$$

($SOC(t_0)$ = initial SOC, Q_{max} = total electrolyte capacity, $i(t)$ = electrical (charging or discharging) current, ΔQ = charge transferred in the time interval $\Delta t = t_1 - t_0$).

By a rearrangement of equation (4-6) and combination with the aforementioned amperometric SOC measurements method, the total electrolyte capacity can be determined according to:

$$Q_{max} = \underbrace{[SOC(t_1) - SOC(t_0)]^{-1}}_{\equiv \Delta SOC} \int_{t_0}^{t_1} i(\tau) d\tau = \frac{\Delta Q}{\Delta SOC}. \quad (4-7)$$

(ΔSOC = changes of the electrolyte SOC)

The possibility to determine the electrolyte capacity enables the calculation of the electrolyte SOH by determining the ratio between the capacity in the n^{th} cycle, Q_{max}^n , to a reference cycle (usually the first) Q_{max}^0 , $SOH^n = Q_{max}^n Q_{max}^0^{-1}$. Alternatively, equation (4-6) can be set up for each individual cycle which yields the following expressions:

$$SOC^0 = SOC^0(t_0) + \frac{\Delta Q}{Q_{max}^0} \quad \text{and} \quad SOC^n = SOC^n(t_0) + \frac{\Delta Q}{Q_{max}^n}. \quad (4-8)$$

By rearrangement of the equation for the n^{th} cycle for ΔQ and inserting it into the equation for the first cycle, a linear relationship between the SOC values of both cycles is obtained:

$$SOC^0(\Delta Q) = \underbrace{\frac{Q_{max}^n}{Q_{max}^0}}_{\equiv SO^n} SOC^n(\Delta Q) + \frac{Q_{max}^n}{Q_{max}^0} SOC^n(t_0) + SOC^0(t_0). \quad (4-9)$$

The slope of the linear equation represents the SOH and can readily be obtained by a linear regression. In the preliminary studies, uncertainties of the SOC of 3 to 7% were observed. To increase the accuracy, possible error sources must be eliminated. When samples with predefined SOC values are used, the measurement errors can mainly be attributed to three possible factors:

- (1) The error of the reference sample preparation (*i.e.*, uncertainty of the reference SOC).
- (2) The error of the current measurement in the micro- to nanoampere range.
- (3) The error in the assumed or measured ratio of the diffusion coefficients, $D_O D_R^{-1}$.

While (1) and (2) can be mitigated using precise measuring equipment and sample preparation, (3) has to be handled by a proper data evaluation. In the preliminary study, it was assumed that $D_O D_R^{-1} \approx 1$. Although, the assumption may be suitable for the magnitude of utilized redox couples, the method's accuracy can be improved by the exact determination of the diffusion

coefficients. This can either be done by a different measurement or by rearrangement of equation (4-4) to:

$$i_{l,c} = \frac{D_o}{D_R} i_{l,a} - 4nFrD_o c. \quad (4-10)$$

A linear regression performed on a plot of $i_{l,c}$ vs. $i_{l,a}$ for samples of unknown but different SOCs yields $D_o D_R^{-1}$ as the slope of this linear equation. To assess the accuracy of this evaluations approach, an offline experiment with different batches of ferri-/ferrocyanide electrolyte samples with SOC of 1%, 5%, 25%, 50%, 75%, 95%, and 99% and concentrations of 0.4, 0.2, and 0.1 M were measured. Instead of the bipolar electrode setup, which was utilized in the first study, ^[69] a two electrode configuration with a gold microelectrode (diameter: 25 μm) as working electrode and a gold macroelectrode (diameter: 2 mm) as counter electrode was used. The SOC was evaluated using three different approaches:

- (1) $D_o D_R^{-1}$ was set to 1,
- (2) $D_o D_R^{-1}$ is calculated from the linear regression of equation (4-9),
- (3) $D_o D_R^{-1}$ is calculated from literature and set to 1.07 ± 0.07 .^[70]

Table 4.3 summarizes the results of the experiments. While setting the ratio of the diffusion coefficients to 1 delivers the highest RSMD, the approaches (2) and (3) are on the same accuracy range over all samples with a slightly better accuracy when the diffusion coefficient ratio is taken from literature. However, in all cases the RMSD is significantly reduced in comparison to the initial study. This emphasizes, that the new regression approach and the two-electrode setup can determine the SOC with high accuracy and, thus, can be utilized for further SOH and capacity investigations. Despite the simplified measuring setup, the previous measurements were still performed with an expensive potentiostat which is unbearable for market ready products. But the amperometric SOC measurement in principle only requires a simple voltage source and an ammeter with sufficient accuracy and precision. To profit from this low hardware requirements, low-cost microcontroller measurement unit (MMU) based on the Arduino Nano was developed and benchmarked against a 100-fold more expensive commercial potentiostat (*cf.* **Table 4.3** and **Table 4.4**)

State of charge and state of health measurement methods for RFB electrolytes

Table 4.3: SOC measurement results for offline samples of different total concentrations of the ferri-/ferrocyanide redox couple in 0.5 M KCl_(aq) solutions as obtained with the Keithley 2400 SMU commercial potentiostat. $\Delta SOC \equiv SOC - SOC_{ref}$ represents the absolute deviation of the measurement value from the true SOC of the sample.

SOC_{ref}	400 mM ^[a]			200 mM ^[b]			100 mM ^[c]		
	$\Delta SOC^{[+]}$	$\Delta SOC_c^{[#]}$	$\Delta SOC_L^{[§]}$	$\Delta SOC^{[+]}$	$\Delta SOC_c^{[#]}$	$\Delta SOC_L^{[§]}$	$\Delta SOC^{[+]}$	$\Delta SOC_c^{[#]}$	$\Delta SOC_L^{[§]}$
[%]	[%]	[%]	[%]	[%]	[%]	[%]	[%]	[%]	[%]
1.01 ± 0.04	0.06 ± 0.04	0.04 ± 0.03	0.04 ± 0.01	0.30 ± 0.27	0.32 ± 0.27	0.22 ± 0.25	0.41 ± 0.13	0.28 ± 0.10	0.32 ± 0.12
5.03 ± 0.03	0.24 ± 0.08	0.15 ± 0.14	0.10 ± 0.06	0.37 ± 0.12	0.45 ± 0.08	0.09 ± 0.03	0.62 ± 0.08	0.11 ± 0.06	0.27 ± 0.07
25.02 ± 0.01	1.29 ± 1.15	1.03 ± 1.43	0.94 ± 1.67	1.11 ± 0.27	1.43 ± 0.13	0.19 ± 0.25	1.80 ± 0.09	0.19 ± 0.08	0.49 ± 0.09
50.00 ± 0.03	1.00 ± 0.12	0.60 ± 0.55	0.69 ± 0.12	1.48 ± 0.33	1.89 ± 0.25	0.30 ± 0.20	2.23 ± 0.26	0.26 ± 0.16	0.55 ± 0.26
74.98 ± 0.03	0.95 ± 0.20	0.61 ± 0.51	0.31 ± 0.20	1.46 ± 0.55	1.75 ± 0.71	0.38 ± 0.43	1.54 ± 0.10	0.30 ± 0.23	0.30 ± 0.10
95.00 ± 0.03	0.19 ± 0.07	0.14 ± 0.12	0.14 ± 0.07	0.26 ± 0.04	0.34 ± 0.02	0.05 ± 0.04	0.16 ± 0.02	0.32 ± 0.05	0.16 ± 0.02
98.99 ± 0.03	0.22 ± 0.19	0.25 ± 0.21	0.30 ± 0.21	0.03 ± 0.01	0.04 ± 0.01	0.04 ± 0.01	0.33 ± 0.08	0.47 ± 0.10	0.42 ± 0.08
RMSD	0.73	0.52	0.47	0.91	1.14	0.22	1.27	0.29	0.38

^[a] Average of three separately prepared sample batches and their standard deviations (batch 1 to 3).

^[b] Prepared by dilution of 400 mM sample (batch 3).

^[c] Prepared by dilution of 400 mM sample (batch 4).

^[+] Calculated from equation (4-5) using the assumption $D_O D_R^{-1} = 1$.

^[#] Calculated from equation (4-9) using the slope of the $i_{l,c}$ vs. $i_{l,a}$ regression line as estimate for $D_O D_R^{-1}$ in each repetition.

^[§] Calculated from equation (4-5) using the average literature value of $D_O D_R^{-1} = 1.07 \pm 0.07$.^[70]

State of charge and state of health measurement methods for RFB electrolytes

Table 4.4: SOC measurement results for offline measurements of different total concentrations of the ferri-/ferrocyanide redox couple in 0.5 M $\text{KCl}_{(\text{aq})}$ solutions as obtained with the microcontroller-based measurement unit. $\Delta\text{SOC} \equiv \text{SOC} - \text{SOC}_{\text{ref}}$ represents the absolute deviation of the measurement value from the true SOC.

SOC_{ref}	400 mM ^[a]			200 mM ^[b]			100 mM ^[c]		
	$\Delta\text{SOC}^{[+]}$	$\Delta\text{SOC}_c^{[\#]}$	$\Delta\text{SOC}_L^{[\S]}$	$\Delta\text{SOC}^{[+]}$	$\Delta\text{SOC}_c^{[\#]}$	$\Delta\text{SOC}_L^{[\S]}$	$\Delta\text{SOC}^{[+]}$	$\Delta\text{SOC}_c^{[\#]}$	$\Delta\text{SOC}_L^{[\S]}$
[%]	[%]	[%]	[%]	[%]	[%]	[%]	[%]	[%]	[%]
1.01 ± 0.04	0.65 ± 0.61	0.65 ± 0.62	0.58 ± 0.55	0.41 ± 0.34	0.45 ± 0.36	0.35 ± 0.27	2.62 ± 2.00	2.45 ± 1.93	2.43 ± 1.81
5.03 ± 0.03	0.44 ± 0.32	0.44 ± 0.30	0.40 ± 0.40	0.66 ± 0.26	0.61 ± 0.25	0.51 ± 0.55	1.34 ± 1.32	1.37 ± 1.41	1.36 ± 1.45
25.02 ± 0.01	1.37 ± 1.18	1.15 ± 1.35	1.12 ± 1.59	1.15 ± 0.83	1.59 ± 1.29	0.57 ± 0.43	3.38 ± 1.37	2.19 ± 1.56	2.03 ± 1.33
50.00 ± 0.03	1.20 ± 0.32	0.90 ± 0.58	0.52 ± 0.27	0.90 ± 0.68	1.29 ± 0.60	0.96 ± 0.94	1.20 ± 1.57	1.17 ± 1.42	1.76 ± 0.49
74.98 ± 0.03	1.23 ± 0.29	1.01 ± 0.51	0.23 ± 0.18	1.68 ± 1.08	2.07 ± 1.52	0.71 ± 0.90	1.74 ± 1.53	1.68 ± 1.46	1.20 ± 0.86
95.00 ± 0.03	0.32 ± 0.26	0.33 ± 0.27	0.39 ± 0.21	0.44 ± 0.29	0.48 ± 0.42	0.58 ± 0.11	4.41 ± 1.94	4.77 ± 2.76	4.57 ± 2.42
98.99 ± 0.03	0.39 ± 0.21	0.40 ± 0.21	0.45 ± 0.24	0.06 ± 0.02	0.04 ± 0.01	0.13 ± 0.02	2.24 ± 1.35	2.38 ± 1.51	2.41 ± 1.52
RMSD	0.90	0.76	0.59	0.91	1.15	0.60	2.65	2.54	2.48

^[a] Average of three separately prepared sample batches and their standard deviations (batch 1 to 3).

^[b] Prepared by dilution of 400 mM sample (batch 3).

^[c] Prepared by dilution of 400 mM sample (batch 4).

^[+] Calculated from equation (4-5) using the assumption $D_O D_R^{-1} = 1$.

^[#] Calculated from equation (4-9) using the slope of the $i_{l,c}$ vs. $i_{l,a}$ regression line as estimate for $D_O D_R^{-1}$ in each repetition.

^[§] Calculated from equation (4-5) using the average literature value of $D_O D_R^{-1} = 1.07 \pm 0.07$.^[70]

In comparison to the 100-fold more expensive SMU, the self-made MMU revealed only a slightly lower accuracy in the commercially more relevant higher concentrations of 0.4 and 0.2 M. With deviations below 1%, the RSMD of the SOC measurement is expected to be sufficiently low for the online evaluation of the electrolyte SOH in an operating RFB. Only the measurements of lower concentrated samples of 0.1 M showed significantly larger RMSDs of approximately 2.5%. However, the uncertainties are still lower in comparison to the first study or the current state of the art.^[69]

After the methodical optimization of the setup and the validation of the MMU, the electrolyte SOC, electrolyte SOH, and the electrolyte capacities of both half-cells in an operating unbalanced compositionally symmetric (UCS) RFB utilizing 1.3 M of TMA-TEMPO (CLS: 17 mL posolyte, NCLS: 24 mL negolyte) were monitored. Herein, the improved amperometric method utilizing MMUs was benchmarked against the commonly applied open circuit voltage (OCV) cell method.^[19] To overcome possible reference potential shifts in the OCV data, the cells were recalibrated in every half cycle according to recently published procedures.^[19, 71]

In a first experiment, the UCS-RFB was cycled for 17.5 consecutive cycles. In order to demonstrate the application possibilities of the amperometric method, three different cycling modes were investigated:

- (1) Complete galvanostatic cycling (CGC) (mostly used for realistic long-term test or industrial applications, cycles 1, 2, 5 to 15),
- (2) incomplete galvanostatic cycling (IGC) (mimic realistic conditions *e.g.*, incomplete charging during the day, cycles 3, 4, and 16),
- (3) mixed galvanostatic and potentiostatic cycling (mostly used in stability investigation during research and development, cycles 0 and 16).

The SOC data for the posolyte (*i.e.*, the CLS) during **complete galvanostatic cycling** (cycles 1, 2, 5 to 15, white background) showed an absolute RMSD of 0.6% to the OCV cell, which represents a three-fold lower statistical variation in comparison to the first study. Nevertheless, the situation for the negolyte differs a bit. Here, a RMSD of 2.5% was observed between the OCV and the amperometric method (*cf.* **Figure 4.1d**). However, the stated RMSD values do not represent the deviation from the true electrolyte SOC but the deviation between the two compared methods and, thus, the cause for the observed higher deviation could be due to either of the two methods. The main differences between the measurement of the negolyte and posolyte is the addressed SOC. While the CLS (posolyte) was cycled between approx. 0% and 100%, the NCLS addressed only 70% of its overall available capacity (*cf.* **Figure 4.1a**).

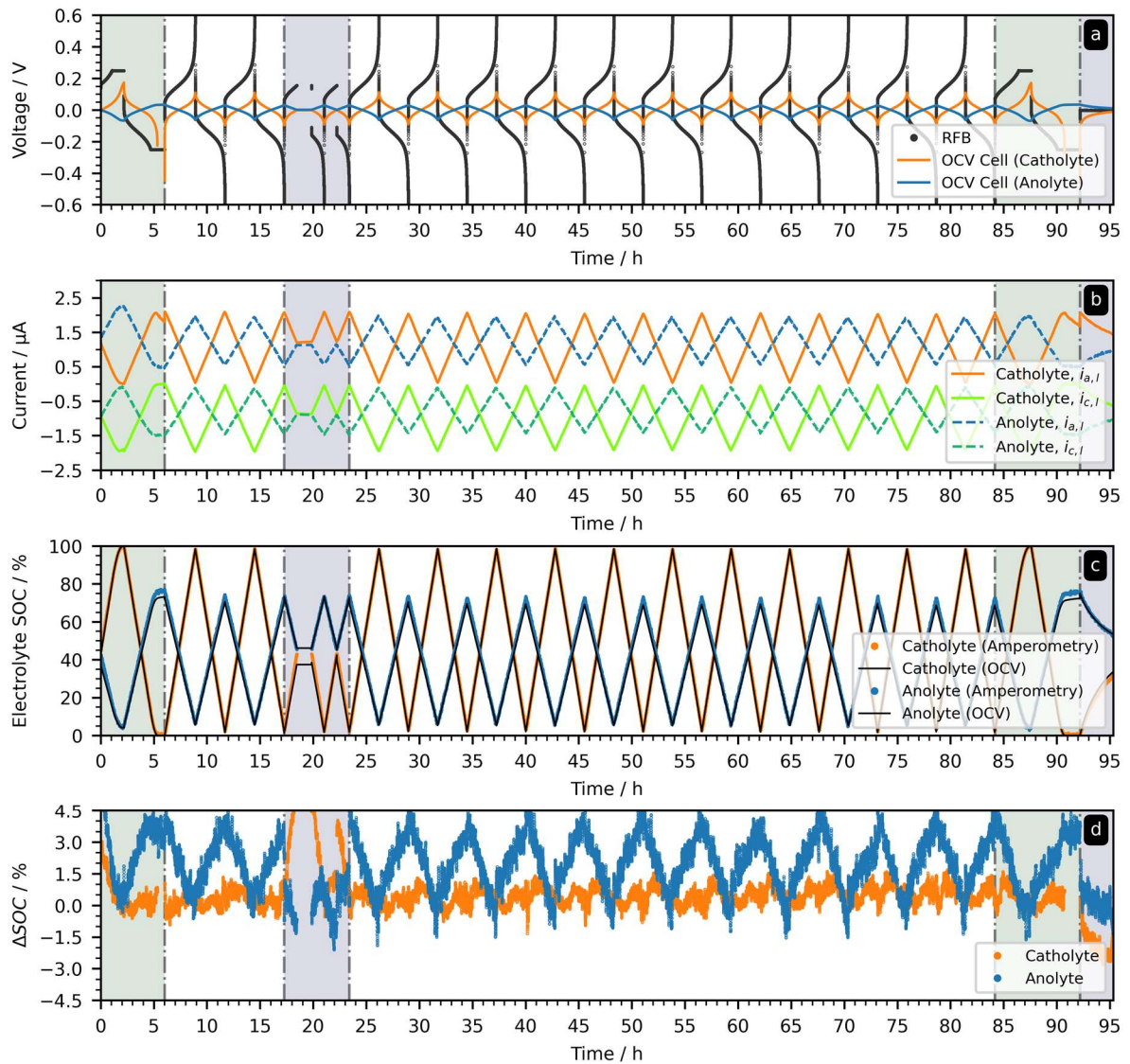


Figure 4.1: Results of the online monitoring of both posolyte (17 mL) and negolyte (24 mL) in a compositionally symmetric, unbalanced aqueous RFB with 1.3 M TEMPTMA in three different cycling modes (green background: mixed galvanostatic and potentiostatic; blue background: incomplete galvanostatic cycling; white background: complete galvanostatic cycling): (a) Cell voltages of the RFB and the symmetric OCV cells used for measuring SOC reference values, (b) the mass-transfer limited currents at the microelectrodes obtained via the microcontroller-based measurement units, (c) the SOC values obtained by both the OCV cell and the amperometric method, and (d) the absolute difference between the SOC values of both methods. In the time range from 18 h to 20 h the experiment was paused to check the data on the MMU (no data recorded in that range). (The figure was taken from P6).^[72]

This has a direct impact on the recalibration of the OCV cells, which relied on a non-linear regression based on the Nernst equation. It was found in this study that an incomplete cycle results in a lower quality of the fit and, as a consequence, in lower accuracies of the received SOC and capacity data. Thus, the larger deviations of the negolyte compared to the posolyte do not originate from the amperometric approach but are linked to the limitation of the OCV cell method.

The measurement of the SOC data for **incomplete galvanostatic cycling** (cycles 3, 4 and 16, blue background) suffers from the same problems as the negolyte during CGC. Both the posolyte (2.5% to 42%) and the negolyte (44% to 73%) do not use the available SOC range (*cf.* **Figure 4.1d**) resulting in higher RMSD (posolyte 2.3% negolyte 0.7%), which supports the previous reasoning.

Mixed galvanostatic and potentiostatic cycling exhibits two deviations from the expected outcome:

- (1) For $SOC < 0.5\%$, the OCV cell data exhibited a deviation from the exponential slope (**Figure 4.2a**).
- (2) For $SOC < 0.5\%$ and $SOC > 99.5\%$, the mass-transfer limited currents on the posolyte side deviated from the expected linear behavior (*cf.* **Figure 4.2b**, orange line on green background).

The first anomaly is linked to the existence of a second redox couple as indicated by the second plateau between -0.20 V and -0.15 V (*cf.* **Figure 4.2a**). The most plausible explanation for this would be the earlier described hydroxylamine-radical couple resulting from the TMA-TEMPO degradation, causing a small offset of the fit curve (*cf.* inset **Figure 4.2a**). The second anomaly is linked to the natural shift of the counter electrode's equilibrium potential with changing SOC in the two-electrode setup as well as the increasing concentration overpotential for the reaction at the microelectrode. Both effects are mainly visible at extreme SOC's and, thus, the values for $SOC < 0.5\%$ are omitted from the fit for the OCV cell data. With that, the RMSD between the approaches are in agreement with the prior findings (RMSD: posolyte 0.7%, negolyte 2.6%). Again, the higher deviations in the negolyte are mainly caused by the aforementioned problems of the OCV cell method with insufficient SOC ranges.

After the amperometric approach could show its capability of measuring the SOC with high accuracy, its capability to simultaneously measure the electrolyte capacity was investigated. Herein, the SOC as obtained by the amperometric sensors was plotted against the transferred charge, ΔQ , for the same half-cycle (*cf.* **Figure 4.2b**). According to equation (4-6) the electrolyte capacity, Q_{max} , can be obtained from the slopes of the ΔQ -SOC-curves. Regardless of that, the capacity was also calculated from the OCV data (*cf.* **Figure 4.2a**). In **Figure 4.2c** and **Figure 4.2d** both values were compared to the expected electrolyte capacities (green line) and the battery capacity measured by the transferred charge in the RFB (black).

Over all three cycling modes, the amperometric approach determines the electrolyte capacity with an average of 576 ± 3 mAh (posolyte) and 820 ± 7 mAh (negolyte). The relative RMSD from the expected capacities for posolyte (575 ± 12 mAh) and negolyte (812 ± 16 mAh) is

below 1%. Again, the OCV cell approach suffers from its inherent problems when not the full SOC range is available for fitting. In general, the posolyte capacity (579 ± 20 mAh) was estimated with a relative RMSD of below 1% (except for the IGC where uncertainties of over 6% (611 ± 43 mAh) were observed). A similar behavior is visible for the negolyte capacity (868 ± 18 mAh) which deviates by approximately 6.7%.

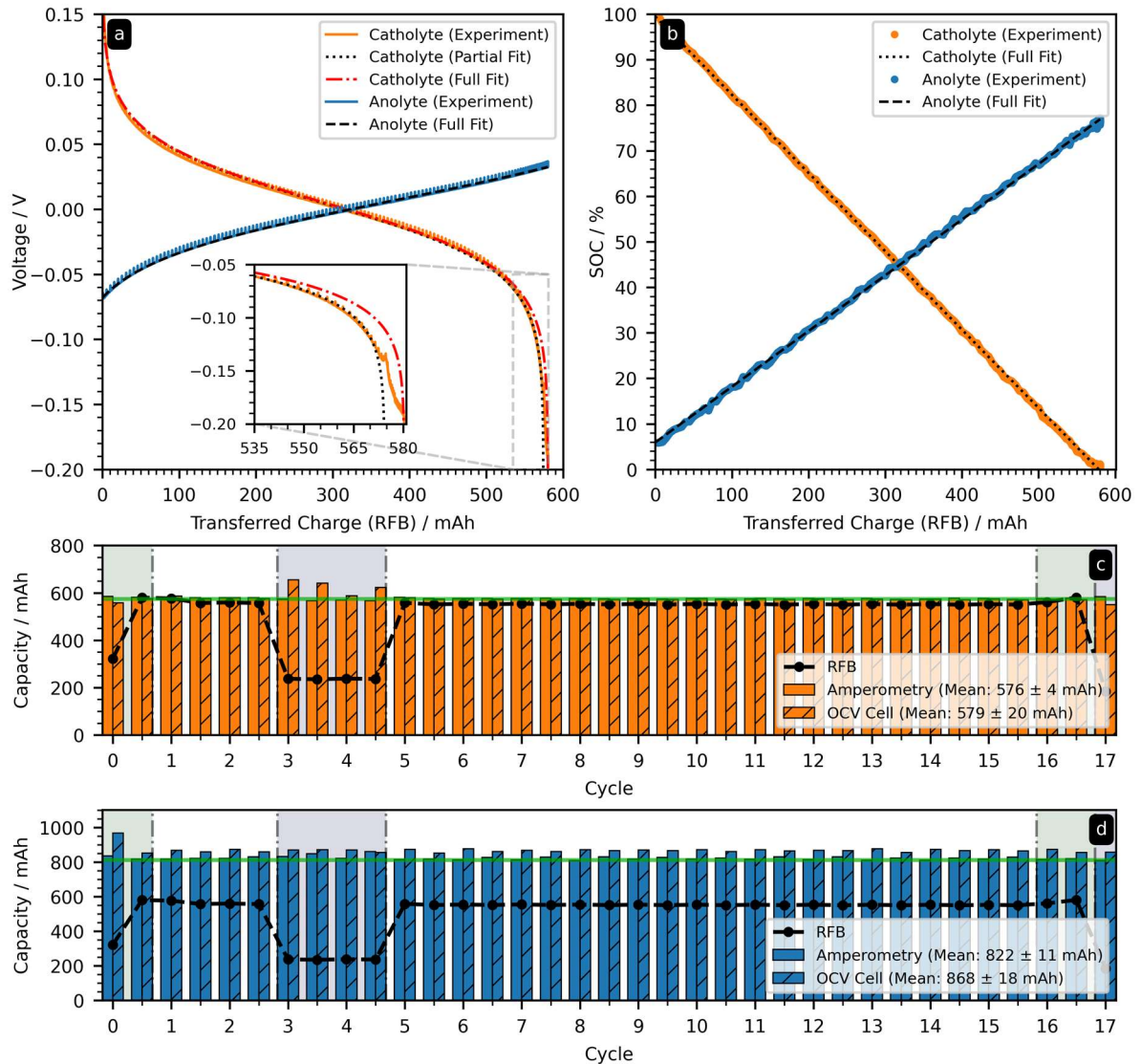


Figure 4.2: Online electrolyte capacity monitoring for the different cycling modes (background colors indicate: Mixed galvanostatic and potentiostatic (green); incomplete galvanostatic cycling (blue); complete galvanostatic cycling (white)): (a) OCV cell voltage over transferred charge for exemplary half-cycle and corresponding fit curves (inset: Deviation indicates a second species); (b) amperometric SOC over transferred charge for capacity measurement; (c) posolyte capacities per half-cycle (amperometric and OCV cell method); (d) negolyte capacities per half-cycle (amperometric and OCV cell method). Red lines in (c) and (d) represent the expected values (posolyte: 575 ± 12 mAh, negolyte: 812 ± 16 mAh). Numbers in the legends represent the average and the standard deviation of all cycles. Discharging half-cycles are indicated as non-integer values. (The figure was taken from P6).^[72]

In a last step, the accuracy of the electrolytes SOH determination was investigated. The most common causes for a decrease of the electrolytes' SOH are side/decomposition reactions or electrolyte leakages. In both cases, the overall available active material and, thus, the battery capacity is reduced. To mimic active material loss due to leakages, aliquots were consecutively extracted once a day from the electrolyte. The volume of the aliquots corresponded to approximately 3.44% of the posolytes initial capacity. Since the amperometry in principle enables two possibilities to calculate the SOH, both were compared to each other.

- (1) SOH calculation *via* determining the ratio of the electrolyte capacities in the different cycles, equation (4-7).
- (2) SOH calculation directly from the slope of a linear regression of the SOC^0 vs. SOC^n plot, equation (4-8).

To estimate the accuracy of the amperometric approaches, the method was benchmarked against the OCV cell protocol. Once again, the amperometric measurement delivers highly accurate values, this time for the SOH of both the posolyte and the negolyte. Both approaches are equally accurate and deliver relative RMSD to the expected value of around 1% (*cf.* **Figure 4.3**). The OCV cell approach in comparison shows similar RMSD for the posolyte but overestimations of up to 7.3% for the negolyte. The reasons are again the incomplete fit data for the OCV cells. In a final experiment for SOH determination, the loss of active material due to decomposition should be simulated. Herein, an aliquot of electrolyte was extracted, and the loss of volume was compensated by adding equal amounts of deionized water. However, the two amperometric evaluation approaches deliver similar accuracies for both the posolyte and the negolyte while the OCV method overestimates the negolyte (*cf.* **Figure 4.3**, grey background).

In final tests the independence of the amperometric approach to elevated temperatures of up to 40 °C as well as the long-term application possibilities (103 cycles over 19 days) were investigated. Under these conditions, the amperometry revealed excellent accuracies with RMSD below 0.5% at 40 °C and 0.6% during long-term testing as well. These results underline the reliability, robustness, and accuracy of the amperometric method for co-estimation of SOC, SOH, and capacity of a redox flow battery electrolyte.

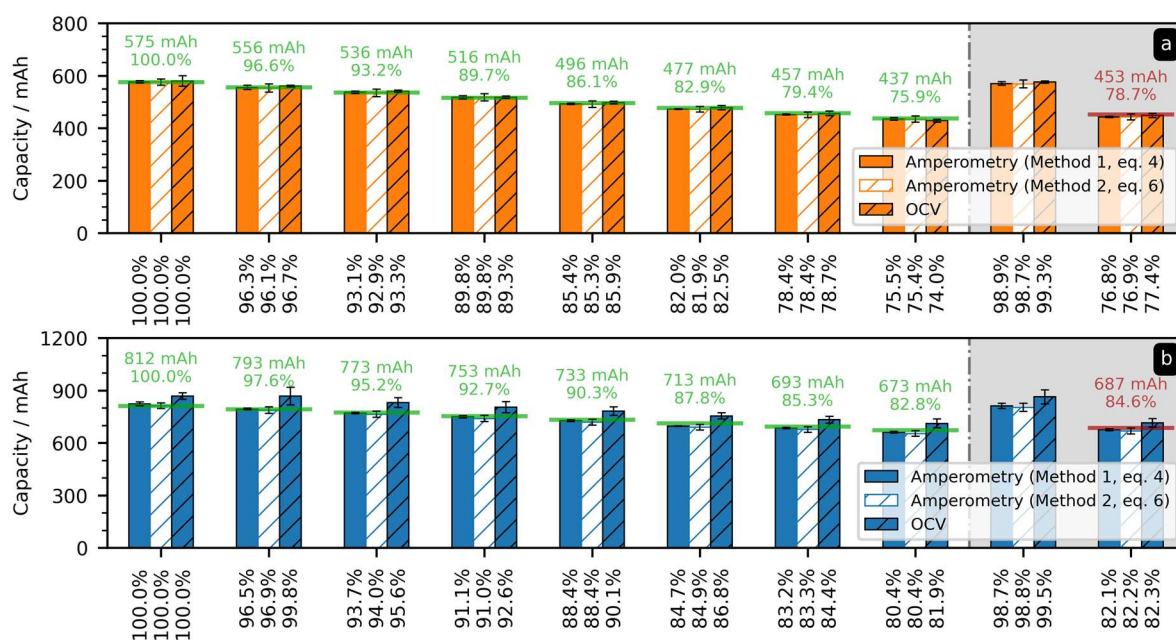


Figure 4.3: Absolute capacity (left axes) and state-of-health values (bottom axes) of both electrolytes determined *via* the amperometric and the OCV cell method after extraction of defined electrolyte aliquots from each tank of the compositionally symmetric, unbalances RFB (1.3 M TEMPTMA). The green values represent the expected values calculated from the measured aliquot masses, electrolyte density, and volumetric electrolyte capacity. All experimental values represent the average of four consecutive cycles and the error bars represent their standard deviations. For the left bar group with grey background all aliquots were filled back to the tanks (no reference value given due to the unknown loss of some microliters of electrolyte during aliquot investigation and refilling). For the right bar group, 3.4 mL of electrolyte were extracted and exchanged with distilled water (red reference value is based on the average SOH values of the left bar group). (The figure was taken from P6).^[72]

4.3 Inexpensive microelectrodes for amperometric SOC, SOH, and capacity co-determination

Parts of this chapter will be published in P6: *A low-cost amperometric sensor for the combined state-of-charge, capacity, and state-of-health monitoring of redox flow battery electrolytes*, C. Stolze, P. Rohland, K. Zub, O. Nolte, M. D. Hager, U. S. Schubert, *Energy Convers. Manag.* **2022**, *14*, 100188. P7: *Inkjet-printed microband electrodes for a cost-efficient state-of-charge monitoring in redox flow batteries*, K. Zub, C. Stolze, P. Rohland, S. Stumpf, S. Hoepfner, M. D. Hager, U. S. Schubert, *Sens. Actuators B Chem.* **2022**, accepted.

The improved amperometric approach towards SOC, SOH and capacity determination showed great potential to become the new state of the art protocol since it is applicable to many electrolytes and does not need difficult mathematic methods or recalibration. Furthermore, it is reliable over a longer measuring time and temperature-independent. But most of all, it does not require cost intensive measuring devices. The above shown MMU based on an Arduino microcontroller has an overall cost of 56.22 € (incl. German VAT, 19%), but without the unnecessary parts like expensive control boards and monitors the price drops to 19.07 € (incl. German VAT, 19%) for a single device (around 40 € for a monitoring both electrolytes). This

represents a significant cost reduction in comparison to the 100-fold more expensive SMU. As a consequence, the most cost-intensive part of the approach is the required microelectrodes. Commercially available electrodes with the required dimensions range in a price segment of over 300 €, increasing the MMU price by one order of magnitude. The development of cheap and reliable microelectrodes has, therefore, a high priority with regard to the amperometric SOC and SOH measurements. Various approaches for the manufacturing of microelectrodes are known from the field of biosensors^[73] or the field of bipolar electrochemistry.^[74]

The main reason for the high prices of commercial microelectrodes is the high quality standards they have to fulfill, *i.e.* in particular the reproducibility of the electrode surface area. Since the amperometric SOC determination is rather robust against these criteria, the manufacturing of new electrodes is comparably uncomplicated. However, one of the greatest challenges is the establishment of a reliable electric contact between the microfiber and a macroscopic current collector for the connection to the potentiostat. In a recent publication, the possibility of a SOC measurements using a bipolar setup gave the starting point for an alternative microelectrode type.^[69] ^[75] Herein, a graphite rod is placed into a tube filled with a SOC 50% of the analyte solution (*cf.* **Figure 4.4a**). The electrode is sealed at the bottom with a carbon fiber embedded in an insulating medium like epoxy resin, where the fiber protrudes into the SOC 50% electrolyte. When placed into an analyte solution with an counter electrode and if a voltage is applied, the overall current flow between this so-called backfilled, bipolar microelectrode (BBME) is limited by the surface area of the fiber tip, while the complementary electrochemical reactions at the longer end of the microfiber and the graphite rod inside the tubing enable a passage of current through the system without establishing a direct electrical contact (*cf.* **Figure 4.4a**). This BBME is a miniaturized version of the previously used bipolar setup^[69, 75] but can be handled and used as any other microelectrode, while the overall material costs of the BBME were estimated to be at around 2 € per unit.

When applied to 1.3 M TMA-TEMPO electrolytes, the BBME delivers accurate SOC values with RMSD of 1.9% (posolyte) and 2.2% (negolyte) over the first four cycles in an operating RFB. However, then the error increases rapidly. In particular the results for the negolyte exhibit string deviations from the expected values (RMSD over 12%), which get less precise with increasing cycle numbers. The main reason for this, is the extreme decay of the mass-transfer limited currents (*cf.* **Figure 4.4d**) which indicates a significant surface change during the electrochemical reactions. This assumption is supported by the fact that the decay was reversible when the electrode surface was polished. The isolating material may either interfere with the highly oxidative TEMPO electrolytes or contaminate the fiber over time. In addition

to that, SEM investigations of the microelectrode tip (*cf.* **Figure 4.4c**) revealed that the fiber is not tightly embedded in the resin, resulting in a non-planar and rod like microelectrode surface circumventing the amperometric microdisc SOC determination approach.

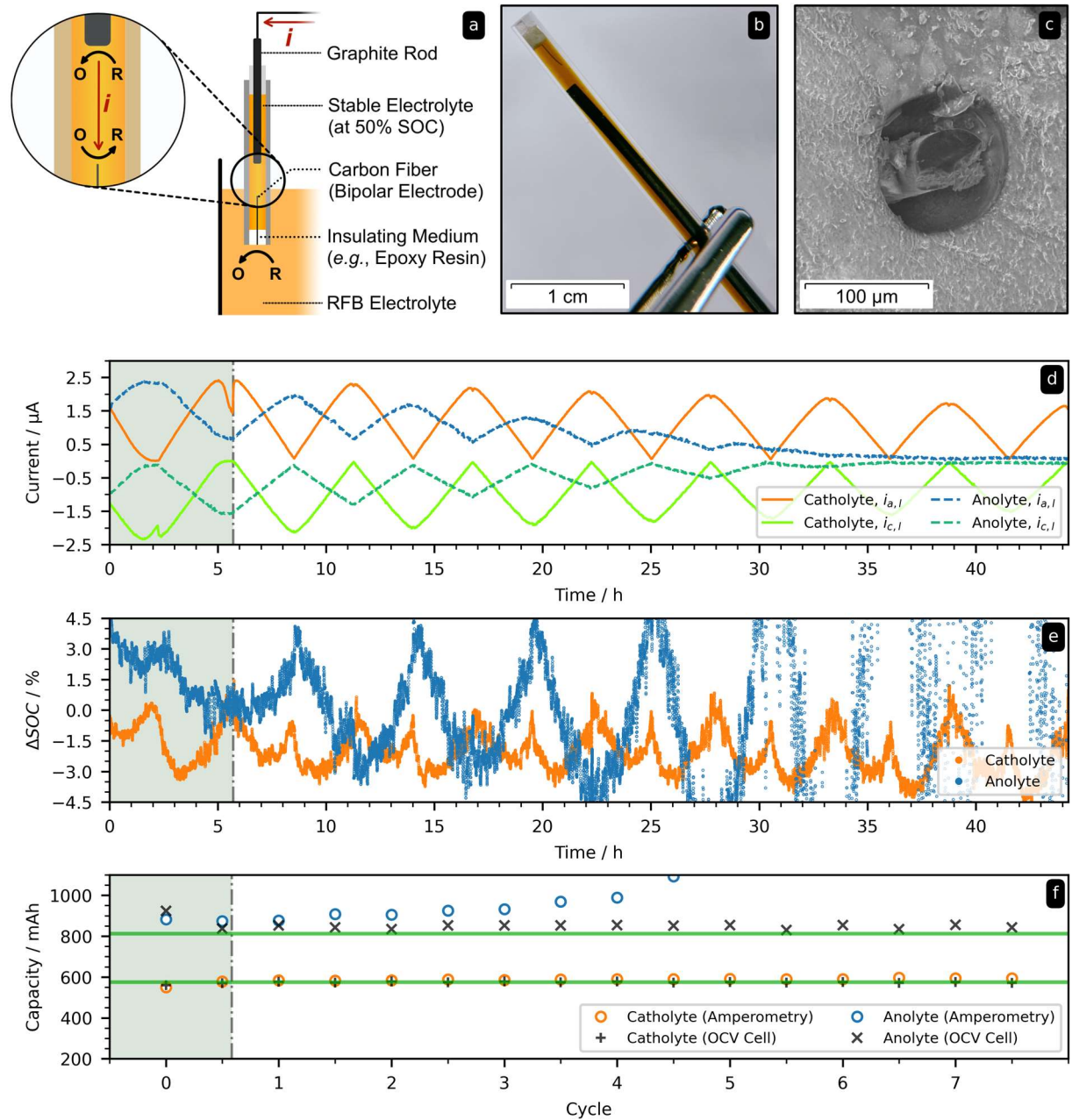


Figure 4.4: (a) Schematical representation of a bipolar, back-filled microelectrode (BBME) illustrating the construction and the bipolar working principle; (b) photograph of a BBME with carbon fiber, graphite rod (1 mm), and 1.3 M TEMPTMA (42% SOC); (c) scanning electron micrograph of the BBME tip showing the carbon fiber surrounded by epoxy resin; (d) mass-transfer limited currents of the two BBMEs utilized for online monitoring of the symmetric TEMPTMA RFB; (e) SOC difference between amperometric and OCV cell SOC; (f) capacity estimates of both the amperometric and OCV cell method (green line: Expected values). (The figure was taken from **P6**).^[72]

Further investigations and improvements during the manufacturing process must be achieved to obtain BBME with sufficient stability. Nevertheless, the recent results confirm two things:

- (1) The bipolar electrochemical mechanism can replace the direct electrical contacting of the carbon fiber,
- (2) the BBME can deliver accurate SOC as well as capacity measurements.

Due to the current limitations of the developed BBME, an alternative approach to produce microelectrodes was investigated. So-called microband electrodes (MBE) are characterized by a microscopic scale in one dimension (width) and a macroscopic scale in a second dimension (length). The advantage is larger electrode surface and, thus, higher current response while maintaining a quasi-stationary behavior. Furthermore, these electrodes can be simply produced in a sandwich style approach where a conducting material (mostly metals) is embedded in an isolator so that only one edge is exposed to the electrolyte. Currently, they are primarily manufactured by placing a metal foil between two glass plates, but since many usable metals are rather expensive, the use of small amounts of metals is preferable. Inkjet-printing or sputtering of the electrodes would allow the economic usage of small amounts of metals in combination with a fast production technique with high spatial resolution.

In this thesis, a polyamide carrier material was firstly cleaned and then printed with a thin layer of platinum ink (*cf.* **Figure 4.5**). After heating the preliminary electrode to evaporate the solvent of the Pt ink, an insulating layer was printed on top. The final step was the irradiation with UV light to harden the insulating layer. To produce the MBE, the tip is cut off to expose only a thin line-like structure the electrode material. SEM revealed that the overall thickness of the microelectrode is around 300 nm (*cf.* **Figure 4.5**). To get a more detailed overview of the influence of the thickness of the Pt layer also sputtered samples with 100 nm and 40 nm were produced.

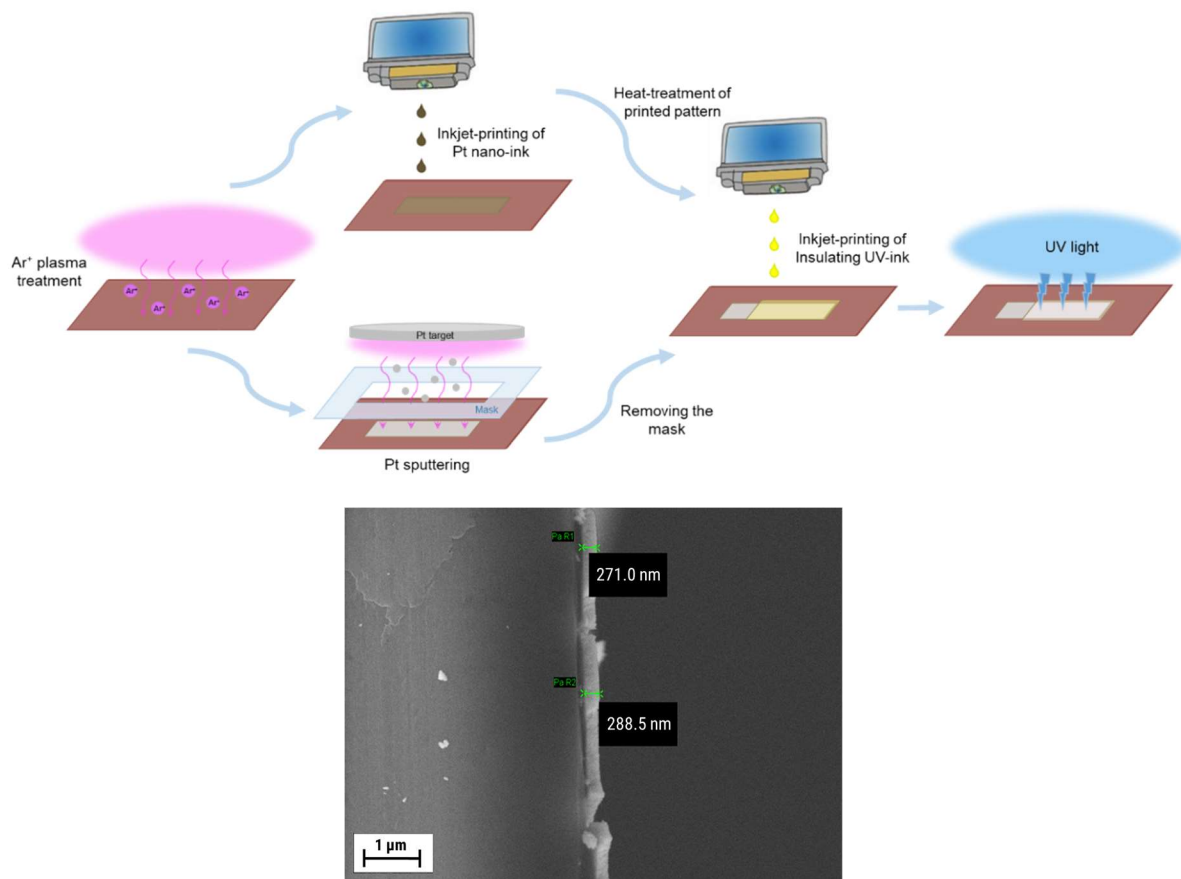


Figure 4.5: Schematic representation of the inkjet-printed / sputtered samples after the tip has been cut off to prepare the microband electrode. The width is in the nanometer range (< 250 nm) and the length in the millimeter range (2.5 mm). (The figure was taken from P7).^[76]

Subsequent to the qualitative evaluation (CV), the electrodes were used for SOC determination utilizing the amperometric approach detailed in the previous section. The ratio of the diffusion coefficients, $D_O D_R^{-1}$ where either set to 1 or 1.07 ± 0.07 as the average of the literature values reported by Konopka^[70a] and Amatore^[70b] for the ferri/ferrocyanide redox couple. Here, the sputtered electrodes with a thickness of 100 nm and the inject printed (300 nm) are in excellent agreement with the true SOC values of the samples with RMSD of below 1% (*cf.* **Table 4.5**), which is equal to the commercial electrodes used in **Chapter 4.2**. In contrast to that, the sputtered electrodes with 40 nm thickness revealed higher deviations with a RMSD of around 3%. This can be attributed to an increased electrical resistance which is connected to the lower thickness of the sputtered samples. However, this RMSD of 3% is also on par with the accuracy of state-of-the-art SOC measurement approaches like the OCV cell and the spectroscopic methods.^[77] This shows the great potential of inkjet-printed and sputtered MBE for amperometric SOC determination. Furthermore, with overall costs of 2.50 € for the self-made

MBE, they are by two magnitude cheaper than commercial microelectrodes (around 350 €), which enables a cost-efficient application in commercial battery management.

Table 4.5 SOC measurement results for samples of different SOC of the 0.4 M ferri-/ferrocyanide in 0.5 M KCl(aq) solutions as obtained from the mass-transfer limited currents at the sputtered and inkjet-printed microband electrodes. $\Delta SOC \equiv SOC - SOC_{ref}$ represents the absolute deviation of the measurement value from the true SOC of the sample. The ΔSOC values are the average of measurements with three electrodes of the same type and its standard deviation.

$SOC_{ref}^{[a]}$	Sputtered, 100 nm		Sputtered, 40 nm		Inkjet-printed	
	$\Delta SOC_1^{[b]}$	$\Delta SOC_{1.07}^{[c]}$	$\Delta SOC_1^{[b]}$	$\Delta SOC_{1.07}^{[c]}$	$\Delta SOC_1^{[b]}$	$\Delta SOC_{1.07}^{[c]}$
	[%]	[%]	[%]	[%]	[%]	[%]
99.01	0.52 ± 0.12	0.62 ± 0.13	0.28 ± 0.12	0.37 ± 0.15	0.36 ± 0.37	0.45 ± 0.39
95.00	0.51 ± 0.61	0.88 ± 0.65	0.46 ± 0.61	0.38 ± 0.09	0.29 ± 0.15	0.11 ± 0.07
75.02	0.90 ± 0.20	1.72 ± 1.03	2.84 ± 0.20	1.65 ± 1.19	0.44 ± 0.61	0.84 ± 0.63
50.00	1.16 ± 0.42	0.53 ± 0.42	4.40 ± 1.20	2.72 ± 1.21	1.48 ± 1.44	1.15 ± 0.42
25.00	0.70 ± 0.40	0.83 ± 0.76	5.60 ± 3.54	5.02 ± 2.20	0.88 ± 0.48	2.09 ± 0.46
5.02	0.66 ± 0.62	0.51 ± 0.30	2.16 ± 0.97	1.93 ± 0.68	0.25 ± 0.17	0.24 ± 0.18
1.02	0.79 ± 0.28	0.68 ± 0.26	0.92 ± 0.79	0.84 ± 0.67	1.04 ± 1.16	0.91 ± 1.09
RMSD	0.78	0.91	3.04	2.39	0.80	1.04

^[a] Reference value calculated from the known molar masses and measured weights of the dry substances. Absolute uncertainties of the reference values are below 0.0003% according to Gaussian error propagation.

^[b] Calculated from equation (4-5) using $D_O D_R^{-1} = 1$.

^[c] Calculated from equation (4-5) using $D_O D_R^{-1} = 1.07 \pm 0.07$ as obtained from literature values.^[70]

5 Summary

To reach the political aims of the Kyoto Protocol and the Paris Agreement, the energy production must change from fossil fuels to sustainable sources like water, sun, and wind. But the fluctuation output of these techniques must be compensated by a smart grid. Herein, the integration of large-scale energy storage systems is inevitable. The possibility to use cheap organic molecules in “green” and non-toxic electrolytes make the emerging technology of organic redox flow batteries a promising candidate for this mission. Nevertheless, this battery concept suffers from many problems. One of the major ones is the insufficient stability of the active materials. To overcome this technical teething trouble, a combination of material and sensor development to investigate and mitigate decomposition processes is required. But currently, the research is more focused on development of new redox-active molecules with intrinsically higher stabilities than on investigating, understanding, and improving the underlying processes. Beside some exceptions, most research groups concentrate on demonstrating stabilities by cycling the material as often as possible. In addition, the influence of the used SOC of the battery is mostly uninvestigated. A battery management system which might limit the used SOC could improve the device lifespan. Therefore, precise, fast, and cheap monitoring systems for SOC and SOH determination are needed. The commonly applied techniques suffer from major drawbacks, like expensive equipment, material limitations, temperature dependency, and the need for (re)calibrations to name only a few. A protocol that is capable of monitoring these parameters on the electrolyte level and not on the battery level could unlock a deeper understanding of the ongoing processes inside the device or electrolyte. Possible device lifespan improvements could then not only be addressed by the material itself but also by the cycling conditions or other external factors.

In this thesis, TMA-TEMPO as the forerunner molecule on the polysolite side of all organic RFBs was investigated in detail (*cf.* **Figure 5.1**). At first, a fundamental understanding of the ongoing processes during the decay of the active material was investigated. Herein, different GC-HRMS techniques and isotopic labeling were used to identify the key intermediates and a decomposition mechanism could be proposed. Interestingly, the major side product is the corresponding hydroxylamine, which can be reoxidized to the radical, reducing the decomposition rate by 75%. But if the mainly applied pure cycling procedures would have been utilized, this reduction-reoxidation mechanism would only barely be noticeable. This led to the utilization of the adapted cycling protocol introduced by Aziz *et al.*, comprising cycling in galvanostatic and potentiostatic mode in combination with hold times in vulnerable states of charge and at elevated temperatures.

Summary

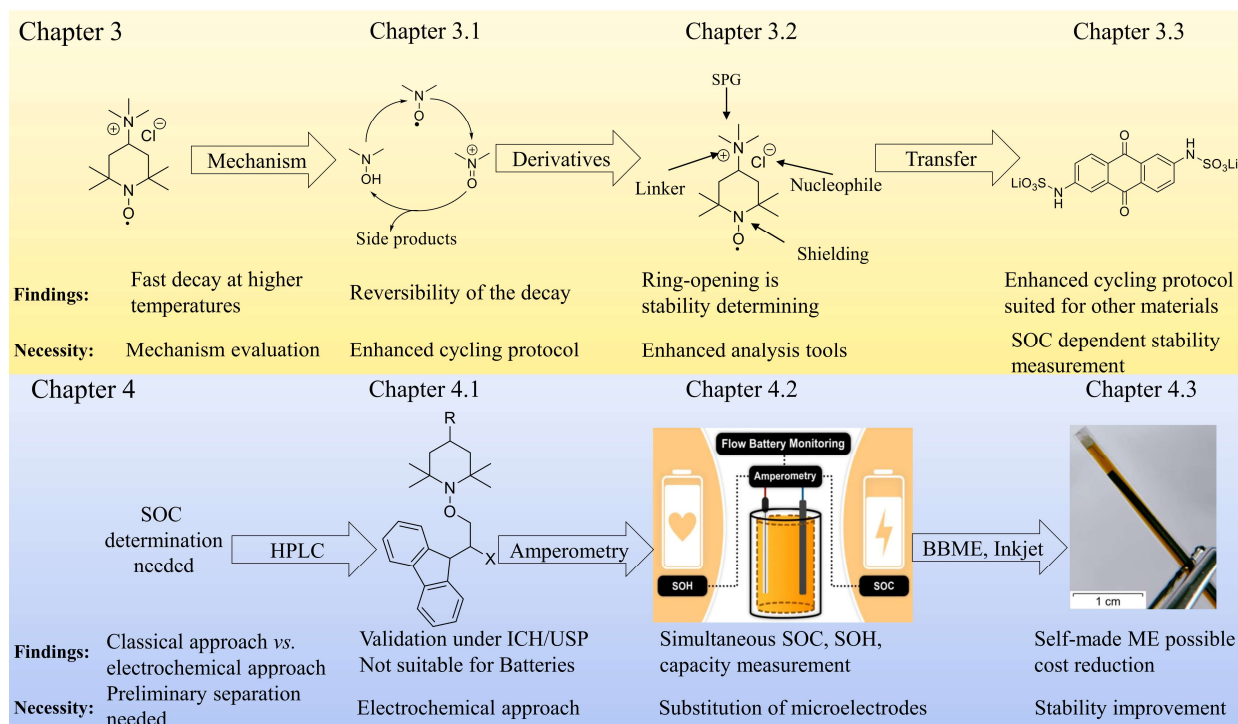


Figure 5.1: Schematic representation of the content of this thesis.

The formation of side products, originated from the vulnerable state, is then visible by a capacity drop after the hold time. In the case of TMA-TEMPO this drop can be partially healed due to the reversibility of the radical reduction to the hydroxyl amine. However, the experiments demonstrate a complex dependency of the decay on the temperature, the concentration, and the SOC. The latter could not be further addressed since the available analytical tools were not capable of determining the electrolyte SOCs with sufficiently high accuracy in an operating RFB at the time of the study. This shows the need for advanced sensors and determination procedures, which were the subject of the next chapter of this thesis.

However, the deeper understanding of the TEMPO decay mechanism allows new possibilities for material development. The decomposition can start with three reactions. The first is a ring opening reaction, which could be hindered by an enhanced shielding of the radical moiety. The second is a Hoffman-like elimination of the SPG. This could be prevented by the introduction of a linker between the piperidyl ring and the SPG. The last starting reaction is the elimination of a chloromethane from the TMA-SPG. Here the nucleophilicity of the counter ion or the nature of the SPG may play an important role. To prove the assumptions, six TEMPO derivatives were synthesized and compared. Each of these derivatives was intended to study at least one of the named starting reactions. Herein, the new cycling protocol was used to test the derivatives under comparable stress conditions. It turned out that all the new molecules showed lower or comparable stabilities compared to TMA-TEMPO. The results of this thesis indicate

that the ring opening reaction is the stability-limiting reaction in the decomposition cascade. An increase in the life span of the TEMPO moiety should, thus, be addressed by the stabilization of the C-N bond adjacent to the radical. This can either be done by substituents vicinal to the named bond or by the introduction of groups with inductive effects in 4-position.

To further exemplify the transferability of the new cycling protocol, a new anthraquinone negolyte was synthesized and tested. Besides the fast and straight forward synthesis procedure, starting with cheap commercial educts and reagents, the anthraquinone has also the advantage that it yields one of the most stable negolytes investigated so far (decay $0.18\% \text{ d}^{-1}$) and the most stable at elevated temperatures of $60\text{ }^{\circ}\text{C}$ (decay $0.17\% \text{ d}^{-1}$). Furthermore, the material is also capable of delivering high-rate capabilities of 40 mA cm^{-2} with high solubilities of up to 0.75 M in water. But the experiments also indicated the usual dependency of the stability on the SOC, underlining the need for reliable, fast, accurate, and widely applicable monitoring procedures for SOC and SOH.

The second part of the thesis deals with the development and improvement of analyzing tools for the accurate SOC and SOH determination (*cf.* **Figure 5.1**). Classical determination methods have problems discriminating between the oxoammonium cation and the radical of the TEMPO species. Thus, a preliminary separation between the species is required. HPLC as standard separation technique for water soluble analytes would target this mission. But due to the high reactivity of the cation and its highly corrosive nature, a derivatization reaction was used to transfer the cation into a more stable and analyzable species. After critical evaluation of the derivatization process, the developed protocol was used to analyze three different TEMPO derivatives. To open the HPLC method not only to the battery community but also to pharmacists and organic chemists, each of the model substances represents one of the most-used TEMPO derivatives in the respective field. Furthermore, the protocol was validated under application of the ICH and USP guidelines. The results demonstrated a general applicability of the method but with limitations. High amounts of radical (over 30%) disturbed the accuracy of the measurement. This might be acceptable for pharmacist or organic chemists who aim for the measurement of the OC content in a drug or a reaction sample. But it is not sufficient for the battery community, where the cation to radical ratio is between approx. 99:1 and 1:99. The switch to electrochemical analysis methods was than required although the method is than focused to the battery community and electrochemists. The starting point for the electrochemical analysis tool was the recently published amperometric approach of Stolze *et al.*, in which the SOC is a function of the ratio between the current response when an anodic and cathodic voltage is applied at a mass-transfer limiting electrode. In its original form, the

amperometric method suffered from the need for expensive equipment and complex measuring setup. However, in this thesis it was shown that the general approach is also functional with cheap self-build microcontroller measurement units and a simplified setup with microelectrodes. In sum, the overall costs are lowered by a factor of 100 while simultaneously increasing the accuracy of the SOC measurement on the electrolyte level to an absolute error of below 1%. The cost reduction enables the building of two sensors, simultaneously monitoring both electrolytes of a running RFB. In the process, the superiority of the new approach in comparison to the current forerunner based on OCV cells was shown and validated. The method not only allows the measurement of the SOC with unprecedented precision but also the determination of SOH and capacity *in situ* in an operating RFB. Furthermore, the method is robust against temperature changes and does not need time-demanding recalibration. Its remaining limitation is the need for cost-intensive microelectrodes. As a consequence, new back-filled, bipolar microelectrodes were investigated as part of this thesis and compared to commercial microelectrodes with respect to the amperometric electrolyte SOC and capacity measurement. With a price of around 2 € per electrode, the costs are reduced to one hundredth, but the stability of the electrodes is not sufficient. Interactions among the investigated electrolyte, the binders, and the epoxy resin limited the life span to a few hours. Nevertheless, a concept of using a bipolar mechanism for the current conduction in a microelectrode was demonstrated. In a subsequent investigation, platinum-based inkjet-printed microband electrodes were investigated in an alternative approach to manufacture inexpensive microelectrodes. The SOC measuring tests showed only a minor accuracy difference in comparison to commercial microelectrodes, while a material cost reduction of more than 90% was achieved.

The results of this thesis show that the dovetailing of sensors and analyzing tools with material development and clever cycling strategies can unlock a deeper insight in the ongoing processes. Decomposition reactions can be revealed, measured and understood. On the one hand, this could lead to the development of intrinsically more stable active materials and, on the other hand, the establishment of a battery management system could offer a lot of set screws to further enhance the lifespan of RFBs. A permanent idea and information exchange between the two topics offers a great potential to boost this rising technology to a new practical alternative for the large-scale energy storage sector to counteract the global climate change.

6 Zusammenfassung

Um die Ziele des Kyoto Protokolls und des Pariser Abkommens zu erreichen, muss die Basis der Energieproduktion von fossilen Rohstoffen auf nachhaltige Quellen wie Wasser-, Sonnen- und Windenergie umgestellt werden. Jedoch sollte die fluktuierende Stromerzeugung dieser Technologien durch ein intelligentes Stromnetz ausgeglichen werden. Dabei spielen Stromspeicher eine entscheidende Rolle. Die Möglichkeit, Energie mithilfe von günstigen organischen Molekülen und „grünen“ Elektrolyten zu speichern, macht die aufkommende Technologie der organischen Redox-Flow-Batterien (RFB) zu einem vielversprechenden Kandidaten für diese Aufgabe. Jedoch leidet dieses Batteriekonzept derzeit noch unter einigen Problemen. Ein Hauptproblem ist die unzureichende Stabilität der genutzten Speicheraktivmaterialien. Zur Überwindung diese technischen Hürden bietet sich eine Kombination aus Materialoptimierung und präziser Sensorik zur Untersuchung der ablaufenden Prozesse an. Derzeit liegt der Forschungsschwerpunkt jedoch eher auf der Entwicklung immer neuer Materialien, die eine intrinsisch höhere Stabilität haben. Die Untersuchung der Zerfallsprozesse und der zugrunde liegenden Mechanismen ist eher zweitrangig. Darüber hinaus liegt das Hauptaugenmerk der meisten Forschungsgruppen darauf, die Stabilität der Materialien durch möglichst häufiges Laden/Entladen zu untersuchen. Des Weiteren ist die Verwendung eines Batteriemanagementsystems, welches z.B. die verwendeten SOC begrenzt, bisher unterrepräsentiert. Hierfür wären jedoch präzise, schnelle, preiswerte SOC- und SOH-Messmethode von Nöten. Die derzeit verwendeten Verfahren leiden jedoch unter großen Problemen, wie zum Beispiel hohen Anschaffungskosten, Limitierungen der untersuchbaren Materialien, Temperaturabhängigkeiten und nötige (Re)Kalibrierungen. Ein Analyseprotokoll, welches diese Nachteile nicht hat und gleichzeitig die Parameter nicht auf der Batterieebene, sondern auf der Elektrolytebene bestimmen kann, würde ein tieferes Verständnis der ablaufenden Prozesse innerhalb der Batterie und der Elektrolyte ermöglichen. Mögliche Verbesserungen der Batterielebensdauer könnten dann nicht nur durch das Material selbst, sondern auch durch die Betriebsbedingungen oder andere äußere Faktoren adressiert werden.

Zusammenfassung

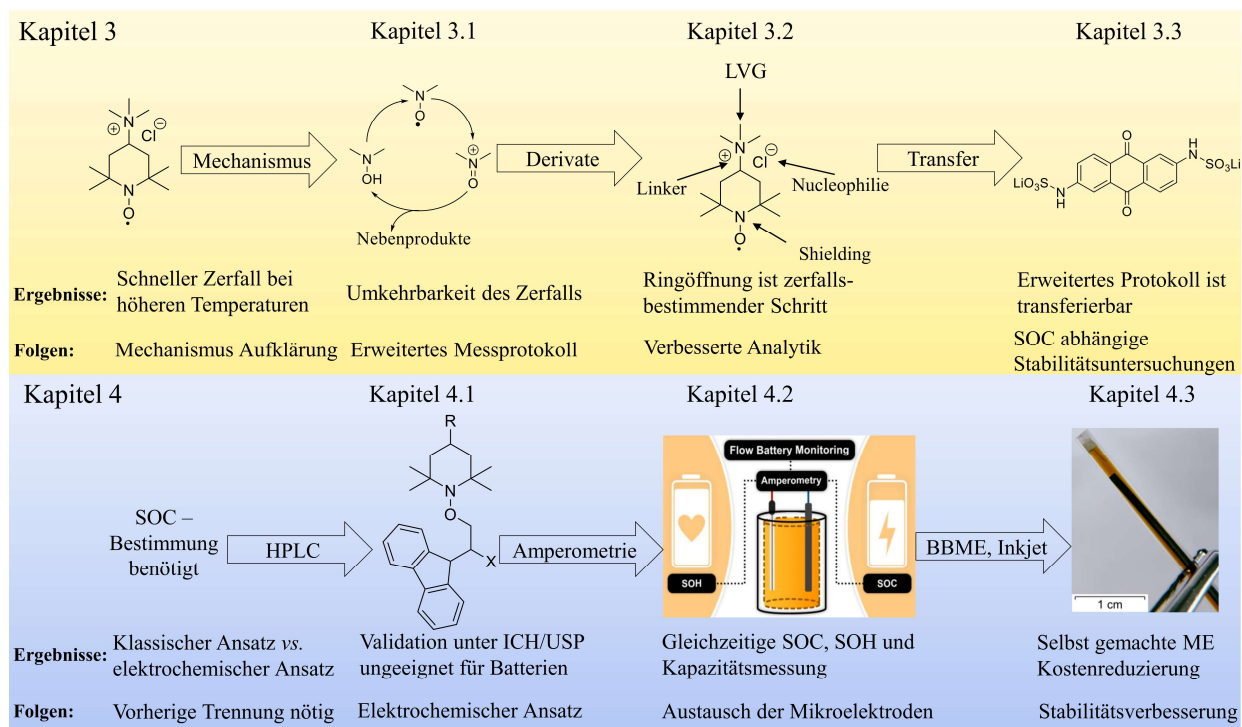


Abbildung 6.1: Schematische Zusammenfassung der Inhalte dieser Arbeit.

Im Zuge dieser Arbeit wurde TMA-TEMPO, das Vorreitermolekül der Katholytseite wässriger ORFBs, eingehend untersucht (*cf.* **Abbildung 6.1**). Dabei stand zunächst das grundlegende Verständnis der ablaufenden Zerfallsprozesse im Vordergrund. Durch den Einsatz verschiedener GC-HRMS-Techniken und der Markierung bestimmter Stellen im Molekül konnten elementare Zwischenprodukte identifiziert und der wahrscheinlichste Zersetzungsmechanismus aufgedeckt werden. Interessanterweise ist das wichtigste Nebenprodukt das korrespondierende Hydroxylamin, welches wieder zum Radikal reoxidiert werden kann. Dadurch wird die Gesamtzersetzungsrate des Moleküls um bis zu 75% reduziert. Dieser Reduktions-Reoxidations-Mechanismus wäre unter Verwendung der häufig benutzten galvanostatischen Lade-/Entladeverfahren kaum zu bemerken gewesen. Dies konnte nur durch die Einführung eines adaptierten Lade-/Entladeprotokolls, welches das Laden/Entladen mit galvanostatischen und potentiostatischen Anteilen in Kombination mit Haltezeiten im instabileren Ladezustand und bei erhöhten Temperaturen umfasst. Dabei ist Bildung von Nebenprodukten, die aus dem instabileren Ladezustand stammen, durch einen Kapazitätsabfall nach der Haltezeit sichtbar. Im Falle von TMA-TEMPO kann dieser Abfall aufgrund der Reversibilität der Radikalreduktion zum Hydroxylamin teilweise geheilt werden. Allerdings zeigt der Test einen komplexen Zusammenhang zwischen der Stabilität und Temperatur, Konzentration sowie SOC. Letzterer Einflussfaktor konnte jedoch nicht näher bestimmt

werden, da die verfügbaren Analysemöglichkeiten nicht in der Lage waren, den SOC mit ausreichend hoher Genauigkeit in einer laufenden RFB zu bestimmen.

Das tiefere Verständnis des TEMPO-Zerfallsmechanismus eröffnet neue Ansatzpunkte für die Materialweiterentwicklung. Die Zersetzung kann mit drei Reaktionen starten, wobei die erste eine Ringöffnungsreaktion ist. Eine verstärkte Abschirmung des Radikals würde vermutlich den Bindungsbruch und somit die Ringöffnung verhindern. Die zweite Reaktion ist eine Hoffmann-Eliminierung der löslichkeitsvermittelnden Gruppe (LVG), welche durch die Einführung eines Linkers zwischen dem Piperidylring und der LVG verhindert werden könnte. Die letzte Startreaktion ist die Eliminierung von Chlormethan aus der Trimethylammonium-LVG. Hier könnte die Nucleophilie des Gegenions oder die Beschaffenheit der LVG eine wichtige Rolle spielen. Um diese Annahmen zu überprüfen, wurden sechs TEMPO-Derivate synthetisiert und miteinander verglichen. Jedes Derivat wurde so konzipiert, dass eine der Zerfallskaskaden verhindert werden sollte. Um die Derivate unter vergleichbaren Stressbedingungen zu testen, wurde dabei das oben genannte adaptierte Lade-/Entladeprotokoll verwendet. Es zeigte sich, dass alle neuen Moleküle geringere oder ähnliche Stabilitäten im Vergleich zu TMA-TEMPO besitzen. Jedoch konnte aus diesen Daten die Vermutung abgeleitet werden, dass die Ringöffnungsreaktion die stabilitätsbestimmende Reaktion in der Zersetzungskaskade ist. Eine Erhöhung der Lebensdauer von TEMPO-Materialien sollte daher durch eine Stabilisierung der C-N-Bindung neben dem Radikal versucht werden. Dies kann entweder durch die Einführung von *para*-ständigen Gruppen mit induktiven Effekten oder durch sterisch anspruchsvolle, vicinal zur genannten Bindung stehende Substituenten erfolgen. Um die Interoperabilität des neuen Protokolls zu zeigen, wurde ein neues Anthrachinon (AQ)-Anolyt synthetisiert und getestet. Neben dem schnellen und unkomplizierten Syntheseverfahren, das mit billigen kommerziellen Edukten und Reagenzien auskommt, hat das AQ auch den Vorteil, dass es eines der bisher stabilsten unter den getesteten Negolyten ist. Der Zerfall beläuft sich dabei auf rund $0,18\% \text{ d}^{-1}$ bei Raumtemperatur und auf $0,17\% \text{ d}^{-1}$ bei $60\text{ }^{\circ}\text{C}$. Darüber hinaus ist das Material auch in der Lage, hohe Stromdichten von bis zu 40 mA cm^{-2} bei hohen Löslichkeiten in Wasser von bis zu $0,75 \text{ M}$ zu liefern. Aber auch dieses Material zeigte während der Tests eine starke Abhängigkeit der Stabilität vom SOC, was einmal mehr die Notwendigkeit von zuverlässigen, schnellen, genauen und vielseitig einsetzbaren SOC- und SOH-Messverfahren zeigt.

Der zweite Teil der Arbeit beschäftigt sich mit neuen Analysemethoden für die SOC-Bestimmung (*cf.* **Abbildung 6.1**). Dabei sollte zunächst auf „klassische“ Methoden, wie UV/Vis, IR o. ä., zurückgegriffen werden. Jedoch können diese Methoden oftmals nicht

zwischen dem Oxoammoniumkation und dem Radikal des TEMPOs unterscheiden. Daher müssen die beiden Spezies vor der Analytik voneinander getrennt werden. Die HPLC als Standardtrenntechnik für wasserlösliche Analyten wäre für diese Aufgabe prädestiniert. Aber aufgrund der hohen Reaktivität des Kations und dessen Fähigkeit, Stahl zu oxidieren, muss eine Derivatisierungsreaktion eingesetzt werden, um vorher das Kation in eine stabilere und analysierbare Spezies zu überführen. Für die Validierung des Derivatisierungsprozesses wurde das Protokoll zur Analyse von drei verschiedenen TEMPO-Derivaten verwendet. Da die HPLC-Methode nicht nur für die Batterieforschung, sondern auch für Anwendung im pharmazeutischen und organisch-chemischen Bereich interessant ist, wurde jeweils ein bekanntes TEMPO-Derivat als Vertreter des jeweiligen Forschungsbereichs ausgewählt und das Protokoll wurde unter den ICH- und USP-Richtlinien validiert. Die Daten zeigten eine allgemeine Verwendbarkeit der Methode, jedoch mit diversen Einschränkungen. So stört ein hoher Radikalanteil (über 30%) die Genauigkeit der Messung. Dies mag für Pharmazeuten oder organische Chemiker akzeptabel sein, wenn z.B. der Gehalt an Oxoammoniumkationen in einem Medikament oder einer Reaktionsprobe gemessen werden soll. Aber es ist nicht ausreichend für die Batterieanwendungen, für die die Analytik auch bei Verhältnissen von Kationen zu Radikalen zwischen ca. 99:1 und 1:99 verwendbar sein muss. Deswegen wurde in der Folge eine alternative, elektrochemische Analysemethode untersucht, obwohl diese Methodik dann primär auf die Batteriecommunity und Electrochemiker fokussiert ist.

Ausgangspunkt für die elektrochemische Analyse war, die kürzlich veröffentlichte amperometrische Messmethode von Stolze *et al.* Der Ansatz beruht auf der Erkenntnis, dass der SOC eine Funktion des Verhältnisses zwischen dem messbaren Strom beim Anlegen einer anodischen und einer kathodischen Spannung unter massentransferlimitierten Bedingungen ist. Jedoch sind für diese amperometrische Methode vergleichsweise teure Geräte und ein komplexer Messaufbau von Nöten. Es konnte aber gezeigt werden, dass der allgemeine Ansatz auch mit einer preiswerten selbstgebauten Mikrocontroller-Messeinheit und einem vereinfachten Aufbau mit Mikroelektroden funktioniert. Dabei konnten die Gesamtkosten um einen Faktor von 100 gesenkt werden, während gleichzeitig die Genauigkeit der SOC-Messung auf Elektrolytebene auf einen absoluten Fehler von unter 1% verbessert wurde. Dies zeigte die Überlegenheit des neuen Ansatzes im Vergleich zum aktuellen Vorreiter unter den Messmethoden auf Basis von OCV-Zellen. Die Methode erlaubt nicht nur die Messung des SOC mit bisher nicht erreichter Präzision, sondern auch die Erfassung des SOH und der Kapazität beider Elektrolyte in einer laufenden RFB. Darüber hinaus ist die Methode robust gegenüber Temperaturänderungen und benötigt keine zeitaufwändige Rekalibrierung. In ihrer

ursprünglichen Form war die Methode jedoch durch den Bedarf an kostenintensiven Mikroelektroden limitiert. Aus diesem Grund wurden im Rahmen der vorliegenden Dissertation neue bipolare Mikroelektroden entwickelt und hinsichtlich ihrer Präzision und Wirtschaftlichkeit mit kommerziellen Mikroelektroden verglichen. Mit einem Preis von ca. 2 € pro Elektrode konnten so die Materialkosten erheblich reduziert werden. Jedoch zeigten die Elektroden eine für die Anwendung nicht ausreichende Stabilität. Wechselwirkungen zwischen den verwendeten Materialien, Bindemitteln und Klebern reduzieren die Lebensdauer auf wenige Stunden. Dennoch konnte der grundsätzliche Nachweis des bipolaren Mechanismus zur Umgehung der sonst eher komplexen Kontaktierung der Kohlenstofffasern geführt werden. Ein möglicher Durchbruch könnten die daraufhin untersuchten durch Tintenstrahltechnik gedruckten Mikrobandelektroden darstellen. SOC-Messversuche zeigten nur eine geringe Verschlechterung im Vergleich zu kommerziellen Mikroelektroden bei einer Materialkostenreduzierung von mehr als 90%.

Die Ergebnisse dieser Arbeit zeigen, dass die Verzahnung von Sensoren und Analysewerkzeugen mit der Materialentwicklung und geschickten Zyklisierungsstrategien einen tiefen Einblick in die ablaufenden Prozesse ermöglichen kann. Dabei können Zersetzungsreaktionen sicht- und messbar gemacht werden, was zu einem tieferen Verständnis der ablaufenden Prozesse führt. Dies könnte zum einen zur Entwicklung intrinsisch stabilerer Aktivmaterialien führen und zum anderen durch die Etablierung eines Batteriemangement-systems viele Stellschrauben bieten, um die Lebensdauer der Batterie weiter erhöhen zu können. Ein ständiger Ideen- und Informationsaustausch zwischen beiden Themenbereichen bietet ein großes Verbesserungspotential, um RFBs zu einer neuen praktischen Alternative im Bereich der Energiespeicherung im Kampf gegen den Klimawandel zu machen.

7 References

- [1] N. N. C. f. E. Information, <https://www.ncei.noaa.gov/access/monitoring/monthly-report/global/202207>, Retrieved on September 12, 2022.
- [2] a) S. Solomon, G. K. Plattner, R. Knutti, P. Friedlingstein, *Proc. Natl. Acad. Sci.* **2009**, *106*, 1704-1709; b) P. M. Cox, R. A. Betts, C. D. Jones, S. A. Spall, I. J. Totterdell, *Nature* **2000**, *408*, 184-187; c) J. Winsberg, T. Hagemann, T. Janoschka, M. D. Hager, U. S. Schubert, *Angew. Chem. Int. Ed.* **2016**, *129*, 702-729; d) N. N. C. f. E. Information, <https://www.ncei.noaa.gov/access/monitoring/monthly-report/global/202113>, Retrieved on September 12, 2022; e) P. T. E. Dlugokencky, <https://www.esrl.noaa.gov/gmd/ccgg/trends/global.html>, Retrieved on September 12, 2022.
- [3] a) B. Obama, *Science* **2017**, *355*, 126-129; b) M. B. Araujo, R. G. Pearson, W. Thuiller, M. Erhard, *Glob. Change Biol. Bioenergy* **2005**, *11*, 1504-1513; c) S. Markkanen, A. Anger-Kraavi, *Clim. Policy* **2019**, *19*, 827-844; d) R. S. J. Tol, *Perspekt. der Wirtschaftspolitik* **2010**, *11*, 13-37.
- [4] a) I. Shishlov, R. Morel, V. Bellassen, *Clim. Policy* **2016**, *16*, 768-782; b) J. Rogelj, M. den Elzen, N. Hohne, T. Fransen, H. Fekete, H. Winkler, R. Schaeffer, F. Sha, K. Riahi, M. Meinshausen, *Nature* **2016**, *534*, 631-639.
- [5] T. N. Foundation., <https://www.nobelprize.org/prizes/chemistry/2019/summary>, Retrieved on May 23, 2022.
- [6] a) C. Menale, F. D'Annibale, B. Mazzarotta, R. Bubbico, *Energy* **2019**, *182*, 57-71; b) D. B. Lu, S. X. Lin, S. W. Hu, W. Cui, T. T. Fang, A. Iqbal, Z. Zhang, W. Peng, *J. Solid State Electrochem.* **2021**, *25*, 315-325.
- [7] a) C. Banza Lubaba Nkulu, L. Casas, V. Haufroid, T. De Putter, N. D. Saenen, T. Kayembe-Kitenge, P. Musa Obadia, D. Kyanika Wa Mukoma, J. M. Lunda Ilunga, T. S. Nawrot, O. Luboya Numbi, E. Smolders, B. Nemery, *Nat. Sustain.* **2018**, *1*, 495-504; b) O. Pourret, M.-P. Faucon, *Encyclopedia of geochemistry: A comprehensive reference source on the chemistry of the earth, Vol. 1*, Springer International Publishing, Cham, Basel, **2017**.
- [8] P. Alotto, M. Guarnieri, F. Moro, *Renew. Sust. Energ. Rev.* **2014**, *29*, 325-335.
- [9] W. Kangro, DE914264C, **1949**.
- [10] a) A. Orita, M. G. Verde, M. Sakai, Y. S. Meng, *Nat. Commun.* **2016**, *7*, 13230; b) T. Janoschka, N. Martin, M. D. Hager, U. S. Schubert, *Angew. Chem. Int. Ed.* **2016**, *55*, 14427-14430.
- [11] a) K. Lin, Q. Chen, M. R. Gerhardt, L. Tong, S. B. Kim, L. Eisenach, A. W. Valle, D. Hardee, R. G. Gordon, M. J. Aziz, M. P. Marshak, *Science* **2015**, *349*, 1529-1532; b) W. Lee, B. W. Kwon, Y. Kwon, *ACS Appl. Mater. Interfaces* **2018**, *10*, 36882-36891.
- [12] a) B. Yang, L. Hooper-Burkhardt, S. Krishnamoorthy, A. Murali, G. K. S. Prakash, S. R. Narayanan, *J. Electrochem. Soc.* **2016**, *163*, A1442-A1449; b) D. G. Kwabi, K. Lin, Y. Ji, E. F. Kerr, M.-A. Goulet, D. De Porcellinis, D. P. Tabor, D. A. Pollack, A. Aspuru-Guzik, R. G. Gordon, M. J. Aziz, *Joule* **2018**, *2*, 1894-1906.
- [13] a) Y. Z. Zhu, F. Yang, Z. H. Niu, H. X. Wu, Y. He, H. F. Zhu, J. Ye, Y. Zhao, X. H. Zhang, *J. Power Sources* **2019**, *417*, 83-89; b) E. S. Beh, D. De Porcellinis, R. L. Gracia, K. T. Xia, R. G. Gordon, M. J. Aziz, *ACS Energy Lett.* **2017**, *2*, 639-644.
- [14] a) T. Janoschka, N. Martin, U. Martin, C. Friebe, S. Morgenstern, H. Hiller, M. D. Hager, U. S. Schubert, *Nature* **2015**, *527*, 78-81; b) J. Winsberg, T. Janoschka, S. Morgenstern, T. Hagemann, S. Muench, G. Hauffman, J. F. Gohy, M. D. Hager, U. S. Schubert, *Adv. Mater.* **2016**, *28*, 2238-2243.

References

- [15] a) J. Luo, B. Hu, C. Debruler, T. L. Liu, *Angew. Chem. Int. Ed.* **2018**, *57*, 231-235; b) C. DeBruler, B. Hu, J. Moss, J. Luo, T. L. Liu, *ACS Energy Lett.* **2018**, *3*, 663-668.
- [16] E. Sánchez-Díez, E. Ventosa, M. Guarnieri, A. Trovò, C. Flox, R. Marcilla, F. Soavi, P. Mazur, E. Aranzabe, R. Ferret, *J. Power Sources* **2021**, *481*, 228804.
- [17] K. Murayama, S. Morimura, T. Yoshioka, *Bull. Chem. Soc. Jpn.* **1969**, *42*, 1640-1643.
- [18] C. Stolze, J. P. Meurer, M. D. Hager, U. S. Schubert, *Chem. Mater.* **2019**, *31*, 5363-5369.
- [19] C. Stolze, M. D. Hager, U. S. Schubert, *J. Power Sources* **2019**, *423*, 60-67.
- [20] a) N. H. Hagedorn, *NASA redox storage system development project, Vol. 1*, U.S. Department of Energy, Washington, D. C., **1984**; b) M. Rychcik, M. Skyllas-Kazacos, *J. Power Sources* **1988**, *22*, 59-67.
- [21] P. Rohland, E. Schröter, O. Nolte, G. R. Newkome, M. D. Hager, U. S. Schubert, *Prog. Polym. Sci.* **2022**, *125*, 101474.
- [22] G. van Loon, S. Duffy, *Environmental chemistry – A global perspective, Vol. 1*, 3 ed., Oxford University Press, Oxford, **2011**.
- [23] a) F. D'Souza, *J. Am. Chem. Soc.* **1996**, *118*, 923-924; b) Hayashi N, Yoshikawa T, Kurakawa M, Ohnuma T, Sugiyama Y, H. H, *Mol. Cryst. Liq.* **2006**, *456*, 133-137; c) V. Milašinović, A. Krawczuk, K. Molčanov, B. Kojić-Prodić, *Cryst. Growth Des.* **2020**, *20*, 5435-5443.
- [24] a) C. Kahlfuss, E. Metay, M. C. Duclos, M. Lemaire, M. Oltean, A. Milet, E. St-Aman, C. Bucher, *C. R. Chim.* **2014**, *17*, 505-511; b) J. W. Park, N. H. Choi, J. H. Kim, *J. Phys. Chem.* **1996**, *100*, 769-774; c) J. Iehl, M. Frascioni, H.-P. Jacquot de Rouville, N. Renaud, S. M. Dyar, N. L. Strutt, R. Carmieli, M. R. Wasielewski, M. A. Ratner, J.-F. Nierengarten, J. F. Stoddart, *Chem. Sci.* **2013**, *4*, 1462-1469.
- [25] D. Reynard, H. Vrabel, C. R. Dennison, A. Battistel, H. Girault, *ChemSusChem* **2019**, *12*, 1222-1228.
- [26] Y. H. Liu, M. A. Goulet, L. C. Tong, Y. Z. Liu, Y. L. Ji, L. Wu, R. G. Gordon, M. J. Aziz, Z. J. Yang, T. W. Xu, *Chem* **2019**, *5*, 1861-1870.
- [27] H. O. Finklea, N. Madhiri, *J. Electroanal. Chem.* **2008**, *621*, 129-133.
- [28] J. F. W. Keana, *Chem. Rev.* **1978**, *78*, 37-64.
- [29] Y. Ma, C. Loyns, P. Price, V. Chechik, *Org. Biomol. Chem.* **2011**, *9*, 5573-5578.
- [30] T. Takata, Y. Tsujino, S. Nakanishi, K. Nakamura, E. Yoshida, T. Endo, *Chem. Lett.* **1999**, *28*, 937-938.
- [31] O. Nolte, P. Rohland, N. Ueberschaar, M. D. Hager, U. S. Schubert, *J. Power Sources* **2022**, *525*, 230996.
- [32] J. D. Milshtein, J. L. Barton, R. M. Darling, F. R. Brushett, *J. Power Sources* **2016**, *327*, 151-159.
- [33] M. A. Goulet, M. J. Aziz, *J. Electrochem. Soc.* **2018**, *165*, A1466-A1477.
- [34] U. S. Schubert, P. Rohland, O. Nolte, K. Schreyer, H. Görls, M. D. Hager, *Adv. Mater.* **2022**, *3*, 4278-4288.
- [35] R. de Levie, *J. Electroanal. Chem.* **1992**, *323*, 347-355.
- [36] T. Hagemann, J. Winsberg, M. Grube, I. Nischang, T. Janoschka, N. Martin, M. D. Hager, U. S. Schubert, *J. Power Sources* **2018**, *378*, 546-554.
- [37] B. Huskinson, M. P. Marshak, C. Suh, S. Er, M. R. Gerhardt, C. J. Galvin, X. Chen, A. Aspuru-Guzik, R. G. Gordon, M. J. Aziz, *Nature* **2014**, *505*, 195-198.
- [38] T. Kusamoto, S. Kume, H. Nishihara, *J. Am. Chem. Soc.* **2008**, *130*, 13844-13845.
- [39] a) A. Fabianska, A. Bialk-Bielinska, P. Stepnowski, S. Stolte, E. M. Siedlecka, *J. Hazard Mater.* **2014**, *280*, 579-587; b) D. A. Song, H. J. Liu, A. Q. Zhang, J. H. Qu, *RSC Adv.* **2014**, *4*, 48426-48432; c) W. W. Ben, Y. W. Shi, W. W. Li, Y. Zhang, Z. M. Qiang, *Chem. Eng. J.* **2017**, *327*, 743-750; d) A. Acosta-Rangel, M. Sanchez-Polo, M.

References

- Rozalen, J. Rivera-Utrilla, A. M. S. Polo, M. S. Berber-Mendoza, M. V. Lopez-Ramon, *J. Environ. Manage.* **2020**, *255*, 109927.
- [40] P. P. Pradhan, J. M. Bobbitt, W. F. Bailey, *J. Org. Chem.* **2009**, *74*, 9524-9527.
- [41] D. G. Kwabi, Y. Ji, M. J. Aziz, *Chem. Rev.* **2020**, *120*, 6467-6489.
- [42] T. Golub, J. Y. Becker, *Org. Biomol. Chem.* **2012**, *10*, 3906-3912.
- [43] K. A. Savin, *Writing reaction mechanisms in organic chemistry*, 3 ed., Academic Press, Waltham, **2014**.
- [44] M. Wu, Y. Jing, A. A. Wong, E. M. Fell, S. J. Jin, Z. J. Tang, R. G. Gordon, M. J. Aziz, *Chem* **2020**, *6*, 1432-1442.
- [45] a) G. L. Perlovich, V. P. Kazachenko, N. N. Strakhova, O. A. Raevsky, *J. Chem. Eng. Data* **2014**, *59*, 4217-4226; b) F. J. Bandelin, W. Malesh, *J. Am. Pharm. Assoc.* **1959**, *48*, 177-181; c) F. Martínez, A. Gomez, *Phys. Chem. Liq.* **2010**, *40*, 411-420.
- [46] C. L. McCormick, P. A. Callais, B. H. Hutchinson, *Macromolecules* **1985**, *18*, 2394-2401.
- [47] D. P. Tabor, R. Gomez-Bombarelli, L. C. Tong, R. G. Gordon, M. J. Aziz, A. Aspuru-Guzik, *J. Mater. Chem. A* **2019**, *7*, 12833-12841.
- [48] P. Rohland, K. Schreyer, M. D. Hager, U. S. Schubert, *RSC Adv.* **2021**, *11*, 38759-38764.
- [49] M. A. Goulet, L. Tong, D. A. Pollack, D. P. Tabor, S. A. Odom, A. Aspuru-Guzik, E. E. Kwan, R. G. Gordon, M. J. Aziz, *J. Am. Chem. Soc.* **2019**, *141*, 8014-8019.
- [50] a) N. Hayashi, T. Yoshikawa, M. Kurakawa, T. Ohnuma, Y. Sugiyama, H. Higuchi, *Mol. Cryst. Liq.* **2006**, *456*, 133-137; b) K. Molčanov, C. Jelsch, B. Landeros, J. Hernández-Trujillo, E. Wenger, V. Stilinović, B. Kojić-Prodić, E. C. Escudero-Adán, *Cryst. Growth Des.* **2018**, *19*, 391-402; c) S. Patai, Z. Rappoport, *The quinonoid compounds: Vol. 1*, John Wiley & Sons Ltd, Hoboken, **1988**.
- [51] a) D. Seebach, *Angew. Chem. Int. Ed.* **1988**, *27*, 1624-1654; b) M. P. Sibi, *J. Am. Chem. Soc.* **1998**, *120*, 2991-2991; c) A. Streitwieser, *J. Mol. Model.* **2006**, *12*, 673-680; d) A. Streitwieser, *J. Org. Chem.* **2009**, *74*, 4433-4446.
- [52] a) T. J. Carney, S. J. Collins, J. S. Moore, F. R. Brushett, *Chem. Mater.* **2017**, *29*, 4801-4810; b) C. Wiberg, T. J. Carney, F. Brushett, E. Ahlberg, E. G. Wang, *Electrochim. Acta* **2019**, *317*, 478-485.
- [53] Y. L. Ji, M. A. Goulet, D. A. Pollack, D. G. Kwabi, S. Y. Jin, D. De Porcellinis, E. F. Kerr, R. G. Gordon, M. J. Aziz, *Adv. Energy Mater.* **2019**, *9*, 1900039.
- [54] a) Y. Jiao, B. Tang, Y. Zhang, J. F. Xu, Z. Wang, X. Zhang, *Angew. Chem. Int. Ed.* **2018**, *57*, 6077-6081; b) E. A. Haidasz, D. Meng, R. Amorati, A. Baschieri, K. U. Ingold, L. Valgimigli, D. A. Pratt, *J. Am. Chem. Soc.* **2016**, *138*, 5290-5298; c) G. Grampp, K. Rasmussen, *Phys. Chem. Chem. Phys.* **2002**, *4*, 5546-5549; d) B. Karimi, S. Vahdati, H. Vali, *RSC Adv.* **2016**, *6*, 63717-63723.
- [55] a) J. M. Bobbitt, N. A. Eddy, C. X. Cady, J. Jin, J. A. Gascon, S. Gelpi-Dominguez, J. Zakrzewski, M. D. Morton, *J. Org. Chem.* **2017**, *82*, 9279-9290; b) M. Mazur, *Anal. Chim. Acta* **2006**, *561*, 1-15.
- [56] a) T. Hagemann, M. Strumpf, E. Schröter, C. Stolze, M. Grube, I. Nischang, M. D. Hager, U. S. Schubert, *Chem. Mater.* **2019**, *31*, 7987-7999; b) T. Duan, T. Zhai, H. Liu, Z. Yan, Y. Zhao, L. Feng, C. Ma, *Org. Biomol. Chem.* **2016**, *14*, 6561-6567; c) M. Gong, J. K. Kim, X. L. Zhao, Y. B. Li, J. Y. Zhang, M. M. Huang, Y. J. Wu, *Green Chem.* **2019**, *21*, 3615-3620.
- [57] C. D. Smith, J. P. Bartley, S. E. Bottle, A. S. Micallef, D. A. Reid, *J. Mass. Spectrom.* **2000**, *35*, 607-611.
- [58] T. Takata, Y. Tsujino, S. Nakanishi, K. Nakamura, E. Yoshida, T. Endo, *Chemistry Lett* **1999**, *28*, 937-938.

References

- [59] a) A. B. V. Silva, E. D. Silva, A. A. dos Santos, J. L. Princival, *Catal. Commun.* **2020**, *137*, 105946; b) K. L. Denlinger, P. Carr, D. C. Waddell, J. Mack, *Molecules* **2020**, *25*, 364-374; c) G. Pierre, C. Punta, C. Delattre, L. Melone, P. Dubessay, A. Fiorati, N. Pastori, Y. M. Galante, P. Michaud, *Carbohydr. Polym.* **2017**, *165*, 71-85.
- [60] a) C. S. Wilcox, A. Pearlman, *Pharmacol. Rev.* **2008**, *60*, 418-469; b) J. A. Zarling, V. E. Brunt, A. K. Vallerger, W. Li, A. Tao, D. A. Zarling, C. T. Minson, *Front. Genet.* **2015**, *6*, 325; c) E. D. Hall, R. A. Vaishnav, A. G. Mustafa, *Neurotherapeutics* **2010**, *7*, 51-61.
- [61] P. Rohland, K. Schreyer, R. Burges, N. Fritz, M. D. Hager, U. S. Schubert, *Chromatographia* **2021**, *84*, 999-1007.
- [62] a) H. G. Rogers, R. A. Gaudiana, W. C. Hollinsed, P. S. Kalyanaraman, J. S. Manello, C. McGowan, R. A. Minns, R. Sahatjian, *Macromolecules* **2002**, *18*, 1058-1068; b) B. J. Barker, J. Rosenfarb, J. A. Caruso, *Angew. Chem.* **1979**, *91*, 560-564; c) R. F. de Farias, C. Airoidi, *J. Therm. Anal. Calorim.* **2002**, *67*, 579-587.
- [63] a) P. Borman, D. Elder, *Q2(R1) Validation of analytical procedures*, John Wiley & Sons, Inc, **2017**; b) U. S. Pharmacopeia, *United States Pharmacopeial Convention*, United States Pharmacopeia, Rockville, **2014**
- [64] C. f. D. Evaluation, a. Research, *Reviewer guidance, validation of chromatographic methods*, United States Pharmacopeia, Rockville, **1994**
- [65] D. L. Marshall, M. L. Christian, G. Gryn'ova, M. L. Coote, P. J. Barker, S. J. Blanksby, *Org. Biomol. Chem.* **2011**, *9*, 4936-4947.
- [66] a) L. Yan, D. Li, S. Li, Z. Xu, J. Dong, W. Jing, W. Xing, *ACS Appl. Mater. Interfaces* **2016**, *8*, 35289-35297; b) H. Prifti, A. Parasuraman, S. Winardi, T. M. Lim, M. Skyllas-Kazacos, *Membranes* **2012**, *2*, 275-306; c) X. F. Li, H. M. Zhang, Z. S. Mai, H. Z. Zhang, I. Vankelecom, *Energy Environ. Sci.* **2011**, *4*, 1147-1160; d) T. Feng, H. N. Wang, Y. Y. Liu, J. Zhang, Y. Xiang, S. F. Lu, *J. Power Sources* **2019**, *436*, 226831.
- [67] a) J. E. Babiarz, G. T. Cunkle, A. D. DeBellis, D. Eveland, S. D. Pastor, S. P. Shum, *J. Org. Chem.* **2002**, *67*, 6831-6834; b) T. Vogler, A. Studer, *Synthesis* **2008**, *2008*, 1979-1993.
- [68] O. Nolte, I. A. Volodin, C. Stolze, M. D. Hager, U. S. Schubert, *Mater Horiz* **2021**, *8*, 1866-1925.
- [69] C. Stolze, J. P. Meurer, M. D. Hager, U. S. Schubert, *Chem. Mater.* **2019**, *31*, 5363-5369.
- [70] a) S. J. Konopka, B. McDuffie, *Anal. Chem.* **2002**, *42*, 1741-1746; b) C. Amatore, S. Szunerits, L. Thouin, J. S. Warkocz, *Electrochem. Commun.* **2000**, *2*, 353-358.
- [71] a) S. Ressel, F. Bill, L. Holtz, N. Janshen, A. Chica, T. Flower, C. Weidlich, T. Struckmann, *J. Power Sources* **2018**, *378*, 776-783; b) T. Struckmann, P. Kuhn, S. Ressel, *Electrochim. Acta* **2020**, *362*, 137174.
- [72] C. Stolze, P. Rohland, K. Zub, O. Nolte, M. D. Hager, U. S. Schubert, *Energy Convers. Manag. X* **2022**, *14*, 100188.
- [73] a) N. Adly, S. Weidlich, S. Seyock, F. Brings, A. Yakushenko, A. Offenhausser, B. Wolfrum, *NPJ Flex. Electron.* **2018**, *2*, 1-9; b) J. Schnitker, N. Adly, S. Seyock, B. Bachmann, A. Yakushenko, B. Wolfrum, A. Offenhausser, *Adv. Biosyst.* **2018**, *2*, 1700136.
- [74] a) F. Mavre, R. K. Anand, D. R. Laws, K. F. Chow, B. Y. Chang, J. A. Crooks, R. M. Crooks, *Anal. Chem.* **2010**, *82*, 8766-8774; b) S. E. Fosdick, K. N. Knust, K. Scida, R. M. Crooks, *Angew. Chem. Int. Ed.* **2013**, *52*, 10438-10456; c) C. A. C. Sequeira, D. S. P. Cardoso, M. L. F. Gameiro, *Chem. Eng. Commun.* **2016**, *203*, 1001-1008; d) S. M. B. Fakhrudin, K. Y. Inoue, R. Tsuga, T. Matsue, *Electrochem. Commun.* **2018**, *93*, 62-65.
- [75] P. Zhong, P. Yu, K. Wang, J. Hao, J. Fei, L. Mao, *Analyst* **2015**, *140*, 7154-7159.

References

- [76] K. Zub, C. Stolze, P. Rohland, S. Stumpf, S. Hoepfner, M. D. Hager, U. S. Schubert, *submitted* **2022**.
- [77] O. Nolte, I. A. Volodin, C. Stolze, M. D. Hager, U. S. Schubert, *Mater. Horiz.* **2021**, *8*, 1866-1925.

Abbreviations

AQ	Anthraquinone
BBME	Backfilled bipolar microelectrode
CE	Coulombic efficiency
CGC	Complete galvanostatic cycling
CLS	Capacity limiting side
CV	Cyclic voltammetry
DoO	Degree of oxidation
ESR	Electron spin resonance
GC-MS	Gas chromatography-mass spectrometry
GHG	Greenhouse gases
HPLC	High-pressure liquid chromatography
HS-GC-MS	Headspace gas chromatography-mass spectrometry
ICH	International council for harmonization
IGC	Incomplete galvanostatic cycling
IR	Infrared
LC	Liquide chromatography
LiAQS	Lithium anthraquinone sulfamic acid
LIB	Lithium-ion battery
LOD	Limit of detection
LOQ	Limit of quantification
LVG	Löslichkeit vermittelnde Gruppe
MGPC	Mixed galvanostatic and potentiostatic cycling
MMU	Microcontroller measurement unit

Abbreviations

NASA	National aeronautics and space administration
NCLS	Capacity non-limiting side
NMR	Nuclear magnetic resonance
OCV	Open circuit voltage
ORFB	Organic redox flow battery
PCET	Proton coupled electron transfer
RDE	Rotating disc electrode
RFB	Redox flow battery
RMSD	Relative mean standard deviation
RSD	Relative standard deviation
SHE	Standard hydrogen electrode
SME	Scanning electron microscope
SMU	Source meter unit
SOC	State of charge
SOH	State of health
SPG	Solubility promoting group
SPME	Solid phase micro extraction
SST	System suitability test
TEA	Triethyl ammonium
TEMPO	2,2,6,6-Tetramethylpiperidine- <i>N</i> -oxyl
TEMPOL	4-Hydroxy-2,2,6,6-tetramethylpiperidine-1-oxyl
TMA-TEMPO	<i>N,N,N</i> -2,2,6,6-Heptamethylpiperidine- <i>N</i> -oxy-4-ammonium chloride
TMU	Tetramethyl urea

Abbreviations

UCS	Unbalanced compositionally symmetric
USP	United states pharmacopeia
UV/vis	Ultra violet/visible
VAT	Value added tax
VRFB	Vanadium redox flow battery

Symbols

Chapter 3

Chapter 4

V_t	Added volume of the titrant	R_s	Resolution
a	Added volume of titrant at the equilibration point	N	Plate count
b	Standard redox potential of the analyte	k'	Capacity factor
c	Standard redox potential of the titrant	T	Tailing factor
f	Pre-factor in the Nernst equation $(\frac{F}{RT} \ln 10)$	R^2	Determination coefficient
x	Measured potential	S	Slope of the calibration curve
$DoO_{opt.}$	DoO from the optical titration DoO from the potentiometric titration	F	Faraday's constant
$DoO_{pot.}$	Half-cell potential determined via CV	n	Number of transferred electrons
$E_{CV}^{1/2}$	Half-cell potential determined via titration	r	Radius of the disk
$E_{tit}^{1/2}$	Half-cell potential determined via titration	$D_{O/R}$	Diffusion coefficient of the oxidized and the reduced form of the redox couple
k^0	Electron-transfer rates,	$c_{O/R}$	Bulk concentrations of the oxidized and the reduced form of the redox couple
D	Diffusion coefficients	$SOC(t_0)$	Initial SOC
α	Transfer coefficients	Q_{max}	Total electrolyte capacity
		$i(t)$	Electrical current
		ΔQ	Transferred charge
		ΔSOC	Change of the electrolyte's SOC

Curriculum vitae



03/05/1990	Born in Zeitz, Germany
1996 – 2008	School education, Wetterzeube / Droyssig
05/07/2008	CJD Christopherusschule Droyssig, Droyssig University entrance certification
08/2008 – 07/2011	Vocational training – Lab technician, Bayer-Bitterfeld GmbH
07/2011 – 09/2011	Lab technician, Bayer-Bitterfeld GmbH
10/2011 – 10/2014	Study of Chemistry (B.Sc.) at the Friedrich Schiller University Jena, Germany Bachelor thesis: “Stereoselective synthesis of dihydropyridines” (group of Prof. Dr. H. D. Arndt)
10/2014 – 10/2016	Study of Chemistry (M.Sc.) at the Friedrich Schiller University Jena, Germany Master thesis: “Synthesis of fluorophores based on 4-hydroxythiazoles” (group of Prof. Dr. R. Beckert)
02/2017 – 12/2021	PhD student at the Laboratory of Macromolecular and Organic Chemistry (IOMC) at the Friedrich Schiller University Jena (group of Prof. Dr. Ulrich S. Schubert)
since 12/2021	Quality Specialist, Quality Life Cycle Management, Bayer Weimar GmbH & Co KG

Jena, der 09.03.2023

.....

Philip Rohland

Publication list

Peer-reviewed publications

- [1] P. Rohland, E. Schröter, O. Nolte, G. R. Newkome, M. D. Hager, U. S. Schubert, “Redox-active polymers: The magic key towards energy storage – A polymer design guideline”, *Prog. Polym. Sci.* **2022**, *125*, 101474.
- [2] P. Rohland, O. Nolte, N. Ueberschaar, N. Martin, M. D. Hager, U. S. Schubert, “Stability of TMA-TEMPO-based aqueous electrolytes for redox-flow batteries”, *J. Power Sources* **2022**, *525*, 230996.
- [3] P. Rohland, O. Nolte, K. Schreyer, H. Goerls, M. D. Hager, U. S. Schubert, “Structural alterations on the TEMPO scaffold and their impact on the performance as active materials for redox flow batteries”, *Mater. Adv.* **2022**, *3*, 4278-4288.
- [4] P. Rohland, K. Schreyer, M. D. Hager, U. S. Schubert, “Anthraquinone-2,6-disulfamidic acid: A negolyte with low decomposition rates at elevated temperatures“ *RSC Adv.* **2021**, *11*, 38759-38764.
- [5] P. Rohland, K. Schreyer, R. Burges, N. Fritz, M. D. Hager, U. S. Schubert, “Liquid chromatography analysis of reactive oxoammonium cations“, *Chromatographia* **2021**, *84*, 999-1007.
- [6] C. Stolze, P. Rohland, K. Zub, O. Nolte, M. D. Hager, U. S. Schubert, “A low-cost amperometric sensor for the combined state-of-charge, capacity, and state-of-health monitoring of redox flow battery electrolyte“, *Energy Convers. Manag. X* **2022**, *14*, 100188.
- [7] K. Zub, C. Stolze, P. Rohland, S. Stumpf, S. Hoepfener, M. D. Hager, U. S. Schubert, “Inkjet-printed microband electrodes for a cost-efficient state-of-charge monitoring in redox flow batteries“, *Sens. Actuators B Chem.* **2022**, accepted.
- [8] O. Nolte, R. Geitner, I. A. Volodin, P. Rohland, M. D. Hager, U. S. Schubert, “State of charge and state of health assessment of viologens in aqueous-organic redox-flow electrolytes using in situ IR spectroscopy and multivariate curve resolution“, *Adv. Sci.* **2022**, 2200535.
- [9] E. Schröter, P. Rohland, K. Schreyer, C. Friebe, M. D. Hager, U. S. Schubert, „Oxidation of N,N,N,2,2,6,6-heptamethyl-piperidine-4-ammonium chloride to water-soluble N-oxyl radicals: A comparative study“, *Eur. J. Org. Chem.* **2022**, accepted.

- [10] S. H. Habenicht, P. Rohland, J. Reichel, T. Biver, P. Minei, D. Jakobi, A. Pucci, D. Weiß, R. Beckert, H. Görls, “Small molecules as long-wavelength fluorophores: Push-pull substituted 4-alkoxy-1,3-thiazoles, *Synthesis* **2018**, *50*, 303-313.

Poster presentation

- [1] O. Nolte, P. Rohland, M. D. Hager, U. S. Schubert, “Testing the stability of TEMPTMA-based electrolytes for redox flow batteries”, *Central European Meeting on Molecular Electrochemistry* **2019**.

Acknowledgements

This work would not have been possible in its current form without the continuous support, advice, and help of several people. First, I wish to express my sincere appreciation to Prof. Dr. Ulrich S. Schubert for giving me the opportunity to work in his group on a highly interesting and interdisciplinary research field. Thank you for offering me a current and interesting interdisciplinary research topic, providing an excellent research infrastructure and the freedom to find and to pursue my own scientific ideas. I am also very grateful to Prof. Dr. Martin Oschatz for the time he invested in the addition evaluation of this thesis.

Furthermore, I would like to thank Dr. Martin Hager for all the invaluable background work. Finding a free spot in your tight schedule might have been very difficult sometimes. Nevertheless, it was always possible to discuss about the further development of my scientific work or talk a few minutes about tea, the upcoming vacation trip to Denmark or the next deuterated TEMPO derivatives Berlin urgently needed. Thank you for the many advice, help in the scientific publication process and funny stories.

I also would like to express my gratitude to all my colleagues within the Schubert group who helped me throughout the years. Although I cannot name all here, I have to thank Dr. Christian Stolze and Dr. Christian Friebe for the nice office atmosphere. Dr. Tobias Klein, Thomas Wloka, Erik Schroeter, Oliver Nolte geb. Zumann and Philip Borchers for the crazy music mix and advices in the lab. Special thanks to Kristin Schreyer for the phenomenal collaboration, all the synthesis and being the next "Labdragon". I am thankful for the support of Rene Burges and his funny stories about the older times. I also need to thank Maria Strumpf for putting so much effort in keeping our labs organized and clean as well as the lab benches unscratched.

I am thankful to the NMR department for their time and all the crazy measurements they did for me. I did not even know that we could measure lithium or sodium NMR. Thanks also to the MS lab. Nicole, thank you for the collaboration and I am sorry for the many TEMPO samples. Grit Festag, Uwe, Koehn, Sandra Koehn, Beate Lendvogt the team from the chemical supply, thanks to all of you.

Acknowledgements

I deeply value Franca Frister, Mandy Hendreich, Katja Gattung, Sylvia Braunsdorf, Ulrike Kaiser, and Doreen Küchler for all the administrative work they did in the background and their open ears and help whenever I had an organizational question, or my project partner got bankrupt and I urgently needed a new contract.

The PhD life can and will be very disappointing, depressing and you need a lot of resilience to go through it. Without “der Niveau” it would have been impossible for me. Thank you for BBQ, beer, the PhD weekend, Russian Hardbass, and all the memories we share.

My very personal and deep gratitude goes to my friends for their unconditional support and the many occasions to find the necessary distraction from this PhD thesis in the time we have spent together. Thank you!

I would also like to thank my parents Birgit and Uwe Rohland as well as my grandparents without your perpetual support during my whole life I would not be at this point.

Last but not least, my dear Melanie, I want to thank you. I know the past years have been challenging in many respects for both of us. I am deeply grateful that we managed all this together, for your understanding throughout this time, your perpetual support and your love. Thank you so much!

Declaration of authorship/Selbstständigkeitserklärung

I certify that the work presented here is, to the best of my knowledge and belief, original and the result of my own investigations, except as acknowledged, and has not been submitted, either in part or whole, for a degree at this or any other university.

(Ich erkläre, dass ich die vorliegende Arbeit selbstständig und unter Verwendung der angegebenen Hilfsmittel, persönlichen Mitteilungen und Quellen angefertigt habe.)

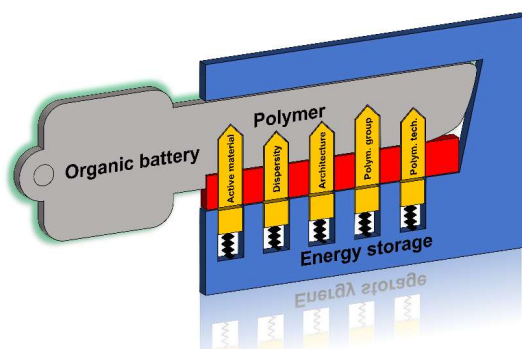
Jena, der 09.03.2023

.....
Philip Rohland

Publications P1

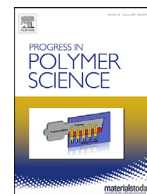
Redox-active polymers: The magic key towards energy storage – A polymer design guideline.

P. Rohland, E. Schröter, O. Nolte, G. R. Newkome, M. D. Hager, U. S. Schubert



Abstract:

Renewable organic batteries represent a valuable option to store sustainably generated energy and can play a major role in phasing out current carbon-based energy production. Several approaches have emerged over the last 80 years that utilize organic redox materials as active components in batteries. In particular, polymers have gained considerable interest among numerous research groups due to their (1) fast redox chemistry, in comparison to conventional active materials, (2) straight-forward syntheses, and (3) tunable solubility, which represent favored properties for diverse electronic devices. Notably, the beginning of redox-active polymers is linked to the discovery of conductive polymers by Heeger, MacDiarmid and Shirakawa in 1977. Nevertheless, redox-active polymers were studied in 1944 making them a familiar class under the broader polymeric framework, which celebrate its 100th birthday in 2020, based on the pioneering publication by Staudinger in 1920. Since their beginning, redox-active polymers have evolved from an interesting phenomenon into a family of promising, tailor-made, battery materials that also made their way to commercialization. In this regard, this review focusses on the design of interesting polymeric, redox-active materials. Polymerization techniques are discussed regarding novel polymer architectures and utilitarian properties. The polymer architectures are subsequently analyzed within the application scenarios of solid-state batteries, pseudo-capacitors, and redox-flow batteries. Redox moieties are compared and an overview of diverse synthetic aspects as well as battery concepts for the optimal assembly of polymeric battery materials are given.



Redox-active polymers: The magic key towards energy storage – a polymer design guideline progress in polymer science

Philip Rohland^{a,b,1}, Erik Schröter^{a,b,1}, Oliver Nolte^{a,b}, George R. Newkome^c,
Martin D. Hager^{a,b}, Ulrich S. Schubert^{a,b,*}

^a Laboratory of Organic and Macromolecular Chemistry (IOMC), Friedrich Schiller University Jena, Humboldtstrasse 10, Jena 07743, Germany

^b Center for Energy and Environmental Chemistry Jena (CEEC Jena), Friedrich Schiller University Jena, Philosophenweg 7a, Jena 07743, Germany

^c Center for Molecular Biology and Biotechnology, Florida Atlantic University, Jupiter, FL 33458, United States

ARTICLE INFO

Article history:

Received 15 March 2021

Revised 16 August 2021

Accepted 29 October 2021

Available online 6 November 2021

Keywords:

Polymer batteries

Material design

Solid state batteries

Redox flow batteries

Pseudo-caps

100 Years of polymer science

Redox polymers

Redox-active organic materials

ABSTRACT

Renewable organic batteries represent a valuable option to store sustainably generated energy and can play a major role in phasing out current carbon-based energy production. Several approaches have emerged over the last 80 years that utilize organic redox materials as active components in batteries. In particular, polymers have gained considerable interest among numerous research groups due to their (1) fast redox chemistry, in comparison to conventional active materials, (2) straight-forward syntheses, and (3) tunable solubility, which represent favored properties for diverse electronic devices. Notably, the beginning of redox-active polymers is linked to the discovery of conductive polymers by Heeger, MacDiarmid and Shirakawa in 1977. Nevertheless, redox-active polymers were studied in 1944 making them a familiar class under the broader polymeric framework, which celebrate its 100th birthday in 2020, based on the pioneering publication by Staudinger in 1920. Since their beginning, redox-active polymers have evolved from an interesting phenomenon into a family of promising, tailor-made, battery materials that also made their way to commercialization. In this regard, this review focusses on the design of interesting polymeric, redox-active materials. Polymerization techniques are discussed regarding novel polymer architectures and utilitarian properties. The polymer architectures are subsequently analyzed within the application scenarios of solid-state batteries, pseudo-capacitors, and redox-flow batteries. Redox moieties are compared and an overview of diverse synthetic aspects as well as battery concepts for the optimal assembly of polymeric battery materials are given.

© 2021 Elsevier B.V. All rights reserved.

Abbreviations: AIBN, azobis(isobutyronitrile); AROP, anionic ring-opening polymerization; ATRP, atom transfer radical polymerization; CP, conjugated polymer; CPDT, 4H-cyclopenta [2,1-b:3,4-b']dithiophene-4-ol; CRP, controlled radical polymerization; D, dispersity; DDQ, 2,3-dichloro-5,6-dicyano-1,4-benzoquinone; DTP, 4H-dithieno [3,2-b:2',3'-d]pyrrole; EDGMA, ethylene glycol dimethacrylate; EDLC, electronic double layer capacitors; COF, covalent organic framework; RAM-COF, redox active moiety covalent organic framework; EO, ethylene oxide; GT, group transfer polymerization; IOT, internet of things; ITO, indium tin oxide; LIB, lithium ion battery; mCPBA, *m*-chloroperoxybenzoic acid; NDI, naphthalene diimide; NMP, nitroxide mediated polymerization; NTCD, naphthalene tetracarboxylic acid dianhydride; OFET, organic field-effect transistors; ORB, organic radical battery; P3HT, poly(3-hexylthiophene); PAN, poly(acrylonitrile); PANI, poly(aniline); PAQS, poly(anthraquinonylsulfide); PBQS, poly(benzoquinonylsulfide); PEDOT, poly(3,4-ethylenedioxythiophene); PEDOT:PSS, poly(3,4-ethylenedioxythiophene):polystyrene sulfonate; PG, polymerizable group; PMDA, pyromellitic acid dianhydride; PMMA, poly(methylmethacrylate); PPEO, poly(proxyethylenoxide); PPy, poly(pyrrole); PROXYL, 2,2,5,5-tetramethyl-1-pyrrolidinyloxy; PS, poly(styrene); PSS, poly(styrene sulfonate); PTCDA, perylene tetracarboxylic acid dianhydride; PTEO, poly(tempoethylene oxide); poly(4-glycidyl-2,2,6,6-tetramethylpiperidine-1-oxyl); PTh, poly(thiophene);

1. Introduction and history

In the last decade, the global battery market has flourished [1]. Electric vehicles, wearable gadgets, the internet-of-things (IOT) as well as smart grids demand more and accurately tailored energy storage systems. The leading technique nowadays is based on lithium ion batteries (LIB) and conveniences with low costs, high voltages, and increasing power densities. The LIB have been

PThPy, poly(dithienopyrrole); PTMA, poly(2,2,6,6-tetramethyl-piperidinyloxy-4-yl methacrylate); PVTMIO, poly(5-vinyl-1,1,3,3-tetramethylisindolin-2-yloxy); RAFT, reversible addition-fragmentation chain-transfer; RAP, redox-active polymer; RFB, redox flow battery; ROMP, ring-opening metathesis polymerization; SOC, state-of-charge; TCAQ, tetracyanoanthraquinone; TEMPO, 2,2,6,6-tetramethylpiperidinyloxy; TEMPOL, 4-hydroxy-2,2,6,6-tetramethyl-piperidinyloxy; TPA, triphenylamine.

* Corresponding author at: Laboratory of Organic and Macromolecular Chemistry (IOMC), Friedrich Schiller University Jena, Humboldtstrasse 10, Jena 07743, Germany.

E-mail address: ulrich.schubert@uni-jena.de (U.S. Schubert).

¹ These authors contributed equally to this work.

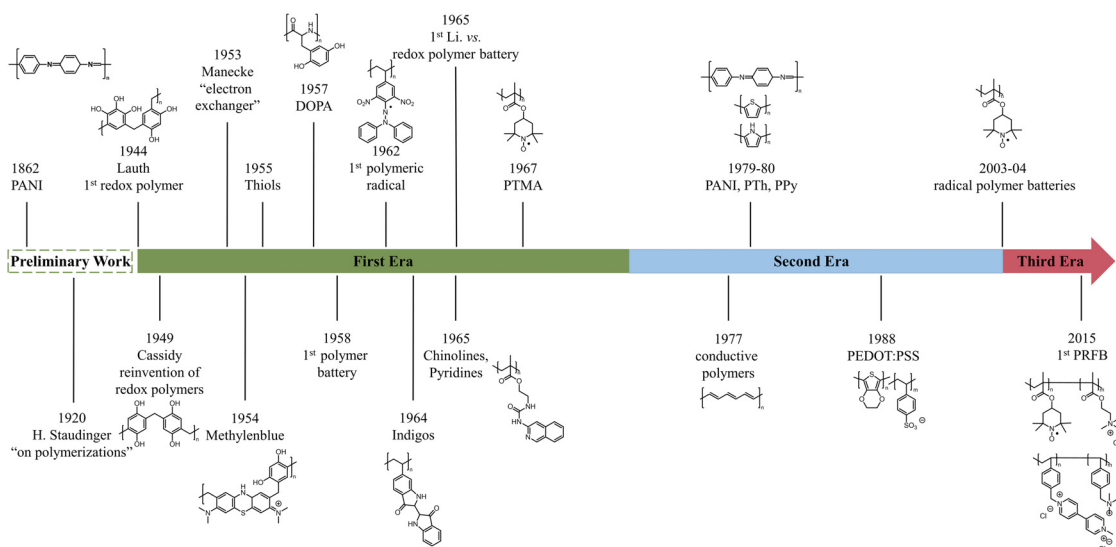


Fig. 1. Timeline with the most noteworthy inventions and scientific milestones in the field of redox-active polymers.

broadly established, which led to a displacement of many other systems and notably their discovery has recently been honored with the Nobel Prize in 2019 [2]. The inorganic lithium technology nevertheless has its limitations. The batteries are stiff and thus bending would lead to leakages and serious hazards [3]. Furthermore, the often required cobalt raw materials are toxic and extracted under unsustainable mining conditions, including the use of children laborers; [4,5] thus, the world market prices for cobalt rose over the last decade [6]. Larger battery packs also require temperature control systems in order to keep them within safe conditions, otherwise serious dangers, e.g., explosions can occur [7,8]. Thus, these disadvantages make inorganic lithium electrodes unfavorable for small and flexible devices in smart clothing, smart packing or other IOT devices as well as resources demanding applications such as battery systems for grid stabilization and on-site storage. Redox polymers, based on organic raw materials, represent a promising alternative approach for battery active materials for these applications. They allow the production of flexible devices largely independent from rare metal commodity prices and use a variety of possible scaffolds, making additional tailoring much easier. Nevertheless, the progress in the field of redox-active polymers is based on nearly eight decades of evolution. However, it must be mentioned that redox active polymers can be divided into two general types in which redox active moieties are located in the polymer backbone or the side chains. The polymers with redox active groups in the backbone can then be subdivided, depending on the individual active moieties being conjugated or isolated from each other. The former polymer type shows intrinsic conductivity. Every polymer architecture reveals its own individual advantages and disadvantages and must be chosen carefully based on the desired application in mind.

The idea of redox active chains is derived from the early studies using ion exchange polymers. Already in 1944, Lauth transferred the concept of reversibly exchanging charged ions to exchanging electrons and synthesized his poly(resorcinol-trihydroxybenzene-formaldehyde) redox polymers for a water deoxygenation application in 1944 [9]. Still, he was not the first to synthesize electroactive polymers, notably, poly(aniline) can be dated back to 1862 [10]. Due to the confusion of World War II, the discovery of redox polymers went basically unacknowledged, leading to an independent conceptualization by Cassidy [11]. The following years were dominated by his research group, who synthesized primarily poly(vinyl quinone)-based systems and investigated their

properties as well as their possible applications [12–15]. Starting in 1953, publications from Manecke et al. concerning "electron exchangers", started a scientific dualism between Cassidy in the US and Manecke in Germany [16,17]. In the ongoing years, both groups focused their research mainly on poly(quinones) and poly(catechols) [18–37]. Other active molecules were also investigated; however, they were rather marginal in the big picture. Nevertheless, many of the nowadays used active scaffolds were first published during this period of time. These include methylene blue in 1954 [38], thiols in 1955 [39], ferrocenes in 1959 [40], indigos in 1964 [41], quinolines in 1964 [41], pyridines in 1965 [42], and even bio-inspired molecules in 1957 [43]. The first synthesis of a macromolecular stable free nitrogen radical was reported by Braun, Loefflund, and Fischer in 1962 [44] which must be in particular emphasized as well as the first synthesis of poly(2,2,6,6-tetramethylpiperidinyloxy-4-yl methacrylate) (PTMA) in 1967 [45]. Unfortunately, the time was not prepared for a significant breakthrough during this initial phase of redox polymers. These materials were only interesting from a scientific point-of-view and their applications were mostly limited to water deoxygenation and hydrogen peroxide production [9,46–50]. Even the first polymeric battery reported in 1958 [51] and the first lithium vs. redox polymer battery in 1965 [52] could not make their future importance realized; thus, these polymers remained a scientific artifact for many years.

The second era of redox polymers (Figure 1) started with the work of Heeger, MacDiarmid and Shirakawa in 1977, who demonstrated the high electric conductivity of oxidized polyacetylene [53]. The initial objective to replace copper in electrical wires [54] was abandoned after it became obvious that this goal could not be achieved and the focus of research moved towards enhancing the polymer properties. New active materials were synthesized or simply rediscovered; Yamamoto et al. [55] in Japan and Kossmehl [56] in Germany were pioneers in the poly(thiophene) area; whereas, Diaz in the US investigated poly(pyrrole) and poly(aniline), [57–59] leading to a better understanding of the physical background responsible for the observed properties. At that time, the focus was more on enhancing the polymer properties, compared to synthesizing an easy-to-process polymer. In particular, the polymer's low solubility in water was problematic for post synthetic processing and could firstly be improved by the self-doping effect of poly(aniline) with sulfuric acid side groups [60]. After the processability challenge was solved, the actual commer-

cialization of conductive polymers opened the door for many research groups. Remarkable innovations were presented by Bridge-stone/Seiko with poly(aniline) and Varta/BASF with polypyrrole for the first commercial polymer that displayed particular electronic properties including conductivity [61]. The next breakthrough was the synthesis of PEDOT [poly(3,4-ethylenedioxythiophene)], which revealed higher conductivity, stability, and biocompatibility when compared to the initial poly(thiophene); [62] however, the poor solution-processability remained [62]. This issue was overcome in 1988 by compromising PEDOT with the water-soluble polymer PSS [poly(styrene sulfonate)] to PEDOT:PSS [poly(3,4-ethylenedioxythiophene):poly(styrene sulfonate)] [63]. It was initially planned to replace indium tin oxide (ITO)-coated glass in polymer light emitting diodes, but the obtained currents were insufficient for practical use; [54] it was, however, found that performance and lifetimes of the devices could be greatly improved by applying a thin film of PEDOT:PSS onto the ITO-glass [64,65]. Later on, the work of Wudl and Holmes about bulk heterojunctions led to the utilization of conductive polymers in the field of organic solar cells [64,65]. Another application for conductive polymers was found in thin film organic field-effect transistors (OFETs), in which polymers such as poly(acetylene) [66] and poly(thiophene)s [67] were the first ones used. The prominent role of conductive polymers in the energy storage sector is superbly summarized in the more in-depth reviews of Novak and Nyholm [68,69]. Overall, the second era was characterized by the fact that conjugated polymers opened up a new dynamic field of research – organic electronics – due to their novel redox properties.

With the ground-breaking works of Nakahara and Nishide, the concept of an organic radical battery (ORB) was developed in the beginning of the 21st century, [70,71] initiating the third era of redox polymers (Figure 1). 2,2,6,6-Tetramethylpiperidinyloxy (TEMPO) units, as redox-active moieties, were linked to a nonconductive methacrylate backbone. The respective polymers revealed a remarkable redox chemistry as well as favorable kinetics. Thus, polymers with stable radical side groups represent the most promising organic battery materials. [72] The currently used active scaffolds are as manifold as their (potential) application fields. [73] Redox-polymers are used for metal ion-based batteries containing Li, [72,74] Na, [75,76] K, [77] Mg, [78,79] Ca, [79] Zn, [79] or Al [79] as well as metal free all-organic batteries [80,81] and even redox flow batteries (RFBs) [82]. Furthermore, besides energy storage applications, electroactive polymers can be utilized in electrochromic devices, [83–85] molecular machines [86,87], sensors, [88–90] drug carriers, [91] or multi-responsive polymers [92]. The materials are increasingly tailored to the desired application. To further match their properties to the specific application, not only the respective active moieties, but also the polymeric architecture, length, and molar mass distribution of the polymer have to be optimized.

Whereas the current literature mainly focuses on the active moieties or the structure of the particular battery and which role a polymeric material can play within this batteries, we want to provide a brief overview of the origins and current trends in the field of electrochemical energy storage devices, based on organic polymers. Furthermore, we wanted to present an in-depth guideline describing which polymerization techniques can be used to produce a certain polymeric architecture. In addition, the compatibility of the polymerization process with the active scaffolds needs to be considered. The aim is to give the reader an overview of the polymeric design principles used in solid state batteries, pseudo-capacitors as well as redox flow batteries as well as their pros and cons for each application field. The knowledge transfer from one to the other should be supported and the reported concepts might also serve as an inspiration for other applications.

Therefore, we initially summarize and compare the most commonly used polymeric architectures in the field of organic batteries. Herein, we also discuss the dependency between the nature of the backbone as well as the integration possibilities of the redox-active moieties into the polymer on the shape of the cell voltage curves. Subsequently, we discuss the mainly used polymerization techniques and which of them are preferable for the polymeric architecture. In conclusion, we discuss the shown possibilities on the example of TEMPO-containing polymers.

In the next two sections, the working principles of solid organic batteries as well as pseudo-capacitors are presented. Then different polymer architectures and each subclass over what active moieties can be used and how good these polymers fulfill the initial presented requirements. The focus lays in the comparison of structural architectures and will highlight the possible advantages and challenges. The next section will deal with the working principle as well as the requirements on polymers for RFBs. In addition, we show the three classes of redox flow batteries – aqueous, organic and hybrid/suspension RFBs – each with its own special demands on the characteristics of the required polymers. We will consider the applied architectures and active materials to overcome the challenges and where room for possible improvements can be considered. Next, a short outlook on future developments is given.

Finally, we summarize the three subordinate topics of solid organic batteries, pseudocapacitors, and redox flow batteries in a short outline to give the reader a tool-in-hand for an optimal design of future redox-active polymer dependent on the implied application field. We finally end with our opinion on which innovation fields will have the most impact towards further commercialization and optimization of electrochemical energy storage application, based on redox-active polymers.

2. Polymer architectures and polymerization techniques

2.1. Influence of the polymer architecture on the cell properties

For further justification for polymers that bear the redox-active moiety in the backbone, the term “backbone polymer” or “backbone RAP (redox-active polymer)” will be used. In a similar manner, polymers that bear a redox-active moiety as a side chain, the term “sidechain polymer” or “sidechain RAP” will be utilized.

Besides the integration of an active material into the polymer, the architecture of the polymer itself represents a crucial factor. Whereas, the architecture is mainly dominated by the manner how and how often branching points are integrated into the polymer. Another important influencing parameter of the polymer properties is their composition and whether they consist of one or more monomers. This can – but not must – influence the structural architecture. All in all, the trend heads towards simple structures that can be easily synthesized *via* known techniques. The increased performances of complex structures are often in contrast to their costs and could stymie future potential commercialization.

Since the groundbreaking work of Heeger, MacDiarmid, and Shirakawa, conjugated polymers were hailed as the active material for the next environmentally friendly battery generation [53]. Their most outstanding property is the conjugated nature of their polymeric backbone, which was composed of the π -conjugated repeating units. Although the intrinsic conductivity is relatively low, it increases by several orders of magnitude upon charging, due to the introduction of delocalized charges along the main chain (*i.e.* doping) [93,94]. This is possible due to the widely expanded π -system of the polymer backbone; however, the introduction of delocalized charges also represents a great disadvantage. Due to the conjugated linkage, the redox moieties are electrostatically influenced by each other. This results in a redox potential that strongly

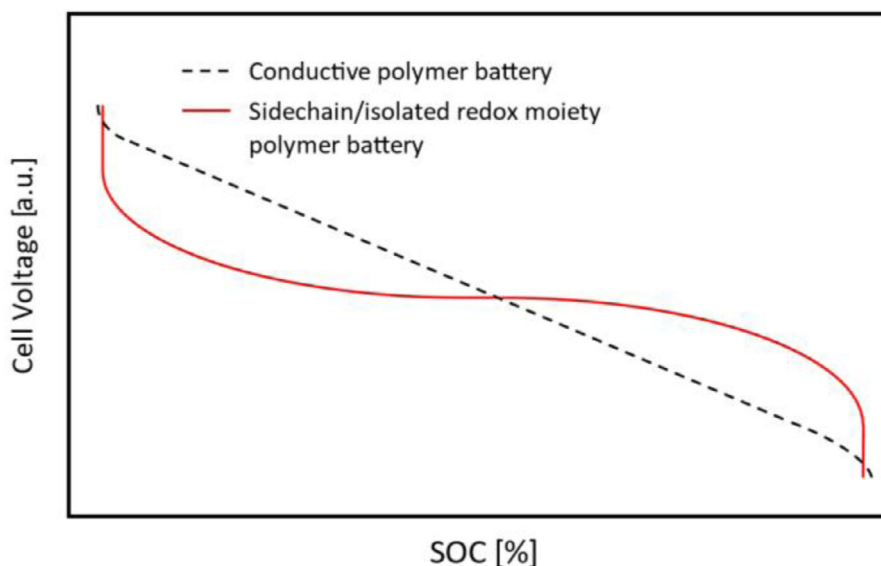


Fig. 2. Schematic comparison of the discharging behavior of batteries, based on conductive polymers (dashed line) and polymers with separated and isolated redox moieties (red solid line). The Figure is inspired by Shacklette et al. [99].

depends on the doping level – which changes with the battery's state-of-charge (SOC) – leading to a slope-like cell voltage (Fig. 3) [72]. Furthermore, the practically achievable doping levels (per monomeric unit) are strongly deviating from unity, with real values ranging from 0.3 to 0.5, causing significantly lower capacities than theoretically possible for 100% doped materials [95]. Even though the doping is not completed, the respective polymers represent highly charged species, resulting in a destabilized polymeric matrix, which could cause unfavorable chain interactions or even chain destruction reactions, [96,97] one drawback that they have in common with most redox polymers, bearing the active moiety in the backbone [96,97]. In contrast, a decoupling of the active site from the backbone into the side chain results in polymers that behave electrochemically more like the corresponding (isolated) monomers. Additionally, higher charging levels are possible, and the usually desired plateau-like cell voltage is obtained over a wide SOC range (Fig. 2) provided that there are no interactions between the side chain moieties [98]. Even though sidechain polymers are favored, based on their superior electrochemical performance; the synthetic routes are often more difficult or economically disfavored. Moreover, due to the lack of intrinsic conductivity, conductive additives are required to form a composite electrode in the battery. In either presented case, the respective polymer backbone defines the electrochemical performance of the material. It is therefore necessary to choose the appropriate polymer design for the intended material application.

2.2. Polymer architecture

2.2.1. Homopolymers

A homopolymer is the simplest possible design and, thus, is often also the cheapest way of producing a redox-active polymer. For them, only one monomer is polymerized to a RAP (Fig. 3). However, in a homopolymer, only this single monomer influences many of the properties of the desired polymer, e.g., polarity and redox kinetics [100]. Since a future fine-tuning of the properties, e.g. solubility, is hardly possible, a complex monomer synthesis might be the consequence. Furthermore, the polymer's length has a substantial influence on the characteristics, such as solubility or film forming ability [101]. Therefore, when using a homopolymer, the utilization of expensive polymerizations may be necessary in order to

obtain the desired chain length [100]. Additionally, during charging and discharging the material characteristics, by, e.g., creation or removal of charge, may significantly change. Therefore, it is often wise to physically decouple the redox-active and the property defining moiety of the polymer by using two different monomers, leading to copolymers.

2.2.2. Copolymers

Copolymers consist of at least two different monomers that will be comprising the polymer chain. This enables a much easier fine-tuning of the desired polymer characteristics [102–104]. This architecture is feasible for both backbone as well as side chain RAPs [100]. In addition, complex structures are often more easily accessible. However, in order to produce such structures like block copolymers, it is often necessary to tune the used comonomers, e.g., by reactivity, to each other.

In alternating copolymers, monomers are incorporated into the polymer alternatingly (see Fig. 3). The respective comonomer(s) can promote the solubility of the polymer or the redox processes of the active moieties. This architecture can be produced easily *via* step-growth polymerization with A_2/B_2 monomers as well as *via* cross coupling reactions [105]. With chain growth polymerizations, like ionic, radical or ring-opening polymerizations, this structure is significantly more difficult to obtain due to the often similar reactivity of the polymerizable groups (PG) [106]. Besides limited examples (e.g., styrene and maleimide in radical polymerizations) [106] statistical / random or gradient-like copolymer are obtained.

2.2.3. Statistical / gradient copolymers

Statistical / gradient copolymers incorporate the monomer into the polymer according to its reactivity (for architecture see Fig. 3). Similar reactivities of both monomers lead to a random distribution of both monomers within the polymer chain. In contrast, a large deviation of both reactivities leads to a gradient copolymer due to the preferred incorporation of the more reactive monomer at the beginning of the polymerization process. A clearly defined and reproducible monomer sequence is for both types barely possible or impossible [107]. Nevertheless, these architectures are most prominent among copolymers, since they are easy to produce and crosslinker can easily be added. Depending on the number of polymerizable groups in the crosslinker, multi-dimensional net-

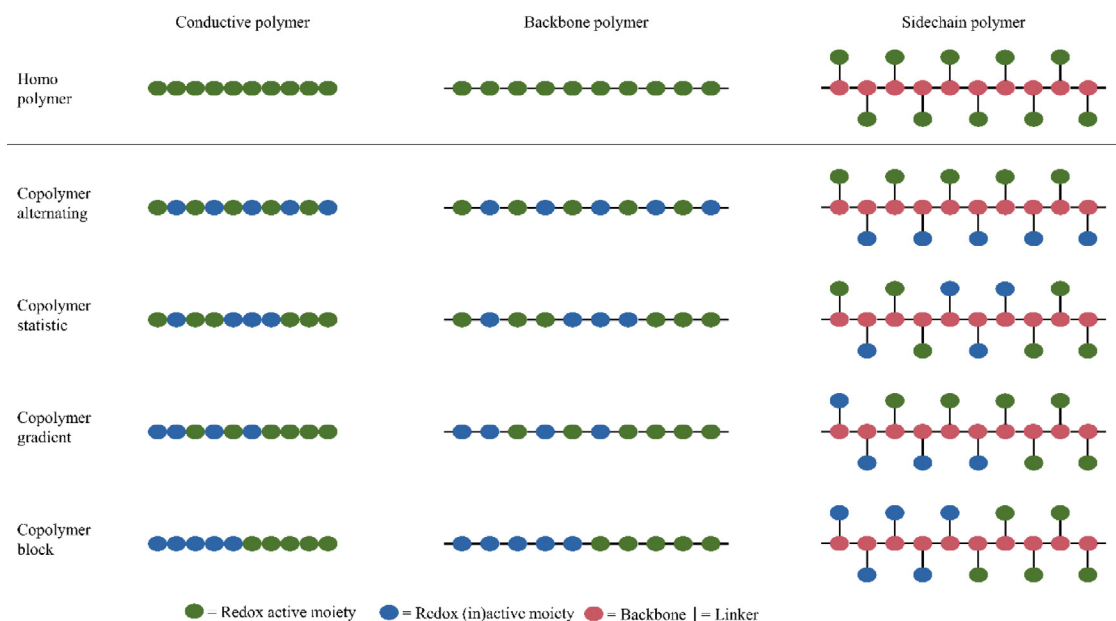


Fig. 3. Schematic representation of different possible polymer designs.

works are possible [108]. A key characteristic for crosslinked polymers is their insolubility in a wide variety of solvents, which is often required for batteries based on solid redox-active polymers or colloidal RFBs [109].

Block copolymers consist of two or more polymeric blocks (see Fig. 3), one for each monomer. While the first block bears the intrinsic electrochemical properties of a homopolymer in the redox-active material, the second block can be used to fine-tune further characteristics like solubility, cross-link-ability or conductivity [110–113]. This architecture is often used to promote self-assembly of the polymer to subordinate structures, like micelles, which can reveal different characteristics, e.g., solubility, compared to the pure polymer [100,114]. Since block copolymers are not easy to synthesize, special techniques must be utilized (see Chapter 2.3 “Polymerization Techniques” and in particular 2.3.2 “Chain-growth polymerization”), resulting in much more expensive polymers [110].

Special polymer architectures are complex architectures like branched, graft, star-shaped, and brush polymers as well as even dendrimers [115–118]. Often, the increased performances of the polymers are in no relation with the expenses incurred. They are, e.g., used to enhance the solubility or attach the polymer to a nanoparticle, but this can be considered as a niche technique only.

2.3. Polymerization techniques

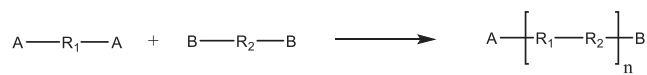
With the desired chosen polymer architecture, a matching polymerization technique has to be considered. In many cases, the redox-active material / moieties limit the number of suitable and matching techniques for the synthesis, even if the polymerizable group, linker or other parts of the molecule would be suitable for the selected technique. PTMA for example, cannot be simply synthesized in a free radical polymerization, since the high concentration of the free TEMPO radical would efficiently hinder the polymerization, in that TEMPO is a well-known polymerization inhibitor [119]. The introduction of a cleavable protecting group or the polymerization of a precursor in combination with a subsequent activation by oxidation can overcome these problems. Furthermore, quinones can also act as an inhibitor / controlling agent. They can be added to the polymerization of styrene resulting in a controlled radical polymerization *via* a quinone-transfer radical polymerization mechanism or to the monomer to sup-

press radical induced auto-polymerization, acting as a scavenger [120,121]. Therefore, radical polymerizations of quinoid moieties can be challenging. In order to circumvent this, either the utilization of an ionic or a metal-catalyzed approach is required. Alternatively, the active moieties must be introduced after polymerization in a polymer analogous reaction. For the latter approach, viologen polymers represent well-known examples. Commercially available poly(chloromethyl-styrene) can be functionalized *via* nucleophilic substitution with mono-alkyl bipyridines [82]. The possibility of using a predefined polymer with the desired properties makes post-polymerization derivatization a very versatile synthetic strategy toward RAPs. Nevertheless, these reactions will never reach full conversion thus resulting in a lowered number of active units attached to the polymer and a reduced ability to store electrical charges. Additionally, undesired side reactions as well as unwanted negative effects of the remaining (still reactive) starting material have to be excluded.

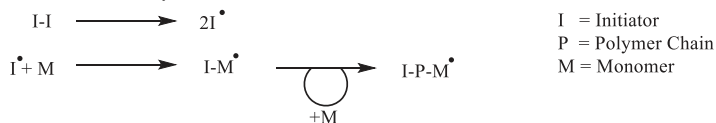
As the aforementioned examples show, the polymerization of the selected monomer may only be successful if the entire parameters, *i.e.* the desired architecture, the chosen active material, and the aspired polymer properties are considered for the polymerization approach. Changing just one small detail can therefore upset the entire system.

2.3.1. Step-growth polymerizations

In general, a step growth polymerization is not initiated by a separately added reactive species, but proceeds due to the intrinsic reactivity of the utilized monomers – a catalyst may also be present. All starting materials and products reveal the same reactivity; thus, it is determined statistically if a new polymerization chain starts or an already existing oligomer / chain adds another monomer unit. Typically, the polymerization is conducted with A_2/B_2 monomers, which are converted to the polymer (see Fig. 4). Therefore, comparably higher molar masses are commonly only possible with very high monomer conversions (well above 95%). Examples for step-growth reactions are polyaddition and polycondensation reactions. The first electron exchangers were synthesized by the polycondensation of quinoid moieties with formaldehyde under basic conditions [9]. Even nowadays, step-growth polymerizations play an important role in the synthesis of poly(diimide)s and hydroquinone resins, e.g., for redox flow batteries [105,122–

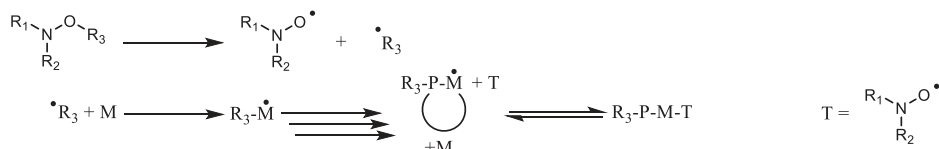
Step Growth Polymerization with A₂+B₂ Monomer

Free Radical Polymerization

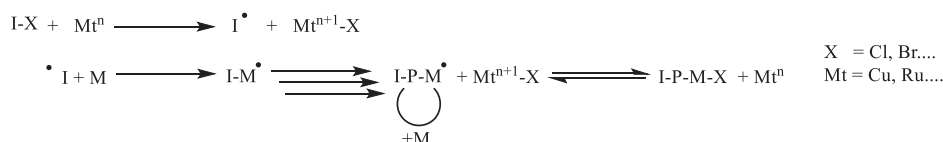


CRP - Controlled Radical Polymerization

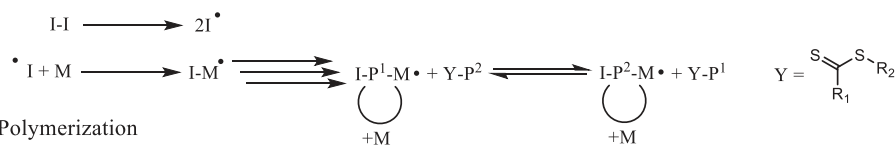
NMP - Nitroxide Mediated Polymerization



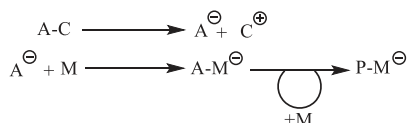
ATRP - Atom Transfer Radical Polymerization



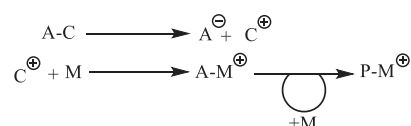
RAFT - Reversible Addition-Fragmentation Chain Transfer



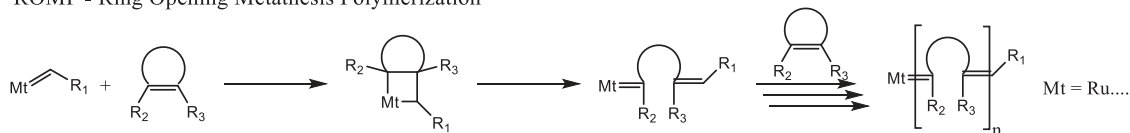
Anionic Polymerization



Cationic Polymerization



ROMP - Ring Opening Metathesis Polymerization



Redox Polymerization

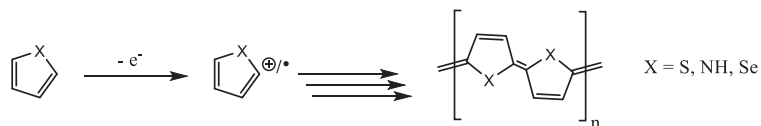


Fig. 4. Schematic summary of the different polymerization techniques.

[128]. Given that the step-growth polymerization represents an easy, cheap and robust technique, it is a commonly employed technique for polymers produced at industrial scale, e.g., polyesters or polyurethanes [129]. Nevertheless, step-growth polymerizations have major drawbacks like poor control over the dispersity (\mathcal{D}), molar mass and reproducibility, resulting in property changes of the polymers [130,131]. The polymerization conditions as well as the stoichiometry of the monomers must be followed exactly to receive polymers of comparable size and dispersity. Special cases

for step-growth reactions are metal-catalyzed coupling reactions, which could be either a step-growth or chain-growth reaction depending on the reaction conditions; even a controlled polymerization mechanism is possible [130,132–135].

2.3.2. Chain-growth polymerizations

The second major polymerization mechanism follows a chain-growth type reaction. At the beginning of the polymerization, a small but highly reactive molecule is generated from an initia-

tor. This reactive molecule attacks the polymerizable group of the monomer and subsequently transfers its reactivity. In the following propagation step, the next monomer is added to the activated monomer. The addition of a monomer to the growing chain is more favored than the start of a new chain. This addition step is repeated until the propagation is terminated. The chain transfer mechanism is, beside of disproportionation, reaction of the active chain with impurities or recombination, one of the major termination possibilities. These steps of initiation, propagation, and transfer / termination have all chain-growth polymerizations in common. But depending on the nature of the initiating species, the polymerization is mainly classified as a radical, cationic, anionic or metathesis polymerization. In contrast to step-growth polymerizations, high molar masses can be achieved relatively rapidly and already at low monomer conversions utilizing chain-growth polymerization.

2.3.3. Radical polymerizations

During a free radical polymerisation, a radical is generated mostly *via* homolytic cleavage of a weak bond in a reactive molecule, *i.e.* the initiator. This process can be triggered by an external stimulus like heat or (ultraviolet) light. This initially formed radical reacts with the polymerizable moiety of the monomer, which is primarily an activated bond with high π -orbital share. In this process, a covalent bond between the initiating radical species and the monomer is formed, while the radical species is shifted to the end of the growing chain, able to add another monomer unit (see Fig. 4). Due to the high monomer concentration compared to the overall radical concentration, the kinetics of the polymerization follows pseudo first order kinetics. In contrast to that, termination reactions like radical recombination typically obey second order kinetics, as two radical species are required. Thus, a comparably low radical concentration in the reaction mixture ensures a low dispersity and high molar masses in the product, while comparably high radical concentrations typically generate polymers with a lower molar mass and a broad molar mass distribution. High amounts of radical recombination reactions broaden the mass distribution more than other terminations, since the molar mass of the resulting chains is much higher when compared to disproportionation where the molar mass before and after termination is nearly the same. Which termination is more prominent is influenced by the nature of the monomer, the viscosity of the reaction mixture and monomer concentration [136]. All in all, the control over the polymer properties, *e.g.*, chain length or mass distribution and their reproducibility remains challenging [137]. Furthermore, a free radical polymerization approach is ineffective to generate block copolymers due to the transitory nature of the carbon-centered radical species. Nevertheless, a free radical polymerization can be used for many monomers and is cost-efficient as well as robust towards external factors, like atmospheric or solvent impurities, making it the polymerization of choice for large scale industrial applications [138,139]. As a consequence, it is not surprising that the FRP is one of the most frequently used polymerization technique for the RAP synthesis. Polymers for RFB and polymer batteries with, *e.g.*, TEMPO [80,98,140–142], other NO-radicals [143,144] (both *via* precursor monomers) as well as BODIPY [145], phthalimide, [146] and viologen [119] containing redox-active units, can be synthesized utilizing free radical polymerization techniques (see Table 1).

2.3.4. CRPs – controlled radical polymerizations

As mentioned for the FRP approach, a high concentration of the highly reactive radical species strongly increases the occurrence of possible termination reactions. Therefore, the conceptual idea of CRPs is a significant decrease of the active radical concentration during chain propagation. To achieve this, different additives are used that enable a reversible termination of the reactive species,

producing an unreactive or ‘sleeping’ chain end. These inactivated molecules exist in an equilibrium with their active counterparts, with the state-of-the-equilibrium strongly shifted toward the inactivated species [147,148]. As long as the polymerization is not finally terminated, though, it can be reinitiated. Thus, by addition of another monomer after completion of the polymerization of a first monomer, a block copolymeric structure or other architectures can be synthesized. Like all radical polymerizations, the reactions are relatively robust against impurities and a wide variety of solvents can be chosen [133,149–151]. All in all, CRP methods can be used to have high control over the polymer characteristics like chain length or dispersity. Furthermore, the reproducibility is increased in comparison to the FRP. We want to (1) highlight the three mostly commonly used techniques for reversible termination of radical polymerizations and (2) discuss their individual advantages and disadvantages for redox polymer synthesis in the following paragraphs.

The **nitroxide-mediated polymerization (NMP)** was firstly described in 1984 and uses a combination-dissociation mechanism [133,152]. The polymerization is mostly started by the cleavage of alkoxyamines but also “conventional” initiators like azobisisobutyronitrile (AIBN) or peroxides can be used in combination with nitroxide radicals [153]. The active chain end reversibly reacts with an aminoxyl radical derivative, forming an unreactive alkoxyamine [154]. The covalent bond formed in the process bond can be homolytically cleaved at higher temperatures, again generating the respective aminoxyl radical as well as an active chain end, which is able to add further monomer units (see Fig. 4) [155]. The cleavage temperature can be adjusted by using different aminoxyl radicals and is in the general range of 120 to 145 °C, but it can also be reduced to 70 °C, under certain conditions [153,156]. The drawbacks of the NMP are the (1) relatively high reaction temperatures, (2) slow reaction kinetics, (3) limited monomer scope (mainly styrenes), (4) difficult end capping and (5) limited commercial availability of the aminoxyl radicals derivatives [153]. Furthermore, sterically hindered double bonds are unfavored due to an impeded combination of the radical with TEMPO [153]. Although, NMP could be used to synthesis defined polymers with high control and reproducibility, the drawbacks predominate the advantages of this method and to the best of our knowledge there are no examples for RAPs synthesized by NMP.

The **atom transfer radical polymerization (ATRP)** was discovered by Matyjaszewski and Sawamoto in 1995 [157,158]. For this technique, transition metal complexes are utilized as halogen atom transfer agents between active and inactive species. Nowadays, the usage of many different metal ions, including Co [159], Fe [160], Ni [161], Pd [162], Re [163], Ti [164] and many others, depending on the monomers and reaction conditions, is common; however, the most frequently used element is copper. [165] The common copper-based ATRP utilizes the single electron redox process between Cu^{I} and Cu^{II} accompanied by the transfer of a halogen atom (mostly bromine) to activate a sleeping chain end and generate the reactive radical species [166]. The $\text{Cu}(\text{II})$ salt can reversibly transfer a halogen atom to the active radical chain end and, thus, regenerating the initial Cu^{I} species as well as the halogenated chain end of the dormant species (see Fig. 4). The copper catalyst is usually a coordination complex with a ligand species, which enhances the solubility in solution for better control [167]. The range of suitable monomers for this technique is limited by both the reactivity of the bond with high π -orbital share as well as the stability of the corresponding radical. Monomers with lower substituted double bonds are, thus, favored, but the ATRP is more sensitive to polar effects compared to steric effects [151,168,169]. Nevertheless, many monomers and solvents are applicable for the ATRP [170–172]. Generally, the reaction temperatures differ from *ca.* 25–130 °C depending on the halogen, pressure, catalyst, and other factors [173–175]. The wide variety of conditions for ATRP

Table 1
Summary of the advantages, disadvantages, and monomer requirements of different polymerization techniques as well as examples for each technique and their occurrence in the field of redox polymers.*The classification was performed according to the subjective feeling of the authors.

Polymerization technique	Advantage	Disadvantage	Monomer requirements	Monomer Scope	Examples	Typical polymer classes	Typical polymer architectures	Occurrence*
Polycondensation/ Polyaddition [130,131]	no inert conditions needed, robust towards impurities and oxygen, cheap, technically matured	often low molar masses and high dispersities, only statistical copolymerization, less control, strict stoichiometric and reaction conditions	AB monomer or A ₂ /B ₂ monomer	low	Poly(diimide), Poly(hydroquinone)-formaldehyde resins [105,123–128], polycoupling reactions [130,132–135]	backbone polymer, conductive polymer	homopolymers, alternating copolymers	often
Free radical polymerization [137,138]	no inert conditions needed, robust towards impurities (and oxygen), cheap, technically matured	high dispersities, only statistical copolymerization, less control	monomer should not inhibit radical formation or be a radical (it is possible but complicates the polymerization)	high	PTMA [80,98,140–142], NO-based Radicals [143,144], BODIPY [145], phthalimides [146], viologens [119]	Side-chain polymer	homopolymers, statistical copolymers	very often
NMP [133,152,154,155]	low dispersities, robust towards impurities, water as solvent possible	high temperatures needed, slow reaction, limited availability of aminoxyl radicals, difficult end-capping	Electron-deficient but reactive double bonds, which do not tend to form sterically hindered radicals	medium		Side-chain polymer	homopolymers, block copolymers	very rare
ATRP [157,158,165,166,170–172]	low dispersities, robust towards impurities, halogenated end group is easy to derivatize	high polymerization temperatures, metal-containing polymer, often colored polymers	limited availability of RAFT agents, often smelly and colored polymers	middle	PTMA [176–179,236]	Side-chain polymer	homopolymers, block copolymers	rare
RAFT [150, 181, 182, 185, 186]	mild reaction conditions, water is possible but no basic conditions [181]	no other reaction with RAFT agent than chain transfer		middle	PTMA [187,188]	Side-chain polymer	homopolymers, block copolymers	rare
Anionic [189,199–201]	very narrow dispersities, high control, very fast, easy end-capping,	high purity monomers and solvents, low reaction temperatures, expensive	electron-deficient polymerizable group, non-reactive toward strong nucleophiles e.g. carbanions	middle	PTMA [45,213,214,237], PTEO [187,188,238]	sidechain polymer	homopolymers, block copolymers, special architectures	very rare
Cationic [206,207]	very narrow dispersities, high control, very fast, easy end-capping,	high purity monomers and solvents, low reaction temperatures, expensive	electron-rich polymerizable group, non-reactive toward carbocations	low	TEMPO-vinyl ether [213,214,237]	sidechain polymer	homopolymers, block copolymers, special architectures	very rare
ROMP [215–217,220,221]	many solvents possible, mild reaction conditions, robust towards impurities and monomer properties	very limited monomer scope, expensive catalysts	norbornenes or strained-ring olefins	low	PTMA [204,205], N and NO based radicals [222]	sidechain polymer	homopolymers, block copolymers, special architectures	very rare
redox polymerization [223,224]	simple, mild and cheap reaction conditions, many possible solvents	very limited monomer selection	5-membered ring heterocycles and derivatives	low	PANI [225–227], PPy [228–230], PTh [231–233]	conductive polymer, sometimes sidechain sidechain polymer	homopolymers	very often
Polymer-analogue reactions [82,119]	commercial polymers can be used	polymers must be derivatized, limited selection of scaffolds for derivatization, no full conversion	derivatization reagent must react with polymer	low	Viologens [239,240], ferrocenes [241]	sidechain sidechain polymer	homopolymers, statistical & block copolymers	moderate

makes it a versatile route for the synthesis of RAP; however, one of the main drawbacks is the residual metal (ions) in the polymers, which can later act as a disruptive factor in the electrochemical processes. Nevertheless, the ATRP technique is used for the synthesis of PTMA-based, redox-active polymers for polymer batteries (see Table 1) [176–180].

The **reversible addition-fragmentation chain transfer (RAFT)** concept was introduced in 1998 [150]. The key element of this concept is the use of a thiocarbonylthio compound (i.e. RAFT agent), which is able to reversibly inactivate the growing chain end. Initially, the active radicals are generated by a radical starter, transferring the radical to the RAFT agent generating the dormant species (see Fig. 4). As for the aforementioned NMP and ATRP methods, activated and deactivated species exist in an equilibrium, in which the deactivated species is favored. In summary, the radical is, thus, reversibly transferred between different species by the RAFT agent [181]. In order to gain more control over the reaction, a relatively high amount of RAFT agent must be added to the polymerization mixture. Products obtained by this polymerization technique are often colored and exhibit a characteristic smell, due to the sulfur content of the RAFT-agents [182]. Since sulfur compounds are known to be electrochemically active the remaining RAFT-agents may influence the electrochemistry of the RAP [183]. However, the possible structural variability of RAFT-agents is high, but for the selection of the agent used, the nature of the monomer(s) has to be considered [168,184]. Unfortunately, the variety of commercially available RAFT agents is limited and the synthesis of the selected agent is often required. Nevertheless, the present reaction conditions are mild and many monomers can thus be used [185,186]. In the field of redox-active polymers, the RAFT technique is in particular used for the synthesis of PTMA containing polymers for redox flow batteries (see Table 1) [187,188].

2.3.5. Anionic polymerization

A polymer, synthesized by an anionic polymerization, was first published in 1954 by Szwarc [189]. The anionic polymerization favors especially monomers with electron deficient double bonds. An initial anion attacks the monomer, forming an anionic kinetic chain end, which is able to add another monomeric unit (see Fig. 4) The initiators have to be adapted to the monomer, but are typically strong nucleophilic compounds, e.g., metal amides [190], alkoxides [191,192], cyanides [193,194] or organometallic compounds like alkyllithium [195,196], Grignard species [197,198] or an active species that can be generated *via* an electron transfer reaction to the monomer, e.g., naphthalene sodium and butadiene [189]. If certain conditions prevail during the polymerization, the anionic chain end can be considered to be a living species, by staying active even if all monomer is consumed and no further monomer is added. Interestingly, this fact was already recognized in the initial publication by Szwarc et al. [189]. In order to achieve this, all possible side reactions, such as reactions with the respective counter ions, impurities and/or the solvent have to be excluded by a careful choice of reaction conditions. This in particular requires extensive purification steps for the monomers and solvents used. Furthermore, due to the high reactivity of the anionic species, the reactions generally require very low temperatures and strictly inert conditions, of course, always depending on the reactivity of the monomer. Controlling the polymeric properties as well as end-capping or generation of block copolymers and even more complex architectures are, thus, accessible [199–201]. In general, anionic polymerizations gave polymers with high molar masses and low dispersities [199]. The most prominent termination reactions occur between the highly reactive anions and impurities of the monomers or solvent, e.g., water. Further termination could be caused by back-biting or hydride elimination [202,203]. The anionic polymerization technique is mostly used for PTMA- and PTEO-based polymers in either redox

flow or solid polymer batteries (Table 1). A special case of the anionic polymerization is the group transfer polymerization in which silylketenacetals are used. This procedure has the same advantages as the anionic polymerization, but is technically less demanding and typically used for PTMA [204,205].

2.3.6. Cationic polymerizations

In this type of polymerization, the active species is positively charged, similar to the negatively charged counterpart in the anionic polymerization. The propagating species is initially generated by an electrophile, which is attacked by a nucleophilic monomer (Fig. 4) [206,207]. The main termination pathways result from a reaction with the counter ion or impurities [208] as well as proton transfer (i.e. chain transfer) [209,210]. Thus, in particular the nucleophilicity of the counter ion is a deciding factor for a successful polymerization. All in all, the cationic polymerization reveals the same advantages and disadvantages as the anionic polymerization, with low dispersities at high molar masses but under difficult reaction conditions [211,212]. The cationic polymerization is also used to polymerize TEMPO bearing vinyl ethers for solid polymer batteries (see Table 1) [213,214].

2.3.7. ROMP – ring-opening metathesis polymerizations

As the name suggests, the ROMP is based on a metathesis reaction involving transition metals e.g., ruthenium [215]. A metal complex coordinates the double bond of the monomer and a subsequent [2+2]-cycloaddition between the metal alkylidene and another monomer occur resulting in a metallacyclobutane. A subsequent cycloelimination then re-forms the metal alkylidene bearing the growing chain (see Fig. 4) [216,217]. The ROMP is very robust towards impurities, solvents, tolerates free radicals, [218] and, in general, the reaction temperatures are moderate [219–221]. However, expensive ruthenium-based catalysts must be used and the range of suitable monomers is rather limited to norbornenes or other strained ring systems containing double bonds [220]. But because of the possibility to directly polymerize free radicals, this technique was used to synthesize polymers with N or NO radicals (see Table 1) [222].

2.3.8. Redox polymerizations

A redox polymerization uses either a chemical redox agent, like FeCl₃ or electric current to oxidize a monomer to a radical cation. These radical cations dimerize and consecutive oxidation leads to dimeric and later oligomeric radicals, which further add monomers (see Fig. 4) [223,224]. This type of polymerization is mainly used for conductive polymers based on five- or six-membered heterocycles and their derivatives, such as anilines [225–227], pyrroles, [228–230] or thiophenes [231–233] (see Table 1). The main limitation of this method is the very lifetime of the generated radicals, which must be sufficiently long enough for the radical recombination reactions. [234,235] As long as the solvent does not interfere with the radical production process, decreases the stability of the radicals or react with the redox agent, the solvent can be freely chosen [234,235].

2.4. Influence of the backbone on the polymer properties

RAPs for battery applications can be further fine-tuned by a careful choice of the polymerizable group on the monomer, since it will determine the key physical properties of the desired product. Additionally, depending on the substitution pattern of the unsaturated polymerizable group, its electron affinity and polarizability as well as the steric accessibility are varied, reflecting their different intrinsic reactivity. This is, in particular, important in conjunction with the respective polymerization technique and may be detrimental for its success.

Due to the widespread scientific use of TEMPO, as an active material in RAPs, the influence of different substituents on the olefinic polymerizable group of TEMPO-bearing monomers is exemplarily shown in the following paragraph and summarized in Table 2 [242]. The TEMPO moiety is often introduced by means of its 4-hydroxy-piperidiny derivative. A prominent example is its methacrylate derivatives, whose polymers are known as poly(TEMPO-methacrylate) (PTMA) [243]. Methacrylic acid derivatives are widely used industrial chemicals. The syntheses of the redox-active monomers are ranging from reactions with acyl chlorides to transesterifications. For methacrylic monomers, numerous polymerization techniques are known, such as free radical [82,119,140,244], anionic [178,245], RAFT [119,177,180,246], ATRP [179] or living single electron transfer (SET) [247,248] mechanisms. However, direct polymerization of TEMPO-bearing monomers is possible but with difficulty. Therefore, most commonly, piperidine precursors are polymerized and subsequently oxidized to generate the TEMPO unit.

At the same time, the achievable architectures are as manifold as the polymerization possibilities, including homopolymers, block copolymers and graft polymers [219,236]. The obtained macromolecules are of medium polarity and reveal solubility in few organic solvents; however, especially challenging for battery applications are those with relatively short polymer chains that dissolve significantly faster when compared to those with longer chains. Therefore, strategies like controlled or living polymerizations are favored to give a low dispersity and high chain length that often are not achievable *via* free radical polymerizations [249]. Another challenge may be the lability of the ester connections between the TEMPO and methacrylic unit, as it is common for ester bonds. Similar properties can be found in polyacrylates. Generally, the ease of monomer synthesis is comparable to that of methacrylates; however, mainly radical-polymerized crosslinked systems have been presented so far [80,250]. The obtained polymers have a medium polarity, are swellable in water, and soluble in some organic solvents. In case of crosslinking, the solubility is expected to be lowered [80].

Styrenic repeating units represent another well-known monomer structure. However, only few TEMPO-containing polystyrenes are known as redox polymers with reference towards batteries. The TEMPO scaffold is typically linked *via* an ether bond to styrene. Those monomers are normally polymerized *via* FRP or CRP (followed by oxidation) and are known for insoluble crosslinked and block copolymers; whereas, the homopolymers often reveal low solubility and only swell in organic solvents [251,252]. Thus for solubility in the desired solvent, comonomers bearing mediating groups must be introduced. Nevertheless, styrenic polymers are, depending on the linker, stable against a wide range of possible reactants. Regardless, the styrenic repeating unit shows a comparably high molar mass when compared to the aforementioned (meth)acrylates, resulting in a lower specific capacity of the respective polymer.

The lowest molar mass and, thus, highest nominal specific capacity for TEMPO-bearing monomers reported in literature can be observed for the vinyl ether derivative. It can be synthesized by reaction of the TEMPOL with an allyl halogenide. The monomers can be polymerized either *via* a cationic or anionic polymerization and homo- and co-polymers are obtainable [45,213,214,237]. As the TEMPO moieties are connected *via* an ether bond, the linker is thus acid labile. Also, the linear backbone supports insolubility for aqueous and many organic solvents [237].

Another well-known monomer is the TEMPO glycidyl ether, that can be readily obtained by the reaction of TEMPOL with epichlorohydrin [238,253]. The epoxide can generate a polyether under AROP conditions. The obtainable molar masses and dispersities are moderate; whereas, the reaction yields are generally high. Homo-

and copolymeric species are accessible *via* this route; however, the elevated toxicity of the necessary epichlorohydrin has to be considered as a safety issue. Due to the high oxygen content of these polymers, the polarity of the backbone is increased leading to a better solubility in polar solvents and a decreased solubility in nonpolar solvents, respectively [187,188,254]. Poly(norbornenes) represent another polymer backbone that can be obtained with a comparably high overall molar mass, resulting in a lower specific capacity of the respective polymer. Norbornenes can be polymerized *via* ROMP; [219] however, the commercial access to highly functionalized norbornenes is often limited and extensive synthesis must be applied. If synthesized, one of the main key derivatives represents the dicarboxylic derivative of norbornene; furthermore, ROMP utilizes expensive transition metal catalysts. But on the other hand, creating crosslinked architectures are possible; thus, graft polymers have been shown to be accessible *via* this route [219]. The resulting polymers exhibit high thermal and chemical stabilities, due to the strong backbone. Nevertheless, their solubility is considerably low, except for those that possess short side chains, that can dissolve in nonpolar organic solvents [219].

3. Solid polymer batteries

Metal ion batteries have emerged as one of the most promising approaches towards energy storage. [72, 260–266] In this context, both organic and inorganic storage materials are used and therefore, this represents the largest group of recently produced energy storage systems for everyday use [266]. Very well-known are Li-, Na-, or Mg-based and, in general, metal-based systems. They can be found in manifold applicable scenarios, from static on-site energy storage systems for the storage of excessive energy, to small wearable storage units for consumer electronics [267,268].

For over 50 years, organic compounds for solid polymer batteries have been investigated, pioneered by Williams et al., who investigated dichloroisocyanuric acid, as the cathode, in a Li solid-state battery systems [269]. Most of the battery development has been performed utilizing inorganic materials, which lead to manifold inorganic battery chemistries that show excellent cycling performance and are commercially available today. Nowadays, many active materials are comprised of Li compounds and are of an ionic nature, such as LiCoO₂, LiNiO₂, LiMn₂O₄ or LiFePO₄. However, rating the sustainability of inorganic battery materials is always an issue, in particular in terms of mining and extraction processes and their energy efficiency [270]. Recently, the search for alternative electrode materials has been strongly focused on organic systems that possibly can be produced in a less environmentally detrimental manner and are comprised of tailor-made electrode systems for batteries. Eventually, organic materials may be synthesized from renewable sources that provide small organic building blocks for single molecule, monomer and polymer syntheses [271–273]. All-organic, solid-state batteries show fascinating new features, such as flexibility, higher voltages, and high current densities [274–277]. This next chapter will deal with the working principle of polymer solid-state batteries, the requirements for the redox-active materials and typical moieties, that can be introduced into and/or onto a polymeric backbone. For a general overview on possible structures for energy storage nanoarchitectures see the very interesting review by Kim et al. [278].

3.1. Working principles

Even though both inorganic and organic solid-state batteries generally rely on the presence of a metal ion in the electrolyte, the charge storage mechanism itself proceeds differently, as presented in Fig. 5. In a Li-based, solid-state anode, Li ions are transported *via* an electrolyte into a porous carbon material, upon charging.

Table 2
Summary of TEMPO bearing polymerizable groups with their inherent properties and subsequent polymer characteristics.

Polymer-izable group	Molar mass (PG)	Molar mass (M_n) of polymer	\bar{D}	Synthetic availability of monomer	Commercial availability	Polymerization mechanism	Shown architectures	Polymer limitations	Polarity and solubility	Ref.
Meth-acrylate	85.08 g mol ⁻¹	free radical: high & low anionic: low RAFT: low, medium ATRP: low Living SET: high	free radical: medium & high anionic: medium RAFT: low ATRP: low Living SET: low	Methacrylic esters can be easily reacted with alcohols or amines to give reactive monomers, that can be post-polymerization functionalized	Methacrylate's available with and without TEMPO moiety, solubility influencing co-monomers, many crosslinkers	free radical, anionic, RAFT, ATRP, Living SET	Block-co-, graft-, Homo polymers	oxidation step required, smaller chains dissolve in electrolyte easily, degradation <i>via</i> transesterification & ester hydrolysis	medium polarity of poly(methacrylates), soluble in many organic solvents	[82,119,140,177–180,219,236,244–247,248,255–257]
Acrylate	71.06 g mol ⁻¹	free radical: high	free radical: high	acrylic esters can be easily reacted with alcohols or amines to give reactive monomers, that can be post-polymerization functionalized	acrylates available but without TEMPO moiety, solubility influencing comonomers, many crosslinkers	free radical	Homo polymers, crosslinked	oxidation step required, smaller chains dissolve in electrolyte easily, degradation <i>via</i> transesterification & ester hydrolysis	medium polarity of poly(acrylate), soluble in most organic solvents, water solubility dependent on pending groups	[80,250]
Styrene	104.15 g mol ⁻¹	free radical: high	free radical: high	TEMPO linked to styrene <i>via</i> an ether or ester bond	polymers are available, styrenic monomers available for linkage	free radical	Block-co-polymer, crosslinked	oxidation step required, soluble in nonpolar, aromatic solvents	solubility in organic solvents	[251,252]
Vinyl ether	43.05 g mol ⁻¹	cationic: high	cationic: low	TEMPO vinyl ether readily synthesized	starting materials available	cationic	co-, homo-polymers	acid labile	insoluble in most organic solvents, rather nonpolar	[45,213,214,237,258]
Glycidyl ether	44.05 g mol ⁻¹	AROP: medium	AROP: medium	monomer available high <i>via</i> etherification, handling of highly reactive and toxic glycidyl compounds often difficult synthetic approach	Epichlorohydrin and TEMPOL available for monomer synthesis	AROP	co-, homo-polymer, crosslinked	acid labile	insoluble in common organic solvents, polar backbone, rather soluble in polar solvents	[187,188,254]
Norbornene	94.16 g mol ⁻¹	ROMP: high	ROMP: low		limited amount of crosslinker available, starting material norbornene dicarboxylic acid available	ROMP	co-, graft- & homo-polymers	high thermal & chemical stability	nonpolar backbone, solubility in some organic solvents, smaller chains easily dissolve in electrolyte	[80,81,219,259]

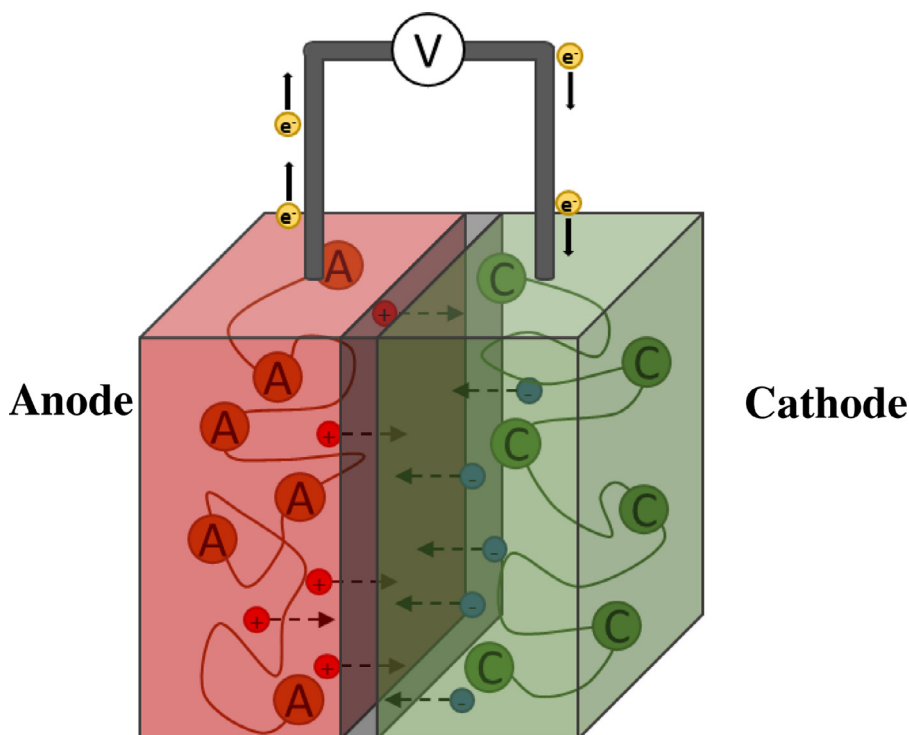


Fig. 5. Working principle of a solid-state organic polymer-based battery, A: Anode active redox unit, C: Cathode active redox unit, semipermeable separator represented in gray between the electrode compartments in red and green (For interpretation of the references to color in this figure legend, the reader is referred to the web version of this article.).

The metal ions are reduced and intercalated into the carbon surface. Therefore, the charging speed is determined by the diffusion and intercalation rate of Li, as an intercalation complex is formed inside the porous carbon electrode. The process is accompanied by a volumetric change of the electrode material. A successive deactivation can be the result of the created mechanical stress inside the cell, limiting the lifetime of the whole battery.

However, in an organic cathode material, a metal ion such as Li, Na, Mg or K is also transferred to the electrode upon charging, but the storage mechanism itself proceeds by direct interaction of the metal ion from the electrolyte and the organic material. Thus, Li can be adsorbed or chemically coordinated by a carbonyl group, when a reduced organic compound is formed. Due to the lack of intercalation, the charging kinetics are less dependent on the kind and the radius-of-electrolyte metal ions and examples for several metals, such as Li, Na, K, or Mg are known [75–79,279–282] However, both the organic and inorganic solid-state systems can suffer from self-discharge, ion-trapping mechanisms, side reactions and/or dissolution behavior of the active electrode material in the desired electrolyte. [283] Therefore, the solubility or insolubility of the active electrode material is one of the most crucial aspects that must be considered during the design phase. Typically, a preferably insoluble electrode material is required to store the applied charge. To promote insolubility of the organic material, several polymerization techniques have been applied to obtain non-soluble electrode materials, by a plethora of working groups. However, to achieve conductivity in organic solid-state electrodes, carbon-based conductive additives are utilized, in order to guarantee an equal charge distribution within the electrode and quick charging, as the desired redox reactions often occur on the conductive agent-active material interface [284].

The total amount of conductive carbon additive may be decreased if π -conjugated polymers are used as the respective storage material, *via* their intrinsic electric conductivity. Furthermore,

in conjugated polymers, the chemical activity does not rely on the presence of distinct redox sites attached to the polymer, but rather is based on the redox activity of the polymer itself, achieved by doping the conjugated π -network [285]. This is achieved by introducing dopant anions or cations that reduce (n-doping) or oxidize (p-doping) the polymer and create an electric charge, as mentioned in Chapter 2.1. The conductivity of the obtained conductive polymer strongly depends on the actual degree-of-doping [285]. Consequently, the redox activity of the conductive polymer also depends on the degree-of-doping. Even though a preferably high degree-of-doping is desired, the material typically suffers from an excessive introduction of charge carriers, as a high amount of electrical charges destabilizes the basic organic network. In many cases, conductive polymers are utilized as cathode materials, since they exhibit mostly stable redox chemistries in their respective p-doped state under reductive conditions. The charge / discharge voltage curves exhibit a sloping shape as the redox potential scales with the amount of doping of the material (Fig. 2). Therefore, obtaining constant battery voltages is always challenging when considering a conductive polymer as a battery active material. In a recent approach to circumvent the aforementioned drawbacks, Esser et al. as well as Facchetti et al. used redox-active units embedded into a conjugated polymer matrix or redox-active groups that have been linked to the polymer chain, to stabilize the redox potential, while maintaining the delocalization of the stored charge in the electrode *via* an electron-transfer mechanism between the redox-active group and the nearby conjugated polymer [233,286].

3.2. Material requirements

The choice of the right active materials requires the consideration of several material aspects, such as design, polymerizable moiety, and solubility-mediating group(s). To this day, battery research as well as industrial applications are based on a large number of known active moieties introducible to polymers; [260,287] how-

ever, the most prominent requirement is the insolubility of the active material in the utilized battery electrolyte. Many research groups have solved this problem by the introduction of additional groups in order to decrease the solubility, or intrinsically insoluble systems, such as cross-linked polymers or low-soluble conjugated polymers are utilized. However, the processability of very low-soluble systems can be challenging. Therefore, *in-situ* polymerizations are often performed to obtain the polymerized electrodes [288].

The active material itself is as important as its low solubility. Since many scaffolds can be attached to a polymer or provided in a polymeric form, the properties of the product can be fine-tuned according to predefined requirements. While every organic redox-active group may have a potential window that can be addressed electrochemically, further attributes or even the exact redox potential can be fine-tuned, largely by molecular changes to the composition of the redox-active moiety. Introduction of solubility-mediating or -preventing, electron donating- or withdrawing-groups to the often conjugated active center are possibilities to tailor the properties. This approach can also be applied to the active groups, that are introduced into or onto the polymeric backbone [289]. The capacity of a solid-state battery is measured in mAhg^{-1} and is directly related to the number of electrons that are stored in the active material. [262] In the case of polymers, an increasing molar mass generally results in an increasing number of redox sites, for which an average molar mass can be assigned. This must be considered when comparing the specific capacities of active materials.

For all of the electrode components, electrochemical stability is mandatory. Mainly, for conductive polymers, electrochemical stability often comes at the expense of a high electrode activity, as in this case both properties are closely linked, due to the doping process [289]. Therefore, conjugated homopolymers, mainly with direct covalent links between the redox-active moieties, are popularly used, since they show a significantly higher specific capacity. This also leads to good charge transport and storage properties that are desired in solid battery electrodes. However, utilizing an organic electrode makes it possible to consider aqueous electrolytes and their advantages, in contrast to the inorganic Li-based materials, which are more or less limited to their usage of organic electrolytes. Nevertheless, aqueous electrolytes only support a narrow potential window of *ca.* 1.2 V, which radically limits the operating voltage of the battery [290,291]. But since non-toxic, renewable and sustainable battery systems are desired, aqueous battery systems are subject to widespread research efforts [292,293].

Similar to the active material(s), the electrolyte composition is a parameter that must be investigated considering sustainability aspects as well. Many solvents for Li-ion batteries are liquid organics that can show high toxicity and flammability. Furthermore, viscosities can be problematic when using liquid organic electrolytes. Also, the ion mobility of the metal ion should be as high as possible to guarantee a high conductivity within the electrode [294].

Further the supporting electrolyte ion mobility inside the electrode can be directly mediated through the porosity of the active polymer matrix [295–298]. While this may be achieved through the addition of a surface-enhancing conductive agent, the high-porosity redox polymers themselves have recently been shown to increase the active surface of the electrode. Increasing the active material surface also increases the availability of the redox active polymer for supporting electrolyte ions, thus facilitating the desired redox behavior. Therefore, it reduces the need of conductive groups from the active material itself, that may go along with the undesired side effects, such as sloping voltage curves, or higher conductive agent ratios, that can decrease the total battery capacity. Recent examples, comprised of two- and three-dimensional networks, use anthraquinone or polyimide active groups. Also, con-

Solid State

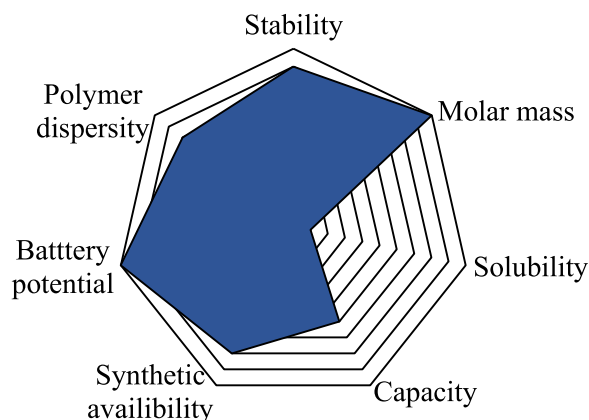


Fig. 6. Spider web diagram of the material requirements for solid-state batteries (from 0 – low to 10 – very high).

ductive polymers both with and without pendant redox active moieties have been demonstrated [295–298].

All in all, polymeric redox-active materials can easily meet all requirements for an active material for a solid-state battery: solubility, cyclability, specific capacity, the applicable potential, and synthetic availability (Fig. 6). Said criteria are summarized into a spiderweb diagram. The necessary values are rated on a scale from 1 to 10 to create an overview about the requirements that must be met for an ideal polymeric, solid-state, battery material (Fig. 6). A multitude of polymers has been utilized by various research groups, differing in polymer architecture and redox-active moiety. The following sub-section outlines active materials (Fig. 7), focusing on the respective redox-active units and their integration into the polymer.

3.3. Architectures

3.3.1. Linear conjugated polymers

Linear conjugated polymers (CP) for the use in solid-state batteries have been investigated intensively for over the past 30 years. Most known systems rely on this architecture, that is readily obtained. The first attempt of energy storage with organic polymers was performed utilizing conjugated polymer materials, initially poly(aniline), with a lithium counter electrode [299]. In the late 80s, Bridgestone-Seiko and Varta/BASF introduced commercial batteries based on poly(pyrrole) and poly(aniline) [61]. Since then, the concept of decreasing the amount of conductive additives by the utilization of intrinsically conductive active materials has gained high interest in the scientific community. However, intrinsic challenges of the redox behavior of conjugated polymers must be met to obtain truly high-performance batteries. The first challenge is the previously mentioned floating redox potentials of CPs. In a CP, π -orbitals of the covalently and conjugated repeating units overlap, creating a semiconducting valence-band [300,301]. If charge carriers are introduced into the conjugated network by doping, a conductive polymer is obtained. The redox potential of the doped CP is strongly dependent on the degree-of-doping, leading to a varying redox potential as a function of the state of charge (SOC) of the battery system [99]. Different approaches, combining the advantage of an isolated redox site with a stable redox potential and the conductivity of a doped CP have been presented in literature for a plethora of different CP systems. For instance, TEMPO, ferrocene or quinoid structures have been linked to con-

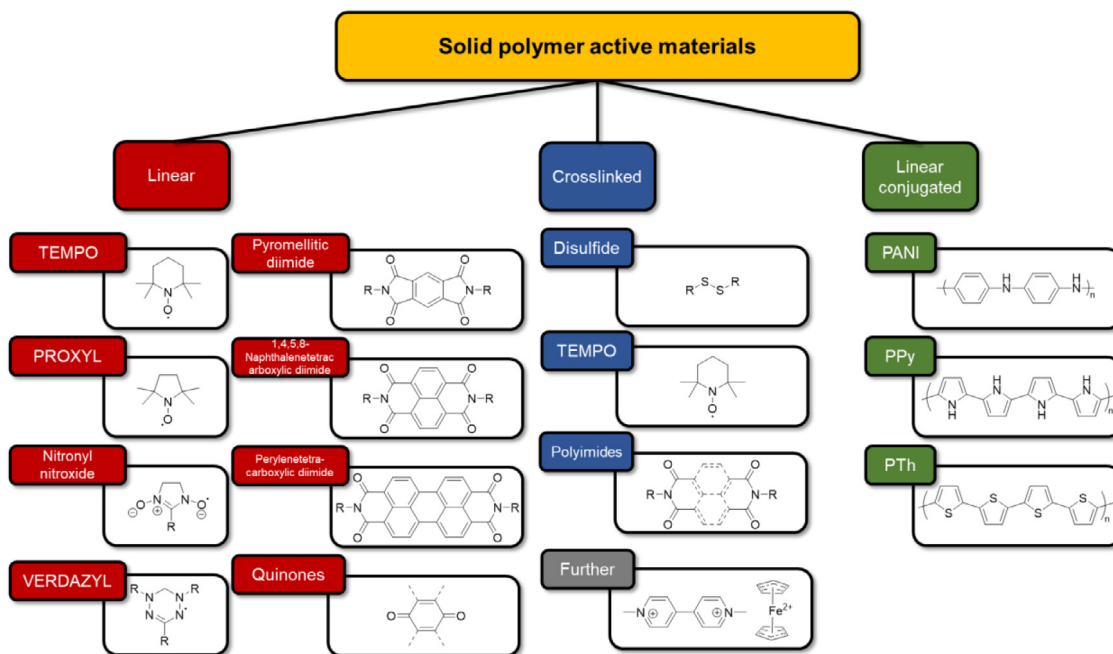


Fig. 7. Summary of the redox active moieties applied for solid polymer batteries, organized by the structure of the polymeric backbone.

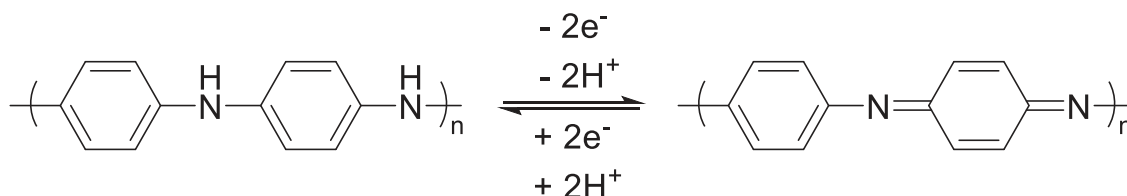


Fig. 8. Schematic representation of the chemical structure and redox reaction of PANI conjugated polymers.

jugated polymers [287,302,303]. However, internal charge transfer processes between the active redox unit and the doped CP-backbone are challenging, since the charge transfer can lead to a non-desired change of the degree-of-doping in the backbone, thus, hindering the redox activity of the side groups or the conductivity properties of the backbone [304]. Also, different dopants have been investigated, that are electrochemically active or inert [287].

Generally, conjugated polymers exhibit intrinsically low solubility, that is often decreased when the backbone is further functionalized; [305] therefore, molar masses and dispersities are not discussed in detail since the main characteristics are obtained by choosing the kind of repeating unit and functionalization. Due to the diverse tuning possibilities, synthetic availability and interesting features, conjugated polymers have been subject to on-going research, that can be seen in a multitude of fascinating review articles. For a detailed overview about poly(aniline), poly(thiophene), and poly(pyrrole), a review of Jia et al. is highly recommended [287]. Akagi also demonstrated in his very comprehensive review, different CPs as well as their possible applications, synthetic approaches and properties [306].

3.3.2. Poly(aniline)

Poly(aniline) (PANI) represents a very well-known conjugated polymer and was investigated among the first redox polymers. The structure and redox reaction of PANI are depicted in Fig. 8. In 2019, a comprehensive review was presented by Jia et al., discussing various groups of conductive polymers and also Luo et al. presented an in-depth overview on PANI materials [287,307]. There, detailed information is given, from the first representatives being quinoid polymers, that derive from hydroxyl or amino functionalized ani-

line derivatives [308,309]. Accordingly, amine-carrying monomers can readily be obtained by classic nitration procedures, followed by reduction with SnCl_2 as shown by Ivashkina et al. in 1984 or obtained commercially [310]. The amino benzoquinoid monomer can be polymerized by an oxidative polymerization utilizing ammonium peroxodisulfate giving, poly(2,5-dimethoxy aniline) in a solventless synthesis [311,312]. Electropolymerizations are also possible. If methoxy derivatives are utilized, a deprotection step comprising BBr_3 must be added, to allow the quinone-hydroquinone redox transition to occur; [313] at low pH values, conductivity was achieved [311]. For a conductive polymer, a high theoretical capacity of 443 mAhg^{-1} was obtained by the Gohy group, due to the additional addressable redox process of the quinoid groups; however, due to the insolubility of the poly(anilines), data about homogeneity or dispersity of the are rarely reported. Further trials have been reported using sulfur, TEMPO or ferrocene moieties in the PANI backbone to further alter the properties, such as: conductivity, capacity or redox potential [225–227].

Sulfur functionalized PANI systems have been published by Komiyama et al. as early as 1997, in which disulfide bridges between two PANI conjugated polymer backbones were reported. Since the polymers are obtained through electropolymerization on an electrode surface, no statements about the molar masses or chain length distribution were made [314]. They, however, obtained a capacity of 270 mAhg^{-1} with a working potential of 2.5 V vs. Li. Higher capacities can be achieved when the respective disulfide moieties are attached to each repeating unit, as side groups. Zhou et al. obtained a poly(α,α' -dithio-3-amino-*o*-xylene), that showed a specific capacity of 370 mAhg^{-1} , due to the availability of a

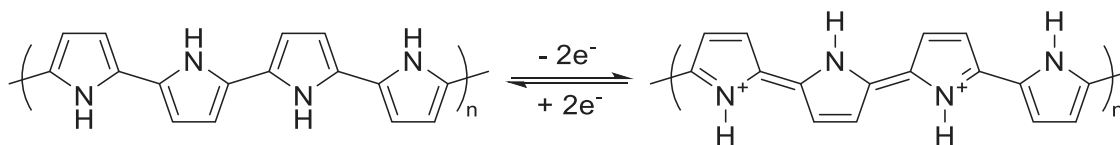


Fig. 9. Schematic representation of the chemical structure and redox reaction of PPy for a two electron redox process.

sulfur redox process [315]. This development is thoroughly documented by Jia et al. in 2019, therefore only more recent developments are herein mentioned [287]. Recent approaches focus on the introduction of active scaffolds, e.g. phenothiazine, into a PANI backbone. Electropolymerization of aniline with phenothiazine led to a flexible battery electrode, that can be operated at $\text{pH} = 5$ and delivers high capacities of 306.3 mAhg^{-1} with an aqueous zinc electrode. High cyclability was achieved, and enormous mechanical stress was shown to be tolerated by the device [316]. Due to the high stability of the redox signal of PANI polymers, Zhang et al. chose PANI as a counter electrode for a low-temperature zinc battery system. The transition of the aromatic anilines towards the quinoid shape exhibited consistent shapes at a large temperature span from 60 to -90 °C. Analogous to previous publications, the PANI was obtained from standard polymerization conditions utilizing $(\text{NH}_4)_2\text{S}_2\text{O}_8$ and later showed a capacity retention of 84.9 mAhg^{-1} after 2000 cycles at -70 °C [317]. For a detailed focus on Li-S batteries comprising said conductive agents, the review of Hong et al. is recommended [318].

3.3.3. Poly(pyrrrole)

As for the other common conjugated heteroaromatic polymers, numerous reviews for poly(pyrrrole) exist [287]. Therefore, the compound is just briefly discussed herein. Poly(pyrrrole) (PPy) is a conjugated polymer with pyrrole repeating units (Fig. 9) that are linked in the respective α -positions to the nitrogen atom and can be substituted at both the β -carbon atoms as well as the nitrogen atom. Often, redox-active groups are linked to this polymer, as an efficient doping can be achieved, by direct linkage [287].

The group of Goodenough presented a poly(pyrrrole) with pendant ferrocene groups, linked *via* a propyl bridge. The capacity could be increased to 65 mAhg^{-1} in comparison to the 20 mAhg^{-1} for the un-modified poly(pyrrrole), which is due to the participation of redox-active ferrocene [228]. The dispersity of the polymer is not discussed and, as the solubility of this pyrrole-based polymer is intrinsically low. The applied synthesis can be considered complex as it comprises firstly, the reduction of 1-(cyanoethyl)pyrrole to the free amino group, then secondly the reaction of thoroughly dried ferrocene carboxylic acid with oxalyl chloride in the dark gave subsequent amide formation, then the electropolymerization, generated the functionalized pol(pyrrrole) films [228].

Also, organic redox-active moieties can be linked to the pyrrole nitrogen. Wang et al. presented poly [6-(1*H*-pyrrol-1-yl)quinoxaline] in a solid electrode setup, making use of the reversible quinoxaline redox chemistry. Amino quinoxaline is reacted with 2,5-dimethoxytetrahydrofuran and iodine in water. A dispersion is then created and bromine is subsequently used to induce polymerization. An insoluble polymer is obtained that was characterized in a composite solid-state electrode. Due to the quinoxaline, the sloping CV curve of the PPy is turned into a rather sharp redox signal; however, the charging and discharging slopes appear rather steep [319]. This effect has also been described by Sjödin and coworkers, after the introduction of benzoquinone units. Depending on the position of the additional redox moiety, sharp signals can be observed, e.g., ethylene spacers between PPy backbone and the quinoid structure can help to sharpen the CV signal, while a direct connection leads to broader reduction signals in acidic aqueous media [229,230]. Also TEMPO and viologen have been in-

vestigated in PPy- linked compounds, but have been extensively discussed elsewhere [287,302,320].

Next to the connection of redox-active moieties, different approaches also focus on investigation of intricate PPy structures, such as nano-pipes created from methyl orange dyes. They are obtained after reaction of methyl orange, FeCl_3 , and pyrrole in water at 25 °C. While the typical sloping potential of CP-composite electrodes can be observed in battery trials vs. Li, the capacity retention reached 93% after 2000 cycles and a stable capacity of 652 mAhg^{-1} . [321] However, while the synthesis is rather straight forward, the characterization of the obtained embedded pyrrole moieties proved to be challenging.

Current efforts utilize polymerized pyrrole rather to trap transition metal oxide particles, creating hybrid materials for battery electrodes without covalent modification. A process to polymerize pyrrole epitaxially on MnO_x platelets was presented by Li et al., who made use of the redox activity of manganese oxide particles to directly induce polymerization [322]. Further attempts to stabilize Ni- and Mo-oxides have been shown by Zhang et al., through formulation of metal oxide microspheres, that are coated with poly(pyrrrole). The resulting electrode revealed an improved capacity and rate capability vs. Zhang et al. [323]. Similar effects have been shown for Co, Mn, and S composites and aqueous Zn batteries [324,325].

However, with PPy being combined with metal oxides, the role of PPy is drawn further away from being an active material itself, towards supporting redox behavior of inorganic active materials. Different approaches with low molar mass active materials have been investigated by Iihama and coworkers, who introduced disulfidic groups onto the polymer. A battery was constructed that reached the 398 mAhg^{-1} of specific capacity, which accounts for a theoretical number of 2.3 electrons, transferred to a repeating unit upon charging [326].

3.3.4. Poly(thiophene)

Next to PANI and PPy, poly(thiophene) is among the most well-known conjugated or conductive polymers. As a result, the compound has been shown in a variety of review articles [287,318]. Another easy to obtain and functionalizable conductive polymeric system is poly(thiophene) (PTh), which shows stable n-doping properties, when functionalized sidechains are introduced [231,287]. They can be obtained by chemical, for instance using FeCl_3 , as well as electrochemical polymerization procedures [232,327]. Recently, the oxidative method was utilized for the preparation of poly(thiophene)/carbon-nanotube composites for application in aluminum batteries [328]. Poly(thiophenes) are easily functionalized in the β -carbon atom and ring sulfur position, for instance doping effects can be achieved when electron withdrawing groups are introduced. Again, side groups affect the electrochemistry of the poly(thiophene) due to their electronic and steric influence [329]. They can be obtained by chemical as well as electrochemical polymerization procedures [232]. Commonly known are TEMPO functionalized poly(thiophene)s as reported by Lutkenhaus et al., that show 68 mAhg^{-1} of cycling capacity. However, a rapid dedoping was observed, which was ascribed to the intramolecular electron transfer from the nitroxide group to the backbone, leading to a deactivation of the charged state [330]. Furthermore, degradation of the backbone is expected to increase with

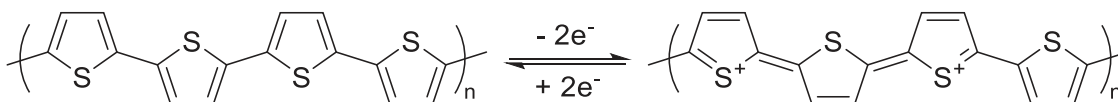


Fig. 10. Schematic representation of the chemical structure and redox reaction of PTH for a two-electron redox reaction.

a redox-active pendant group such as TEMPO that can mediate redox processes such as alcohol oxidation. It is expected that also UV active groups can produce singlet oxygen, which is able to further degrade the polymer backbone [331–333].

Apart from functionalization on the thiophene groups, also different polymer structures are accessible, while maintaining the conjugated properties (Fig. 10). As reviewed by Jia et al., Liang and coworkers created poly(imide-co-thiophene) polymers, starting from dimeric thiophene species, that exhibit stable n-doping with high conductivity. The synthesis is performed from a dibrominated rylene dye, which was polymerized via a Stille-type coupling reaction with a twice stannated dithiophene. A copolymer was obtained, that is comprised of both conjugated properties and distinct redox sites [334]. If the material was reacted with metallic Li, a conductive active material was obtained with a capacity of 54.2 mAhg⁻¹. The stability of this material is extraordinarily high, since 96% of the initial capacity can be retained after cycling at 100 C for 3000 cycles [233,287].

As an alternative, sulfur chains could also be introduced to poly(3-hexylthiophene-2,5-diyl) (P3HT), by inverse vulcanization, leading to an improved battery performance. This synthetic route is actually comprised of a two step of polymerization, as an allyl terminated P3HT was prepared by Grignard metathesis reaction, utilizing *t*-BuMgCl and Ni(dppp)Cl₂. Subsequently, the polymer chains were interconnected via an inverse vulcanization at 170 °C with elemental sulfur. This presents a straightforward approach towards insolubilizing shorter polymer chains, while increasing the capacity of the active material through the additional sulfur. The initial capacity of 799 mAhg⁻¹ was obtained at 0.5 C after 100 cycles for the sulfur composite, while the unfunctionalized polymer only showed 544 mAhg⁻¹, when investigated as a non-covalently linked mixture [335].

Another prominent thiophene-based polymer is poly(3,4-ethylenedioxythiophene) (PEDOT), which found wide-spread application for organic electronic devices [287,336]. To further increase the properties for solid-state batteries, the solubility was efficiently decreased by addition of benzoquinone and anthraquinone as pendant group to the PEDOT homopolymer. However, capacities and voltage slopes are typically unfavored for application in high capacity solid-state batteries [337]. Another PEDOT-based approach uses PEDOT-anthraquinone and benzoquinone active material in a proton exchanging battery by Sjödin and coworkers; the battery exhibited up to 120 mAhg⁻¹ and reversibility for 1000 cycles [338]. Further approaches again investigated the combination of inorganic active materials with conductive PEDOT chains [339,340].

3.3.5. Other conjugated polymers

Apart from conjugated polymers using the aforementioned redox moieties, a wide variety of additional CPs can be obtained from numerous different monomers. Furthermore, 2D conductive polymeric networks can be synthesized by the utilization of multifunctional monomers like the commonly utilized triphenylamine (TPA), which was shown to give poly-TPA with a specific capacity of 100 mAhg⁻¹, which was stable over 200 cycles [341]. Various pore sizes were obtained by replacement of some of the triphenylamine moieties with triphenyl-benzene, resulting in a slightly higher rate capability. Additionally, poly-TPA-based active materials can even be used without conductive additives, due to the intrinsic conductivity of the active material [342,343]. Next to the

mentioned frontrunner for conductive polymers, manifold completely different scaffolds can be obtained and investigated with respect to battery applications. Only to mention a few examples: Polymers of 5-cyanoindole, [342,343] carbazole, [344] dihydroacridine, [345] phenazine, [342,343], phenothiazine, [346] thianthrene, [347] diaminorubicene, [348] coronone, [348] and azobenzene [349].

3.3.6. Non-conjugated linear homopolymers

In terms of ease of synthesis, linear homopolymers represent the most straightforward approach towards a polymeric architecture for solid-state batteries, as only one monomer is introduced into the backbone. However, this has drawbacks, as key properties of the resulting polymer, such as its redox potential, are strongly defined by the monomer itself. On the other hand, many homopolymers intrinsically show the required insolubility in the desired electrolyte, as the solubility decreases with increasing molar mass of the polymers [101]. Additionally, the solubility of the active material can be further decreased by use of various electrolytes or mixtures thereof. With regard to the synthesis of homopolymers, various different strategies are suitable, depending on the utilized monomer (see Section 2.3).

3.3.7. TEMPO

Among the highest number of literature-known redox-active moieties, stable organic radicals, such as 2,2,6,6-tetramethylpiperidine-1-oxyl (TEMPO) (Fig. 11), have gained considerable interest. First reports of polymer-attached stable radicals emerged nearly 60 years ago, when Braun and coworkers and later Braun et al. synthesized the polymers by free radical polymerization and, subsequently, investigated this new kind of polymers as spin-labeling compounds [44,140]. Already, two strategies comprising polymerization of a nitroxide monomer species was compared to the non-radical species. However, it was reported that only “non ideal” polymers, regarding “chain length and stereoregularity”, were obtained. In particular, early on TEMPO bearing chains gained high interest, as shown in the works of Calvin and Griffith et al. [45,350] With a potential of 3.6 V vs. Li and many available starting materials such as alcohols, amines or carbonyl-derivatives, especially the TEMPO moiety represents a potent active group that can be introduced into a polymer matrix by various means, for instance as methacrylate or methacrylamide [71,257] As a battery material, it was first used by Nakahara and coworkers in 2002, who built the first organic radical battery (ORB). However, as the counter electrode was composed of metallic Li, it did not represent the first full-organic radical battery published, [71] which was presented by Nishide and coworkers in 2009, utilizing a TEMPO-poly(norbornyl) electrode and a polystyrene-bound galvinoxyl radical, as a counter electrode. The authors obtained a working voltage of 0.6 V in their first publication, which was exceeded in future attempts. Later on, many different TEMPO-functionalized polymers have been presented by various groups [80,81,259,351].

Of all TEMPO-containing RAPs, poly(TEMPO-methacrylate) (PTMA) is the most well-known, since it is easy to synthesize and poorly soluble in the prominently-used carbonate solvents and exhibits a specific capacity of 111 mAhg⁻¹ [71]. The typical synthetic route includes the linking of a tetramethyl piperidyl derivative onto the monomer, often via transesterification of an alcoholic

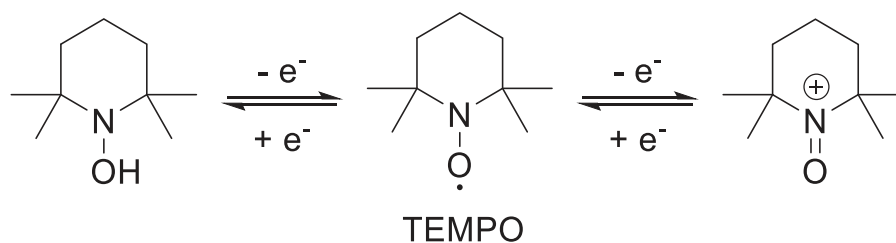


Fig. 11. Schematic representation of the redox reactions of TEMPO radicals.

moiety, followed by polymerization and oxidation. Different radical polymerization procedures have been applied for methacrylic monomers, generating different PTMA derivatives, after oxidation of the piperidiny groups. Until now, free radical polymerizations have been the most prominent, since they represent a simple, robust, and cheap technique. Polymers with high molar masses, up to 89 kg mol^{-1} but with also high dispersities can be achieved. [80,98,140–142] (See Section 2.4) Polymers obtained by controlled radical strategies exhibit smaller dispersities ($\mathfrak{D} < 1.2$) but significantly lower molar masses due to the chain transfer [71,352] When reversible addition-fragmentation chain transfer is used for the synthesis of PTMA, polymers with molar masses of $24\text{--}70 \text{ kg mol}^{-1}$ and dispersities of $\mathfrak{D} \sim 1.3$ can be obtained [176,177,246] With ATRP, polymers of 24.7 kg mol^{-1} and < 1.2 were obtained [176–179].

Since living (ionic) polymerizations are known for their achievable high molar masses while still maintaining low dispersities, these methods have also been used to synthesize TEMPO-bearing polymers. When applied to the synthesis of PTMA, polymers with high molar masses of 169 kg mol^{-1} can be synthesized [247,248] Gohy, Monteiro and their coworkers were able to obtain M_n -values of *ca.* 131 kg mol^{-1} by living single electron transfer polymerization [247,248]. Furthermore, anionic polymerizations for TEMPO-bearing polymers have been investigated as early as 1967, but without direct reference towards battery systems [45]. Nishide, Nakahara and coworkers were the first to use this approach to produce TEMPO-bearing polymers for ORBs [45,213,214,237] Molar masses of up to 30.4 kg mol^{-1} and dispersities of $\mathfrak{D} = 1.2$ have been obtained [213,214,237]. Group transfer polymerization (GTP) has been applied for PTMA as well, to further optimize the molar masses and dispersities [204,205]. Cationic polymerizations gave molar masses ranging from 36 to 130 kg mol^{-1} and broad dispersities ($\mathfrak{D} = 1.4$ to 3.5) [204,205,237]. Also, group transfer polymerizations can give in to TEMPO carrying polymers, such as poly(TEMPO-vinyl ether) or PTMA, but the obtained dispersities ($\mathfrak{D} = 3.2$) are comparably high. [204,205,237]

Recently, TEMPO has been linked to various polymeric backbones, such as oxiranes, norbornenes, or even conjugated backbones to further tailor the properties of the corresponding polymers. [187,188,254] Anionic, ring-opening polymerization [187,188] is a typical polymerization technique for oxiranes and was utilized for poly(TEMPO-glycidyl ether) (PTEO) to generate polymers of $M_n = 40 \text{ kg mol}^{-1}$ and $\mathfrak{D} = 2.1$. [187,188,254] Poly(norbornene) polymers, bearing TEMPO side chains, have been synthesized *via* ROMP. The polymer can be obtained *via* a polymer analogous reaction by reacting a poly(norbornyldicarboxylic anhydride) backbone with TEMPOL [177,246,353,354]. Conductive polymers are often synthesized by linking the TEMPO scaffold to a desired five-membered heterocycle, followed by a subsequent electro-polymerization. Additionally, introducing the TEMPO-moiety into polymers can be achieved by various means, such as *in situ* polymerization in the electrode material, co-dispersion with a CP or encapsulation or grafting onto a CP-backbone [355–357]. Popular CP-backbones utilized with TEMPO moieties are poly(thiophene), poly(pyrrole),

poly(3,4-ethylendioxythiophene), poly(dithienopyrrole) (PThPy) or poly(3-hexylthiophene-2,5-diyl) [302,358–361].

All these strategies aim at optimizing the solubility behavior of the obtained PTMA products, as low-molar mass polymeric compounds, that can differ immensely in solubility behavior [101]. Even the tacticity of polymeric TEMPO compounds was reported to influence material properties, such as redox potential and reversibility [362]. CV investigations revealed that PTMA produced *via* GTP revealed two distinct redox processes, of which one proved to be reversible, while the second was shown to be irreversible. The reversible process was ascribed to the redox reaction of the TEMPO moieties from isotactic domains in the polymer. The irreversible process, which had not been reported previously, was linked to smaller heterotactic and syndiotactic domains in the PTMA polymer. Apart from the generally used aminoxyl radical / oxoammonium cation redox process, the TEMPO scaffold itself has been shown to exhibit a second redox process, in which the radical can be reduced to the respective hydroxylamine (Fig. 11). The normally irreversible process can be stabilized when TEMPO is polymerized and embedded in graphite or cellulose, surpassing the specific capacity of 111 mAhg^{-1} and reaching up to 222 mAhg^{-1} specific capacity [363,364].

For most polymerization procedures, the oxidation of the tetramethylpiperidine ring nitrogen is performed after the polymerization, as the resulting polymers show more uniform chain lengths [119] A high degree-of-oxidation is favorable, as it corresponds to a high storage capacity. Typical oxidative procedures employ peroxides, such as *m*-chloroperbenzoic acid (*m*CPBA) or hydrogen peroxide combined with tungsten trioxide under high temperatures [176,365]. While both oxidative strategies deliver similar radical loadings, hydrogen peroxide is often preferred, as *m*CPBA-based oxidations tend to result in a higher amount of overoxidation and higher dispersities, while being less cost efficient [176,177,248]. Even though the reaction procedures are very similar, the obtained radical loadings differ significantly, with values between 46 to 100% for identical synthetic procedures published [204,248,352,366]. As an alternative, an already oxidized derivative, TEMPOL, can be linked to a poly(methyl methacrylate) (PMMA) backbone *via* transesterification. However, the obtained degree-of-functionalization with TEMPO moieties in the polymer is relatively low [367]. While the conductivity of the linear PTMA itself is often not high enough for use in a solid-state battery electrode, charge transport over the TEMPO groups can be observed. As the TEMPO ring itself remains very stable after oxidation due to the charge being located on the nitroxide group and not the ring itself. This leads to a very similar structure in the oxidized state and ground state as well as a visible charge transport inside the polymer, caused by the redox gradient of the polymer chains. Charges will be distributed equally between the TEMPO groups, even in parts of the electrode that show low carbon content [368].

While the PTMA backbone shows low electron conductivity, AROP polymerized poly(TEMPO-glycidyl ether) (PTEO) has been presented by Boudouris et al. to exhibit excellent conductivities up to 28 S m^{-1} [254]. Here, the authors accounted the conductive ef-

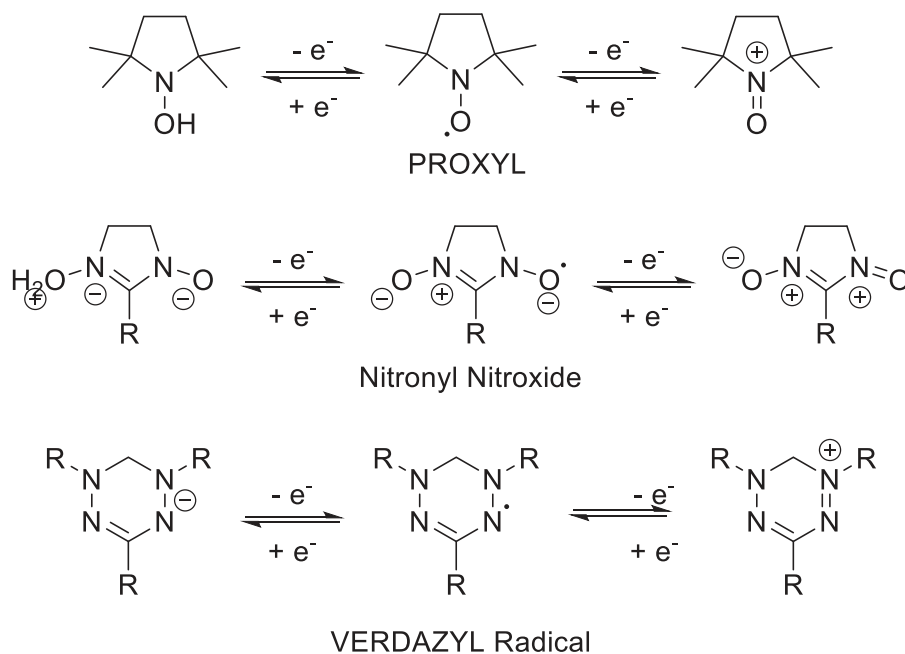


Fig. 12. Schematic representation of the chemical structures and redox processes of PROXYL, nitronyl nitroxide, and VERDAZYL radicals.

fect of the TEMPO moieties for the excellent charge transport properties. Hence, if conductive materials are desired, the amount of carbon additive and liquid electrolyte can be reduced with the introduction of the TEMPO moiety in a conductive polymer (CP).

3.3.8. Other stable radicals

Apart from the TEMPO-radical, other nitroxide-based radical species have been investigated as solid-state, battery-active materials. However, as noted earlier, radical-bearing monomers in general are not suitable for most polymerization strategies. ROMP polymerizations present an efficient alternative and have been investigated widely for this case, as verdazyl, nitronyl nitroxide, and proxyl groups (Fig. 12) are tolerated under ROMP conditions [369].

Verdazyl compounds display reversible redox-processes and have been introduced into a polynorbornene backbone by Gilroy and Anghel et al. [222] Here, an aliphatic linker was used to connect the verdazyl group to norbornene dicarbonyl, which was later polymerized *via* ROMP using a Grubbs' catalyst. The compound exhibited an amphoteric behavior by showing a reduction signal (Fig. 12) at -0.96 V and oxidation process at 0.49 V vs. ferrocene. Polymer molar masses of $M_n = 46.6$ kg mol $^{-1}$ and low dispersities of $\mathcal{D} = 1.11$ were obtained.

Following a similar strategy, a nitronyl nitroxide polymer was obtained. The reactive unit was again linked to a norbornyl backbone that was polymerized *via* a ROMP [222]. The obtained nitronyl nitroxide polymer exhibited an oxidation potential of 0.44 V vs. ferrocene, a dispersity of $\mathcal{D} = 1.18$, and $M_n = 51.4$ kg mol $^{-1}$. In another approach, poly(5-vinyl-1,1,3,3-tetramethylisindolin-2-yloxy) (PVTMIO) was prepared from a vinylic starting material *via* FRP with AIBN. Successively, the methyl-protected nitroxide group is oxidatively cleaved with *m*-CPBA, generating the redox-active aminoxyl-radical. The polymer exhibits an oxidation potential of 3.7 V vs. Li and was introduced into a Li organic battery with 104.7 mAh $^{-1}$. The 90% capacity was retained after 100 cycles at varying charging rates with a high operating voltage of 3.69 V [143]. A different poly(arylnitroxide), poly(4-(*N*-*tert*-butyl-*N*-oxylamino)-3-trifluoromethylstyrene), has been prepared by Nishide et al. from a styrene derivative utilizing a free radical polymerization. The

system exhibited a redox potential of 0.76 V vs. Ag/AgCl [144]. The same group also investigated a bipolar radical battery, utilizing poly(nitronylnitroxylstyrene) as anode and cathode material, due to their amphoteric redox behavior. The utilized redox processes exhibit potentials of -0.61 V and 0.72 V vs. Ag/AgCl. The polymer is obtained in a free radical polymerization and shows a $M_n = 52$ kg mol $^{-1}$ and $\mathcal{D} = 3.2$. A full organic battery was prepared, showing a capacity of 44 mAh $^{-1}$ and a lifetime of over 250 cycles at a working voltage of 1.3 V [81,370].

In a further study, Xiong et al. linked a 2,2,5,5-tetramethyl-1-pyrrolidinyloxy (didehydro-PROXYL) radical to a triphenylamine polymer, which was then oxidatively polymerized using FeCl $_3$. The polymer exhibited a broad redox process at 3.62 to 3.89 V vs. Li. The prepared Li-organic thin-film battery, showed two voltage plateaus at 3.7 V and 2.7 V. The two plateaus are linked to the two used active units, PROXYL (3.7 V) and triphenylamine (2.7 V). A capacity of 120 mAh $^{-1}$ was obtained, that decreased by 10% after 100 cycles at various charging rates [370].

Furthermore, RAPs, based on phenoxyl-radical compounds, have been shown by Schubert and coworkers. The redox-active units were introduced as side-groups to a norbornene monomer backbone that was subsequently polymerized *via* ROMP. The radical groups led to a reversible reduction at -0.6 to -0.8 V vs. Ag/AgCl. The corresponding battery tests showed a capacity of 60 mAh $^{-1}$ and a 20% loss after 100 cycles [371].

3.3.9. Quinones

Redox-active polymeric quinoid systems have been known for over 75 years. In 1944, D. H. Lauth transferred the polymerization process of phenol with formaldehyde to quinoid systems and synthesized redox-active resins, initially intended for oxygen removal from water [9]. Since then, a large variety of applications, demanding redox-active polymers, have relied on quinoid systems, as they show reversible two-electron reduction processes and can be readily adjusted in terms of redox potential and solubility. When reduced, these quinoid systems deliver alcoholates that can be used to trap metal-ions to enable metal-ion loading of quinone-based active materials [372] Popular quinoid core systems are benzoquinone, naphthoquinone, anthraquinone, and phenan-

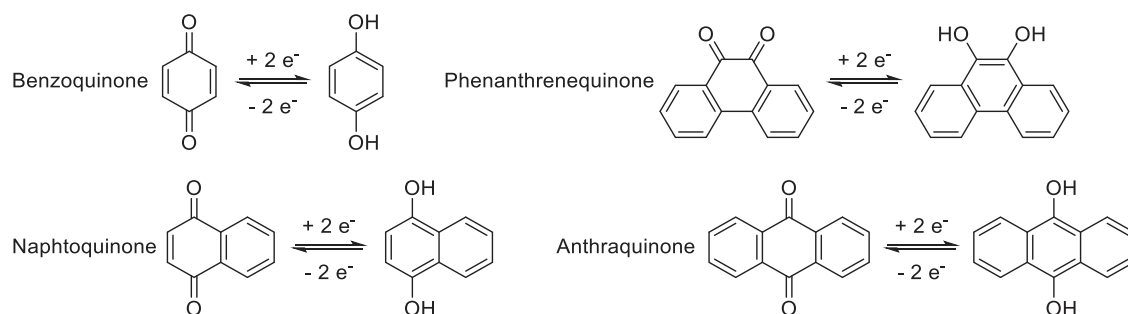


Fig. 13. Schematic representation of the redox reactions for different quinoid systems.

threnequinone (see Fig. 13). Theoretical capacities are exceptionally high with 496 mAhg^{-1} for benzoquinone, 339 mAhg^{-1} for naphthoquinone and 259 mAhg^{-1} for anthraquinone as well as phenanthrenequinone [373–375]. Due to the fact, that many quinoid systems can be found in nature and biological processes, it is often attempted to use these resources for sustainable energy storage systems [374].

The first quinone investigation, as cathode material, was performed in the early 70 s by Sandstede et al., who used duroquinone and chloranil in aqueous and organic media to examine the reversibility of their reduction process [376]. In 2008, the first polymeric quinoid material utilized in a solid-state battery was an anthraquinone-based system by Song et al., who introduced a dichloroanthraquinone building block into a poly(anthraquinonylsulfide) backbone [377–379]

3.3.10. Poly(benzoquinones)

Various research groups have used benzoquinones in solid state batteries, [380–382] as shown in Fig. 13; however, the solubility of the benzoquinoid materials must be optimized, as the intrinsic solubility of the small aromatic compounds is often too high. Therefore, polymeric connections between the low molar mass active groups are an effective strategy to mediate insolubility. Also, the π -conjugated systems can be obtained in this way, as shown by Song et al., who used a sulfidic linker [372,377]. The authors synthesized poly(benzoquinonylsulfide) (PBQS) via a redox polymerization mechanism from dichlorobenzoquinone and an excess of lithium sulfide at 160°C in *N*-methyl pyrrolidone. After delithiation with HCl, the partially reduced compound was reoxidized with 2,3-dichloro-5,6-dicyano-1,4-benzoquinone (DDQ). A solid-state battery with a considerably high capacity of 232 mAhg^{-1} was obtained, which revealed an 86% capacity retention after 1000 cycles at 500 mAg^{-1} and up to 72% capacity retention after 10 cycles at 5000 mAg^{-1} [378]. An equal investigation using the dihydroxy derivative poly(2,5-dihydroxy-*p*-benzoquinonyl sulfide) of the aforementioned active material was performed by the same group [383]. Due to the hydroxyl groups, the material is able to stabilize more Li-ions, leading to a comparably high capacity of 268 mAhg^{-1} with a capacity retention of 90% after 1500 cycles at 500 mAg^{-1} [383]. Further approaches using sulfur-linked benzoquinoid RAPs were presented by Zhang et al. [384,385].

3.3.11. Poly(naphthoquinone)

Naphthoquinones are based on the naphthalene structure, as shown in Fig. 13. Compared to benzoquinones, they show a lower solubility while maintaining reversible redox properties. Park et al. showed the fact, that the naphthoquinone scaffold can be modified, while still keeping the intrinsic redox behavior, when they compared naphthoquinone with its close homologues “lawsone” (2-hydroxy-) and “menadione” (2-methyl)-[386]. Functionalization of the naphthoquinone scaffold delivers modified charge transport properties, which can be up to five times higher when compared

to the unmodified naphthoquinone [386]. As one of the first polymers with naphthoquinone active units, Haas et al. synthesized a poly(aniline) derivative from 5-aminonaphthoquinone and investigated its electronic properties [308]. Häringer et al. then showed the first utilization of poly(aniline), as an electrode material. With a capacity of 290 mAhg^{-1} , 17 cycles were performed at 0.07 C and a capacity retention of 70% was achieved [308,309].

Similar approaches were investigated by Yao et al, who showed both a molecular naphthoquinone as well as the corresponding polymer with $M_n = 910 \text{ kg mol}^{-1}$ and $\bar{D} = 1.1$. [387,388] The polymer was synthesized from 5,8-dihydroxy-1,4-naphthoquinone and formaldehyde via polycondensation in acidic medium. After lithiation, a capacity of 256 mAhg^{-1} was obtained, exceeding the monomer capacity, which was not discussed further. However, the capacity fades quickly in the first cycles to 150 mAhg^{-1} . From then on, the decrease slows down and after 100 cycles, a remaining capacity of 133 mAhg^{-1} could be achieved [388]. A more recent approach by Xu et al. showed a poly(norbornene) polymer with pendant naphthoquinone and benzoquinone groups. The polymer was obtained by ROMP utilizing a Grubbs’ catalyst with (1*R*,4*S*,4*aS*,8*bR*)-1,4,4*a*,10*b*-methanonaphthalene-5,10-dione. This monomer was obtained by a pericyclic reaction of naphthoquinone and quadricyclane. The resulting polymer exhibited a capacity of 190 mAhg^{-1} at 0.1 C with 94.1% capacity retention after 200 cycles and 76 % capacity retention after 500 cycles [389].

3.3.12. Poly(anthraquinone)

Amongst the quinoid systems, anthraquinones have gained considerable interest, due to their excellent redox behavior and comparably poor solubility [272,390,391] First reports for the reversibility of the reduction process of polymeric anthraquinone-based materials were presented by Manecke and Stork in the early 60s. [31,392]

Anthraquinone revealed a two-electron reduction process with a potential of approximately 2.20 V vs. Li. [393,394] (Fig. 13) If reduced, the carbonyl moieties become an alcoholate radical anion during the first reduction step and give a dianion after the second reduction. The anion is generally stabilized by alkaline earth metal ions, such as Li-ions. However, when molecular anthraquinone is utilized as active material in a battery electrode, the active material can migrate out of the electrode matrix during cycling, leading to irreversible capacity loss. Often, connecting the active group to a long polymer chain reduces the migratory ability and therefore enables a stable capacity retention [72]. For instance, Zhou et al. investigated a high molecular-weight poly(anthraquinone) with 230 kDa and 530 Whkg^{-1} . It showed a capacity retention of 94 % after 1000 cycles at 0.2 C. As a comparison, unbound anthraquinone showed only 18% capacity retention after 100 cycles under the same conditions. Also, a smaller polymer with 2.3 kDa was investigated and compared; after 100 cycles, a capacity retention of 68% was achieved. Therefore, it was concluded, that a

higher molecular mass effectively decreases the migration-caused capacity losses in the battery electrode [377].

The initial investigations of poly(anthraquinone)-based batteries were performed by Song et al., who polymerized a 1,4-chloroanthraquinone with sodium sulfide, following the Phillips method; this polymerization strategy, utilizing sodium sulfide, was patented by Phillips in 1977 [395]. A battery material with a capacity of 189 mAhg⁻¹ and a capacity retention of 88% after 200 cycles at 0.22 C vs. Li was obtained [379]. Polymers, based on the same anthraquinone as well as the respective 1,5-dichloroanthraquinone derivative, were also synthesized using different alkali sulfides or Ni-catalyzed coupling reactions [377–379]. Unfortunately, Ni-catalyzed polymerizations gave poly(anthraquinonylsulfide) (PAQS) as well as directly covalently linked anthraquinone polymers. For poly(1,4-anthraquinonyl-sulfide), the battery electrode showed a capacity of 263 mAhg⁻¹, while a capacity retention of 98% was achieved after 1000 cycles at 0.2 C (99% at 1 and 2 C after 1000 cycles). The high cyclability was accounted to the high polymer molar masses of 230 kg mol⁻¹. Lithiated PAQS derivatives were shown by Petronico et al., who used lithium sulfide in the Phillips procedure [396]. They were able to stabilize 4 Li-ions per repeating unit of poly(dihydroxyanthraquinone) and a high capacity of 300 mAhg⁻¹ was achieved. The polymer exhibited a molar mass of 25 kDa. The capacity initially decreased to 210 mAhg⁻¹, and then remained stable for 1200 consecutive cycles at a voltage of 2.5 V [396].

Nitrogen-linked anthraquinones have been investigated as well. Zhao et al. reported poly(5-amino-1,4-dihydroxyanthraquinone), as a cathode material [397]. The polymer was obtained by oxidative polymerization of 5-amino-1,4-dihydroxyanthraquinone with ammonium peroxydisulfate in acetic acid, generating a poly(aniline)-analogous backbone in the resulting polymer with anthraquinone active groups. The initial capacity of 101 mAhg⁻¹ increased to 143 mAhg⁻¹ within 14 cycles at 400 and 126 mAhg⁻¹ could be retained after 50 cycles [397]. A direct linkage of anthraquinone cores without bridging heteroatoms was achieved by Pan et al., who connected anthraquinones *via* Pd-catalyzed coupling reactions of the respective chloro- and bromo-anthraquinones. The obtained poly(anthraquinones) were investigated in a Mg-ion battery, showing constant capacities and high cycling stabilities [398].

A further anthraquinone-based structure has gained interest in research; tetracyanoanthraquinone (TCAQ) was shown to exhibit reversible redox chemistry when employed as a cathode active material in a solid-state battery. At a working voltage of 3.05 V at charging and 2.25 V at discharging, the Schubert group reported a battery with a high capacity retention of 95% after 1000 cycles. While performing a two-electron redox reaction, the material exhibited only one charge/discharge plateau, with excellent material usage and cyclability [399]. However, the TCAQ molecule itself was reported to show higher capacity fade rates when compared to unsubstituted anthraquinone [391]. The TCAQ scaffold was obtained from a vinylic anthraquinone derivative that can be reacted with malononitrile in a Knoevenagel condensation. Polymerization gives a poly(ethylene) backbone with pendant TCAQ groups and a $M_n = 26.4 \text{ kg mol}^{-1}$ and $\mathcal{D} = 1.87$. [399]. In a similar approach published by the Schubert group, a thiophene-fused quinone pendant polymer was used for battery studies [400]. Polymers with molar masses between 2.49 and 4.72 kg mol⁻¹ were obtained. The shown composite electrode exhibited a capacity of 217 mAhg⁻¹ at a cell voltage of 2.45 V and cycling at high rates of 10 C, only with minor capacity decreases [400]. Further thiophene-containing poly(quinone)s were presented by Jing et al., [401] who polymerized a thiophene derivative with Ni-catalysis in DMF; polymers of 0.88 and 1.25 kg mol⁻¹ could be obtained. Battery electrodes exhibited a capacity of 214 mAhg⁻¹ and a capacity retention of 96% after 250 cycles at 5 C and a discharge voltage of 2.52 V [401].

3.3.13. Linear copolymers

Copolymeric compounds have been investigated to further optimize the battery performance of polymeric active materials. While physical properties of homopolymeric compounds are generally predefined through the monomeric attributes, features can be fine-tuned when one or more co-monomer(s) is (are) added during the synthesis. As a typical example, the solubility of the desired redox-active polymeric material can be drastically changed by addition of suitable comonomers. Copolymers can be readily obtained by various polymeric strategies, highly organized structures like block-copolymers, however, can only be obtained by controlled or living polymerization procedures (see Section 2.3.2.2). This allows for an opportunity to obtain micellar or nanoparticulate battery materials, that can show fascinating features [236,402]. Nonetheless, random, statistical or alternating copolymers are often favored, due to their ease of synthesis and possible on-site or *in situ* production under various conditions [403]. Further fine-tuning of solubility properties may be possible with the introduction of a comonomer; however, this generally comes at the expense of a decreased specific capacity of the obtained electrode material (see 2.2.2).

3.3.14. TEMPO

Typically, PTMA electrodes exhibit high coulomb efficiencies and high electron transfer rates. However, due to soluble, small polymer chains, self-discharge effects can be a problem, as these chains can act as redox shuttles in the cell [256]. In order to minimize solution processes and avoid conductivity problems for PTMA homopolymers, copolymeric species like block copolymers, bearing an insoluble and electrochemically inert block, such as poly(styrene) (PS), have been investigated [404]. Apart from these systems, different approaches aiming at an improved polymer conductivity have been examined by Nishide et al, who created a poly(TEMPO-co-TFSI) polymer [405]. Due to the high Li-conductivity of the polymer itself, a liquid electrolyte can be omitted. Upon charging, the lithium ions initially coordinated by the TFSI units are released from the polymer giving way for the TEMPO groups to be coordinated by the TFSI groups. A battery was prepared and performed 30 consecutive cycles with a working voltage 3.7 V, as no liquid is present that could restrict the obtainable redox potential [405].

3.3.15. Poly(imides)

Poly(imides) have been widely investigated by various researchers after the first investigation of their stability by Mazur and Viehbeck in the 1980s. [406,407] The integration of poly(imides) in solid state batteries then began with the groups of Nishide and Zhou in 2010. [408,409] RAPs featuring this scaffold generally show a reversible two-electron reduction, high thermal and mechanic stability, and good electron mobility when employed as electrode materials [410]. The reduction potentials for pyromellitic diimide are reported at 2.25 and 1.9 V vs. Li, [411] 2.5 V vs. for naphthalene tetracarboxylic diimide and perylene-based diimides [412,413].

Upon reduction, the two imide carbonyl groups in the molecule will reversibly form radical-anionic species (Fig. 14). Mostly, only two of the four theoretically available carbonyl groups show these reversible reductions, as the radical intermediate created in the first step will be easily stabilized by a second reduction leading to a dianionic species. A further reduction leading to four negative charges per species is highly unfavored, as the additional negative charges cannot be stabilized within the molecule, resulting in decomposition [414]. When used in a solid polymer electrode, high molar masses and a narrow molar mass distribution are usually not required, as poly(imides) are intrinsically poorly soluble [415]. The main compound properties are derived from the building block properties introduced during synthesis.

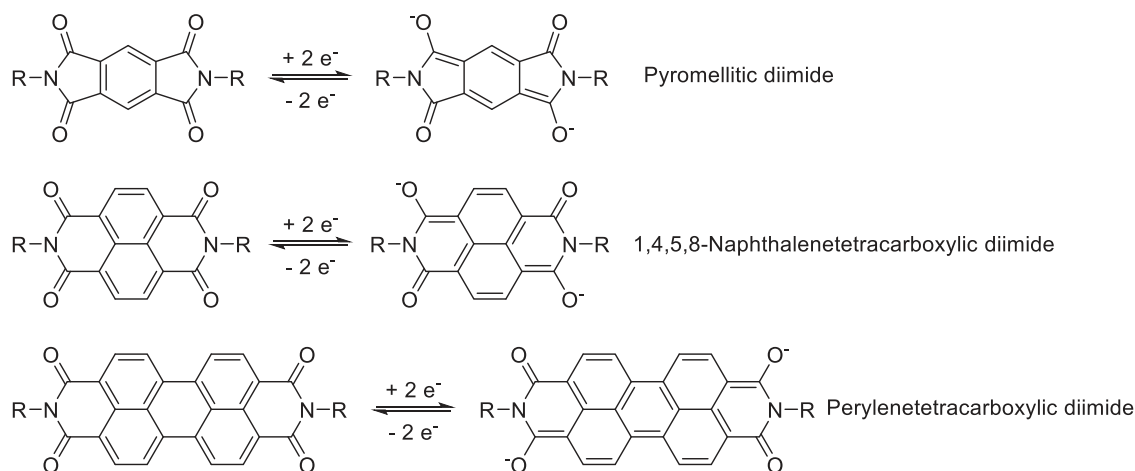


Fig. 14. Schematic representation of the redox reaction of imides. The number of aromatic rings between the amide groups can be varied. Depicted are the most well-known systems, pyromellitic diimide, 1,4,5,8-naphthalenetetracarboxylic diimide and perylenetetracarboxylic diimide. The redox reaction performs with creation of an enolate group or a carbonyl group, respectively.

In a typical synthesis of a diimide battery compound, a dianhydride precursor is reacted with a diamino compound at elevated temperatures in a step-growth process, giving a polymer chain that contains the diimide groups in its backbone. Commonly used starting materials for these procedures include pyromellitic acid dianhydride (PMDA), naphthalene tetracarboxylic acid dianhydride (NTCDA), and perylene tetracarboxylic acid dianhydride (PTCDA), combined with a variety of diamine linkers [416]. The simplest diimide compounds are phenylene diimides, which are readily available from PMDA and different diamine linkers; however, compared to the higher homologues of polyaromatic starting materials, this class exhibits lower capacity retention rates due to a generally higher solubility [417,418]. Also, the specific capacity of pyromellitic derivatives is higher, than for the larger analogues, due to its lower molar mass. While the ethyl-bridged pyromellitic diimides exhibit a specific capacity of 442.7 mAhg⁻¹, the naphthalene derivative reaches 366.8 mAhg⁻¹ [409]. Furthermore, the conjugated system of naphthalene diimide and perylene diimide is significantly bigger, leading to a better stabilization of the electronic charges upon reduction. Additionally, the ring tension of the imide ring is considerably lower in naphthalene- and perylene-based imides, resulting in more stable compounds that are more prominently used as battery material [417,418].

In 2010, Oyaizu et al. presented a poly(phenylene-diimide) anode material via a polycondensation of *p*-phenylenediamine and pyromellitic anhydride [408]. When the polymer was added to a composite anode material, a capacity of 95 mAhg⁻¹ was obtained. The capacity rapidly decreased by a third within the first ten cycles and then remained stable for over 100 cycles [408]. Similar polymeric pyromellitic diimides have also been prepared by a direct Pd-catalyzed Hartwig-Buchwald type polymerization, involving a pyromellitic diimide building block and *p*-dibromobenzene, utilizing a Pd-catalyst [411]. In 2010, Song et al. presented two pyromellitic polycondensation products, using both *p*-phenylenediamine and hydrazine, as composite cathode materials, showing initial capacities of 155 mAhg⁻¹ and 206 mAhg⁻¹, respectively. After 100 cycles at 0.2 C, capacities of 129 and 171 mAhg⁻¹ were retained [409]. As the selection of possibly usable linkers for polyimide groups is great, many of them have been investigated showing that their length does not significantly influence the polymer's electrochemical behavior, compared to the electrochemical and aromatic properties of different aromatic basic structure [372].

As previously mentioned, naphthalene tetracarboxylic acid diimides are the most investigated species among poly(imides) for

use as electrode materials [270]. Pioneered by Zhou et al., the corresponding diimides are prepared from NTCDA via condensation with an alkylic or aromatic diamine [409]. Hydrazine and *p*-diaminobenzene-linked organic polymers gave cathodes with capacities of 202 and 181 mAhg⁻¹, respectively. Both capacities decreased over 100 cycles at 0.2 C to 183 and 173 mAhg⁻¹ [409]. Another hydrazine-linked naphthalene diimide derivative was presented by Lordache et al. for the usage in Mg-ion batteries [419]. While at the beginning, due to swelling processes, only a capacity of 30 mAhg⁻¹ could be achieved, the capacity of the battery material increased to 75 mAhg⁻¹ after 100 cycles. Afterwards, the capacity was well-retained for 100 cycles [419]. Chen et al. presented a cathode material that is obtained by condensation of NTCDA with urea in *N*-methylpyrrolidone at 180 °C and imidization at 300 °C [412]. In a Li-organic battery, reversible capacities of 20, 50 and 500 mAhg⁻¹ were obtained. 92% of the initial capacity was retained after 60 cycles at 50 mAhg⁻¹ [412]. Triethylene glycol bridged NDI polymers were synthesized by Mecerreyes et al. These materials had a specific capacity of 127 mAhg⁻¹, discharge capacity of 80 mAhg⁻¹ at cycling at 250 mAhg⁻¹ and were stable over 100 cycles. [416] Different linkers like sulfonyl or carbonyl groups were also investigated [412,420]. In case of carbonyl linkers, higher initial capacities compared to the carbonyl-lacking compounds could be obtained, as the linker itself is redox-active, leading to a capacity of 160 mAhg⁻¹, stable for 50 cycles [412]. A full organic polymer battery was prepared with an ethylene-linked NDI and a poly(triphenylamine) counter electrode. A comparably low capacity loss of 15% after 700 cycles was demonstrated [421]. Furthermore, in attempts to increase the specific capacity of the resulting poly(diimides), different redox-active groups have been incorporated as linkers, giving alternating copolymers with two different redox potentials. Such strategies have been shown by many groups, for instance by introducing quinoid systems as linking groups in a poly(imide) polymer [422–427].

Apart from naphthalene diimides, perylene-based structures are well known [372]. Due to the extended π -system, a higher stabilization of the dianionic state and significantly lower solubility in the reduced state can be observed; [428] however, the theoretical capacity is lower than for the previously mentioned core systems, as the molar mass is significantly higher [72]. Cao et al. created a lithium-storing non-polymeric cathode from a perylenediimide dye that gave a capacity of 110 mAhg⁻¹. After 200 cycles, a remarkably high capacity retention of 80% was achieved, mainly due

to the intrinsically low solubility of the perylene core [429]. In a fully-organic approach, Picard et al. introduced a Li-storing perylene tetracarboxylic acid, as cathode material, and hexyl-bridged perylene diimide, as anode. The battery was cycled at 1 V and an initial capacity of 80 mAhg⁻¹ was obtained, which then decreased by 20% after 200 cycles [413].

Another approach was performed by Meccerreyes et al., who connected perylenediimide *via* a phenothiazine linker, leading to a bifunctional battery material [430]. It was possible to create a fully organic symmetrical battery, utilizing the same material in both electrodes and approaching a different redox process in each electrode while using the same material. The battery showed stable performance for 1000 cycles with a working voltage of 1.5 V with retained 94% of the initial 77 mAhg⁻¹. The battery was cycled at a rate of 800 mAg⁻¹ [430].

3.3.16. Crosslinked polymers

In order to further mediate insolubility and tune mechanical properties of the polymers, crosslinks are often introduced [431]. In solid polymer batteries, this generally reduces redox-shuttling processes promoted by crossover of soluble oligomeric chain fragments, which can lead to irreversible self-discharging and capacity loss of the battery. Therefore, in many battery systems, the cycling behavior of crosslinked electrode materials is more stable when compared to the respective linear compounds [204]. However, due to their poor solubility, crosslinked materials are difficult to synthesize and process, requiring *in-situ* or *in situ* polymerizations. Further, it is possible to synthesize the crosslinked material and obtain composite battery active materials by milling and mixing steps. However, solution-based crosslinking polymerizations often suffer from impurities, due to encapsulation. Thus, battery electrode processing can later be challenging. Also, the availability of redox-active groups can be hindered in crosslinked materials, as swelling is hindered and diffusion pathways can be blocked when compared to non-crosslinked analogues. This accounts for both the conductive salt and the electrolyte itself, leading to suffering material usage and lower addressable capacities [353,432–434]. Possible strategies to rapidly obtain crosslinked materials represent photopolymerizations, thermally initiated polymerization methods or electrochemical polymerizations [353,432].

3.3.17. TEMPO

Since TEMPO is among the most investigated redox-active moieties, it is not surprising that also a wide range of different crosslinkers have been reported [204,353,434,435]. The strategy has been applied widely and the solubility of TEMPO bearing polymers could be significantly reduced [435,436]. However, as mentioned before, the processability of crosslinked polymers is challenging. Therefore, *in situ* crosslinking strategies are investigated and photo-crosslinking involving norbornene-based or benzophenone-based linkers as well as thermal crosslinking with an epoxide have been reported [353,432–434]. Nevertheless, penetration of electrolyte and conducting salt are hindered in a crosslinked polymer matrix, leading to a lower cycle stability, and lower specific capacity of the electrode material [353,432–434].

A crosslinked TEMPO polymer was presented by Nishide et al., who photo-crosslinked a TEMPO carrying norbornyl monomer on a glass template [353]. The obtained film revealed a stable redox signal at 0.84 V vs. Ag/AgCl and a stable capacity of 109 mAhg⁻¹ at 50C for 1000 cycles. The used crosslinkers were based on phenylic dinorbornyl compounds as well as diazides. The obtained products were reported to be insoluble; however, a slight swelling of the polymers was observed [353]. Bugnon et al. synthesized PTMA cross-linked with ethylene glycol dimethacrylate (EDGMA) *via* a group transfer polymerization (GTP) and obtained an insoluble battery material [204]. Compared to a similarly prepared non-

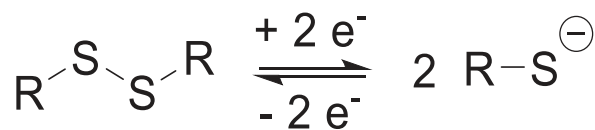


Fig. 15. Schematic representation of the reversible cleavage of disulfides, resulting in sulfidic species.

crosslinked PTMA, the material exhibited high cyclic stabilities for 200 cycles with a capacity retention of 95% and a high initial capacity of 105 mAhg⁻¹. The non-crosslinked material suffered from strong capacity decreases, already evident after 25 cycles [204]. A PEO-derivative was shown by Nishide et al. The TEMPO glycidyl ether was copolymerized with 1,4-butanediol diglycidyl ether in an anionic ring-opening polymerization. A composite electrode was prepared, showing an initial capacity of 80 mAhg⁻¹, that declined to 70% of its initial capacity after 200 cycles [238].

3.3.18. Poly(imides)

As mentioned before, poly(imides) show an intrinsically low solubility in common battery electrolytes, which can be further decreased by the introduction of crosslinks. Such poly(imides) have, for example, been prepared from NTCDA and trianilinobenzene by Sharma and Tian et al. [437,438]. The copolymerization with the C₃-symmetric amino-linking groups resulted in a crosslinked polymeric network, exhibiting very low solubility [436,437]. Further polymers, bearing naphthalenediimides, as side groups, are known. For instance, Nishide et al. presented a crosslinked poly(norbornene) obtained by ROMP with naphthalene diimides, as side groups, that are linked to the backbone *via* methylene groups [439]. The pendant groups participated almost completely in the charge/discharge process and gave a discharge capacity of 138 mAhg⁻¹ at 5C. At higher rates (20C), capacities of 70% could be retained, which was related to a rather high electron diffusion in the electrode. Also, the capacities were demonstrated to remain stable over 1000 cycles, leading to a promising approach towards a quickly chargeable battery material [439]. By functionalization of the pendant group with aromatic compounds, very high stabilities were observed. But only 70% capacity retention was obtained at 20 C for the *N*-methylated derivative, which is attributed to an increased solubility of the polymer. The respective *N*-phenyl compound showed very low capacity losses over 500 cycles at 1C and 80% capacity retention at cycling with 10 C as well as insolubility in most organic solvents [440].

Furthermore, a crosslinked 3D framework was created by Seferos et al., who synthesized a triptycene diimide derivative, from both naphthalene and perylene aromatic cores. While the naphthalene-triptycene network showed no conductivity and low cyclability, the perylene-triptycene formed evenly structured domains, leading to an 80% capacity retention after 500 consecutive cycles, while the unpolymerized monomer showed only 7.5% capacity retention after 500 cycles. However, the molar mass of the triptycene-diimide monomer is relatively high, resulting in an overall low battery capacity [441].

3.3.19. Disulfides

Sulfur has been used for Li-based solid-state batteries in manifold systems, as the specific energy density of 2600 Whkg⁻¹ for such systems is extremely promising, with a potential of 2.0 to 2.4 V vs. Li (Huang et al.) [183,442,443]. Elemental sulfur is a low-cost material and the sustainability of sulfuric materials is considered high; [444] however, sulfuric composites or poly(sulfides) used for electrochemical energy storage often decompose, gave insoluble sulfide or bisulfide salts (Fig. 15), lowering the accessible sulfur content in the battery and, therefore,

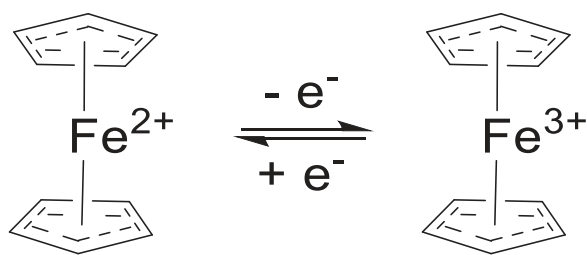


Fig. 16. Schematic representation of the redox reaction of ferrocene.

lowering the cyclability [445,446]. Several approaches have been performed, aimed at stabilizing sulfuric compounds in solid-state batteries, amongst which polymeric systems have also been reported. One approach is the introducing of small sulfuric side groups onto a backbone [447]. This strategy was initially published in 1997 by Naoi et al., who created a poly(dithiodianiline) system with capacity of 270 mAhg⁻¹ [314]. However, sulfur is often only used as a linker between redox-active groups, as mentioned before [398,448]. Hawker et al., who created a polymeric crosslinked network by oxidative formation of dithio bridges between hexathiolated benzene units, which can trap Li-ions in the discharging process. A theoretical specific capacity of 609 mAhg⁻¹ was calculated, although this is based on a complete breakup of the crosslinked network. However, during the performed cycling tests at 0.1C over 200 cycles, only roughly a quarter of the theoretical capacity of the material was used, albeit with high coulombic efficiencies, hinting at a low rate of parasitic redox-shuttling processes inevitable for other active materials relying on dithiolate redox chemistries [449].

A promising approach towards polymeric sulfur systems was presented by Pyun and coworkers, who created a crosslinked polysulfuric network via so-called “inverse vulcanization” [450,451]. Here, elemental sulfur is molten to form the diradical and a divinyl compound is added to the liquid sulfur phase. After cooling, a crosslinked material is obtained, in which the average sulfur chain length depends on the amount of crosslinker added [450,451]. The material, utilized in a solid-state battery, showed an extraordinary high capacity of 1100 mAhg⁻¹. After cycling for 100 cycles, 75% of capacity was retained. The amount of crosslinker, here 1,3-diisopropenylbenzene, was optimized. The best performance showed a 10% crosslinked poly(sulfur) material with 91% capacity retention after 100 cycles and 74% capacity retention after 300 cycles [452]. This strategy was adapted by different working groups, for example by Armand et al., who utilized a four-armed crosslinker, based on pentaerythritol to generate poly(S-pentaerythritol tetraacrylate) [453]. A sodium-sulfur battery was constructed to give 877 mAhg⁻¹ with a capacity retention of 91% after 100 cycles at 0.1C [453]. Furthermore, oligomeric sulfur chains can be introduced onto conjugated polymeric backbones, as shown by Buchmeiser et al. They functionalized poly(acrylonitrile) (PAN) with elemental sulfur under high temperatures, leading to PAN with oligomeric sulfur sidechains attached to the backbone with terminal sulfur groups. A composite cathode material was obtained with a capacity of 800 mAhg⁻¹ that decreased to 90% after the first 5 cycles, but then remained stable for 380 cycles [454].

3.3.20. Further architectures and active materials

Ferrocenes

The ferrocene redox moiety is widely known for its stable and highly reversible redox chemistry (Fig. 16). Thus, various applications were proposed, ranging from electrochromic devices, [455] redox-responsive polymers, [456] bio sensors, [457] self-healing materials [458] to drug carriers [91]. However, compared to other often-used redox moieties, the use of ferrocene in battery-related applications has thus far been limited. This may be at-

tributed to the high molecular mass of the ferrocene scaffold itself and the resulting low specific capacity. The ferrocene unit in all these examples showed a redox peak at nearly the same potential, 0.1 to 0.3 vs. Ag/AgCl, and 3.4 to 3.6 vs. Li/Li⁺, respectively. Most commonly, ferrocene-based RAPs can be synthesized by electropolymerization of heterocycles attached to the redox unit, generating linear conjugated homopolymers. There are manifold examples including thiophene-based CPDT, [459] pyrroles, [228,460] such as DTP, [459] and PANI [226]. Like for most conductive polymers, the solubilities are relatively low. Nevertheless, the bulky ferrocene hinders a tight stacking of the linear backbone. As a result, the polymers show an increased residual solubility as well as a higher electrochemical accessibility of the redox-active unit. Attainable capacities differ slightly, depending on the particular backbones used, but lie mostly at ca. 50 to 70 mAhg⁻¹. The polymers show high cycle stability and fast redox kinetics, enabling charging speeds up to 500 mAg⁻¹. Nevertheless, the CPDT-Ferrocene and DTP-Ferrocene polymers showed strongly fading capacities over the published 50 cycles, which may be caused by an irreversible oxidation involving the backbone [459]. Statements about the dispersity and molar masses cannot be made, since all conductive polymers are mostly insoluble and, thus, difficult to analyze. In any case, the main polymer design factors for these polymers are rather the synthetic accessibility of the monomer than the properties of the corresponding polymer.

Furthermore, it is possible to use a ferrocene unit itself, as a redox-active backbone. Tamura et al. synthesized a poly(ferrocene) by polycondensation of 1,1'-dibromoferrocene with magnesium and a nickel catalyst [461]. The polymer showed a capacity of ca. 95 mAhg⁻¹, which strongly decreases within the first cycles of the battery. This might be due to an interaction or charge transfer between neighboring ferrocene moieties in different oxidation states, possible due to the conjugated network. In an attempt to isolate the ferrocene cores from each other, Zhong et al. reported a poly(ferrocenyl-methylsilane), in which the ferrocene units are bridged by silanes [462]. The polymer was synthesized via ring-opening polymerization ($M_n = 80 \text{ kgmol}^{-1}$) showing a typical redox potential of 3.35 V vs. Li/Li⁺ and delivered a capacity of 110 mAhg⁻¹ at 50C with high cycle stability. Compared with the aforementioned example, this impressively shows the effect that the isolation of the ferrocene cores has on the electrochemical performance of the material. The same strategy was also utilized by Xiang et al. [463] in which they coupled ferrocene to fluorenylethynylene and polymerized this compound in a Sonogashira reaction with diiodothiophene (50 mAhg⁻¹) and 4,4'-diiodotriphenylamine (100 mAhg⁻¹), respectively. Both polymers showed the ferrocene-typical redox chemistry; whereas for the triphenylamine unit, an additional redox peak at ca. 1.0 V vs. Ag/AgCl was observed. Batteries, based on these polymers, were able to be cycled for 100 cycles with up to 10C. While an initial loss is recognizable, the capacity subsequently stabilizes.

Another possibility for the isolation of the ferrocene core is its use in a side chain of the polymer. Tamura et al. published vinyl ferrocene homopolymers, which were synthesized via FRP with AIBN [461]. Polymers with rather low molar masses could be obtained ($M_n = 2.2$ to 5.1 kgmol^{-1}). These materials showed low dispersities from 1.5 to 1.8. They could also show that the initial capacity of 105 mAhg⁻¹ is stable over the first four cycles. An additional conjugated ethynylferrocene polymer, synthesized via rhodium-catalyzed olefin polymerization, showed a similar starting capacity; however, it took a much higher drop of ca. 15 % over the first four cycles, again showing the necessity of isolating the ferrocene cores from each other. Vinylferrocene was also used by Xiang et al., who copolymerized it with *N*-vinylphenyl-*N,N'*-diphenylamine utilizing AIBN [464]. Two polymers with different comonomer ratios were synthesized. Both showed the typical re-

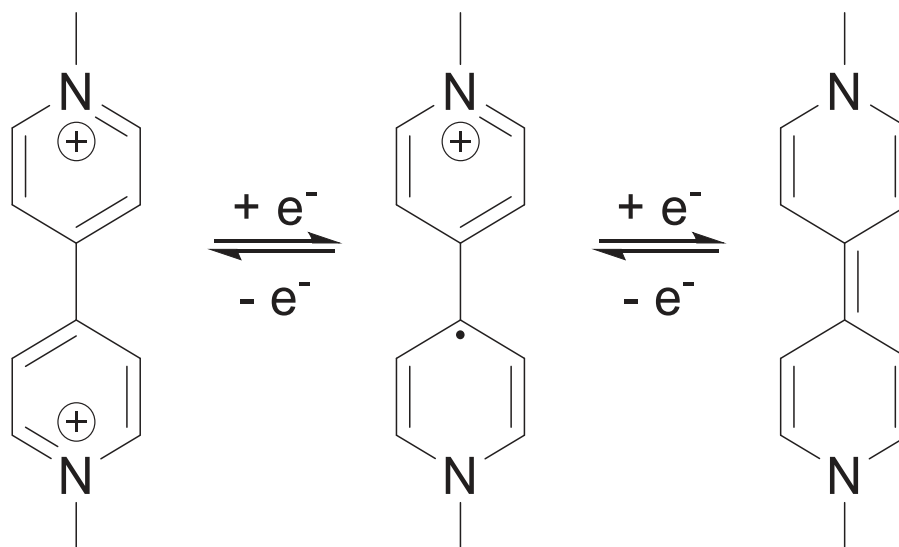


Fig. 17. Schematic representation of the redox reactions of methyl viologen.

dox peaks for ferrocene and triphenylamine. Interestingly, a lower content of ferrocene in the polymer corresponded to a higher capacity as well as a better performance in the battery.

Viologens

With a redox potential of *ca.* -0.8 V and -1.2 V against Fc^+/Fc for methylviologen, viologen represents a promising scaffold for anodes in full-organic solid polymer batteries [465]. The aromatic compound has been known for a long time [466]. Viologens typically show two one-electron reductions, generating a radical cation in the first step that is generally regarded as reversible, while a further reduction generates the neutral, less stable form (Fig. 17) [467]. Reduced viologen species are sensitive towards oxygen, which represents a challenge for many applications. However, it has been shown that the stability against re-oxidation in air can be increased by attaching the viologen core to a polymeric backbone, which can stabilize the radical species for several days [468]. Kvarnström et al. presented branched viologen compounds that were synthesized from three-armed monomers bearing cyanopyridines. These were electropolymerized in aqueous medium to generate linked viologen compounds. The success of the reaction was proven *via* electrochemistry. However, no battery was constructed, but the crosslinked structure of the material was confirmed [469]. Palmore et al. linked viologen groups to a poly(pyridine) backbone using an aliphatic C5-linker. [320]. The material was introduced into a composite electrode and cycled 100 times; 70% of the initial capacity of 55 mAhg^{-1} was retained after cycling at a working voltage of 1.2 V. It is expected that the degradation of the active material was derived partly from degradation of the backbone and partly from trace oxygen in the cell and is not due to irreversibility of the addressed redox processes [320]. The research groups of Poizot and Gaubicher presented oligomeric systems that were compromised of viologen groups covalently linked naphthalene tetracarboxylic acid diimides. A battery with an aqueous electrolyte was investigated and showed 85 mAhg^{-1} of capacity and a capacity retention of 83 % after 3000 cycles at 4 C [470]. Furthermore, Walder et al. investigated poly(viologen)s that are linked *via* aromatic groups such as biphenyls or xylenes; these polymers were embedded into graphene oxide. Theoretical capacities of 159 to 252 mAhg^{-1} were calculated and capacities of 138 to 216 mAhg^{-1} could be measured. They created flexible electrode films and achieved excellent capacity retentions of 98 to 99 % after 50 cycles at 5 Ag^{-1} [470]. An alternative viologen compound was presented by Stolar et al. [471] in which they

utilized the previously known 2,7-diazadibenzophosphole oxide as starting material for their polymerization. It was condensed with di(bromomethylene)benzene and the anion was changed to triflate, reaching molar masses of 0.70 to 1.29 kg mol^{-1} . The xylene-bridged phosphaviologen polymer showed a reversible two electron reduction at very low potentials, due to the electron withdrawing effect of the phosphoryl group. Battery testing showed 84% capacity retention after 150 cycles at multiple C-rates.

4. Redox-active polymers in capacitor-based systems

4.1. Working principles and material requirements

Apart from batteries, which can be regarded as classic electrochemical storage systems, novel energy storage systems have evolved in recent years [472]. One of the highly investigated approaches represent capacitor-based concepts [473]. Electrical double layer capacitors (EDLCs) combine high power outputs and rapid charging with high discharge rates. The capacitance of the system is determined by the electrodes' surface area, while the cell voltage is linked to the state-of-charge of the capacitor [474]. Therefore, the voltage is limited by the stability window of the electrolyte [475]. A capacitor half-cell is composed of a porous carbon material in an electrolyte salt solution. Two of these half-cells are connected by a mesoporous separator. When a potential difference between the electrodes is applied, ions within the electrolyte migrate towards the electrode surface to counter-balance the accumulating charges within the electrode, storing the applied charge in the electric field of respective electrical double layer of the electrode. This charge storage process is of physical nature, in contrast to typical battery systems that revealed electrochemical charge storage, based on faradaic charge transfer processes, accompanied by a change in chemical structure of the active material. Capacitors of the aforementioned-type are labeled as (EDLCs) and do not require the application of redox-active polymers. Most prominently, conductive carbon materials are applied for EDLCs, as the surface of the chemical capacitor is maximized for maximum charge storage [476].

Apart from the purely electrostatic storage concept of capacitors, faradaic charge transfer processes can lead to an increased charge storage capability of the device. This can be achieved by integrating redox-active groups, such as inorganic oxides or organic polymers into a capacitors' active material, leading to a pseudoca-

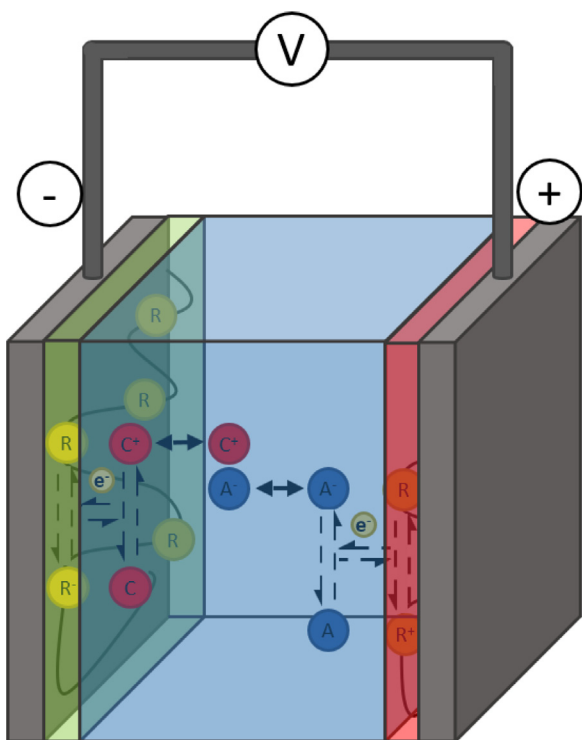


Fig. 18. Working principle of pseudocapacitor-based energy storage systems. Upon charging, an electrochemical double layer is formed after diffusion of supporting electrolyte salt ions (M^+ and I^-) towards the electrode surfaces. At the same time, redox reactions occur in the electrode due to the redox-active materials (R and R^+), leading to both faradaic and capacitive energy storage.

capacitance. The resulting hybrid storing device is called a pseudocapacitor. Here, a combination of the fast charging and discharging rates of capacitor-based approaches is combined with the stable voltage output of faradaic storage systems. Requirements for a well-performing organic active material are high conductivity, low solubility within the electrolyte and fast redox kinetics, generally without subsequent changes of the chemical structure of the active material as shown in Fig. 18. Often, the solubility of the redox-active species must be optimized, making redox-active polymers reasonable contenders to inorganic alternatives (Fig. 18). For pseudocapacitors, electrolytes can be freely chosen from organic, aqueous solvents or ionic liquids and further polymeric solid electrolytes can be used, without the need for a liquid solvent at all [73].

In pseudocapacitors, redox reactions do not only occur at the electrode surface but also within the electrode composite material, as the redox groups are distributed over the complete conductive material. Thus, the capacity, the ability to faradaically store the applied charge, will increase, if both the density as well as the accessibility of the redox-active groups in the polymer matrix are increased. The system capacitance increases significantly, when the surface area is increased, as the area to form an electrical double layer is increased. Both lead to an improved performance of the device, as more energy can be stored. In order to further increase the accessibility of the redox-active groups, they are often linked to conductive polymers, providing access to polymer domains that bear redox-active groups, but are not easily accessible for migrating ions [477]. Approaches to increase the availability of the redox active groups through significant an increase of active material porosity may be interesting for further improvement of the redox behavior. This has been shown for solid polymer batteries and was discussed in Section 3.2.

Recently, covalent-organic frameworks (COFs) with redox active moieties (RAM-COF) have gained increasing interest. The concept refers to a multi-dimensional network within cooperating electrochemical active groups. Currently, the research focuses more on two rather than three-dimensional networks due to the higher accessibility and lower synthetic expenditure for both the monomers and products. In general, RAM-COFs consist of rigid highly organized frameworks constructed from conjugated polymers, that lead to inner pores, through which metal ions can migrate freely. The high porosity of these materials produces an overall extraordinary high specific surface area. RAM-COFs have, in comparison to standard active materials, based on linear polymeric chains or cross-linked networks, the following advantages: 1) The π - π interactions between the 2D layers enable a pathway for efficient electronic charge transport, 2) the ionic diffusion is enhanced and 3) possible tailoring the pore size and charge to the utilized mobile ion [295]. The high surface area and the named advantages make them a good active alternative (electrode) material for electrochemical applications, in particular for super capacitors. However, due to the limited thermal performance, the challenging synthetic procedures, and complicated processability, they do not appear to be standard materials in battery electrodes, until now. The topic of RAM-COFs is summarized in several excellent reviews by Kandambeth et al. [295], Li et al. [296], Pei et al. [297], and Zhang et al. [298].

However, typical challenges inherited from solid-state batteries are present as well, which are, in particular, a lower cycle stability as well as volume changes during the charging and discharging process [473,478].

The most prominent materials for pseudocapacitors are conductive polymers and conductive carbons composites thereof. Frequent representatives are polymers, e.g., poly(pyrrole), poly(thiophene), and poly(aniline) [479]. Graphene is the most commonly used carbon material in composite electrodes as it shows high conductivity and conductive polymers can be grown easily on the carbon surface due to sp^2 -hybridization. Due to the high conductivity, bulk-located redox centers can be addressed efficiently. Additionally, if three-dimensional carbon materials are used, volume changes can be controlled more efficiently in the electrode, increasing the stability over higher cycle numbers.

4.2. Architectures and active materials

The most-studied conductive polymer type for pseudocapacitors are the poly(aniline)s, since they exhibit high stabilities, straightforward synthetic procedures are known and the respective devices show high pseudocapacitance. Most importantly, morphology plays an important role for PANIs and has, therefore, been widely investigated [480]. Chen et al. presented different nanostructures with high surface areas [481]. For PANIs, protic electrolytes, often also acidic and protic ionic liquids can be used. [231,482] As discussed in Section 3.3.1.1, chemical or electrochemical procedures are followed to form polymers, since they give the opportunity to rapidly form composites *in situ*. For instance, Wand et al. performed the *in situ* polymerization on graphene for a PANI-based pseudocapacitor, showing a peak capacitance of 233 Fg^{-1} and 135 Fcm^3 [481,482] Li et al. utilized graphene nanosheets for the *in situ* polymerization, leading to a peak capacitance of 1130 Fg^{-1} in $1 \text{ M H}_2\text{SO}_4$ with a 87% capacitance retention after 1000 cycles [483,484,485].

Poly(pyrrole)s (PPy)s represent another important pseudocapacitor material, since it can be implemented in systems with aqueous, organic, and/or aprotic solvents. In particular, aqueous systems perform efficiently, since the electron conductivity of PPy is high and ions can migrate rather freely into PPy pores. Furthermore, it is mechanically stable and readily available, both synthetically and commercially [486,487]. However, the specific capacitances of PPy

systems are lower than for PANI systems and the stability is often decreased when PPy is not combined with a graphene material, which can act as an adsorbing agent [231,482]. Typically, graphene and the pyrrole monomer are combined and oxidized with ammonium persulfate or FeCl_3 [488]. A different approach was followed by Zhu et al., who investigated cauliflower-shaped aggregates of small PPy particles [489]. They influenced the PPy shaping by addition of graphene, inducing the formation of homogenous nanosheets, where the surface area is easier accessible for migrating ions. A pseudocapacitance of 255.7 Fg^{-1} at 0.2 Ag^{-1} and 199.6 Fg^{-1} at 25.6 Ag^{-1} in 3 M KCl with a 93% capacitance retention after 1000 cycles could be achieved [490]. Recent approaches focus on highly porous hydro- and aero-gels, respectively, as they show even higher surfaces as well as high mechanical stability. He et al. synthesized a PPy / graphene hybrid aerogel through a freeze-drying process [486,487]. Stabilization of the graphene layers in a 3D network prevents the folding of graphene to areas, which are inaccessible for ions. The built devices showed a pseudocapacitance of 417 Fg^{-1} at 0.5 Ag^{-1} with 74% capacitance retention after 2000 cycles in 1 M aqueous KOH.

Poly(3,4-ethylenedioxythiophene):poly(styrene sulfonate) (PEDOT:PSS) is another important material used for pseudocapacitors. The resulting pseudocapacitors benefit from the high insolubility, high pseudocapacitance and low toxicity [491]. PEDOT:PSS can be synthesized *in situ* analogously to the procedures for PPy. PSS is dissolved in an aqueous electrolyte and EDOT is added. Subsequently, an oxidizing agent, such as a peroxydisulfate salt or FeCl_3 , is added to induce the polymerization [492]. A specific capacitance of 70 to 130 Fg^{-1} can be achieved, depending on the polymerization technique. However, the morphology of the desired electrode structure also depends on the required polymerization parameters. Consequently, these properties can influence the capacitor performance [493–495]. Also, PEDOT can be used in a supercapacitor without PSS, showing high cycle stability, but low specific capacitances [496]. A graphene-PEDOT system was investigated by Alvi et al., in which they achieved a specific capacitance of 304 Fg^{-1} in 2 M HCl and 261 Fg^{-1} in 2 M HCl at 10 nVs^{-1} . [492] Österholm et al. showed that PEDOT-graphene oxide composites exhibit an even surface morphology; however, due to aggregate formation, the electron and ion conductivity are reduced, resulting in a lower redox current and charge compared to PEDOT:PSS [497]. Zhou et al. investigated a graphene-PEDOT hydrogel, bearing stable mechanic stress resistance and high conductivity. The material was formed *via an in situ* polymerization. Carbonyl moieties that can be found in graphene oxide, lead to the formation of PEDOT clusters, which show a conductivity of 0.73 Scm^{-1} and a specific capacitance of 174.4 Fg^{-1} . The mechanical stability was reported with an compressive fracture stress of 29.6 MPa and 2.1 MPa at 10 rads^{-1} [498].

5. Summary – solid state batteries and capacitor-based applications

Redox-active polymers represent promising materials for the transition away from metal-based electrochemical energy storage devices, as evidenced by the various active materials and polymeric designs that have been shown until now. According to our hands-on approach, both battery- and capacitor-based devices require varying polymer designs, which can be classified by the respective active materials, but may as well be distinguished by their integration into the polymer or the architecture of the polymer network itself. In this regard, linear polymers can contain the active materials attached as pendant side groups, but the backbone of the polymer can as well be constructed of the reactive moiety itself. This leads to varying electrochemical and physical properties, which may further be varied upon changing the polymer architecture by formation of crosslinks, as shown for the example of

the TEMPO scaffold. Apart from the working principle, the material requirements for solid polymer batteries and capacitor-based storage devices have been outlined and illustrated, focusing on key factors, such as: solubility, synthetic availability and/or stability of the polymeric materials.

Starting from a macroscopic point-of-view, the overall polymer architecture was initially regarded, followed by the polymer type, e.g., type of linkage of the active moiety to and within the polymer, before the respective redox-active unit is discussed in conjunction with this hierarchy.

The linear architecture has been utilized for both conductive and non-conductive polymers. Linear homopolymers show a simple construction that is often mirrored by a straight-forward synthesis. However, fine-tuning of the polymer properties is hardly possible, since the redox-active monomer often mediates the majority of the polymer's properties. Non-conducting linear polymers often show a distinct redox potential, as the redox properties of a redox-active monomer are typically maintained. TEMPO and different radicals have been introduced as side groups; whereas, quinones are often introduced into the backbone. Benzo-, naphtho-, and anthra-quinone are the front-runners for quinoidic systems utilized in linear architectures. The direct connection of aromatic or conjugated monomers in the backbone leads to conjugated polymers. The redox activity of these conjugated polymers is obtained via doping of the polymer by introducing positive or negative charges, accompanied by an increased electrical conductivity. As a drawback, conductive polymers do not show steady redox potentials. Nevertheless, batteries may be constructed with less conductive additives. Poly(aniline), poly(pyrrole), and poly(thiophene) are amongst the most-studied representatives. Also, side group functionalization was investigated for most conductive polymers.

Apart from homopolymers, copolymers have been investigated to further optimize solubility and redox properties of the RAPs by the introduction of solubility-mediating monomers or blocks. Mainly, TEMPO and polyimidic systems have been widely investigated. For polyimidic systems, a plethora of linking molecules was shown to further alter the performance of the active material. When crosslinkers are introduced, new multi-dimensional structures can be obtained that are favorable from a synthetic viewpoint. Mainly C_3 -symmetric crosslinkers and monomers bearing two polymerizable groups are known. In general, crosslinked active materials often revealed high cycle stability and very low solubility but are hardly processible and can contain trace impurities from the synthesis.

Conductive polymers have been further utilized in another interesting energy storage approach, based on pseudocapacitors. These devices are comprised of the rapid charge storage mechanisms of capacitors and energy storage, based on fast faradaic charge transfers. By combining the electrochemical double layer-based capacitance of EDLCs with a chemical redox process in the electrode, so-called “pseudocapacitance” is obtained and is significantly higher compared to the capacitances of a classical capacitor. However, the charging and discharging speeds are intrinsically lower, as the fast redox reactions that are addressed during charge storage do not proceed as fast as the formation and deformation of the electrochemical double layer. Nevertheless, studying hybrid systems is an important means for finding charge storage solutions for manifold applications.

6. Redox flow batteries

6.1. Introduction

Since Kangro patented the first RFB in 1949, [499] using chromium and titanium species as redox couples, a wide range of new and promising alternatives has evolved. Nowadays, the most

Pseudocapacitor

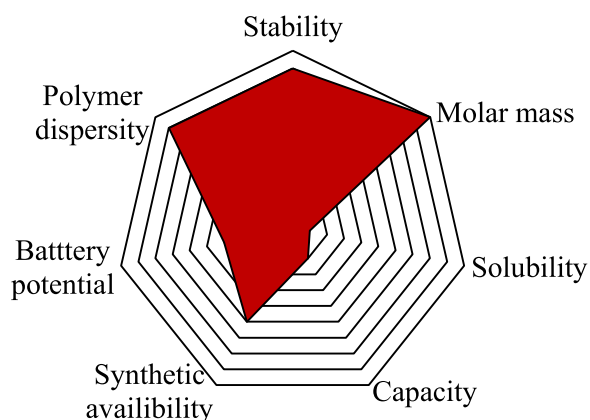


Fig. 19. Spider web diagram of the material requirements for pseudocapacitors.

developed concept is the all-vanadium RFB (VRFB); however, utilizing vanadium-based electrolytes has major drawbacks, such as the use of corrosive electrolytes, a strong dependency on commodity prices, and toxicity. This leads to the development of the (all-)organic RFBs, which use organic molecules, as storage materials [500–503]. Due to the manifold usable scaffolds, the design of a cheap battery with tailor-made electrochemical properties, based on non-corrosive and non-toxic electrolytes, is possible [504,505].

In general, every RFB is using the same working principle (see Fig. 19). The storage materials are dissolved in the electrolyte and kept in tanks, one for each half-cell. Both electrolytes (*i.e.* posolyte and negolyte) are pumped into the galvanic cell, in which the actual electrochemical reaction takes place. Both half cells are separated by a semipermeable, mostly ion selective membrane. As the membrane represents a crucial factor, not only for the cell performance but also for the cost of the whole system; great efforts were made to improve selectivity and longevity along with simultaneous cost reductions [82]. A promising concept are membranes with a separation mechanism, based on the size of the active material as compared to its charge. In 2011, this idea was first realized by Zhang et al., who used nano-filtration membranes in vanadium redox flow batteries, which were able to shuttle hydronium ions but could also prevent a crossover of vanadium ions [506]. In order to further improve the selectivity, the size of the restrained material has to be enlarged. In 2013, the group of Liao showed a water-based poly(aniline)-zinc hybrid flow cell and introduced the usage of polymers as active materials in RFBs [507]. Nagajuna et al. expanded the concept towards non-aqueous systems by using poly(styrene) polymers with viologen side groups in a potential-controlled bulk electrolysis in MeCN [239]. The first all-polymeric redox flow battery was then published by the Schubert group in 2015 [508]. The concept focused on a poly(styrene)-based polymer with viologen side groups, as the negolyte, and a poly(methacrylate)-based polymer with TEMPO side groups, as the posolyte, in aqueous NaCl, separated by a cheap dialysis membrane. However, with the usage of polymers as active materials, new requirements for potential storage materials arose.

6.2. Material requirements

The market share of large-scale energy store technologies is largely price-driven, pushing the system costs for a competitive RFB below \$100 per kWh of storage capacity [504,505,509]. For these costs, the main influencing factor remains the active mate-

rial, as its molecular complexity and synthetic availability scale the initial system costs, while its physical and electrochemical properties largely define the cost of long-term energy storage [510]. Thus, storage material optimization has been singled out in order to achieve high cost efficiency. This, of course, applies for all utilized RFB redox-active materials, however, the strongest cost reductions have been forecast for organic storage materials. Further cost reductions may be achieved with polymeric active materials, as their utilization allows for the advantage of using comparably cheap size exclusion membranes. In comparison to proton exchange membranes, *e.g.*, Nafion®, or ion selective membranes, these separators are *ca.* one order of magnitude cheaper [511]. Given that the membrane may equal up to a sixth of the overall system costs for RFBs, the presented approach is highly promising [510].

When designing organic, redox-active materials for electrochemical applications, the electrochemical properties of both the active material and the electrolyte have to be considered. In contrast to solid state batteries, where the solubility of the active material within the electrolyte should be as low as possible, for classical RFBs, the solubility should be as high as possible, as the theoretical capacity of the battery scales directly with the solubility of the storage material (see Fig. 20). Organic molecules are often only soluble in organic solvents, but these electrolytes have several disadvantages, such as higher toxicity, flammability, cost and low ion and electric conductivity. Nonetheless, their often-wide electrochemical stability window, a higher inertness and better solution properties of the solvent are the deciding advantages of organic electrolytes (see Fig. 23). [319,512] Aqueous systems mainly suffer from their small electrochemical stability window, low solubility of many active scaffolds and the nucleophilic and protic properties of water. However, its high conductivity, solubility for ionic substances, cost efficiency, non-toxicity and inflammability makes it the solvent of choice for many RFB systems [501,513–515] Furthermore, with the solvent, additional electrolyte properties have to be considered, *e.g.*, supporting electrolyte and pH-values. For example, anthraquinones show good properties as active materials, but require extreme pH-values in aqueous solutions due to their proton-coupled electron transfer mechanism during charge and discharge, making their respective redox potentials pH-dependent. Thus, the pH-value must be adjusted using respective supporting electrolytes [516]. However, TEMPO-based materials cannot be implemented under strongly basic conditions, because of a disproportionation reaction of the oxoammonium cation, that is formed upon oxidation of the TEMPO-moiety [517]. However, as not every active material exhibits a pH-dependent redox equilibrium, an arbitrary combination of negolytes and posolytes remains challenging due to both osmotic and ion crossover effects through the membrane in the long term, requiring additional buffer equilibria and special membranes [518]. Additionally, the solubility of the active material within the electrolyte mixture for all addressed redox states remains a challenging point for suitable redox-active materials, but may be synthetically altered in case of organics [519].

While the general requirements for active materials in RFBs are summed up in the reviews of Luo et al. [519] and Ding et al. [520], we wanted to give a more in-depth overview on the special requirements, which must be fulfilled when using polymeric materials.

Of paramount importance in this context is the polymer's degree-of-polymerization. The ability to retain a molecule of a certain size by the employed dialysis membranes is defined by their molecular weight cut off (MWCO), which can be regarded as a measure of the pore size of the membranes. Thus, the employed polymer has to have a certain degree-of-polymerization in order to be retained by the membrane. However, depending on the polymers' molar mass distribution, a relevant portion of the polymer chains may be small enough to not be retained by the membrane.

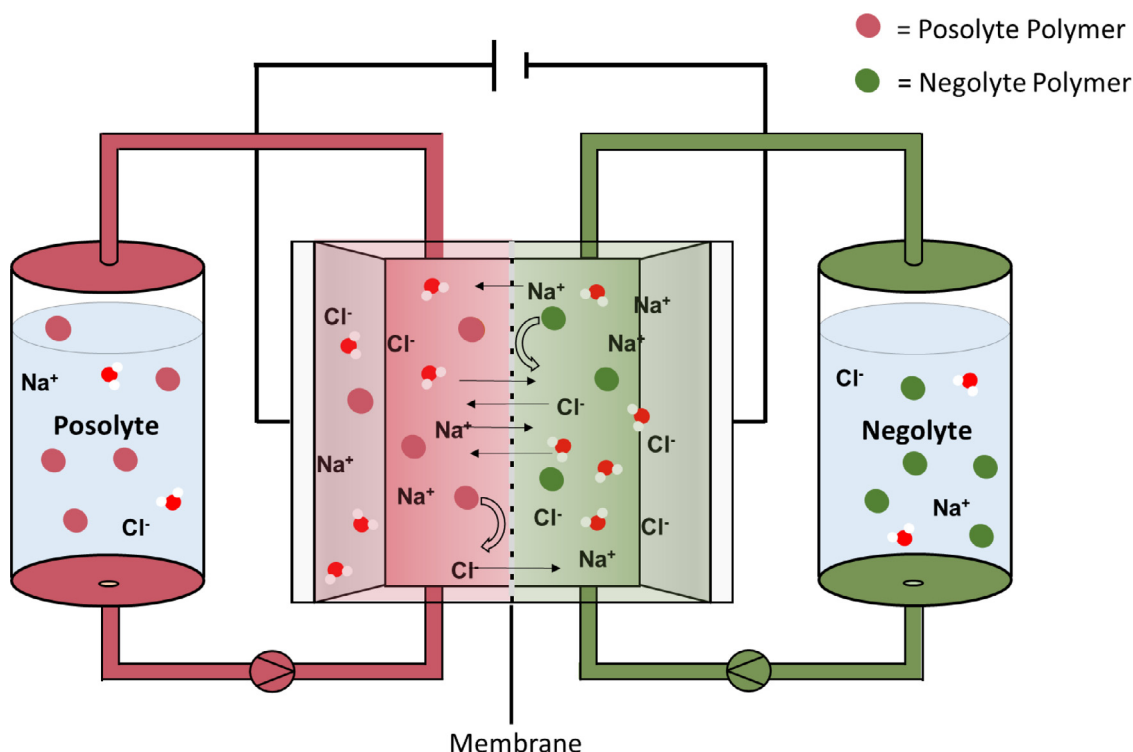


Fig. 20. Schematic representation of a redox flow battery based on redox-active polymers in aqueous electrolytes.

Thus, not only the molar mass M_n is crucial to the performance of such systems, but the dispersity \mathcal{D} of the polymer is as well, as low molar mass portions of the polymer directly contribute to crossover through the membrane. Therefore, it is necessary to have the M_n to be at least a few times larger than the MWCO, depending of the dispersity.

A further challenge for the use of polymeric redox-active substances in RFB electrolytes may be their solubility. Depending on the nature of the solvent, this parameter may be addressed during the polymer synthesis by using mediating comonomers. Additionally, the viscosity of polymer solutions in comparisons to small molecules is usually higher. A high electrolyte viscosity is associated with a higher energy consumption of the pumps, lowering the round-trip efficiency of the battery and raising operating costs [518,521,522]. In order to achieve lower viscosities, the molar mass has to be limited; however, the above mentioned retention by the SEC membrane has to be still ensured.

All of these special requirements have to be finally addressed by using the proper polymerization technique that is as well rated from an economic point-of-view. All in all, polymeric RFB (PRFB) not only offer promising opportunities, but also pose new challenges, which must be overcome by smart polymeric design processes. A summary of the literature known redox moieties for polymeric flow batteries is given in Fig. 21 and Table 3.

6.3. Battery types

6.3.1. Aqueous polymer redox flow batteries

Since organics are widely investigated for aqueous organic redox flow batteries, [523–526] it is surprising that there are very few examples for polymeric active materials, which can be attributed to the aforementioned challenges (see Fig. 22). The main issue for their use is the insolubility of most monomers and their corresponding polymers in aqueous media. In these cases, it is necessary to utilize solubility promoting comonomers that are mostly redox inactive and can lower the specific capacity of the material.

The amount of comonomer added is critical to the overall performance of the battery.

6.3.2. Homopolymers

As discussed, a polymer solely consisting of the respective redox-active monomer may be advantageous in terms of specific capacity for use in PRFBs. Unfortunately, the monomer must also provide the required degree-of-solubility (see Fig. 22). The only known example that utilizes the double-cationic viologen scaffold by the Schubert group. Here, a 1-methyl-1'-(4-vinylbenzyl)-4,4'-bipyridine monomer was directly polymerized with potassium peroxodisulfate [119]. The received linear homopolymer showed molar masses between 13 and 32 kg mol⁻¹ with high dispersities of $\mathcal{D} = 2.8$ to 7.2. Lower dispersities were achieved by adding thioacetic acid, as chain transfer agent during the radical polymerization. Even if only the general properties of the polymer and not its electrochemistry were investigated, a future utilization as negolyte active material in RFBs was intended. Nevertheless, the loss of a positive charge inside the molecule during the charging process with the coupled formation of a radical could lead to solubility decrease. Furthermore, adjacent viologen radicals show the tendency to partially dimerize irreversibly, leading to a decreasing accessible capacity with every charge / discharge cycle. These drawbacks make the viologen homopolymer unfavorable for application in RFBs.

6.3.3. Copolymers

In a preliminary study, Janoschka et al. investigated the influence of methacrylamide, as comonomer for 1-methyl-1'-(4-vinylbenzyl)-4,4'-bipyridine polymers. The authors synthesized different linear statistic copolymers with comonomer fractions ranging from 0.14 to 0.50 [119]. The dispersities of the resulting copolymers were between 2.1 and 2.5 making the utilization of chain transfer agents obsolete. Furthermore, the received molar masses of 38 to 39 kg mol⁻¹ are higher and more favored for RFBs with size-exclusion membranes. Nevertheless, the

Table 3

Summary of so far presented RAPs for RFB applications or intended usage. *The shown TEMPO precursor was not oxidized nor used in a battery but was synthesized for a further battery application and thus included in the list. Refs. [82,119,122,145,146,180,219,236,239,240,241,244,250,255,303,319,528,536,537,540,544] are used in the last column of this table.

Redox-active Monomer / Precursor	Comonomer	Comonomer ratio	Polymerization Characteristics	Polymerization Technique	M_n [kg mol ⁻¹]	\bar{D}	Viscosity	$E_{1/2}$	Battery properties	Cell OCV	Membrane	Ref.
Aqueous PRFBs												
		n. a.	homopolymer	FRP	13 to 32	2.8 to 7.2	7 to 30 mPa·s (41 mg/mL) in 1.5 M NaCl at 20 °C	-0.40 V, -0.80 V vs. Ag/AgCl	n. a.	n. a.	n. a.	[119]
		0.14 to 0.5	statistic, post-polymerization functionalization	FRP	38 to 39	2.1 to 2.5	n. a.	n. a.	n. a.	n. a.	n. a.	[119]
		0.15	statistic, post-polymerization functionalization	FRP	30.9	2.4	5 mPa·s (10 AhL ⁻¹) in 1.5 M NaCl at 20 °C	-0.40 V, -0.53 V vs. Ag/AgCl	40 to 100 mAcm ⁻² 10000 cycles, 10 WhL ⁻¹	0.5 V vs. TEMPO polymer	size-exclusion membrane	[82]
		0.14 to 0.5	statistic	FRP, without chain transfer agent	46 to 95	1.9 to 2.8	n. a.	n. a.	n. a.	n. a.	n. a.	[119]*
		0.33 to 0.67	statistic	FRP with and without chain transfer agent	9 to 169	1.5 to 4.3	n. a.	n. a.	n. a.	n. a.	n. a.	[119]*
		0.22 to 0.5	statistic, post-polymerization oxidation	RAFT	52-80	1.26 to 1.62	pseudo-plastic shear-thinning behavior (5.6 wt%) in 0.5 M NaCl	0.72 V vs. Ag/AgCl	n. a.	n. a.	n. a.	[119]*
		0.5	statistic, post-polymerization oxidation	FRP with and without chain transfer agent	7 to 134	1.7 to 4.9	29 mPa·s (5.6 wt%) in 33 mmolL ⁻¹ NaCl	n. a.	n. a.	n. a.	n. a.	[119]*
			statistic, post-polymerization oxidation	FRP with chain transfer agent	20.2	1.7	17 mPa·s (10 AhL ⁻¹) in 1.5 mmolL ⁻¹ NaCl	0.72 V vs. Ag/AgCl	40 to 100 mAcm ⁻² 10000 cycles, 10.0 WhL ⁻¹	1.1 V vs. viologen polymer	size-exclusion membrane	[82]
	0.5	statistic, post-polymerization oxidation	not specified	20.2	1.71	n. a.	0.72 V vs. Ag/AgCl	1 to 16 mAcm ⁻² 2500 cycles, 3.6 WhL ⁻¹	1.1 V vs. methyl viologen	anion exchange membrane	[255]	
		Organic PRFBs										
			0.5	statistic, post-polymerization oxidation	FRP	20.7	2.6	n. a.	0.75 V vs. Ag/AgCl	1 to 20 mAcm ⁻² 50 cycles 4.1 WhL ⁻¹	1.7 V vs. zinc	size-exclusion membrane
statistic, post-polymerization oxidation	FRP with chain transfer agent			14.4	2.4	n. a.	0.75 V vs. Ag/AgCl	1 to 12 mAcm ⁻² 1000 cycles 1.9 WhL ⁻¹	1.7 V vs. zinc	size-exclusion membrane	[180]	
0.5	statistic, post-polymerization oxidation		FRP with chain transfer agent	38.1	1.39	4.59 mPa·s (10 AhL ⁻¹) in 1.5 molL ⁻¹ NaCl	0.70 V vs. Ag/AgCl	8 mAcm ⁻² 125 cycles >26 WhL ⁻¹	1.1 V vs. methyl viologen	size-exclusion membrane, anion exchange membrane	[244]	
		n. a.	post-polymerization functionalization	RAFT	21 to 318	1.9 to 1.6	9.1 to 220 mPa·s (0.01 M to 1.0 M)	-0.7 V, -1.1 V vs. Ag ⁺	12 cycles MeCN	bulk electrolysis	nano porous membrane, Celgard	[239]

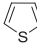
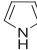
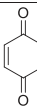
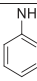
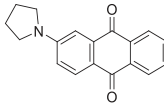
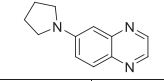
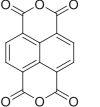
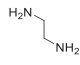
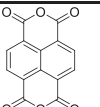
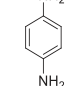
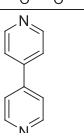
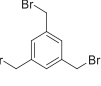
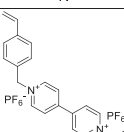
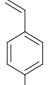
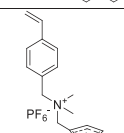
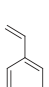
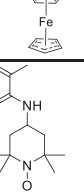
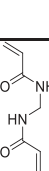
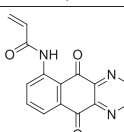
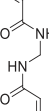
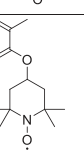
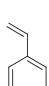
Table 3 (continued)

Redox-active Monomer / Precursor	Comonomer	Comonomer ratio	Polymerization Characteristics	Polymerization Technique	M_n [kg mol ⁻¹]	\bar{D}	Viscosity	$E_{1/2}$	Battery properties	Cell OCV	Membrane	Ref.
		n. a.	post-polymerization functionalization, ortho and para derivatives	RAFT	53 to 80	1.4 to 1.9	9 mPa·s	-0.7 V, -1.2 V vs. Ag ⁺	6 cycles MeCN	bulk electrolysis	nano porous membrane, Celgard	[240]
		n. a.	post-polymerization functionalization	not specified	271	1.6	n. a.	0.26 V vs. Ag ⁺	0.9 mAcm ⁻² 50 cycles, 0.2 WhL ⁻¹ MeCN	0.9 V vs. viologen polymer	anion exchange membrane	[241]
		n. a.	homopolymer	RAFT	4.9 to 11.1	1.0 to 1.1	n. a.	0.96 V vs. Ag ⁺	100 cycles MeCN	bulk electrolysis	nano porous membrane Celgard	[522]
		0.45 to 0.8	statistic	FRP	6 to 88	2.2 to 2.7	n. a.	-1.9 V vs. Ag/AgN O ₃	0.5 mAcm ⁻² 10 cycles, 0.3 WhL ⁻¹ , DMF	2.2 V vs. TEMPO polymer	polyolefin foil Celgard	[146]
		0.2	statistic	FRP	17	2.3	n. a.	-1.4 V, 0.6 V vs. Ag/AgN O ₃	0.025 mAcm ⁻² 100 cycles, 0.5 WhL ⁻¹ PC	1.6 V vs. p(BODIPY)-co-TAST	size-exclusion membrane	[145]
		0.2	statistic	FRP	4	1.5	n. a.	-1.4 V and 0.6 V vs. Ag/AgN O ₃	0.025 mAcm ⁻² 100 cycles 0.5 WhL ⁻¹ PC	1.6 V vs. p(BODIPY)-co-TEGST	size-exclusion membrane	[145]
		0.2	statistic	FRP	17	2.3	n. a.	-1.4 V and 0.6 V vs. Ag/AgN O ₃	0.25 mAcm ⁻² 100 cycles 0.5 WhL ⁻¹ , PC	1.6 V vs. TEMPO polymer	size-exclusion membrane	[145]
		0.22	statistic, post-polymerization functionalization	RAFT	53	1.3	n. a.	0.5 V vs. Ag/AgN O ₃	4 mAcm ⁻² 500 cycles 8.1 WhL ⁻¹ EC/DMC/DEC	1.2 V vs. zinc	size-exclusion membrane	[180]
		n. a.	graft polymer	anionic and ROMP	32 to 230	1.4 to 1.9	n. a.	0.8 V vs. Ag/AgCl	100 cycles EC/DEC	Half-cell setup	nano porous membrane, Celgard	[219]

Suspension PRFBs

(continued on next page)

Table 3 (continued)

Redox-active Monomer / Precursor	Comonomer	Comonomer ratio	Polymerization Characteristics	Polymerization Technique	M_n [kg mol ⁻¹]	\bar{D}	Viscosity	$E_{1/2}$	Battery properties	Cell OCV	Membrane	Ref.
		n. a.	homopolymer	electro-polymerization	n. a.	n. a.	n. a.	-2.0 V and 0.5 V vs. Ag ⁺	5 mAcm ⁻² , 30 cycles, PC	2.7 V vs. itself	anion exchange membrane	[536]
		n. a.	homopolymer	electro-polymerization	n. a.	n. a.	n. a.	0.2 V vs. SCE	15 mAcm ⁻² , 90 cycles, water, 170 mAhg ⁻¹	1.25 V vs. MnO ₂	polyolefin foil	[531]
		n. a.	homopolymer	oxidative polymerization	3.4	n. a.	7.8 mPa·s (1.0 M)	0.7 V vs. SHE	20 mAcm ⁻² , 5000 cycles, 6.3 WhL ⁻¹ , water	0.7 V vs. phthalimide polymer	size-exclusion membrane, Nafion 117	[122]
		n. a.	homopolymer	electro-polymerization	n. a.	n. a.	10 to 400 mPa·s 50 to 400 gL ⁻¹	0.2 V vs. SCE	30 mAcm ⁻² : 32 cycles, water, 117 mAhg ⁻¹	1.25 V vs. zinc	polyolefin foil	[540]
		n. a.	homopolymer,	oxidative polymerization	1.5 to 4.7	n. a.	n. a.	-0.2 V vs. SHE	2 Ag ⁺ , 100 cycles, water, 61 mAhg ⁻¹	1.1 V vs. TEMPO amine	Nafion 112	[303]
		n. a.	homopolymer	oxidative polymerization	5.5	1.22	n. a.	-0.79 V vs. SHE	5 Ag ⁺ , 1000 cycles, water, 120 mAhg ⁻¹	1.3 V vs. potassium hexacyanoferrate	Nafion 112	[319]
		0.5	alternating copolymer	polycondensation	n. a.	n. a.	3.1 mPa·s (1.0 M)	-0.15 to 0.2 V vs. SHE	20 mAcm ⁻² , 5000 cycles, 6.3 WhL ⁻¹ , water	0.7 V vs. Quinone polymer	size-exclusion membrane, Nafion 117	[122]
		0.5	alternating copolymer	polycondensation	n. a.	n. a.	2.3 mPa·s (1.0 M)	-0.1 V vs. SHE	5-20 mAcm ⁻² , 50 cycles, 8.3 WhL ⁻¹ , water	0.8 V vs. quinone polymer	size-exclusion membrane, Nafion 117	[122]
		0.6	suspension	polyaddition	n. a.	n. a.	1.31 to 14.2 mPa·s (0.001 to 1.0 M)	-0.4 V vs. Ag/AgCl	100 cycles, water, 15 WhL ⁻¹	1.0 vs. TEMPO-polymer	size-exclusion membrane	[250]
		n. a.	crosslinked colloidal PVBC, post-polymerization functionalization	n. a.	n. a.	n. a.	<10 mPa·s (0.56 M)	-0.5 V vs. Ag ⁺	0.043 mAcm ⁻² , 12 cycles, MeCN, 0.1 WhL ⁻¹	0.9 V vs. ferrocene polymer	nano porous membrane, Celgard	[538]
		n. a.	crosslinked colloidal PVBC, post-polymerization functionalization	n. a.	n. a.	n. a.	n. a.	0.4 V vs. Ag ⁺	0.043 mAcm ⁻² , 12 cycles, MeCN, 0.1 WhL ⁻¹	0.9 V vs. viologen polymer	nano porous membrane, Celgard	[538]
		0.064	dispersion polymerization	FRP	n. a.	n. a.	1.12 to 7.94 mPa·s (0.001-1.0 M)	0.6 V vs. Ag/AgCl	100 cycles, water, 15 WhL ⁻¹	1.0 vs. viologen polymer 1.2 V vs. anthraquinone polymer	size-exclusion membrane	[250]
		0.044	dispersion polymerization	FRP	n. a.	n. a.	n. a.	-0.7 V vs. Ag/AgCl	100 cycles, water, 15 WhL ⁻¹	1.2 vs. TEMPO-polymer	size-exclusion membrane	[250]
		0.33	block copolymer, post-polymerization oxidation, micelle	ATRP	41	1.1	3.5 mPa·s (13 mg/ml)	0.5 V vs. Ag/AgN O ₃	5 mAcm ⁻² , 1000 cycles, 1.6 WhL ⁻¹ EC/DMC/DEC	1.3 V vs. zinc	size-exclusion membrane	[524]

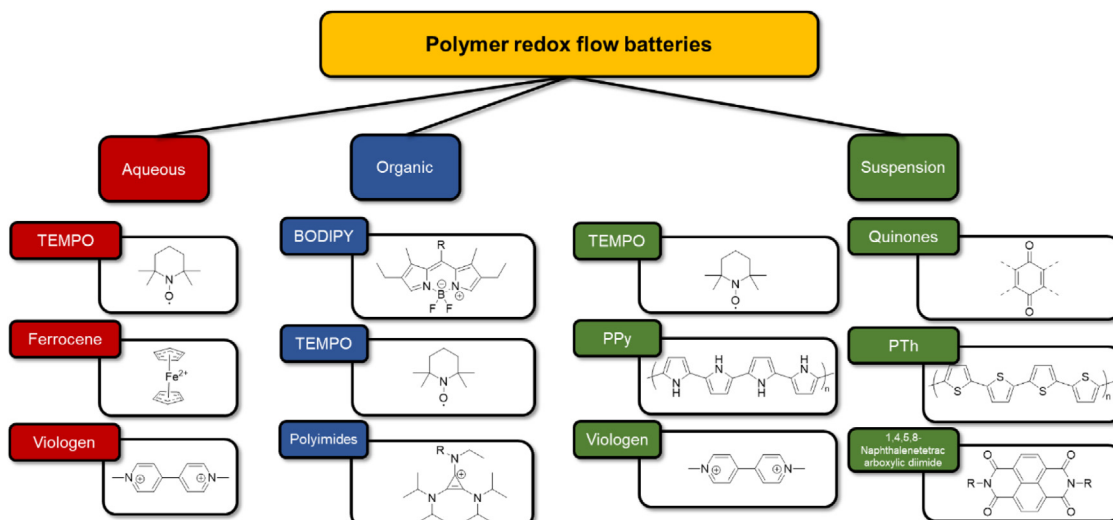


Fig. 21. Summary of the redox active moieties applied in polymeric redox flow batteries, organized by the type of electrolyte.

Redox Flow aqueous

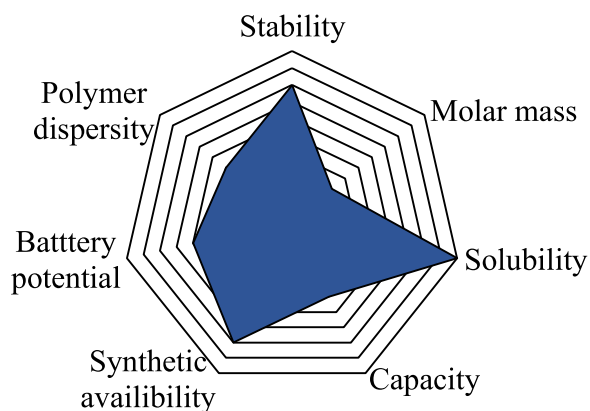


Fig. 22. Spider web diagram of the material requirements for aq. redox flow batteries.

positive influence of the methacrylamide on the solubility and prevention of radical recombination is not enough for the intended application. The first viologen polymer used in an RFB was synthesized via a post-polymerization derivatization approach: In which 4-chloromethylstyrene was copolymerized with *para*-trimethylammoniumstyrene (15 mol%) in a FRP. The viologen moieties were later introduced via nucleophilic substitution of the chloride with mono-methylated 4,4'-bipyridine. The resultant polymer showed a molar mass of 30.9 kgmol^{-1} with a \bar{D} of 2.4 [508]. A relatively low amount of solubility-promoting comonomer was needed to suppress radical-radical as well as π - π -interactions of the viologens during the charge/discharge process and to enhance solubility. Furthermore, the specific viscosity of the polymer is much lower in comparison to the homopolymer (viologen-copolymer: $5 \text{ mPa}\cdot\text{s}$ (10 AhL^{-1}) in 1.5 M NaCl at 20°C vs. viologen homopolymer: 7 to $30 \text{ mPa}\cdot\text{s}$ ($41 \text{ mg mL}^{-1} \triangleq 1.5 \text{ AhL}^{-1}$) in 1.5 M NaCl at 20°C). However, polymer-analogous modifications usually suffer from low yields, as this is directly proportional to the degree-of-functionalization. In order to circumvent this issue, the direct use of a redox-active monomer may be advantageous. Nevertheless, the shown *para*-trimethylammoniumstyrene represents

the most efficient comonomer for viologen polymers thus far as it significantly improves desired polymer properties, addressing the aforementioned issues.

As potential posolyte copolymeric materials for aqueous PRFBs, TEMPO-based polymers have been investigated. Since the TEMPO scaffold does not intrinsically bear any highly polar or charged moieties, the hydrophilicity is far too low for the intended solubility in water. Comonomers enhancing the solubility are, thus, mandatory. Furthermore, as discussed previously, the direct polymerization of the radical is challenging and requires special polymerization techniques. Thus, the main route to the respective redox-active polymers represents a post-polymerization oxidation of precursor polymers using hydrogen peroxide or *m*CPBA [176,365].

Due to the high availability of the methacrylic TEMPO precursor and its versatile polymerization possibilities, the PTMA-based polymers are the most widely used TEMPO-bearing polymers. The general synthetic route involves a free radical polymerization with different comonomers. Schubert et al. used 2,2,6,6-tetramethylpiperidin-4-ol coupled to methacrylic acid and statistically copolymerized it with (methacryloyloxy)-*N,N,N*-trimethylethylammonium chloride (METAC), with a subsequent oxidation using hydrogen peroxide and sodium tungstate [508]. The obtained molar mass of 20.2 kgmol^{-1} is sufficiently large for using a simple and cheap size-exclusion membrane, while the electrolyte viscosities are sufficiently low. The expected high molar mass distribution was narrowed by utilization of mercaptoethanol, as a chain transfer reagent. In a subsequent, more in-depth study, Janoschka et al. investigated the influence of comonomers and mercaptoethanol on the dispersity, molar mass, and water solubility on the unoxidized PTMA copolymers [119]. The poly(ethylene-glycol)methacrylate (EGMA), di(ethyleneglycol)methyl ether methacrylate (DEGMA), methacrylamide (MA) and METAC-containing copolymers were synthesized via a free radical polymerization and showed dispersities ranging from 1.5 to 4.9 as well as molar masses between 7 and 169 kg mol^{-1} . Again, mercaptoethanol was used as a chain-transfer agent. While the unoxidized P(TMA-co-METAC) showed suitable properties, the solubility of unoxidized P(TMA-co-MA) and non-oxidized P(TMA-co-DEGMA) were too low and dispersity as well as molar mass of non-oxidized P(TMA-co-PEGMA) was too high. The utilization of PEGMA macroinitiators, synthesized via RAFT polymerization, lead to more control over both size and mass distribution of the P(TMA-co-PEGMA) polymers, but the electrochem-

Redox Flow organic

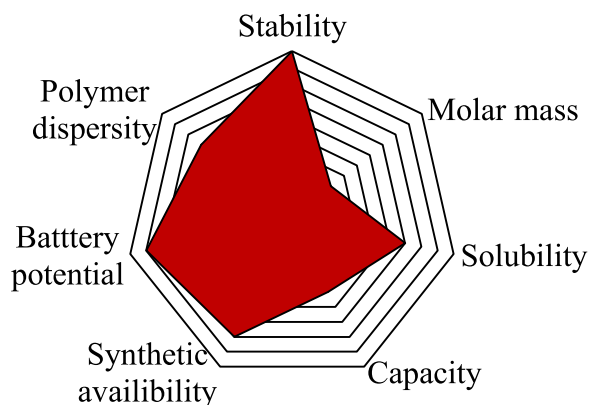


Fig. 23. Spider web diagram of the material requirements for organ. redox flow batteries.

ical properties of the subsequent oxidized RAP showed no significant improvement in comparison to P(TMA-co-METAC). Flow cells using methyl viologen and zinc half-cells could be realized [180,255]. In a recent publication, PTMA was polymerized with 2-[(methacryloxy)ethyl]dimethyl(3-sulfopropyl)ammonium hydroxide [244]. The zwitterionic character of the copolymer enhanced the solubility, in particular in connection with high concentrations of supporting electrolyte. Furthermore, the achieved viscosities are in comparison much lower and the degree-of-oxidation higher, making it superior to comparable PTMA-co-METAC solutions. In a recent publication from the Schubert group, a new ferrocene RAP, synthesized by FRP was reported [527]. The ferrocene propyl methacrylamide (FPMAM) METAC copolymer had molar masses of 6.9 to 11.7 kg mol⁻¹ and dispersities of 1.3 to 2.3 [527]. Nevertheless, the polymer showed a relatively low, but ferrocene typical, redox potential of 0.52 V vs. Ag/AgCl, the combination with a viologen derivative results in cell voltage of ca. 1 V. The authors could also show the high solubility of the p(FPMAM-co-METAC) polymers of over 1 M. The most outstanding property of the material is its stability against elevated working temperatures. Even at 60 °C, the battery showed a stable cycling behavior over 100 consecutive cycles with an average coulombic efficiency of 99.8%. This was the first example for a PRFB operated stable at elevated temperatures.

6.3.4. Organic redox flow batteries

In order to overcome the limited electrochemical stability window of water and, thus, to improve the power density of the battery, a transition to organic solvents, as electrolytes, can be useful (Fig. 23). Additionally, the nucleophilicity of aqueous solutions is a problem for many redox-active scaffolds, making organic electrolytes mandatory. Furthermore, the copolymerization of solubility-mediating monomers can often be omitted, depending on the solubility of the resulting polymers in the desired organic electrolyte.

6.3.5. Homopolymers

The prominent usage of the viologen scaffold in negolyte materials for water-based PRFBs is also reflected in organic PRFBs. The group of Rodriguez-Lopez showed two examples for post-polymerization derivatization of polymers with viologen moieties. One was based on the RAFT polymerization of 1-(chloromethyl)-4-vinylbenzene with a consecutive nucleophilic substitution, using monoethylbipyridine. In order to improve the solubility in organic solvents, the halogenide counter ions were exchanged

by hexafluorophosphate ions (see Fig. 23) [239]. The second approach used the same synthetic strategy, however, *meta* and *ortho* bis(chloromethyl)benzyl cores were utilized to attach two viologen moieties to each repeating unit [240]. Both approaches lead to polymers with CRP-typical dispersities of $\bar{D} \leq 1.9$ and high molar masses of M_n up to 318 kg mol⁻¹. The polymers revealed two redox peaks at ca. -0.7 V and -1.1 V vs Ag⁺, as expected for the viologen cores. They could demonstrate 6 and 12 reversible charge and discharging cycles by using bulk electrolysis but with significant capacity decrease of up to 12% over 12 cycles. This may be explained by an irreversible radical-radical interaction between the reduced viologen cores. To prove this hypothesis, the distance between the two viologen scaffolds in the *meta* and *ortho* bis(chloromethyl)benzyl derivatives was calculated. It could be shown that the gap between both rings halved upon charging, suggesting a possible intramolecular interaction leading to the dimerization of radical cations. This could also take place in a 1-(chloromethyl)-4-vinylbenzene-viologen homopolymer. Similar to the aforementioned copolymerization strategies used for the respective aqueous counterparts, a copolymerization with an inert comonomer might suppress these interactions.

On the posolyte (e.g., the separation of positive and negative solutions) side, ferrocenes are known for their extraordinary stability and reversible redox chemistry as well as redox potentials ca. 0.2 to 0.3 V vs. Ag⁺. The group of Rodriguez-Lopez synthesized the first polymer utilizing the post-polymerization derivatization route. A commercial poly(chloromethyl)styrene was functionalized with (dimethylaminomethyl)ferrocene (DMAMFc), followed by an ion exchange with hexafluorophosphate [241]. The battery against a viologen polymer showed an open circuit voltage (OCV) of ca. 0.9 V and could be cycled at least for 50 cycles with a current density of up to 0.9 mAcm⁻². The power density of 0.2 WhL⁻¹ was, due to their used concentration of 10 mM, very low. Unfortunately, the redox potential of the ferrocene scaffold is inferior to other posolyte materials, e.g. TEMPO or triaryl amines, resulting in a lower cell voltage. To fully utilize the advantage of the wide stability window of many organic solvents, other materials may be used.

The group of Rodriguez-Lopez further published a polymer that was based on a cyclopropenium active scaffold [528]. The active moiety was linked to a styrene-based monomer and polymerized via RAFT. The linker was utilized in order to adequately address the steric repulsion of the bulky cyclopropenium monomers. Nevertheless, the polymers showed low molar masses ($M_n = 4.9$ to 11.1 kg mol⁻¹), presumably due to the bulkiness of the monomer. The extraordinarily low dispersities of < 1.1 are, however, desirable for the intended use in RFBs with size-exclusion membranes. Furthermore, the high redox potential of ca. 1.0 V vs. Ag⁺ makes the presented scaffold an interesting candidate for use in high energy density batteries; however, an operating RFB has not been demonstrated and only the cell properties have been investigated in a bulk electrolysis setup.

Interestingly, based on our literature survey, we found that all homopolymers of this category are based on styrenic monomers. In this regard, the commercial availability of monomers as well as respective polymers for post polymerization derivatization and the well-understood and versatile polymerization possibilities for styrenes may be the explanation.

6.3.6. Copolymers

Since organic RFBs require polar organic solvents, e.g., organocarbonates, to solubilize a significant sum of supporting electrolyte, polar co-monomers enhance the solubility of non-polar polymers in the desired electrolyte. Thus, Winsberg published a new poly(*p*-vinylbenzylphthalimide)-co-poly(vinylbenzyl triethylene glycol monomethylether) P(PSt-co-TEGSt) polymer

($M_n = 6$ to 88 kg mol^{-1} , $\bar{D} = 2.2$ to 2.7), as the negolyte material [146]. The polar TEGSt, as discussed before, promotes solubility in polar organic solvent and suppresses phthalimide-phthalimide stacking. The styrenic backbone was chosen because of its easy polymerizability, enabling a free radical polymerization and the utilization of commercially available comonomers. The polymer showed a remarkably low reversible one-electron redox process at $-1.9 \text{ V vs Ag/AgNO}_3$. Despite the high OCV of $2.2 \text{ V vs. a TEMPO}$ -based polymer, the power density does, with 0.3 WhL^{-1} , need further improvement.

Advantageous for battery designs are materials, which can be applied as both negolyte and posolyte, simultaneously, as crossover through the membrane can be easily mediated by rebalancing schemes, as seen for VRFBs [529]. This can be achieved by utilizing redox amphoteric scaffolds, as shown by the Schubert group, using poly(boron-dipyrromethene) (BODIPY) polymers [145]. The remarkable property of this active material is the two reversible one-electron redox processes at 0.6 V and $-1.4 \text{ V vs. Ag/AgNO}_3$, resulting in an OCV of 2.0 V . These authors synthesized two different polymers: a P(BODIPY-co-TEGSt) polymer ($M_n = 17 \text{ kg mol}^{-1}$, $\bar{D} = 2.3$) and a p(BODIPY-co-trimethylammoniumstyrene) (TASSt) polymer ($M_n = 4 \text{ kg mol}^{-1}$, $\bar{D} = 1.5$). The commercially available TEGSt and TASSt comonomers were chosen for the solubility improvement. In electrochemical investigations, the TASSt-containing copolymer showed slightly better electrochemical properties. This might be because of the charge repulsion between the positive BODIPY unit and the positive TASSt monomer, resulting in a greater isolation of the redox moieties in comparison to the neutral and, thus, more interfering TEGSt comonomer.

Comonomers with ethylene glycol-based sidechains were further used in combination with other active materials. Winsberg et al. adapted them to TEMPO-polymers for organic RFBs [180]. They used a RAFT polymerization for a P(TMA-co-EGMA) polymer with a M_n of 53 kg mol^{-1} and \bar{D} of 1.3 . Unlike its inferior performance in aqueous RFB tests, this polymer showed a superior solubility in organic media. The demonstrated hybrid redox cell with zinc perchlorate in ethylene carbonate/dimethylene carbonate/diethylene carbonate achieved charge densities up to 4 mAcm^{-2} with a high energy density of 8.1 WhL^{-1} .

The most complex architecture thus far, was shown by Nishide et al., who synthesized a norbornene-grafted PTMA [219]. The ROMP of the norbornene macromonomer generated bottle brush-like polymers with M_n between 32 and 230 kg mol^{-1} and $\bar{D} = 1.17$ to 2.73 . The polymers showed a reversible redox reaction at 0.8 V against Ag/AgCl , typical for the TEMPO scaffold. But neither in the shown two cycles in a half cell setup with $0.1 \text{ M } (n\text{-C}_4\text{H}_9)_4\text{NClO}_4$ in ethylene carbonate/diethylene carbonate, as electrolyte, nor during the other electrochemical investigations; a significant improvement in comparison to other TEMPO polymers was demonstrated.

However, all of the presented organic polymer RFBs did not go beyond the prove-of-concept stage, which may be due to the low electric conductivity of the organic solvents used. Both current and energy densities are comparably low, with less than 5 mAcm^{-2} , and 8.1 WhL^{-1} , respectively, and, thus, do not match the requirements for commercial applications.

6.3.7. Suspension redox flow batteries

Suspension redox flow batteries (SRFBs) represent a promising design, aiming at a performance boost by overcoming solubility-related restrictions of the energy density in RFB electrolytes. This idea originates from the lithium battery sector. Goodenough thought about a battery using lithium as anode and a redox-active solution, as cathode [530]. The combination of the flexibility of RFBs with the high redox potential of lithium would lead to a highly competitive battery; [531,532] however, the solubility of the

Redox Flow suspension

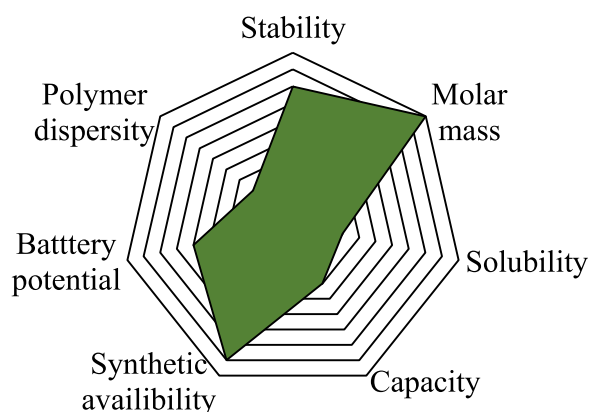


Fig. 24. Spider web diagram of the material requirements for suspension redox flow batteries.

lithium species is too low to achieve high power densities. Such a system has been firstly presented in 2011; Duduta et al. showed that suspensions of typical lithium ion battery materials in a flow cell setup achieved extraordinarily high energy densities [533]. Due to the tailor-ability of the solution properties for RAPs, this concept can be realized as a green way of using organic redox-active moieties, making a high number of scaffolds accessible for a precise adjustment of redox properties. Furthermore, assuming spherical particles, the viscosity of the resultant mixture is generally lower than for a comparable amount of RAPs in solution [528,534,535].

6.3.8. Homopolymers

As the storage medium has not to be soluble in the electrolyte, simple synthetic pathways to polymers with highly stable electrochemistry become more attractive (see Fig. 24). Conductive polymers have been investigated for this purpose. They bear the advantage that electrical conductivity within the colloidal particle is easily implemented by doping, even though they do not show stable voltage outputs over a wide range of the SOC [72]. Furthermore, they can be produced in an easy and cheap manner by electro/redox polymerization, generating linear backbone homopolymers. The key design and selection criteria are, therefore, focused on the electrochemical properties, e.g., the redox potential, of the active material.

One of the first conductive polymers for SPRFB was poly(thiophene). The electropolymerized PTh showed reversible redox processes at -2.0 V and 0.5 V vs. Ag^+ after n- and p-doping, respectively, and a symmetrical RFB with 2.7 V OCV could be built, showing low coulombic efficiencies and sloping voltage outputs [536]. In consecutive years, more conductive polymers like the poly(pyrrole)s were used. The first PPy example was a battery paired with manganese dioxide with an OCV of 1.25 V [537]. A subsequent study showed that the electrochemical properties could be further improved by the use of anthraquinone-2-sulfonate, as a supporting salt in the electrolyte [538]. In 2019, Yan et al. showed a full colloid water-based PRFB with 6.3 WhL^{-1} and a maximum current density of 20 mAcm^{-2} by utilizing a poly(1,4-hydroquinone) (PHQ), as the posolyte, vs. poly(naphthalenetetracarboxylic diimide) p(NTCDI), as the negolyte [122]. The PHQ was simply produced by an oxidative polymerization of the corresponding hydroquinone.

Even though poly(aniline) is known since the 1860s, it was firstly used in a redox flow cell in 2013 by Liao et al. [10,507]. The

authors reported a suspension flow battery with an operating voltage of 1.25 V paired with zinc and current density of 30 mAcm⁻². This is the highest current density ever reached for a colloidal PRFB so far and the electrochemical properties can be further improved by doping the PANI with silver ions [539]. Thus, it is not surprising that PANI was under investigation for a longer period and other battery setups could be realized, e.g., vs. lead oxide [540–542].

A very interesting modification of the suspension flow battery concept is represented by the idea to use so-called solid boosters, also known as “redox targeting”, to increase the storage capabilities of known RFB designs. The concept is based on the reversible redox reaction of solids introduced into the RFB electrolyte that are, in contrast to a SRFB, not addressed directly within the electrochemical cell, but by the redox potential of the dissolved active components in the RFB electrolyte, boosting the overall cell capacity. These solid ingredients are not pumped through the cell, but are instead kept in the tanks, allowing an unobstructed electrolyte flow.

For this purpose, PANI was prominently used by Zanzola et al. in order to significantly improve the capacity of an iron-vanadium redox flow battery by adding insoluble PANI to the tanks [543]. While the redox kinetics of the primary vanadium species was not influenced by the polymer, the volumetric capacity was improved by a factor of three.

In a further development looking for an improvement of the unstable voltage output of conjugated RAPs, pyrrole was functionalized with anthraquinone and quinoxaline then oxidatively polymerized [303,319]. The resulting polymers can be regarded as a crossover between a pure RAP with redox-active side-chain moieties and a conductive and redox-active backbone polymer, thus aiming for a combination of the electric conductivity of the backbone with the more stable voltage output of isolated redox moieties. Nevertheless, a sloping cell voltage over the SOC range of the battery, due to the high conjugation ratio, is observed. Both polymers were used as negolytes, paired with either TEMPO-amines or potassium ferrocyanide and showed surprisingly high current densities with acceptable power densities.

6.3.9. Copolymers

As mentioned above, in order to overcome the unstable voltage output of conjugated RAPs, it is necessary to isolate the redox-active moieties from each other. This can be achieved by incorporating inert comonomers or by isolation in a side chain. Nevertheless, in particular in the side chain approach, the need for insoluble copolymers or crosslinkers may arise to decrease the solubility. In most cases, the residual solubility of homopolymers bearing ionic charges is too high and precipitation as well as agglomeration in the electrochemical cell upon depletion of the ionic charges would be the consequence (see Fig. 24). Here, an in-depth investigation of the literature of solid polymer batteries could be a guiding line for a development of new polymers, as SPBs and SSPRFBs suffer from many identical problems.

Known for their insolubility and extraordinary good electrochemistry, poly(diimide)s are commonly used in solid polymer batteries. (see chapter 3.3.1) Although they are backbone polymers, the redox-active centers are separated by linkers. In 2019, Yan et al. were the first to synthesize a poly(naphthalenetetracarboxylic diimide) NTCDI for application in a RFB [122]. The polymers were prepared by the condensation of naphthalenetetracarboxylic acid with both 1,2-diaminoethane or *p*-phenylenediamine. Whereas, the diaminoethane derivative showed four reversible one-electron redox reactions with a mean potential of 0.1 V vs. standard hydrogen electrode (SHE), the aromatic-linked derivative only showed one two-electron redox reaction but with a slightly lower potential of -0.1 V vs. SHE. Subsequent battery tests revealed a much higher stability for the diaminoethylene-based particle dispersions.

Another approach leading to backbone polymers by a step-growth polymerization was presented by Hatakeyama-Sato et al. [250]. The authors synthesized a multi-dimensional polymeric network with tribromomesitylene and 4,4'-bipyridine. Incorporated within the network and separated by a linker, the viologen subunit showed the expected redox properties, while the polymer was completely insoluble. The generated nanoparticles were dispersed in an aqueous RFB electrolyte. The batteries used size-exclusion membranes and showed remarkably high-power densities of up to 15 WhL⁻¹, which are comparable to classical RFBs based on redox-active organic scaffolds.

Apart from the shown polyaddition reactions of multifunctional monomers, the addition of a crosslinker during polymerization is a common way to produce multidimensional polymeric networks. Nishide used this approach by addition of a bifunctional acrylamide crosslinker during the free radical polymerization of TEMPO- and anthraquinone acrylamides [250]. The simple addition of the crosslinker formed particles, which could directly be used in a RFB.

Rodriguez-Lopez was one-step ahead and derivatized commercially available crosslinked poly(vinylbenzylchloride) (PVBC) nanoparticles with monoethylviologen as well as a ferrocene unit [544]. This approach can by far be regarded as the simplest and cheapest pathway towards redox-active colloids (RACs). The authors could demonstrate a full suspension PRFB with MeCN, as electrolyte; however, the system suffered from the organic inherent low conductivity.

A more exotic way to produce suspensions is the use of self-assembled polymeric macrostructures. Winsberg et al. demonstrated a flow battery of self-assembled PTMA-*b*-PS micelles paired with zinc [236]. Since self-assembly processes need well-defined polymers, a commonly used free radical polymerization could not be utilized. An ATRP polymerization approach was therefore used to initially synthesize the hydrophobic PS core, followed by a block of the aminic PTMA precursor. After self-assembly to micelles, the PTMA precursor was subsequently oxidized, generating the redox-active aminoxyl radicals. The obtained polymer had a very low dispersity of $\mathcal{D} = 1.1$ with a M_n of 41 kg mol⁻¹ and showed a redox peak at 0.5 V vs. Ag/AgNO₃; however, the power density measured during battery tests of the material could not reach the level previously reported for the PTMA-co-PEGMA solution-based system [180].

6.4. Summary – redox flow batteries

In comparison to solid state batteries, the hitherto investigated options for active materials in soluble PRFB are relatively limited; mainly viologen and TEMPO-based scaffolds have been proposed, as well as ferrocenes or propenium-based materials. These often-used active materials are attached to styrene and methacrylate-based monomers, respectively. These groups are characterized by their synthetic availability; the possibility to use versatile polymerization techniques and a great variety of commercially available comonomers is noteworthy. Additionally, the solubility of most homopolymers in the desired electrolyte is often too low and may, thus, be adjusted using solubility-promoting comonomers. The known examples for aqueous systems mainly use cationic ammonium salt monomers, although a zwitterionic monomer was used as well as anionic groups, such as sulfonates, may also be possible. The solubility in organic-based electrolytes on the other hand, can be increased by the introduction of non-ionic polar groups, such as ethylene glycol bearing co-monomers. Often, there is no need for perfectly defined polymers in terms of molar masses, dispersity or polymeric architecture; thus, and a free radical polymerization producing statistic copolymers can be considered. The main requirement for the electrochemical performance of the respective

polymers is a preferably low crossover through the utilized size-exclusion membrane, achievable by an adequately high degree-of-polymerization. Furthermore, the molar mass should not be too high, since it directly influences the electrolytes' viscosity.

Suspension RFBs represent a relatively new, albeit not less interesting, concept, aiming for an increased energy density in RFBs. Compared to the classical PRFB concept, a greater variety of active materials has been investigated, mainly because the polymer is not required to exhibit a minimum solubility in the electrolyte. Thus, numerous suitable homopolymers, especially conjugated polymers, is higher than for classical RFBs. Nevertheless, in order to further promote insolubility in distinct redox states, comonomers or crosslinks are usually introduced.

7. Conclusion and perspective

The design of the best-fitting redox-active polymers for a desired application may prove to be a challenging task, particularly, considering the large variety of potential redox moieties, polymerizable groups, possible comonomers and the multitude of polymerization techniques. With the review at hand, we intended to provide a guideline for the structured design of redox-active polymers in the field of energy storage applications. Thus, at the very beginning, we focused on the basis of the design process: a comprehensive overview of the possibilities that a polymeric design offers. Starting with the position that the redox-active unit has within the polymer chain, then key differences in the resulting polymer properties can be spotted. Based on this, different possible polymer architectures are usable, increasing in complexity from simple linear polymers to polymer networks. Several polymerization processes are possible, whereby the most important polymerization techniques and synthetic pathways were briefly discussed. The choice of polymerization and polymer backbone will influence the final polymeric properties.

We dedicated the three following parts of this review to a literature survey of the previously examples of redox-active polymers in the topics of solid polymer batteries, capacitor-based systems as well as redox-flow batteries. These sections were structured by imaginary zooming in from a macroscopic point-of-view, based on polymer architecture, the position of the active moiety within the polymer and the active scaffold itself.

Here, we would like to summarize the following key findings of this review:

- Redox-active polymers date back almost 80 years and have been proposed for varying purposes. Many of the investigated uses are related to the storage of electrical energy, driven by an increasing environmental awareness.
- By incorporating redox-active moieties into a polymeric network, both physical and electrochemical properties of a redox-active material are influenced. Apart from the redox moiety itself, we identified the positioning of the redox-active moiety within the polymer, the polymer architecture and the structure of the polymer backbone, as key influencing factors.
- The positioning of the redox moiety within the macromolecule strongly influences the ability to transport a charge along the polymeric chain. While an isolation of the respective redox moieties leads to electrically non-conductive polymers that show distinct redox potentials, conjugation and physical proximity of the redox moieties leading to an increased electrical conductivity and less defined redox potentials.
- A multitude of different polymerization techniques are available for the synthesis of polymeric materials, determining the degree-of-control over the molar mass, molar mass distribution, and polymer shape. In that, the desired redox-active moiety may interfere with the propagating species, special syn-

thetic precautionary measures have to be taken, as seen for the TEMPO scaffold, which cannot be easily polymerized by radical polymerization techniques in its aminoxyl radical form due to parasitic recombination reactions.

- As shown for the example of the TEMPO moiety, a wide range of different backbone structures can be accessed by linking a redox-active moiety to different monomeric structures. This enables the use of different polymerization strategies to circumvent the mentioned chemical interferences. Furthermore, the specific capacity of the materials can be tuned by variations of the monomeric nature.
- Depending on the type of electrochemical storage technology, RAPs have to be tuned in terms of solubility in order to assure maximum performance of the electrochemical device. Due to the polymeric nature of the materials, this can be achieved in a relatively simple manner by incorporating solubility-mediating comonomers or in the other direction by introduction of crosslinks between polymer chains.
- Solid polymer batteries are based on the use of solid polymeric active materials exhibiting low solubility in the used electrolytes. While first examples have been based on conductive RAPs, showing unstable voltage outputs, more recent designs have focused on the use of non-conjugated RAPs that generally show distinct redox potentials preferred in battery applications.
- In order to ensure a low solubility of the used RAPs in SPBs, comonomers are often introduced, as the residual solubility of purely homopolymers is commonly too high.
- RAPs can further be used in capacitor-based applications, increasing the overall capacitance by enabling energy storage, based on faradaic charge transfer that adds to the static capacitance, creating a strong pseudocapacitance. Conductive polymers are preferred for these applications, as their redox reactions often show fast kinetics.
- RAPs can as well be used as active materials in PRFBs. This enables the use of comparably inexpensive size-exclusion membranes. Arising issues, such as an increased viscosity of the resulting solutions, can be addressed by changes of the degree-of-polymerization or the targeted architecture as well as the use of different comonomers.
- For a use in PRFBs, the solubility may be fine-tuned to ensure both high and low solubility, depending on the design. While PRFBs with active materials dissolved in the electrolyte can be constructed, suspension-based systems rely on the insolubility of the respective RAPs.
- As the requirements of RAPs for different applications can reveal strong communalities, we want to encourage fellow researchers to also follow the progress of related fields of use for RAPs as well as to have a look at the early publications concerning this field, as these may hide interesting ideas and concepts, albeit intending different applications.

The current state of research, in particular in the field of secondary batteries, is at a point that brings commercialization of new environmentally friendly and possibly metal-free batteries within reach. Redox-active polymers have a key role within these concepts, as they represent a smart way of addressing the environmental concerns of many consumers (e.g., material sources or recyclability) while still combining cheap and easy synthetic pathways for an industrial-scale production. However, some critical issues, such as the intrinsic stability of the active materials or the ability to retain the applied charge over an extended period of time, often remain unaddressed. Furthermore, the toxicity of the polymers has hardly been investigated. A graphical overview of the development process, that is necessary for novel polymeric active material for organic batteries is depicted in Fig. 25.

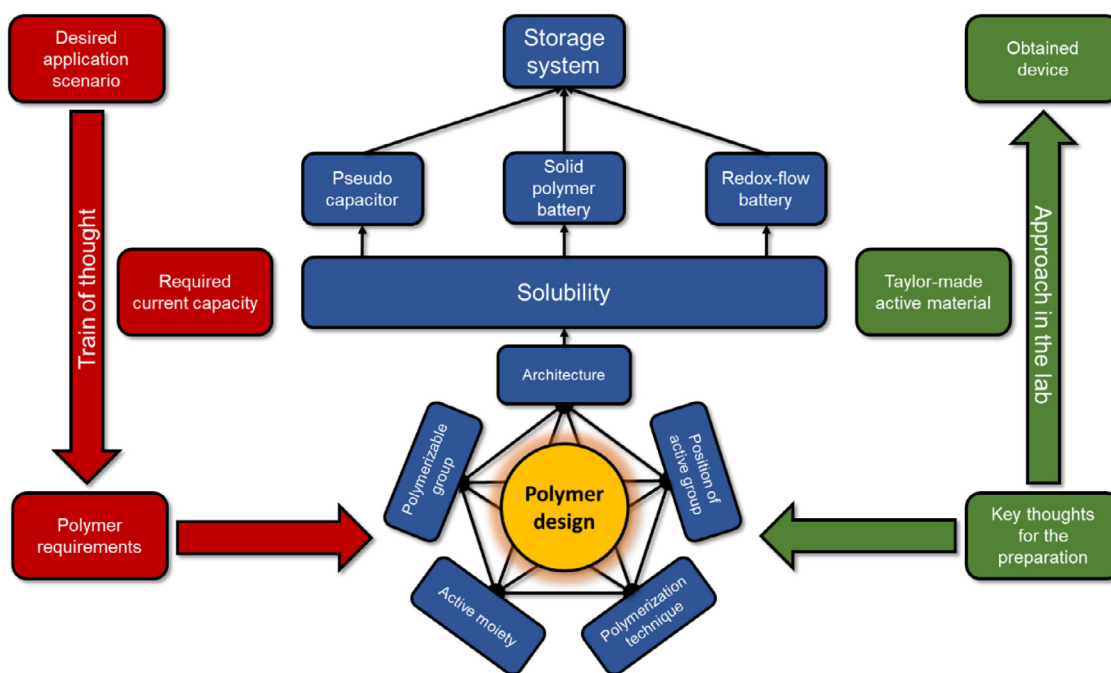


Fig. 25. Schematic representation of the approach and considerations towards polymers for organic redox active polymers.

Even though the use of RAPs in RFBs has been rather limited so far, the presented literature still outlines trending concepts within this field of research. In particular, the use of solid additives in the electrolytes promises strongly increased energy densities exceeding the known benchmarks for these systems in the near future, further boosting their competitiveness among the known battery technologies.

Other concepts, such as the presented capacitor concepts, may benefit equally from the use of RAPs in terms of economic viability.

Furthermore, in the future, the general origin of organic raw materials will inevitably shift from the currently exploited fossil resources to more environmentally benign sources, such as raw materials derived by plant plants, or produced by bacteria or fungi.

Considering the usage of polymeric materials in energy storage, these represent currently almost exclusively the pure carrier of the redox moieties. In recent years, polymers have gained particular interest in the context of stimuli-responsive materials / smart materials; enabling a multitude of potential applications – e.g. in soft robotics [545] or as sensors [546]. Hence, we anticipate that the utilization of other properties / functionalities of polymers as well as stimuli-responsive behavior will also find their way into the field of polymers for electrical energy storage [547].

Declaration of Competing Interest

The authors declare that they have no known competing financial interests or personal relationships that could have appeared to influence the work reported in this paper.

Acknowledgment

The authors thank the European Regional Development Fund (EFRE), the Thuringian Ministry for Economic Affairs, Science and Digital Society (TMWWdG), and the Thuringer Aufbaubank (TAB) for financial support. Furthermore, the German Research Foundation (DFG) is acknowledged for funding within the framework of SPP 2248 “Polymer-based Batteries”.

This project received funding from the European Union’s Horizon 2020 research and innovation program under the Marie Skłodowska-Curie grant agreement No 860403.

References

- [1] Figgner J, Stenzel P, Kairies KP, Linssen J, Haberschusz D, Wessels O, et al. The development of stationary battery storage systems in germany - a market review. *J Energy Storage* 2020;29:101153.
- [2] The Nobel Foundation. The Nobel Prize in Chemistry 2019, <https://www.nobelprize.org/prizes/chemistry/2019/summary>; 2019 [accessed 10.03.2021].
- [3] Liu K, Liu Y, Lin D, Pei A, Cui Y. Materials for lithium-ion battery safety. *Sci Adv* 2018;4:eas9820.
- [4] Banza Lubaba Nkulu C, Casas L, Haufroid V, De Putter T, Saenen ND, Kayembe-Kitenge T, et al. Sustainability of artisanal mining of cobalt in DR Congo. *Nat Sustain* 2018;1:495–504.
- [5] Pourret O, Faucon MP. Cobalt. In: White WM, editor. *Encyclopedia of geochemistry: a comprehensive reference source on the chemistry of the earth*. Cham: Springer International Publishing; 2017. p. 1–4.
- [6] . *Mineral commodity summaries*. VA: Reston; 2020. p. 204.
- [7] Menale C, D’Annibale F, Mazzarotta B, Bubbico R. Thermal management of lithium-ion batteries: an experimental investigation. *Energy* 2019;182:57–71.
- [8] Lu DB, Lin SX, Hu SW, Cui W, Fang TT, Iqbal A, et al. Thermal behavior and failure mechanism of large format lithium-ion battery. *J Solid State Electr* 2020;25:315–25.
- [9] H. Lauth, Verfahren zur fortlaufenden entfernung von sauerstoff aus wässern, 1944, DE 972626.
- [10] Letheby XH. On the production of a blue substance by the electrolysis of sulphate of aniline. *J Chem Soc* 1862;15:161–3.
- [11] Cassidy HG. Electron exchange-polymers. I. *J Am Chem Soc* 1949;71:402–6.
- [12] Updegraff IH, Cassidy HG. Electron exchange-polymers. II. Vinylhydroquinone monomer and polymer. *J Am Chem Soc* 1949;71:407–10.
- [13] Cassidy HG. Electron exchange-polymers. *Proc Natl Acad Sci U S A* 1952;38:934–7.
- [14] Cassidy HG, Ezrin M, Updegraff IH. Electron exchange polymers. IV. Counter-current applications. *J Am Chem Soc* 1953;75:1615–17.
- [15] Ezrin M, Cassidy HG. Electron exchange polymers; present status of the problem. *Ann N Y Acad Sci* 1953;57:79–86.
- [16] Sansoni B. Eine neuartige anwendung von ionenaustauscharzen als elektro-nenaustauscher. *Sci Nat* 1952;39:281.
- [17] Manecke G. Electron exchangers. *Z Elektrochem Angew Phys Chem* 1953;57:189–94.
- [18] Ezrin M, Cassidy HG. Electron exchange polymers. VI. Preparation of water-soluble and water-swellaable polymers. *J Am Chem Soc* 1956;78:2525–6.
- [19] Luttinger L, Cassidy HG. Electron exchange polymers. VIII. The redox potentials of polymeric hydroquinones. *J Polym Sci* 1956;22:271–90.
- [20] Verplanck V, Cassidy HG. Electron exchange-polymers. V. Hydroquinone-formaldehyde polymers. *J Polym Sci* 1956;19:307–10.

- [21] Robinson ID, Fernandez-Rofojo M, Cassidy HG. Electron exchange polymers. XI. Oxidation potentials and spectra of water-soluble hydroquinones and polymeric hydroquinones. *J Polym Sci* 1959;39:47–61.
- [22] Kun KA, Cassidy HG. Electron exchange polymers. XV. NMR spectra of some methylated hydroquinones and their derivatives. *J Org Chem* 1961;26:3223–6.
- [23] Moser RE, Cassidy HG. Electron transfer polymers. XXIV. Photosensitization with a polymer sensitizer in a heterogeneous and a homogeneous system. *J Polym Sci B* 1964;2:545–7.
- [24] Moser RE, Kamogawa H, Hartmann H, Cassidy HG. Electron exchange polymers. XX. Preparation and polymerization of vinylbis(1-ethoxyethyl)-hydroquinone. *J Polym Sci A* 1964;2:2401–8.
- [25] Cassidy HG, Kun KA. Oxidation-reduction polymers (redox polymers). *Polym Rev* 1965;11:307.
- [26] Kun KA. Macroreticular redox polymers. II. Further synthesis and properties of some redox polymers. *J Polym Sci A* 1966;4:847–57.
- [27] Moser RE, Cassidy HG. Electron-transfer polymers. XXVI. Synthesis of oligomeric hydroquinones and p-benzoquinones. *J Org Chem* 1965;30:2602–7.
- [28] Cassidy HG. Electron-transfer polymers (oxidation-reduction polymers). *J Polym Sci Macromol Rev* 1972;6:1–58.
- [29] Wegner G, Nakabayashi N, Cassidy HG. Electron-transfer polymers. XXXI. Preparation of difunctional benzoquinones and related derivatives and polymers. *J Org Chem* 1967;32:3155–9.
- [30] Kun KA, Kunin R. Macroreticular redox polymers. III. Characterization of some hydroquinone-quinone redox polymers. *J Polym Sci A* 1966;4:859–68.
- [31] Manecke G, Storck W. Redoxharze auf der basis von vinyl-anthracinonen-(9.10). *Angew Chem Int Ed* 1962;74:903–4.
- [32] Manecke G, Förster HJ. Über die synthese und das redoxverhalten von molekulareinheitlichen hydrochinon-phenol-formaldehydkondensaten. *Macromol Chem Phys* 1962;52:147–63.
- [33] Manecke G, Panoch HJ. Über die synthese und das redoxverhalten von molekulareinheitlichen hydrochinon-phenol-formaldehyd-kondensaten. II. *Macromol Chem Phys* 1966;96:1–16.
- [34] Manecke VG, Beyer HJ. Über die synthese und das redoxverhalten von molekulareinheitlichen hydrochinon-phenol-formaldehyd-kondensaten. III. *Macromol Chem Phys* 1967;105:59–72.
- [35] Manecke G, Mölleken R. Über die synthese und das redoxverhalten molekular-einheitlicher hydrochinon-phenol-formaldehyd-kondensate. IV. *Macromol Chem Phys* 1967;105:73–83.
- [36] Manecke VG, Zerpner D. Über die synthese und das redoxverhalten einiger modellsubstanzen für polymere hydrochinon-chinon-redoxsysteme. VI. *Macromol Chem Phys* 1967;108:198–209.
- [37] Förster HJ, Manecke G. Bis-trimethylchinon-1.4-yl-alkane als modellsubstanzen für polymere hydrochinon-chinon-redoxsysteme. VI. Synthese und untersuchung des redoxverhaltens durch potentiometrische titration und polarographie. *Macromol Chem Phys* 1969;129:165–82.
- [38] Sansoni B. Leukomethylenblau methylenblau-redoxite. *Sci Nat* 1954;41:212–13.
- [39] Overberger CG, Lebovits A. The synthesis of poly-p-thiolstyrene, an oxidation reduction polymer. *J Am Chem Soc* 1955;77:3675–6.
- [40] Chen Y-H, Fernandez-Refojo M, Cassidy HG. Electron exchange polymers. XII. Potentiometric titration of dicyclopentadienyliron ("ferrocene") and some derivatives. *J Polym Sci* 1959;40:433–41.
- [41] Manecke G, Kossmehl G. Über indigoide Farbstoffe enthaltende Redoxharze. *Macromol Chem Phys* 1964;70:112–29.
- [42] M. Bruxelles, M.J. Bruxelles, Nouveaux polymères du nitrile acrylique, 1965, BE666862 (A).
- [43] Harwood HJ, Cassidy HG. Electron exchange polymers. IX. Synthesis of polymers of 2,5-dihydroxyphenylalanine and of 3,4-dihydroxyphenylalanine (DOPA). *J Am Chem Soc* 1957;79:4360–5.
- [44] Braun D, Löflund I, Fischer H. Macromolecular stable free nitrogen radicals. *J Polym Sci* 1962;58:667–80.
- [45] Griffith OH, Keana JFW, Rottschaefer S, Warlick TA. Preparation and magnetic resonance of nitroxide polymers. *J Am Chem Soc* 1967;89:5072.
- [46] Manecke G. Entfernung von sauerstoff aus lösungen mit hilfe von redoxharzen (Elektronenaustauschern). *Angew Chem* 1955;67:613–15.
- [47] Manecke G. Darstellung von H₂O₂ mit hilfe von redoxharzen. *Angew Chem Int Ed* 1956;68:582.
- [48] Helfferich F, Luten DB. Oxygen-transfer resins, a new type of oxidation-reduction polymers. *J Appl Polym Sci* 1964;8:2899–908.
- [49] Sansoni B. Redoxaustauscher und ihre Anwendungen—XVI Entfernung von Wasserstoffperoxid aus wässriger lösung an redox- und Ionenaustauschern. *Talanta* 1970;17:987–97.
- [50] Manecke G. Verfahren zur herstellung von wasserstoffperoxyd. DE; 1958.
- [51] M.S. Harding, Battery, 1958, US 2831045.
- [52] S.W. Mayer, D.E. McKenzie, Lightweight secondary battery, 1965, US 3185590.
- [53] Shirakawa H, Louis EJ, Macdiarmid AG, Chiang CK, Heeger AJ. Synthesis of electrically conducting organic polymers - halogen derivatives of polyacetylene. *J Chem Soc Chem Comm* 1977:578–80.
- [54] Eftekhari A. Nanostructured conductive polymers. Chichester, United Kingdom: John Wiley & Sons, Ltd; 2010.
- [55] Yamamoto T, Sanechika K, Yamamoto A. Preparation of thermostable and electric-conducting poly(2,5-thienylene). *J Polym Sci C* 1980;18:9–12.
- [56] Koßmehl G, Chatzitheodorou G. Electrical conductivity of poly(2,5-thiophenediyl)-AsF₅-complexes. *Macromol Rapid Commun* 1981;2:551–5.
- [57] Bargon J, Mohmand S, Waltman RJ. Electrochemical synthesis of electrically conducting polymers from aromatic-compounds. *IBM J Res Dev* 1983;27:330–41.
- [58] Scott JC, Pfluger P, Krounbi MT, Street GB. Electron-spin-resonance studies of pyrrole polymers - evidence for bipolarons. *Phys Rev B* 1983;28:2140–5.
- [59] Scott JC, Bredas JL, Yakushi K, Pfluger P, Street GB. The evidence for bipolarons in pyrrole polymers. *Synthetic Met* 1984;9:165–72.
- [60] Yue J, Wang ZH, Cromack KR, Epstein AJ, Macdiarmid AG. Effect of sulfonic-acid group on polyaniline backbone. *J Am Chem Soc* 1991;113:2665–71.
- [61] Miller JS. Conducting polymers? Materials of commerce. *Adv Mat* 1993;5:671–6.
- [62] Wen YP, Xu JK. Scientific importance of water-processable PEDOT-PSS and preparation, challenge and new application in sensors of its film electrode: a review. *J Polym Sci A Polym Chem* 2017;55:1121–50.
- [63] F. Jonas, G. Heywang, W. Schmidtberg, J. Heinze, M. Dietrich Method of imparting antistatic properties to a substrate by coating the substrate with a novel polythiophene, 1991, DE 5035926.
- [64] Lee CH, Yu G, Moses D, Pakbaz K, Zhang C, Sariciftci NS, et al. Sensitization of the photoconductivity of conducting polymers by C60: photoinduced electron transfer. *Phys Rev B Condens Matter* 1993;48:15425–33.
- [65] Halls JJM, Pichler K, Friend RH, Moratti SC, Holmes AB. Exciton diffusion and dissociation in a poly(p-phenylenevinylene)/C60 heterojunction photovoltaic cell. *Appl Phys Lett* 1996;68:3120–2.
- [66] Ebisawa F, Kurokawa T, Nara S. Electrical-properties of polyacetylene polysiloxane interface. *J Appl Phys* 1983;54:3255–9.
- [67] Koezuka H, Tsumura A, Ando T. Field-effect transistor with polythiophene thin-film. *Synthetic Met* 1987;18:699–704.
- [68] Novak P, Muller K, Santhanam KS, Haas O. Electrochemically active polymers for rechargeable batteries. *Chem Rev* 1997;97:207–82.
- [69] Nyholm L, Nystrom G, Mhramyan A, Stromme M. Toward flexible polymer and paper-based energy storage devices. *Adv Mater* 2011;23:3751–69.
- [70] Nishide H, Iwasa S, Pu YJ, Suga T, Nakahara K, Satoh M. Organic radical battery: nitroxide polymers as a cathode-active material. *Electrochim Acta* 2004;50:827–31.
- [71] Nakahara K, Iwasa S, Satoh M, Morioka Y, Iriyama J, Suguro M, et al. Rechargeable batteries with organic radical cathodes. *Chem Phys Lett* 2002;359:351–4.
- [72] Muench S, Wild A, Friebe C, Haupler B, Janoschka T, Schubert US. Polymer-based organic batteries. *Chem Rev* 2016;116:9438–84.
- [73] Chen R, Bresser D, Saraf M, Gerlach P, Balducci A, Kunz S, et al. A comparative review of electrolytes for organic-material-based energy-storage devices employing solid electrodes and redox fluids. *ChemSusChem* 2020;13:2205–19.
- [74] Liang YL, Tao ZL, Chen J. Organic electrode materials for rechargeable lithium batteries. *Adv Energy Mater* 2012;2:742–69.
- [75] Zhao Q, Lu Y, Chen J. Advanced organic electrode materials for rechargeable sodium-ion batteries. *Adv Energy Mater* 2017;7:1601792.
- [76] Lu Y, Zhang Q, Li L, Niu ZQ, Chen J. Design strategies toward enhancing the performance of organic electrode materials in metal-ion batteries. *Chem* 2018;4:2786–813.
- [77] Pramudita JC, Sehrawat D, Goonetilleke D, Sharma N. An initial review of the status of electrode materials for potassium-ion batteries. *Adv Energy Mater* 2017;7:1602911.
- [78] Chen L, Bao JL, Dong X, Truhlar DG, Wang Y, Wang C, et al. Aqueous Mg-ion battery based on polyimide anode and prussian blue cathode. *ACS Energy Lett* 2017;2:1115–21.
- [79] Xie J, Zhang Q. Recent progress in multivalent metal (Mg, Zn, Ca, and Al) and metal-ion rechargeable batteries with organic materials as promising electrodes. *Small* 2019;15:e1805061.
- [80] Koshika K, Chikushi N, Sano N, Oyaizu K, Nishide H. A TEMPO-substituted polyacrylamide as a new cathode material: an organic rechargeable device composed of polymer electrodes and aqueous electrolyte. *Green Chem* 2010;12:1573–5.
- [81] Suga T, Sugita S, Ohshiro H, Oyaizu K, Nishide H. p- and n-type bipolar redox-active radical polymer: toward totally organic polymer-based rechargeable devices with variable configuration. *Adv Mater* 2011;23:751–4.
- [82] Janoschka T, Martin N, Martin U, Friebe C, Morgenstern S, Hiller H, et al. An aqueous, polymer-based redox-flow battery using non-corrosive, safe, and low-cost materials. *Nature* 2015;527:78–81.
- [83] Yasa M, Sürmeli S, Depci T, Toppare L, Hacıoğlu SO. Synthesis of a multifunctional quinoxaline and benzodithiophene bearing polymer and its electrochromic device applications. *Macromol Chem Phys* 2020;221:1900470.
- [84] Zhang H, Ming SL, Liang YZ, Feng L, Xu T. A multi-color electrochromic material based on organic polymer. *Int J Electrochem Sci* 2020;15:1044–57.
- [85] Cao KL, Shen DE, Osterholm AM, Kerszulis JA, Reynolds JR. Tuning color, contrast, and redox stability in high gap cathodically coloring electrochromic polymers. *Macromolecules* 2016;49:8498–507.
- [86] Zou S, Korczagin I, Hempenius MA, Schonherr H, Vancso GJ. Single molecule force spectroscopy of smart poly(ferrocenylsilane) macromolecules: towards highly controlled redox-driven single chain motors. *Polymer* 2006;47:2483–92.
- [87] Shi W, Giannotti MI, Zhang X, Hempenius MA, Schonherr H, Vancso GJ. Closed mechanochemical cycles of individual single-chain macromolecular motors by AFM. *Angew Chem Int Ed Engl* 2007;46:8400–4.

- [88] Stoian IA, Iacob BC, Dudas CL, Barbu-Tudoran L, Bogdan D, Marian IO, et al. Biomimetic electrochemical sensor for the highly selective detection of azithromycin in biological samples. *Biosens Bioelectron* 2020;155:112098.
- [89] Hartmann V, Ruff A, Schuhmann W, Rogner M, Nowaczyk MM. Analysis of photosystem II electron transfer with natural PsaA-variants by redox polymer/protein biophotoelectrochemistry. *Photosynthetica* 2018;56:229–35.
- [90] Saleem M, Yu H, Wang L, Zain ul A, Khalid H, Akram M, et al. Review on synthesis of ferrocene-based redox polymers and derivatives and their application in glucose sensing. *Anal Chim Acta* 2015;876:9–25.
- [91] Na Y, Lee JS, Woo J, Ahn S, Lee E, Il Choi W, et al. Reactive oxygen species (ROS)-responsive ferrocene-polymer-based nanoparticles for controlled release of drugs. *J Mater Chem B* 2020;8:1906–13.
- [92] Behzadi S, Gallei M, Elbert J, Appold M, Glasser G, Landfester K, et al. A triblock terpolymer vs. blends of diblock copolymers for nanocapsules addressed by three independent stimuli. *Polym Chem* 2016;7:3434–43.
- [93] Zhang Z, Liao M, Lou H, Hu Y, Sun X, Peng H. Conjugated polymers for flexible energy harvesting and storage. *Adv Mater* 2018;30:e1704261.
- [94] Bredas JL, Street GB. Polarons, bipolarons, and solitons in conducting polymers. *Acc Chem Res* 2002;18:309–15.
- [95] Heinze J, Frontana-Urbe BA, Ludwigs S. Electrochemistry of conducting polymers—persistent models and new concepts. *Chem Rev* 2010;110:4724–71.
- [96] Levi MD, Aurbach D. A short review on the strategy towards development of π -conjugated polymers with highly reversible p- and n-doping. *J Power Sources* 2008;180:902–8.
- [97] Krische B, Zagorska M. Overoxidation in conducting polymers. *Synth Met* 1989;28 C257–C62.
- [98] Janoschka T, Hager MD, Schubert US. Powering up the future: radical polymers for battery applications. *Adv Mater* 2012;24:6397–409.
- [99] Shacklette LW, Maxfield M, Gould S, Wolf JF, Jow TR, Baughman RH. Secondary batteries with electroactive polymer electrodes. *Synthetic Met* 1987;18:611–18.
- [100] Schroot R, Jager M, Schubert US. Synthetic approaches towards structurally-defined electrochemically and (photo)redox-active polymer architectures. *Chem Soc Rev* 2017;46:2754–98.
- [101] Wolf BA. Solubility of polymers. *Pure Appl Chem* 1985;57:323–36.
- [102] Topham PD, Parnell AJ, Hiorns RC. Block copolymer strategies for solar cell technology. *J Polym Sci Pol Phys* 2011;49:1131–56.
- [103] Lee YM, Gomez ED. Challenges and opportunities in the development of conjugated block copolymers for photovoltaics. *Macromolecules* 2015;48:7385–95.
- [104] Wang J, Higashihara T. Synthesis of all-conjugated donor acceptor block copolymers and their application in all-polymer solar cells. *Polym Chem* 2013;4:5518–26.
- [105] Liaw DJ, Wang KL, Huang YC, Lee KR, Lai JY, Ha CS. Advanced polyimide materials: Syntheses, physical properties and applications. *Prog Polym Sci* 2012;37:907–74.
- [106] Nishimori K, Ouchi M. AB-alternating copolymers via chain-growth polymerization: synthesis, characterization, self-assembly, and functions. *Chem Commun* 2020;56:3473–83.
- [107] Xia L, Zhang Z, Hong CY, You YZ. Synthesis of copolymer via hybrid polymerization: From random to well-defined sequence. *Eur Polym J* 2020;122:109374.
- [108] Ha S, La Y, Kim KT. Polymer cubosomes: infinite cubic mazes and possibilities. *Acc Chem Res* 2020;53:620–31.
- [109] Dyson RW. *Polymer structures and general properties*, Boston, MA: Springer; 1987. 1 ed.
- [110] Shin JJ, Kim EJ, Ku KH, Lee YJ, Hawker CJ, Kim BJ. 100th anniversary of macromolecular science viewpoint: Block copolymer particles: Tuning shape, interfaces, and morphology. *ACS Macro Lett* 2020;9:306–17.
- [111] Rudolph T, Schacher FH. Selective crosslinking or addressing of individual domains within block copolymer nanostructures. *Eur Polym J* 2016;80:317–31.
- [112] Li C, Li Q, Kaneti YV, Hou D, Yamauchi Y, Mai Y. Self-assembly of block copolymers towards mesoporous materials for energy storage and conversion systems. *Chem Soc Rev* 2020;49:4681–736.
- [113] Yang Z, Li L, Jin AJ, Huang W, Chen XY. Rational design of semiconducting polymer brushes as cancer theranostics. *Mater Horiz* 2020;7:1474–94.
- [114] Lu Y, Lin J, Wang L, Zhang L, Cai C. Self-assembly of copolymer micelles: Higher-level assembly for constructing hierarchical structure. *Chem Rev* 2020;120:4111–40.
- [115] Feng C, Li Y, Yang D, Hu J, Zhang X, Huang X. Well-defined graft copolymers: from controlled synthesis to multipurpose applications. *Chem Soc Rev* 2011;40:1282–95.
- [116] Ilgach DM, Meleshko TK, Yakimansky AV. Methods of controlled radical polymerization for the synthesis of polymer brushes. *Polym Sci Ser C* 2015;57:3–19.
- [117] Verdusco R, Li X, Pesek SL, Stein GE. Structure, function, self-assembly, and applications of bottlebrush copolymers. *Chem Soc Rev* 2015;44:2405–20.
- [118] Kutsevol NV, Bezuglaya TN, Bezuglyi MY. Features of the intramolecular structure of branched polymer systems in solution. *J Struct Chem* 2014;55:548–59.
- [119] Janoschka T, Morgenstern S, Hiller H, Friebe C, Wolkersdorfer K, Haupler B, et al. Synthesis and characterization of TEMPO- and viologen-polymers for water-based redox-flow batteries. *Polym Chem* 2015;6:7801–11.
- [120] Takahashi T, Ikejiri Y, Himori S, Gotoh H. Polymerization inhibition mechanism of 1,4-naphthoquinone by experimentation and DFT calculations. *Polym J* 2019;51:929–34.
- [121] Caille JR, Debuigne A, Jerome R. Controlled radical polymerization of styrene by quinone transfer radical polymerization (QTRP). *Macromolecules* 2005;38:27–32.
- [122] Yan W, Wang C, Tian J, Zhu G, Ma L, Wang Y, et al. All-polymer particulate slurry batteries. *Nat Commun* 2019;10:2513–24.
- [123] Tapaswi PK, Ha CS. Recent trends on transparent colorless polyimides with balanced thermal and optical properties: design and synthesis. *Macromol Chem Phys* 2019;220:1800313.
- [124] Ji D, Li T, Hu W, Fuchs H. Recent progress in aromatic polyimide dielectrics for organic electronic devices and circuits. *Adv Mater* 2019;31:e1806070.
- [125] Yen HJ. Arylamine-based high performance polymers for electrochromic applications. *RSC Smart Mater* 2019;33:323–71.
- [126] Yi L, Huang W, Yan DY. Polyimides with side groups: synthesis and effects of side groups on their properties. *J Polym Sci A Polym Chem* 2017;55:533–59.
- [127] Hodge P, Gautrot JE. Polymers containing in-chain quinone moieties: synthesis and properties. *Polym Int* 2009;58:261–6.
- [128] A.S. Lindsey *Polymeric quinones* 1974.
- [129] Dove AP, Meier MAR. Step-growth polymerization in the 21st century. *Macromol Chem Phys* 2014;215:2135–7.
- [130] Leone AK, Mueller EA, McNeil AJ. The history of palladium-catalyzed cross-couplings should inspire the future of catalyst-transfer polymerization. *J Am Chem Soc* 2018;140:15126–39.
- [131] Lee SM, Park KH, Jung S, Park H, Yang C. Stepwise heating in Stille polycondensation toward no batch-to-batch variations in polymer solar cell performance. *Nat Commun* 2018;9:1867–75.
- [132] Baker MA, Tsai CH, Noonan KJT. Diversifying cross-coupling strategies, catalysts and monomers for the controlled synthesis of conjugated polymers. *Chem* 2018;24:13078–88.
- [133] Mansfeld U, Pietsch C, Hoogenboom R, Becer CR, Schubert US. Clickable initiators, monomers and polymers in controlled radical polymerizations - a prospective combination in polymer science. *Polym Chem* 2010;1:1560–98.
- [134] Boffa LS. An overview of transition metal-mediated polymerizations: catalysts for the 21st century. In: *Applied Polymer Science: 21st Century*. Elsevier Science Ltd; 2000. p. 1021–42. 21st century.
- [135] Verheyen L, Leysen P, Van den Eede MP, Ceunen W, Hardeman T, Koecelberghs G. Advances in the controlled polymerization of conjugated polymers. *Polymer* 2017;108:521–46.
- [136] Smith GB, Heuts JPA, Russell GT. New paradigms in free-radical polymerization kinetics. *Macromol Symp* 2005;226:133–46.
- [137] Noble BB, Coote ML. First principles modelling of free-radical polymerisation kinetics. *Int Rev Phys Chem* 2013;32:467–513.
- [138] Braslau R. *Handbook of radical polymerization*. Hoboken: John Wiley & Sons, Inc; 2003.
- [139] Nesvadba P. *Radical polymerization in industry*. Hoboken: John Wiley & Sons, Ltd; 2012.
- [140] Kurosaki T, Lee KW, Okawara M. Polymers having stable radicals. I. Synthesis of nitroxyl polymers from 4-methacryloyl derivatives of 2,2,6,6-tetramethylpiperidine. *J Polym Sci A* 1972;10:3295–310.
- [141] Sato K, Ichinoi R, Mizukami R, Serikawa T, Sasaki Y, Lutkenhaus J, et al. Diffusion-cooperative model for charge transport by redox-active nonconjugated polymers. *J Am Chem Soc* 2018;140:1049–56.
- [142] Zhang XH, Li HQ, Li LT, Lu GL, Zhang S, Go LN, et al. Polyallene with pendant nitroxyl radicals. *Polymer* 2008;49:3393–8.
- [143] Hansen KA, Nerker J, Thomas K, Bottle SE, O'Mullane AP, Talbot PC, et al. New spin on organic radical batteries—an isoindoline nitroxide-based high-voltage cathode material. *ACS Appl Mater Interfaces* 2018;10:7982–8.
- [144] Suga T, Pu YJ, Kasatori S, Nishide H. Cathode- and anode-active poly(nitroxylstyrene)s for rechargeable batteries: p- and n-type redox switching via substituent effects. *Macromolecules* 2007;40:3167–73.
- [145] Winsberg J, Hagemann T, Muench S, Friebe C, Haupler B, Janoschka T, et al. Poly(boron-dipyrromethene)-a redox-active polymer class for polymer redox-flow batteries. *Chem Mater* 2016;28:3401–5.
- [146] Winsberg J, Benndorf S, Wild A, Hager MD, Schubert US. Synthesis and characterization of a phthalimide-containing redox-active polymer for high-voltage polymer-based redox-flow batteries. *Macromol Chem Phys* 2018;219:1700267.
- [147] Ribelli TG, Lorandi F, Fantin M, Matyjaszewski K. Atom transfer radical polymerization: billion times more active catalysts and new initiation systems. *Macromol Rapid Commun* 2019;40:e1800616.
- [148] Kreutzer J, Yagci Y. Metal free reversible-deactivation radical polymerizations: advances, challenges, and opportunities. *Polymers* 2017;10:1–52.
- [149] Wu L, Glebe U, Boker A. Surface-initiated controlled radical polymerizations from silica nanoparticles, gold nanocrystals, and bionanoparticles. *Polym Chem* 2015;6:5143–84.
- [150] Chiefari J, Chong YK, Ercole F, Krstina J, Jeffery J, Le TPT, et al. Living free-radical polymerization by reversible addition-fragmentation chain transfer: the RAFT process. *Macromolecules* 1998;31:5559–62.
- [151] Matyjaszewski K. Atom transfer radical polymerization (ATRP): current status and future perspectives. *Macromolecules* 2012;45:4015–39.
- [152] D.H. Solomon, E. Rizzardo, P. Cacioli, *Free radical polymerization and the produced polymers*, 1985, EP135280A2.
- [153] Nicolas J, Guillauneuf Y, Lefay C, Bertin D, Gïgmes D, Charleux B. Nitroxide-mediated polymerization. *Prog Polym Sci* 2013;38:63–235.
- [154] Maric M. Application of nitroxide mediated polymerization in different monomer systems. *Curr Org Chem* 2018;22:1264–84.

- [155] Tebben L, Nitroxide SA. Anwendungen in der synthese und in der polymerchemie. *Angew Chem* 2011;123:5138–74.
- [156] Nicolas J, Guillaneuf Y. Living radical polymerization: nitroxide-mediated polymerization. Berlin Heidelberg: Springer-Verlag Berlin Heidelberg; 2014.
- [157] Kato M, Kamigaito M, Sawamoto M, Higashimura T. Polymerization of methyl-methacrylate with the carbon-tetrachloride dichlorotris(triphenylphosphine)ruthenium(ii) methylaluminum bis(2,6-di-tert-butylphenoxide) initiating system - Possibility of living radical polymerization. *Macromolecules* 1995;28:1721–3.
- [158] Wang JS, Matyjaszewski K. Controlled living radical polymerization - atom-transfer radical polymerization in the presence of transition-metal complexes. *J Am Chem Soc* 1995;117:5614–15.
- [159] Bao F, Feng L, Gao J, Tan Z, Xing B, Ma R, et al. New cobalt-mediated radical polymerization (CMRP) of methyl methacrylate initiated by two single-component dinuclear beta-diketone cobalt (II) catalysts. *PLoS One* 2010;5:e13629.
- [160] Matyjaszewski K, Wei M, Xia J, McDermott NE. Controlled/"living" radical polymerization of styrene and methyl methacrylate catalyzed by iron complexes. *Macromolecules* 1997;30:8161–4.
- [161] Granel C, Dubois P, Jerome R, Teyssie P. Controlled radical polymerization of methacrylic monomers in the presence of a bis(ortho-chelated) arylnickel(II) complex and different activated alkyl halides. *Macromolecules* 1996;29:8576–82.
- [162] Lecomte P, Drapier I, Dubois P, Teyssie P, Jerome R. Controlled radical polymerization of methyl methacrylate in the presence of palladium acetate, triphenylphosphine, and carbon tetrachloride. *Macromolecules* 1997;30:7631–3.
- [163] Kotani Y, Kamigaito M, Sawamoto M. $Re(v)$ -mediated living radical polymerization of styrene: $^1ReO_2i(PPh_3)_2/r-i$ initiating systems. *Macromolecules* 1999;32:2420–4.
- [164] Kabachii YA, Kochev SY, Bronstein LM, Blagodatikh IB, Valetsky PM. Atom transfer radical polymerization with Ti(III) halides and alkoxides. *Polym Bull* 2003;50:271–8.
- [165] di Lena F, Matyjaszewski K. Transition metal catalysts for controlled radical polymerization. *Prog Polym Sci* 2010;35:959–1021.
- [166] Matyjaszewski K, Xia J. Atom transfer radical polymerization. *Chem Rev* 2001;101:2921–90.
- [167] Patten TE, Xia J, Abernathy T, Matyjaszewski K. Polymers with very low polydispersities from atom transfer radical polymerization. *Science* 1996;272:866–8.
- [168] Braunecker WA, Matyjaszewski K. Controlled/living radical polymerization: Features, developments, and perspectives. *Prog Polym Sci* 2007;32:93–146.
- [169] Lin CY, Marque SRA, Matyjaszewski K, Coote ML. Linear-free energy relationships for modeling structure-reactivity trends in controlled radical polymerization. *Macromolecules* 2011;44:7568–83.
- [170] Acar AE, Yagci MB, Mathias LJ. Adventitious effect of air in atom transfer radical polymerization: Air-induced (reverse) atom transfer radical polymerization of methacrylates in the absence of an added initiator. *Macromolecules* 2000;33:7700–6.
- [171] de la Fuente JL, Fernández-Sanz M, Fernández-García M, Madruga EL. Solvent effects on the synthesis of poly(methyl methacrylate) by atom-transfer radical polymerization (atrp). *Macromol Chem Phys* 2001;202:2565–71.
- [172] Coullerez G, Malmstrom E, Jonsson M. Solvent effects on the redox properties of Cu complexes used as mediators in atom transfer radical polymerization. *J Phys Chem A* 2006;110:10355–60.
- [173] Percec V, Guliasvili T, Ladislav JS, Wistrand A, Stjern Dahl A, Sienkowska MJ, et al. Ultrafast synthesis of ultrahigh molar mass polymers by metal-catalyzed living radical polymerization of acrylates, methacrylates, and vinyl chloride mediated by SET at 25°C. *J Am Chem Soc* 2006;128:14156–65.
- [174] Krys P, Matyjaszewski K. Kinetics of atom transfer radical polymerization. *Eur Polym J* 2017;89:482–523.
- [175] Coessens VMC, Matyjaszewski K. Fundamentals of atom transfer radical polymerization. *J Chem Educ* 2010;87:916–19.
- [176] Zhang Y, Park A, Cintora A, McMillan SR, Harmon NJ, Moehle A, et al. Impact of the synthesis method on the solid-state charge transport of radical polymers. *J Mater Chem C Mater* 2018;6:111–18.
- [177] Qin HR, Liu X, Huang JB, Liang H, Zhang ZS, Lu J. Design and synthesis of a facile solution-processing and ultrastable crosslinkable branched nitroxide polymer. *Macromol Chem Phys* 2019;220 1900068.
- [178] Sukeyawa T, Omata H, Masuko I, Oyaizu K, Nishide H. Anionic polymerization of 4-methacryloyloxy-TEMPO using an MMA-capped initiator. *ACS Macro Lett* 2014;3:240–3.
- [179] Hergué N, Ernoult B, Minoia A, Lazzaroni R, Gohy JF, Dubois P, et al. Improving the performance of batteries by using multi-pyrene PTMA structures. *Batter Supercaps* 2018;1:102–9.
- [180] Winsberg J, Janoschka T, Morgenstern S, Hagemann T, Muench S, Hauffman G, et al. Poly(TEMPO)/zinc hybrid-flow battery: a novel, "green," high voltage, and safe energy storage system. *Adv Mater* 2016;28:2238–43.
- [181] Moad G. Mechanism and kinetics of dithiobenzoate-mediated RAFT polymerization - Status of the dilemma. *Macromol Chem Phys* 2014;215:9–26.
- [182] Moad G, Rizzardo E, Thang SH. Living radical polymerization by the RAFT process - a second update. *Aust J Chem* 2009;62:1402–72.
- [183] Huang X, Luo B, Chen P, Searles DJ, Wang D, Wang L. Sulfur-based redox chemistry for electrochemical energy storage. *Coord Chem Rev* 2020;422:213445.
- [184] Favier A, Charreyre MT. Experimental requirements for an efficient control of free-radical polymerizations via the reversible addition-fragmentation chain transfer (RAFT) process. *Macromol Rapid Commun* 2006;27:653–92.
- [185] Moad G, Rizzardo E, Thang SH. Radical addition-fragmentation chemistry in polymer synthesis. *Polymer* 2008;49:1079–131.
- [186] Mayadunne RTA, Rizzardo E, Chiefari J, Chong YK, Moad G, Thang SH. Living radical polymerization with reversible addition-fragmentation chain transfer (RAFT polymerization) using dithiocarbamates as chain transfer agents. *Macromolecules* 1999;32:6977–80.
- [187] Oyaizu K, Suga T, Yoshimura K, Nishide H. Synthesis and characterization of radical-bearing polyethers as an electrode-active material for organic secondary batteries. *Macromolecules* 2008;41:6646–52.
- [188] Oyaizu K, Kawamoto T, Suga T, Nishide H. Synthesis and charge transport properties of redox-active nitroxide polyethers with large site density. *Macromolecules* 2010;43:10382–9.
- [189] Szwarc M, Levy M, Milkovich R. Polymerization initiated by electron transfer to monomer. a new method of formation of block polymers. *J Am Chem Soc* 1956;78:2656–7.
- [190] Kitaura T, Kitayama T. Anionic polymerization of methyl methacrylate by difunctional lithium amide initiators with trialkylsilyl protection. *Polym J* 2013;45:1013–18.
- [191] Forens A, Roos K, Gadenne B, Carlotti S. Anionic polymerization of butadiene by dialkylmagnesium /alkali metal alkoxide systems in apolar medium: Polybutadiene microstructure and polymerization control. *Polymer* 2020;205:122864.
- [192] Rabiee Kenaree A, Gillies ER. Controlled polymerization of ethyl glyoxylate using alkylolithium and alkoxide initiators. *Macromolecules* 2018;51:5501–10.
- [193] Beneš MJ, Peška J. Anionic polymerization of propionitrile. *Collect Czechoslov Chem Commun* 1973;38:3762–8.
- [194] Eromosele IC, Pepper DC. Anionic-polymerization of butyl isocyanate (Bic) by NACN. *J Polym Sci A* 1987;25:3499–503.
- [195] Aida T. Living and immortal polymerizations. *Prog Polym Sci* 1994;19:469–528.
- [196] Rempp P, Franta E, Herz JE. Macromolecular engineering by anionic methods. *Adv Polym Sci* 2005:145–74.
- [197] Kobayashi M, Ishizone T, Nakahama S. Synthesis of highly isotactic poly(n,n-diethylacrylamide) by anionic polymerization with grignard reagents and diethylzinc. *J Polym Sci A* 2000;38:4677–85.
- [198] Habaue S, Morita M, Okamoto Y. Stereospecific anionic polymerization of α -(alkoxymethyl)acrylate derivatives affording novel vinyl polymers with macrocyclic side chains. *Polymer* 2002;43:3469–74.
- [199] Natori I, Natori S, Sekikawa H, Takahashi T, Sato H. Bipolar polymer semiconductor blends of C60-end-capped poly(4-diphenylaminostyrene) and poly(4-diphenylaminostyrene): one-pot synthesis and charge-transport properties. *J Appl Polym Sci* 2011;121:3433–8.
- [200] Jagur-Grodzinski J. Functional polymers by living anionic polymerization. *J Polym Sci Part A 1 Polym Chem* 2002;40:2116–33.
- [201] Kang BG, Jang J, Song Y, Kim MJ, Lee T, Lee JS. Facile anionic synthesis of a well-controlled thermally cross-linkable block copolymer for polymer-based resistive memory device applications. *Polym Chem* 2015;6:4264–70.
- [202] Tanaka R, Shinto Y, Matsuzaki R, Nakayama Y, Shiono T. Stereospecific polymerization of conjugated dienes using neodymium alkylborohydride complexes. *Dalton Trans* 2019;48:7267–73.
- [203] Baskaran D. Strategic developments in living anionic polymerization of alkyl (meth)acrylates. *Prog Polym Sci* 2003;28:521–81.
- [204] Bugnon L, Morton CJH, Novak P, Vetter J, Nesvadba P. Synthesis of poly(4-methacryloyloxy-TEMPO) via group-transfer polymerization and its evaluation in organic radical battery. *Chem Mater* 2007;19:2910–14.
- [205] Lopez-Pena HA, Hernandez-Munoz LS, Frontana-Urbe BA, Gonzalez FJ, Gonzalez I, Frontana C, et al. Tacticity influence on the electrochemical reactivity of group transfer polymerization-synthesized PTMA. *J Phys Chem B* 2012;116:5542–50.
- [206] Webster OW. Living polymerization methods. *Synthetic* 1991;251:887–93.
- [207] Miyamoto M, Sawamoto M, Higashimura T. Living polymerization of isobutyl vinyl ether with the hydrogen iodide iodine initiating system. *Macromolecules* 1984;17:265–8.
- [208] Dimitrov P, Faust R. Structure-reactivity scales in carbocationic polymerizations: the case of α -methylstyrene. *Macromolecules* 2010;43:1724–9.
- [209] Zsuga M, Faust R, Kennedy JP. Living carbocationic polymerization. *Polym Bull* 1989;21:273–80.
- [210] Han L, Wu YB, Dan Y, Wang H, Zhang XQ, Wei XL, et al. Characteristics and mechanism of styrene cationic polymerization in 1-butyl-3-methylimidazolium hexafluorophosphate ionic liquid. *RSC Adv* 2016;6:105322–30.
- [211] Ouardad S, Deffieux A, Peruch F. Polyisoprene synthesized via cationic polymerization: state of the art. *Pure Appl Chem* 2012;84:2065–80.
- [212] Kamigaito M, Sawamoto M. Synergistic advances in living cationic and radical polymerizations. *Macromolecules* 2020;53:6749–53.
- [213] Suguro M, Iwasa S, Nakahara K. Fabrication of a practical and polymer-rich organic radical polymer electrode and its rate dependence. *Macromol Rapid Commun* 2008;29:1635–9.
- [214] Koshiika K, Sano N, Oyaizu K, Nishide H. An ultrafast chargeable polymer electrode based on the combination of nitroxide radical and aqueous electrolyte. *Chem Commun* 2009:836–8.
- [215] Truett WL, Johnson DR, Robinson IM, Montague BA. Polynorbornene by coordination polymerization. *J Am Chem Soc* 1960;82:2337–40.

- [216] Jean-Louis Hérisson P, Chauvin Y. Catalyse de transformation des oléfines par les complexes du tungstène. II. Télomérisation des oléfines cycliques en présence d'oléfinacycliques. *Macromol Chem Phys* 1971;141:161–76.
- [217] Suthasupa S, Shiotsuki M, Sanda F. Recent advances in ring-opening metathesis polymerization, and application to synthesis of functional materials. *Polym J* 2010;42:905–15.
- [218] Leitgeb A, Wappel J, Slugovc C. The ROMP toolbox upgraded. *Polymer* 2010;51:2927–46.
- [219] Sukegawa T, Masuko I, Oyaizu K, Nishide H. Expanding the dimensionality of polymers populated with organic robust radicals toward flow cell application: Synthesis of TEMPO-crowded bottlebrush polymers using anionic polymerization and romp. *Macromolecules* 2014;47:8611–17.
- [220] Slugovc C. The ring opening metathesis polymerisation toolbox. *Macromol Rapid Comm* 2004;25:1283–97.
- [221] Demel S, Schoefberger W, Slugovc C, Stelzer F. Benchmarking of ruthenium initiators for the ROMP of a norbornenedicarboxylic acid ester. *J Mol Catal A Chem* 2003;200:11–19.
- [222] Anghel M, Magnan F, Catingan SD, McCreedy MA, Aawani E, Wong V, et al. Redox polymers incorporating pendant 6-oxoverdazyl and nitronyl nitroxide radicals. *J Polym Sci* 2020;58:309–19.
- [223] Sadki S, Schottland P, Brodie N, Sabouraud G. The mechanisms of pyrrole electropolymerization. *Chem Soc Rev* 2000;29:283–93.
- [224] Friebe C, Hager MD, Winter A, Schubert US. Metal-containing polymers via electropolymerization. *Adv Mater* 2012;24:332–45.
- [225] Oyaizu K, Tatsuhira H, Nishide H. Facile charge transport and storage by a TEMPO-populated redox mediating polymer integrated with polyaniline as electrical conducting path. *Polym J* 2015;47:212–19.
- [226] Su C, Ji LL, Xu LH, Zhu XG, He HH, Lv YK, et al. A novel ferrocene-containing aniline copolymer: Its synthesis and electrochemical performance. *RSC Adv* 2015;5:14053–60.
- [227] Sato M, Tanaka S, Kaeriyama K. Electrochemical preparation of highly conducting polythiophene films. *J Chem Soc Chem Comm* 1985:713–14.
- [228] Park KS, Schougaard SB, Goodenough JB. Conducting-polymer/iron-redox-couple composite cathodes for lithium secondary batteries. *Adv Mater* 2007;19:848–52.
- [229] Karlsson C, Huang H, Stromme M, Gogoll A, Sjodin M. Quinone pendant group kinetics in poly(pyrrol-3-ylhydroquinone). *J Electroanal Chem Inter Electrochem* 2014;735:95–8.
- [230] Emanuelsson R, Huang H, Gogoll A, Stromme M, Sjodin M. Entropic versus enthalpic contribution to the quinone formal potential in a polypyrrole-based conducting redox polymer. *J Phys Chem C* 2016;120:21178–83.
- [231] Snook GA, Kao P, Best AS. Conducting-polymer-based supercapacitor devices and electrodes. *J Power Sources* 2011;196:1–12.
- [232] Nezakati T, Seifalian A, Tan A, Seifalian AM. Conductive polymers: opportunities and challenges in biomedical applications. *Chem Rev* 2018;118:6766–843.
- [233] Liang Y, Chen Z, Jing Y, Rong Y, Facchetti A, Yao Y. Heavily n-dopable pi-conjugated redox polymers with ultrafast energy storage capability. *J Am Chem Soc* 2015;137:4956–9.
- [234] Misra GS, Bajpai UDN. Redox polymerization. *Prog Polym Sci* 1982;8:61–131.
- [235] Sarac AS. Redox polymerization. *Prog Polym Sci* 1999;24:1149–204.
- [236] Winsberg J, Muench S, Hagemann T, Morgenstern S, Janoschka T, Billing M, et al. Polymer/zinc hybrid-flow battery using block copolymer micelles featuring a TEMPO corona as catholyte. *Polym Chem* 2016;7:1711–18.
- [237] Suguro M, Iwasa S, Kusachi Y, Morioka Y, Nakahara K. Cationic polymerization of poly(vinyl ether) bearing a TEMPO radical: a new cathode-active material for organic radical batteries. *Macromol Rapid Comm* 2007;28:1929–33.
- [238] Sukegawa T, Sato K, Oyaizu K, Nishide H. Efficient charge transport of a radical polyether/SWCNT composite electrode for an organic radical battery with high charge-storage density. *RSC Adv* 2015;5:15448–52.
- [239] Nagarjuna G, Hui J, Cheng KJ, Lichtenstein T, Shen M, Moore JS, et al. Impact of redox-active polymer molecular weight on the electrochemical properties and transport across porous separators in nonaqueous solvents. *J Am Chem Soc* 2014;136:16309–16.
- [240] Burgess M, Chenard E, Hernandez-Burgos K, Nagarjuna G, Assary RS, Hui JS, et al. Impact of backbone tether length and structure on the electrochemical performance of viologen redox active polymers. *Chem Mater* 2016;28:7362–74.
- [241] Montoto EC, Nagarjuna G, Moore JS, Rodriguez-Lopez J. Redox active polymers for non-aqueous redox flow batteries: Validation of the size-exclusion approach. *J Electrochem Soc* 2017;164:A1688–A1A94.
- [242] Liu S, Wang H, Xing Y, Chu X, Zhao F, Tang E. TEMPO functionalized polymers: synthesis and applications. *Curr Org Chem* 2016;20:1389–403.
- [243] Xue WW, Mutlu H, Theato P. Post-polymerization modification of polymeric active esters towards TEMPO containing polymers: a systematic study. *Eur Polym J* 2020;130:109660.
- [244] Hagemann T, Strumpf M, Schröter E, Stolze C, Grube M, Nischang I, et al. (2,2,6,6-tetramethylpiperidin-1-yl)oxyl-containing zwitterionic polymer as catholyte species for high-capacity aqueous polymer redox flow batteries. *Chem Mater* 2019;31:7987–99.
- [245] Allgaier J, Finkelman H. Anionic-polymerization of 4-methacryloyloxy-2,2,6,6-tetramethylpiperidin-1-oxyl and the magnetic-properties of the polymer. *Makromol Chem Rapid Comm* 1993;14:267–71.
- [246] Rostro L, Baradwaj AG, Boudouris BW. Controlled radical polymerization and quantification of solid state electrical conductivities of macromolecules bearing pendant stable radical groups. *ACS Appl Mater Interfaces* 2013;5:9896–901.
- [247] Bertrand O, Ernould B, Boujioui F, Vlad A, Gohy JF. Synthesis of polymer precursors of electroactive materials by SET-LRP. *Polym Chem* 2015;6:6067–72.
- [248] Zhang K, Hu YX, Wang LZ, Fan JY, Monteiro MJ, Jia ZF. The impact of the molecular weight on the electrochemical properties of poly(TEMPO methacrylate). *Polym Chem* 2017;8:1815–23.
- [249] Tian X, Ding J, Zhang B, Qiu F, Zhuang X, Chen Y. Recent advances in RAFT polymerization: Novel initiation mechanisms and optoelectronic applications. *Polymers* 2018;10:318–44.
- [250] Hatakeyama-Sato K, Nagano T, Noguchi S, Sugai Y, Du J, Nishide H, et al. Hydrophilic organic redox-active polymer nanoparticles for higher energy density flow batteries. *ACS Appl Polym Mater* 2019;1:188–96.
- [251] Shashni B, Alshwimi A, Minami K, Furukawa T, Nagasaki Y. Nitroxide radical-containing nanoparticles as potential candidates for overcoming drug resistance in epidermoid cancers. *Polymer* 2017;116:429–38.
- [252] Chen JY, He JP, Tao YF, Li CM, Yang YL. Synthesis of thermosensitive gel by living free radical polymerization mediated by an alkoxyamine inimer. *Polymer* 2010;51:4769–75.
- [253] Sato K, Sukegawa T, Oyaizu K, Nishide H. Synthesis of poly(TEMPO-substituted glycidyl ether) by utilizing t-BuOK/18-crown-6 for an organic cathode-active material. *Macromol Symp* 2015;351:90–6.
- [254] Joo Y, Agarkar V, Sung SH, Savoie BM, Boudouris BW. A nonconjugated radical polymer glass with high electrical conductivity. *Science* 2018;359:1391–5.
- [255] Hagemann T, Winsberg J, Grube M, Nischang I, Janoschka T, Martin N, et al. An aqueous all-organic redox-flow battery employing a (2,2,6,6-tetramethylpiperidin-1-yl)oxyl-containing polymer as catholyte and dimethyl viologen dichloride as anolyte. *J Power Sources* 2018;378:546–54.
- [256] Nakahara K, Iriyama J, Iwasa S, Suguro M, Satoh M, Cairns EJ. Cell properties for modified PTMA cathodes of organic radical batteries. *J Power Sources* 2007;165:398–402.
- [257] Hatakeyama-Sato K, Wakamatsu H, Yamagishi K, Fujie T, Takeoka S, Oyaizu K, et al. Ultrathin and stretchable rechargeable devices with organic polymer nanosheets conformable to skin surface. *Small* 2019;15:e1805296.
- [258] Guo W, Su J, Li YH, Wan LJ, Guo YG. Nitroxide radical polymer/graphene nanocomposite as an improved cathode material for rechargeable lithium batteries. *Electrochim Acta* 2012;72:81–6.
- [259] Oyaizu K, Choi W, Nishide H. Functionalization of poly(4-chloromethylstyrene) with anthraquinone pendants for organic anode-active materials. *Polym Adv Technol* 2011;22:1242–7.
- [260] Friebe C, Lex-Balducci A, Schubert US. Sustainable energy storage: Recent trends and developments toward fully organic batteries. *ChemSusChem* 2019;12:4093–115.
- [261] Mecerreyes D, Porcarelli L, Casado N. Innovative polymers for next-generation batteries. *Macromol Chem Phys* 2020;221:1900490.
- [262] Yang MX, Liu KW, Shkrob IA, Liao C. Redox-active polymers (redoxmers) for electrochemical energy storage. *Mrs Commun* 2019;9:1151–67.
- [263] Chen R, Li Q, Yu X, Chen L, Li H. Approaching practically accessible solid-state batteries: Stability issues related to solid electrolytes and interfaces. *Chem Rev* 2020;120:6820–77.
- [264] Zhao C, Liu L, Qi X, Lu Y, Wu F, Zhao J, et al. Solid-state sodium batteries. *Adv Energy Mater* 2018;8:1703012.
- [265] Zhao Q, Stalin S, Zhao CZ, Archer LA. Designing solid-state electrolytes for safe, energy-dense batteries. *Nat Rev Mater* 2020;5:229–52.
- [266] Lu Y, Chen J. Prospects of organic electrode materials for practical lithium batteries. *Nat Rev Chem* 2020;4:127–42.
- [267] Miao Y, Hynan P, von Jouanne A, Yokochi A. Current Li-ion battery technologies in electric vehicles and opportunities for advancements. *Energies* 2019;12:1074–94.
- [268] Ahmadi L, Young SB, Fowler M, Fraser RA, Achachlouei MA. A cascaded life cycle: reuse of electric vehicle lithium-ion battery packs in energy storage systems. *Int J Life Cycle Ass* 2017;22:111–24.
- [269] Williams DL, Byrne JJ, Driscoll JS. A high energy density lithium/dichloroisocyanuric acid battery system. *J Electrochem Soc* 1969;116:2–4.
- [270] Oubaha H, Gohy JF, Melinte S. Carbonyl-based pi-conjugated materials: From synthesis to applications in lithium-ion batteries. *ChemSusChem* 2019;84:1179–214.
- [271] Gao Z, Zhang YY, Song NN, Li XD. Biomass-derived renewable carbon materials for electrochemical energy storage. *Mater Res Lett* 2017;5:69–88.
- [272] Hu P, Wang H, Yang Y, Yang J, Lin J, Guo L. Renewable-biomolecule-based full lithium-ion batteries. *Adv Mater* 2016;28:3486–92.
- [273] Lee B, Ko Y, Kwon G, Lee S, Ku K, Kim J, et al. Exploiting biological systems: toward eco-friendly and high-efficiency rechargeable batteries. *Joule* 2018;2:61–75.
- [274] Yu ZJ, Jiao SQ, Li S, Chen XD, Song WL, Teng T, et al. Flexible stable solid-state Al-ion batteries. *Adv Funct Mater* 2019;29:1806799.
- [275] Chen Z, Kim GT, Wang ZL, Bresser D, Qin BS, Geiger D, et al. 4-V flexible all-solid-state lithium polymer batteries. *Nano Energy* 2019;64:103986.
- [276] López-Aranguren P, Judez X, Chakir M, Armand M, Buannic L. High voltage solid state batteries: Targeting high energy density with polymer composite electrolytes. *J Electrochem Soc* 2020;167:020548.
- [277] Randau S, Weber DA, Kotz O, Koerver R, Braun P, Weber A, et al. Benchmarking the performance of all-solid-state lithium batteries. *Nat Energy* 2020;5:259–70.
- [278] Kim J, Kim JH, Ariga K. Redox-active polymers for energy storage nanoarchitectonics. *Joule* 2017;1:739–68.

- [279] Song ZP, Zhou HS. Towards sustainable and versatile energy storage devices: an overview of organic electrode materials. *Energy Environ Sci* 2013;6:2280–301.
- [280] Liang Y, Jing Y, Gheytni S, Lee KY, Liu P, Facchetti A, et al. Universal quinone electrodes for long cycle life aqueous rechargeable batteries. *Nat Mater* 2017;16:841–8.
- [281] Dong XL, Guo ZW, Guo ZY, Wang YG, Xia YY. Organic batteries operated at -70°C . *Joule* 2018;2:902–13.
- [282] Xie J, Gu PY, Zhang QC. Nanostructured conjugated polymers: toward high-performance organic electrodes for rechargeable batteries. *ACS Energy Lett* 2017;2:1985–96.
- [283] Kaneko F, Wada S, Nakayama M, Wakihara M, Koki J, Kuroki S. Capacity fading mechanism in all solid-state lithium polymer secondary batteries using PEG-borate/aluminate ester as plasticizer for polymer electrolytes. *Adv Funct Mater* 2009;19:918–25.
- [284] Prosin PP, Passerini S. The role of conductive carbon in PEO-based composite cathodes. *Eur Polym J* 2001;37:65–9.
- [285] Huang Y, Kormakov S, He X, Gao X, Zheng X, Liu Y, et al. Conductive polymer composites from renewable resources: an overview of preparation, properties, and applications. *Polymers* 2019;11:187–219.
- [286] Acker P, Rzesny L, Marchiori CFN, Araujo CM, Esser B. Π -conjugation enables ultra-high rate capabilities and cycling stabilities in phenothiazine copolymers as cathode-active battery materials. *Adv Funct Mater* 2019;29:1906436.
- [287] Jia XT, Ge Y, Shao L, Wang CY, Wallace GG. Tunable conducting polymers: toward sustainable and versatile batteries. *ACS Sustain Chem Eng* 2019;7:14321–40.
- [288] Liu TT, Zhang JJ, Han W, Zhang JN, Ding GL, Dong SM, et al. Review-*in situ* polymerization for integration and interfacial protection towards solid state lithium batteries. *J Electrochem Soc* 2020;167:070527.
- [289] Tang M, Zhu S, Liu Z, Jiang C, Wu Y, Li H, et al. Tailoring π -conjugated systems: from π - π stacking to high-rate-performance organic cathodes. *Chem* 2018;4:2600–14.
- [290] Ibanez JG, Rincon ME, Gutierrez-Granados S, Chahma M, Jaramillo-Quintero OA, Frontana-Urbe BA. Conducting polymers in the fields of energy, environmental remediation, and chemical-chiral sensors. *Chem Rev* 2018;118:4731–816.
- [291] Yang Q, Zhang Z, Sun XG, Hu YS, Xing H, Dai S. Ionic liquids and derived materials for lithium and sodium batteries. *Chem Soc Rev* 2018;47:2020–64.
- [292] Watanabe M, Thomas ML, Zhang S, Ueno K, Yasuda T, Dokko K. Application of ionic liquids to energy storage and conversion materials and devices. *Chem Rev* 2017;117:7190–239.
- [293] Liu J, Xu C, Chen Z, Ni S, Shen ZX. Progress in aqueous rechargeable batteries. *Green Energy Environ* 2018;3:20–41.
- [294] Kalhoff J, Eshetu GG, Bresser D, Passerini S. Safer electrolytes for lithium-ion batteries: state of the art and perspectives. *ChemSusChem* 2015;8:2154–75.
- [295] Kandambeth S, Kale VS, Shekhar O, Alshareef HN, Eddaoudi M. 2D Covalent-organic framework electrodes for supercapacitors and rechargeable metal-ion batteries. *Adv Energy Mater* 2021:2100177.
- [296] Li M, Liu J, Zhang T, Song X, Chen W, Chen L. 2D Redox-active covalent organic frameworks for supercapacitors: design, synthesis, and challenges. *Small* 2021;17:e2005073.
- [297] Pei C, Choi MS, Yu X, Xue H, Xia BY, Park HS. Recent progress in emerging metal and covalent organic frameworks for electrochemical and functional capacitors. *J Mat Chem A* 2021;9:8832–69.
- [298] Zhang Y, Riduan SN, Wang J. Redox active metal- and covalent organic frameworks for energy storage: Balancing porosity and electrical conductivity. *Chemistry* 2017;23:16419–31.
- [299] Goto F, Abe K, Okabayashi K, Yoshida T, Morimoto H. The polyaniline lithium battery. *J Power Sources* 1987;20:243–8.
- [300] Mike JF, Lutkenhaus JL. Recent advances in conjugated polymer energy storage. *J Polym Sci Pol Phys* 2013;51:468–80.
- [301] Bäuerle P. Intrinsically conducting polymers—quo vadis? *Adv Mater* 1993;5:879–86.
- [302] Xu LH, Yang F, Su C, Ji LL, Zhang C. Synthesis and properties of novel TEMPO-contained polypyrrole derivatives as the cathode material of organic radical battery. *Electrochim Acta* 2014;130:148–55.
- [303] Cao JY, Ding FF, Chen HP, Wang HN, Wang WC, Chen ZD, et al. A new redox-active conjugated polymer containing anthraquinone pendants as anode material for aqueous all-organic hybrid-flow battery. *J Power Sources* 2019;423:316–22.
- [304] Wang SY, Easley AD, Lutkenhaus J. 100th anniversary of macromolecular science viewpoint: Fundamentals for the future of macromolecular nitroxide radicals. *ACS Macro Lett* 2020;9:358–70.
- [305] Yang Y, Liu Z, Zhang G, Zhang X, Zhang D. The effects of side chains on the charge mobilities and functionalities of semiconducting conjugated polymers beyond solubilities. *Adv Mater* 2019;31:e1903104.
- [306] Akagi K. Interdisciplinary chemistry based on integration of liquid crystals and conjugated polymers: development and progress. *Bull Chem Soc Jpn* 2019;92:1509–655.
- [307] Luo Y, Guo R, Li T, Li F, Liu Z, Zheng M, et al. Application of polyaniline for Li-ion batteries, lithium-sulfur batteries, and supercapacitors. *ChemSusChem* 2019;12:1591–611.
- [308] Pham MC, Piro B, Bazzouai EA, Hedayatullah M, Lacroix JC, Novak P, et al. Anodic oxidation of 5-amino-1,4-naphthoquinone (ANQ) and synthesis of a conducting polymer (PANQ). *Synth Met* 1998;92:197–205.
- [309] Häring D, Novák P, Haas O, Piro B, Pham MC. Poly(5-amino-1,4-naphthoquinone), a novel lithium-inserting electroactive polymer with high specific charge. *J Electrochem Soc* 2019;146:2393–6.
- [310] Ivashkina NV, Romanov VS, Moroz AA, Shvartsberg MS. 5-Arylethynyl-1,4-naphthoquinones. *Bull Acad Sci USSR Chem* 1984;33:2345–8.
- [311] Palaniappan S, Chang YT, Liu CM, Manisankar P. Mechanochemical synthesis and characterization of poly(2,5-dimethoxy aniline) salts. *J Appl Polym Sci* 2012;124:4281–8.
- [312] Vlad A, Arnould K, Ernould B, Sieuw L, Rolland J, Gohy JF. Exploring the potential of polymer battery cathodes with electrically conductive molecular backbone. *J Mater Chem A* 2015;3:11189–93.
- [313] Sieuw L, Ernould B, Gohy JF, Vlad A. On the improved electrochemistry of hybrid conducting-redox polymer electrodes. *Sci Rep* 2017;7:4847–56.
- [314] Naoi K, Kawase K, Mori M, Komiya M. Electrochemistry of poly(2,2'-dithiodianiline): A new class of high energy conducting polymer interconnected with S-S bonds. *J Electrochem Soc* 1997;144:L173–LL75.
- [315] Li JX, Zhan H, Zhou L, Deng SR, Li ZY, Zhou YH. Aniline-based polyorganodisulfide redox system of high energy for secondary lithium batteries. *Electrochim Commun* 2004;6:515–19.
- [316] Li P, Fang ZS, Zhang Y, Mo CS, Hu XH, Jian JH, et al. A high-performance, highly bendable quasi-solid-state zinc-organic battery enabled by intelligent proton-self-buffering copolymer cathodes. *J Mater Chem A* 2019;7:17292–8.
- [317] Zhang Q, Ma Y, Lu Y, Li L, Wan F, Zhang K, et al. Modulating electrolyte structure for ultralow temperature aqueous zinc batteries. *Nat Commun* 2020;11:4463–73.
- [318] Hong X, Liu Y, Li Y, Wang X, Fu J, Wang X. Application progress of polyaniline, polypyrrole and polythiophene in lithium-sulfur batteries. *Polymers* 2020;12:331–58.
- [319] Wang BB, Zhang Y, Zhu Y, Shen YM, Wang WC, Chen ZD, et al. Redox-active poly(6-(1H-pyrrol-1-yl)quinoxaline) as a novel organic anode material for aqueous hybrid flow batteries. *J Power Sources* 2020;451:227788.
- [320] Sen S, Saraidaridis J, Kim SY, Palmore GT. Viologens as charge carriers in a polymer-based battery anode. *ACS Appl Mater Interfaces* 2013;5:7825–30.
- [321] Dubal D, Jagadale A, Chodankar NR, Kim DH, Gomez-Romero P, Holze R. Polypyrrole nanopipes as a promising cathode material for Li-ion batteries and Li-ion capacitors: Two-in-one approach. *Energy Technol* 2019;7:193–200.
- [322] Zang X, Wang X, Liu H, Ma X, Wang W, Ji J, et al. Enhanced ion conduction via epitaxially polymerized two-dimensional conducting polymer for high-performance cathode in zinc-ion batteries. *ACS Appl Mater Interfaces* 2020;12:9347–54.
- [323] Zhang JH, Yue HG, Ma YQ, Han X, Mei J, Zhao JS, et al. Fabrication of NiO-NiMoO₄/PPy microspheres as high-performance anode material for lithium-ion battery. *Ionics* 2020;26:3823–30.
- [324] Gao LL, Cao YX, Wang J, Ren HB, Wang JH, Huang JR. Construction of polypyrrole coated hollow cobalt manganese nanocages as an effective sulfur host for lithium-sulfur batteries. *Ceram Int* 2020;46:18224–33.
- [325] Zhang Y, Xu GB, Liu X, Wei XL, Cao JX, Yang LW. Scalable *in situ* reactive assembly of polypyrrole-coated MnO₂ nanowire and carbon nanotube composite as freestanding cathodes for high performance aqueous zn-ion batteries. *ChemElectrochem* 2020;7:2762–70.
- [326] Amakie M, lihama T. Chemical polymerization of pyrrole with disulfide structure and the application to lithium secondary batteries. *Synthetic Met* 2006;156:239–43.
- [327] Thanasamy D, Jesuraj D, Kannan SKK, Avadhanam V. A novel route to synthesis polythiophene with great yield and high electrical conductivity without post doping process. *Polymer* 2019;175:32–40.
- [328] Raju V, Rani JV, Basak P. Self-arranged polythiophene on multi-walled carbon nanotube templated composites: synthesis and application in rechargeable aluminium battery. *Electrochim Acta* 2020;361:137097.
- [329] Sarker H, Gofer Y, Killian JG, Poehler TO, Searson PC. Synthesis and characterization of fluoro-substituted polyphenylthiophenes for charge storage applications. *Synth Met* 1997;88:179–85.
- [330] Li F, Gore DN, Wang S, Lutkenhaus JL. Unusual internal electron transfer in conjugated radical polymers. *Angew Chem Int Ed* 2017;56:9856–9.
- [331] Kunz TK, Wolf MO. Electrodeposition and properties of TEMPO functionalized polythiophene thin films. *Polym Chem* 2011;2:640–4.
- [332] Manceau M, Rivaton A, Gardette JL, Guillerez S, Lemaître N. The mechanism of photo- and thermooxidation of poly(3-hexylthiophene) (P3HT) reconsidered. *Polym Degrad Stab* 2009;94:898–907.
- [333] Manceau M, Rivaton A, Gardette JL. Involvement of singlet oxygen in the solid-state photochemistry of P3HT. *Macromol Rapid Commun* 2008;29:1823–7.
- [334] Chen Z, Zheng Y, Yan H, Facchetti A. Naphthalenedicarboximide- vs perylenedicarboximide-based copolymers. Synthesis and semiconducting properties in bottom-gate N-channel organic transistors. *J Am Chem Soc* 2009;131:8–9.
- [335] Oschmann B, Park J, Kim C, Char K, Sung YE, Zentel R. Copolymerization of polythiophene and sulfur to improve the electrochemical performance in lithium-sulfur batteries. *Chem Mater* 2015;27:7011–17.
- [336] Fan X, Nie W, Tsai H, Wang N, Huang H, Cheng Y, et al. PEDOT:PSS for flexible and stretchable electronics: modifications, strategies, and applications. *Adv Sci* 2019;6:1900813.
- [337] Emanuelsson R, Sterby M, Stromme M, Sjödin M. An all-organic proton battery. *J Am Chem Soc* 2017;139:4828–34.

- [338] Cíntora-Juárez D, Pérez-Vicente C, Ahmad S, Tirado JL. Improving the cycling performance of LiFePO₄ cathode material by poly(3,4-ethylenedioxythiophene) coating. *RSC Adv* 2014;4:26108–14.
- [339] Wang X, Wang BQ, Tang YX, Xu BB, Liang C, Yan M, et al. Manganese hexacyanoferrate reinforced by PEDOT coating towards high-rate and long-life sodium-ion battery cathode. *J Mater Chem A* 2020;8:3222–7.
- [340] Ozerova VV, Stenina IA, Kuz'mina AA, Kulova TL, Yaroslavtsev AB. Cathode materials based on lithium iron phosphate/PEDOT composites for lithium-ion batteries. *Inorg Mater* 2020;56:648–56.
- [341] Chen ZX, Li WJ, Dai YY, Xu N, Su C, Liu JL, et al. Conjugated microporous polymer based on star-shaped triphenylamine-benzene structure with improved electrochemical performances as the organic cathode material of Li-ion battery. *Electrochim Acta* 2018;286:187–94.
- [342] Fan L, Liu Q, Xu Z, Lu BG. An organic cathode for potassium dual-ion full battery. *ACS Energy Lett* 2017;2:1614–20.
- [343] Xu T, Xiong JQ, Du XL, Zhang Y, Song SK, Xiong CX, et al. Polytriphenylamine derivative and carbon nanotubes as cathode materials for high-performance polymer-based batteries. *J Phys Chem C* 2018;122:20057–63.
- [344] Nayana V, Kandasubramanian B. Polycarbazole and its derivatives: progress, synthesis, and applications. *J Polym Res* 2020;27:285–309.
- [345] Shimizu T, Yamamoto K, Pandit P, Yoshikawa H, Higashibayashi S. Application of hydrazine-embedded heterocyclic compounds to high voltage rechargeable lithium organic batteries. *Sci Rep* 2018;8:579–85.
- [346] Kolek M, Otteny F, Schmidt P, Mück-Lichtenfeld C, Einholz C, Becking J, et al. Ultra-high cycling stability of poly(vinylphenothiazine) as a battery cathode material resulting from π - π interactions. *Energy Environ Sci* 2017;10:2334–41.
- [347] Wild A, Strumpf M, Hauptler B, Hager MD, Schubert US. All-organic battery composed of thianthrene- and TCAQ-based polymers. *Adv Energy Mater* 2017;7:1601415.
- [348] Rodríguez-Pérez IA, Jian Z, Waldenmaier PK, Palmisano JW, Chandrabose RS, Wang X, et al. A hydrocarbon cathode for dual-ion batteries. *ACS Energy Lett* 2016;1:719–23.
- [349] Luo C, Xu GL, Ji X, Hou S, Chen L, Wang F, et al. Reversible redox chemistry of azo compounds for sodium-ion batteries. *Angew Chem Int Ed* 2018;57:2879–83.
- [350] Ferruti P, Gill D, Klein MP, Wang HH, Entine G, Calvin M. Synthesis of mono-, di-, and polynitroxides. Classification of electron spin resonance spectra of flexible dinitroxides dissolved in liquids and glasses. *J Am Chem Soc* 1970;92:3704–13.
- [351] Suga T, Ohshiro H, Sugita S, Oyaizu K, Nishide H. Emerging n-type redox-active radical polymer for a totally organic polymer-based rechargeable battery. *Adv Mater* 2009;21:1627–31.
- [352] Wang S, Li F, Easley AD, Lutkenhaus JL. Real-time insight into the doping mechanism of redox-active organic radical polymers. *Nat Mater* 2019;18:69–75.
- [353] Suga T, Konishi H, Nishide H. Photocrosslinked nitroxide polymer cathode-active materials for application in an organic-based paper battery. *Chem Commun* 2007:1730–2.
- [354] Katsumata T, Qu J, Shiotsuki M, Satoh M, Wada J, Igarashi J, et al. Synthesis, characterization, and charge/discharge properties of polynorbornenes carrying 2,2,6,6-tetramethylpiperidine-1-oxyl radicals at high density. *Macromolecules* 2008;41:1175–83.
- [355] Kim TS, Lim JE, Oh MS, Kim JK. Carbon conductor- and binder-free organic electrode for flexible organic rechargeable batteries with high energy density. *J Power Sources* 2017;361:15–20.
- [356] Ernoult B, Bertrand O, Minoia A, Lazzaroni R, Vlad A, Gohy JF. Electroactive polymer/carbon nanotube hybrid materials for energy storage synthesized via a "grafting to" approach. *RSC Adv* 2017;7:17301–10.
- [357] Zhang K, Hu Y, Wang L, Monteiro MJ, Jia Z. Pyrene-functionalized PTMA by NRC for greater pi-pi stacking with RGO and enhanced electrochemical properties. *ACS Appl Mater Interfaces* 2017;9:34900–8.
- [358] Li F, Zhang YP, Kwon SR, Lutkenhaus JL. Electropolymerized polythiophenes bearing pendant nitroxide radicals. *ACS Macro Lett* 2016;5:337–41.
- [359] Zhang YR, Park AM, McMillan SR, Harmon NJ, Flatte ME, Fuchs GD, et al. Charge transport in conjugated polymers with pendent stable radical groups. *Chem Mater* 2018;30:4799–807.
- [360] Casado N, Hernandez G, Veloso A, Devaraj S, Mecerreyes D, Armand M. Pedot radical polymer with synergetic redox and electrical properties. *ACS Macro Lett* 2016;5:59–64.
- [361] Li F, Wang SY, Zhang YP, Lutkenhaus JL. Electrochemical energy storage in poly(dithieno [3,2-b:2',3'-d]pyrrole) bearing pendant nitroxide radicals. *Chem Mater* 2018;30:5169–74.
- [362] López-Peña HA, Hernández-Muñoz LS, Cardoso J, González FJ, González I, Frontana C. Electrochemical and spectroelectrochemical properties of nitroxyl radical species in PTMA, an organic radical polymer. Influence of the microstructure. *Electrochem Commun* 2009;11:1369–72.
- [363] Guo W, Yin YX, Xin S, Guo YG, Wan LJ. Superior radical polymer cathode material with a two-electron process redox reaction promoted by graphene. *Energy Environ Sci* 2012;5:5221–5.
- [364] Qu JQ, Khan FZ, Satoh M, Wada J, Hayashi HY, Mizoguchi KJ, et al. Synthesis and charge/discharge properties of cellulose derivatives carrying free radicals. *Polymer* 2008;49:1490–6.
- [365] Wingate AJ, Boudouris BW. Recent advances in the syntheses of radical-containing macromolecules. *J Polym Sci Pol Chem* 2016;54:1875–94.
- [366] Endo T, Takuma K, Takata T, Hirose C. Synthesis and polymerization of 4-(glycidyoxy)-2,2,6,6-tetramethylpiperidine-1-oxyl. *Macromolecules* 1993;26:3227–9.
- [367] Vekšli Z, Miller WG. The effect of good solvents on molecular motion of nitroxide free radicals in covalently labeled polystyrene and poly(methyl methacrylate). *Macromolecules* 1977;10:686–92.
- [368] Oyaizu K, Nishide H. Radical polymers for organic electronic devices: a radical departure from conjugated polymers? *Adv Mater* 2009;21:2339–44.
- [369] Zhang K, Monteiro MJ, Jia ZF. Stable organic radical polymers: synthesis and applications. *Polym Chem* 2016;7:5589–614.
- [370] Xiong JQ, Wei Z, Xu T, Zhang Y, Xiong CX, Dong LJ. Polytriphenylamine derivative with enhanced electrochemical performance as the organic cathode material for rechargeable batteries. *Polymer* 2017;130:135–42.
- [371] Jahnert T, Hager MD, Schubert US. Assorted phenoxyl-radical polymers and their application in lithium-organic batteries. *Macromol Rapid Commun* 2016;37:725–30.
- [372] Häupler B, Wild A, Schubert US. Carbonyls: Powerful organic materials for secondary batteries. *Adv Energy Mater* 2015;5:1402034.
- [373] Wu YW, Zeng RH, Nan JM, Shu D, Qiu YC, Chou SL. Quinone electrode materials for rechargeable lithium/sodium ion batteries. *Adv Energy Mater* 2017;7:1700278.
- [374] Miroshnikov M, Divya KP, Babu G, Meiyazhagan A, Arava LMR, Ajayan PM, et al. Power from nature: designing green battery materials from electroactive quinone derivatives and organic polymers. *J Mater Chem A* 2016;4:12370–86.
- [375] Xie J, Zhang QC. Recent progress in rechargeable lithium batteries with organic materials as promising electrodes. *J Mater Chem A* 2016;4:7091–106.
- [376] Alt H, Binder H, Köhling A, Sandstedt G. Investigation into the use of quinone compounds-for battery cathodes. *Electrochim Acta* 1972;17:873–87.
- [377] Song Z, Qian Y, Gordin ML, Tang D, Xu T, Otani M, et al. Polyanthraquinone as a reliable organic electrode for stable and fast lithium storage. *Angew Chem Int Ed* 2015;54:13947–51.
- [378] Song Z, Qian Y, Zhang T, Otani M, Zhou H. Poly(benzoquinonyl sulfide) as a high-energy organic cathode for rechargeable Li and Na batteries. *Adv Sci* 2015;2:1500124.
- [379] Song Z, Zhan H, Zhou Y. Anthraquinone based polymer as high performance cathode material for rechargeable lithium batteries. *Chem Commun* 2009:448–50.
- [380] Chi X, Liang Y, Hao F, Zhang Y, Whiteley J, Dong H, et al. Tailored organic electrode material compatible with sulfide electrolyte for stable all-solid-state sodium batteries. *Angew Chem Int Ed* 2018;57:2630–4.
- [381] Yokoji T, Kameyama Y, Maruyama N, Matsubara H. High-capacity organic cathode active materials of 2,2'-bis-p-benzoquinone derivatives for rechargeable batteries. *J Mater Chem A* 2016;4:5457–66.
- [382] Kwon JE, Hyun CS, Ryu YJ, Lee J, Min DJ, Park MJ, et al. Triptycene-based quinone molecules showing multi-electron redox reactions for large capacity and high energy organic cathode materials in Li-ion batteries. *J Mater Chem A* 2018;6:3134–40.
- [383] Song ZP, Qian YM, Liu XZ, Zhang T, Zhu YB, Yu HJ, et al. A quinone-based oligomeric lithium salt for superior Li-organic batteries. *Energy Environ Sci* 2014;7:4077–86.
- [384] Xie J, Wang ZL, Gu PY, Zhao Y, Xu ZCJ, Zhang QC. A novel quinone-based polymer electrode for high performance lithium-ion batteries. *Sci China Mater* 2016;59:6–11.
- [385] Wei WF, Li L, Zhang L, Hong JH, He G. A benzoquinone-based cathode for Li-organic batteries. *Mater Lett* 2018;213:126–30.
- [386] Lee J, Park MJ. Tattooing dye as a green electrode material for lithium batteries. *Adv Energy Mater* 2017;7:1602279.
- [387] Yao M, Umetani S, Ando H, Kiyobayashi T, Takeichi N, Kondo R, et al. Rechargeable organic batteries using chloro-substituted naphthazarin derivatives as positive electrode materials. *J Mater Sci* 2017;52:12401–8.
- [388] Yao M, Numoto T, Ando H, Kondo R, Takeshita HT, Kiyobayashi T. Improving the cycle-life of naphthoquinone-based active materials by their polymerization for rechargeable organic batteries. *Energy Procedia* 2016;89:213–21.
- [389] Shi Y, Sun P, Yang J, Xu Y. Benzoquinone- and naphthoquinone-bearing polymers synthesized by ring-opening metathesis polymerization as cathode materials for lithium-ion batteries. *ChemSusChem* 2020;13:334–40.
- [390] Zhao J, Yang JX, Sun PF, Xu YH. Sodium sulfonate groups substituted anthraquinone as an organic cathode for potassium batteries. *Electrochem Commun* 2018;86:34–7.
- [391] Takeda T, Taniki R, Masuda A, Honma I, Akutagawa T. Electron-deficient anthraquinone derivatives as cathodic material for lithium ion batteries. *J Power Sources* 2016;328:228–34.
- [392] Manecke G, Storck W. Polyvinylanthraquinone redox resins (electron exchange polymers). *J Polym Sci C* 2007;4:1457–66.
- [393] Katsumi J, Nakayama T, Esaka Y, Uno B. Mechanistic study on the electrochemical reduction of 9,10-anthraquinone in the presence of hydrogen-bond and proton donating additives. *Anal Sci* 2012;28:257–65.
- [394] Bachman JE, Curtiss LA, Assary RS. Investigation of the redox chemistry of anthraquinone derivatives using density functional theory. *J Phys Chem A* 2014;118:8852–60.
- [395] R.W. Campbell, J.J.T. Edmonds, Production of p-phenylene sulfide polymers, 1975, US4038259A.
- [396] Petronico A, Bassett KL, Nicolau BG, Gewirth AA, Nuzzo RG. Toward a four-electron redox quinone polymer for high capacity lithium ion storage. *Adv Energy Mater* 2018;8:1700960.

- [397] Zhao L, Wang WK, Wang AB, Yuan KG, Chen S, Yang YS. A novel polyquinone cathode material for rechargeable lithium batteries. *J Power Sources* 2013;233:23–7.
- [398] Pan BF, Huang JH, Feng ZX, Zeng L, He MN, Zhang L, et al. Polyanthraquinone-based organic cathode for high-performance rechargeable magnesium-ion batteries. *Adv Energy Mater* 2016;6:1600140.
- [399] Häupler B, Burges R, Janoschka T, Jähner T, Wild A, Schubert US. PolyTCAQ in organic batteries: enhanced capacity at constant cell potential using two-electron-redox-reactions. *J Mater Chem A* 2014;2:8999–9001.
- [400] Häupler B, Hagemann T, Friebe C, Wild A, Schubert US. Dithiophenedione-containing polymers for battery application. *ACS Appl Mater Interfaces* 2015;7:3473–9.
- [401] Jing Y, Liang YL, Gheyhani S, Yao Y. Cross-conjugated oligomeric quinones for high performance organic batteries. *Nano Energy* 2017;37:46–52.
- [402] Hauffman G, Maguin Q, Bourgeois JP, Vlad A, Gohy JF. Micellar cathodes from self-assembled nitroxide-containing block copolymers in battery electrolytes. *Macromol Rapid Commun* 2014;35:228–33.
- [403] Hammad AS, Noby H, Elkady MF, El-Shazly AH. In-situ polymerization of polyaniline/polypyrrole copolymer using different techniques. *Iop Conf Ser Mat Sci* 2018;290:012001.
- [404] Hauffman G, Rolland J, Bourgeois JP, Vlad A, Gohy JF. Synthesis of nitroxide-containing block copolymers for the formation of organic cathodes. *J Polym Sci Pol Chem* 2013;51:101–8.
- [405] Tokue H, Murata T, Agatsuma H, Nishide H, Oyaizu K. Charge discharge with rocking-chair-type Li⁺ migration characteristics in a zwitterionic radical copolymer composed of TEMPO and trifluoromethanesulfonylimide with carbonate electrolytes for a high-rate Li-ion battery. *Macromolecules* 2017;50:1950–8.
- [406] Mazur S, Lugg PS, Yarnitzky C. Electrochemistry of aromatic polyimides. *J Electrochem Soc* 1987;134:346–53.
- [407] Viehbeck A, Goldberg MJ, Kovac CA. Electrochemical properties of polyimides and related imide compounds. *J Electrochem Soc* 1990;137:1460–6.
- [408] Oyaizu K, Hatemata A, Choi W, Nishide H. Redox-active polyimide/carbon nanocomposite electrodes for reversible charge storage at negative potentials: expanding the functional horizon of polyimides. *J Mater Chem* 2010;20:5404–10.
- [409] Song Z, Zhan H, Zhou Y. Polyimides: promising energy-storage materials. *Angew Chem Int Ed* 2010;49:8444–8.
- [410] Ostroverkhova O. Organic optoelectronic materials: Mechanisms and applications. *Chem Rev* 2016;116:13279–412.
- [411] Zindy N, Blaskovits JT, Beaumont C, Michaud-Valcourt J, Saneifar H, Johnson PA, et al. Pyromellitic diimide-based copolymers and their application as stable cathode active materials in lithium and sodium-ion batteries. *Chem Mater* 2018;30:6821–30.
- [412] Chen CY, Zhao X, Li HB, Gan F, Zhang JX, Dong J, et al. Naphthalene-based polyimide derivatives as organic electrode materials for lithium-ion batteries. *Electrochim Acta* 2017;229:387–95.
- [413] Iordache A, Delhorbe V, Bardet M, Dubois L, Gutel T, Picard L. Perylene-based all-organic redox battery with excellent cycling stability. *ACS Appl Mater Interfaces* 2016;8:22762–7.
- [414] Luo W, Allen M, Raju V, Ji XL. An organic pigment as a high-performance cathode for sodium-ion batteries. *Adv Energy Mater* 2014;4:1400554.
- [415] Ghosh A, Sen SK, Banerjee S, Voit B. Solubility improvements in aromatic polyimides by macromolecular engineering. *Rsc Adv* 2012;2:5900–26.
- [416] Hernández G, Salsamendi M, Morozova SM, Lozinskaya EI, Devaraj S, Vygodskii YS, et al. Polyimides as cathodic materials in lithium batteries: effect of the chemical structure of the diamine monomer. *J Polym Sci A Polym Chem* 2018;56:714–23.
- [417] Medabalmi V, Kuanr N, Ramanujam K. Reversible sodium storage behavior of aromatic diimide disodium carboxylates. *J Electrochem Soc* 2016;164:A6147–A6A53.
- [418] Veerababu M, Varadaraju UV, Kothandaraman R. Reversible lithium storage behaviour of aromatic diimide dilithium carboxylates. *Electrochim Acta* 2016;193:80–7.
- [419] Bančić T, Bitenc J, Pirnat K, Kopač Lautar A, Grdadolnik J, Randon Vitanova A, et al. Electrochemical performance and redox mechanism of naphthalene-hydrazine diimide polymer as a cathode in magnesium battery. *J Power Sources* 2018;395:25–30.
- [420] Xu F, Xia JT, Shi W, Cao SA. Sulfonyl-based polyimide cathode for lithium and sodium secondary batteries: Enhancing the cycling performance by the electrolyte. *Mater Chem Phys* 2016;169:192–7.
- [421] Dong X, Yu H, Ma Y, Bao JL, Truhlar DG, Wang Y, et al. All-organic rechargeable battery with reversibility supported by "water-in-salt" electrolyte. *Chem* 2017;23:2560–5.
- [422] Jung MH, Ghorpade RV. Polyimide containing tricarbonyl moiety as an active cathode for rechargeable Li-ion batteries. *J Electrochem Soc* 2018;165:A2476–A2A82.
- [423] Xu F, Wang HT, Wu MY, Nan JS, Li T, Cao SA. Electrochemical properties of poly(anthraquinonyl imide)s as high-capacity organic cathode materials for Li-ion batteries. *Mater Chem Phys* 2018;214:120–5.
- [424] Wu HP, Yang Q, Meng QH, Ahmad A, Zhang M, Zhu LY, et al. A polyimide derivative containing different carbonyl groups for flexible lithium ion batteries. *J Mater Chem A* 2016;4:2115–21.
- [425] Tian BB, Ning GH, Tang W, Peng CX, Yu DY, Chen ZX, et al. Polyquinoneimines for lithium storage: more than the sum of its parts. *Mater Horiz* 2016;3:429–33.
- [426] Xu F, Wang H, Lin J, Luo X, Cao S-a, Yang H. Poly(anthraquinonyl imide) as a high capacity organic cathode material for Na-ion batteries. *J Mater Chem A* 2016;4:11491–7.
- [427] Xu F, Xia JT, Shi W. Anthraquinone-based polyimide cathodes for sodium secondary batteries. *Electrochem Commun* 2015;60:117–20.
- [428] Iron MA, Cohen R, Rybtechinski B. On the unexpected stability of the dianion of perylene diimide in water—a computational study. *J Phys Chem A* 2011;115:2047–56.
- [429] Zhu XM, Liu XL, Deng WW, Xiao LF, Yang HX, Cao YL. Perylenediimide dyes as a cheap and sustainable cathode for lithium ion batteries. *Mater Lett* 2016;175:191–4.
- [430] Casado N, Mantione D, Shanmukaraj D, Mecerreyes D. Symmetric all-organic battery containing a dual redox-active polymer as cathode and anode material. *ChemSusChem* 2020;13:2464–70.
- [431] Miller-Chou BA, Koenig JL. A review of polymer dissolution. *Prog Polym Sci* 2003;28:1223–70.
- [432] Wang S, Park AMG, Flouda P, Easley AD, Li F, Ma T, et al. Solution-processable thermally crosslinked organic radical polymer battery cathodes. *ChemSusChem* 2020;13:2371–8.
- [433] Zheng LY, Mukherjee S, Wang K, Hay ME, Boudouris BW, Gong X. Radical polymers as interfacial layers in inverted hybrid perovskite solar cells. *J Mater Chem A* 2017;5:23831–9.
- [434] Janoschka T, Teichler A, Häupler B, Jähner T, Hager MD, Schubert US. Reactive inkjet printing of cathodes for organic radical batteries. *Adv Energy Mater* 2013;3:1025–8.
- [435] Vlad A, Rolland J, Hauffman G, Ernoult B, Gohy JF. Melt-polymerization of TEMPO methacrylates with nano carbons enables superior battery materials. *ChemSusChem* 2015;8:1692–6.
- [436] Iwasa S, Nishi T, Sato H, Nakamura S. Flexibility and high-rate discharge properties of organic radical batteries with gel-state electrodes. *J Electrochem Soc* 2017;164:A884–AA88.
- [437] Sharma P, Damien D, Nagarajan K, Shaijumon MM, Hariharan M. Perylene-polyimide-based organic electrode materials for rechargeable lithium batteries. *J Phys Chem Lett* 2013;4:3192–7.
- [438] Tian D, Zhang HZ, Zhang DS, Chang Z, Han J, Gao XP, et al. Li-ion storage and gas adsorption properties of porous polyimides (PIs). *RSC Adv* 2014;4:7506–10.
- [439] Sasada Y, Langford SJ, Oyaizu K, Nishide H. Poly(norbornyl-NDIs) as a potential cathode-active material in rechargeable charge storage devices. *RSC Adv* 2016;6:42911–16.
- [440] Maniam S, Oka K, Nishide H. N-Phenyl naphthalene diimide pendant polymer as a charge storage material with high rate capability and cyclability. *MRS Commun* 2017;7:967–73.
- [441] Schon TB, Tilley AJ, Kynaston EL, Seferos DS. Three-dimensional aryene diimide frameworks for highly stable lithium ion batteries. *ACS Appl Mater Interfaces* 2017;9:15631–7.
- [442] Liu YT, Liu S, Li GR, Yan TY, Gao XP. High volumetric energy density sulfur cathode with heavy and catalytic metal oxide host for lithium-sulfur battery. *Adv Sci* 2020;7:1903693.
- [443] Kong L, Peng HJ, Huang JQ, Zhu W, Zhang G, Zhang ZW, et al. Beaver-dam-like membrane: a robust and sulphophilic MgBO₃(OH)/CNT/PP nest separator in Li-S batteries. *Energy Storage Mater* 2017;8:153–60.
- [444] Larcher D, Tarascon JM. Towards greener and more sustainable batteries for electrical energy storage. *Nat Chem* 2015;7:19–29.
- [445] Umeshbabu E, Zheng B, Yang Y. Recent progress in all-solid-state lithium-sulfur batteries using high Li-ion conductive solid electrolytes. *Electrochem Energy Rev* 2019;2:199–230.
- [446] Yang X, Luo J, Sun X. Towards high-performance solid-state Li-S batteries: from fundamental understanding to engineering design. *Chem Soc Rev* 2020;49:2140–95.
- [447] Naoi K, Kawase K, Inoue Y. A new energy storage material: organosulfur compounds based on multiple sulfur-sulfur bonds. *J Electrochem Soc* 1997;144:L170–LL72.
- [448] Zhu XM, Zhao RR, Deng WW, Ai XP, Yang HX, Cao YL. An all-solid-state and all-organic sodium-ion battery based on redox-active polymers and plastic crystal electrolyte. *Electrochim Acta* 2015;53:178–55–9.
- [449] Preefer MB, Oschmann B, Hawker CJ, Seshadri R, Wudl F. High sulfur content material with stable cycling in lithium-sulfur batteries. *Angew Chem Int Ed* 2017;56:15118–22.
- [450] Chung WJ, Griebel JJ, Kim ET, Yoon H, Simmonds AG, Ji HJ, et al. The use of elemental sulfur as an alternative feedstock for polymeric materials. *Nat Chem* 2013;5:518–24.
- [451] Griebel JJ, Li GX, Glass RS, Char K, Pyun J. Kilogram scale inverse vulcanization of elemental sulfur to prepare high capacity polymer electrodes for li-s batteries. *Polym Sci Pol Chem* 2015;53:173–7.
- [452] Simmonds AG, Griebel JJ, Park J, Kim KR, Chung WJ, Oleshko VP, et al. Inverse vulcanization of elemental sulfur to prepare polymeric electrode materials for li-s batteries. *ACS Macro Lett* 2014;3:229–32.
- [453] Zhou D, Chen Y, Li B, Fan H, Cheng F, Shanmukaraj D, et al. A stable quasi-solid-state sodium-sulfur battery. *Angew Chem Int Ed* 2018;57:10168–72.
- [454] Fanous J, Wegner M, Grimminger J, Andresen A, Buchmeiser MR. Structure-related electrochemistry of sulfur-poly(acrylonitrile) composite cathode materials for rechargeable lithium batteries. *Chem Mater* 2011;23:5024–8.
- [455] Manners I. Polyferrocenylsilanes: metallopolymers for electronic and photonic applications. *J Opt A Pure Appl Opt* 2002;4:S221–SS23.

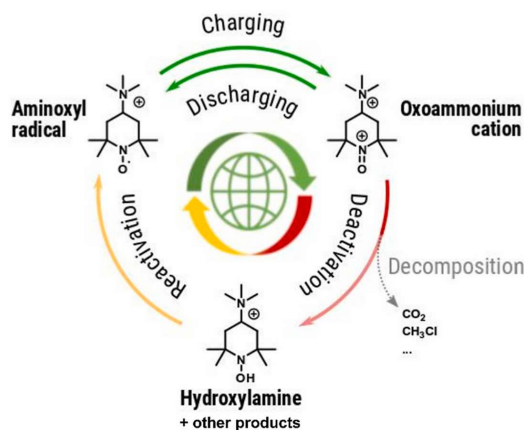
- [456] Akhoury A, Bromberg L, Hatton TA. Redox-responsive gels with tunable hydrophobicity for controlled solubilization and release of organics. *ACS Appl Mater Interfaces* 2011;3:1167–74.
- [457] Dursun F, Ozoner SK, Demirci A, Gorur M, Yilmaz F, Erhan E. Vinylferrocene copolymers based biosensors for phenol derivatives. *J Chem Technol Biot* 2012;87:95–104.
- [458] Yan Q, Feng AC, Zhang HJ, Yin YW, Yuan JY. Redox-switchable supramolecular polymers for responsive self-healing nanofibers in water. *Polym Chem* 2013;4:1216–20.
- [459] Schwartz PO, Fortsch S, Mena-Osteritz E, Weirather-Kostner D, Wachtler M, Bauerle P. Ferrocene-functionalized polyheteroarenes for the use as cathode active material in rechargeable batteries. *Rsc Adv* 2018;8:14193–200.
- [460] Su C, Wang LM, Xu LH, Zhang C. Synthesis of a novel ferrocene-contained polypyrrole derivative and its performance as a cathode material for Li-ion batteries. *Electrochim Acta* 2013;104:302–7.
- [461] Tamura K, Akutagawa N, Satoh M, Wada J, Masuda T. Charge/discharge properties of organometallic batteries fabricated with ferrocene-containing polymers. *Macromol Rapid Commun* 2008;29:1944–9.
- [462] Zhong H, Wang G, Song Z, Li X, Tang H, Zhou Y, et al. Organometallic polymer material for energy storage. *Chem Commun* 2014;50:6768–70.
- [463] Xiang J, Burges R, Haupler B, Wild A, Schubert US, Ho CL, et al. Synthesis, characterization and charge-discharge studies of ferrocene-containing poly(fluorenylethynylene) derivatives as organic cathode materials. *Polymer* 2015;68:328–34.
- [464] Xiang J, Sato K, Tokue H, Oyaizu K, Ho CL, Nishide H, et al. Synthesis and charge-discharge properties of organometallic co-polymers of ferrocene and triphenylamine as cathode active materials for organic-battery applications. *Eur J Inorg Chem* 2016;2016:1030–5.
- [465] Hu D, Liu Q, Chen C. Polymer hydrogel based materials for supercapacitors. *Huaxue Tongbao* 2018;81:483–92.
- [466] Michaelis L, Hill ES. The viologen indicators. *J Gen Physiol* 1933;16:859–73.
- [467] Bird CL, Kuhn AT. Electrochemistry of the viologens. *Chem Soc Rev* 1981;10:49–82.
- [468] Yamaguchi I, Yamamoto M. Synthesis and chemical properties of polyphenylenes cross-linked by electron-accepting viologen moiety. *Polym Bull* 2015;73:1827–39.
- [469] Wang NX, Kahkonen A, Damlin P, Aaritalo T, Kankare J, Kvarnstrom C. Electrochemical synthesis and characterization of branched viologen derivatives. *Electrochim Acta* 2015;154:361–9.
- [470] Beladi-Mousavi SM, Sadaf S, Mahmood AM, Walder L. High performance poly(viologen)-graphene nanocomposite battery materials with puff paste architecture. *ACS Nano* 2017;11:8730–40.
- [471] Stolar M, Reus C, Baumgartner T. Xylene-bridged phosphaviologen oligomers and polymers as high-performance electrode-modifiers for li-ion batteries. *Adv Energy Mater* 2016;6:1600944.
- [472] Mahlia TMI, Saktisandan TJ, Jannifar A, Hasan MH, Matseelar HSC. A review of available methods and development on energy storage; technology update. *Renew Sust Energ Rev* 2014;33:532–45.
- [473] Li Q, Horn M, Wang Y, MacLeod J, Motta N, Liu J. A review of supercapacitors based on graphene and redox-active organic materials. *Materials* 2019;12:703–33.
- [474] González A, Goikolea E, Barrena JA, Mysyk R. Review on supercapacitors: technologies and materials. *Renew Sust Energ Rev* 2016;58:1189–206.
- [475] Kumar Y, Rawal S, Joshi B, Hashmi SA. Background, fundamental understanding and progress in electrochemical capacitors. *J Solid State Electr* 2019;23:667–92.
- [476] Wang Y, Song Y, Xia Y. Electrochemical capacitors: mechanism, materials, systems, characterization and applications. *Chem Soc Rev* 2016;45:5925–50.
- [477] Pell WG, Conway BE. Peculiarities and requirements of asymmetric capacitor devices based on combination of capacitor and battery-type electrodes. *J Power Sources* 2004;136:334–45.
- [478] Simon P, Gogotsi Y. Materials for electrochemical capacitors. *Nat Mater* 2008;7:845–54.
- [479] Ehsani A, Heidari AA, Shirri HM. Electrochemical pseudocapacitors based on ternary nanocomposite of conductive polymer/graphene/metal oxide: An introduction and review to it in recent studies. *Chem Rev* 2019;19:908–26.
- [480] Park HW, Kim T, Huh J, Kang M, Lee JE, Yoon H. Anisotropic growth control of polyaniline nanostructures and their morphology-dependent electrochemical characteristics. *ACS Nano* 2012;6:7624–33.
- [481] Chen W, Rakhi RB, Alshareef HN. Morphology-dependent enhancement of the pseudocapacitance of template-guided tunable polyaniline nanostructures. *J Phys Chem C* 2013;117:15009–19.
- [482] Wu MQ, Snook GA, Gupta V, Shaffer M, Fray DJ, Chen GZ. Electrochemical fabrication and capacitance of composite films of carbon nanotubes and polyaniline. *J Mater Chem* 2005;15:2297–303.
- [483] Wu JF, Zhang QE, Wang JJ, Huang XP, Bai H. A self-assembly route to porous polyaniline/reduced graphene oxide composite materials with molecular-level uniformity for high-performance supercapacitors. *Energy Environ Sci* 2018;11:1280–6.
- [484] Wang DW, Li F, Zhao J, Ren W, Chen ZG, Tan J, et al. Fabrication of graphene/polyaniline composite paper via *in situ* anodic electropolymerization for high-performance flexible electrode. *ACS Nano* 2009;3:1745–52.
- [485] Li J, Xie HQ, Li Y, Liu J, Li ZX. Electrochemical properties of graphene nanosheets/polyaniline nanofibers composites as electrode for supercapacitors. *J Power Sources* 2011;196:10775–81.
- [486] Wang LX, Li XG, Yang YL. Preparation, properties and applications of polypyrroles. *React Funct Polym* 2001;47:125–39.
- [487] Zhou M, Xiong Y, Cao YL, Ai XP, Yang HX. Electroactive organic anion-doped polypyrrole as a low cost and renewable cathode for sodium-ion batteries. *J Polym Sci Pol Phys* 2013;51:114–18.
- [488] Li J, Xie HQ. Synthesis of graphene oxide/polypyrrole nanowire composites for supercapacitors. *Mater Lett* 2012;78:106–9.
- [489] Sanches EA, Alves SF, Soares JC, da Silva AM, da Silva CG, de Souza SM, et al. Nanostructured polypyrrole powder: a structural and morphological characterization. *J Nanomater* 2015;2015:1–8.
- [490] Zhu J, Xu Y, Wang J, Wang J, Bai Y, Du X. Morphology controllable nano-sheet polypyrrole-graphene composites for high-rate supercapacitor. *Phys Chem Chem Phys* 2015;17:19885–94.
- [491] Snook GA, Peng C, Fray DJ, Chen GZ. Achieving high electrode specific capacitance with materials of low mass specific capacitance: potentiostatically grown thick micro-nanoporous PEDOT films. *Electrochem Commun* 2007;9:83–8.
- [492] Alvi F, Ram MK, Basnayaka PA, Stefanakos E, Goswami Y, Kumar A. Graphene-polyethylenedioxythiophene conducting polymer nanocomposite based supercapacitor. *Electrochim Acta* 2011;56:9406–12.
- [493] Liu K, Hu ZL, Xue R, Zhang JR, Zhu JJ. Electropolymerization of high stable poly(3,4-ethylenedioxythiophene) in ionic liquids and its potential applications in electrochemical capacitor. *J Power Sources* 2008;179:858–62.
- [494] Zhao Z, Richardson GF, Meng Q, Zhu S, Kuan HC, Ma J. PEDOT-based composites as electrode materials for supercapacitors. *Nanotechnology* 2016;27:042001.
- [495] Ryu KS, Lee YG, Hong YS, Park YJ, Wu XL, Kim KM, et al. Poly(ethylenedioxythiophene) (PEDOT) as polymer electrode in redox supercapacitor. *Electrochim Acta* 2004;50:843–7.
- [496] Lei CH, Wilson P, Lekakou C. Effect of poly(3,4-ethylenedioxythiophene) (PEDOT) in carbon-based composite electrodes for electrochemical supercapacitors. *J Power Sources* 2011;196:7823–7.
- [497] He YB, Bai YL, Yang XF, Zhang JY, Kang LP, Xu H, et al. Holey graphene/polypyrrole nanoparticle hybrid aerogels with three-dimensional hierarchical porous structure for high performance supercapacitor. *J Power Sources* 2016;317:10–18.
- [498] Zhou H, Yao W, Li G, Wang J, Lu Y. Graphene/poly(3,4-ethylenedioxythiophene) hydrogel with excellent mechanical performance and high conductivity. *Carbon* 2013;59:495–502.
- [499] W. Kangro, Verfahren zur Speicherung von elektrischer Energie, 1949.
- [500] Alotto P, Guarnieri M, Moro F. Redox flow batteries for the storage of renewable energy: a review. *Renew Sust Energ Rev* 2014;29:325–35.
- [501] Noack J, Roznyatovskaya N, Herr T, Fischer P. The chemistry of redox-flow batteries. *Angew Chem Int Ed* 2015;54:9776–809.
- [502] Wang W, Luo QT, Li B, Wei XL, Li LY, Yang ZG. Recent progress in redox flow battery research and development. *Adv Funct Mater* 2013;23:970–86.
- [503] Wei X, Xu W, Vijayakumar M, Cosimbescu L, Liu T, Sprengle V, et al. TEM-PO-based catholyte for high-energy density nonaqueous redox flow batteries. *Adv Mater* 2014;26:7649–53.
- [504] Ziegler MS, Mueller JM, Pereira GD, Song J, Ferrara M, Chiang Y-M, et al. Storage requirements and costs of shaping renewable energy toward grid decarbonization. *Joule* 2019;3:2134–53.
- [505] Brushett FR, Aziz MJ, Rodby KE. On lifetime and cost of redox-active organics for aqueous flow batteries. *ACS Energy Lett* 2020;5:879–84.
- [506] Zhang HQ, Zhang HM, Li XF, Mai ZS, Zhang JL. Nanofiltration (NF) membranes: the next generation separators for all vanadium redox flow batteries (VRBs)? *Energy Environ Sci* 2011;4:1676–9.
- [507] Zhao Y, Si S, Liao C. A single flow zinc/polyaniline suspension rechargeable battery. *J Power Sources* 2013;241:449–53.
- [508] Janoschka T, Martin N, Martin U, Friebe C, Morgenstern S, Hiller H, et al. An aqueous, polymer-based redox-flow battery using non-corrosive, safe, and low-cost materials. *Nature* 2016;534:S9–S10.
- [509] Energy storage program plan february 2011, https://www.energy.gov/sites/prod/files/oeprod/DocumentsandMedia/OE_Energy_Storage_Program_Plan_February_2011v3.pdf; 2011 [accessed 22.07.2021].
- [510] Ha S, Gallagher KG. Estimating the system price of redox flow batteries for grid storage. *J Power Sources* 2015;296:122–32.
- [511] Lai YY, Li X, Zhu Y. Polymeric active materials for redox flow battery application. *ACS Appl Polym Mater* 2020;2:113–28.
- [512] Leung P, Shah AA, Sanz L, Flox C, Morante JR, Xu Q, et al. Recent developments in organic redox flow batteries: a critical review. *J Power Sources* 2017;360:243–83.
- [513] Hofmann JD, Schröder D. Which parameter is governing for aqueous redox flow batteries with organic active material? *Chem Ing Tech* 2019;91:786–94.
- [514] Chakrabarti MH, Mjalli FS, AlNashef IM, Hashim MA, Hussain MA, Bahadori L, et al. Prospects of applying ionic liquids and deep eutectic solvents for renewable energy storage by means of redox flow batteries. *Renew Sustain Energ Rev* 2014;30:254–70.
- [515] Chen RY. Toward high-voltage, energy-dense, and durable aqueous organic redox flow batteries: role of the supporting electrolytes. *Chemelectrochem* 2019;6:603–12.
- [516] Gerhardt CR, Tong LC, Gomez-Bombarelli R, Chen Q, Marshak MP, Galvin CJ, et al. Anthraquinone derivatives in aqueous flow batteries. *Adv Energy Mater* 2017;7:1601488.

- [517] Israeli A, Patt M, Oron M, Samuni A, Kohen R, Goldstein S. Kinetics and mechanism of the comproportionation reaction between oxoammonium cation and hydroxylamine derived from cyclic nitroxides. *Free Radic Biol Med* 2005;38:317–24.
- [518] Khataee A, Wedege K, Dražević E, Bontien A. Differential pH as a method for increasing cell potential in organic aqueous flow batteries. *J Mater Chem A* 2017;5:21875–82.
- [519] Luo JA, Hu B, Hu MW, Zhao Y, Liu TL. Status and prospects of organic redox flow batteries toward sustainable energy storage. *ACS Energy Lett* 2019;4:2220–40.
- [520] Ding Y, Zhang C, Zhang L, Zhou Y, Yu G. Molecular engineering of organic electroactive materials for redox flow batteries. *Chem Soc Rev* 2018;47:69–103.
- [521] Liu M, Tan L, Cao S. Influence of viscosity on energy performance and flow field of a multiphase pump. *Renew Energy* 2020;162:1151–60.
- [522] Morrison G, Yin W, Agarwal R, Patil A. Development of modified affinity law for centrifugal pump to predict the effect of viscosity. *J Energy Res Tech* 2018;140:092005.
- [523] Zhao Q, Zhu Z, Chen J. Molecular engineering with organic carbonyl electrode materials for advanced stationary and redox flow rechargeable batteries. *Adv Mater* 2017;29:1607007.
- [524] Winsberg J, Hagemann T, Janoschka T, Hager MD, Schubert US. Redox-flow batteries: From metals to organic redox-active materials. *Angew Chem Int Ed* 2017;56:686–711.
- [525] Park M, Ryu J, Wang W, Cho J. Material design and engineering of next-generation flow-battery technologies. *Nat Rev Mater* 2016;2:1–18.
- [526] Zhang SP, Guo WJ, Yang FC, Zheng PN, Qiao R, Li Z. Recent progress in polysulfide redox-flow batteries. *Batter Supercaps* 2019;2:627–37.
- [527] Borchers PS, Strumpf M, Friebe C, Nischang I, Hager MD, Elbert J, et al. Aqueous redox flow battery suitable for high temperature applications based on a tailor-made ferrocene copolymer. *Adv Energy Mater* 2020;10:2001825.
- [528] Montoto EC, Cao Y, Hernandez-Burgos K, Sevov CS, Braten MN, Helms BA, et al. Effect of the backbone tether on the electrochemical properties of soluble cyclopropenium redox-active polymers. *Macromolecules* 2018;51:3539–46.
- [529] Jirabovornwisut T, Arpornwihanop A. A review on the electrolyte imbalance in vanadium redox flow batteries. *Int J Hydrog Energy* 2019;44:24485–509.
- [530] Lu YH, Goodenough JB. Rechargeable alkali-ion cathode-flow battery. *J Mater Chem* 2011;21:10113–17.
- [531] Wang Y, Wang Y, Zhou H. A Li-liquid cathode battery based on a hybrid electrolyte. *ChemSusChem* 2011;4:1087–90.
- [532] Zhao Y, Ding Y, Song J, Peng L, Goodenough JB, Yu G. A reversible Br₂/Br⁻ redox couple in the aqueous phase as a high-performance catholyte for alkali-ion batteries. *Energy Environ Sci* 2014;7:1990–5.
- [533] Duduta M, Ho B, Wood VC, Limthongkul P, Brunini VE, Carter WC, et al. Semi-solid lithium rechargeable flow battery. *Adv Energy Mater* 2011;1:511–16.
- [534] Hao T. Viscosities of liquids, colloidal suspensions, and polymeric systems under zero or non-zero electric field. *Adv Colloid Interface Sci* 2008;142:1–19.
- [535] Simon M, Schneck E, Noirez L, Rahn S, Davidovich I, Talmon Y, et al. Effect of polymer architecture on the phase behavior and structure of polyelectrolyte/microemulsion complexes (PEMECs). *Macromolecules* 2020;53:4055–67.
- [536] Oh SH, Lee CW, Chun DH, Jeon JD, Shim J, Shin KH, et al. A metal-free and all-organic redox flow battery with polythiophene as the electroactive species. *J Mater Chem A* 2014;2:19994–8.
- [537] Zhao YF, Si SH, Wang L, Liao C, Tang P, Cao HJ. Electrochemical study on polypyrrole microparticle suspension as flowing anode for manganese dioxide rechargeable flow battery. *J Power Sources* 2014;248:962–8.
- [538] Nagaoka T, Ahmed SM, Ogura K. Electroactivity of polypyrrole colloids enhanced by quinone mediation. *J Electrochem Soc* 1999;146:3378–82.
- [539] Wu S, Zhao Y, Li D, Xia Y, Si S. An asymmetric Zn//Ag doped polyaniline microparticle suspension flow battery with high discharge capacity. *J Power Sources* 2015;275:305–11.
- [540] Zhao Y, Si S, Wang L, Tang P, Cao H. Electrochemical behavior of polyaniline microparticle suspension as flowing anode for rechargeable lead dioxide flow battery. *J Electrochem Soc* 2013;161:A330–AA35.
- [541] Jugović BZ, Trišović TL, Stevanović J, Maksimović M, Grgur BN. Novel electrolyte for zinc-polyaniline batteries. *J Power Sources* 2006;160:1447–50.
- [542] Karami H, Mousavi MF, Shamsipur M. A new design for dry polyaniline rechargeable batteries. *J Power Sources* 2003;117:255–9.
- [543] Zanzola E, Dennison CR, Battistel A, Peljo P, Vrabel H, Amstutz V, et al. Redox solid energy boosters for flow batteries: polyaniline as a case study. *Electrochim Acta* 2017;235:664–71.
- [544] Montoto EC, Nagarjuna G, Hui J, Burgess M, Sekerak NM, Hernandez-Burgos K, et al. Redox active colloids as discrete energy storage carriers. *J Am Chem Soc* 2016;138:13230–7.
- [545] Shen Z, Chen F, Zhu X, Yong KT, Gu G. Stimuli-responsive functional materials for soft robotics. *J Mater Chem B* 2020;8972–91.
- [546] Shu T, Shen Q, Zhang X, Serpe MJ. Stimuli-responsive polymer/nanomaterial hybrids for sensing applications. *Analyst* 2020;145:5713–24.
- [547] Schattling P, Jochum FD, Theato P. Multi-stimuli responsive polymers - the all-in-one talents. *Polym Chem* 2014;5:25–36.

Publications P2

Stability of TMA-TEMPO-based aqueous electrolytes for redox-flow batteries.

P. Rohland, O. Nolte, N. Ueberschaar, M. D. Hager, U. S. Schubert



Abstract:

The TEMPO scaffold is one of the most prominent used polysolite systems in organic redox flow batteries (RFBs). While the aminoxyl radical is well known for his extraordinary stability, there are only a few studies investigating the stability of the respective oxoammonium cation. In this study, we utilize battery experiments to quantify the fade rate of the oxoammonium cation derived from *N,N,N*-2,2,6,6-heptamethylpiperidinyloxy-4-ammonium chloride (TMA-TEMPO) in correlation with temperature and time. The observed capacity decay is mostly caused by a deactivation of the oxidized TMA-TEMPO yielding the corresponding hydroxylamine, which can mostly be regenerated by reoxidation. Additionally, unbalanced compositionally symmetric flow cells are used to compare the fade rate at different temperatures combined with varying hold times showing a strong dependency on temperature and residence time in high states of charge. The acquired results are used for a use-oriented cycling program comprising a single cycle per day. Furthermore, GC-HRMS and isotopic labeling are used to analyze the volatile decomposition products of heated and oxidized TMA-TEMPO, identifying key intermediates of the decomposition mechanism and the role of an aqueous environment.



Stability of TMA-TEMPO-based aqueous electrolytes for redox-flow batteries

Oliver Nolte^{a,b,1}, Philip Rohland^{a,b,1}, Nico Ueberschaar^c, Martin D. Hager^{a,b}, Ulrich S. Schubert^{a,b,*}

^a Laboratory of Organic and Macromolecular Chemistry (IOMC), Friedrich Schiller University Jena, Humboldtstrasse 10, 07743, Jena, Germany

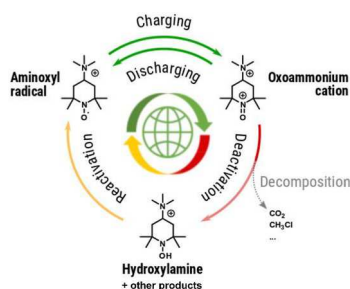
^b Center for Energy and Environmental Chemistry Jena (CEEC Jena), Friedrich Schiller University Jena, Philosophenweg 7a, 07743, Jena, Germany

^c Mass Spectrometry Platform, Faculty of Chemistry and Earth Sciences, Friedrich Schiller University Jena, Humboldtstrasse 8, 07743 Jena, Germany

HIGHLIGHTS

- Key intermediates in the TEMPO decomposition mechanism were identified by GC-HRMS.
- Time- and temperature-depending decomposition studies with different concentrations.
- Capacity fade can almost entirely be reversed by oxidation of the side product.
- Imitation of commercial cycling profiles with highly concentrated electrolytes.

GRAPHICAL ABSTRACT



ARTICLE INFO

Keywords:

Redox flow battery
Aminoxyl radical
Decomposition
Capacity fade rates
Electrolyte reactivation
Use-oriented cycling

ABSTRACT

The TEMPO scaffold is one of the most prominent used polysolite systems in organic redox flow batteries (RFBs). While the aminoxyl radical is well known for his extraordinary stability, there are only a few studies investigating the stability of the respective oxoammonium cation. In this study, we utilize battery experiments to quantify the fade rate of the oxoammonium cation derived from *N,N,N',N',N',N'*-2,2,6,6-heptamethylpiperidinyloxy-4-ammonium chloride (TMA-TEMPO) in correlation with temperature and time. The observed capacity decay is mostly caused by a deactivation of the oxidized TMA-TEMPO yielding the corresponding hydroxylamine, which can mostly be regenerated by reoxidation. Additionally, unbalanced compositionally symmetric flow cells are used to compare the fade rate at different temperatures combined with varying hold times showing a strong dependency on temperature and residence time in high states of charge. The acquired results are used for a use-oriented cycling program comprising a single cycle per day. Furthermore, GC-HRMS and isotopic labeling are used to analyze the volatile decomposition products of heated and oxidized TMA-TEMPO, identifying key intermediates of the decomposition mechanism and the role of an aqueous environment.

* Corresponding author. Laboratory of Organic and Macromolecular Chemistry (IOMC), Friedrich Schiller University Jena, Humboldtstrasse 10, 07743, Jena, Germany.

E-mail address: ulrich.schubert@uni-jena.de (U.S. Schubert).

¹ Both authors contributed equally to the manuscript.

<https://doi.org/10.1016/j.jpowsour.2022.230996>

Received 5 July 2021; Received in revised form 13 December 2021; Accepted 9 January 2022

Available online 10 February 2022

0378-7753/© 2022 The Authors. Published by Elsevier B.V. This is an open access article under the CC BY license (<http://creativecommons.org/licenses/by/4.0/>).

1. Introduction

In the quest for large-scale energy-storage capabilities for renewables, redox-flow-batteries (RFBs) represent a promising technology due to their independent scalability of power output and capacity. However, current commercially available systems, such as the vanadium redox flow battery (VRFB) or zinc/bromine redox flow battery, use precious metals or toxic and corrosive materials and electrolytes [1–4]. In order to overcome these drawbacks, organic redox-active molecules are heavily investigated as replacement [3,5,6]. Of the manifold variety of organic redox-active moieties, aminoxyl-based radicals, such as 2,2,4,4-tetramethylpiperidinyloxy (TEMPO) derivatives are promising candidates due to their accessibility, low cost and fast redox kinetics [7,8].

The redox activity of TEMPO radicals has been in the focus of intense studies, due to their redox-amphoteric behavior. While oxidation leads to the respective oxoammonium cations, which are capable of oxidizing primary and secondary alcohols, reduction yields hydroxylamines [5, 9–16]. Despite their amphoteric behavior, battery applications favor the aminoxyl radical/oxoammonium cation redox step due to suitable (high) redox potentials and pH independence [11].

Although TEMPO radicals are widely considered to be stable upon storage at increased temperatures [17], the respective oxoammonium cation may undergo decomposition reactions by self-oxidation, as discussed later on. However, when used in a battery, the respective redox states must be stable enough to retain the applied charge, ensuring a high energy efficiency and sufficient stability in order to approach decadal lifetimes. Regardless, common tests for novel active materials focus on the cyclability of the material rather than the investigation of the stability of its different redox states, often failing to meet important requirements towards commercialization, although an increasing number of recent studies focuses on the stability assessment of redox-active materials as well [18,19].

To this date, only a limited number of publications regarding the stability of TEMPO-based materials have been issued. In 1969, Murayama et al. [20] investigated the thermal decomposition of 4-oxo-TEMPO, discovering that the main components of the resulting mixture were the respective hydroxylamine and phorone. Even though the decomposition of 4-oxo-TEMPO was ascribed to the acidity of the alpha-hydrogen atoms adjacent to the keto group, the decomposition pathway is similar to that of a TEMPO-based oxoammonium cation, as published by Ma et al. [21] in 2011. They investigated the thermal decomposition of TEMPO in acidic media and distinguished between two different decay mechanisms, a hydrogen abstraction and formation of a carbon-centered radical on the one hand as well as a ring-opening reaction on the other hand. Furthermore, the authors identified key intermediates for the proposed reactions like 2,2,6,6-tetramethyl-1,2,3,6-tetrahydropyridinyloxy radicals, the *N,N*-2,2,6,6-hexamethylpiperidin-4-amine and (poly)unsaturated hydrocarbons as well as ketones. Further work regarding the stability of TEMPO-based active materials in RFB electrolytes has been presented by Zhou et al., who investigated the influence of several structural modifications on the battery performance of the TEMPO scaffold [22], while the influence of the pH on the cycling behavior of a TEMPO-based polysolite was investigated by Xu et al. [23].

In this work, we present the thorough investigation of the decomposition of one of the currently most promising TEMPO-based molecules for aqueous RFB applications, *N,N,N*-2,2,6,6-heptamethylpiperidinyloxy-4-ammonium chloride (TMA-TEMPO), utilized as polysolite material in an all-organic RFB [7]. We assess the influence of temperature and cycling modes on the depletion of the oxoammonium cation by both GC-MS and electrochemical methods and demonstrate an improved cycling protocol, representing a more realistic grid-scale galvanostatic cycling with roughly one cycle per day.

2. Experimental

2.1. MS measurements

Gas-chromatographic quantification of the chloromethane and carbon dioxide in dependency of the temperature were executed on a Thermo Fisher Scientific (Germany) Trace 1310 gas chromatograph. A Thermo Fisher Scientific TSQ 8000 electron-ionization (EI) triple quadrupole mass spectrometer was used for detection. The relative amounts of the monitored substances were calculated using argon, which was used as inert gas in the glovebox where the sample preparation was performed, as internal standard.

Substance identification was carried out by retention time comparison to air for argon and CO₂. Additionally, for CO₂ and CH₃Cl, the exact masses were checked using the same GC coupled to a Q Exactive GC mass spectrometer (Thermo Fisher Scientific, Germany).

For solid-phase-microextraction–gas-chromatography–high-resolution mass-spectrometry (SPME-GC-HRMS) measurements, a Q-Exactive GC (Thermo Fisher Scientific, Germany) with the GC trace 1310 (Thermo Fisher Scientific, Germany) was used. Samples were loaded onto SPME fibers (50/30 μm, 24Ga, StableFlex Divinylbenzene/Carboxen®/PDMS, Supelco, USA) during 10 min at room temperature inside the capped reaction vessels using the manual holder.

Additional details are accessible in the Supporting Information.

2.2. Flow cell tests

The used flow cell was designed as a flat type cell by JenaBatteries GmbH (Germany) and was equipped with graphite felts (GFA6, SGL SE, Germany) as porous electrodes and an anion-selective membrane (FAA-3-50, Fumasep GmbH, Germany). The TMA-TEMPO solutions were charged with 75 mA cm⁻² galvanostatically until a cell voltage of 1.45 V was reached. Afterwards, the cell was further charged potentiostatically until the current density decreased to less than 0.5 mA cm⁻² to receive charged TMA-TEMPO solutions.

Galvanostatic cycling experiments for stability studies were conducted using a current density of 10 mA cm⁻². If a potentiostatic regime was included, the cells were first cycled galvanostatically with 10 mA cm⁻² up to the designated potential and then charged further potentiostatically until the applied current density dropped below 0.5 mA cm⁻².

The explicit conditions and settings are described in detail in the corresponding experimental descriptions in the Supporting Information.

3. Results and discussion

Recent publications regarding TEMPO-based molecules for aqueous RFB applications showed a significant capacity loss over the cycling duration [7,8,24]. As published by Ma et al., this capacity loss may be caused by a self-oxidation of the TEMPO scaffold [21]. In view of a better understanding of the ongoing processes and their impact on the charge storage performance of TMA-TEMPO, we started an investigation of the occurring processes *via* monitoring of the ongoing side reactions using different measurement techniques. Unfortunately, analytical standard tools, such as ¹H NMR spectroscopy or LC-MS, are not applicable to this particular problem due to the high radical content and corrosive nature of the electrolyte solutions. Thus, the volatile substances in the headspace gas phase were analyzed quantitatively and qualitatively *via* gas chromatography-mass spectrometry (GC-MS).

3.1. GC-MS experiments

In a first experiment, deoxygenated charged and uncharged aqueous TMA-TEMPO solutions [7] with a concentration of 1.3 M were transferred into a glovebox in order to avoid atmospheric influence on the measurement, split in several samples and stored for two days at

different temperatures. Analysis of the gas phase using headspace-GC-MS revealed the presence of carbon dioxide as well as chloromethane. As shown in Fig. 1a, carbon dioxide levels increases nearly fivefold upon heating and by one order of magnitude upon oxidation, while chloromethane is only present when charged electrolytes are used.

In order to map the influence of the temperature on the decomposition processes, different samples of a charged 1.3 M TMA-TEMPO solution were prepared in the glovebox as described above and stored in GC-vials at different temperatures (ranging from room temperature to 60 °C) over time (up to 16 d). The amount of the emerging carbon dioxide and chloromethane was analyzed (Fig. 1b). Notably, values for 60 °C show a great variation due to overpressure in the vessels and, thus, are omitted for clarity (see Fig. S2 for a complete data view). This may also be causing deviations at lower temperatures (e.g., for the sample of 16 d/50 °C). The remaining data show that the amounts of carbon dioxide and chloromethane increase with increasing temperature. However, neither a fit of the data for first- nor second-order kinetics shows linear behavior, indicating more complex interdependencies (see Figs. S3 and S4). Nevertheless, the applied method may be too inaccurate for detailed kinetic studies, requiring an analysis of the liquid phase.

A qualitative gas-phase analysis with SPME-Headspace-GC-MS of heated and unheated samples of charged as well as uncharged TMA-TEMPO solutions shows several other volatile substances prominent in the chromatograms (see Fig. S5, Fig. S6 and Table S1), suggesting possible pathways for capacity loss. Firstly, a decomposition product lacking the solubility-promoting ammonium group in 4-position is imaginable, apparently yielded by a Hoffmann-like elimination (see Scheme 1). As a second pathway, a ring-opening oxidation of the C–N bond of the oxoammonium cation is assumed, leading to a nitroso group with a subsequent elimination of nitrous acid or other nitro compounds [21,25]. Both ways would lead to unsaturated hydrocarbons, able to form hydrated intermediates which may be oxidized in the strongly oxidizing milieu. Consequently, carbon dioxide as final product and hydroxylamine (as described for the aminoxyl radical mediated oxidation of alcohols) [26] as a side product can form, with water involved as an oxygen source. As a third pathway for capacity loss, we propose an elimination of chloromethane, resulting in less soluble TEMPO moieties.

In order to study the influence of water, both ^{18}O -labeled and deuterated water were used as solvent in separate tempering experiments. The isotopic pattern of the emerging carbon dioxide, chloromethane and other volatile substances were analyzed, confirming the assumption that water is indeed involved in the decomposition pathways of TMA-TEMPO (see Fig. S7 and Fig. S8). While isotopic labelling with ^{18}O produces C^{18}O_2 and other labeled intermediates of the proposed self-oxidation of the TEMPO scaffold, deuterated water does not

change the isotopic pattern of the generated products, as verified by software-supported analysis of isotopologues (see Table S2) [27].

3.2. Battery experiments

Since a quantification of the TMA-TEMPO decay via ^1H NMR or LC-MS is not possible, charge/discharge battery experiments were chosen as the basis for time-dependent decomposition measurements.

All following electrochemical experiments were conducted at 40 °C due to several reasons:

- (1) As shown in the GC-MS data, the temperature has a great influence on the rate of the molecular decomposition of the active material. By increasing the temperature, decomposition reactions should be more pronounced and, thus, better detectable.
- (2) At this temperature, the vapor pressure of water should be low enough to prevent evaporation effects of the electrolyte.
- (3) 40 °C may well be within the considerable temperature limits for a commercially employed redox-flow battery management system.
- (4) Previously reported capacity fade rates were mostly published without any indication of temperature. Since the ambient conditions may vary due to experimental (e.g., by cycling in a glovebox), geographic or climatic conditions, creating an easily implementable common ground seems to be appropriate.

In order to observe the impact of temperature and the changes in composition on the electrolyte performance of a concentrated TMA-TEMPO solution, a 35 Ah L^{-1} (1.3 M) solution was charged galvanostatically and potentiostatically in a cell against methyl viologen (MV). Upon successful charging, the posolyte was removed and split in several samples in order to eliminate the influences of the negolyte or the cell setup and create an easily manageable sample set.

The error of electrolyte fractioning was assessed by discharging several samples individually, yielding a variation of 0.6% (see Fig. S9). However, based on the data collected in the GC-MS experiments, the error due to sample variations for experiments at ambient temperature is estimated to be in the range of the expected fade rate and, thus, these experiments are conducted solely at 40 °C.

The TMA-TEMPO solutions were stored for four, eight and sixteen days at 40 °C and compared to the starting solution, which was not stored. For each data point, two samples were measured. After the storage phase, the solutions were discharged against charged MV in a redox flow cell at ambient temperature in order to determine the residual capacity of the electrolyte. Charging and discharging were conducted galvanostatically at a low current density of 10 mA cm^{-2} .

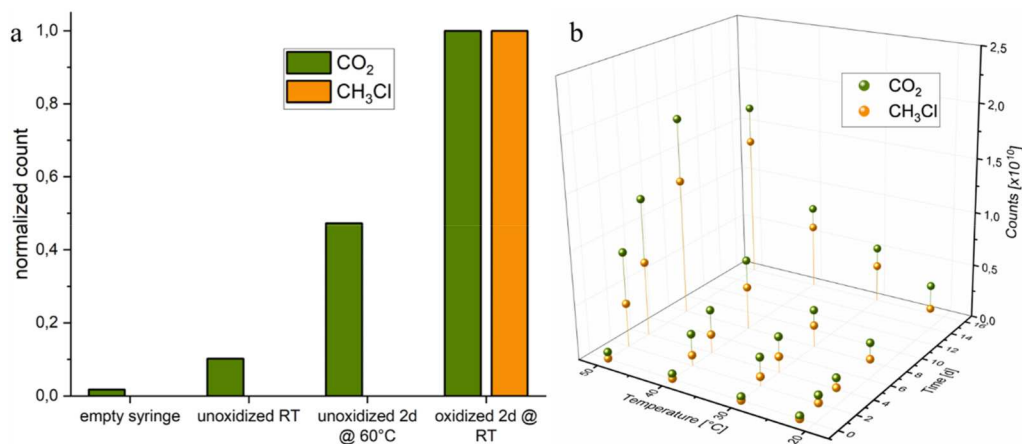
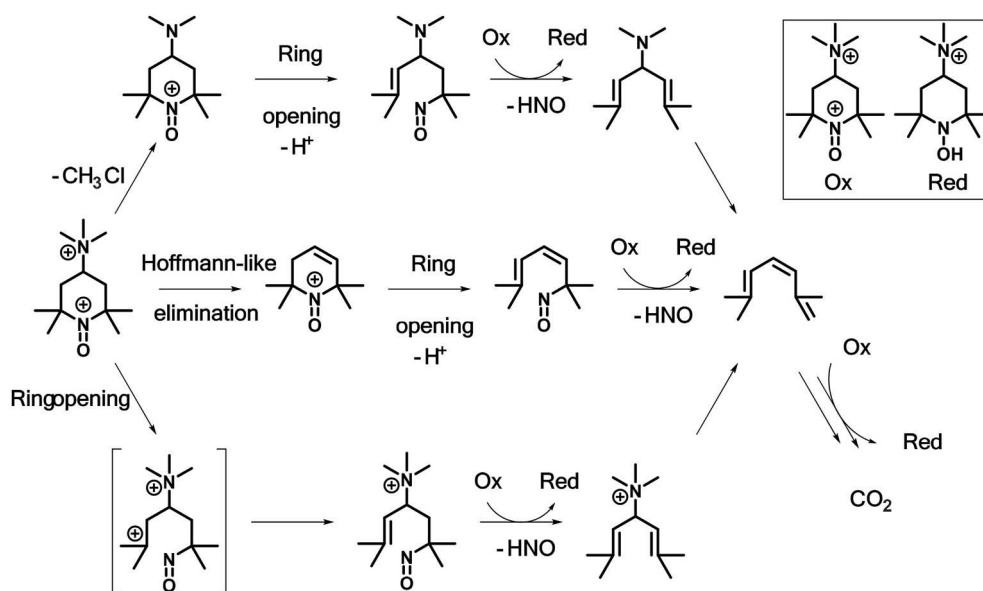


Fig. 1. Headspace-GC-MS results: (a) comparison of emerging carbon dioxide and chloromethane of charged and uncharged TMA-TEMPO-solutions after tempering; (b) influence of temperature and time on the amount of emerging carbon dioxide and chloromethane of charged TMA-TEMPO solutions.



Scheme 1. Proposed decomposition pathways of TMA-TEMPO towards carbon dioxide.

Fig. 2a–c shows typical discharge voltage curves obtained during the experiment at 40 °C. As the storage time progresses, the retained capacity drops relatively fast to a level that would render an operation of

the cell uneconomic. The capacity loss over time at 40 °C is consistent among the samples and is calculated to be 1.15% d⁻¹ (see Fig. 2d and S11 as well as Table S4) directly after tempering.

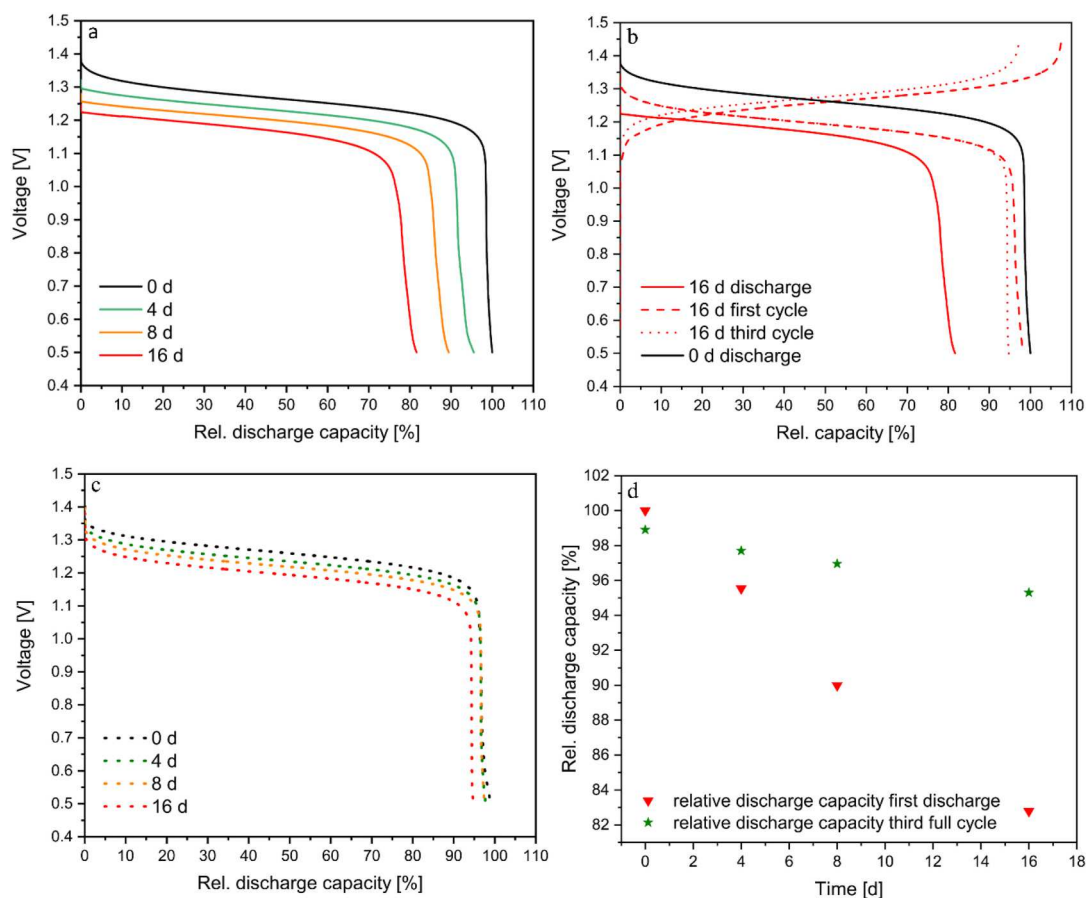


Fig. 2. Battery performance of 1.3 M aq. TMA-TEMPO solutions tempered at 40 °C (vs. excess MV solution). a) Representative discharge curves after 0 d (black), 4 d (green), 8 d (orange) and 16 d (red); b) representative charge/discharge curves after 0 d (black) and first discharge (red solid line), first full cycle (red dashed line) and third full cycle (red dotted line) after 16 d; c) representative discharge curves of the third full cycle after 0 d (black), 4 d (green), 8 d (orange) and 16 d (red); d) relative discharge capacity over time of the first discharge (red) and of the third full cycle (green). (For interpretation of the references to colour in this figure legend, the reader is referred to the Web version of this article.)

We furthermore investigated the possibility to partly regain the lost capacity. In slightly acidic media, hydroxylamines are known to undergo a comproportionation reaction with oxoammonium cations, forming aminoxyl radicals [28]. If hydroxylamine is the main product of the deactivation reaction, it may be electrochemically reoxidizable by simply cycling the battery.

Therefore, the solutions stored at 40 °C were cycled galvanostatically at ambient temperature after the initial discharge. Since reactivating the hydroxylamine electrochemically requires a higher amount of charge, an increase in the apparent charge capacity of the cell well over its nominal capacity is observable (overcharging). This overcharging in the first cycle increases with increasing storage time. After three full cycles, almost no overcharging is apparent while a significant amount of the initially lost discharge capacity is regained. The obtained charge-discharge curves (see Fig. 2b and S10) show a low coulombic efficiency for the first full cycle, converging 100% again within three full cycles. The absence of an additional charging plateau in Fig. 2b supports the hypothesis that the reoxidation of the present hydroxylamine occurs indirectly *via* a comproportionation reaction with an oxoammonium cation. Thus, the discharge curves of the third cycles show a drastically reduced capacity loss and an increase in cell voltage compared to the initial discharge experiment (Fig. 2b). The additional amount of charge required to regenerate the formed hydroxylamine is in good agreement with the reversed capacity loss. Through the described electrochemical regeneration, around 80% of the initially lost capacity could be regained. The remaining capacity loss of the battery is most likely attributed to the irreversible molecular decomposition of the TEMPO moiety itself, leading to an effective decomposition rate of $0.22\% \cdot \text{d}^{-1}$ (Fig. 2d, green stars), which is in good agreement with the estimated amount of hydroxylamine generated and is consistent among the samples [21].

Nevertheless, one has to keep in mind that the electrochemical reoxidation of the formed hydroxylamine to the aminoxyl radical in the capacity-limiting half-cell requires an equal amount of reducible material in the second half-cell, which therefore needs to be over-sized in order to not become capacity-limiting. In case of methyl viologen as negolyte material, this would require a higher amount of the uncharged dication in the initial electrolytes and is, therefore, easily implementable.

3.3. Symmetric cell tests

In order to get a more detailed insight into the decomposition of TMA-TEMPO, a symmetric cell setup was used, in which only TMA-TEMPO is employed as both posolyte and anolyte, avoiding possible influences of the oxygen-sensitive MV.

In 2016, the group of Brushett [14] introduced the symmetric cell cycling method for RFBs, which uses the same electrolyte with an initial state of charge (SOC) of 50% in both half cells. Because the same

electrolyte is used, the involved half-cell reactions are identical and the cell has a voltage of around 0 V (see Fig. 3). This concept was further developed by Goulet and Aziz [19], who confirmed the method's advantages by applying it to other redox-active materials. Furthermore, they developed an elaborate cycling protocol for the electrochemical investigation of active materials, comprising capacity limitation of one half-cell as well as potentiostatic charging and the introduction of hold times in different states of charge.

Thus, we assembled an unbalanced compositionally symmetric cell, which was cycled potentiostatically (limiting current was 0.5 mA cm^{-2}). The employed cycling protocol, inspired by Goulet and Aziz [19], should stress the cell and mimic unfavorable but realistic conditions.

Cycling was performed at room temperature for a total number of 175 cycles with hold phases of 24 h at maximum SOC after 50, 100 and 150 cycles, respectively. The cell was then left with the CLS in its discharged state before repeating this protocol at 40 °C by immersing the capacity limiting reservoir tank in a tempered oil bath. The purpose of this protocol was the determination of capacity fade rates at different temperatures as well as the comparison of capacity fade rates obtained during cycling and during extended hold periods in the fully charged state. The concentration was chosen to be comparably low (0.10 M), in order to keep the length of the experiment in a manageable time frame.

Fig. 4 shows the results of this experiment. After an initial capacity stabilization, the attainable capacity slightly fades, with relatively high coulombic efficiencies. When the cell is then charged to its maximum SOC and left in OCV mode for 24 h, a large capacity drop is observable. In the following few cycles, this drop can partially be recovered by electrochemical re-oxidation of the generated hydroxylamine, apparent by an increasing discharge capacity in the subsequent cycles following each rest time. However, this process seems to be relatively slow compared to the fast redox kinetics of the charging/discharging of the aminoxyl radical/oxoammonium cation redox pair. As a consequence, the cell needs 2–3 cycles to equilibrate after each hold time.

Increasing the reservoir temperature of the capacity-limiting side results in an initial equilibration period with both increased capacity fade and charging capacity and, later on, to a continuation of the capacity fade trend observed at room temperature in cycling mode. During the applied hold times, however, the capacity fade is significantly increased, reflecting the trend observed upon temperature increase in the GC-MS experiments. Fortunately, these larger drops in capacity are still partially reversible by electrochemical re-oxidation.

Table 1 summarizes the results of the experiment. The cell loses an average of 1.50% of its capacity per day in pure cycling mode (without the equilibration sequence at the start of the experiment) and 2.34% per day during hold times at maximum SOC at room temperature. The average capacity fade rate at 40 °C is calculated as 3.12% per day during the hold times and 1.09% per day in cycling mode. A great difference in the cycle-based fade rate assessment between unit and increased cycling rates can be seen (entries one and two as well as three and four),

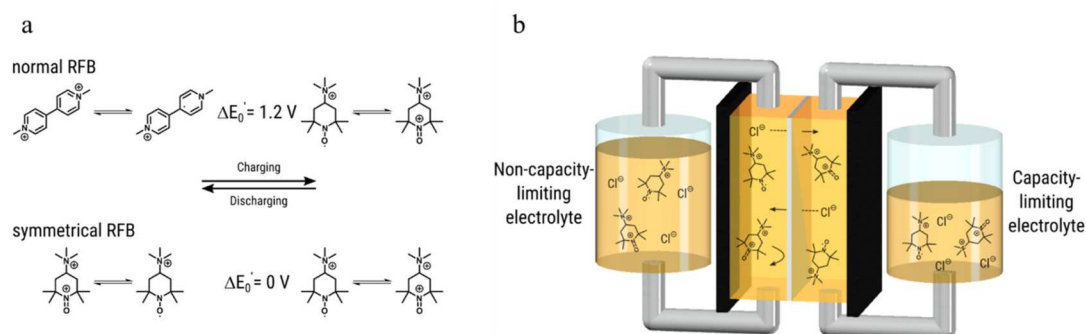


Fig. 3. (a) Cell reactions of a “normal” (asymmetric) RFB represented by the MV/TMA-TEMPO system (top) and a symmetric TMA-TEMPO RFB (bottom); (b) Schematic illustration of an unbalanced compositionally symmetric RFB.

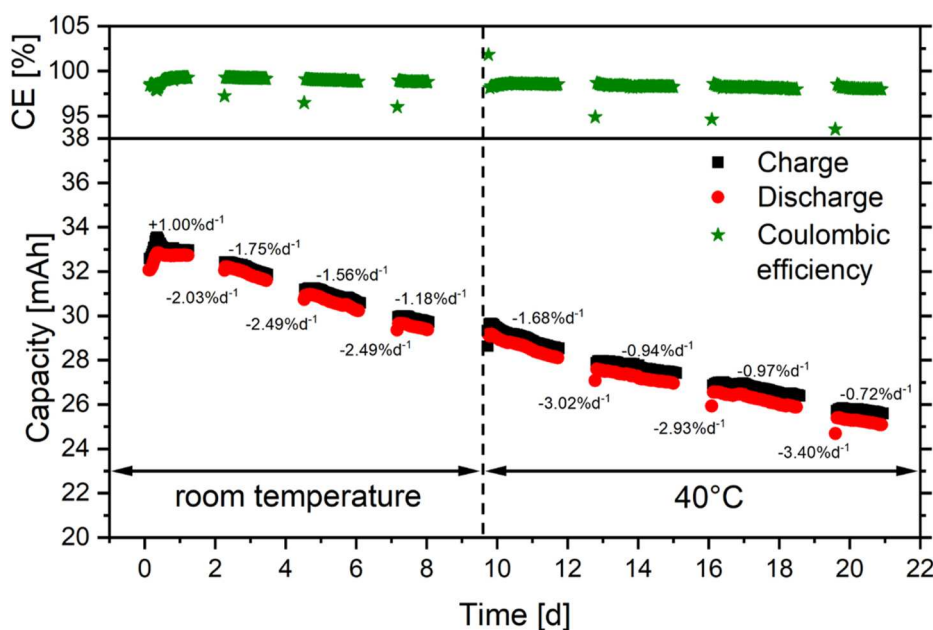


Fig. 4. Charge and discharge capacities as a function of time of an unbalanced compositionally symmetric cell with potentiostatic cycling and hold times. The cell used 0.1 M solutions of TMA-TEMPO; 15 mL on the capacity-limiting side (CLS) and 25 mL on the non-capacity-limiting side (NCLS). Temperatures indicate the reservoir temperature. Temporal fade rates were determined by linear regression of the respective cycling sequences (for continuous cycling sequences, the initial capacity drop was omitted).

Table 1

Experimentally obtained average capacity fade rates for the experiment of Fig. 4. Fade rates were obtained by linear regression.

Entry	Average capacity fade rate		Experimental conditions	
	cyclic [%]	temporal [% d ⁻¹]	cycles per day	reservoir temperature
1	2.34	2.34	1	RT (23 °C)
2	0.046	1.50	32.3	RT (23 °C)
3	3.12	3.12	1	40 °C
4	0.052	1.09	21.1	40 °C

verifying the proposed use of a temporal fade rate measure [19]. However, even the average temporal fade rates for unit and increased cycling rates at both temperatures differ, hinting at an SOC dependency of the capacity fade rate, as both differ in the temporal average SOC that the electrolyte is being kept at. However, the measurements also indicate a more complex relationship between the overall active material concentration of the TMA-TEMPO electrolyte and its capacity fade rate, as higher fade rates compared to the highly concentrated solutions are observed.

Further noticeable is the increasing cycle duration over the course of the experiment. While this is certainly caused by the more sluggish kinetics of the hydroxylamine/aminoxyl radical redox pair, we do not know how electrode kinetics of the battery may be influenced by further decomposition products.

After each rest time, the subsequent cycle shows a stark decline of the CE, which mainly relates to the charge lost during deactivation. Nevertheless, over the course of the whole experiment, only a slight decline is noticeable ($CE_{\text{Start}} = 99.2$, $CE_{\text{End}} = 98.0$). This may be due to an accumulation of hydroxylamine over time since not all of it may be re-oxidized and accessible due to the slow reaction rates. No half-cell showed visible gas evolution over the course of the experiment.

The experiment in particular shows a great difference of cycle and time-based fade rates among different cycling modes and emphasizes the need for a common measure for fade rates. As evidenced by our findings, time-based fade rates are an important measure for the stability of an RFB electrolyte, however, the time that a cell resides in a particular SOC may influence the fade rate measurements. Unfortunately, quantifying the SOC dependence of fade rates requires SOC determination tools that have to provide reliable outputs over an increased period of

time, which are currently not available.

3.4. Symmetric cell cycling with extended rest times and higher concentration

For a final test, we again used a 1.3 M solution of TMA-TEMPO in a compositionally symmetric cell with galvanostatic cycling at both ambient temperature and 40 °C. In this experiment, the electrolyte was first charged and discharged for 20 consecutive cycles, followed by 10 cycles with 12 h rest time each after charge and discharge in order to model an RFB operation of roughly one cycle per day. Both cells were cycled with 10 mA cm⁻² to ensure a high active material utilization. A symmetric setup was chosen due to less crossover and osmotic effects as well as the absence of any influence by possible side reactions with the negolyte (e.g., the oxygen-sensitivity of MV).

Fig. 5 shows the obtained data for both tested temperatures. Pure cycling without rest times for an increased amount of time (about 8 d) shows only a slight variation of the accessible capacity, with almost no capacity fade visible for both ambient temperature and 40 °C. This may be attributed to the relatively short periods of time in a reactive redox state at high SOC. Additionally, due to galvanostatic cycling, the maximum SOC in this experiment is restricted to values lower than attainable by potentiostatic charging. While the average SOC throughout the whole experiment does not change greatly, the average time the system is held in the more reactive redox state increases with increasing rest time. As shown recently, limitations of the SOC may have a great influence in the effective fade rate of flow battery electrolytes [29]. Furthermore, due to the long charging process (in comparison to the experiments at low concentrations), the emerging hydroxylamine has more time to be reoxidized to the corresponding radical, which can be reintroduced in the charging/discharging cycle.

When cycling pauses are introduced, the cell at room temperature shows no measurable capacity fade, whereas a capacity fade slowly starts to evolve in the elevated-temperature cell. At the end of the 12 h cycling pause segment of the experiment, the electrolyte tempered at 40 °C loses roughly 0.35% of its capacity per day which is in the range of previously published data but for room temperature [8,18]. The obtained fade rate is comparable to those obtained during the asymmetric full-cell experiments, where the same storing temperature and concentration are applied to the posolyte.

Furthermore, as already observed in the earlier experiments,

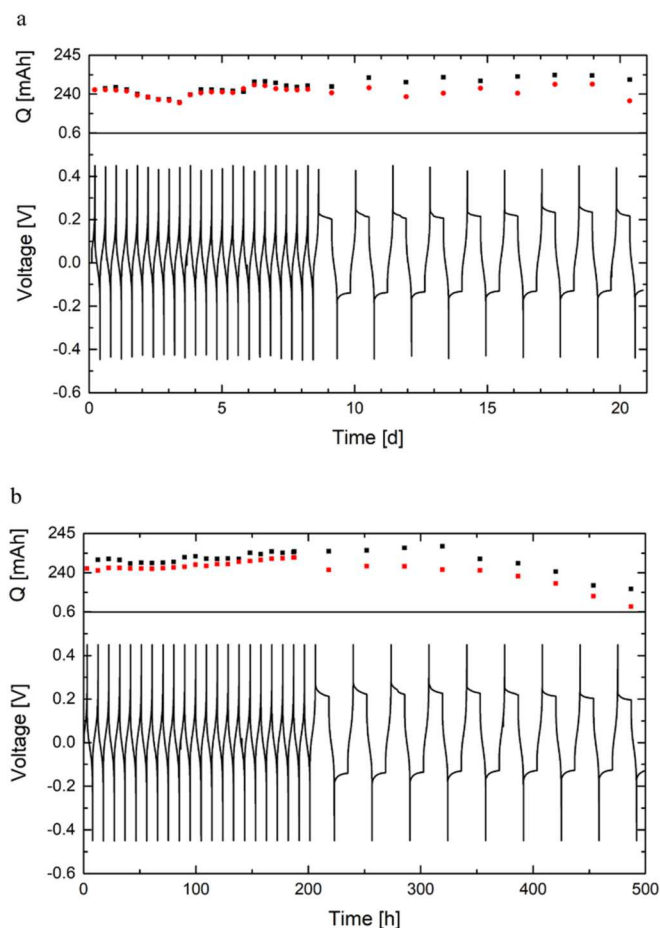


Fig. 5. Traces of voltage and capacity over time for two symmetric cells of TMA-TEMPO (1.3 M), (a) cycled at room temperature and (b) by tempering the capacity-limiting reservoir at 40 °C. In both cases, the cells were cycled galvanostatically at 10 mA cm⁻² throughout the experiment, hold times of 12 h (after each charge and discharge, respectively) were applied during the second phase in order to approximate use-oriented cycling. Black data points for the capacity denote the charging capacity, while red is used for the discharge capacity, respectively. (For interpretation of the references to colour in this figure legend, the reader is referred to the Web version of this article.)

coulombic efficiencies were relatively high during the initial cycling mode without rest periods. While the cell kept at ambient temperature generally higher coulombic efficiencies, they drop significantly with the introduction of rest times for both temperatures (see Fig. S12), which might be explained by a mixture of self-discharge processes as well as degradation reactions.

Based on these findings, it would be interesting to further investigate the influence of SOC restrictions to the fade rates. However, this is beyond the scope of this publication and subject of ongoing studies.

4. Conclusion

With the study at hand, we tried to investigate the capacity fade occurring in TMA-TEMPO solutions, used as RFB posolytes, when influenced by key parameters. In order to get more detailed insights into the decomposition mechanism, we tempered charged TMA-TEMPO solutions, applying different storage times and temperatures. Emerging volatile substances were analyzed via GC-MS, revealing a complex correlation between the amount of decomposition products (CH₃Cl and CO₂), time and storage temperature. The liquid phase was analyzed using both compositionally asymmetric and symmetric battery experiments conducted at ambient temperature and 40 °C.

The performed experiments show influence of time and different cycling modes as well as the importance of tempering protocols. We additionally showed that the initial capacity loss can largely be recovered by reoxidation of the generated hydroxylamine. In order to mimic a use-oriented life of an RFB, an experiment comprising hold times in high and low SOCs was designed in order to simulate cycling on a daily basis. All in all, compared to other molecules suitable for the use in posolyte compositions for all-organic aqueous redox flow batteries, the employed TMA-TEMPO molecule shows a good stability, in case key factors like temperature and state of charge are managed, e.g., by a proper battery management system.

At this point, we want to emphasize again the use of time-dependent capacity fade rates or the indication of half-life (fraction-life) values instead of cycle-dependent decomposition rates. To further develop this approach published by Aziz, we added temperature-dependent measurements, resulting in more pronounced fade rates, which may be exceptionally helpful for testing relatively stable electrolyte compositions with slow fade rates. Furthermore, investigations on higher temperatures may be interesting for industrial applications. A similar protocol may even be used to compare active materials with exceptionally small capacity fade rates.

CRediT authorship contribution statement

Oliver Nolte: Conceptualization, Investigation, Data curation, Writing – original draft, Visualization. **Philip Rohland:** Conceptualization, Investigation, Data curation, Writing – original draft, Visualization. **Nico Ueberschaar:** Investigation, Data curation, Writing – original draft. **Martin D. Hager:** Writing – review & editing, Supervision, Project administration. **Ulrich S. Schubert:** Writing – review & editing, Supervision, Funding acquisition.

Declaration of competing interest

The authors declare that they have no known competing financial interests or personal relationships that could have appeared to influence the work reported in this paper.

Acknowledgement

We acknowledge the Thüringer Aufbaubank (TAB), the European Social Fund (ESF), the Thuringian Ministry of Economic Affairs, Science and Digital Society (TMWWdG) for financial support. The study was co-financed by the state of Thuringia (2015 FGI 0021) with means of the EU in the framework of the EFRE program.

Appendix A. Supplementary data

Supplementary data to this article can be found online at <https://doi.org/10.1016/j.jpowsour.2022.230996>.

References

- [1] L.Y. Li, S. Kim, W. Wang, M. Vijayakumar, Z.M. Nie, B.W. Chen, J.L. Zhang, G. G. Xia, J.Z. Hu, G. Graff, J. Liu, Z.G. Yang, A stable vanadium redox-flow battery with high energy density for large-scale energy storage, *Adv. Energy Mater.* 1 (2011) 394–400, <https://doi.org/10.1002/aenm.201100008>.
- [2] J. Noack, N. Roznyatovskaya, T. Herr, P. Fischer, Die Chemie der redox-flow-batterien, *Angew. Chem.* 127 (2015) 9912–9947, <https://doi.org/10.1002/ange.201410823>.
- [3] J. Winsberg, C. Stolze, A. Schwenke, S. Muench, M.D. Hager, U.S. Schubert, Aqueous 2,2,6,6-tetramethylpiperidine-n-oxyl catholytes for a high-capacity and high current density oxygen-insensitive hybrid-flow battery, *ACS Energy Lett.* 2 (2017) 411–416, <https://doi.org/10.1021/acsenenergylett.6b00655>.
- [4] L. Zhang, Q. Lai, J. Zhang, H. Zhang, A high-energy-density redox flow battery based on zinc/polyhalide chemistry, *ChemSusChem* 5 (2012) 867–869, <https://doi.org/10.1002/cssc.201100530>.
- [5] P. Leung, A.A. Shah, L. Sanz, C. Flox, J.R. Morante, Q. Xu, M.R. Mohamed, C.P. de Leon, F.C. Walsh, Recent developments in organic redox flow batteries: a critical

- review, *J. Power Sources* 360 (2017) 243–283, <https://doi.org/10.1016/j.jpowsour.2017.05.057>.
- [6] F.R. Brushett, M.J. Aziz, K.E. Rodby, On lifetime and cost of redox-active organics for aqueous flow batteries, *ACS Energy Lett.* 5 (2020) 879–884, <https://doi.org/10.1021/acseenergylett.0c00140>.
- [7] T. Janoschka, N. Martin, M.D. Hager, U.S. Schubert, An aqueous redox-flow battery with high capacity and power: the TEMPTMA/MV system, *Angew. Chem. Int. Ed.* 55 (2016) 14427–14430, <https://doi.org/10.1002/anie.201606472>.
- [8] Y.H. Liu, M.A. Goulet, L.C. Tong, Y.Z. Liu, Y.L. Ji, L. Wu, R.G. Gordon, M.J. Aziz, Z. J. Yang, T.W. Xu, A long-lifetime all-organic aqueous flow battery utilizing TMAP-TEMPO radical, *Inside Chem.* 5 (2019) 1861–1870, <https://doi.org/10.1016/j.chempr.2019.04.021>.
- [9] J. Cong, Y. Hao, G. Boschloo, L. Kloo, Electrolytes based on TEMPO-co tandem redox systems outperform single redox systems in dye-sensitized solar cells, *ChemSusChem* 8 (2015) 264–268, <https://doi.org/10.1002/cssc.201402780>.
- [10] A. Dhar, N.S. Kumar, M. Asif, R.L. Vekariya, Systematic study of mono- and tri-TEMPO-based electrolytes for highly efficient next-generation dye-sensitized photo harvesting, *J. Photochem. Photobiol., A* 363 (2018) 1–6, <https://doi.org/10.1016/j.jphotochem.2018.05.021>.
- [11] H.O. Finklea, N. Madhiri, Reorganization energies of TEMPO/TEMPO+ in water, *J. Electroanal. Chem.* 621 (2008) 129–133, <https://doi.org/10.1016/j.jelechem.2007.07.026>.
- [12] G. Grampp, K. Rasmussen, Solvent dynamical effects on the electron self-exchange rate of the TEMPO/TEMPO+ couple (TEMPO=2,2,6,6-tetramethyl-1-piperidinyloxyradical): Part I. ESR -linebroadening measurements at T= 298K, *Phys. Chem. Chem. Phys.* 4 (2002) 5546–5549, <https://doi.org/10.1039/b206313a>.
- [13] S.J. Liu, H.L. Wang, Y.B. Xing, X.M. Chu, F.Q. Zhao, E.J. Tang, TEMPO functionalized polymers: synthesis and applications, *Curr. Org. Chem.* 20 (2016) 1389–1403, <https://doi.org/10.2174/1385272820666151120000657>.
- [14] J.D. Milshtein, J.L. Barton, R.M. Darling, F.R. Brushett, 4-acetamido-2,2,6,6-tetramethylpiperidine-1-oxyl as a model organic redox active compound for nonaqueous flow batteries, *J. Power Sources* 327 (2016) 151–159, <https://doi.org/10.1016/j.jpowsour.2016.06.125>.
- [15] A. Studer, T. Vogler, Applications of TEMPO in synthesis, *Synthesis* 2008 (2008) 1979–1993, <https://doi.org/10.1055/s-2008-1078445>.
- [16] X. Wei, W. Xu, M. Vijayakumar, L. Cosimbescu, T. Liu, V. Sprenkle, W. Wang, TEMPO-based catholyte for high-energy density nonaqueous redox flow batteries, *Adv. Mater.* 26 (2014) 7649–7653, <https://doi.org/10.1002/adma.201403746>.
- [17] J.F.W. Keana, Newer aspects of the synthesis and chemistry of nitroxide spin labels, *Chem. Rev.* 78 (1978) 37–64, <https://doi.org/10.1021/cr60311a004>.
- [18] D.G. Kwabi, Y. Ji, M.J. Aziz, Electrolyte lifetime in aqueous organic redox flow batteries: a critical review, *Chem. Rev.* 120 (2020) 6467–6489, <https://doi.org/10.1021/acs.chemrev.9b00599>.
- [19] M.A. Goulet, M.J. Aziz, Flow battery molecular reactant stability determined by symmetric cell cycling methods, *J. Electroanal. Chem.* 165 (2018) A1466–A1477, <https://doi.org/10.1149/2.0891807jes>.
- [20] K. Murayama, T. Yoshioka, Studies on stable free radicals. Iv. Decomposition of stable nitroxide radicals, *Bull. Chem. Soc. Jpn.* 42 (1969) 2307–2309, <https://doi.org/10.1246/bcsj.42.2307>.
- [21] Y. Ma, C. Loynes, P. Price, V. Chechik, Thermal decay of TEMPO in acidic media via an N-oxoammonium salt intermediate, *Org. Biomol. Chem.* 9 (2011) 5573–5578, <https://doi.org/10.1039/c1ob05475a>.
- [22] W. Zhou, W. Liu, M. Qin, Z. Chen, J. Xu, J. Cao, J. Li, Fundamental properties of TEMPO-based catholytes for aqueous redox flow batteries: effects of substituent groups and electrolytes on electrochemical properties, solubilities and battery performance, *RSC Adv.* 10 (2020) 21839–21844, <https://doi.org/10.1039/d0ra03424j>.
- [23] X. Junhui, W. Yi, W. Hui, D. Li, L. Chen, Enhanced cyclability of organic aqueous redox flow battery by control of electrolyte pH value, *Chem. Lett.* 50 (2021) 1301–1303, <https://doi.org/10.1246/cl.200967>.
- [24] J. Winsberg, T. Hagemann, T. Janoschka, M.D. Hager, U.S. Schubert, Redox-flow batteries: from metals to organic redox-active materials, *Angew. Chem. Int. Ed.* 56 (2017) 686–711, <https://doi.org/10.1002/anie.201604925>.
- [25] R. Ballini, A. Palmieri, Formation of carbon-carbon double bonds: recent developments via nitrous acid elimination (NAE) from aliphatic nitro compounds, *Adv. Synth. Catal.* 361 (2019) 5070–5097, <https://doi.org/10.1002/adsc.201900563>.
- [26] R. Ciriminna, M. Ghahremani, B. Karimi, M. Pagliaro, Electrochemical alcohol oxidation mediated by TEMPO-like nitroxyl radicals, *ChemistryOpen* 6 (2017) 5–10, <https://doi.org/10.1002/open.201600086>.
- [27] T.U.H. Baumeister, N. Ueberschaar, W. Schmidt-Heck, J.F. Mohr, M. Deicke, T. Wichard, R. Guthke, G. Pohnert, DeltaMS: a tool to track isotopologues in GC- and LC-MS data, *Metabolomics* 14 (2018) 41–51, <https://doi.org/10.1007/s11306-018-1336-x>.
- [28] A.E.J.d. Nooy, A.C. Besemer, H.v. Bekkum, On the use of stable organic nitroxyl radicals for the oxidation of primary and secondary alcohols, *Synthesis* 1996 (1996) 1153–1176, <https://doi.org/10.1055/s-1996-4369>.
- [29] M.A. Goulet, L. Tong, D.A. Pollack, D.P. Tabor, S.A. Odom, A. Aspuru-Guzik, E. E. Kwan, R.G. Gordon, M.J. Aziz, Extending the lifetime of organic flow batteries via redox state management, *J. Am. Chem. Soc.* 141 (2019) 8014–8019, <https://doi.org/10.1021/jacs.8b13295>.

Supporting Information

for

Stability of TEMPO-based aqueous electrolytes for Redox-Flow Batteries

Oliver Nolte^{a,b}, Philip Rohland^{a,b}, Nico Überschaar^c, Martin D. Hager^{a,b}, Ulrich S. Schubert^{*,a,b}

^a Laboratory of Organic and Macromolecular Chemistry (IOMC), Friedrich Schiller University Jena, Humboldtstrasse 10, 07743 Jena, Germany

* E-mail: ulrich.schubert@uni-jena.de

^b Center for Energy and Environmental Chemistry Jena (CEEC Jena), Friedrich Schiller University Jena, Philosophenweg 7a, 07743 Jena, Germany

^c Mass Spectrometry Platform, Faculty of Chemistry and Earth Sciences, Friedrich-Schiller University Jena, Humboldtstrasse 8, 07743 Jena, Germany

Version: 09/03/2023

Table of Content:

General information	1
Chemicals and Materials	1
Cell Assembly:	1
Equipment and settings.....	2
Preparation of charged TMA-TEMPO solutions.....	2
Procedure for GC-MS measurement of carbon dioxide and chloromethane determination: .	3
Procedure for SPME-GC-HRMS measurement for decomposition product determination ..	5
Isotopic labelling procedure	6
Decomposition Experiments.....	7
Headspace-GC-MS experiments for determination of temperature and time dependence evolution of chloromethane and carbon dioxide	7
GC-HRMS measurement for decomposition product determination:	9
Isotopic labelling	14
Cell tests	16
Long-term stability test.....	16
Cycling and hold-time-cycling tests with low-concentrated TMA-TEMPO solutions	21
Cycling and Hold Time-Cycling tests with concentrated TMA-TEMPO solutions.....	22
Literature	23

1 General information

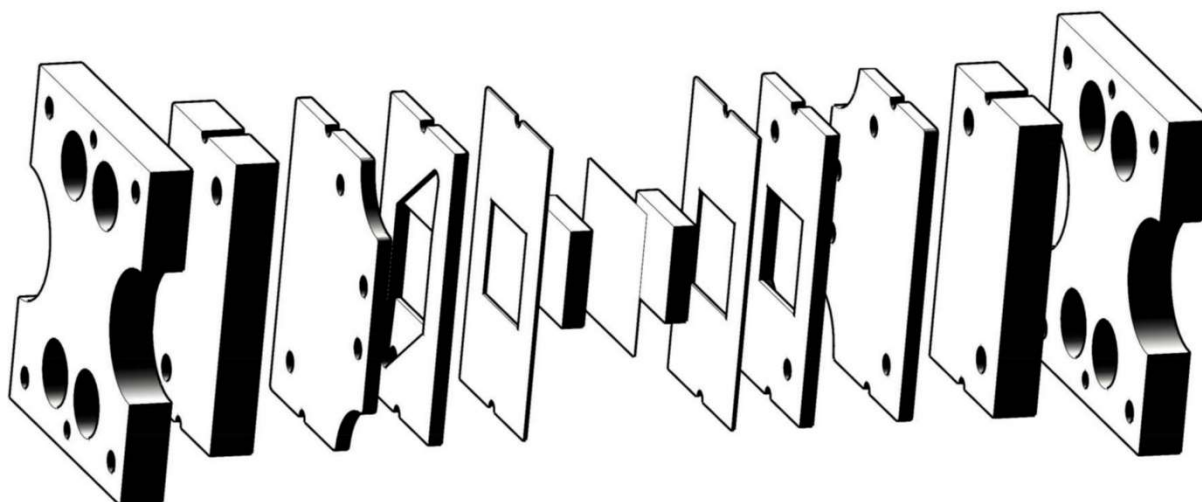
2 Chemicals and Materials

3 Sodium chloride ($\geq 99.5\%$, Fisher Scientific Ltd., United Kingdom), water (97 atom % ^{18}O ,
4 Sigma Aldrich, Germany), deuterium oxide (99.90 atom % deuterium, Eurisotop, France)
5 *N,N,N*-2,2,6,6-heptamethylpiperidinyloxy-4-ammonium chloride (TMA-TEMPO) and *N,N'*-
6 dimethyl-4,4'-bipyridinium dichloride (MV) were used as described previously.^[1] The FAA-3-
7 50 (Fumasep GmbH, Germany) ion-selective membrane for cell assembly was cut into pieces
8 and prewetted at least 24 h in a 1.5 M aq. NaCl solution before installation. GFA6 graphite felts
9 (SGL SE, Germany) were used as porous electrodes.

10 Cell Assembly:

11 The redox flow cell was designed as a flat type with a membrane active area of 5 cm² by
12 JenaBatteries GmbH, Germany. The Fehler! Verweisquelle konnte nicht gefunden werden.
13 displays a detailed overview of the cell components.

a) b) c) d) e) f) g)



14
15 *Figure S1: Schematic presentation of the electrochemical cell. One half cell consists of a metal frame (a), PTFE block with*
16 *hose connections and rubber seal (b), graphite current collector (c), PTFE flow frame (d), rubber sealing (e), graphite felt (f).*
17 *The half cells are separated by an ion-selective membrane (g).*

18 *Equipment and settings*

19 All charge/discharge tests were performed with a VMP3 potentiostat/galvanostat (BioLogic,
20 France). The electrolyte solution was pumped through the cell with a flow rate of approx.
21 20 mL min⁻¹ using a peristaltic pump (Hei-Flow Value 01 Multi equipped with a multi-channel
22 pumping head adapter and C8 multi-channel pumping head, Heidolph, Germany) or at
23 25 mL min⁻¹ using a membrane pump (Simdos 10, KNF Neuberger, Germany). The membrane
24 pump was only used for the long-term cycling experiments with low electrolyte concentration.
25 Tygon® 2375 (ϕ_{inn} 1.6 mm, ϕ_{out} 4.8 mm, Saint-Gobain, France) tubes were used with both
26 pumps. If not specified otherwise, all charging experiments were performed under an argon
27 atmosphere.

28 All inert experiments were performed in a glovebox (UNIlab Plus Eco, MBraun, Germany,
29 O₂ < 1ppm, H₂O < 1 ppm, Ar as protective gas).

30 Room temperature was measured multiple times and assumed as 22 °C. Long-term storage
31 experiments at 40 °C, 50 °C and 60 °C were carried out in a drying oven (M 53, Binder
32 Labortechnik GmbH, Germany). For 30 °C, a 1000 mL beaker was filled with 500 mL sand
33 (Grüssing GmbH, Germany) and placed on a heating plate (Hei-Tec, Heildoph, Germany)
34 equipped with an external temperature sensor (PT 1000, Heidolph, Germany). The temperature
35 of the sand was equilibrated for at least one hour before the samples were placed in the sand.
36 For tempering of the tanks in the long-term cycling experiments, an oil bath heated to 40 °C by
37 a heating plate (Hei-Tec, Heildoph, Germany) equipped with an external temperature sensor
38 (PT 1000, Heidolph, Germany) was used.

39 *Preparation of charged TMA-TEMPO solutions*

40 1.3 M aq. TMA-TEMPO solution was charged galvanostatically against a 1.5 M aq. MV
41 solution with 80 mA cm⁻² until a cell voltage of 1.45 V was reached, followed by potentiostatic
42 charging until the current density dropped below 0.5 mA cm⁻².

43 *Procedure for GC-MS measurement of carbon dioxide and chloromethane determination:*

44 The charged TMA-TEMPO solution was transferred into the glovebox. For each data point,
45 300 μL were transferred with a microlitre pipette (Transferpette® S 100-1000 μL , Brand
46 GmbH & Co. KG, Germany) into a GC-vial (2 mL WO Screw Vials + ND9 Screw Cap with
47 PTFE septa, AppliChrom, Germany). The vials were tempered for 2, 4, 8 and 16 d at room
48 temperature, 30 °C, 40 °C, 50 °C, and 60 °C. For each condition, two vials were prepared, and
49 the gas phase of each vial was analysed twice. The average of these data points was used to
50 create the displayed data.

51 Gas-chromatographic analyses were executed on a Trace 1310 gas chromatograph (Thermo,
52 Germany) equipped with a TriPlus RSH auto sampler. A TSQ 8000 electron ionization (EI)
53 triple quadrupole mass spectrometer (THERMO, Germany) was used for detection. Separation
54 was performed on a Zebron ZB-SemiVolatiles column (Phenomenex, Germany) with the
55 following dimensions: 30+10 m length, 0.25 mm inner diameter and 0.25 μm film thickness.
56 The column was operated with helium carrier gas using an S/SL injector with a column flow of
57 1 mL min^{-1} and a split-less (1 min) injection. Injector temperature was set to 280 °C. After a
58 split-less time of 1 min, the split flow was set to 10 mL min^{-1} . The 50 μL gas-tight syringe was
59 cleaned three times with air pre-injection and rinsed with five plunger strokes inside the sample
60 vial with 25 μL gaseous sample before the injection was performed with 25 μL . After injection,
61 the syringe was rinsed ten times with air (25 μL each). The headspace injection was performed
62 using standard 2 mL vials with a sample volume of 300 μL . The needle penetration depth was
63 set to 10 mm for a proper headspace sampling. The GC oven was held at 40 °C for 5 min and
64 was subsequently raised to 320 °C at 50 °C min^{-1} . This temperature was held for 2 min before
65 cooling and re-equilibration. The mass spectrometer was set to monitor the mass range between
66 30 and 300 m/z in EI+ (70 eV) mode. The MS transfer line and the ion-source temperature were
67 set to 300 °C.

68 The relative amounts of the monitored substances were calculated using the internal standard
69 argon, which was used as inert gas in the glovebox where the sample preparation was
70 performed. Peak detection and integration were carried out using the Thermo Scientific™
71 Xcalibur™ 3.0.63 Quan Browser software with the following settings: mass tolerance
72 500 mmu; mass precision 1 decimal; compounds: argon, carbon dioxide, chloromethane;
73 retention time window 30 s; signal XIC from full scan experiment; peak detection algorithm
74 genesis (Smoothing points 11); peak detection setting “highest peak”. Area ratios of each
75 analyte were determined relative to the internal standard argon. Each replicate sample was
76 measured two times using sample list with a sample order of increasing storage temperatures.
77 The quantification was carried out using the molecular ion for quantification and additionally
78 the ³⁷Cl isotope peak for chloromethane.

79 Substance identification was carried out by retention-time comparison to air for argon and
80 carbon dioxide. For carbon dioxide and chloromethane, additionally, the exact masses were
81 determined on the same GC coupled to a Q Exactive GC mass spectrometer (Thermo Fisher
82 Scientific, Germany). Carbon dioxide: 43.9892 u, error: -0.95 ppm; chloromethane, 49.9918 u,
83 error: -0.34 ppm. Separation was performed on a Zebron ZB-SemiVolatiles column
84 (Phenomenex, Germany) with the following dimensions: 30+10 m length, 0.25 mm inner
85 diameter and 0.25 μm film thickness. Instrument settings: The resolution was set to
86 120,000 (FWHM); mass range was set from 40 to 400 u; automated gain control (AGC target)
87 was set to 1×10^6 and maximum inject time was set to “auto”; auxiliary temperatures were set
88 to 280 °C for both transfer lines 1 and 2; MS transfer line temperature was set to 250 °C and
89 the temperature of the EI source was set to 300 °C; EI was performed at 70 eV energy. Nitrogen
90 for supply of the C-Trap and HCD cell of the GC Orbitrap had a minimum purity of 99.999%
91 (Linde AG, Munich, Germany) and was further dried using a moisture filter (the vendor
92 specifies a gas quality of 6.0 after passage; Thermo, Germany).

93 *Procedure for SPME-GC-HRMS measurement for decomposition product determination*

94 The preparation of the charged solution was carried out like the GC-MS measurements of
95 carbon dioxide and chloromethane. 5 mL samples of the 1.3 M aq. TMA-TEMPO solution were
96 transferred in 25 mL glass bottles (Duran® GL45, Schott AG, Germany) using a 5 mL
97 volumetric pipette (Duran®, Germany) and sealed with a membrane screw cap (screw cap:
98 BOLA PPS EX, GL45, borehole $\varnothing = 34$ mm, Bohlender GmbH, Germany, membrane: silicon
99 elastomer with PTFE coating, 3.3 mm thickness). The samples were tempered at room
100 temperature and 60 °C for two days. For the uncharged samples, the 1.3 M TMA-TEMPO
101 solution was transferred to the glovebox and treated like the charged solution.

102 For SPME-GC-HRMS-measurements, a Q-Exactive GC (Thermo Fisher Scientific, Germany)
103 was used. Separation was performed on a Zebron ZB-SemiVolatiles column (Phenomenex,
104 Germany) with the following dimensions: 30+10 m length, 0.25 mm inner diameter and
105 0.25 μm film thickness. The following MS parameters were set: Resolution 120,000; AGC
106 target 1×10^6 ; maximum ion time: “auto”; scan range 40 to 450 m/z; transfer line 1, 2 were at
107 280 °C and transfer line 3 at the MS at 250 °C. The ion-source temperature was 300 °C and an
108 EI ion volume was installed. The filament delay was turned off and the acquisition was
109 performed between 0.5 and 24 min. The GC trace 1310 (Thermo Fisher Scientific, Germany)
110 was used with the following parameters: After 3 min at 40 °C, the GC oven temperature was
111 raised to 200 °C with 15 °C min^{-1} , then to 320 °C with 30 °C min^{-1} and held for 1 min at
112 320 °C. The S/SL injector was operated in split mode at 260 °C with a flow rate of 10 mL min^{-1} ,
113 split flow was 10 and the column flow 1 mL min^{-1} in constant flow mode. The septum pure
114 flow was set to 1 mL min^{-1} . The sample was loaded onto SPME fiber (50/30 μm , 24Ga,
115 StableFlex Divinylbenzene/Carboxen/PDMS, Supelco, USA) over 10 min at room temperature
116 inside the capped reaction vessels using the manual holder. Injection was performed by keeping
117 the SPME fiber in the injector for 10 min.

118 *Isotopic labelling procedure*

119 The charged TMA-TEMPO solution was freeze-dried with a Christ alpha 2-4 LDplus (Martin
120 Christ Gefriertrocknungsanlagen GmbH, Germany). Afterwards, an appropriate amount for a
121 1.3 M solution of charged TMA-TEMPO was weighed into a GC-Vial (2 mL WO Scew
122 Vials + ND9 Screw Cap with PTFE septa, AppliChrom, Germany), transferred into the
123 Glovebox and 300 μL D_2O or H_2^{18}O was added with a microliter pipette (Transferpette® S 100-
124 1000 μL , Brand GmbH & Co. KG, Germany). The 1.3 M TMA-TEMPO solutions were
125 tempered at 40 °C for four days. The SPME-GC-MS run for the full spectra and the Headspace-
126 GC-MS run were performed as described before.

127

128

129

130

131

132

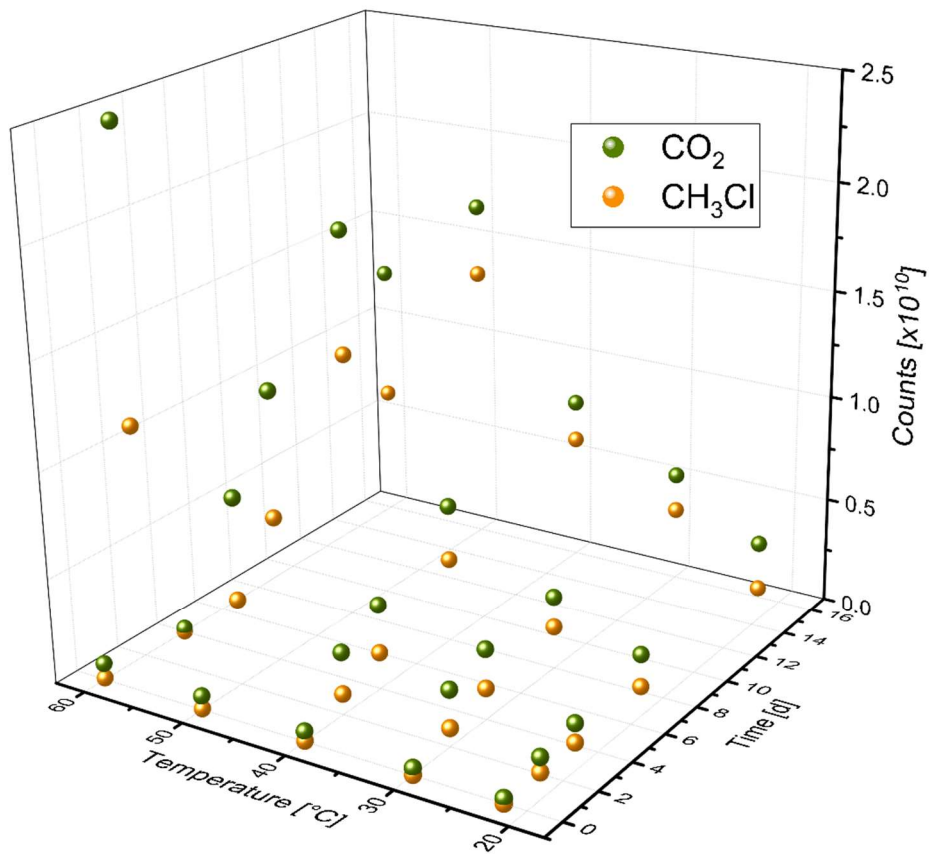
133

134

135 *Decomposition Experiments*

136 Headspace-GC-MS experiments for determination of temperature and time dependent

137 evolution of chloromethane and carbon dioxide

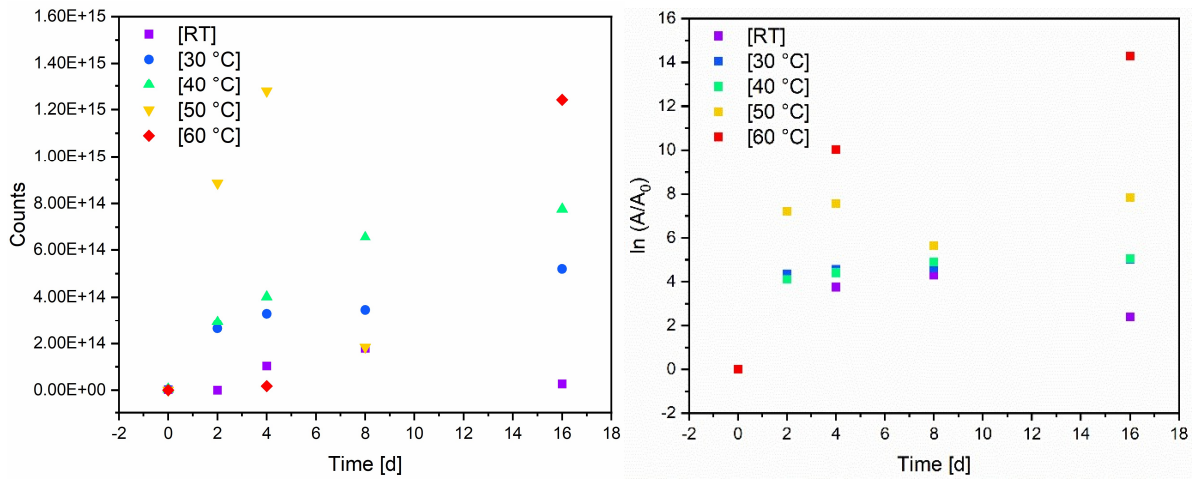


138

139 *Figure S2: Influence of temperature and time on the amount of emerging carbon dioxide and chloromethane of charged TMA-*
140 *TEMPO solutions.*

141

142

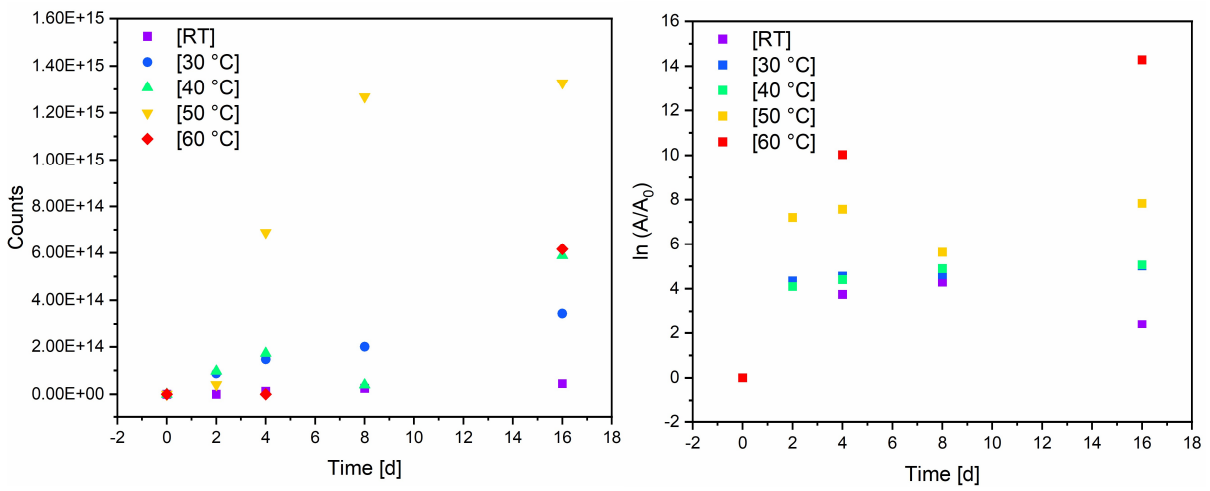


143

144

145

Figure S3: Influence of the tempering time on the amount of emerging carbon dioxide at different temperatures (left) and linearized plot for first order reaction order appraisal (right).



146

147

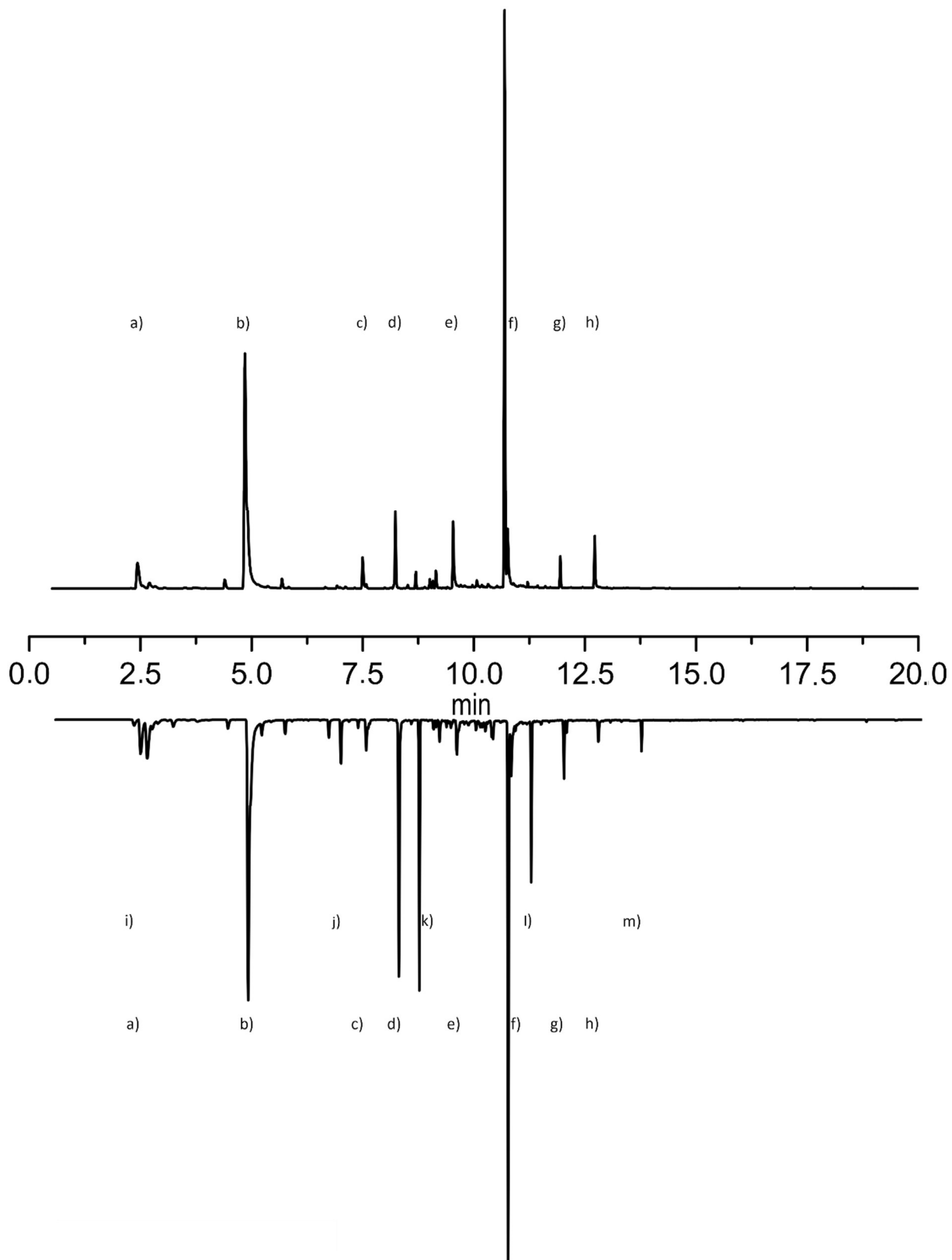
148

149

150

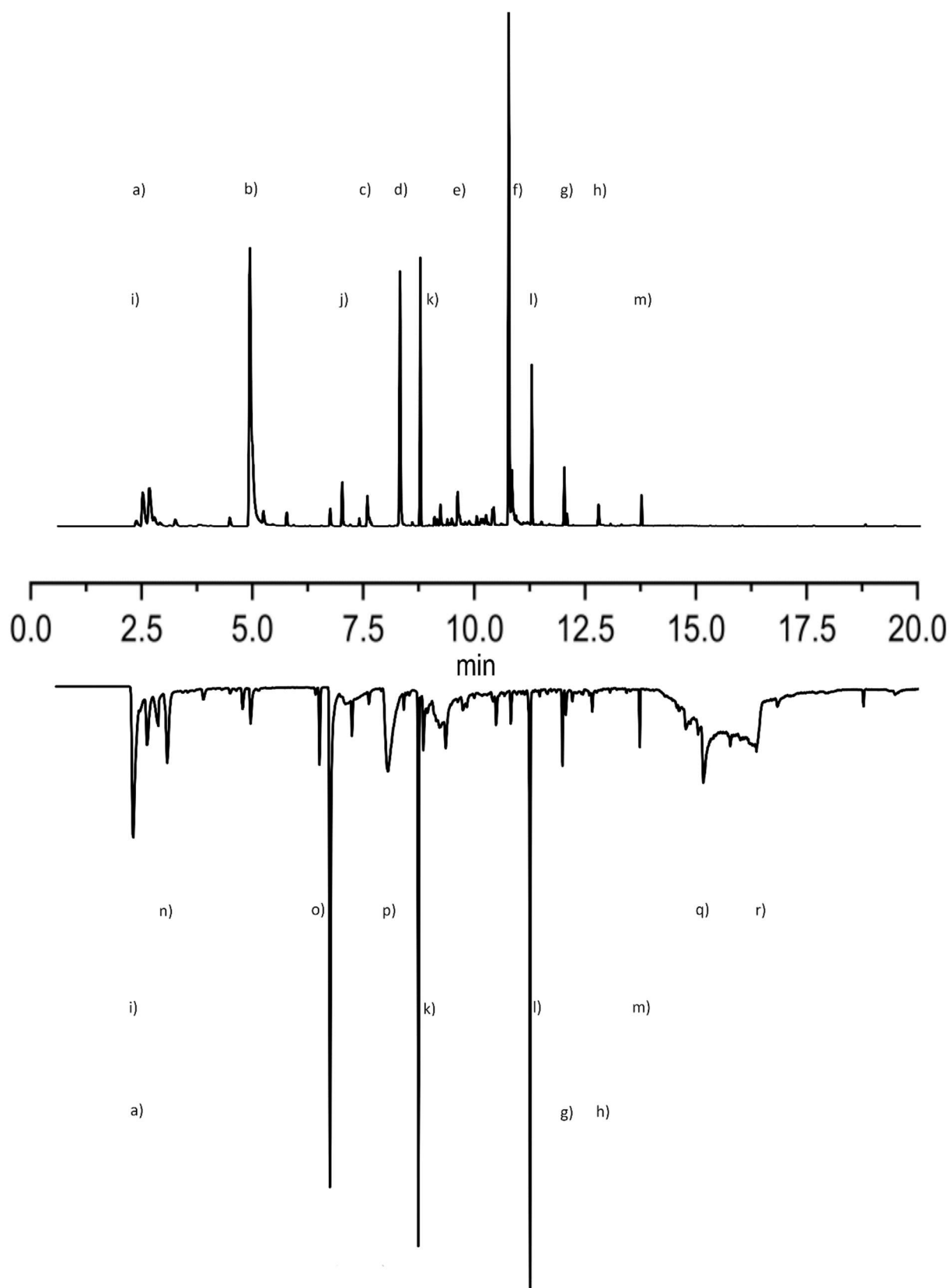
Figure S4: Influence of the tempering time on the amount of emerging chloromethane at different temperatures (left) and linearized plot for first order reaction order appraisal (right).

151 GC-HRMS measurement for decomposition product determination:



152

153 *Figure S5: Full SPME-GC-MS runs of uncharged 1.3 M aq. TMA-TEMPO tempered at room temperature (top) and 60 °C for*
154 *two days (bottom). For assignment of the signals see Table S1.*



155

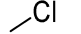
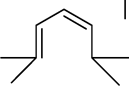
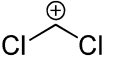
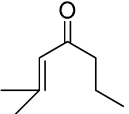
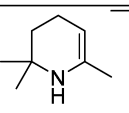
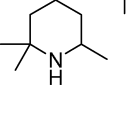
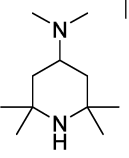
156 *Figure S6: Full SPME-GC-MS runs of uncharged (top) and charged (bottom) 1.3 M aq. TMA-TEMPO tempered at 60 °C for*
 157 *two days. For assignment of the signals see Table S1.*

158

159 Table S1: Peak determination for the SPME-GC-MS runs of charged and uncharged 1.3 M aq. TMA-TEMPO solution at room
 160 temperature and 60 °C.

161 Note: The peaks k, l and m are signals from silicones which have been extracted during the
 162 incubation process from the vial sealing (PTFE coated silicone septa).

peak	conditions	RT [min]	Predicted formula	sum	m/z found	m/z calc.	suggested structure or fragment
a	uncharged, RT, 2d	2.44	[C ₂ H ₃ O] ⁺		43.0178	43.0184	
b	uncharged, RT, 2d	4.85	[C ₇ H ₇] ⁺		91.0543		
b2	uncharged, RT, 2d	4.90	[C ₅ H ₇ N] ⁺		81.0573	81.0573	
c	uncharged, RT, 2d	7.50	[C ₈ H ₁₄ N] ⁺		124.1121	124.1121	
d	uncharged, RT, 2d	8.24	[C ₄ H ₈ O] ⁺		72.0568	72.0575	
e	uncharged, RT, 2d	9.53	[C ₇ H ₁₃] ⁺		93.1012	93.1012	
f	uncharged, RT, 2d	10.69	[C ₉ H ₁₆ ON] ⁺		154.1227	154.1232	
g	uncharged, RT, 2d	11.95	[C ₁₃ H ₂₄] ⁺		180.1870	180.1878	
h	uncharged, RT, 2d	12.72	[C ₉ H ₁₅] ⁺		123.1168	123.1168	

i	uncharged, 60°C, 2d	2.27	[CH ₃ Cl] ⁺⁺	49.9916	49.9923	
j	uncharged, 60°C, 2d	6.93	[C ₉ H ₁₆] ⁺⁺	124.1246	124.1252	
n	charged, 60°C, 2d	3.02	[CHCl ₂] ⁺⁺	82.9449	82.9455	
o	charged, 60°C, 2d	6.46	[C ₈ H ₁₃ O] ⁺	125.0962	125.0966	
p	charged, 60°C, 2d	8.00	[C ₈ H ₁₄ N] ⁺	124.1126	124.1121	
q	charged, 60°C, 2d	15.13	[C ₈ H ₁₇ N] ⁺⁺	127.1353	127.1361	
r	charged, 60°C, 2d	15.99- 16.33	[C ₁₁ H ₂₄ N ₂] ⁺⁺	184.1931	184.1939	

163

164 Even in the uncharged state without extra heating, various ketones and decomposition products
165 of ketones were detected (**Fehler! Verweisquelle konnte nicht gefunden werden.**5, ret. time:
166 2.44 min, 8.24 min, 9.53 min), which may be attributed to manufacturing processes. On the
167 other hand, Hoffmann-like elimination products of the TMA solubility-promoting group were
168 visible (**Fehler! Verweisquelle konnte nicht gefunden werden.**5, ret. time: 7.50 min). This
169 indicates that there are two first main steps in the decomposition pathway of TMA-TEMPO.
170 One may be a ring-opening reaction and loss of a NO-species, like described by Ma *et al.*,^[2]
171 while the other way starts with the elimination of the TMA-group. Both reactions lead to
172 unsaturated hydrocarbons (**Fehler! Verweisquelle konnte nicht gefunden werden.**5, ret. time:

173 12.72 min), which can add water to form the detected ketones/aldehydes. The
174 decomposition/oxidation of these compounds then leads to an accumulation of carbon dioxide.

175

176

177 Heating the uncharged solution didn't seem to alter the composition of the spectra considerably,
178 indicating that the decomposition pathway of TMA-TEMPO is dependent on the formation of
179 the oxoammonium cation as reactive species. However, the detection of chloromethane
180 (**Fehler! Verweisquelle konnte nicht gefunden werden.**, ret. time 2.27 min) and an
181 unsaturated intermediate (**Fehler! Verweisquelle konnte nicht gefunden werden.**, ret. time
182 6.93 min) may hint at an increased rate of the disproportionation reaction at elevated
183 temperatures, generating the reactive oxoammonium cation species.

184 The presence of demethylated TMA-TEMPO in the charged state (**Fehler! Verweisquelle**
185 **konnte nicht gefunden werden.**, ret. time: 15.99-16.33 min) suggests an elimination at the
186 trimethylammonium group as origin of chloromethane. Furthermore, the existence of poly-
187 unsaturated hydrocarbons also points out that elimination reactions must be present. As
188 discussed before, a Hoffmann-like elimination in
189 4-position of the ring as well as a ring opening reaction and subsequent elimination reaction of
190 a NO-species are the dominant decomposition pathways. The oxidative decomposition of the
191 emerging unsaturated compounds then leads to the detected rise of carbon dioxide. The TMA-
192 TEMPO oxoammonium cation serves as oxidant and is reduced to the corresponding
193 hydroxylamine.

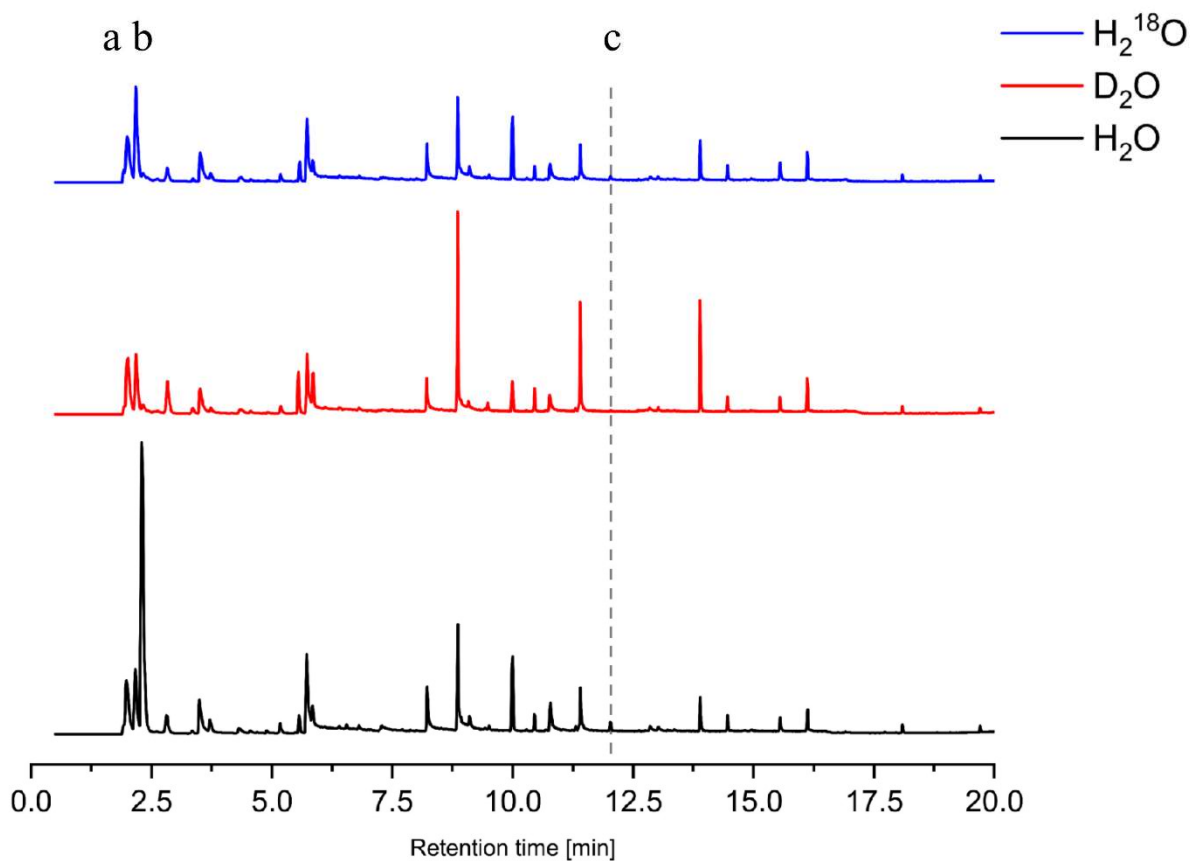
194 The inclusion of water in the reaction pathway was investigated *via* temperature tests in isotope-
195 labeled water and GC-MS investigation.

196 *Isotopic labelling*

197 10 mL of a 1.3 M solution of TEMPTMA were charged against MV potentiostatically (current
198 limit 0.5 mA). The solution was subsequently placed into a 500 mL round-bottom flask and
199 lyophilized. The obtained solid was then introduced into a glovebox, together with degassed
200 samples of H₂O, D₂O and H₂¹⁸O. Solutions in the respective solvents having the initial 1.3 M
201 concentration were then prepared and stored in closed vials. These were afterwards stored at
202 increased temperature (40°C) for two days and used for the headspace GC-MS experiments.

203 As expected, the full SPME-GC-MS runs of the TMA-TEMPO in H₂O, D₂O and H₂¹⁸O do not
204 show big differences in the spectra. Interestingly, beside carbon dioxide and C₂H₃O () only a
205 few isotopically labeled substances (**Fehler! Verweisquelle konnte nicht gefunden werden.**,
206 *e.g.*, ret. time: 12.30 min) were detected, confirming the inclusion of water in the decomposition
207 pathway of TMA-TEMPO but imposing the suspicion that the addition of water leads directly
208 to the formation of carbon dioxide with really fast kinetics.

209 A Headspace-GC-MS was carried out in order to get a more detailed overview of the emerging
210 carbon dioxide and chloromethane (**Fehler! Verweisquelle konnte nicht gefunden werden.**).
211 The chloromethane showed no isotopic labelling, indicating the absence of water in its
212 formation pathway. In contrast, almost all carbon dioxide was present in form of C¹⁸O₂ (m/z =
213 47.9978) when H₂¹⁸O is used, showing that the origin of the oxygen of carbon dioxide is the
214 water. The small amount of C¹⁶O¹⁸O can be explained by the usage of 97 atom% ¹⁸O-labeled
215 water and residual moisture remaining after freeze-drying.



216

217 *Figure S7: SPME-GC-MS runs of 1.3 M aq. TMA-TEMPO solution tempered at 60 °C for 2 d using H₂O, D₂O and H₂¹⁸O as*
 218 *solvent.*

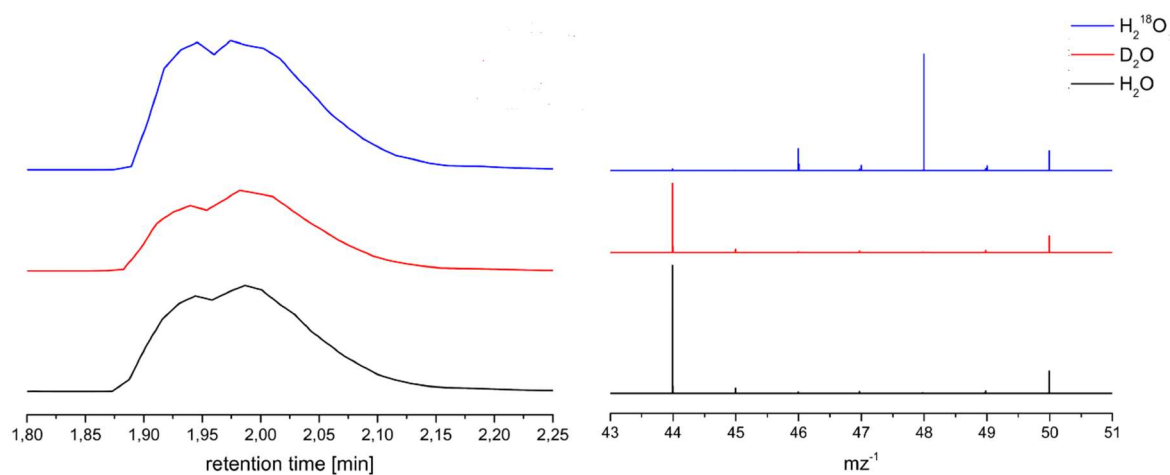


Figure S8: Headspace-GC-MS run of charged 1.3 M aq. TMA-TEMPO solution tempered at 60 °C for two days using normal and isotopic labeled water as solvent and the corresponding mass spectra of the two peaks between 1.90 and 2.15 min.

219 *Table S 2: Peak determination for the SPME-GC-MS runs of charged 1.3 M aq. TMA-TEMPO solution tempered at 60 °C for*
 220 *2 d using H₂O, D₂O and H₂¹⁸O as solvent.*

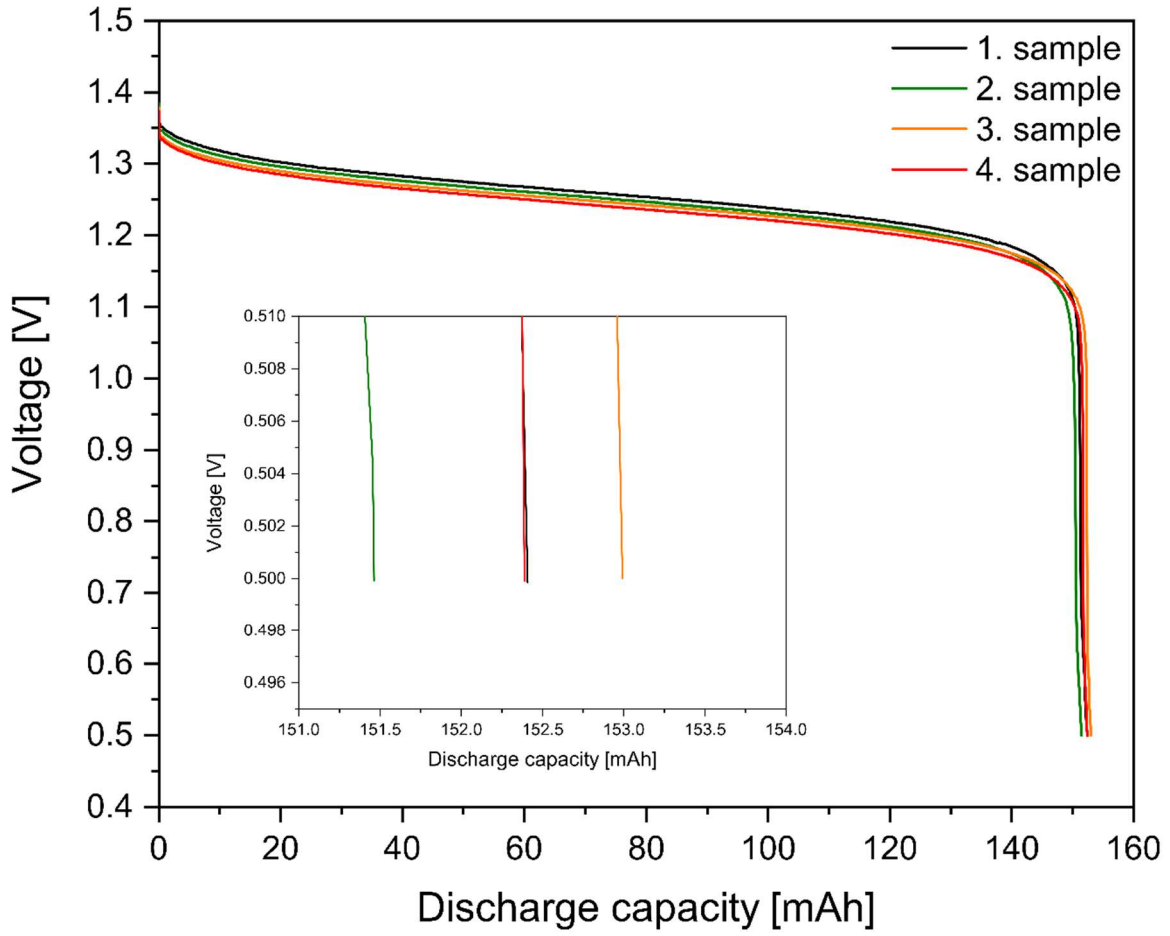
peak	solvent	retention time [min]	Observed species:	<i>m/z</i> found	<i>m/z</i> calculated
a	H ₂ O	1.98	[CO ₂] ⁺⁺ [CH ₃ Cl] ⁺⁺	43.9893 49.9918	43.9898 49.9923
a	D ₂ O	2.01	[CO ₂] ⁺⁺ [CH ₃ Cl] ⁺⁺	43.9893 49.9918	43.9898 49.9923
a	H ₂ ¹⁸ O	1.98	[C ¹⁶ O ¹⁸ O] ⁺⁺ [C ¹⁸ O ₂] ⁺⁺ [CH ₃ Cl] ⁺⁺	45.9935 47.9978 49.9918	45.9941 47.9984 49.9923
b	H ₂ O	2.17	[C ₂ H ₃ O] ⁺	43.0178	43.0184
b	D ₂ O	2.18	[C ₂ H ₃ O] ⁺	43.0178	43.0184
b	H ₂ ¹⁸ O	2.17	[C ₂ H ₃ ¹⁸ O] ⁺	45.0221	45.0221
c	H ₂ O	12.30	[C ₉ H ₁₃ NO ₂] ⁺	167.0941	167.0946
c	D ₂ O	12.30	[C ₉ H ₁₃ NO ₂] ⁺	167.0941	167.0946
c	H ₂ ¹⁸ O	12.30	[C ₉ H ₁₃ NO ¹⁸ O] ⁺	169.0984	169.0983

221 *Cell tests*

222 *Long-term stability test*

223 A 1.3 M aq. TMA-TEMPO solution was charged as described above. For each sample, 5 mL
224 of the charged 1.3 M aq. TMA-TEMPO solution was transferred in a 25 mL glass bottle
225 (Duran® GL45, Schott AG, Germany), sealed with a membrane screw cap (screw cap: BOLA
226 PPS EX, GL45, borehole $\varnothing = 34$ mm, Bohlender GmbH, Germany, membrane: silicon
227 elastomer with PTFE coating, 3.3 mm thickness), using a 5 mL volumetric pipette (Duran®,
228 Germany). The samples were tempered at 40 °C for 4, 8 or 16 d. For each time, two samples
229 were prepared. The previously charged MV solution was used to discharge the tempered TMA-
230 TEMPO solutions after storage. In order to make sure that the discharge capacity is not limited
231 by MV, an excess was used (at least four times volume of 1.5 M MV in comparison to the

232 TMA-TEMPO). Before the experiment argone was bubbled through the MV solution for
233 15 min and the MV solution was held under argon for the whole subsequeunt experiment. All
234 samples were mixed with 5 mL 1.5 NaCl solution, using a 5 mL volumetric pipette (Duran®,
235 Germany), directly before the discharge, in order to ensure a sample volume that is sufficiently
236 large to be manageable in our system, and held under argon during the whole experiment.
237 Sodium chloride was used to minimize osmotic effects. The discharge capacity obtained in the
238 first discharge experiment without storage was taken as 100% for the following experiments.
239 In order to determine the error of sample splitting, we prepared four extra samples and
240 discharged them against MV without further storage. The samples were mixed with 5 mL
241 1.5 NaCl solution, using a 5 mL volumetric pipette (Duran®, Germany), directly before the
242 discharge and held under argon during the whole experiment. The discharge curves showed
243 similar behavior and only narrow discrepancies in discharge capacity among the samples
244 (**Fehler! Verweisquelle konnte nicht gefunden werden.**). The results (see **Fehler!**
245 **Verweisquelle konnte nicht gefunden werden.** for exact data) did prove that the splitting
246 method is suitable for the experiments.



247

248 *Figure S9: Discharge capacity curve for four samples for the evaluation of the influence of the splitting method.*

249 *Table S 3: Data for four samples for the evaluation of the influence of the splitting method.*

Sample	discharge capacity [mAh]
1	152.4
2	151.5
3	153.0
4	152.4
average	152.3
standard deviation [%]	0.55
error interval	152.3 +/- 1.1

250

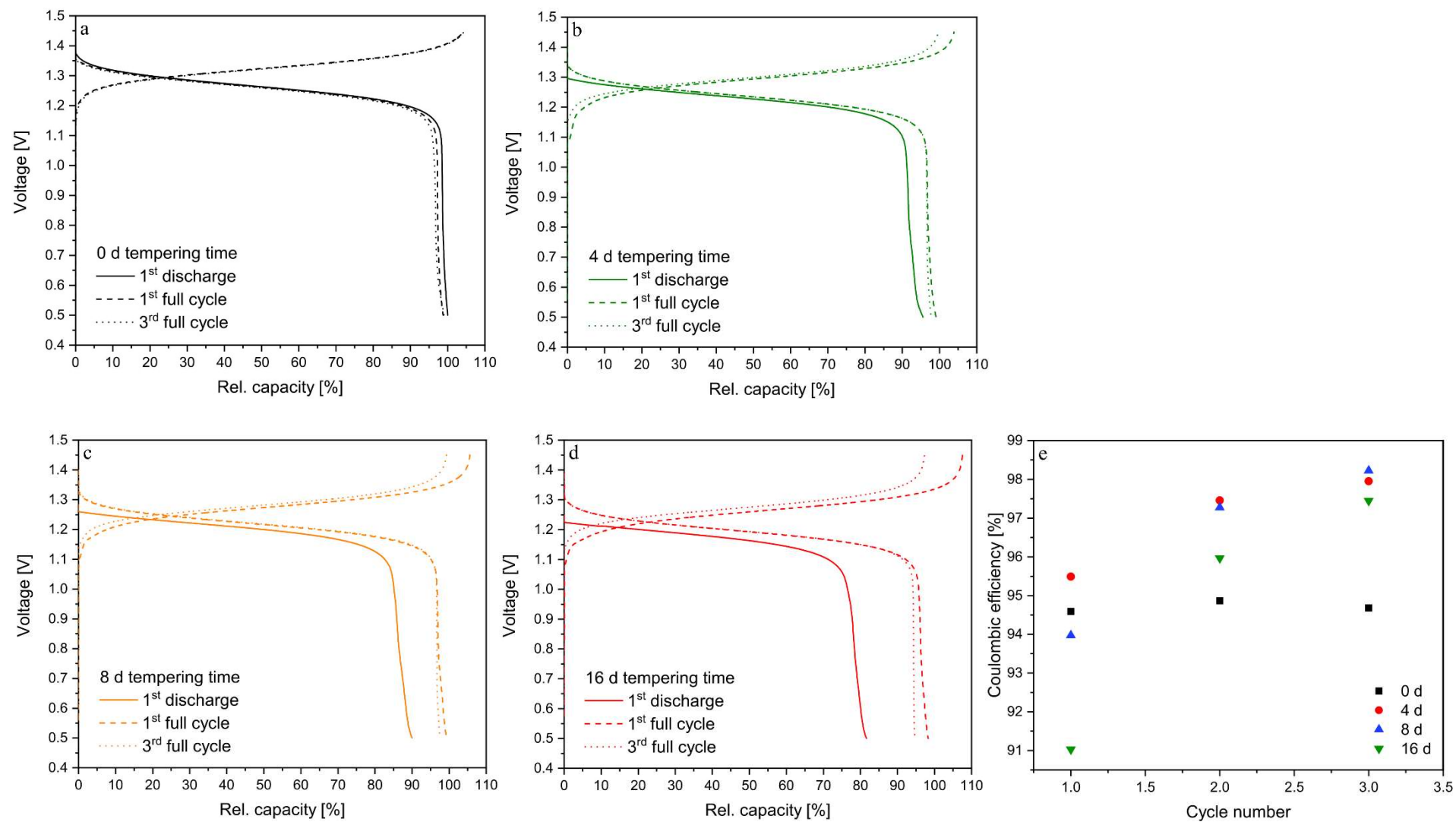


Figure S50: Charge and discharge curves for the tempered, charged TMA-TEMPO solutions for 0 (a), 4 (b), 8 (c), 16 d (d) and coulombic efficiency (e) after storage at 40 °C.

Table S 4: Absolute and rel. charge/discharge capacities in dependency of the tempering and cycle.

t = 0 d, 1st sample	<i>charge capacity [mAh]</i>	<i>discharge capacity [mAh]</i>	<i>rel. charge capacity [%]</i>	<i>rel. discharge capacity [%]</i>
<i>first discharge</i>		152		100.0
<i>first full cycle</i>	158	150	104.4	98.7
<i>third full cycle</i>	158	150	104.5	98.9
t = 4 d, 1st sample				
<i>first discharge</i>		145		95.5
<i>first full cycle</i>	157	150	103.9	99.1
<i>third full cycle</i>	151	148	99.6	97.7
t = 4 d, 2nd sample				
<i>first discharge</i>		143		94.4
<i>first full cycle</i>	156	149	103.1	98.6
<i>third full cycle</i>	151	148	99.9	97.7
t = 8 d, 1st sample				
<i>first discharge</i>		136.7		90.0
<i>first full cycle</i>	160	151	105.6	99.4
<i>third full cycle</i>	150	148	99.3	97.5
t = 8 d, 2nd sample				
<i>first discharge</i>		136		89.5
<i>first full cycle</i>	159	149	104.9	98.5
<i>third full cycle</i>	148	146	97.8	96.4

t = 16 d, 1st sample	<i>charge capacity [mAh]</i>	<i>discharge capacity [mAh]</i>	<i>rel. charge capacity [%]</i>	<i>rel. discharge capacity [%]</i>
first discharge		125		82.8
first full cycle	166	150	109.3	99.1
third full cycle	149	145	98.3	95.9
t = 16 d, 2nd sample				
first discharge		123		81.7
first full cycle	163	149	107.5	98.3
third full cycle	147	144	97.2	94.7

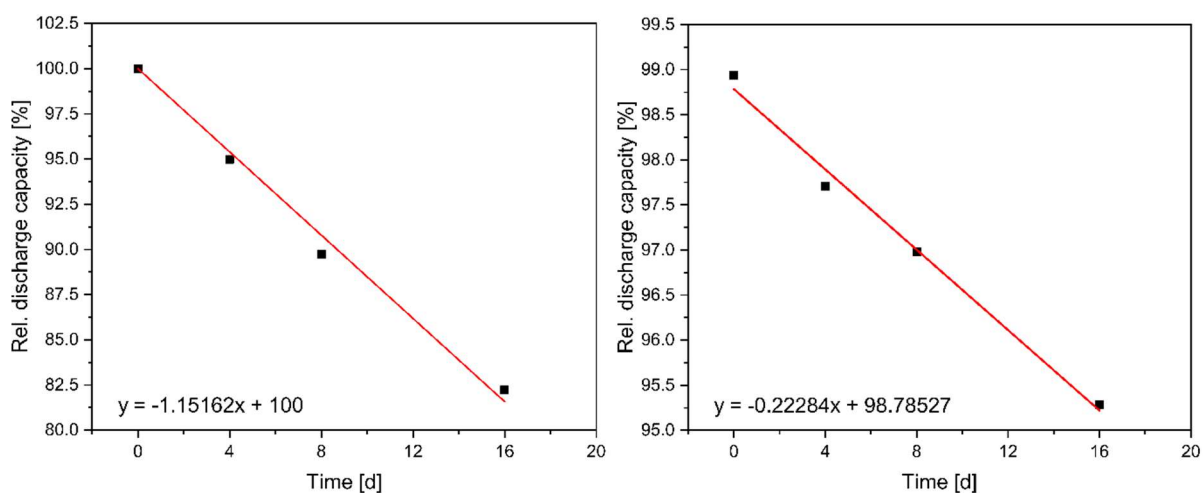


Figure S61: Linear regression of the average discharge capacity over time directly after the tempering (left) and in the third full cycle (right).

Cycling and hold-time-cycling tests with low-concentrated TMA-TEMPO solutions

0.1 M TMA-TEMPO (20 mL) solution was charged against 25 mL 0.13 M MV in 1 M aq. sodium chloride with 80 mA cm^{-2} until 1.45 V cell voltage was reached. Afterwards the cell was charged potentiostatically until the current density dropped under 0.5 mA cm^{-2} . The posolyte was then combined with 20 mL of a 0.1 M uncharged TMA-TEMPO solution and pumped through the TEMPO half-cell for 10 min to receive a 50%-SOC solution.

The 50%-SOC solution was then used to build a compositionally symmetric cell with 25 mL for the non-capacity-limiting and 15 mL for the capacity-limiting half-cell. For this long-term cycling test, two Simdos 10 pumps (KNF Neugebauer, Germany) were used.

The battery was cycled at room temperature 50 times between +0.45 V and -0.45 V with 76 mA cm⁻². After the target cell voltage was reached, the cell was charged potentiostatically until the current density dropped below 2.5 mA cm⁻². After the 50 cycles, a hold time of 24 h at maximum SOC was applied. The complete sequence was repeated two more times.

Afterwards, the tank of the capacity-limiting half-cell was placed in an oil bath and heated to 40 °C by a heating plate (Hei-Tec, Heidolph, Germany) equipped with an external temperature sensor (PT 1000, Heidolph, Germany) and the above described cycling protocol with hold times of 24 h at maximum SOC was applied again.

Cycling and hold time-cycling tests with concentrated TMA-TEMPO solutions

The 50%-SOC solution was created as described above, except for a 55 mL TMA-TEMPO with a target concentration of 1.3 M (using a 1.5 M MV solution). The received solution was split into two samples and two identical symmetric cell setups were built, using 15 mL for the non-capacity limiting side and 8 mL for the capacity limiting half-cell. One setup was held at room temperature and the tank of the capacity-limiting side of the other setup was tempered at 40 °C in an oil bath on a heating plate (Hei-Tec, Heidolph, Germany) equipped with an external temperature sensor (PT 1000, Heidolph, Germany).

For both cell setups, the following cycling procedure was applied: the cell was cycled galvanostatically with 10 mA cm⁻² between +0.45 V and -0.45 V for 20 cycles, followed by 10 cycles with same limiters but with 12 h hold time at each maximum and minimum SOC.

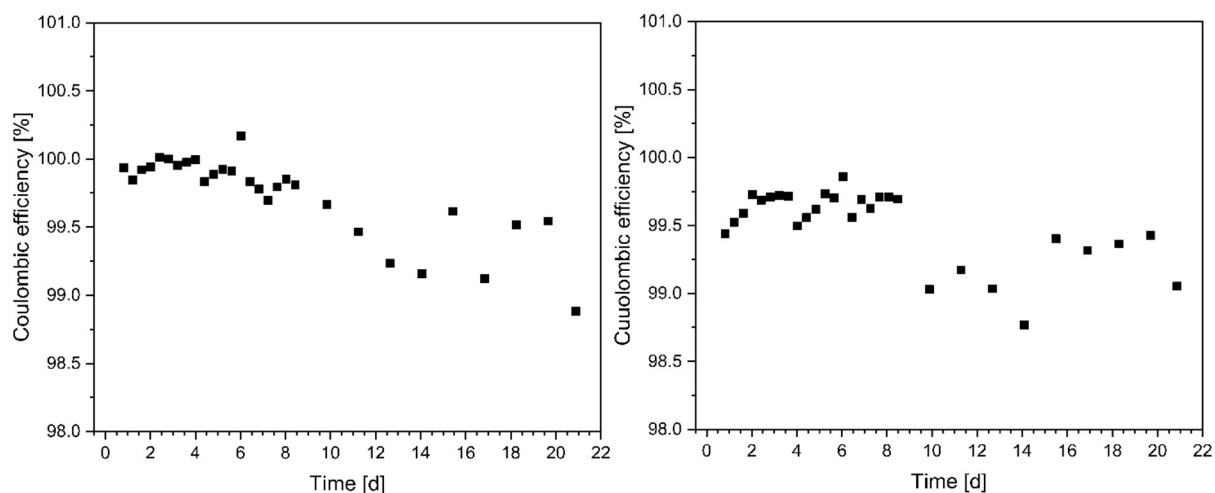


Figure S72: Impact of hold times on the coulombic efficiencies over time when cycling a 1.3 M TMA-TEMPO solution in a symmetric cell setup at room temperature (left) and 40 °C (right).

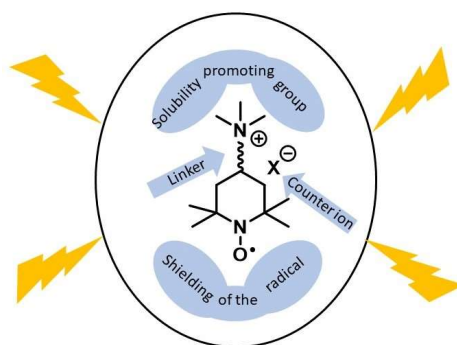
Literature

- [1] T. Janoschka, N. Martin, M.D. Hager, U.S. Schubert, An aqueous redox-flow battery with high capacity and power: the TEMPTMA/MV system, *Angew. Chem. Int. Ed.* 55 (2016) 14427–14430, doi:10.1002/anie.201606472.
- [2] Y. Ma, C. Loyns, P. Price, V. Chechik, Thermal decay of TEMPO in acidic media via an N-oxoammonium salt intermediate, *Org. Biomol. Chem.* 9 (2011) 5573-5578, <https://doi.org/10.1039/c1ob05475a>.

Publications P3

Structural alterations on the TEMPO scaffold and their impact on the performance as active materials for redox flow batteries.

P. Rohland, O. Nolte, K. Schreyer, H. Goerls, M. D. Hager, U. S. Schubert



Abstract:



Trimethylammonium-2,2,6,6-tetramethylpiperidine-1-oxyl chloride (TMA-TEMPO) has been intensively studied for its usage in aqueous organic redox flow batteries. Straightforward synthesis, reliable electrochemistry, fast kinetics and high cycling stability are the advantages of this active material. Nevertheless, it has been shown that elevated temperatures and high states of charge accelerate the decomposition of this material. Hence, a comparative study was performed with five new and one known TEMPO derivatives, to elucidate the structure–stability relationship of the TEMPO scaffold and to investigate the influence on the battery performance. The results show that the introduction of linkers between the solubility-promoting group and the piperidyl core or enhanced shielding of the radical has a great impact on the stability during cycling.

Cite this: *Mater. Adv.*, 2022, **3**, 4278Received 29th July 2021,
Accepted 21st March 2022

DOI: 10.1039/d1ma00663k

rsc.li/materials-advances

Structural alterations on the TEMPO scaffold and their impact on the performance as active materials for redox flow batteries†

Philip Rohland,^{ab} Oliver Nolte,^{ab} Kristin Schreyer,^{ab} Helmar Görls,^c
Martin D. Hager ^{ab} and Ulrich S. Schubert ^{*ab}

Trimethylammonium-2,2,6,6-tetramethylpiperidine-1-oxyl chloride (TMA-TEMPO) has been intensively studied for its usage in aqueous organic redox flow batteries. Straightforward synthesis, reliable electrochemistry, fast kinetics and high cycling stability are the advantages of this active material. Nevertheless, it has been shown that elevated temperatures and high states of charge accelerate the decomposition of this material. Hence, a comparative study was performed with five new and one known TEMPO derivatives, to elucidate the structure–stability relationship of the TEMPO scaffold and to investigate the influence on the battery performance. The results show that the introduction of linkers between the solubility-promoting group and the piperidyl core or enhanced shielding of the radical has a great impact on the stability during cycling.

Introduction

Conventional energy production based on fossil energy sources, such as coal or natural gas, contributes to increasing amounts of greenhouse gasses in the atmosphere. Therefore, there is an urgent need for decarbonization of the energy production around the world. Renewables offer a viable alternative, with solar and wind power being the most prominent representatives.^{3–6} However, unlike conventional power plants based on nuclear power or fossil fuels, these technologies suffer from a discontinuous power output, depending on weather conditions and daytime. To compensate supply shortages or overproduction in a smart grid, the implementation of large-scale energy storage capabilities is highly important. Nowadays, many different technologies have been evaluated for long-term storage of electrical energy.⁷ Since they enable decentralized and scalable applications, electrochemical storage technologies, in particular battery systems, are by far the most practical and promising solution. Among other batteries based on lead and lithium ions, redox flow batteries (RFB) stand out due to

the possibility of tailoring their characteristics according to a broad range of applications with long lifetimes and low self-discharge.⁸ Until now, the all-vanadium RFB is the most technologically advanced RFB type. However, the technology failed to reach high market share in the large-scale battery sector.^{8–10} The main reason is the cost-intensive, toxic and highly corrosive vanadium electrolyte based on concentrated sulphuric acid.¹¹ Organic-based RFB electrolytes may be able to overcome these drawbacks by providing inexpensive water-based electrolytes, making the technology environmentally benign and even more competitive to the widely used lithium and sodium batteries.

Currently developed organic and all organic redox flow batteries (AORFB) use, *e.g.*, alloxazine,^{12,13} flavine,¹⁴ quinones,^{15–17} ferrocene,^{18,19} stable organic radicals^{20–22} and viologen derivatives,^{21,23,24} showing the wide range of possible scaffolds and the possibility to tailor the characteristics of the storage materials. Nevertheless, many organic electrolytes do not meet the requirements for long cycle stability and additionally only a narrow number of molecules were tested under more realistic conditions, *e.g.*, at higher temperatures or dwell times in vulnerable redox state like high state of charge (SOC).^{17,25}

Scaffolds based on the 2,2,6,6-tetramethylpiperidinyloxy (TEMPO) radicals are among the best-investigated active materials and considered as one of the most promising catholyte materials.²⁶ However, there are a few studies reporting about the thermal decomposition of TEMPO radicals and their associated oxoammonium cations.¹ Thus, we developed a new

^a Laboratory of Organic and Macromolecular Chemistry (IOMC),
Friedrich Schiller University Jena, Humboldtstrasse 10, 07743 Jena, Germany.
E-mail: ulrich.schubert@uni-jena.de

^b Center for Energy and Environmental Chemistry Jena (CEEC Jena),
Friedrich Schiller University Jena, Philosophenweg 7a, 07743 Jena, Germany

^c Institute for Inorganic and Analytical Chemistry (IAAC), Friedrich-Schiller
University Jena, Humboldtstrasse 8, 07743 Jena, Germany

† Electronic supplementary information (ESI) available. See DOI: <https://doi.org/10.1039/d1ma00663k>



battery cycling protocol to investigate the influence of temperature and dwell time at high SOC on the lifetime of the active material.²⁷

In this work, we study six TEMPO derivatives with five of them being synthesised for the first time. The molecules are then compared with *N,N,N*-2,2,6,6-heptamethylpiperidinyloxy-4-ammonium chloride (TMA-TEMPO), the current forerunner, regarding their suitability as new catholyte materials for ORFBs and to elucidate a structure–stability relationship. We therefore focus on the influence of structural changes on the TEMPO scaffold and on the molecular stability of the compounds upon thermal stresses and dwell times at high SOC. We were able to demonstrate that the introduction of a linker between the piperidyl core and the solubility promoting group or enhanced shielding of the radical has a great impact on the stability, leading to a TEMPO derivative which is stable at room temperature even if dwell times are applied. However, the compound was found to be less stable at an elevated temperature of 40 °C.

Scope

In a recent publication from our group, we investigated the decomposition of TMA-TEMPO (**1**) and the associated oxoammonium cation **1**⁺ in detail. The results of the extensive gas chromatography–mass spectrometry experiments support the findings by Ma *et al.* and Takata *et al.*^{1,2} The proposed mechanism is summarized in Scheme 1. Furthermore, the findings of the study suggest three possible decomposition pathways (see Scheme 2).²⁷ The first starts with a Hoffmann-like elimination of the trimethylammonium group and generation of a double bond. Liu *et al.* recently proposed that the introduction of a linker between the solubility-promoting group (SPG) and the piperidyl core may result in an increase of the stability of the active material.²⁶ The authors suggested that the decoupling of the strong electron-withdrawing trimethyl ammonium group from the piperidine core reduces electronic effects, like

inductive effects, that can promote ring opening reactions. Furthermore, the introduction of a linker may prevent the Hoffmann-like elimination that results in the formation of endocyclic double bonds. To investigate these effects, we decided to synthesise the amide molecule **2** as well as the sulfonamide derivative **3** and compare them to the ether system **4**, which Liu²⁶ had introduced previously. The electron-withdrawing effect expected for both the amide and the sulfonamide groups is lower compared to that of the ether **4** and, thus, the decomposition rate may be further reduced. Additionally, these linkers may be more stable towards possible pH changes, caused by water splitting or other side reactions during battery cycling.

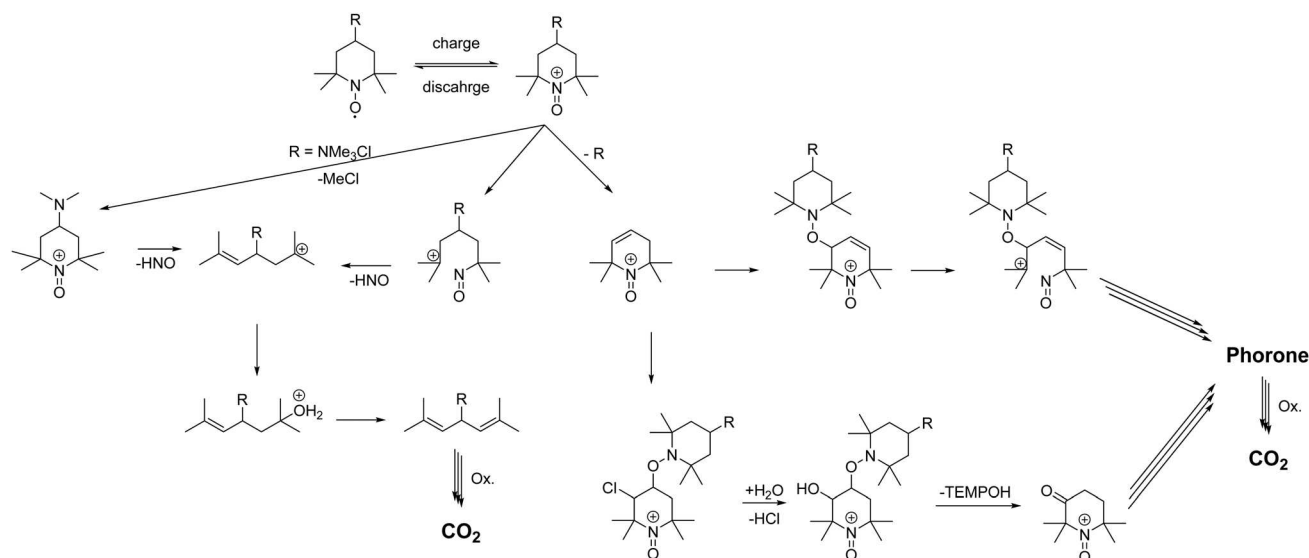
The second decomposition pathway starts directly with a ring-opening reaction by breaking one of the C–N bonds next to the oxoammonium cation. As the TEMPO radical and its oxoammonium cation are stabilised by the shielding effect of the four neighbouring methyl groups, we intended to enhance this shielding effect by introducing tetrahydropyran rings. In the resulting spiro-TEMPO compound **5**, the reactive site of the molecule should be better protected and, thus, possible ring-opening reactions with subsequent decomposition reactions may be hindered.

The last pathway includes the loss of chloromethane. Here, the nucleophilic character of the counterion may play an important role. Thus, we decided to substitute the chloride ion with the less nucleophilic tetrafluoroborate counterion to yield the TMA-TEMPO BF₄ salt **6**. Furthermore, we intended to investigate if the switch to a triethyl-ammonium-bearing derivative **7** might suppress the formation of halogenoalkanes or the elimination of pathway one.

Experimental section

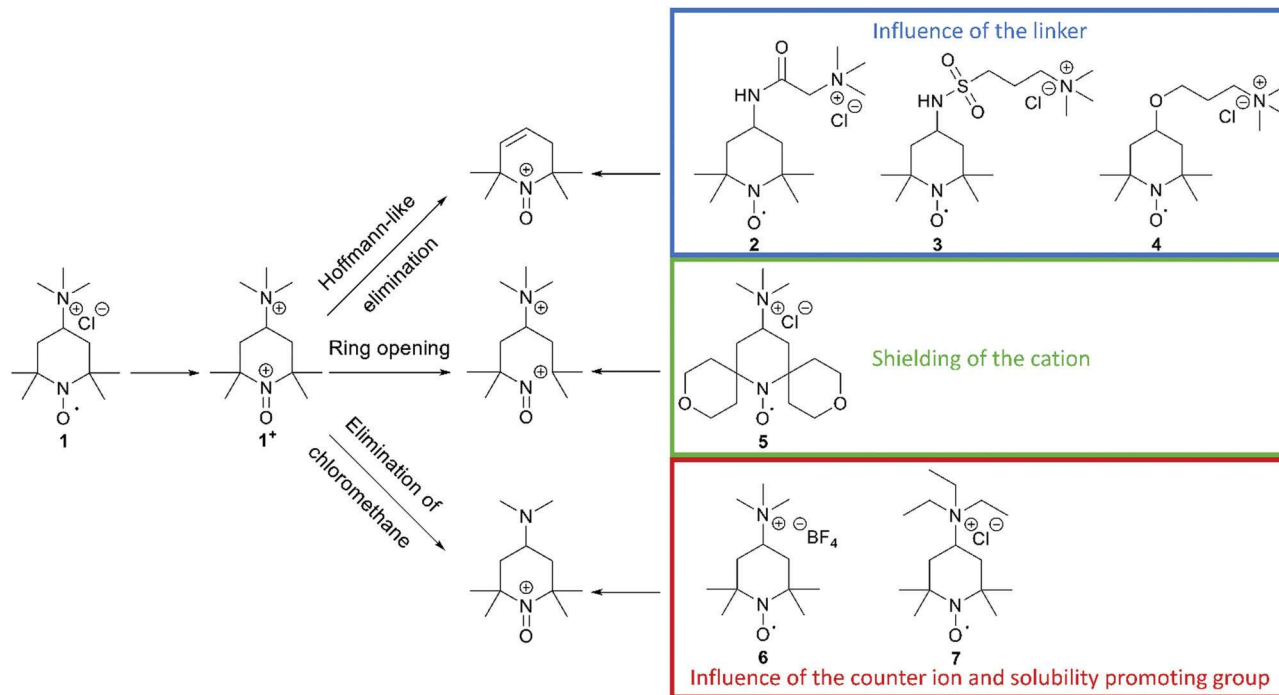
Chemicals and materials

Chemicals for synthesis were purchased with a purity exceeding 95% and were used as received. Details can be obtained from



Scheme 1 Schematic representation of the proposed decomposition mechanism of TEMPO derivatives according to Ma *et al.* and Takata *et al.*^{1,2}





Scheme 2 Schematic representation of the three suggested decomposition pathways of TMA-TEMPO **1** and the proposed TEMPO derivatives **2–7** to influence the respective decomposition pathway by the introduction of different linkers between the solubilizing group and the TEMPO moiety (top), a shielding of the formed cation utilizing a spiro derivate (middle) and influencing the elimination of chloromethane by different anions and the exchange of methyl to ethyl (bottom).

the ESL.† Deionized water was used for all experiments. The ion-selective membrane (FAA-3-50, Fumasep GmbH, Germany) was cut into appropriate pieces and prewetted for at least 24 h in 1.5 M aq. sodium chloride or sodium tetrafluoroborate solution. GFA-6 graphite felts from SGL SE, Germany, were used as porous electrodes.

Electrochemical analytics

Cyclic voltammetry (CV)

Cyclic voltammetry was performed using a VMP-3 (Bio-Logic, France) potentiostat/galvanostat using a standard three-electrode setup with an AgCl/Ag reference electrode (Ag wire in 3 M aq. potassium chloride solution), a platinum wire counter electrode and a glassy carbon working electrode (GCWE) with a diameter of 1.6 mm.

The diffusion coefficients for the oxidized TEMPO derivatives were calculated according to the Randles-Sevcik approach.²⁸

$$i_p = 0.4463nFAC_0 \left(\frac{nFvD}{RT} \right)^{1/2} \quad (1)$$

(peak current of the oxidation of the active material i_p , number of transferred electrons $n = 1$, Faraday constant $F = 96485 \text{ C mol}^{-1}$, electrode surface $A = 0.08 \text{ cm}^2$, the bulk concentration c_0 of the active material, the scan rate of the CV v , the diffusion coefficient D , the universal gas constant $R = 8.314 \text{ J mol}^{-1} \text{ K}^{-1}$ and the measuring temperature $T = 22 \text{ }^\circ\text{C}$.)

The rate constant was determined using the Nicholson approach.^{29,30}

$$\Psi = k^0 \left(\frac{\pi D n F}{RT} \right)^{-1/2} \nu^{-1/2} \quad (2)$$

(the Nicholson parameter Ψ , the rate constant k^0 and mathematical constant π)

Rotating-disk electrode voltammetry (RDE)

Measurements were conducted with the same setup but with a GCWE diameter of 5 mm and an EDI 101 rotator controlled by a CTV101 (Radiometer analytical, France). The Data of the RDE measurements were analyzed using the Levich equation,

$$i_{\text{lim}} = 0.62nFAD^{2/3}\omega^{1/2}\nu^{-1/6}c_0 \quad (3)$$

(electrode surface $A = 0.2 \text{ cm}^2$ and the kinematic viscosity of a 0.1 M aq. sodium chloride solution²¹ $\nu = 1.01 \times 10^{-6} \text{ m}^2 \text{ s}^{-1}$) yielding the diffusion coefficient D .

The applied Koutecký-Levich equation,

$$\frac{1}{i} = \frac{1}{i_k} + \frac{1}{0.62nFAD^{2/3}\omega^{1/2}\nu^{-1/6}c_0} \quad (4)$$

delivered the mass-transfer-independent kinetic currents i_k . These were fitted using the Butler-Volmer equation with a Tafel Plot. The determined slope allows the calculation of i_0



and k^0 with $i_0 = Fk^0c_0$ by

$$\text{Tafel slope} = \frac{-\alpha F}{2.3RT} \text{ or } \frac{(1-\alpha)F}{2.3RT} \quad (5)$$

General optical titration procedure

Standard solution preparation

The purchased 0.1 M cerium(IV)-sulphate solution was diluted with water to obtain a 0.025 M solution.

Titer determination

Approx. 0.125 mmol ammonium iron(II) sulphate was dissolved in 45 mL of water, and 5 mL of 10 vol% sulfuric acid as well as two drops of ferroin solution were added.

Sample preparation

Approx. 0.125 mmol TEMPO derivative was dissolved in 45 mL of water, and 5 mL 10 vol% sulfuric acid as well as two drops of ferroin solution were added.

Titration

The sample/titer solution was continuously stirred and the standard solution was added dropwise using a 10 mL burette (AS grade, Duran[®], Germany) until the color of the sample solution turned from red to slightly yellow and the color change remained at least for 5 seconds.

General potentiometric titration procedure

The same sample, titer and standard solution preparation procedures as described for optical titration were used but without the ferroin indicator. The dispensing voluminal interval was adjusted according to the expected equivalence point, derived from optical titration. To measure the redox potential, a GMH 3530 digital pH/mV-/thermometer (Greisinger electronic GmbH, Germany) equipped with a GR 105 redox electrode (Greisinger electronic GmbH, Germany, reference electrode: Ag wire in 3 M aq. potassium chloride solution) was used.

The added volume of cerium(IV)-sulphate solution was plotted over the measured potential and an adjusted eqn (6) according to Levie³¹ was fitted to the data set.

$$V_t = a \frac{10^{(-fb)}(10^{-fx} + 10^{-fc})}{10^{(-fx)}(10^{-fx} + 10^{-fb})} \quad (6)$$

(added volume of the titrant V_t , added volume of titrant at the equilibration point a , standard redox potential of the analyte b , standard redox potential of the titrant c , $f = \frac{F}{RT} \ln 10$, which describes the pre-factor in the Nernst equation and was set to a value of 17.2, measured potential x)

Battery experiments

All battery tests were performed under normal atmosphere. As a potentiostat/galvanostat a VMP3 (BioLogic, France) was used. The electrolyte was pumped by a Hei-Flow Value 01 equipped with a C8 multi-channel pumping head (Heidolph, Germany) at a flow rate of approx. 25 mL min⁻¹ through Norprene[®] A-60-G (ϕ_{inn} 1.6 mm, ϕ_{out} 4.8 mm, Saint-Gobain, France) peristaltic tubes into the cell. For all battery tests, a flat-type redox flow cell according to the design of Jena Batteries GmbH, Germany, with an active membrane area of 5 cm² was utilized. A detailed overview of the cell components is provided in the ESI[†]

The room temperature was 22 °C. For tempering, the samples were placed into an oil bath and heated to 40 °C using a magnetic stirrer/hot plate (Hei-Tec, Heidolph, Germany) equipped with an external temperature sensor (PT 1000, Heidolph, Germany).

General method for SOC 50% samples

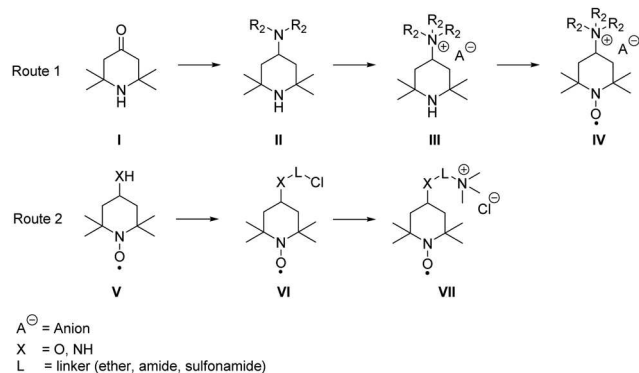
2 mmol of the synthesized TEMPO derivative was mixed with 20 mL of water and 20 mmol of the appropriate supporting electrolyte (sodium chloride or tetrafluoroborate). The sample was charged against 25 mL of 0.1 M aq. methyl viologen solution mixed with 20 mmol sodium chloride or tetrafluoroborate. The applied current was 80 mA cm⁻² until a cell voltage of 1.45 V was reached. Afterwards, the battery was charged potentiostatically at 1.45 V until the current decreased below 0.5 mA cm⁻². This electrolyte was considered as fully charged and mixed with a solution of 2 mmol of the same TEMPO derivative and 20 mmol sodium chloride or tetrafluoroborate in 20 mL of water. The solution was pumped through the cell for approx. 10 min and the SOC of the obtained sample was considered as 50%.

General cycling protocol

The received SOC-50% sample was split into 12 mL of 0.1 M aq. TEMPO derivative solution for the capacity-limiting side (CLS) and 18 mL of 0.1 M aq. TEMPO derivative solution for the capacity non-limiting side (CNLS), except for TMA-TEMPO, where 15 mL of 0.1 M aq. solution for CLS and 20 mL of 0.1 M aq. solution as CNLS were used. For all splitting processes, the same 1, 2, 5 and 10 mL volumetric pipettes (Duran[®], Germany) were used.

The unbalanced, compositionally symmetric cell was cycled 50 times between +0.45 V and -0.45 V with 76 mA cm⁻². After the cell voltage limits were reached, the battery was charged/discharged potentiostatically until the current dropped below the threshold of 0.5 mA cm⁻². After finishing the 50 cycles, the battery was charged to maximal SOC and a hold time of 24 h was applied. During these hold times the pumps of the battery were not paused or slowed down. This cycling protocol was repeated three times and 25 additional cycles were applied at the end. Afterwards, the reservoir of the capacity-limiting side was heated up to 40 °C and the cycling protocol described above was applied again (see ESI[†] Fig. S15).





Scheme 3 Schematic representation of the used general synthesis routes for the desired TEMPO derivatives.

Synthesis

In general, the syntheses of the desired derivatives can be classified in two different approaches (see Scheme 3): the first starts with a reductive amination of the triacetone amine precursors I with subsequent quaternization, leading to the trialkylammonium derivative III, which is oxidized to the radical IV in the final step. The second route starts with the respective aminoxyl radical V bearing an amino or hydroxyl group in the 4-position and the introduction of halogen-bearing linkers (VI). The desired product VII is subsequently synthesised *via* nucleophilic substitution with trimethyl amine. Detailed synthesis procedures of all compounds are available in the ESI.†

Results and discussion

Electrochemical characteristics

In order to elucidate the structure–stability relationship the degree of oxidation (DoO) of the TEMPO derivatives was first analysed, followed by electrochemical characterisation studies, before battery experiments were conducted.

The DoOs of the TEMPO derivatives were determined using a cerimetric redox titration procedure with the indicator ferroin. To overcome the subjective titration endpoint determination based on color change, the change of the redox potential during the titration was measured using a potentiometer (see Fig. S2 and S3, ESI†).

As the curve for eqn (6) depends on the redox potential of the TEMPO derivative, we tried to validate our new fitting approach by comparing with the redox potential delivered by CV measurements. The differences between the redox potentials obtained by the CV method and from the fitting curve are mostly below 10 mV (see Table 1) with standard deviation of 7 mV or below. The shape of the CV curves (see ESI† chapter: CV-RDE-Measurements) is typical for TEMPO derivatives. The plot of the peak currents over the square root of the scan speed revealed linear behavior except for the spiro-Tempo 5 where the curves flattened at low scan speeds, indicating a non-reversible redox reaction upon oxidation. Furthermore, compound 5 could not be determined by titration. This may be caused by the hydrolyzation of the ether bonds of the attached rings and the subsequent oxidation of the resulting alcohols in the acidic environment. Using both titration methods, neither a stable color change during optical titration nor a significant change in the potential could be observed. Thus, we assumed that the oxoammonium cation is not stable and decomposes within a short time frame.

In contrast to the redox potentials of the other TEMPO derivatives determined by titration and by CV (Table 1), TEA-TEMPO 7 exhibited an extraordinarily high difference of 85 mV. Up to now, we do not have a plausible explanation for this observation and an in-depth investigation of this behavior is the topic of further research. Our first assumption is that derivatives with a DoO of below approx. 80% are not suitable for a simultaneous determination of the redox potential and the DoO.

The DoOs of the other TEMPO derivatives were mostly over 80% with two derivatives with approx. 100% degree of oxidation. Lower radical contents might be caused by the reduction or disproportionation reactions during the purification processes. However, a reduced DoO may only affect the overall electrolyte capacity but not the cyclability.^{20,22,32} Thus, we assumed that the stability of the TEMPO derivatives in the following experiments is not compromised by the residual amount of the respective nonoxidized precursors. All in all, we were able to develop a new titration protocol for water-soluble TEMPO derivatives, which is independent from subjective visual perception of the titrator and furthermore enables the direct measurement of the redox potential of the analyte within the same measurement.

Furthermore, the titration procedure can be automated using a titration machine. However, the main drawback of the method is its long measuring time caused by the equilibration time of the redox electrode. Additional electrochemical

Table 1 Overview of the redox potentials of different TEMPO derivatives determined by CV ($E_{CV}^{1/2}$) and by titration ($E_{tit}^{1/2}$) with the corresponding standard deviation as well as the degrees of oxidation determined by optical (DoO_{opt.}) and potentiometric titration (DoO_{opt.}). The data points were triple determined. — Data could not be obtained

Compound	$E_{CV}^{1/2}$ [V]	$E_{tit}^{1/2}$ [V]	$\Delta E^{1/2}$ [mV]	DoO _{opt.} [%]	DoO _{opt.} [%]
1 ²¹	0.754+/-1 mV	0.747+/-1 mV	6	99+/-0.3	103+/-0.5
2	0.644+/-1 mV	0.652+/-1 mV	7	86+/-0.1	88+/-0.2
3	0.648+/-1 mV	0.652+/-1 mV	4	101+/-0.1	100+/-0.8
4 ²⁶	0.623+/-2 mV	0.610+/-2 mV	13	81+/-0.1	74+/-0.7
5	0.883+/-7 mV	—	—	—	—
6	0.755+/-1 mV	0.753+/-1 mV	2	79+/-0.2	78+/-0.2
7	0.841+/-6 mV	0.754+/-1 mV	85	59+/-0.6	58+/-1



Table 2 Overview of the electron-transfer rates obtained by the Koutecký–Levich approach k_{KL}^0 and the Nicholson approach k_{N}^0 , diffusion coefficients obtained by the Koutecký–Levich approach D_{KL} and the Randles–Sevcik approach D_{RS} , transfer coefficients α as well as the solubility S of the different TEMPO-derivatives. No data could be obtained for **5** and **7**

Compound	k_{KL}^0 [$10^{-3} \text{ cm s}^{-1}$]	k_{N}^0	D_{KL} [$10^{-6} \text{ cm}^2 \text{ s}^{-1}$]	D_{RS}	α	S [mol L^{-1}]
1	2.43	15.48	4.7	3.5	0.66	3.2 ²¹
2	1.97	0.98	3.8	2.63	0.54	3.8
3	3.04	8.01	4.0	1.88	0.60	3.0
4	1.61	3.64	3.7	2.04	0.55	4.6 ²⁶
6	2.61	5.00	3.9	2.9	0.6	0.1

properties were determined by rotating disk electrode (RDE) voltammetry (see ESI† section: CV-RDE Measurements).

The electron-transfer rates k^0 , the diffusion coefficients D and the transfer coefficients α , determined *via* RDE, were found to be 1.6 to $3.0 \times 10^{-3} \text{ cm s}^{-1}$, 3.7 to $4.7 \times 10^{-6} \text{ cm}^2 \text{ s}^{-1}$ and 0.54 to 0.66 , respectively (see Table 2). To overcome some potential errors due to the fast redox kinetics of the analyte material, the electron-transfer rates k^0 and the diffusion coefficients D were also determined using both the Nicholson and the Randles–Sevcik approach.^{28–30} The findings of the different methods are comparable to each other and to the published data for TMA-TEMPO in aq. solutions at glassy carbon electrodes and other organic active materials, like quinones.^{21,33} It seems that structural deviations at the TEMPO scaffold do not affect the electrochemical properties or kinetic parameters significantly. This is not surprising since the molecular orbitals of the radical as well as the oxoammonium cation that are involved in the redox reaction are mainly located at the NO moiety of the TEMPO scaffold.³⁴

As already indicated during the CV measurements, the spiro-TEMPO **5** cannot be analysed using RDE due to the absence of a plateau during the oxidation process (see ESI† section: CV-RDE measurements), likely because of stability problems of the attached cyclic ethers, as discussed above.

The TEA-TEMPO **7** likewise cannot be analyzed (see ESI† section: CV-RDE measurements), most likely due to the high content of non-oxidized educt and possible interactions between an educt and a product. A simple evaluation with the Levich equations was thus not possible.

While compound **5** is not stable enough for battery applications, triethyl ammonium TEMPO-derivative **7** was excluded due to its low DoO and insufficient yields in the synthesis, which make them both unsuitable candidates for further large-scale applications. Based on these findings, compounds **5** and **7** were not investigated further.

Battery experiments

In order to test the stability of the proposed active materials in a battery setup, the unbalanced, compositionally symmetric cell setup was employed. The main advantage is that the utilization

of the same active material as a posolyte as well as a negolyte largely avoids crossover. This concept was firstly introduced by the group of Brushett³⁵ in 2016, who used the same electrolyte with an initial SOC of 50% for both half-cells, creating a battery that cycles around a cell voltage of 0 V (Fig. 2). Goulet and Aziz further developed this idea and reported an elaborate cycling protocol including a capacity-limiting half-cell, hold times and potentiostatic charging.²⁵

In order to study the influence of temperature and rest times at high SOC values, the cycling protocol was adapted by our group. The adapted protocol featured potentiostatic cycling near the extreme SOC values of the capacity-limiting electrolyte with a limiting current of 0.5 mA cm^{-2} . Every 50 cycles, a hold time of 24 h at maximum SOC was applied. After 175 cycles, the capacity-limiting reservoir was placed in an oil bath at $40 \text{ }^\circ\text{C}$ and the described protocol was repeated. This stress test should mimic unfavorable, but still realistic conditions.

The utilized low concentration of 0.1 M was used to keep the experiment in a manageable time frame. For comparability reasons, we normalized the highest achieved capacity during the test protocol for each derivative to 100% and calculated every other datapoint relative to this capacity.

At first, we investigated the TMA-TEMPO system **1** in order to create a benchmark to which we can then compare our new derivatives. TMA-TEMPO **1** showed a relatively stable charge and discharge capacity in the first 50 cycles; however, after an initial peak the electrolyte capacity started to decay with an increased dip after the first hold time of 24 h. While under room temperature conditions ($22 \text{ }^\circ\text{C}$) the capacity loss during the hold times is only moderately higher than that during cycling ($1.5\% \text{ d}^{-1}$ and $0.9\% \text{ d}^{-1}$, respectively, see Table 3), increasing the temperature to $40 \text{ }^\circ\text{C}$ results in an increased decay during hold times ($2.0\% \text{ d}^{-1}$). Interestingly, the capacity fade during cycling is comparable to that at room temperature ($0.8\% \text{ d}^{-1}$). After the completion of the test protocol, 73.0% rest capacity could be recovered (see Table 3).

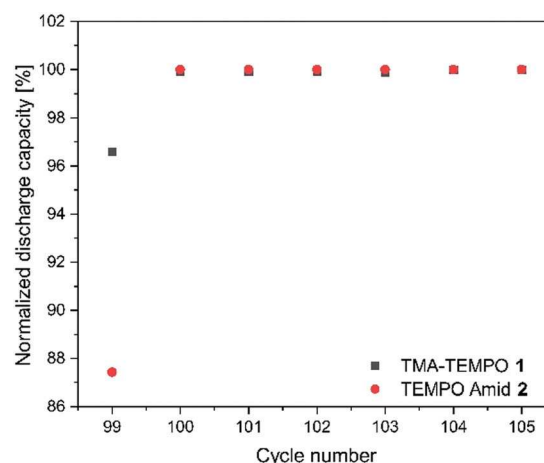


Fig. 1 Illustration of the discharge capacity of the first seven cycles of the TMA-TEMPO **1** and the amide **2** after the second hold time of 24 h. The capacity was normalized to the highest capacity in the shown interval. The first cycle showed a massively reduced discharge capacity.



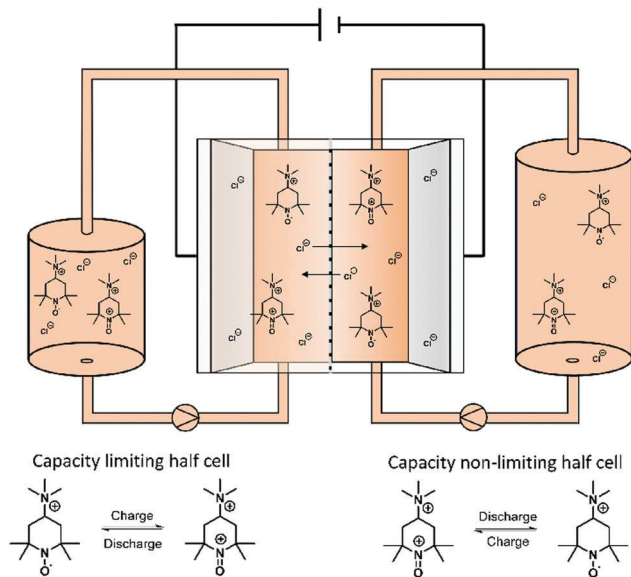


Fig. 2 Illustration of a symmetric TMA-TEMPO redox flow battery set up as well as the corresponding half-cell reaction.

As mentioned before, the nature of the linker to the solubilizing moiety may have a pronounced influence on the stability of the active material during battery experiments. We first investigated the TEMPO-amide system **2**. While 6.6% of the capacity is lost during the first 50 cycles, the decay stabilizes during the next 100 cycles and declines linearly afterwards until the end of the experiment. All in all, it is comparable to TMA-TEMPO **1** (0.9% d^{-1} 20 °C, 0.8% d^{-1} 40 °C). In contrast, the loss during the hold time is, with an average of 11.6% d^{-1} , much higher (1.5% d^{-1} **1**, see Table 3).

This decay can mostly be reversed during the next consecutive charging (see Fig. 1), indicating a much more pronounced but also highly reversible capacity loss mechanism. A self-discharge mechanism whose kinetics are relatively slow, so it cannot be measured during cycling, is the most plausible explanation (a possible mechanism is explained below). Nevertheless, the TEMPO-amide compound **2**, even with the initial comparably high loss, shows a similar stability as the known TMA-TEMPO system **1** (see Fig. 3). In comparison, the TEMPO-sulfamide molecule **3** is significantly more unstable. The experiment showed an exponential capacity decay (see Fig. 3), and only 50% of the initial capacity remained after the first 50 cycles, which corresponds to a decay of over 20% d^{-1} . This trend continues over the next cycles, although not that pronounced. After the first 175 cycles, only 32% of the initial capacity can be recovered. At higher temperatures, the decay is 1.2% per day (Fig. 3), which is comparable to that of the other derivatives. All in all, the sulfamide system **3** revealed a strongly pronounced capacity decay during cycling, which shows its insufficiency as a battery active material. Originally intended to be a more stable linker for the SPG, the amide compound **2** and sulfamide molecule **3** failed to improve the stability of the TEMPO scaffold. Whereas the amide revealed a similar stability to TMA-TEMPO, the sulfamide is much more prone to capacity decay. We think that oxidative cleavage of the linker might be

Table 3 Overview of the capacity decay of different TEMPO derivatives during cell test for pure cycling (50 cycles 1–3 period, 25 cycles 4 period) and hold times of 24 h at room temperature and 40 °C. — Data could not be obtained

Start rel. dis-charge capacity	Decay 22 °C [% d^{-1}]										Decay 40 °C [% d^{-1}]									
	1. Cycling period	1. Hold time	2. Cycling period	2. Hold time	3. Cycling period	3. Hold time	4. Cycling period	4. Hold time	1. Cycling period	1. Hold time	2. Cycling period	2. Hold time	3. Cycling period	3. Hold time	4. Cycling period	4. Hold time				
1B 89.07	0.28	1.25	1.24	1.63	1.36	1.57	0.55	1.00	2.06	0.51	1.90	0.92	2.14	0.60	72.95					
2 94.74	6.79	12.80	2.10	10.36	1.01	10.18	0.84	0.45	11.32	0.92	11.35	0.97	11.44	0.97	71.33					
3 99.24	20.45	13.75	2.57	10.02	0.92	8.90	0.35	0.76	8.98	0.35	8.47	0.15	8.10	0.43	27.09					
4 99.95	28.31	16.35	3.30	9.77	1.52	8.15	1.11	1.16	10.60	0.87	9.00	0.60	8.80	0.97	28.47					
6 80.43	+1.98	+1.12	0.16	—	—	—	—	—	—	—	—	—	—	—	—	—				



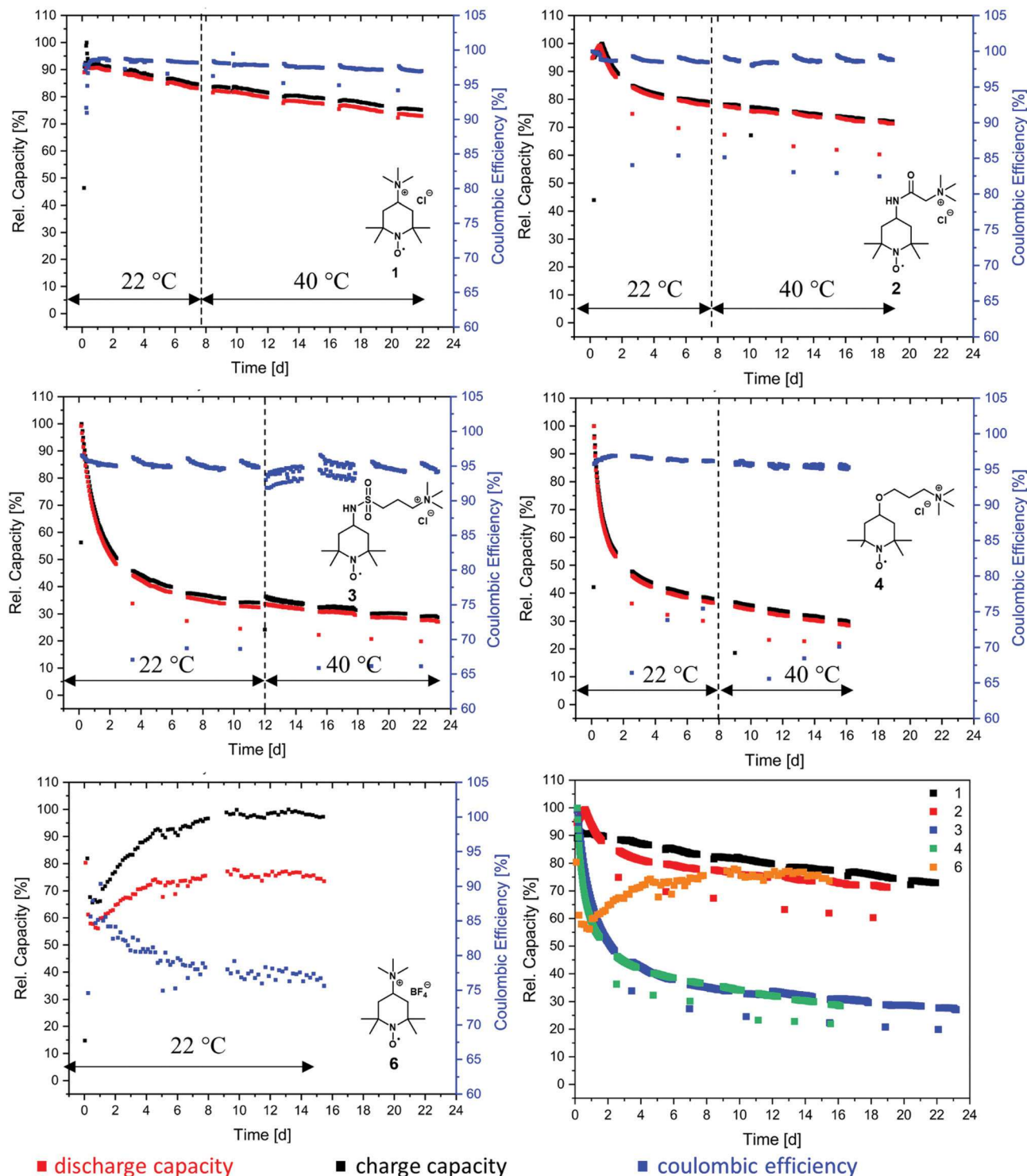


Fig. 3 Overview of the battery performance of different TEMPO-derivatives in symmetrical redox flow cell tests cycled potentiostatically with 76 mA cm^{-2} with a consecutively added galvanostatic part (current limitation of 0.5 mA cm^{-2}). The cells consist of 12 mL vs. 18 mL 0.1 M active material solution, except for TMA-TEMPO, where 15 mL vs. 20 mL solutions were used. All electrolytes consist of 1.5 M appropriate supporting salt in water. The charge capacity is represented in black, the discharge capacity in red and the coulombic efficiency in blue. (Lower right) Comparison of the discharge capacity of the TEMPO derivatives.

the most probable explanation. While amides are stable against the oxidative cleavage of the C–N bond up to a potential of approx. 1.25 V vs. Ag/AgCl,³⁶ it was shown that the N–S bond of

sulfamides can be cleaved at a redox potential of 0.75 to 0.95 V vs. Ag/AgCl,^{37–40} which is similar to the oxidation potential of the TEMPO derivatives.



Thus, an autoxidative cleavage of the N–S sulfamide bond by the oxoammonium cation itself is considered as a reason for the fast decay of the battery capacity. The resulting 4-amino-TEMPO is more likely to undergo degradation reactions than TMA-TEMPO **1**, the amide **2** or the sulfamide **3**.⁴¹ This trend was also demonstrated for the 4-hydroxy-TEMPO, which was shown to be significantly more unstable compared to TMA-TEMPO.⁴² During hold times, the capacity loss of **3** is much more pronounced than that of the TMA-TEMPO system **1** and is 10.2% d⁻¹ (see Table 3), which is in the range of the amide compound **2**. The loss can be largely recovered in the next cycle. Once again, a reversible self-discharge mechanism with slow kinetics is a good explanation for this behavior.

The TEMPO-ether molecule **4** shows a comparable behaviour of the battery capacity to the sulfamide system **3**. After an initial exponential decay within the first 50 cycles, the fade stabilizes and becomes linear. At the end of the segment conducted at room temperature, only 36% of the initial capacity can be retained and 28% remaining capacity was accessible after the consecutive test at 40 °C (see Table 3). TEMPO-based oxoammonium cations are known to be capable of cleaving ether bonds oxidatively.⁴³ The resulting 4-hydroxy TEMPO undergoes further irreversible degradation reactions, as discussed before. The finding of Liu that the introduction of an ether between the solubility-promoting trimethylammonium group and the TEMPO scaffold increases the stability²⁶ could not be confirmed by our setup (under the used conditions, *e.g.*, no hold times in vulnerable SOC, other voltage limits).

Ma *et al.* showed that TEMPO can undergo multiple bond breaking reactions in acidic aqueous media resulting in unsaturated phorones (see Scheme 1).¹ Takata and co-workers demonstrated that oxoammonium cations undergo rapid 1,2 electrophilic additions with double bonds.² Subsequent cleavage of the addition products leads to acid formation, reduction of the oxoammonium cation to hydroxylamine and oxidation of the double bond to an alcohol/ketone (see Scheme 1). Ma *et al.* stated that for every decomposed TEMPO molecule approx. four hydroxylamine molecules are formed, which is in good agreement with the mechanism formulated by Takata *et al.* and our findings in the GC-MS study.²⁷

These findings could possibly explain why the coulombic efficiencies of the molecules **1** to **4** are comparably low. Fast cycling of the active material, avoidance of hold times in the oxidized state and high cut off currents would lower the oxoammonium cation concentration and, thus, bypass the described mechanism. Furthermore, the formed acids do not only catalyse the processes Ma *et al.* described, but they also influence the cleavage of the linker. The amide **2**, sulfonamide **3** and the ether **4** linkers are thus under double stress; on the one hand the oxidative cleavage and on the other hand the acidic catalysed cleavage could take place. Nevertheless, the low coulombic efficiency and the huge healable capacity drop after hold times is most likely attributed to the formed hydroxylamine, which needs to be electrochemically reoxidized to the radical. However, we repeated the measurements of Liu *et al.* of the TEMPO-ether **4** with lower cut-off voltages and higher cut-

off currents (see ESI† Fig. S22). The results show that the decay rate can be massively reduced by carefully adjusting the cycling parameter of the molecule. However, the decomposition rate is with 3.1% d⁻¹, during pure cycling, reduced but the TEMPO-amide **2** or the TMA-TEMPO **1** is still more stable. Further post-mortem analyses like pH, CV or NMR (see ESI† Fig. S23 and S24) support these findings, but give no additional hints on the ongoing processes.

Compared to halogenide anions, the BF₄⁻ anion is known to be less nucleophilic.^{44,45} Therefore, compound **6** was synthesised to investigate the influence of the counterion on the stability of TMA-TEMPO. As expected, the salt revealed only a low solubility in the used aqueous electrolyte, with a maximum concentration of around 0.1 M. During the cycling test, only 50% of the theoretical capacity (see ESI† section: battery experiments) can be addressed. Furthermore, the achieved charge and discharge current densities are relatively low, resulting in exceptionally long cycling times.

Although the membrane was prewetted for 24 h in a 1.5 M aq. sodium tetrafluoroborate solution, the anion exchange might be hindered, which would explain the long charging and discharging times.

However, over the first cycles the capacity slowly increases before remaining nearly stable for the rest of the experiment. This atypical behavior could be explained by the low solubility and possible dissolution-participation equilibria which would also explain the low accessible capacity of the electrolyte. The influence of the counter ion on the stability could thus not be derived. Furthermore, the test could not be completed as the solubility of the BF₄-salt was insufficiently low and precipitation took place in the cell. After 79 cycles, the membrane was perforated either because of clogging and the associated pressure increase or because of conductive-salt crystals, which had grown through the membrane (see pictures in the ESI† section: photos of BF₄-salt precipitate).

As discussed above, we think that the main reason for the low coulombic efficiencies is attributed to the formal oxidation of a double bond to an alcohol by an oxoammonium cation with its reduction to the hydroxylamine as discussed by Takata (see Scheme 1).² The alcohol is then oxidized to the ketone and the corresponding keto–enol-tautomerism produces additional double bonds which are oxidized. This mechanism continues until CO₂ is formed.¹

The formation of these double bonds needs to be avoided for a more stable TEMPO derivative. The ether **4** and the sulfonamide **3** linked compound can be cleaved oxidatively and/or acid catalysed resulting in a lesser stable 4-hydroxy or 4-amino TEMPO. These compounds can be oxidized easily to the carbonylic or carbonyl-equivalent. The subsequent keto–enol-tautomerism produces double bonds which needs to be avoided. Since the amide **2** is (more) stable against the decay mechanism, linker cleavage as the decomposition starting point can be omitted. Furthermore, the amide **2** should also hinder the Hoffman-like elimination pathway and decomposition of the solubility promoting group *via* chloromethane evolution. Nevertheless, the amide **2** and the TMA-TEMPO



system **1** are comparably stable. We thus hypothesize that the comparable capacity loss of the TMA-TEMPO system **1** and the TEMPO-amide compound **2** is attributed to the N–C bond break in the TEMPO scaffold and the subsequent formation of oxidizable double bonds. A cleavage of this bond must be prevented either by further shielding of the radical or stabilization *via* electronic effects caused by substituents vicinal to the N–O radical.

Conclusions

TMA-TEMPO is among the best investigated and most stable posolyte materials for redox batteries. Nevertheless, it does suffer from decomposition and reversible self-discharge reactions. We synthesised five new TEMPO derivatives as well as one known and compared their electrochemical parameters as well as their stability with those of TMA-TEMPO.

At first, we developed a new evaluation method for redox titration with which, in one measurement, the DoO and the half-cell potential of the analyte can be obtained, which were validated by both CV and optical titrations. However, while the DoO is accurate even at lower values, the half-cell potentials are only precise when the degree of oxidation is sufficiently high. While the method needs a comparably long measuring time, it nevertheless reveals great potential due to its possible automatization.

In subsequent battery experiments, a selection of promising candidates were tested using a cycling protocol involving dwell times at high SOC's at room temperature and 40 °C. The introduction of a tetra fluoroborate counter ion to TMA-TEMPO lowered the solubility so much that no reliable statements about possible introduced stability changes could be made.

The usage of an amide linker revealed no significant stability changes in comparison to TMA-TEMPO. Nevertheless, a more pronounced but also highly reversible self-discharge mechanism was visible, whose details are the subject of ongoing studies.

However, linkers connected *via* a sulfonamide or an ether unit did show pronounced signs of capacity loss even at low temperatures; these were less accentuated for TMA-TEMPO. The main reason for this may be a possible oxidative cleavage of the linker by the corresponding oxoammonium cation, although Liu *et al.* did not observe such a degradation process during their investigation of the ether-linked compound **5**.²⁶ This may be caused by the differences in the cycling protocols. We are intending to emphasise concentration-dependent studies as well as dwell times in vulnerable SOC's for future investigations.

Author contributions

Philip Rohland: conceptualization, methodology, formal analysis, data curation, visualization, writing – original draft (lead) investigation, and synthesis (equal); Oliver Nolte: investigation

(equal), formal analysis (supporting), writing – original draft (supporting), and writing – review and editing: critical review (equal); Kristin Schreyer: synthesis (equal), investigation (supporting), and writing – review and editing: critical review (equal); Helmar Görls: XRC (lead), investigation (supporting), and writing – review and editing: critical review (equal); Martin D. Hager: writing – review and editing: critical review (equal), supervision of P. R., O. N., and K. S. (equal), and funding acquisition (equal); Ulrich S. Schubert: writing – review and editing: critical review (equal), supervision of P. R., O. N., and K. S. (equal), and funding acquisition (equal).

Conflicts of interest

The authors declare no conflicts of interest.

Acknowledgements

We acknowledge the European Social Fund (ESF), the Thüringer Aufbaubank (TAB) and the Thuringian Ministry of Economic Affairs, Science and Digital Society (TMWWdG) for financial support. We further want to thank Christian Friebe and Christian Stolze for their help and suggestions.

References

- 1 Y. Ma, C. Loynes, P. Price and V. Chechik, *Org. Biomol. Chem.*, 2011, **9**, 5573–5578.
- 2 T. Takata, Y. Tsujino, S. Nakanishi, K. Nakamura, E. Yoshida and T. Endo, *Chem. Lett.*, 1999, 937–938.
- 3 C. R. Chamorro, M. E. Mondéjar, R. Ramos, J. J. Segovia, M. C. Martín and M. A. Villamañán, *Energy*, 2012, **42**, 10–18.
- 4 E. von Sperling, *Energy Proc.*, 2012, **18**, 110–118.
- 5 B. Obama, *Science*, 2017, **355**, 126–129.
- 6 S. Chu and A. Majumdar, *Nature*, 2012, **488**, 294–303.
- 7 I. Hadjipaschalis, A. Poullikkas and V. Efthimiou, *Renewable Sustainable Energy Rev.*, 2009, **13**, 1513–1522.
- 8 P. Alotto, M. Guarnieri and F. Moro, *Renewable Sustainable Energy Rev.*, 2014, **29**, 325–335.
- 9 J. Winsberg, T. Hagemann, T. Janoschka, M. D. Hager and U. S. Schubert, *Angew. Chem., Int. Ed.*, 2017, **129**, 702–729.
- 10 A. Z. Weber, M. M. Mench, J. P. Meyers, P. N. Ross, J. T. Gostick and Q. Liu, *J. Appl. Electrochem.*, 2011, **41**, 1137.
- 11 J. Noack, N. Roznyatovskaya, T. Herr and P. Fischer, *Angew. Chem., Int. Ed.*, 2015, **54**, 9776–9809.
- 12 K. Lin, R. Gómez-Bombarelli, E. S. Beh, L. Tong, Q. Chen, A. Valle, A. Aspuru-Guzik, M. J. Aziz and R. G. Gordon, *Nat. Energy*, 2016, **1**.
- 13 W. Lee, B. W. Kwon and Y. Kwon, *ACS Appl. Mater. Interfaces*, 2018, **10**, 36882–36891.
- 14 A. Orita, M. G. Verde, M. Sakai and Y. S. Meng, *Nat. Commun.*, 2016, **7**, 13230.
- 15 B. Yang, L. Hooper-Burkhardt, S. Krishnamoorthy, A. Murali, G. K. S. Prakash and S. R. Narayanan, *J. Electrochem. Soc.*, 2016, **163**, A1442–A1449.



- 16 K. Lin, Q. Chen, M. R. Gerhardt, L. Tong, S. B. Kim, L. Eisenach, A. W. Valle, D. Hardee, R. G. Gordon, M. J. Aziz and M. P. Marshak, *Science*, 2015, **349**, 1529–1532.
- 17 D. G. Kwabi, K. Lin, Y. Ji, E. F. Kerr, M.-A. Goulet, D. De Porcellinis, D. P. Tabor, D. A. Pollack, A. Aspuru-Guzik, R. G. Gordon and M. J. Aziz, *Joule*, 2018, **2**, 1907–1908.
- 18 Y. Zhu, F. Yang, Z. Niu, H. Wu, Y. He, H. Zhu, J. Ye, Y. Zhao and X. Zhang, *J. Power Sources*, 2019, **417**, 83–89.
- 19 E. S. Beh, D. De Porcellinis, R. L. Gracia, K. T. Xia, R. G. Gordon and M. J. Aziz, *ACS Energy Lett.*, 2017, **2**, 639–644.
- 20 T. Janoschka, N. Martin, U. Martin, C. Friebe, S. Morgenstern, H. Hiller, M. D. Hager and U. S. Schubert, *Nature*, 2015, **527**, 78–81.
- 21 T. Janoschka, N. Martin, M. D. Hager and U. S. Schubert, *Angew. Chem., Int. Ed.*, 2016, **55**, 14427–14430.
- 22 J. Winsberg, T. Janoschka, S. Morgenstern, T. Hagemann, S. Muench, G. Hauffman, J. F. Gohy, M. D. Hager and U. S. Schubert, *Adv. Mater.*, 2016, **28**, 2238–2243.
- 23 J. Luo, B. Hu, C. Debruler and T. L. Liu, *Angew. Chem., Int. Ed.*, 2018, **57**, 231–235.
- 24 C. DeBruler, B. Hu, J. Moss, J. Luo and T. L. Liu, *ACS Energy Lett.*, 2018, **3**, 663–668.
- 25 M.-A. Goulet and M. J. Aziz, *J. Electrochem. Soc.*, 2018, **165**, A1466–A1477.
- 26 Y. Liu, M.-A. Goulet, L. Tong, Y. Liu, Y. Ji, L. Wu, R. G. Gordon, M. J. Aziz, Z. Yang and T. Xu, *Chemistry*, 2019, **5**, 1861–1870.
- 27 O. Nolte, P. Rohland, N. Ueberschaar, M. D. Hager and U. S. Schubert, *J. Power Sources*, 2022, **525**, 230996.
- 28 P. Zanello, *Inorganic Electrochemistry: Theory, Practice and Application*, The Royal Society of Chemistry, Milton Road, Cambridge, UK, 2003.
- 29 R. S. Nicholson, *Anal. Chem.*, 2002, **37**, 1351–1355.
- 30 J. Luo, B. Hu, M. Hu, Y. Zhao and T. L. Liu, *ACS Energy Lett.*, 2019, **4**, 2220–2240.
- 31 R. de Levie, *J. Electroanal. Chem.*, 1992, **323**, 347–355.
- 32 T. Hagemann, J. Winsberg, M. Grube, I. Nischang, T. Janoschka, N. Martin, M. D. Hager and U. S. Schubert, *J. Power Sources*, 2018, **378**, 546–554.
- 33 B. Huskinson, M. P. Marshak, C. Suh, S. Er, M. R. Gerhardt, C. J. Galvin, X. Chen, A. Aspuru-Guzik, R. G. Gordon and M. J. Aziz, *Nature*, 2014, **505**, 195–198.
- 34 T. Kusamoto, S. Kume and H. Nishihara, *J. Am. Chem. Soc.*, 2008, **130**, 13844–13845.
- 35 J. D. Milshtein, J. L. Barton, R. M. Darling and F. R. Brushett, *J. Power Sources*, 2016, **327**, 151–159.
- 36 T. Golub and J. Y. Becker, *Org. Biomol. Chem.*, 2012, **10**, 3906–3912.
- 37 A. Fabianska, A. Bialk-Bielinska, P. Stepnowski, S. Stolte and E. M. Siedlecka, *J. Hazard. Mater.*, 2014, **280**, 579–587.
- 38 D. Song, H. Liu, A. Zhang and J. Qu, *RSC Adv.*, 2014, **4**, 48426–48432.
- 39 W. Ben, Y. Shi, W. Li, Y. Zhang and Z. Qiang, *Chem. Eng. J.*, 2017, **327**, 743–750.
- 40 A. Acosta-Rangel, M. Sanchez-Polo, M. Rozalen, J. Rivera-Utrilla, A. M. S. Polo, M. S. Berber-Mendoza and M. V. Lopez-Ramon, *J. Environ. Manage.*, 2020, **255**, 109927.
- 41 W. Zhou, W. Liu, M. Qin, Z. Chen, J. Xu, J. Cao and J. Li, *RSC Adv.*, 2020, **10**, 21839–21844.
- 42 D. G. Kwabi, Y. Ji and M. J. Aziz, *Chem. Rev.*, 2020, **120**, 6467–6489.
- 43 P. P. Pradhan, J. M. Bobbitt and W. F. Bailey, *J. Org. Chem.*, 2009, **74**, 9524–9527.
- 44 K. A. Savin, *Writing Reaction Mechanisms in Organic Chemistry*, Academic Press – Elsevier Inc, Waltham, USA, 3 edn, 2014.
- 45 M. S. Puar, *J. Chem. Educ.*, 1970, **47**, 473–474.



1 Supplemental Information

2 Structural influence of TEMPO derivatives on their performance as battery material

3

4 Philip Rohland^{a,b}, Oliver Nolte^{a,b}, Kristin Schreyer^{a,b}, Helmar Görls^c, Martin D. Hager^{a,b},

5 Ulrich S. Schubert^{*,a,b}

6

7 * E-mail: ulrich.schubert@uni-jena.de

8 ^a Laboratory of Organic and Macromolecular Chemistry (IOMC), Friedrich Schiller University

9 Jena, Humboldtstrasse 10, 07743 Jena, Germany

10 ^b Center for Energy and Environmental Chemistry Jena (CEEC Jena), Friedrich Schiller

11 University Jena, Philosophenweg 7a, 07743 Jena, Germany

12 ^c Institute for Inorganic and Analytical Chemistry (IAAC), Friedrich-Schiller University Jena,

13 Humboldtstrasse 8, 07743 Jena, Germany

14

15 Version: Wednesday, 02 February 2022

16

17 *Table of Content:*

18	Synthesis	1
19	General analytical instruments:.....	1
20	Cell assembly	2
21	Structure determinations.	2
22	Chemicals and materials	3
23	Synthesis overview	5
24	Synthesis of <i>N,N</i> -2,2,6,6-hexamethylpiperidin-4-amine (1b):	6
25	Synthesis of <i>N,N,N</i> -2,2,6,6-heptamethylpiperidin-4-ammonium chloride (1c):	7
26	Synthesis of <i>N,N,N</i> -2,2,6,6-heptamethylpiperidinyloxyl-4-ammonium chloride (1):	8
27	Synthesis of 2-chloro- <i>N</i> -(2,2,6,6-tetramethylpiperidin-4-yloxy)acetamide (2b):	10
28	Synthesis of <i>N,N,N</i> -trimethyl-2-oxo-2-((2,2,6,6-tetramethylpiperidin-4-yloxy)amino)ethan-	
29	1-amonium chloride (2):	11
30	Synthesis of 3-chloro- <i>N</i> -(2,2,6,6-tetramethylpiperidin-4-yloxy)propane-1-sulfonamide	
31	(3a):.....	12
32	Synthesis of <i>N,N,N</i> -trimethyl-3-(<i>N</i> -(2,2,6,6-tetramethylpiperidin-4-	
33	yloxy)sulfamoyl)propan-1-amonium chloride (3):.....	13
34	Synthesis of 4-(3-chloropropoxy)-2,2,6,6-tetramethylpiperidin-1-yloxy (4b):.....	14
35	Synthesis of <i>N,N,N</i> -trimethyl-3-((2,2,6,6-tetramethylpiperidin-4-yloxy)oxy)propan-1-	
36	amonium chloride (4):.....	15
37	Synthesis of 1,2,2,6,6-pentamethylpiperidin-4-one (5a):	16
38	Synthesis of 3,11-dioxa-7-azadispiro[5.1.5.3]hexadecan-15-one (5b):.....	17
39	Synthesis of <i>N,N</i> -dimethyl-3,11-dioxa-7-azadispiro[5.1.5.3]hexadecan-15-amine (5c):.....	19
40	Synthesis of <i>N,N,N</i> -trimethyl-3,11-dioxa-7-azadispiro[5.1.5.3]hexadecan-15-amonium	
41	chloride (5d):	20
42	Synthesis of <i>N,N,N</i> -trimethyl-3,11-dioxa-7-azadispiro[5.1.5.3]hexadecan-15-amonium	
43	chloride aminoxyl free radical (5):	21
44	Synthesis of <i>N,N,N</i> -2,2,6,6-heptamethylpiperidin-4-ammonium tetrafluoroborate (6a):	23

45	Synthesis of <i>N,N,N</i> -2,2,6,6-heptamethylpiperidinyloxy-4-ammonium tetrafluoroborate (6):	
46	24
47	Synthesis of <i>N,N</i> -diethyl-2,2,6,6-tetramethylpiperidin-4-amine (7a):.....	25
48	Synthesis of <i>N,N,N</i> -triethyl-2,2,6,6-tetramethylpiperidin-4-ammonium chloride (7b):.....	26
49	Synthesis of <i>N,N,N</i> -triethyl-2,2,6,6-tetramethylpiperidinyloxy-4-ammonium chloride (7):	
50	27
51	Synthesis of 1,1'-Dimethyl-4,4'-bipyridinium dichloride:.....	28
52	Synthesis of 1,1'-Dimethyl-4,4'-bipyridinium ditetrafluoroborate:.....	29
53	Potentiostatic titration.....	30
54	CV-RDE measurements.....	33
55	EPR spectra.....	41
56	Battery experiments.....	44
57	X-Ray crystallographic data.....	53
58	Photos of BF ₄ -salt precipitate.....	57
59	Literature.....	57
60		

61 *Synthesis*

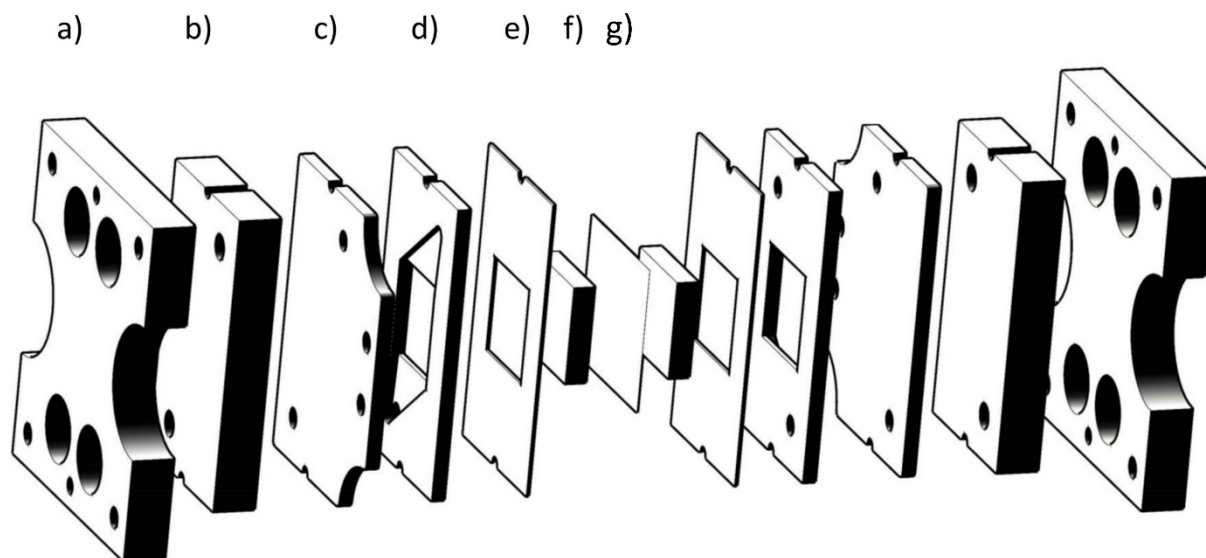
62 *General analytical instruments:*

63 The NMR spectra were obtained utilizing an Advance I 300 MHz (Bruker, Germany)
64 and X-band EPR spectra on an EMXmicro CW-EPR spectrometer (Bruker, Germany)
65 using an AquaX cell for acetonitrile and ER 221TUB for dichloromethane
66 measurements. The ESI-Q-TOF MS measurements were performed utilizing a
67 micrOTOF QII mass spectrometer (Bruker, Germany) with an automatic syringe pump
68 (KD Scientific, USA). An ESI source was used to generate ions and the calibrated
69 instrument measured in a m/z range between 50 and 3000. As calibration standard, an
70 ESI-L Low concentration tuning mix from Agilent was used. The sample concentration
71 ranged between 1 and 10 $\mu\text{g mL}^{-1}$ and was injected into the instrument with a constant
72 flow of 3 $\mu\text{L min}^{-1}$ (= 180 $\mu\text{L hr}^{-1}$). The data were evaluated with the Bruker Data
73 Analysis software version 4.2. For elemental analysis, an EA 3000 (HEKAtech GmbH,
74 Germany) was used.

75 GC-MS analyses were performed utilizing a GC-2010 gas chromatograph with an AOC-20s
76 autosampler and an AOC-20i injector (all Shimadzu, Japan). A GC-QP2010S electron
77 ionization (EI) quadrupole mass spectrometer (Shimadzu, Japan) was used for detection.
78 Separation was performed on a Restek Rxi-5Sil MS column (Restek, USA) with the following
79 dimensions: 30 m length, 0.25 mm inner diameter and 0.25 μm film thickness. The column was
80 operated with helium carrier gas using a S/SL injector with a column flow of 0.9 mL min^{-1} . The
81 injector temperature was set to 250 $^{\circ}\text{C}$. The GC oven was held at 80 $^{\circ}\text{C}$ for 1 min and was
82 subsequently heated to 300 $^{\circ}\text{C}$ at 25 $^{\circ}\text{C min}^{-1}$. This temperature was held for 7 min before
83 cooling and re-equilibration. The mass spectrometer was set to monitor the mass range between
84 40 and 600 m/z in EI+ (70 eV) mode. The MS transfer line was set to 250 $^{\circ}\text{C}$ and the ion-source
85 temperature to 200 $^{\circ}\text{C}$.

86 *Cell assembly*

87 The redox flow cell was designed as a flat type with an active membrane area of 5 cm² by
88 JenaBatteries GmbH, Germany. The Figure S1 displays a detailed overview of the cell
89 components.



90

91 *Figure S1: Schematic presentation of the electrochemical cell. One half-cell consists of a metal frame (a), PTFE block with*
92 *tubing connectors and rubber gasket (b), graphite current collector (c), PTFE flow frame (d), rubber gasket (e) and graphite*
93 *felt (f). The half-cells are separated by an ion-selective membrane (g).*

94 *Structure determinations.*

95 The intensity data for the compounds were collected on a Nonius KappaCCD diffractometer
96 using graphite-monochromated Mo-K_α radiation. The data were corrected for Lorentz and
97 polarization effects; absorption was taken into account on a semi-empirical basis using multiple-
98 scans¹⁻³. The structures were solved by intrinsic phases (SHELXT⁴) and refined by full-matrix
99 least squares techniques against Fo⁴. All hydrogen atoms of **3a** and the hydrogen atoms bonded to
100 the amino group of compounds **2** and **2b** were included at calculated positions with fixed thermal
101 parameters. All other hydrogen atoms were included at calculated positions with fixed thermal
102 parameters. All non-hydrogen atoms were refined anisotropically⁴. Crystallographic data as well
103 as structure solution and refinement details are summarized in Table 2. XP (SIEMENS
104 Analytical X-ray Instruments, Inc.) was used for structure representations.

105 **Further information available:** Crystallographic data (excluding structure factors) has been
106 deposited with the Cambridge Crystallographic Data Centre as supplementary publication
107 CCDC-2085767 for **2**, CCDC-2085768 for **2b**, and CCDC-2085769 for **3a**. Copies of the data
108 can be obtained free of charge on application to CCDC, 12 Union Road, Cambridge CB2 1EZ,
109 UK [E- mail: deposit@ccdc.cam.ac.uk].

110 *Chemicals and materials*

111 If not noted otherwise, the solvents were purchased from standard suppliers and distilled prior
112 to usage. If solvents were used from a solvent purification system (SPS), they were obtained
113 from a MB-SPS-800 (MBraun Inertgas-Systeme GmbH, Germany) and stored under argon. If
114 water is used, deionized water was utilized. Acetonitrile (HPLC Grade, Fisher Scientific Ltd.,
115 United Kingdom), chloromethane (Linde AG, Germany), sodium tungstate (Carl Roth GmbH
116 & Co. KG, Germany), hydrogen peroxide (35% & 50%, Carl Roth GmbH & Co. KG,
117 Germany), hydrochloric acid (37%, Fisher Scientific Ltd., United Kingdom), manganese
118 dioxide (VEB Laborchemie Apolda, Germany), 4-amino-2,2,6,6-tetramethylpiperidine-1-oxyl
119 (Apollo Scientific Ltd, United Kingdom), potassium carbonate (Grüssing GmbH, Germany),
120 chloroacetyl chloride (Alfa Aesar, USA), sodium sulphate (Grüssing GmbH, Germany),
121 trimethylamine (13% in THF, TCI, Japan), *N,N*-diisopropylethylamine (Sigma Aldrich, USA),
122 3-chloropropane sulfonyl chloride (Alfa Aesar, USA), trimethylamine (33% in ethanol, Sigma
123 Aldrich, USA), 4-hydroxy-2,2,6,6-tetramethylpiperidin-1-oxl (ABCR GmbH, Germany)
124 ammonium chloride (Grüssing GmbH, Germany), trimethyloxonium tetrafluoroborate (TCI,
125 Japan), diethylamine (Alfa Aesar, USA), iodethane (TCI, Japan), sodium hydrogencarbonate
126 (Fisher Scientific Ltd., United Kingdom), sodium periodate (Sigma Aldrich, USA),
127 *m*-chloroperoxybenzoic acid (Fisher Scientific Ltd., United Kingdom), 4,4' bipyridine (Alfa
128 Aesar, USA), 2-chloroacetyl chloride (Sigma Aldrich, USA), silver tetrafluoroborate (TCI,
129 Japan), sodium chloride ($\geq 99.5\%$, Fisher Scientific Ltd., United Kingdom), cerium(IV)-

130 sulphate solution 0.1 M (Carl Roth GmbH & Co. KG, Germany), sulphuric acid (min. 95%,
131 Fisher Scientific Ltd., United Kingdom), ammonium iron(II) sulphate hexahydrate (VEB
132 Laborchemie Apolda, Germany), ferroin indicator solution 1:40 (Lachema, Chemapol, Czech
133 Republic), 2,2,6,6-tetramethylpiperidin-4-one (TCI, Japan), paraformaldehyde (VWR
134 International GmbH, Germany), formic acid (85%, Grüssing GmbH, Germany), sodium (Sigma
135 Aldrich, USA), benzophenone (Acros Organics, Belgium), sodium hydroxide (Carl Roth
136 GmbH & Co. KG, Germany), tetrahydro-4H-pyran-4-one (TCI, Japan), Triton B (40 wt.% in
137 methanol, Sigma Aldrich, USA), 2,2,6,6-tetramethyl-4-piperidone (TCI, Japan), palladium on
138 activated charcoal (10% Pd, Sigma Aldrich, USA), dimethylamine (Linde AG, Germany) and
139 hydrogen (Linde Ag, Germany) were used as received.

140

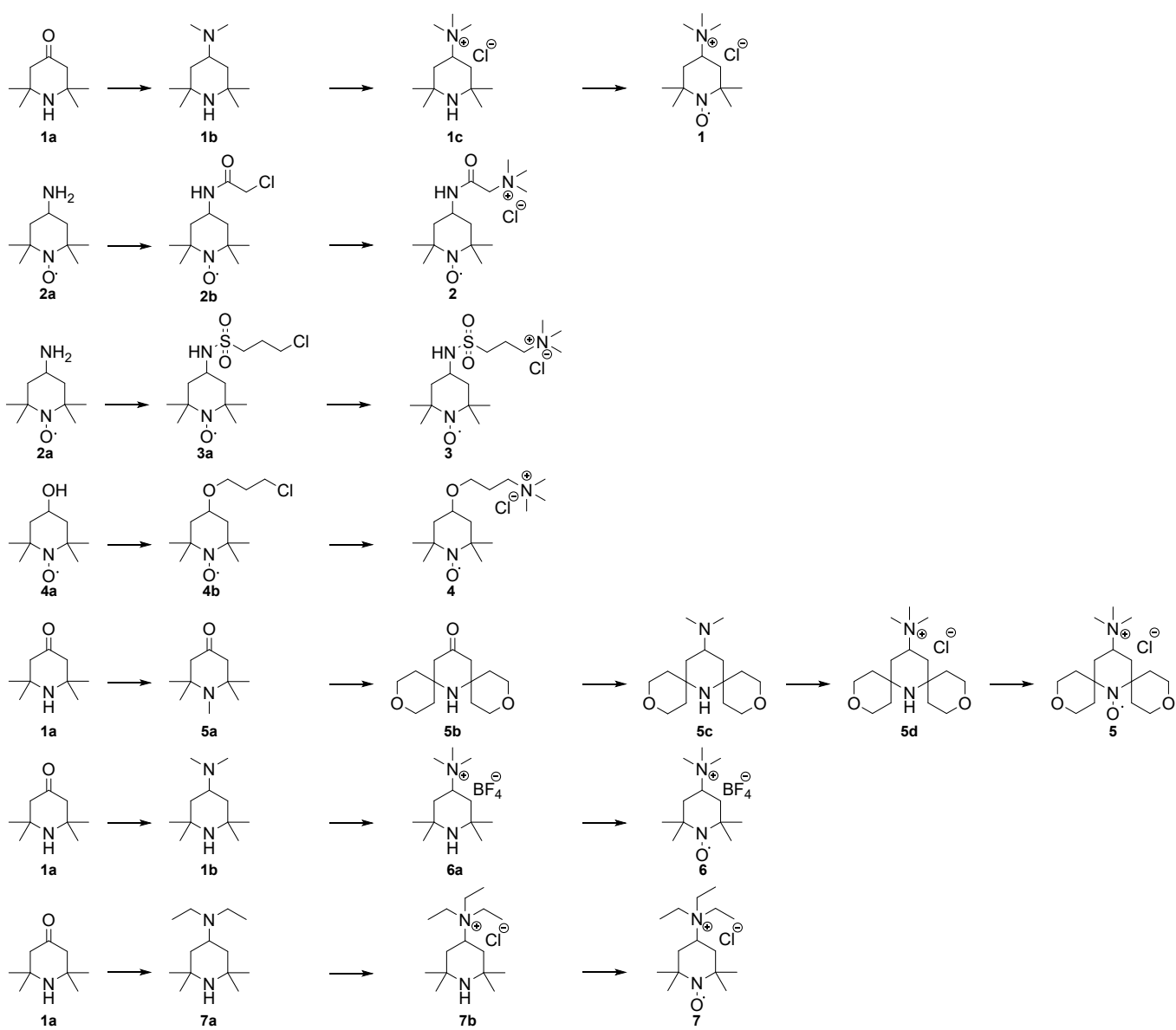
141

142

143

144

145



Scheme S1: Schematic representation of the performed synthetic routes.

146 Synthesis overview

147

148

149

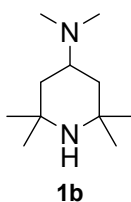
150

151

152

153

154 *Synthesis of N,N-2,2,6,6-hexamethylpiperidin-4-amine (1b):*



155

156 The synthesis was performed based on the protocol published by Janoschka *et al.*⁵

157 2,2,6,6-Tetramethylpiperidine-4-one (**1a**) (150 g, 970 mmol) was dissolved in 300 mL

158 methanol, transferred to a Büchi ecoclave pressure reactor and cooled to $-20\text{ }^{\circ}\text{C}$.

159 Subsequently, palladium on activated charcoal (10% Pd, 8 g, 7.36 mmol) and liquid

160 ($-10\text{ }^{\circ}\text{C}$) dimethylamine were added. The reaction mixture was heated to $60\text{ }^{\circ}\text{C}$ and

161 hydrogen (approx. 3 bar) was added. The pressure of the ecoclave was checked

162 frequently and re-adjusted to 3 bar until it remained stable. The mixture was heated to

163 $80\text{ }^{\circ}\text{C}$ and if necessary, hydrogen or dimethylamine were added until GC-MS analytics

164 revealed full conversion of the reaction. The catalyst was removed by filtration and the

165 product was obtained as colourless liquid after distillation under reduced pressure.

166 (1.0×10^{-3} mbar, 42 to $44\text{ }^{\circ}\text{C}$) (165.0 mmol, 92.3%). ^1H NMR (CDCl_3 , 300 MHz):

167 δ [ppm] = 0.65 (1 H, br s, NH), 0.97 (2 H, t, $J = 12.24$ Hz, CH_2), 1.16

168 (12 H, d, $J = 17.33$ Hz, CCH_3), 1.75 (2 H, dd, $J = 12.62, 3.20$ Hz, CH_2), 2.27

169 (6 H, s, NCH_3), 2.65 (1 H, tt, $J = 12.13, 3.23$ Hz, CH); ^{13}C NMR (CDCl_3 , 75 MHz):

170 δ [ppm] = 28.65 (CCH_3), 35.35 (CCH_3), 41.11 (CH_2), 41.25 (NCH_3), 51.00 (C), 56.27

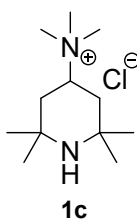
171 (CH); HR-MS (ESI m/z): calc. for $[\text{C}_{11}\text{H}_{24}\text{N}_2]^{\text{H}^+}$ 185.2012, found: 185.2015. Elemental

172 analysis: found C, 70.45; H, 12.7; N, 14.7. Calc. for $\text{C}_{11}\text{H}_{24}\text{N}_2$: C, 70.3; H, 13.1; N,

173 14.9%.

174

175 *Synthesis of N,N,N-2,2,6,6-heptamethylpiperidin-4-ammonium chloride (1c):*

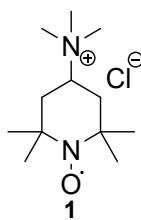


176

177 The synthesis was performed based on the protocol of Janoschka *et al.*⁵ *N,N*-2,2,6,6-
178 Hexamethylpiperidin-4-amine (**1b**) (159.0 g, 862 mmol) was dissolved in 800 mL
179 acetonitrile:toluene (50:50 v:v) and transferred into a Büchi ecoclave pressure reactor.
180 The mixture was heated to 70 °C and chloromethane was added until a pressure of 3 bar
181 was reached. Afterwards, the mixture was kept at 70 °C and chloromethane was added
182 until the pressure was stable at 3 bar. The mixture was then cooled to room temperature
183 and the received suspension was filtered of, washed with toluene, acetone and
184 acetonitrile. The solvents of the filtrate were evaporated under reduced pressure. The
185 received solid was washed with low amounts of acetonitrile and united with the first
186 filtrate. The desired product was received as white solid (157.05 g, 668 mmol, 77.5 %)
187 after drying under reduced pressure. ¹H NMR (D₂O, 300 MHz): δ [ppm] = 1.15
188 (12 H, d, *J* = 5.65 Hz, CH₃), 1.35 (2 H, t, *J* = 12.24 Hz, CH₂), 2.09
189 (2 H, d, *J* = 10.93 Hz, CH₂), 3.00 (9 H, s, N(CH₃)₃), 3.72
190 (1 H, tt, *J* = 12.55, 2.80 Hz, NCH); ¹³C NMR (CDCl₃, 75 MHz): δ [ppm] = 26.25
191 (CCH₃), 32.88 (CCH₃), 37.08 (CH₂), 50.46 (N(CH₃)₃), 51.85 (C), 69.21 (CH); HR-MS
192 (ESI): calc. for [C₁₂H₂₇N₂]⁺ 199.2169, found: 199.2171. Elemental analysis: found C,
193 61.2; H, 11.9; N, 11.8; Cl, 15.2. Calc. for C₁₂H₂₆ClN₂O: C, 61.4; H, 11.6; N, 11.9; Cl,
194 15.1%.

195

196 *Synthesis of N,N,N-2,2,6,6-heptamethylpiperidinyloxyl-4-ammonium chloride (1)*:



197

198 The synthesis was performed based on the protocol of Janoschka *et al.*⁵ *N,N,N-2,2,6,6-*

199 *Heptamethylpiperidin-4-ammonium chloride (1c)* (155 g, 660 mmol) was dissolved in

200 1000 mL water, sodium tungstate (10.89 g, 33 mmol) dissolved in 550 mL water and

201 45 mL (660 mmol) of 50% hydrogen peroxide were added. The pH-value was checked

202 and adjusted to pH = 10 and the solution was stirred for three days at room temperature.

203 Every day, 1 eq. of hydrogen peroxide (35%) was added, the pH-value checked and if

204 necessary, re-adjusted with sodium hydroxide (35%) to pH = 10. Afterwards, the

205 solution was acidified with 1 M hydrochloric acid to a pH-value of 4. Catalytic amounts

206 of manganese dioxide were added, stirred for additional 3 h and filtered off. The filtrate

207 was evaporated under reduced pressure and the residue was lyophilized. Afterwards, the

208 orange solid was suspended in acetonitrile and filtered. The solvent was removed under

209 reduced pressure. The received solid contains the pure product. This suspension-

210 filtration procedure was repeated until only a slightly reddish residue remained on the

211 filter. The desired product could be obtained after drying as orange solid

212 (163.74 g, 655 mmol, quantitative). ¹H NMR (D₂O, 300 MHz): δ [ppm] = 1.14

213 (12 H, d, *J* = 17.71 Hz, CCH₃), 1.61 (2 H, t, *J* = 12.34 Hz, CH₂), 2.03

214 (2 H, d, *J* = 10.17 Hz, CH₂), 2.91 (9 H, s, N(CH₃)₃), 3.55 (1 H, tt, *J* = 12,67, 3.06 Hz,

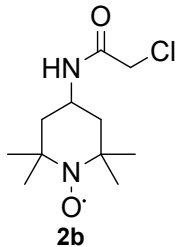
215 NCH) (quenched with phenyl hydrazine); ¹³C NMR (D₂O, 75 MHz): δ [ppm] = 19.59

216 (CCH₃), 30.90 (C_CH₃), 37.37 (CH₂), 50.87 (N(CH₃)₃), 59.46 (C), 66.72 (CH) (quenched

217 with phenyl hydrazine); HR-MS (ESI): calc. for [C₁₂H₂₆N₂O]⁺ 214.2040, found:

218 214.2039. Elemental analysis: found C, 57.0; H, 10.4; N, 11.1; Cl, 14.0. Calc. for
219 $C_{12}H_{26}ClN_2O + 0.15 H_2O$: C, 57.1; H, 10.5; N, 11.1; Cl, 14.0%; ESR: $g = 2.0067$.

220 *Synthesis of 2-chloro-N-(2,2,6,6-tetramethylpiperidin-4-yl)acetamide (2b)*:



221

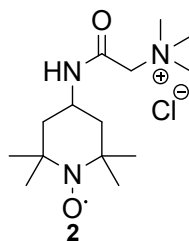
222 4-Amino-2,2,6,6-tetramethylpiperidine-1-oxyl (**2a**) (8.00 g, 46.71 mmol) was
223 suspended in 50 mL dichloromethane (SPS) and potassium carbonate (6.46 g,
224 46.71 mmol) was added. The mixture was stirred vigorously and chloroacetyl chloride,
225 dissolved in 10 mL dichloromethane (SPS), was added dropwise. The mixture was
226 subsequently heated under reflux for 3 h. After cooling to room temperature, 20 mL
227 water were added. The organic solution was removed and the water phase was extracted
228 with 2×100 mL dichloromethane. All organic phases were united and extracted with
229 2×100 mL water and dried with sodium sulphate before the solvent was removed under
230 reduced pressure. The product was obtained after column chromatography with
231 hexane:ethyl acetate (8:2 v:v) and slowly evaporating of the solvents at room
232 temperature as red crystals (7.41 g, 29.91 mmol, 64%, suitable for X-ray
233 crystallography). 1H NMR ($CDCl_3$, 300 MHz): δ [ppm] = 1.14 (12 H, s, CH_3), 1.38
234 (2 H, t, $J = 12.34$ Hz, CH_2), 1.73 - 1.86 (2 H, m, CH_2), 3.93 (2 H, s, CH_2Cl), 4.01 - 4.22
235 (1 H, m, CH) (quenched with phenyl hydrazine); ^{13}C NMR ($CDCl_3$, 75 MHz):
236 δ [ppm] = 19.94 (CH_3), 31.37 (CH_3), 41.29 (CH), 42.61 (CH_2Cl), 44.38 (CH_2) 61.25 (C),
237 165.37 (CO) (quenched with phenyl hydrazine); HR-MS (ESI m/z): calc. for
238 $[C_{11}H_{20}ClN_2O_2]^+$ 247.1208 found 247.1201. Elemental analysis: found: C, 53.6; H, 8.2;

239 N, 11.4; Cl, 14.5. Calc. for $C_{11}H_{20}ClN_2O_2$: C, 53.3; H, 8.1; N, 11.3; Cl, 14.3%; ESR:

240 $g = 2.0064$.

241

242 *Synthesis of N,N,N-trimethyl-2-oxo-2-((2,2,6,6-tetramethylpiperidin-4-yloxy)amino)ethan-1-*
243 *amonium chloride (2):*

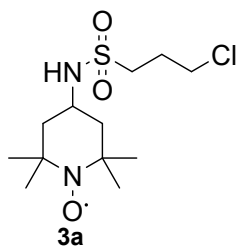


244

245 2-Chloro-*N*-(2,2,6,6-tetramethylpiperidin-4- yloxy)acetamide (2b) (7.00 g,
246 28.26 mmol) was dissolved in 50 mL dichloromethane (SPS) and argon was bubbled
247 through the solution for 15 min. Trimethylamine solution (13% in THF,
248 18 mL, 16.0 g, 35.2 mmol) was added dropwise and the reaction mixture was stirred for
249 16 h at room temperature. The received orange suspension was filtered and washed with
250 small amounts of dichloromethane. The solvent of the filtrate was removed under
251 reduced pressure till only 5 mL was left and the mixture was left at 4 °C overnight. The
252 precipitate was filtered off and washed with a small amount of dichloromethane. Both
253 solid fractions were united and dried to receive the product as orange solid (4.86 g,
254 15.83 mmol, 56%). ¹H NMR (D₂O, 300 MHz): δ [ppm] = 1.14
255 (12 H, d, *J* = 6.59 Hz, CH₃), 1.35 - 1.50 (2 H, m, CH₂), 1.76 - 1.91 (2 H, m, CH₂), 3.15
256 (9 H s, N(CH₃)₃) 3.87 (2 H, s, CH₂Cl), 4.08 (1 H, tt., *J* = 12.32, 3.89 Hz, CH)
257 (quenched with phenyl hydrazine); ¹³C NMR (D₂O, 75 MHz): δ [ppm] = 19.72 (CH₃),
258 30.38 (CH₃), 41.52 (CH), 43.22 (CH₂), 54.23 (N(CH₃)₃) 59.96 (C), 65.27 (CH₂Cl)
259 163.09 (CO) (quenched with phenyl hydrazine); HR-MS (ESI *m/z*): calc. for
260 [C₁₄H₂₉N₃O₂]⁺ 271.2254 found 271.2255. Elemental analysis: found: C, 54.6; H, 9.5; N,
261 13.65; Cl, 11.25. Calc. for C₁₄H₂₉ClN₃O₂: C, 54.8; H, 9.5; N, 13.7; Cl, 11.55%. ESR:
262 *g* = 2.0063.

263

264 *Synthesis of 3-chloro-N-(2,2,6,6-tetramethylpiperidin-4-yloxy)propane-1-sulfonamide (3a):*

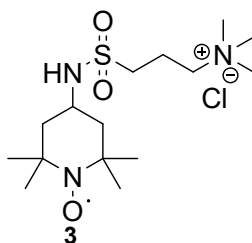


265

266 4-Amino-2,2,6,6-tetramethylpiperidine-1-oxyl (**2a**) (3.0 g, 17.5 mmol) was suspended
267 in 200 mL dichloromethane (SPS), which completely dissolves after addition of 4.57 mL
268 *N,N*-diisopropylethylamine (3.39 g, 26.25 mmol). The solution was cooled with a
269 sodium chloride ice bath below 0 °C and 3-chloropropanesulfonyl chloride (2.08 mL,
270 3.10 g, 26.25 mmol) dissolved in 50 mL dichloromethane (SPS) was added dropwise
271 over one hour. The reaction mixture was extracted three times with 150 mL brine and
272 the organic solution was dried with sodium sulphate. The solvent was removed under
273 reduced pressure. The desired product was received after column chromatography with
274 heptane:ethyl acetate (50:50 v:v) and slow evaporation of the solvents at room
275 temperature as red crystals (4.13 g, 13.24 mmol, 75.7%, suitable for X-ray
276 crystallography). ¹H NMR (CDCl₃, 300 MHz): δ [ppm] = 1.10
277 (12 H, d, *J* = 5.84 Hz, CH₃), 1.33 - 1.49 (2 H, m, CHCH₂C), 1.76 - 1.88
278 (2 H, m, CHCH₂C), 2.16 (2 H, dq, *J* = 8.95, 6.06 Hz, CH₂CH₂CH₂), 3.07
279 (2 H, t, *J* = 7.35 Hz, SO₂ CH₂), 3.57 (2 H, t, *J* = 6.12 Hz, CH₂Cl), 4.75
280 (1 H, d, *J* = 7.35 Hz, CH) (quenched with phenyl hydrazine); ¹³C NMR (CDCl₃,
281 75 MHz): δ [ppm] = 19.88 (CH₃), 27.03 (CH₂CH₂CH₂), 31.59 (CH₃), 42.87 (CH₂Cl),
282 45.64 (CH), 46.40 (CHCH₂C), 51.29 (SO₂CH₂) 60.56 (C) (quenched with phenyl
283 hydrazine); HR-MS (ESI *m/z*): calc. for [C₁₂H₂₄ClN₂O₃S]⁺ 311.1191 found 311.1192.
284 Elemental analysis: found C, 46.4; H, 7.8; N, 8.9; S, 10.4; Cl, 11.15. Calc. for
285 C₁₂H₂₄ClN₂O₃S: C, 46.2; H, 7.8; N, 9.0; S, 10.3; Cl, 11.4%; ESR: *g* = 2.0064.

286

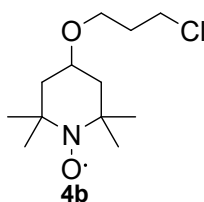
287 *Synthesis of N,N,N-trimethyl-3-(N-(2,2,6,6-tetramethylpiperidin-4-yloxy)sulfamoyl)propan-1-*
288 *amonium chloride (3):*



289

290 3-Chloro-*N*-(2,2,6,6-tetramethylpiperidin-4-yloxy)propane-1-sulfonamide (**3a**) (2.5 g,
291 8.02 mmol) was placed in a microwave vial, 18.2 mL (14.36 g, 80.2 mmol)
292 33% trimethylamine solution in ethanol was added and the vial was capped. The vial
293 was placed in an oil bath at 50 °C for two days until TLC (hexane: ethyl acetate 1:1, v:v)
294 indicated quantitative conversion. Afterwards, the solvents were removed under reduced
295 pressure and the residue was dissolved in as less water as possible. The desired product
296 was received after precipitation in acetone and subsequently drying as red solid (2.3 g,
297 6.20 mmol, 77.3%). ¹H NMR (D₂O, 300 MHz): δ [ppm] = 1.12
298 (12 H, d, *J* = 2.64 Hz, CH₃), 1.49 (2 H, t, *J* = 12.62 Hz, CH₂), 1.88 (2 H, dd, *J* = 13.19,
299 3.77 Hz, CH₂), 2.07 - 2.25 (2 H, m, CH₂CH₂CH₂), 3.01 (9 H, s, N(CH₃)₃),
300 3.17 (2 H, t, *J* = 7.16 Hz, SO₂CH₂), 3.28 - 3.42 (2 H, m, CH₂-N), 3.50 - 3.70
301 (1 H, m, CH) (quenched with phenyl hydrazine); ¹³C NMR (D₂O, 75 MHz):
302 δ [ppm] = 17.73 (CH₂CH₂CH₂), 19.74 (CH₃), 30.43 (CH₃), 45.32 (CH), 45.51
303 (CHCH₂C), 49.61 (SO₂CH₂) 52.93 (N(CH₃)₃), 60.04 (C), 64.15 (CH₂N) (quenched with
304 phenyl hydrazine); HR-MS (ESI *m/z*): calc. for [C₁₅H₃₃N₃O₃S]⁺ 335.2237 found
305 335.2233. Elemental analysis: found: C, 46.7; H, 9.2; N, 10.55; S, 8.2; Cl, 9.2. Calc. for
306 C₁₅H₃₃ClN₃O₃S + 0.9 H₂O: C, 46.5; H, 9.1; N, 10.85; S, 8.3; Cl, 9.2%; ESR: *g* = 2.0063.
307

308 Synthesis of 4-(3-chloropropoxy)-2,2,6,6-tetramethylpiperidin-1-yloxy (**4b**):

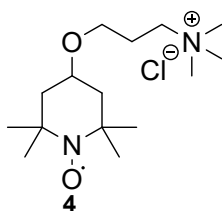


309

310 The synthesis was based on the procedure described by Liu *et al.*⁶ 4-Hydroxy-2,2,6,6-
311 tetramethylpiperidin-1-oxy (**4a**) (20 g, 116 mmol), tetrabutylammonium-bromide
312 (1.73 g, 5.33 mmol), 1-bromo-3-chloropropane (44.7 mL, 71.5 g, 453.4 mmol) were
313 dissolved in a mixture of 4.5 mL toluene and 67 mL 50% aq. sodium hydroxide. The
314 mixture was stirred vigorously for 96 h. After completion, 400 mL diethyl ether was
315 added and the organic solution was extracted with water until the water had only a
316 slightly orange color. The organic phase was dried with sodium sulphate and the solvents
317 were removed under reduced pressure. The desired product was received after column
318 chromatography with pure ethyl acetate as viscous red liquid (10.1 g, 40.6 mmol, 35%).
319 ¹H NMR (CDCl₃, 300 MHz): δ [ppm] = 1.21 (12 H, d, J = 18.65 Hz, CH₃), 1.50
320 (2 H, t, J = 11.77 Hz, CH₂), 1.89 - 2.07 (4 H, m, CH₂ + CH₂CH₂CH₂), 3.54 - 3.72
321 (4 H, m, OCH₂ + CH₂Cl + CH) (quenched with phenyl hydrazine); ¹³C NMR (CDCl₃,
322 75 MHz): δ [ppm] = 21.81 (CH₃), 30.70 (CH₃), 33.34 (CH₂CH₂CH₂), 42.36 (CH₂Cl),
323 44.02 (CH₂), 62.13 (C) 64.88 (CH₂O), 70.86 (CH) (quenched with phenyl hydrazine);
324 HR-MS (ESI m/z): calc. for [C₁₂H₂₃ClNO₂]⁺ 248.1412 found 248.1418. Elemental
325 analysis: found: C, 58.1; H, 9.3; N, 5.5; Cl, 13.5. Calc. for C₁₂H₂₃ClNO₂: C, 57.9; H,
326 9.3; N, 5.6; Cl, 14.2%; ESR: g = 2.0063.

327

328 Synthesis of *N,N,N*-trimethyl-3-((2,2,6,6-tetramethylpiperidin-4-yloxy)oxy)propan-1-
329 amonium chloride (**4**):

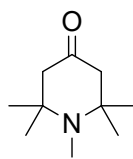


330

331 The synthesis was based on the procedure described by Liu *et al.*⁶ 4-(3-Chloropropoxy)-
332 2,2,6,6-tetramethylpiperidin-1-yloxy (**4b**) (9.00 g, 36.26 mmol) was dissolved in
333 85 mL trimethylamine solution (33% in ethanol, 362 mmol) and stirred for 96 h until
334 TLC (pure ethyl acetate) revealed full conversion. The mixture was concentrated under
335 reduced pressure. The received red liquid was dissolved in water and extracted with
336 dichloromethane until only a slightly red color remained in the organic phase. The
337 aqueous solution was concentrated to approx. 50 mL and then freeze-dried to obtain the
338 desired product as a hygroscopic orange solid (7.43 g, 25.38 mmol, 66.6%). ¹H NMR
339 (D₂O, 300 MHz): δ [ppm] = 1.15 (d, J = 6.22 Hz, 12 H, CH₃), 1.38
340 (t, J = 11.96 Hz, 2 H, CH₂), 1.85 - 2.09 (m, 4 H, CH₂ + CH₂CH₂CH₂), 3.01
341 (s, 2H, N(CH₃)₃) 3.23 - 3.35 (m, 2H, CH₂N) 3.55 (t, J = 5.84 Hz, 2 H, OCH₂), 3.75
342 (tt, J = 11.33, 4.03 Hz, 1 H, CH) (quenched with phenyl hydrazine); ¹³C NMR (D₂O,
343 75 MHz): δ [ppm] = 20.31 (CH₃), 23.27 (CH₂CH₂CH₂), 30.32 (CH₃), 43.43 (CH₂),
344 52.97 (N(CH₃)₃), 60.60 (C), 64.35 (CH₂N), 64.51 (CH₂O), 70.92 (CH) (quenched with
345 phenyl hydrazine); HR-MS (ESI m/z): calc. for [C₁₅H₃₂N₂O₂]⁺ 272.2458 found
346 272.2466. Elemental analysis: found: C, 57.3; H, 10.4; N, 8.9; Cl, 11.3. Calc. for
347 C₁₅H₃₂ClN₂O₂ + 0.35 H₂O: C, 57.3; H, 10.5; N, 8.9; Cl, 11.3%; ESR: g = 2.0065.

348

349 *Synthesis of 1,2,2,6,6-pentamethylpiperidin-4-one (5a):*



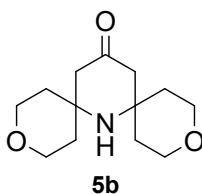
350

5a

351 The synthesis was performed based on a procedure reported by Paletta *et al.*⁷ Sodium
352 and benzophenone were added to toluene and the mixture was heated to reflux until the
353 solution became deep blue. The toluene was subsequently distilled in an argon-flushed
354 Schlenk flask. 2,2,6,6-Tetramethylpiperin-4-one (**1a**) (20 g, 129 mmol) and
355 paraformaldehyde (5.56 g, 185 mmol) were suspended in the freshly distilled toluene
356 (100 mL). The mixture was stirred for 1 h at 90 °C, followed by dropwise addition of
357 formic acid (85%, 6.6 mL, 149 mmol) and held at 90 °C for an additional hour.
358 Afterwards, the solution was heated to 100 °C for 45 min. During this time, a water-
359 toluene mixture was removed *via* distillation. The residue was cooled to room
360 temperature using an ice bath, sodium hydroxide (700 mg, 17.5 mmol) was added and
361 the mixture was stirred for one hour at room temperature. The solution was purified by
362 filtration and the solvent of the filtrate was removed under reduced pressure. The
363 received brown liquid was distilled under reduced pressure (1.6×10^{-2} mmbar,
364 42 to 44 °C) to provide the desired product (11.16 g, 66 mmol, 51.2%) as greenish oil.
365 ¹H NMR (CDCl₃, 300 MHz): δ [ppm] = 1.13 (12 H, s, CCH₃), 2.32 (3 H, s, NCH₃), 2.36
366 (4 H, s, CH₂); ¹³C NMR (CDCl₃, 75 MHz): δ [ppm] = 27.19 (C_CH₃), 28.55 (NCH₃),
367 55.62 (CH₂), 58.71 (C), 209.99 (CO); HR-MS (ESI): calc. for [C₁₀H₁₉NO+H]⁺
368 170.1539, found:170.1542. Elemental analysis: found: C, 70.4; H, 11.1; N, 7.9. Calc for
369 C₁₀H₁₉NO + 0.1 H₂O: C, 70.2; H, 11.3; N, 8.2%.

370

371 Synthesis of 3,11-dioxo-7-azadispiro[5.1.5.3]hexadecan-15-one (**5b**):

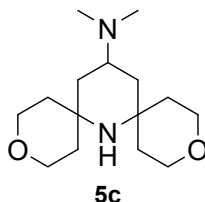


372

373 The synthesis was performed based on the protocol by Morisako *et al.* and Haugland *et*
374 *al.*^{8, 9 8, 9 8, 9 8, 9} 1,2,2,6,6-Pentamethylpiperidin-4-one (**5a**) (19.23 g, 114 mmol) and
375 tetrahydro-4H-pyran-4-one (35.48 g, 32.60 mL, 354 mmol) were dissolved in 130 mL
376 DMSO. Afterwards, ammonium chloride (37.87 g, 708 mmol) was added portion-wise.
377 Subsequently, 18 mL Triton B (40 wt.% in methanol) were added, and the mixture was
378 stirred at 55 °C for 8 h, followed by addition of 200 mL water. The mixture was held at
379 room temperature for 12 h. Afterwards, the solution was acidified with 7 vol% aq. HCl
380 to pH 1. The mixture was extracted with diethyl ether (3 × 150 mL). The aq. solution
381 was basified with 10% aq. K₂CO₃ to a pH value of around 9. The complete mixture was
382 extracted with ethyl acetate (2 × 200 mL) and chloroform (4 × 150 mL). The organic
383 solutions were dried with sodium sulphate and the solvent was removed under reduced
384 pressure. The resulting oil was kept in the fridge over night for crystallisation.
385 Afterwards, the solid was recrystallized in ethyl acetate multiple times until GC-MS
386 measurements indicated pure product. The desired product is a white crystalline solid
387 (6.1 g, 25.5 mmol, 21.6%). ¹H NMR (CDCl₃, 300 MHz): δ [ppm] = 1.50 - 1.72 (8 H, m,
388 CCH₂CH₂O), 2.38 (4 H, s, CH₂), 3.46 - 3.65 (4 H, m, CCH₂CH₂O), 3.70 - 3.95
389 (4 H, m, CCH₂CH₂O); ¹³C NMR (CDCl₃, 75 MHz): δ [ppm] = 40.52 (CCH₂CH₂O),
390 50.29 (C), 54.82 (CH₂), 63.73 (CCH₂CH₂O), 209.18 (CO); HR-MS (ESI): calc. for
391 [C₁₃H₂₁NO₃+H]⁺ 240.1594, found: 240.1606. Elemental analysis: found: C, 65.7; H,
392 8.95; N, 6.00. Calc for C₁₃H₂₁NO₃: C, 65.25; H, 8.85; N, 5.85%. Since the HR-MS data

393 fit to the requirements, the deviation of the carbon content in the elemental analysis of
394 <0.5% and >0.3% was found to be uncritical.

395 *Synthesis of N,N-dimethyl-3,11-dioxo-7-azadispiro[5.1.5.3]hexadecan-15-amine (5c):*

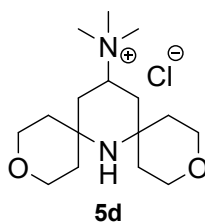


396

397 The synthesis was performed similar to the procedure described for **1a** with 3,11-dioxo-
398 7-azadispiro[5.1.5.3]hexadecan-15-one (**5b**) (5.54 g, 23.15 mmol) in 100 mL methanol
399 and palladium on activated charcoal (10% Pd, 1.05 g, 0.96 mmol). The product was
400 obtained as color less solid (5.71 mmol, 91.9%). ¹H NMR (CDCl₃, 300 MHz):
401 δ [ppm] = 0.48 (1 H, s br, NH), 0.97 (2 H, t, *J* = 12.34 Hz, CH₂), 1.34 - 1.59
402 (4 H, m, CCH₂CH₂O), 1.60 - 1.75 (4 H, m, CCH₂CH₂O), 1.99
403 (2 H, dd, *J* = 12.62, 3.01 Hz, CH₂), 2.28 (6 H, s, N(CH₃)₂), 2.64
404 (1 H, tt, *J* = 12.22, 3.13 Hz, CH), 3.49 - 3.68 (4 H, m, CCH₂CH₂O), 3.74 - 3.90
405 (4 H, m, CCH₂CH₂O); ¹³C NMR (CDCl₃, 75 MHz): δ [ppm] = 38.25 (CH₂), 39.03
406 (CH₂) 40.96 (N(CH₃)₂), 43.42 (CCH₂CH₂O), 50.56 (C), 54.25 (CH), 63.74
407 (CCH₂CH₂O), 64.19 (CCH₂CH₂O); HR-MS (ESI *m/z*): calc. for [C₁₅H₂₈N₂O₂+H]⁺
408 269.2224, found: 269.2223. Elemental analysis: found: C, 66.6; H, 10.6; N, 10.3. Calc.
409 for C₁₅H₂₈N₂O₂ + 0.1 H₂O: C, 66.7; H, 10.5; N, 10.4%.

410

411 Synthesis of *N,N,N*-trimethyl-3,11-dioxa-7-azadispiro[5.1.5.3]hexadecan-15-amonium
412 chloride (**5d**):



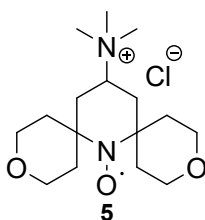
413

414 The synthesis was performed as described for **1b** with *N,N*-dimethyl-3,11-dioxa-7-
415 azadispiro[5.1.5.3]hexadecan-15-amine (**5c**) (5.3 g, 19.75 mmol). The desired product
416 was received as a colorless solid (6.2 g, 19.44 mmol, quant.). ¹H NMR (D₂O, 300 MHz):
417 δ [ppm] = 1.37 (2 H, t, J = 12.53 Hz, CH₂), 1.50 - 1.60 (2 H, m, CCH₂CH₂O), 1.69
418 (4 H, tdd, J = 13.96, 9.84, 4.24 Hz, CCH₂CH₂O), 1.82 (2 H, m, CCH₂CH₂O), 2.56
419 (2 H, d, J = 11.30 Hz, CH₂), 3.07 (9 H, s, N(CH₃)₃), 3.46 - 3.72
420 (5 H m, CCH₂CH₂O + CH), 3.81 (4 H, td, J = 8.15, 4.43 Hz, CCH₂CH₂O); ¹³C NMR
421 (D₂O, 75 MHz): δ [ppm] = 33.30 (CH₂), 36.46 (CCH₂CH₂O) 40.57 (CCH₂CH₂O), 50.67
422 (N(CH₃)₃), 51.62 (C), 63.44 (CCH₂CH₂O), 63.90 (CCH₂CH₂O) 67.64 (CH); HR-MS
423 (ESI m/z): calc. for [C₁₆H₃₁N₂O₂]⁺ 283.2380, found: 283.2381; Elemental analysis:
424 found: C, 54.4; H, 10.0; N, 7.9; Cl, 9.15. Calc. for C₁₆H₃₁ClN₂O₂ + 2 H₂O: C, 54.15; H,
425 10.0; N: 7.9; Cl: 10.0%. Since the HR-MS data fit to the requirements, the deviation of
426 the chlorine content in the elemental analysis was found to be uncritical.

427

428

429 Synthesis of *N,N,N*-trimethyl-3,11-dioxa-7-azadispiro[5.1.5.3]hexadecan-15-amonium
430 chloride aminoxyl free radical (**5**):

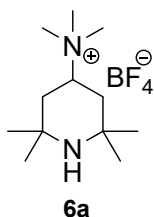


431

432 The synthesis was performed based on a reported protocol of Janoschka *et al.*⁵ *N,N,N*-
433 Trimethyl-3,11-dioxa-7-azadispiro[5.1.5.3]hexadecan-15-amonium chloride (**5d**)
434 (3.0 g, 9.41 mmol) and sodium tungstate (155 mg, 0.47 mmol) were dissolved in 30 mL
435 water. The pH-value of the solution was adjusted to 11.5 with 20 μ L 35% aq. sodium
436 hydroxide and 633 μ L hydrogen peroxide (50%) were added. The colorless solution
437 turned slowly to yellow and was stirred at room temperature for 18 h, before another
438 633 μ L of hydrogen peroxide (50%) were added. The pH-value dropped to 10.5 and the
439 orange solution was stirred for additional 48 h with again adding 633 μ L of 50%
440 hydrogen peroxide solution. Afterwards, the pH-value was adjusted with 1 M HCl to 4,
441 the precipitate was filtered off and catalytic amounts of manganese dioxide were added.
442 The suspension was stirred at room temperature for 2 h, subsequently filtered and freeze
443 dried. The orange solid was dissolved in dichloromethane/ethanol (20:1 v:v) and filtered
444 off to remove residual salts. The title compound was obtained after removing the
445 solvents under reduced pressure as orange solid (2.8 g, 8.4 mmol, 89%) ¹H NMR (D₂O,
446 300 MHz): δ [ppm] = 1.08 (2 H, t, J = 7.06 Hz, CH₂), 1.43 (5 H, m, CCH₂CH₂O),
447 2.04 - 2.28 (4 H, m, CCH₂CH₂O), 2.61 (2 H, d, J = 12.06, CH₂), 2.91 - 3.11
448 (9 H, m, N(CH₃)₃), 3.38 - 3.92 (9 H, m, CCH₂CH₂O + CH) (quenched with phenyl
449 hydrazine); ¹³C NMR (D₂O, 75 MHz): δ [ppm] = 16.95 (CH₂), 37.15 (CCH₂CH₂O),
450 50.96 (N(CH₃)₃), 57.51 (CCH₂CH₂O), 60.29 (C), 63.55 (CCH₂CH₂O), 64.08
451 (CCH₂CH₂O), 66.12 (CH) (quenched with phenyl hydrazine); HR-MS (ESI m/z): calc.

452 for $[\text{C}_{16}\text{H}_{30}\text{N}_2\text{O}_3]^+$ 298.2251 found 298.2253; Elemental analysis: found: C, 55.2; H, 9.4;
453 N, 7.55; Cl, 10.1. Calc. for $\text{C}_{16}\text{H}_{30}\text{ClN}_2\text{O}_3 + 0.9 \text{H}_2\text{O}$: C, 54.9; H, 9.2; N, 8.0; Cl, 10.1%;
454 Since the HR-MS data fit to the requirements, the deviation of the nitrogen content in
455 the elemental analysis of $<0.5\%$ and $>0.3\%$ was found to be uncritical. ESR: $g = 2.0069$.
456

457 *Synthesis of N,N,N-2,2,6,6-heptamethylpiperidin-4-ammonium tetrafluoroborate (6a):*

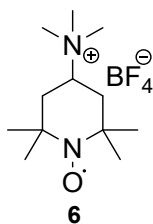


458

459 The synthesis was performed using argon as protection gas. *N,N*-2,2,6,6-
460 Hexamethylpiperidin-4-amine (**1b**) (6.23 g, 33.8 mmol) was dissolved in 400 mL
461 dichloromethane (DCM) and trimethyloxonium tetrafluoroborate (5.00 g, 33.8 mmol),
462 dissolved in 200 mL dichloromethane, was added. The mixture was stirred at room
463 temperature for two days. The received suspension was filtered off and the solvent of
464 the filtrate was removed under reduced pressure until approx. 50 mL remained. The
465 solution was kept overnight at 4 °C and the received crystals were filtered off. The
466 desired product was received as white solid (6.08 g, 21.2 mmol, 61.6%). ¹H NMR
467 (CD₃CN, 300 MHz): δ [ppm] = 1.16 (12 H, d, *J* = 10.93 Hz, CCH₃), 1.28
468 (2 H, t, *J* = 12.15 Hz, CH₂), 2.01 (2 H, dd, *J* = 11.87, 1.51 Hz, CH₂) 2.96 (9 H, s,
469 N(CH₃)₃); 3.64 (1 H, tt, *J* = 12.67, 3.06 Hz, NCH); ¹³C NMR (CD₃CN, 75 MHz):
470 δ [ppm] = 28.70 (CCH₃), 34.86 (CCH₃), 38.46 (CH₂), 51.53 (N(CH₃)₃), 52.67 (C), 70.97
471 (CH); HR-MS (ESI): calc. for [C₁₂H₂₇N₂]⁺ 199.2169, found: 199.2175; Elemental
472 analysis: found: C, 50.2; H, 9.6; N, 9.65. Calc. for C₁₂H₂₇N₂BF₄: C, 50.4; H, 9.5; N,
473 9.8%.

474

475 *Synthesis of N,N,N-2,2,6,6-heptamethylpiperidinyloxyl-4-ammonium tetrafluoroborate (6):*

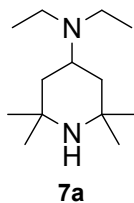


476

477 The synthesis was performed as described for compound **1**. The desired product was
478 received as orange solid (1.77 g, 5.8 mmol, 83.8%). ¹H NMR (CD₃CN, 300 MHz):
479 δ [ppm] = 1.16 (12 H, d, J = 15.26 Hz, CH₃), 1.57 - 1.71 (2 H, m, CH₂), 2.02
480 (2 H, dd, J = 12.15, 2.35 Hz, CH₂) 2.96 (9 H, s, N(CH₃)₃), 3.52
481 (1 H, tt, J = 12.65, 3.18 Hz, CH) (quenched with phenyl hydrazine); ¹³C NMR (CD₃CN,
482 75 MHz): δ [ppm] = 19.57 (CCH₃), 32.79 (CCH₃), 38.74 (CH₂), 51.64 (N(CH₃)₃), 59.39
483 (C), 68.02 (CH) (quenched with phenyl hydrazine); HR-MS (ESI): calc. for
484 [C₁₂H₂₆N₂O]⁺ 214.2040, found: 214.2040; Elemental analysis: found: C, 47.35; H, 8.9;
485 N, 9.7. Calc. for C₁₂H₂₇N₂BF₄ + 0.05 H₂O: C, 47.7; H, 8.7; N; 9.3%; Since the HR-MS
486 data fit to the requirements, the deviation of the nitrogen content in the elemental
487 analysis of <0.5% and >0.3% was found to be uncritical. ESR: g = 2.0066.

488

489 *Synthesis of N,N-diethyl-2,2,6,6-tetramethylpiperidin-4-amine (7a):*

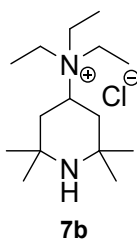


490

491 The synthesis was performed as described for compound **1a** with 2,2,6,6-
492 tetramethylpiperidin-4-one (10.0 g, 64.4 mmol), diethylamine (7.07 g, 96.6 mmol) and
493 palladium on activated charcoal (10% Pd, 1 g, 0.92 mmol). The product was obtained as
494 slightly yellow oil (2.6 mmol, 19.0%). ¹H NMR (CDCl₃, 300 MHz): δ [ppm] = 0.77 -
495 1.35 (20 H, m, CCH₃ + CH₂CH₃ + CH₂), 1.70 (2 H, dd, *J* = 12.62, 3.01 Hz, CH₂), 2.56
496 (4 H, q, *J* = 7.16, CH₂CH₃) 3.07 (1 H, tt, *J* = 12.20, 3.16 Hz, CH); ¹³C NMR (CDCl₃, 75
497 MHz): δ [ppm] = 13.94 (CH₂CH₃), 28.58 (CCH₃), 35.39 (CCH₃), 41.49 (CH₂), 43.40
498 (N(CH₂)), 51.29 (C), 51.53 (CH) HR-MS (ESI): calc. for [C₁₃H₂₈N₂+H]⁺ 213.2325,
499 found: 213.2325; Elemental analysis: No data could be obtain due to possible
500 decomposition.

501

502 *Synthesis of N,N,N-triethyl-2,2,6,6-tetramethylpiperidin-4-amonium chloride (7b):*

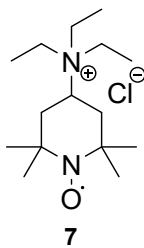


503

504 *N,N*-Diethyl-2,2,6,6-tetramethylpiperidin-4-amine (7a) (2.49 g, 11.72 mmol) and iodoethane
505 (4.7 mL, 9.14 g, 58.62 mmol) were dissolved in 20 mL acetonitrile and heated to 140 °C for
506 16 h in a microwave (Initiator, Biotage, Sweden). The off-white precipitate was filtered off,
507 washed with dichloromethane and dried. The white solid was dissolved in water and 10 g
508 Marathon A2 ion exchange resin was added. The mixture was stirred for 16 h, filtered and the
509 water was removed under reduced pressure. The desired product was received as white solid
510 (0.9 g, 3.2 mmol, 27.7%). ¹H NMR (D₂O, 300 MHz): δ [ppm] = 1.26
511 (9 H, t, *J* = 7.16 Hz, N(CH₂CH₃)₃), 1.43 (12 H, d, *J* = 14.32 Hz, CH₃), 1.95
512 (2 H, t, *J* = 12.90, CH₂), 2.33 (2 H, d, *J* = 12.90, CH₂), 3.39 (6 H, q, *J* = 7.16, N(CH₂CH₃)₃),
513 3.72 (1 H, t, *J* = 12.62, CH); ¹³C NMR (D₂O, 75 MHz): δ [ppm] = 8.57 (N(CH₂CH₃)₃), 23.49
514 (CCH₃), 29.71 (CCH₃), 35.01 (CH₂), 53.55 (N(CH₂CH₃)₃), 57.78 (C), 62.17 (CH); HR-MS
515 (ESI): calc. for [C₁₅H₃₃N₂]⁺ 241.2638, found: 241.2641; Elemental analysis: No data could be
516 obtain due to possible decomposition.

517

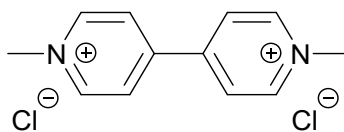
518 *Synthesis of N,N,N-triethyl-2,2,6,6-tetramethylpiperidinyloxy-4-ammonium chloride (7):*



519

520 *N,N,N*-Triethyl-2,2,6,6-tetramethylpiperidin-4-ammonium chloride (**7b**) (0.8 g, 2.90 mmol) was
521 dissolved in 30 mL water and 100 mL sodium hydrogen carbonate solution (0.7 M) was added.
522 After the solution was cooled to 0 °C, *m*-chloroperoxybenzoic acid 2.36 g (13.70 mmol),
523 dissolved in dichloromethane, was added. The mixture was kept at 0 °C for an hour and
524 afterwards, 1.76 g (8.22 mmol) sodium periodate, dissolved in 35 mL water, was added. After
525 the mixture was stirred at room temperature for two additional hours, the organic solution was
526 separated. The solvent of the orange aqueous solution was evaporated under reduced pressure.
527 The orange solid was washed several times with acetonitrile until only a slightly off-white solid
528 was left. The acetonitrile solution was filtered with a syringe filter and subsequently the solvent
529 was removed under reduced pressure. The desired product was received as orange solid (0.8 g,
530 2.7 mmol, 94.8%). ¹H NMR (D₂O, 300 MHz): δ [ppm] = 1.09 (12 H, d, *J* = 6.97 Hz, (CH₃), =
531 1.20 (9 H, t, *J* = 7.16 Hz, N(CH₂CH₃)₃), 1.73 (2 H, t, *J* = 12.43, CH₂), 2.02
532 (2 H, d, *J* = 11.11, CH₂), 3.27 (6 H, q, *J* = 7.10, N(CH₂CH₃)₃), 3.49 (1 H, t, *J* = 12.53, CH);
533 ¹³C NMR (D₂O, 300 MHz): δ [ppm] = 8.47 (N(CH₂CH₃)₃), 19.21 (CCH₃), 30.76 (CCH₃),
534 37.74 (CH₂), 53.02 (N(CH₂CH₃)₃), 60.08 (C), 63.10 (CH); HR-MS (ESI): calc. for
535 [C₁₅H₃₃N₂O]⁺ 256.2509, found: 256.2505; Elemental analysis: No data could be obtain due to
536 possible decomposition. ESR: *g* = 2.0069

537 *Synthesis of 1,1'-Dimethyl-4,4'-bipyridinium dichloride:*

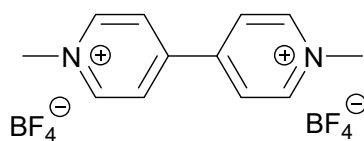


538

539 The synthesis was performed based on the protocol published by Janoschka *et al.*⁵ 4,4'-
540 Bipyridine (200 g, 1.28 mmol) and 2-chloroacetyl chloride (266.2 g, 2.82 mmol) were
541 suspended in 1 L of dimethylformamide and heated to 160 °C oil bath temperature. After one
542 hour, all solids were dissolved. The solution was stirred for additional 16 h. The off-white
543 precipitate was filtered off, resuspended in 500 mL dimethylformamide and stirred for 1 h at
544 170 °C. The mixture was filtered as hot as possible, and the filter cake was washed with acetone
545 and dichloromethane. The desired product was received after drying as slightly grey solid
546 (283 g, 1.1 mmol, 86%). The analytical data matched with the published values.

547

548 *Synthesis of 1,1'-Dimethyl-4,4'-bipyridinium ditetrafluoroborate:*



549

550 1,1'-Dimethyl-4,4'-bipyridinium dichloride (2.0 g, 7.78 mmol) was dissolved in 10 mL water.

551 To this aq. methyl viologen solution, a solution of silver tetrafluoroborate (3.03 g, 15.55 mmol)

552 in 15 mL water was added dropwise. The mixture was stirred for 1 h and left to settle for an

553 additional hour. The silver chloride was filtered off and the solvent of the filtrate was freeze-

554 dried to receive the desired product as white solid (2.80 g, 7.78 mol, quantitative) ¹H NMR

555 (D₂O, 300 MHz): δ [ppm] = 4.39 (6 H, s, CH₃), 8.40 (4 H, d, *J* = 6.78, CH₂), 8.93

556 (4 H, d, *J* = 6.78, CH₂); ¹³C NMR (D₂O, 75 MHz): δ [ppm] = 48.38 (CH₃), 126.70 (CH₂),

557 146.33 (CH₂N), 149.96 (C); HR-MS (ESI): calc. for [C₁₂H₁₄N₂]²⁺ 93.0573, found: 93.0574;

558 Elemental analysis: found: C, 39.7; H, 3.9; N, 7.6. Calc. for C₁₂H₁₄N₂B₂F₈ + 0.25 H₂O: C, 39.6;

559 H, 4.0; N, 7.6%.

560

561 *Potentiostatic titration*

562 As published by Levie, equations (1) and (2) are a simple expression of the entire titration curve
 563 for a potentiometric titration of Fe²⁺ to Fe³⁺ ions using Ce⁴⁺ salts.¹⁰ These equations could be
 564 generalized for all potentiometric titrations when only one electron is exchanged or applied to
 565 every redox titration by introduction of exponents in dependency of the exchanged electrons.

566

$$\Phi = \frac{10^{(-f * b)} * (10^{-f * x} + 10^{-f * c})}{10^{(-f * x)} * (10^{-f * x} + 10^{-f * b})}$$

567
568 (1)

569

$$V_t = \frac{\Phi C V}{C_t}$$

570 (2)

571 (b = standard redox potential of the analyte; c = standard redox potential of the titrant; f = F/RT
 572 ln 10, which describes the pre-factor in the Nernst equation; C = concentration of analyte; V =
 573 volume of the analyte; C_t = concentration of the titrant; V_t = volume of the titrant; x = measured
 574 potential).

575

576 By substitution of equation (1) into equation (2) and solving for x, a curve for volume of the
 577 titrant vs. the measured potential can be obtained. As the DoO is determined by the inflection
 578 point of the curve, the second derivation must be formed. However, this equation would be very
 579 complex, and thus, a simplification was used that introduces a prefactor a in equation (1) which
 580 corresponds to the added volume of titrant at the equilibrium point. Equation (3) was then fitted
 581 to a plot of the measured potential vs. the added volume.

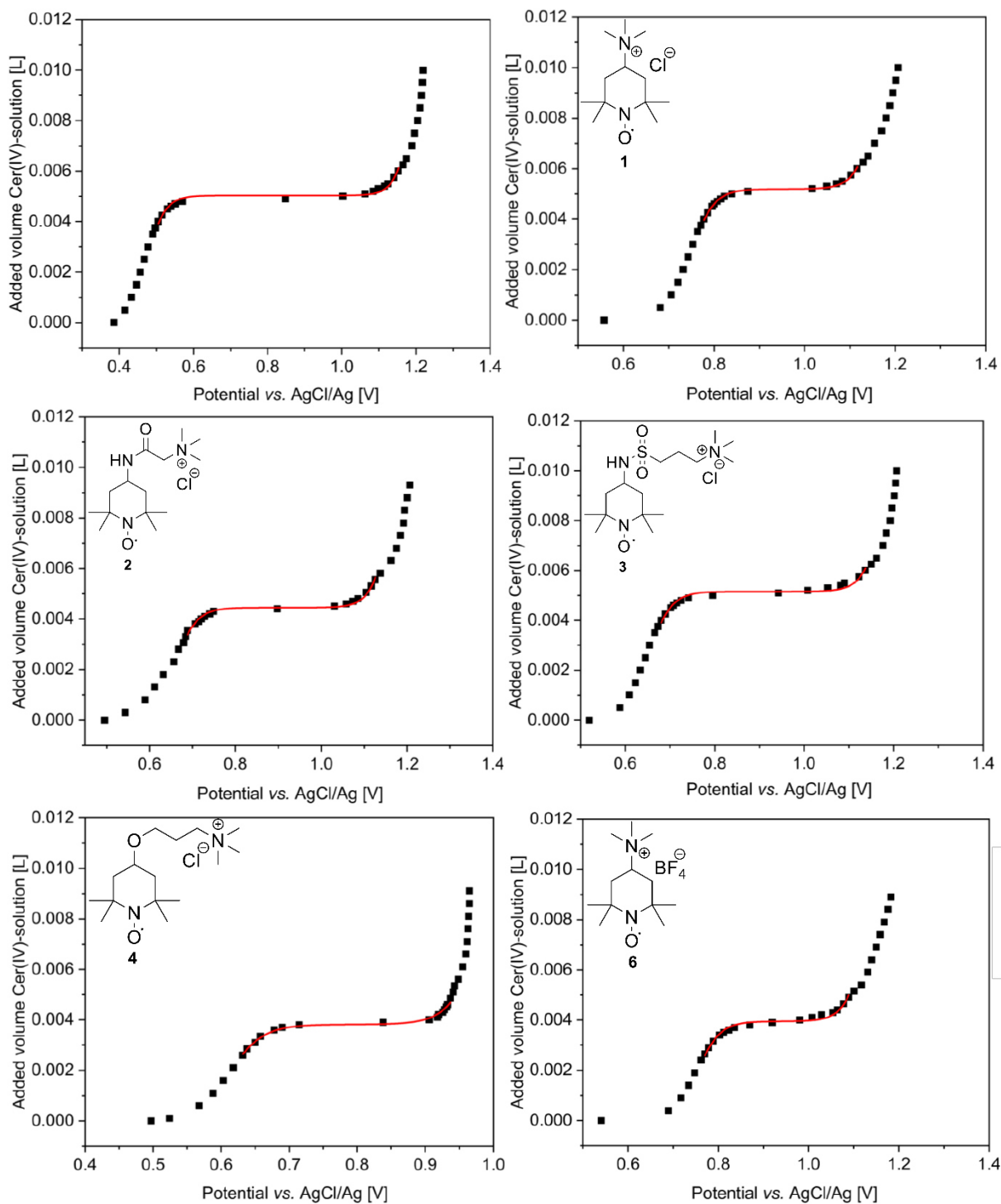
582

$$V_t = a * \frac{10^{(-f * b)} * (10^{-f * x} + 10^{-f * c})}{10^{(-f * x)} * (10^{-f * x} + 10^{-f * b})}$$

583
584 (3)

585

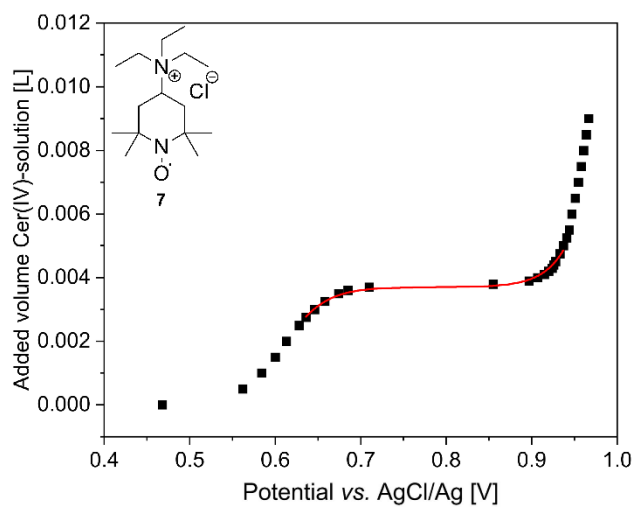
586



587

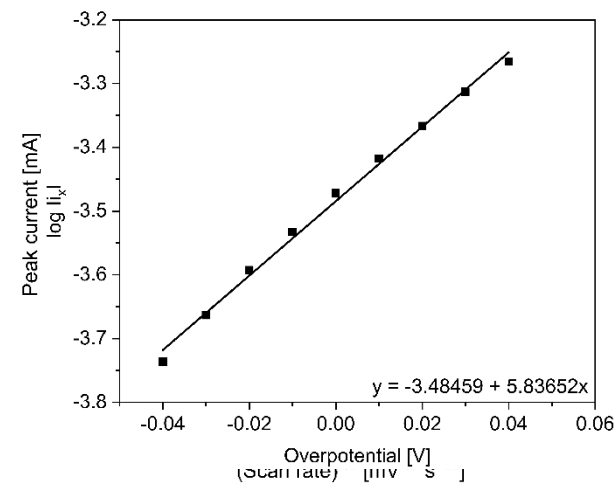
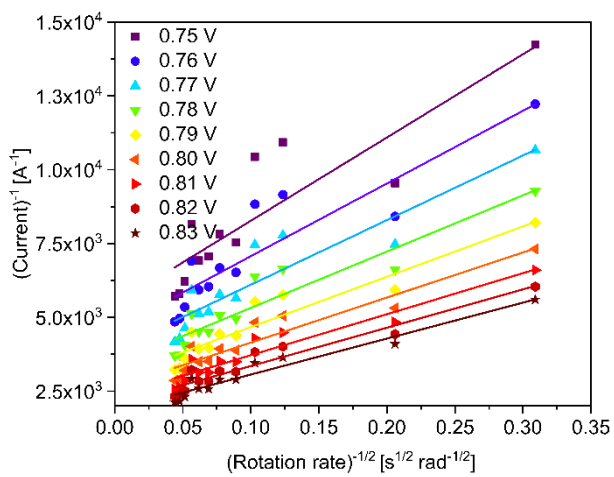
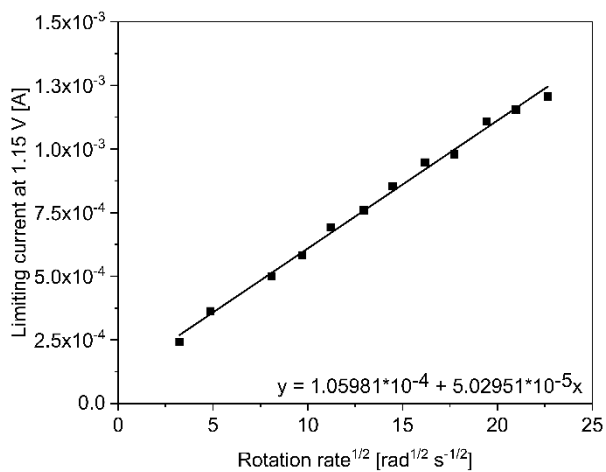
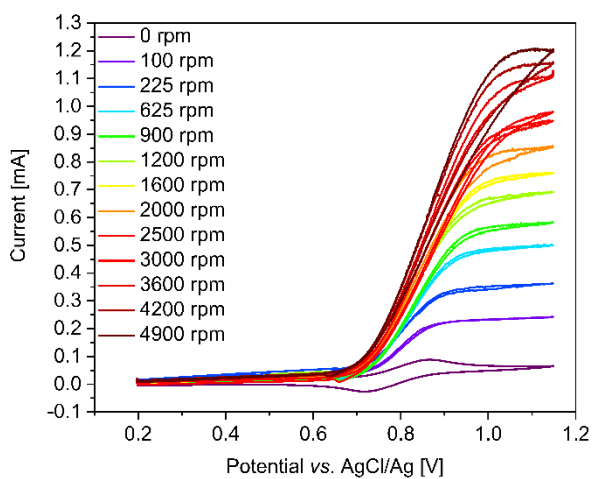
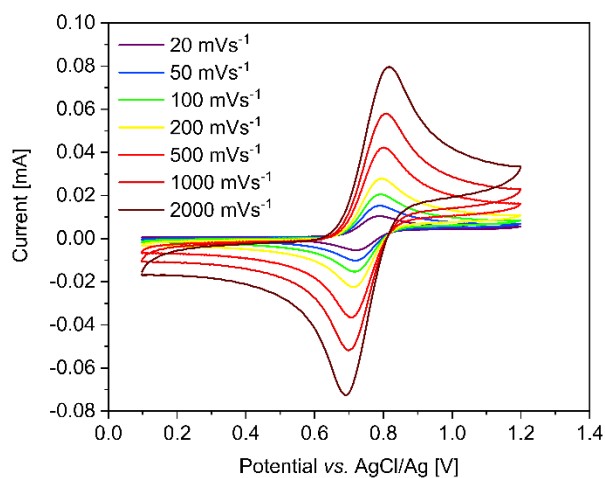
588 *Figure S2: Representative potentiometric titration curves of ammonium iron (II) sulphate (upper left), TMA-TEMPO 1 (upper*
 589 *right), TEMPO-amide 2 (middle left), TEMPO-sulfamide 3 (middle right), TEMPO-ether 4 (lower left) and TMA-TEMPO-BF₄*
 590 *salt 6 (lower right).*

591



593 *Figure S3: Representative potentiometric titration curves of TEA-TEMPO 7.*

594



599

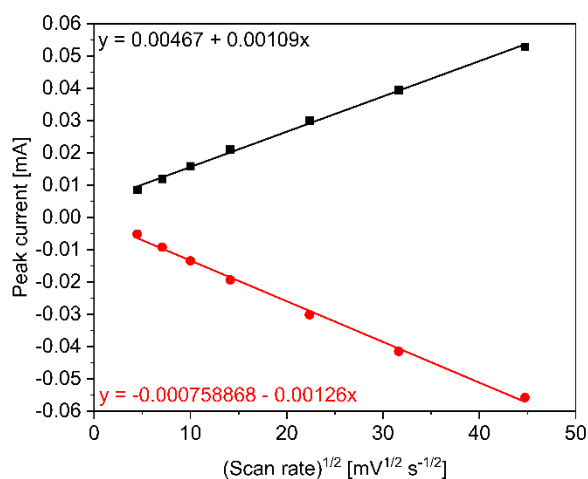
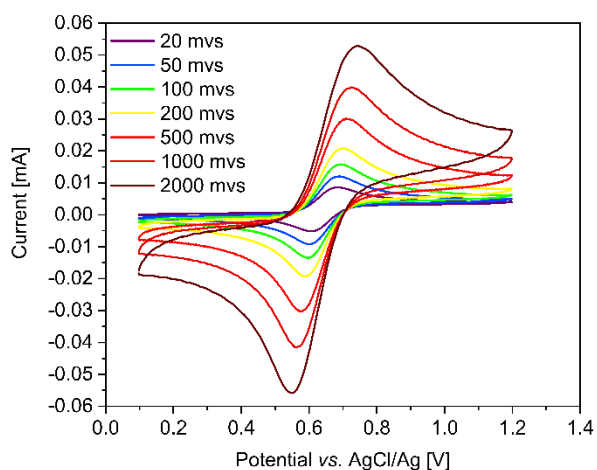
600

601

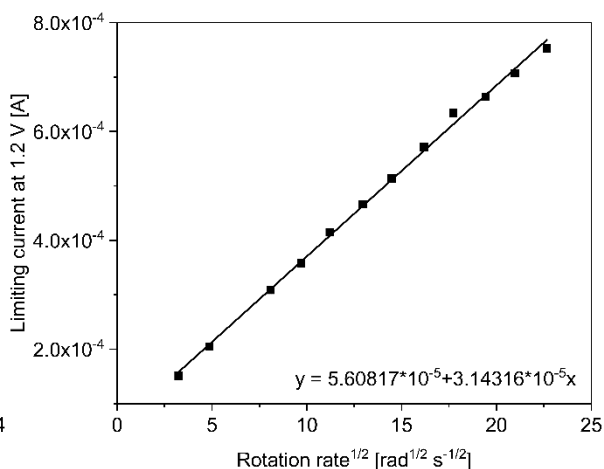
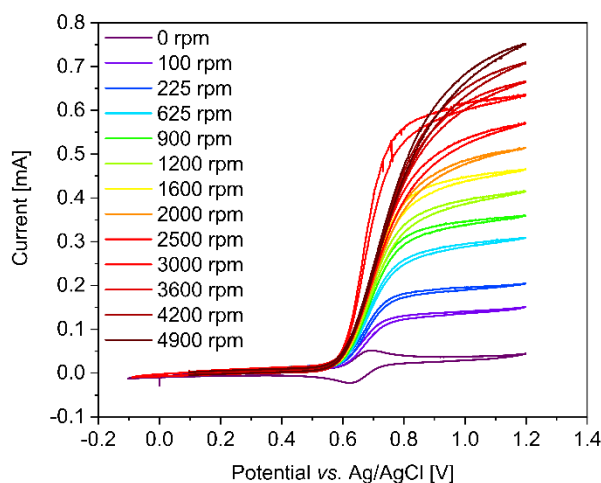
602

603

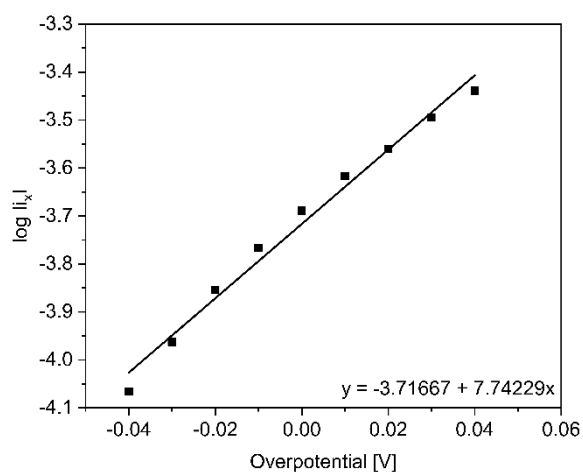
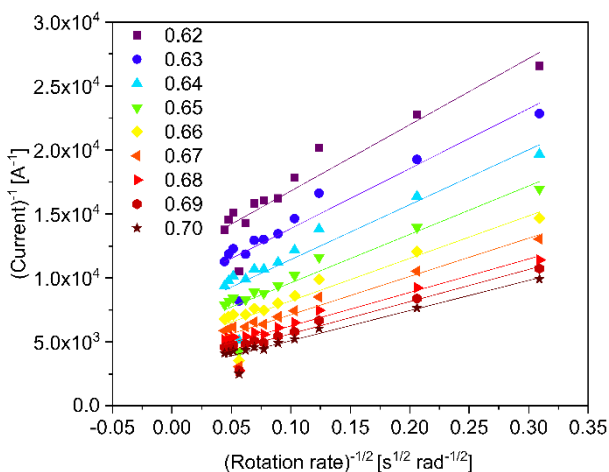
604 *Figure S4: Cyclic voltammograms of a 5.0 mmol L⁻¹ TMA-TEMPO 1 in 0.1 M sodium chloride as supporting electrolyte at*
605 *different scan speeds (upper left) and peak current vs. square root of scan speed (upper right, oxidation black and re-reduction*
606 *red). Rotating disk electrode voltammetry results (RDE) of a 7.0 mmolL⁻¹ TMA-TEMPO 1 in 0.1 M sodium chloride as*
607 *supporting electrolyte: RDE voltammograms (middle left), Levich Plot (middle right), Koutecký-Levich plot (lower left) and*
608 *Tafel plot (lower right). The following constants were calculated according to the above-described procedure: Reaction*
609 *constant $k^0 = 2.42 * 10^{-3} \text{ cm s}^{-1}$, diffusion coefficient $D = 4.7 * 10^{-6} \text{ cm}^2\text{s}^{-1}$ and a transfer coefficient $\alpha = 0.66$.*



610



611

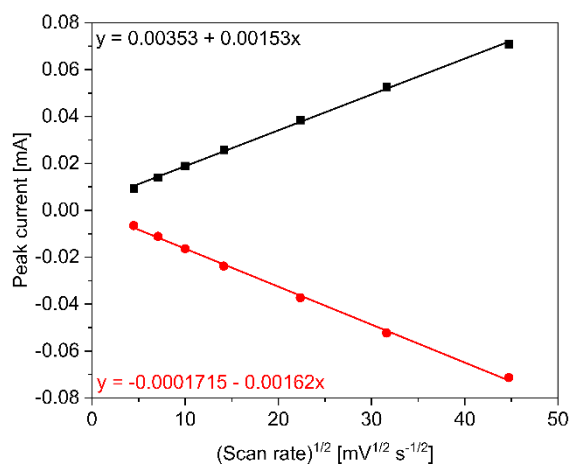
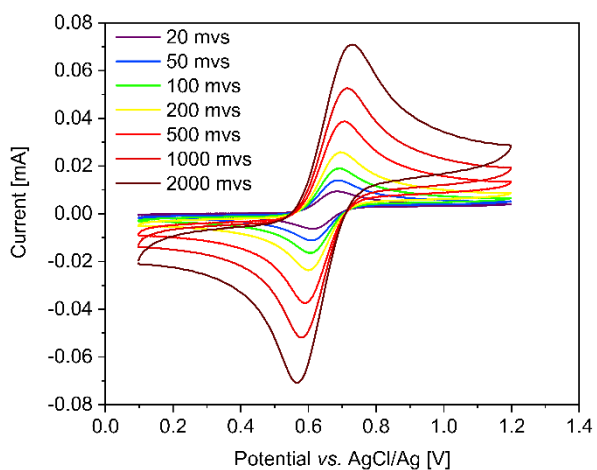


612

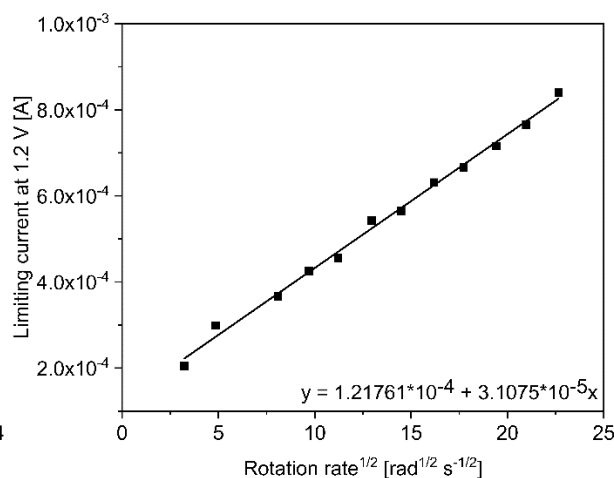
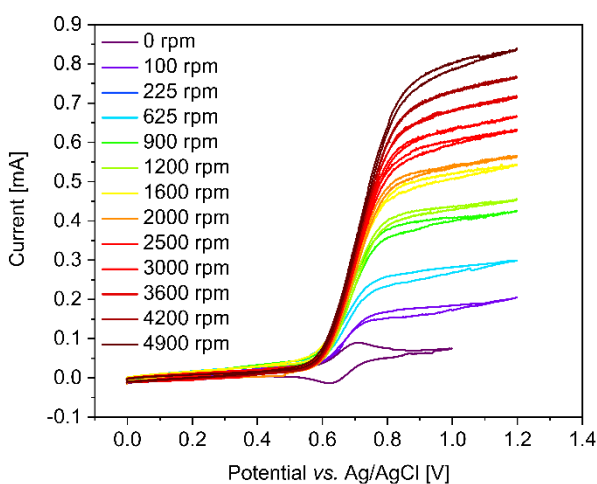
613

614

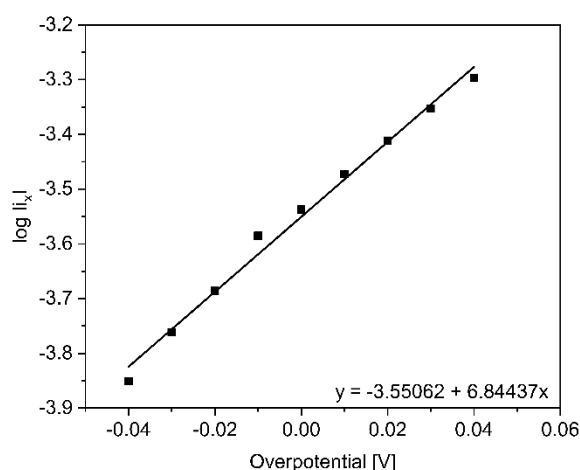
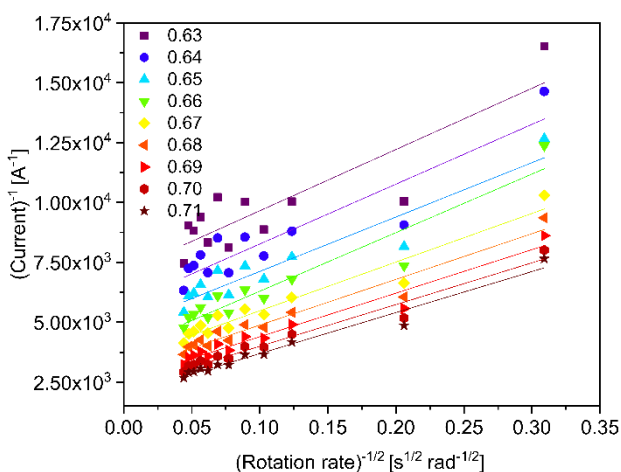
Figure S5: Cyclic voltammograms of a 5.0 mmol L⁻¹ TEMPO-amide 2 in 0.1 M sodium chloride as supporting electrolyte at different scan speeds (upper left) and peak current vs. square root of scan speed (upper right, oxidation black and re-reduction red). Rotating disk electrode voltammetry results (RDE) of a 5.0 mmolL⁻¹ TEMPO-amide 2 in 0.1 M sodium chloride as supporting electrolyte: RDE voltammograms (middle left), Levich Plot (middle right), Koutecký-Levich plot (lower left) and Tafel plot (lower right). The following constants were calculated according to the above-described procedure: Reaction constant k , diffusion coefficient D and a transfer coefficient α .



616



617



618

619

620

621

622

623

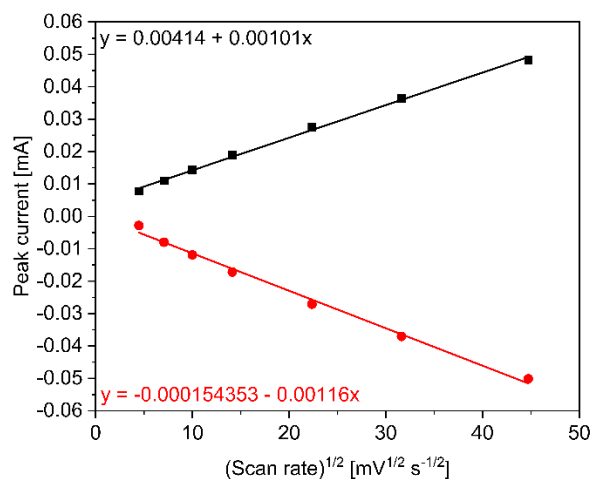
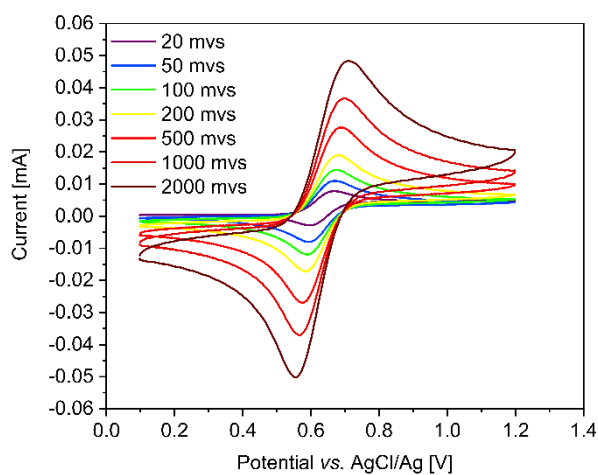
624

625

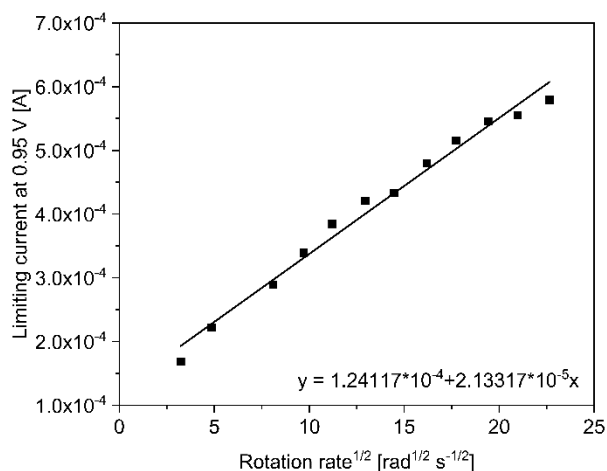
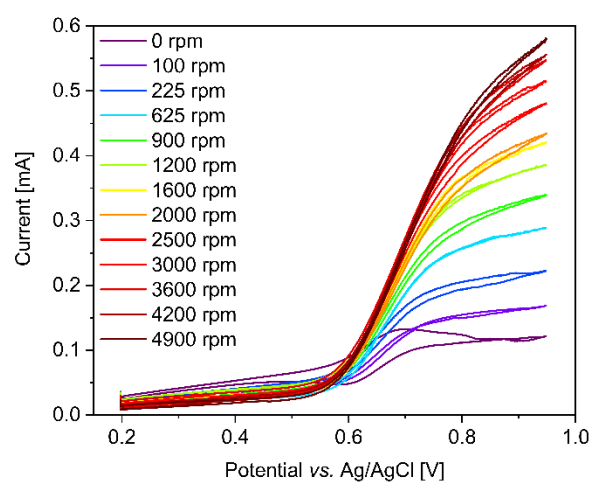
626

Figure S6: Cyclic voltammograms of a 16.0 mmol L⁻¹ TEMPO-sulfamide 3 in 0.1 M sodium chloride as supporting electrolyte at different scan speeds (upper left) and peak current vs. square root of scan speed (upper right, oxidation black and reduction red). Rotating disk electrode voltammetry results (RDE) of a 4.8 mmol L⁻¹ TEMPO-sulfamide 3 in 0.25 M sodium chloride as supporting electrolyte: RDE voltammograms (middle left), Levich Plot (middle right), Koutecký-Levich plot (lower left) and Tafel plot (lower right). The following constants were calculated according to the above-described procedure:

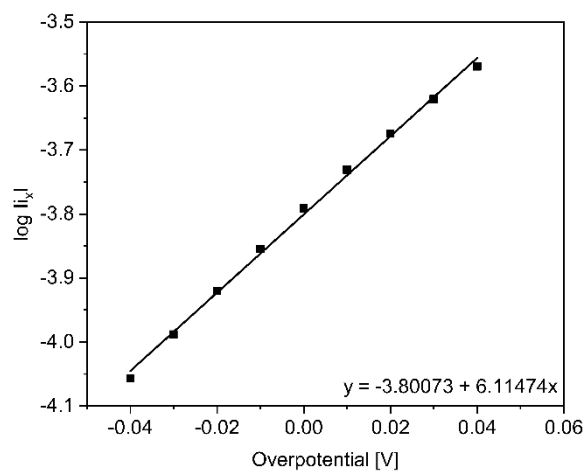
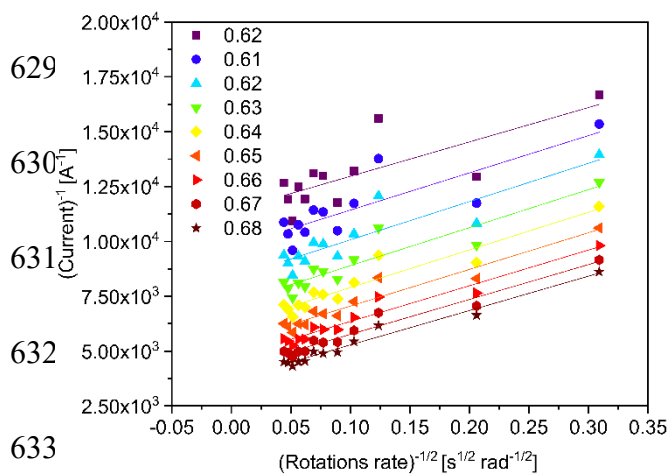
Reaction constant, diffusion coefficient and a transfer coefficient



627



628

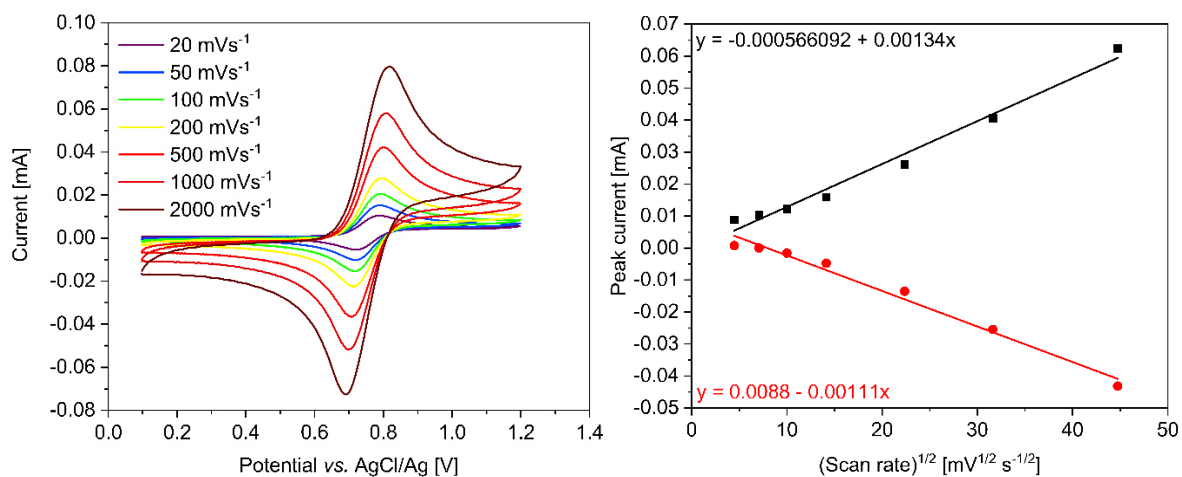


634 Figure S7: Cyclic voltammograms of a 5.0 mmol L^{-1} TEMPO-ether **4** in 0.1 M sodium chloride as supporting electrolyte at different scan speeds (upper left) and peak current vs. square root of scan speed (upper right, oxidation black and re-reduction red).

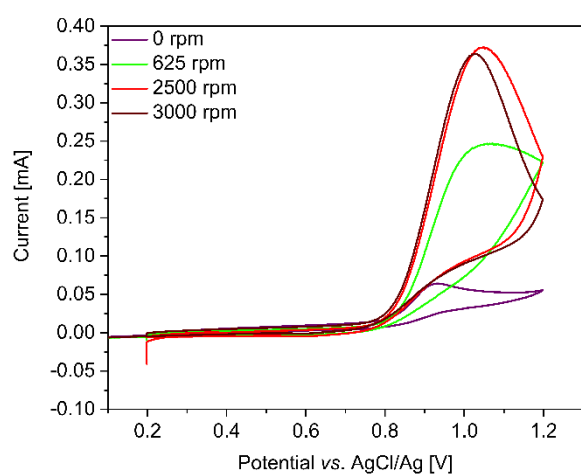
635 Rotating disk electrode voltammetry results (RDE) of a 5.0 mmol L^{-1} TEMPO-ether **4** in 0.1 M sodium chloride as supporting electrolyte: RDE voltammograms (middle left), Levich Plot (middle right), Koutecký-Levich plot (lower left) and Tafel plot (lower right).

636 The following constants were calculated according to the above-described procedure: Reaction constant k_{red} , diffusion coefficient D and a transfer coefficient α .

637

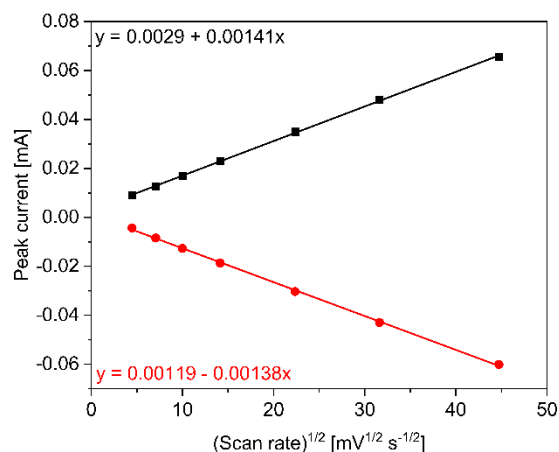
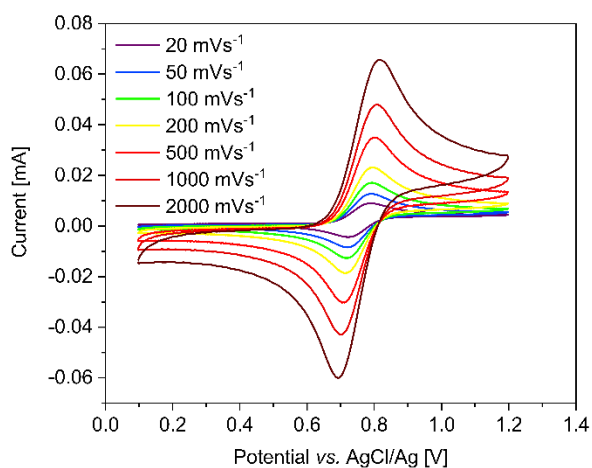


638

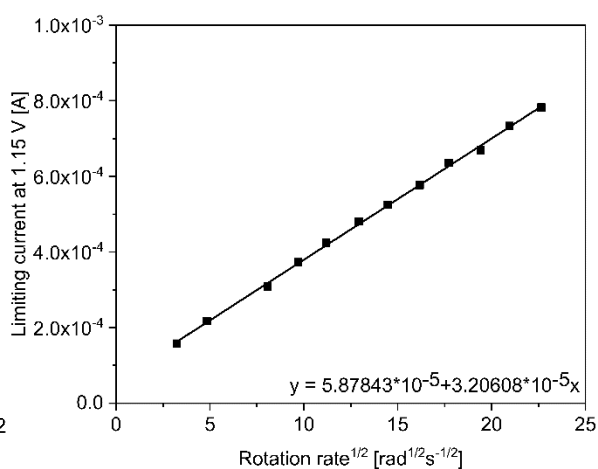
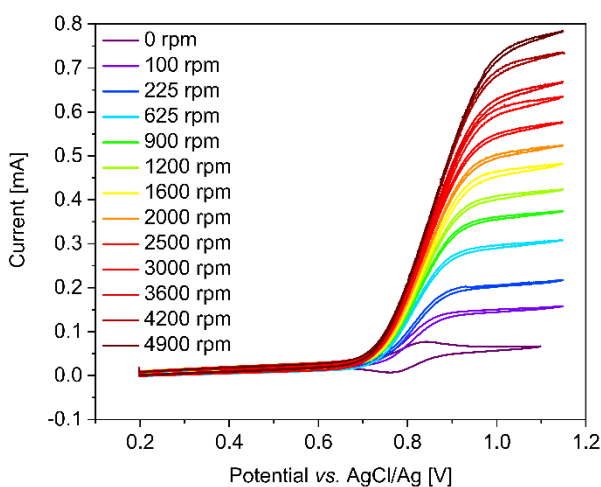


639

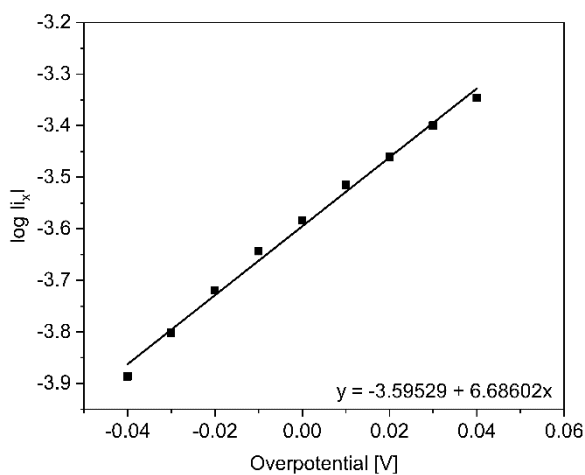
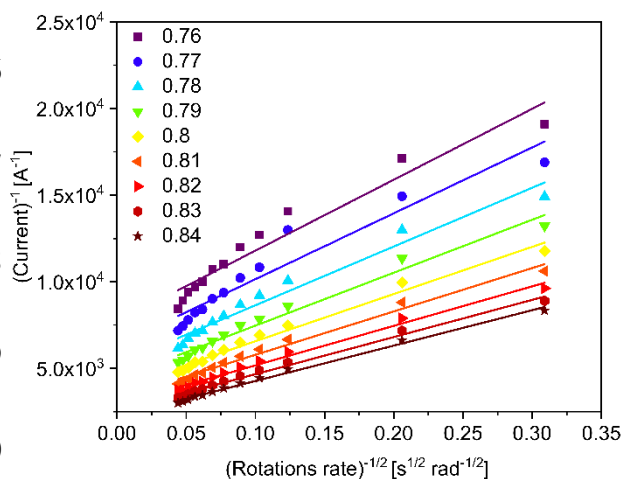
640 Figure S8: Cyclic voltammograms of a 5.0 mmol L⁻¹ spiro-TEMPO 5 in 0.1 M sodium chloride as supporting electrolyte at
 641 different scan speeds (upper left) and peak current vs. square root of scan speed (upper right, oxidation black and rereduction
 642 red). Rotating disk electrode voltammograms (RDE) of a 4.8 mmol L⁻¹ spiro-TEMPO 5 in 0.25 M sodium chloride as supporting
 643 electrolyte.



644



645



646

647

648

649

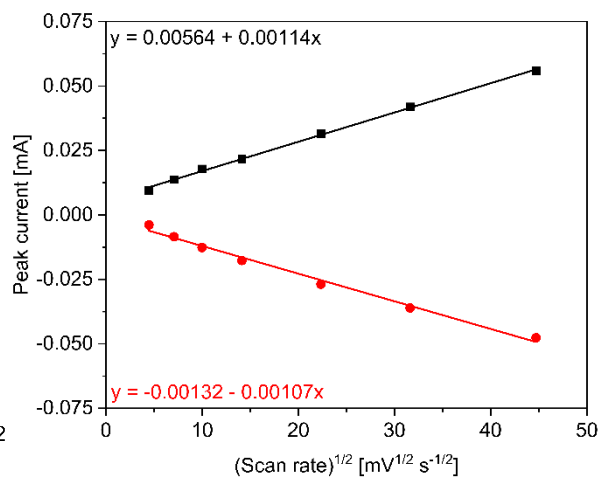
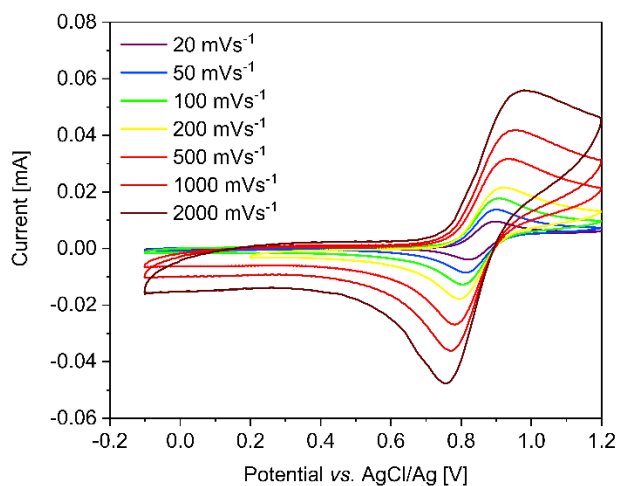
650

651

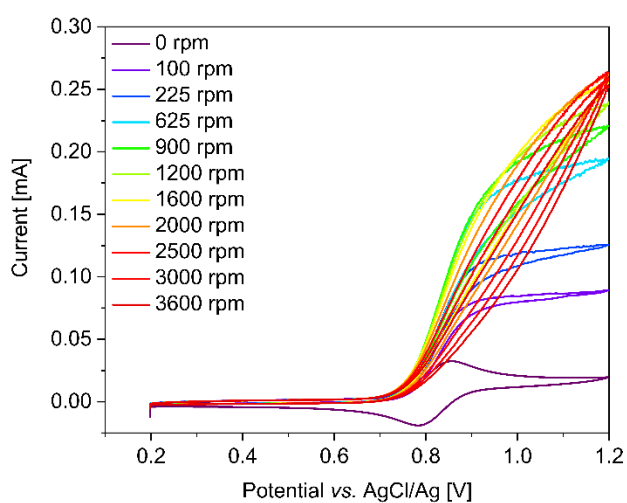
652

653

Figure S9: Cyclic voltammograms of a 5.0 mmol L^{-1} TMA-TEMPO- BF_4 **6** in 0.1 M sodium tetrafluoroborate as supporting electrolyte at different scan speeds (upper left) and peak current vs. square root of scan speed (upper right, oxidation black and re-reduction red). Rotating disk electrode voltammetry results (RDE) of a 5.1 mmol L^{-1} TMA-TEMPO- BF_4 **6** in 0.1 M sodium tetrafluoroborate as supporting electrolyte: RDE voltammograms (middle left), Levich Plot (middle right), Koutecký-Levich plot (lower left) and Tafel plot (lower right). The following constants were calculated according to the above-described procedure: Reaction constant k , diffusion coefficient D and a transfer coefficient α .



654

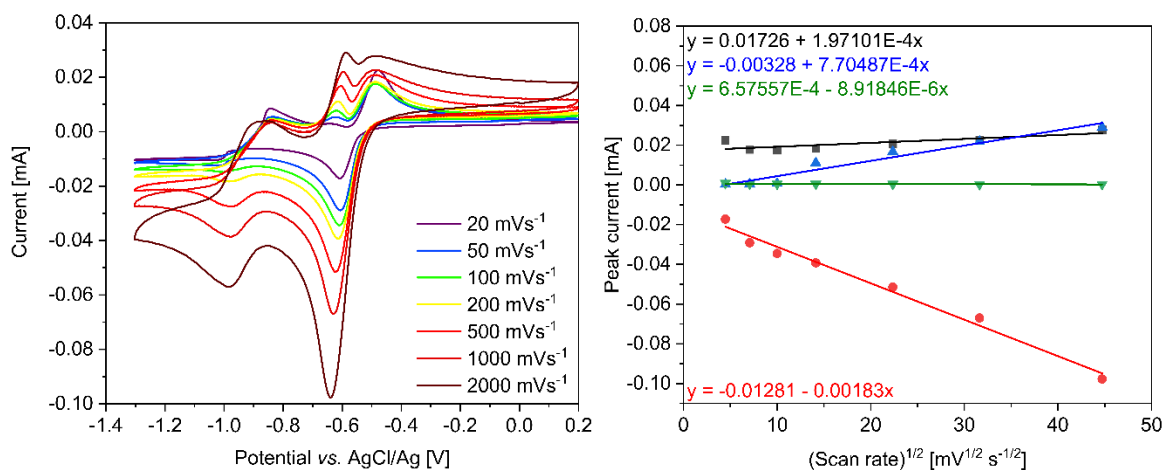


655

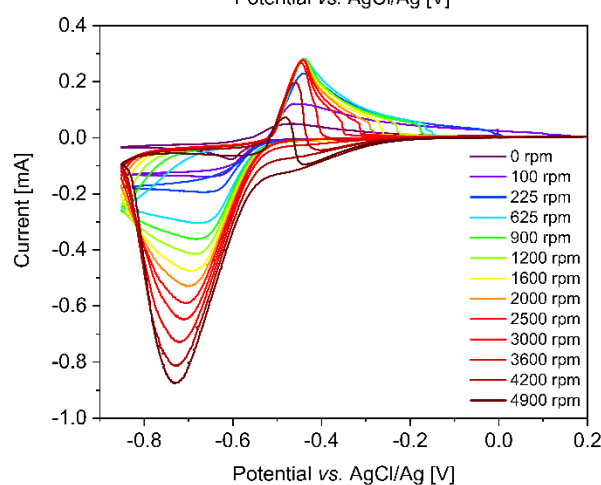
656 Figure S10: Cyclic voltammograms of a 5.0 mmol L⁻¹ TEA-TEMPO 7 in 0.1 M sodium chloride as supporting electrolyte at
 657 different scan speeds (upper left) and peak current vs. square root of scan speed (upper right, oxidation black and re-reduction
 658 red). Rotating disk electrode voltammograms (RDE) of a 4.8 mmol L⁻¹ TEA-TEMPO 7 in 0.1 M sodium chloride as supporting
 659 electrolyte. The Data for 4200 rpm and 4900 rpm shows great fluctuation due to productions of bubbles in solution and where
 660 thus omitted.

661

662



663



664

665 Figure S11: Cyclic voltammograms of a 5.0 mmol L⁻¹ methyl viologen – BF₄ salt in 0.1 M sodium tetrafluoroborate as
 666 supporting electrolyte at different scan speeds (upper left) and peak current vs. square root of scan speed (upper right, oxidation
 667 process at -0.5 V black, oxidation process at -0.65 V blue, oxidation process at -0.85 V green and re-reduction red). Rotating
 668 disk electrode voltammograms (RDE) of a 5.0 mmol L⁻¹ methyl viologen – BF₄ salt in 0.1 M sodium tetrafluoroborate as
 669 supporting electrolyte.

670 Depending on the scan speed, the methyl viologen – BF₄ salt revealed different redox process.

671 This is mainly due to the lower solubility of the BF₄ salt in comparison to the methyl viologen

672 chloride and the even lower solubility of the reduced species. The reduction of the doubly-

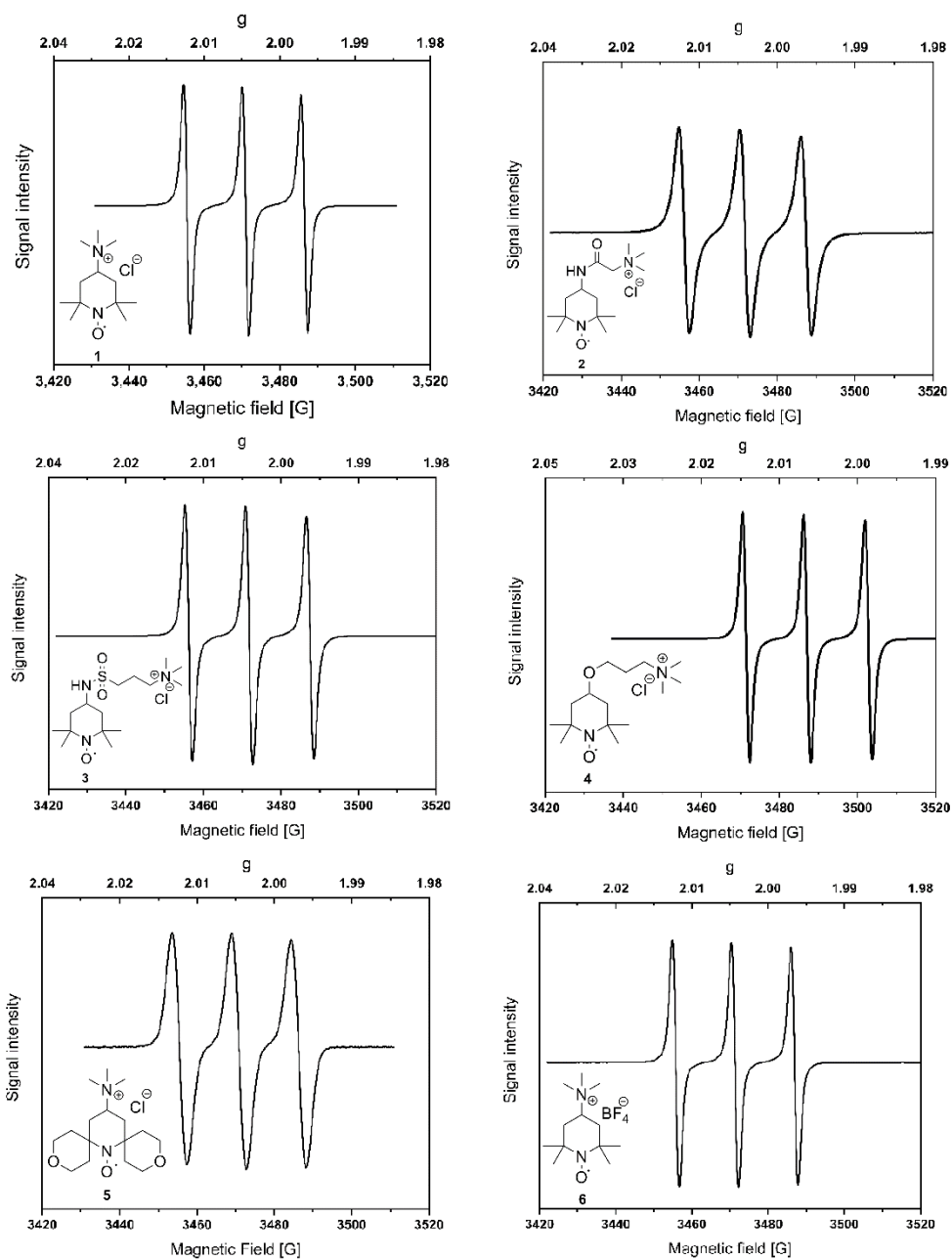
673 charged cations lead to mono-cationic and uncharged species, respectively, which deposit onto

674 the electrode surface. This also explains the nonlinear behavior of the current at the limiting

675 potential during the RDE measurements. A simple evaluation, using the Levich equations is

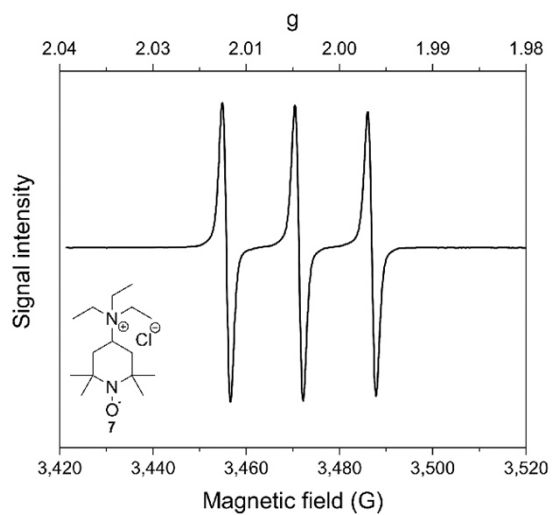
676 thus not possible.

677 EPR spectra



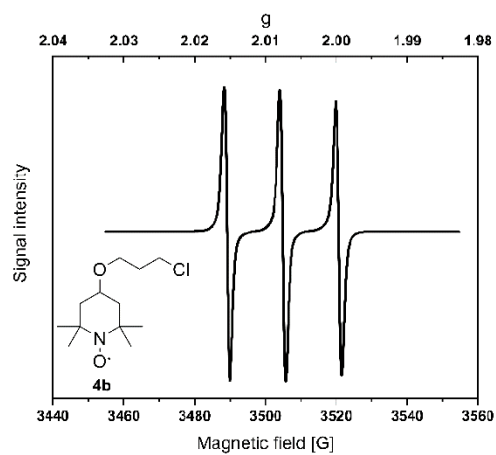
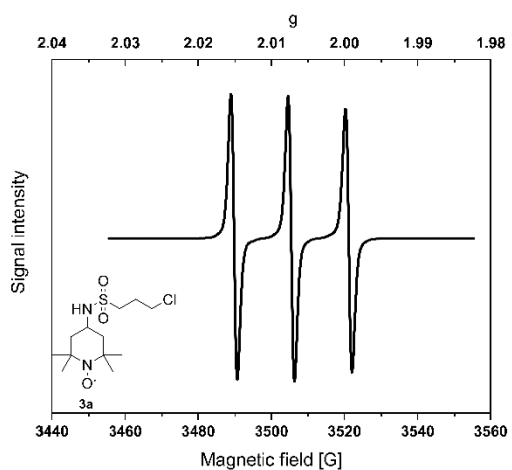
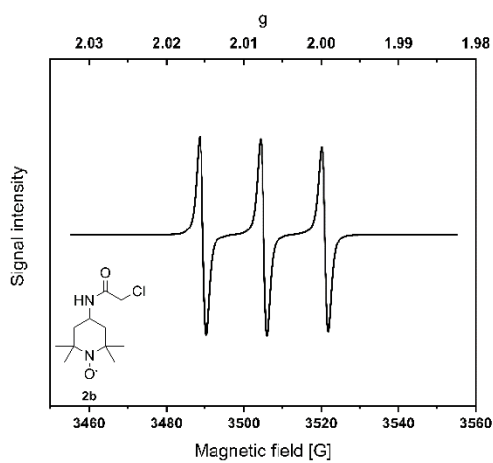
678

679 Figure S12: EPR spectra of 1 mg mL^{-1} TEMPO derivatives solutions in acetonitrile: TMA-TEMPO **1** (upper left), TEMPO-amide
 680 **2** (upper right), TEMPO-sulfamide **3** (middle left), TEMPO-ether **4** (middle right), spiro-TEMPO **5** (lower left), TMA-TEMPO-
 681 BF_4 **6** (lower right).



682

683 Figure S13: EPR spectrum of 1 mg mL⁻¹ TEA-TEMPO 7 solution in acetonitrile.



684

685 Figure S14: EPR spectrum of 1 mg mL⁻¹ TEMPO precursor solutions in dichloromethane: TEMPO-amide 2 (upper left),

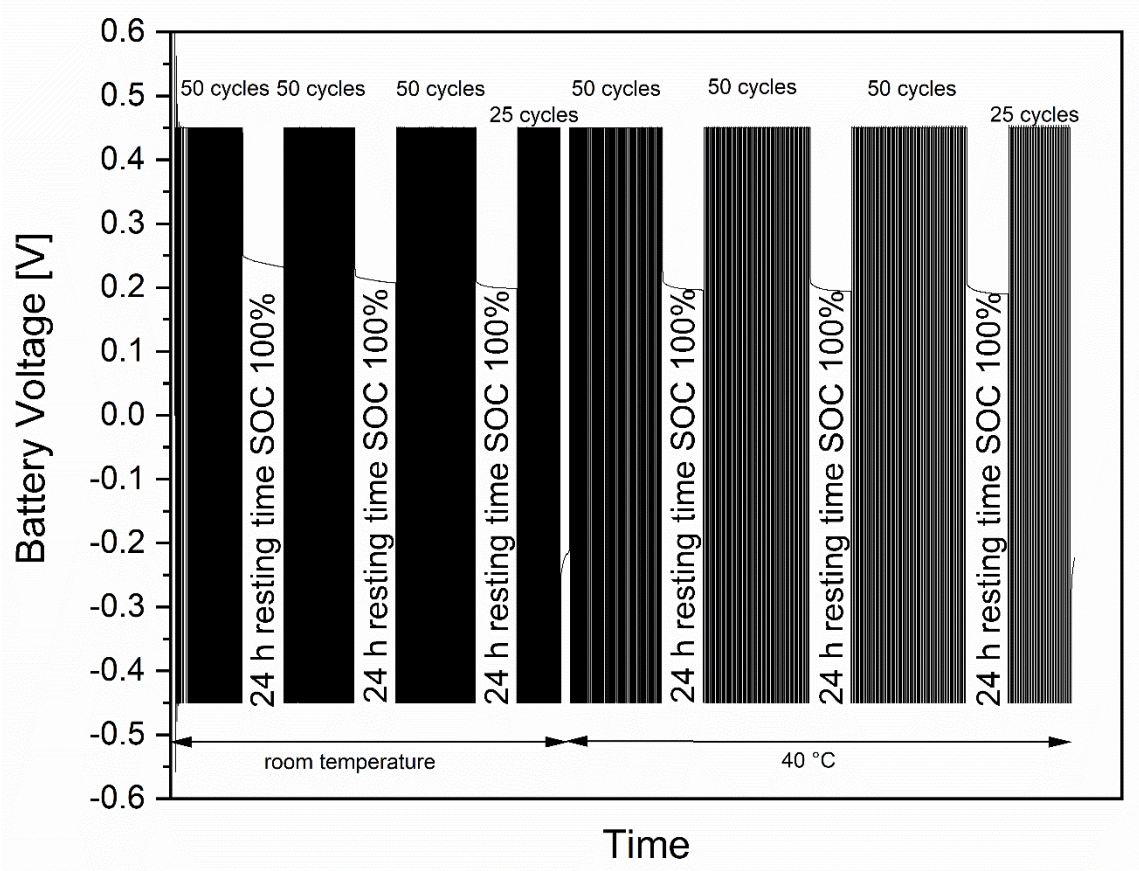
686 TEMPO-sulfamide 3 (upper right) TEMPO-ether 4 (lower left).

687

688 *Solubility tests of compound 2 and 3*

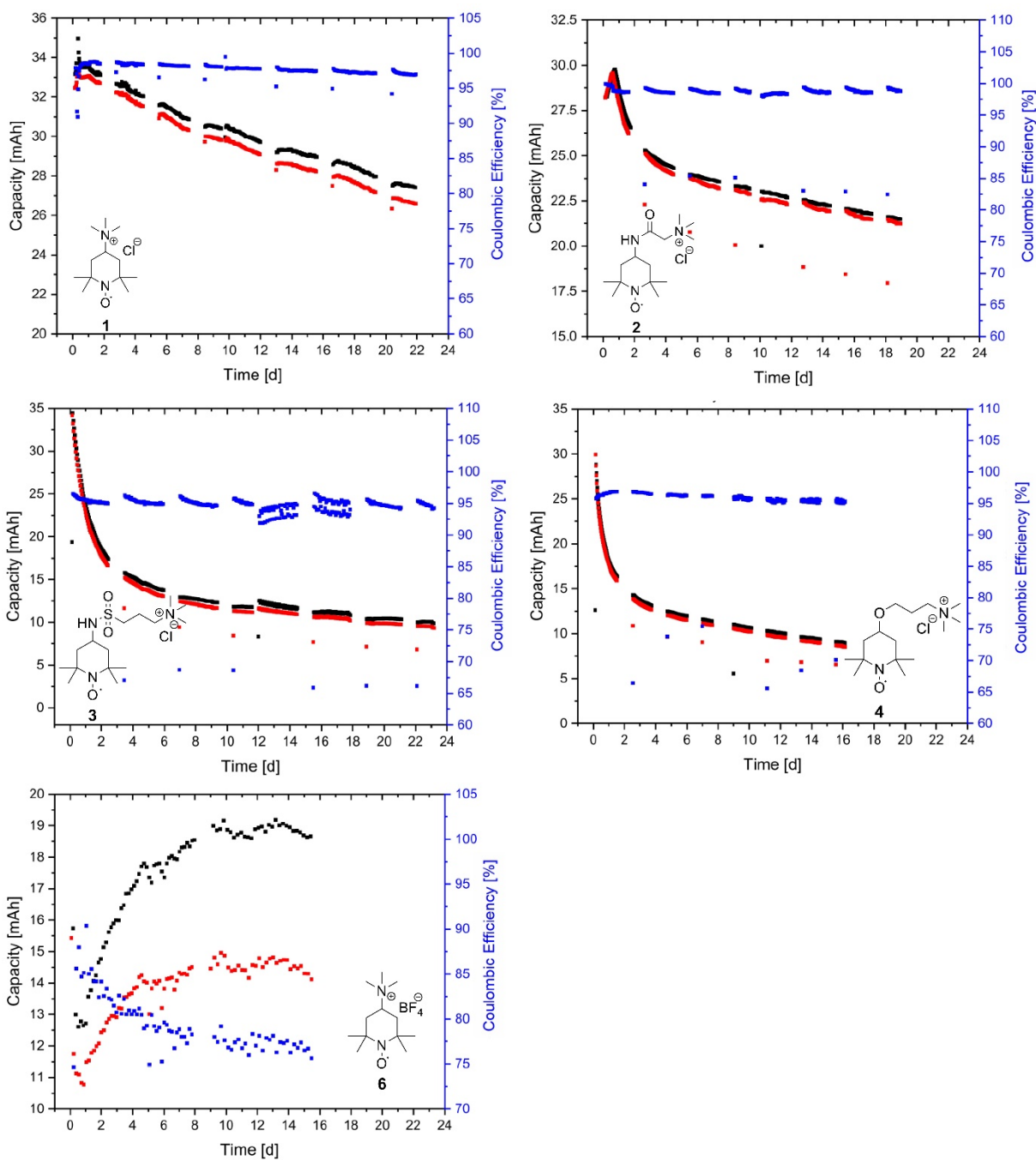
689 The maximum solubility of the TEMPO-amide **2** was determined by dissolving 2 g in 400 μL
690 pure water. The volume of the solution increased to over 1.5 mL and a very viscous liquid was
691 received. Further added 100 mg portions of the amide were dissolved but also the volume of
692 the liquid increased, thus we assumed that we received the maximum concentration. Three
693 100 μL aliquotes of the amide solution were transferred into 1.5 mL HPLC-vials and freeze
694 dried. The residue of the amide solution was weighted and the concentration was calculated.
695 The average concentration was 3.8 mol L^{-1} , which corresponds to an average half-cell capacity
696 of 101.8 AhL^{-1} or a battery capacity of 50.9 AhL^{-1} .

697 The maximum concentration of the tempo-sulfonamide **3** was determined accordingly. The
698 material also revealed a volume increase upon dissolution to approximately four times of the
699 starting volume, but the apparent viscosity stayed rather low. The average maximum
700 concentration of three replicates was determined to be 4.0 mol L^{-1} , which corresponds to a half-
701 cell capacity of 107.2 AhL^{-1} or a battery capacity of 53.6 AhL^{-1} .



703

704 Figure S15: Schematic representation of the used cycling protocol. Each cycle consists of a galvanostatic charging with
 705 76 mA cm⁻². After the cell voltage limits were reached, the battery was charged / discharged potentiostatically until the current
 706 dropped below the threshold of 0.5 mA cm⁻².



707

708 Figure S16: Symmetric battery tests of 12 mL 0.1 M aq. TEMPO derivative solution vs. 18 mL 0.1 M aq. TEMPO derivative in
 709 1.5 M sodium chloride. Except for TMA-TEMPO, where 15 mL 0.1 M aq. solution vs. 20 mL aq. solution were used. The first
 710 three blocks consist of 50 consecutive charge-discharge cycles and the fourth block of 25 cycles. Each block is separated by a
 711 hold time of 24 h in maximal SOC. The experiments were performed at first at room temperature and then repeated at 40 °C.

712

713

714

715 Table S1: Decay rates in %d⁻¹ of different TEMPO derivatives at room temperature and 40 °C during hold times and pure
 716 cycling. Every cycling period consist of 50 consecutive cycles, except for the fourth cycling period, where 25 cycles were
 717 applied. Every cycling period was separated by a hold time of 24 h in maximal SOC.

	decay 22 °C [% d ⁻¹]									decay 40 °C [%d ⁻¹]							
	Start rel. Discharge Capacity	1. Cycling period	1. Hold time	2. Cycling period	2. Hold time	3. Cycling period	3. Hold time	4. Cycling period	End rel. Discharge Capacity	1. Cycling period	1. Hold time	2. Cycling period	2. Hold time	3. Cycling period	3. Hold time	4. Cycling period	End rel. Discharge Capacity
1	89.07	0.39	1.29	1.13	1.68	1.13	1.63	0.53	81.80	0.89	2.14	0.42	2.00	0.77	2.26	0.23	72.95
2	94.74	4.37	13.21	2.12	10.72	1.02	10.53	0.92	76.84	0.50	11.67	0.98	11.69	0.96	11.79	0.98	71.33
3	99.24	22.12	14.46	2.51	10.51	0.92	9.32	0.33	32.47	0.79	9.42	0.45	8.86	0.21	8.46	0.62	27.09
4	99.95	33.51	16.86	3.28	10.00	1.37	8.35	1.07	36.59	1.05	10.84	0.98	9.00	0.60	8.07	0.97	28.47
6	80.43	0.61	0.21	0.58		n. a.			73.60					n. a.			

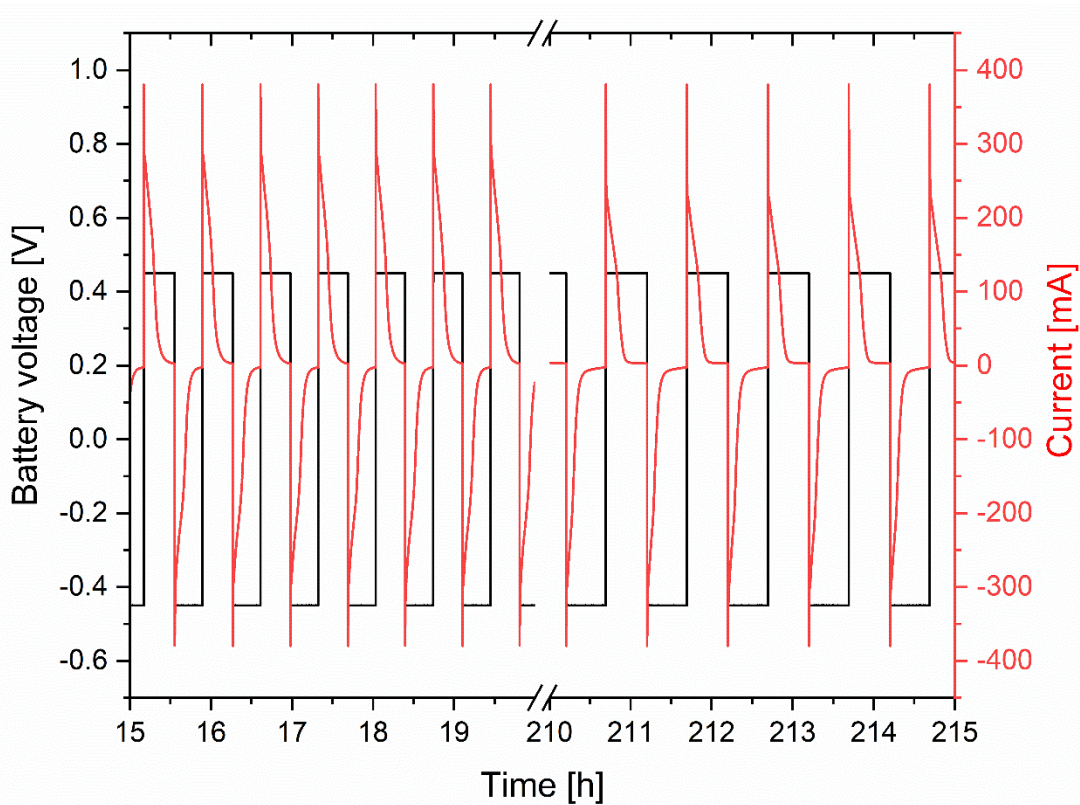
718

719

720 Table S2: Summary of the batteries' theoretical capacities as well as capacity utilizations. The theoretical capacity is calculated
 721 with the volume of the CLS at a concentration of 0.1 M.

	Starting capacity [mAh]	Volume CLS [mL]	Theoretical capacity [mAh]	Capacity utilization [%]
1	36.4	15	40.2	90.5
2	29.3	12	32.1	91.2
3	34.4	12	32.1	107.1
4	29.9	12	32.1	93.1
6	18.6	12	32.1	58.0

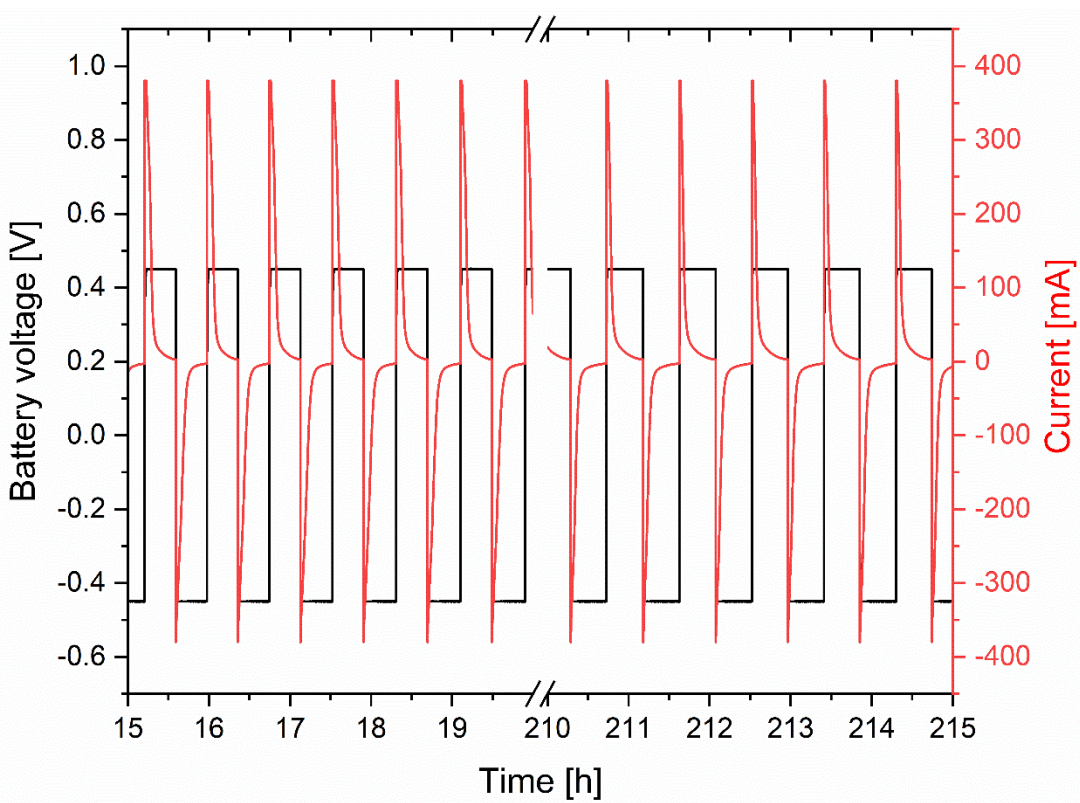
722



723

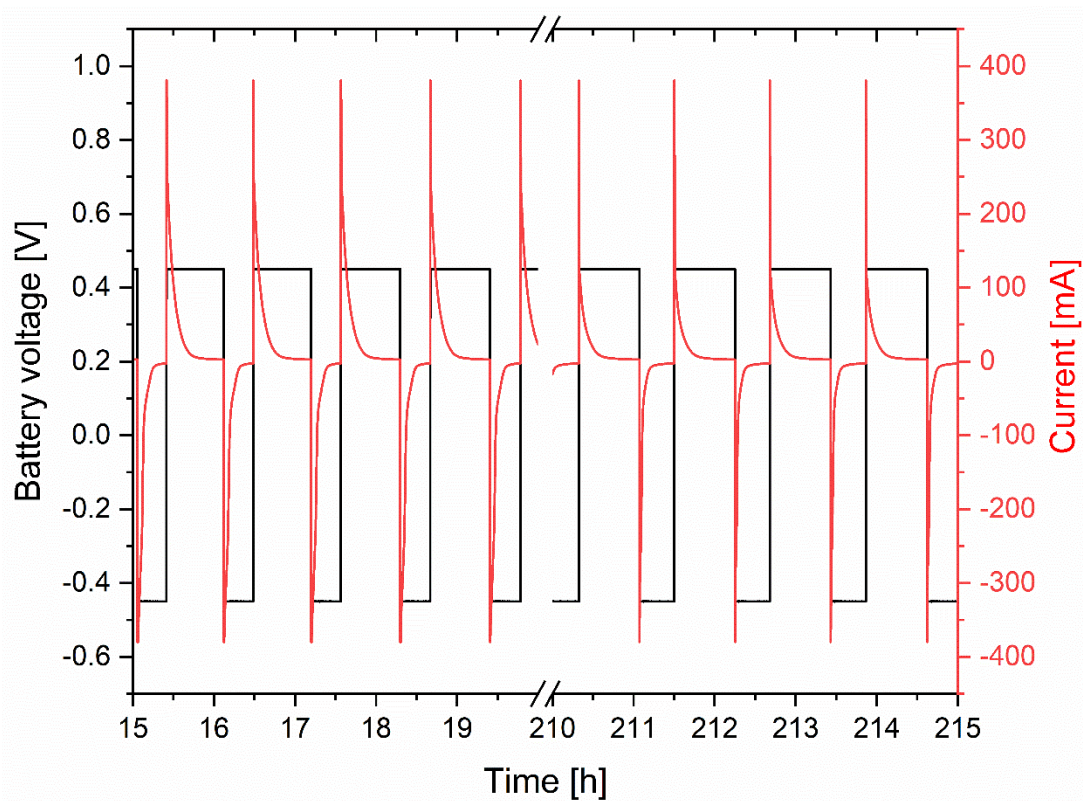
724 *Figure S17: Typical charge/discharge profile of TMA-TEMPO 1.*

725



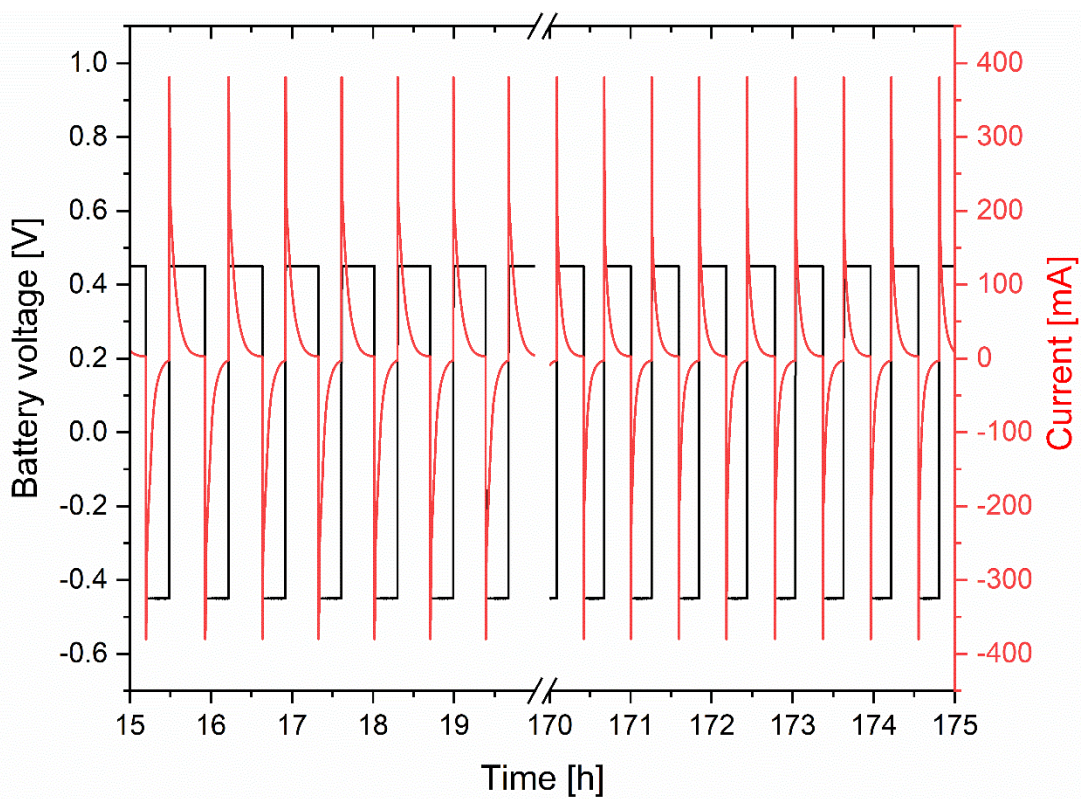
726

727 *Figure S18: Typical charge/discharge profile of TEMPO-amide 2.*



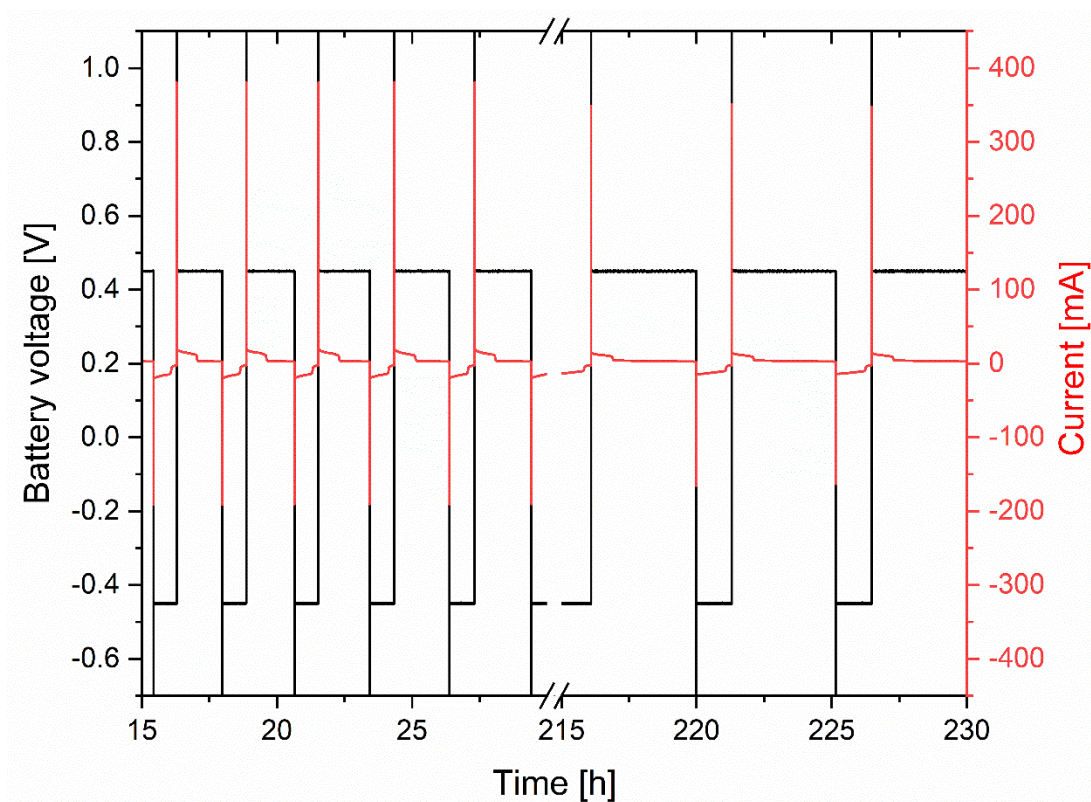
728

729 Figure S19: Typical charge/discharge profile of TEMPO-sulfonamide 3.



730

731 Figure S20: Typical charge/discharge profile of TEMPO-ether 4.



732

733 *Figure S21: Typical charge/discharge profile of TMA-TEMPO-BF₄ 6.*

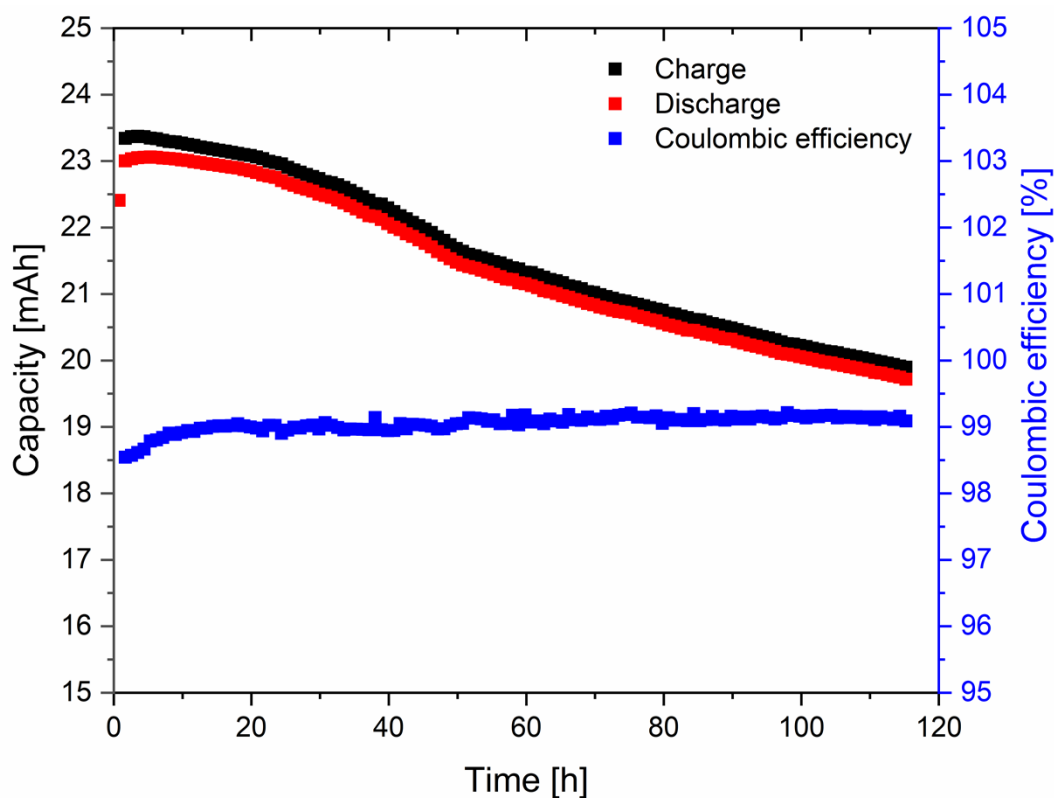
734

735 *Repetition of the TEMPO-ether battery test*

736 To investigate the effect of overpotentials and the limiting voltage the TEMPO-ether
 737 experiment was repeated but with the cycling condition Liu *et al.* used (limiting current of
 738 1 mA cm⁻² instead of 0.5 mA cm⁻², a voltage cut-off of ± 0.2 V instead of ± 0.45 V and no hold
 739 times in vulnerable SOC).⁶ Since the redox potential of the TEMPO derivatives are close to the
 740 edge of the water working window to high cut-off voltage may result in water splitting
 741 processes causing the pH-value to drop and maybe catalyse cleave reactions.

742 In comparison to the preliminary experiments the coulomb efficiency increased from 96% to
 743 over 99% and the decomposition rates are massively reduced (see *Figure S22*). Nevertheless,
 744 the decay rate was determined to be 0.14% h⁻¹ or 3.1% d⁻¹. In comparison to the data of Liu *et*
 745 *al.* (0.023% h⁻¹ or 0.5 % d⁻¹) these values are higher. pH-Measurements showed an increase of
 746 the hydronium ion concentration. While the SOC = 0% mixture of 0.1 M TEMPO-ether **3** in
 747 1.5 M sodium chloride has a pH value of 8.01 the pH drops to 3.44 for a the SOC 50% solution
 748 (used for the test). At the end of the battery experiment the CLS has a pH value of 1.45 and the
 749 CLNS of 2.05. The decrease must not only be caused by water splitting. It can also caused by

750 the 1,2 electrophilic addition and subsequently cleavage of the hydroxylamine under acid
751 formation¹¹. A pH-drop is also visible in the data of Liu *et al.* where the end pH after the cycling
752 experiment is at approx. 3. We think that the higher pH drop is linked to the higher
753 decomposition rates.

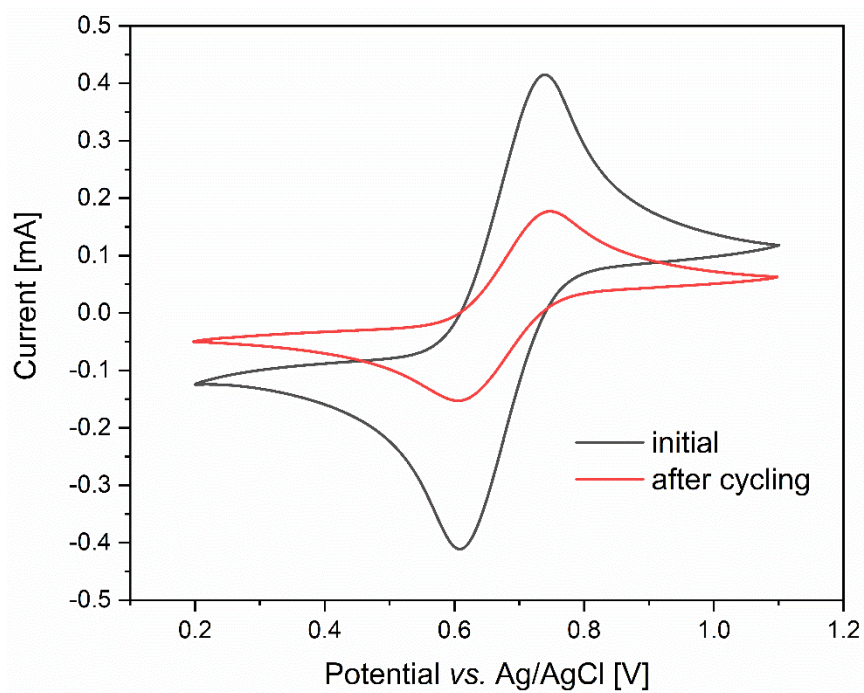


754

755 Figure S22: Battery test of the TEMPO-ether **3** with the cycling conditions of Liu *et al.*⁶

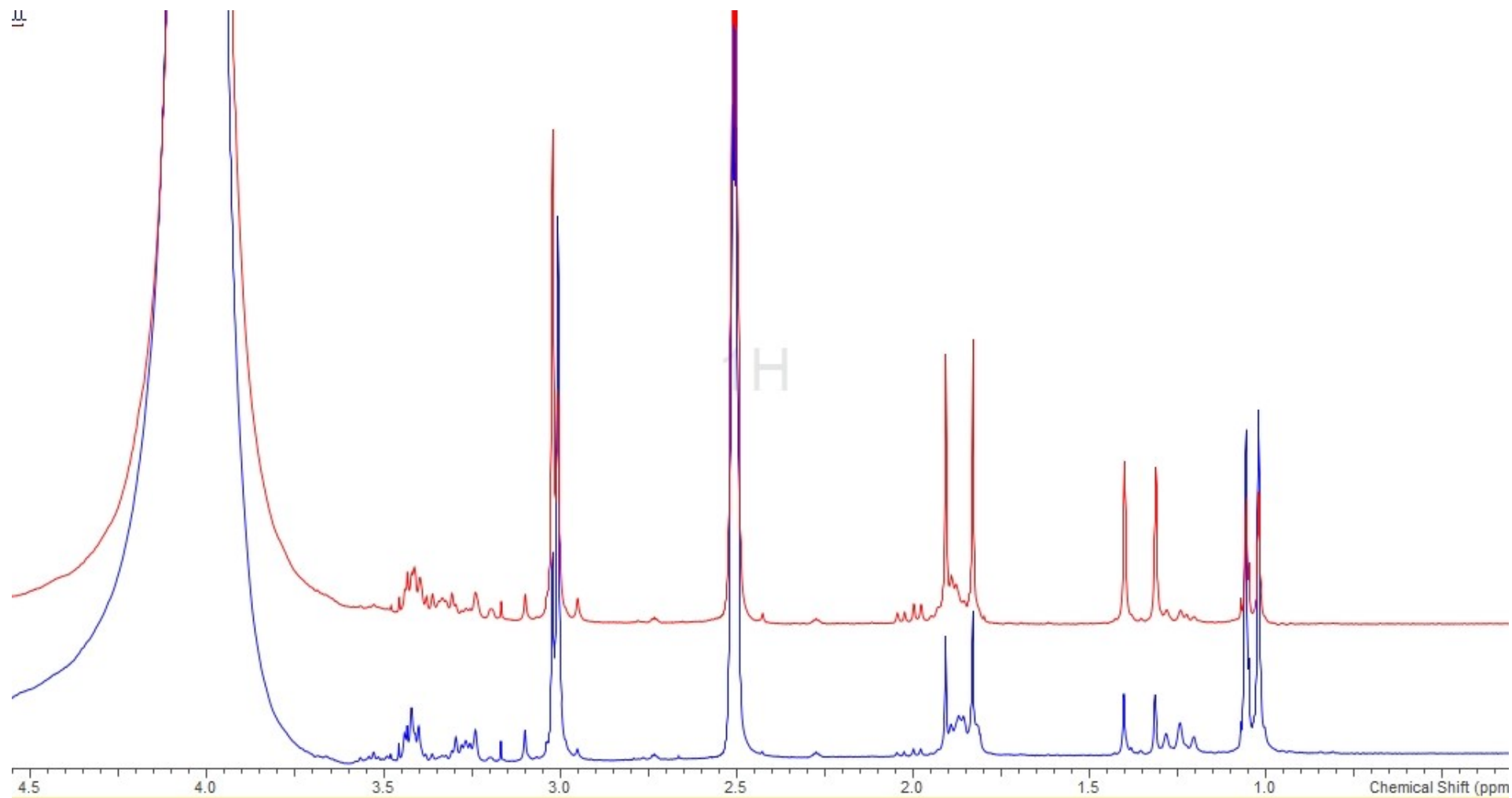
756

757 To have more details about the ongoing processes we also conducted CV measurements, which
758 revealed a decrease in the peak heights by 60%, which is also in alignment to the data of Liu *et*
759 *al.* but once again more pronounced (60 to 24%) (see Figure S23). Similar results were achieved
760 by NMR measurement. Here, a 50 to 60% reduction of the signal intensity upon cycling is
761 visible as well (see Figure S24).



762

763 Figure S23: Cyclic voltammogram measurement of the TEMPO-ether before and after the battery experiment.



764

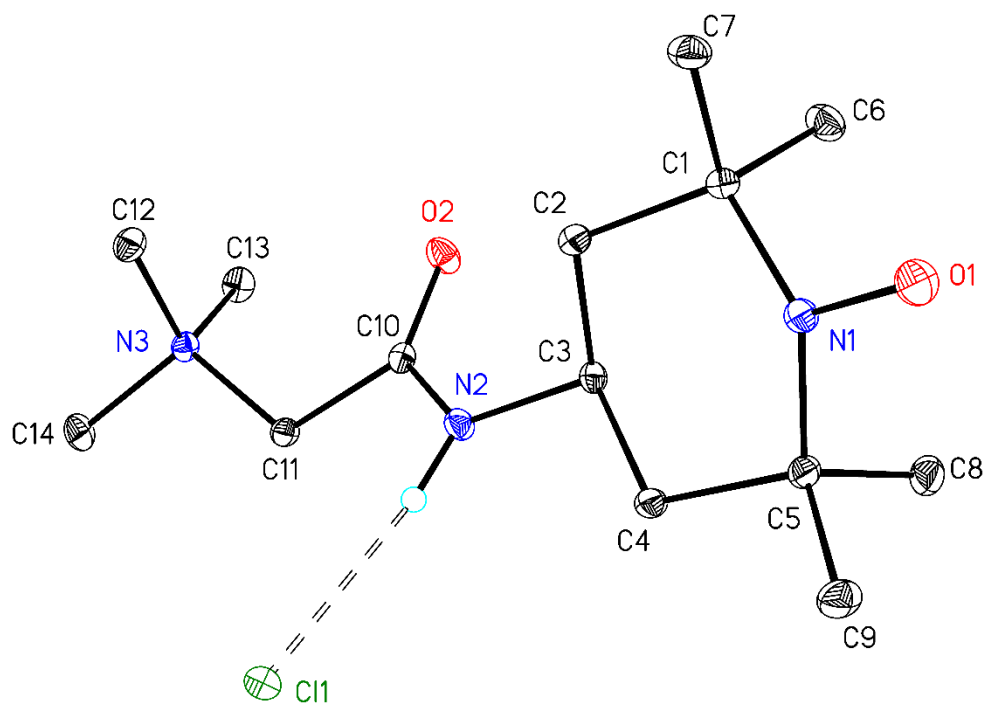
765 *Figure S24: Stacked ¹H NMR spectra of the initial TEMPO-ether (blue) and the cycled (green). 100 μL aliquots were taken and mixed with 700 μL d₆-DMSO and appropriate amounts of phenyl*
766 *hydrazine. No new decomposition products could be detected. The signal of the d₆-DMSO rest protons was used as internal standard after baseline correction and phasing. Integration of the TEMPO*
767 *ether peaks towards the DMSO signal revealed a 50 to 60% loss of signal intensity in comparison to the initial signal integral.*

769 Table S3: Crystal data and refinement details for the X-ray structure determinations.

Compound	2	2b	3a
Formula	C ₁₄ H ₂₉ ClN ₃ O ₂	C ₁₁ H ₂₀ ClN ₂ O ₂	C ₁₂ H ₂₄ ClN ₂ O ₃ S
fw (g·mol ⁻¹)	306.85	247.74	311.84
T/°C	-140(2)	-140(2)	-140(2)
crystal system	orthorhombic	monoclinic	triclinic
space group	P 2 ₁ 2 ₁ 2 ₁	C c	P $\bar{1}$
<i>a</i> /Å	5.94210(10)	17.3461(5)	7.7329(3)
<i>b</i> /Å	10.7976(2)	9.9064(4)	9.7637(3)
<i>c</i> /Å	25.7468(4)	8.9377(3)	10.9893(3)
α /°	90	90	87.709(2)
β /°	90	120.426(2)	79.419(2)
γ /°	90	90	72.4440(10)
<i>V</i> /Å ³	1651.93(5)	1324.32(8)	777.51(4)
<i>Z</i>	4	4	2
ρ (g·cm ⁻³)	1.234	1.243	1.332
μ (cm ⁻¹)	2.38	2.78	3.86
measured data	13055	8989	9432
data with <i>I</i> > 2 σ (<i>I</i>)	3692	2880	3252
unique data (<i>R</i> _{int})	3765/0.0357	2971/0.0335	3544/0.0218
w <i>R</i> ₂ (all data, on <i>F</i> ²) ^{a)}	0.0597	0.0643	0.0714
<i>R</i> ₁ (<i>I</i> > 2 σ (<i>I</i>)) ^{a)}	0.0251	0.0275	0.0301
<i>S</i> ^{b)}	1.063	1.050	1.061
Res. dens./e·Å ⁻³	0.211/-0.149	0.296/-0.156	0.358/-0.388
Flack-parameter	0.02(3)	0.06(2)	-
absorpt method	multi-scan	multi-scan	multi-scan
absorpt corr T _{min} /max	0.7170/0.7456	0.6777/0.7456	0.6988/0.7456
CCDC No.	2085767	2085768	2085769

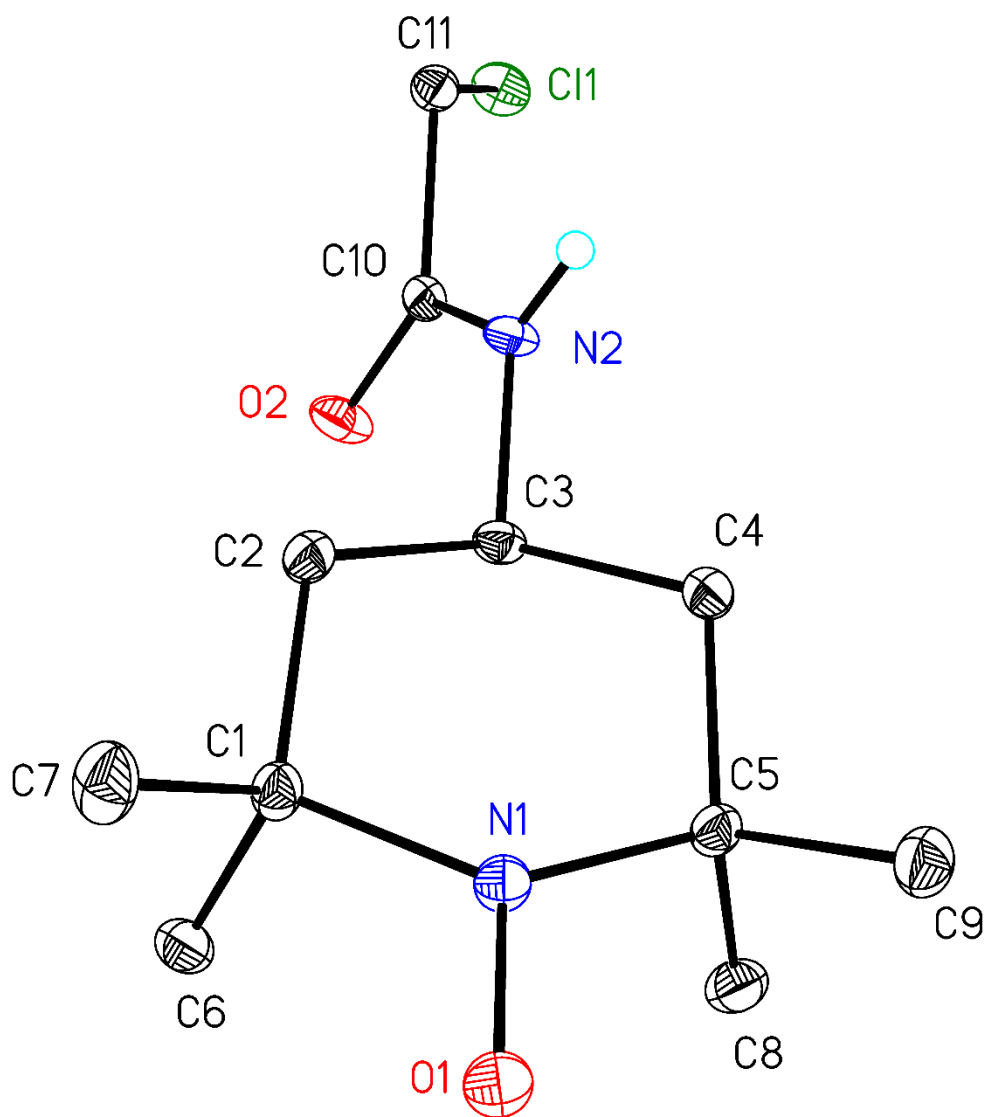
770 ^{a)} Definition of the *R* indices: $R_1 = (\sum ||F_o| - |F_c||) / \sum |F_o|$;771 $wR_2 = \{\sum [w(F_o^2 - F_c^2)^2] / \sum [w(F_o^2)^2]\}^{1/2}$ with $w^{-1} = \sigma^2(F_o^2) + (aP)^2 + bP$; $P = [2F_c^2 + \text{Max}(F_o^2)]/3$;772 ^{b)} $S = \{\sum [w(F_o^2 - F_c^2)^2] / (N_o - N_p)\}^{1/2}$.

773



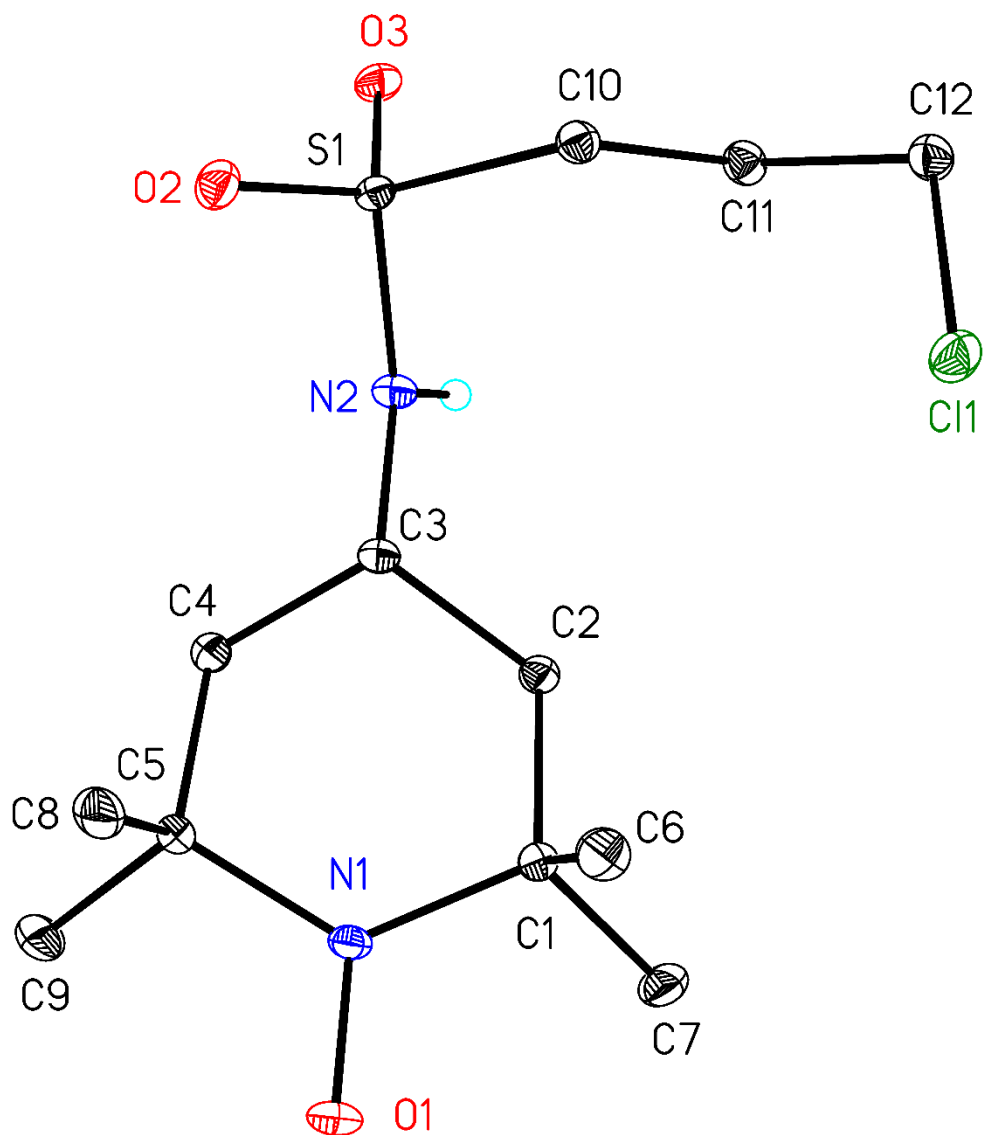
774

775 *Figure S25: Molecular structure and atom numbering schemes of 2. The ellipsoids represent a probability of 30 %, H atom for*
 776 *the amino group is drawn with arbitrary radii. All other hydrogen atoms are omitted for clarity.*



777

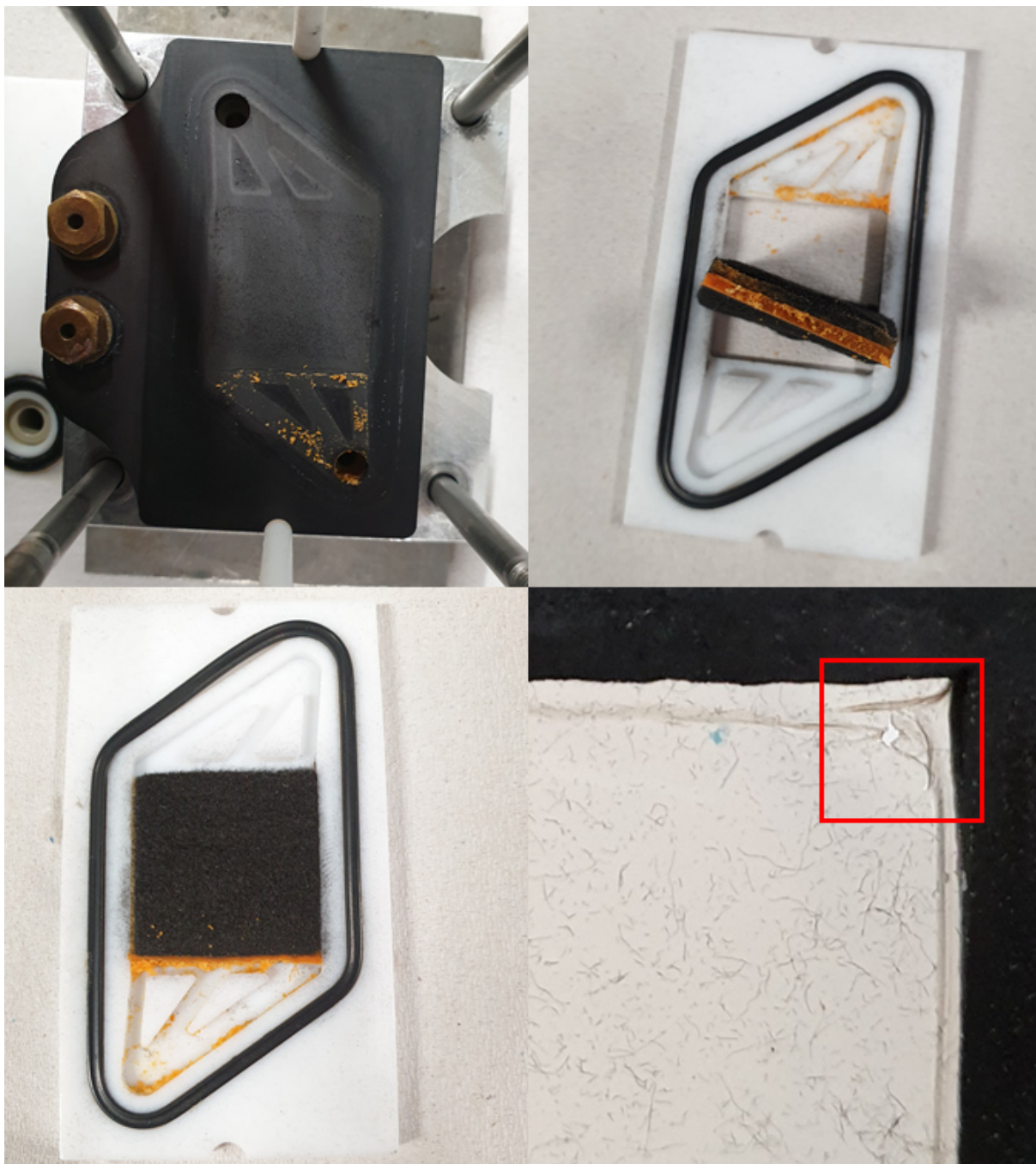
778 *Figure S26: Molecular structure and atom numbering schemes of 2b. The ellipsoids represent a probability of 30%, H atom*
779 *for the amino group is drawn with arbitrary radii. All other hydrogen atoms are omitted for clarity.*



780

781 *Figure S27: Molecular structure and atom numbering schemes of 3a. The ellipsoids represent a probability of 30%, H atom*
782 *for the amino group is drawn with arbitrary radii. All other hydrogen atoms are omitted for clarity.*

783 *Photos of BF₄-salt precipitate*



784

785 *Figure 28: Photos of the BF₄-salt precipitate and used membrane. Hole in the membrane highlighted by the red square (lower*
786 *right).*

787

788

789

790

791 *Literature*

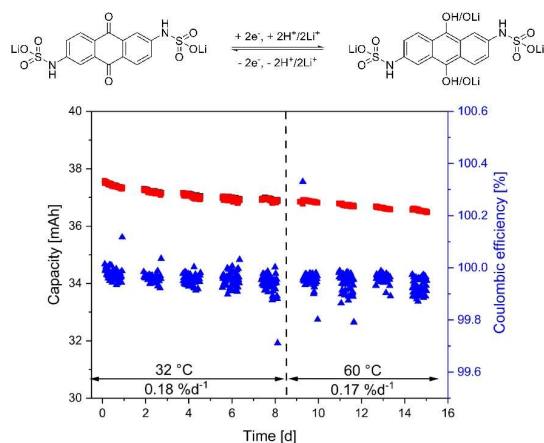
- 792 1. A. Gzella, *Acta Crystallogr. C*, 1999, **55**, 1730-1733.
793 2. Z. Otwinowski and W. Minor, *Processing of X-ray diffraction data collected in*
794 *oscillation mode*, Academic Press, 1997.
795 3. L. Krause, R. Herbst-Irmer, G. M. Sheldrick and D. Stalke, *J. Appl. Crystallogr.*, 2015,
796 **48**, 3-10.
797 4. G. M. Sheldrick, *Acta Crystallogr. A*, 2015, **71**, 3-8.
798 5. T. Janoschka, N. Martin, M. D. Hager and U. S. Schubert, *Angew. Chem. Int. Ed.*, 2016,
799 **55**, 14427-14430.
800 6. Y. Liu, M.-A. Goulet, L. Tong, Y. Liu, Y. Ji, L. Wu, R. G. Gordon, M. J. Aziz, Z. Yang
801 and T. Xu, *Chem*, 2019, **5**, 1861-1870.
802 7. J. T. Paletta, M. Pink, B. Foley, S. Rajca and A. Rajca, *Org. Lett.*, 2012, **14**, 5322-5325.
803 8. S. Morisako, R. Shang and Y. Yamamoto, *Inorg. Chem.*, 2016, **55**, 10767-10773.
804 9. M. M. Haugland, A. H. El-Sagheer, R. J. Porter, J. Pena, T. Brown, E. A. Anderson and
805 J. E. Lovett, *J. Am. Chem. Soc.*, 2016, **138**, 9069-9072.
806 10. R. de Levie, *J. Electroanal. Chem.*, 1992, **323**, 347-355.
807 11. T. Takata, Y. Tsujino, S. Nakanishi, K. Nakamura, E. Yoshida and T. Endo, *Chem. Lett*,
808 1999, **28**, 937-938.

809

Publications P4

Anthraquinone-2,6-disulfamidic acid: An anolyte with low decomposition rates at elevated temperatures.

P. Rohland, K. Schreyer, M. D. Hager, U. S. Schubert



Abstract:

A new sulfamidic acid anthraquinone derivative was synthesized from 2,6-diaminoanthraquinone with high yields, designed for utilization in redox flow batteries. The active material was investigated with cyclic voltammetry, revealing a reversible redox reaction at approximately -0.65 V vs. Ag/AgCl at pH-values above 12. A stress test in a redox flow battery was applied with hold times at critical states of charge and at 32 °C as well as at 60 °C. Furthermore, the stability was investigated at the maximum concentration of the anolyte. All in all, the material showed the lowest decomposition rates at 60 °C reported so far for an organic anolyte in a redox flow battery.


 Cite this: *RSC Adv.*, 2021, 11, 38759

 Received 19th July 2021
 Accepted 9th November 2021

DOI: 10.1039/d1ra05545c

rsc.li/rsc-advances

Anthraquinone-2,6-disulfamidic acid: an anolyte with low decomposition rates at elevated temperatures†

 Philip Rohland,^{ab} Kristin Schreyer,^{ab} Martin D. Hager ^{ab} and Ulrich S. Schubert ^{*ab}

A new sulfamidic acid anthraquinone derivative was synthesized from 2,6-diaminoanthraquinone with high yields, designed for utilization in redox flow batteries. The active material was investigated with cyclic voltammetry, revealing a reversible redox reaction at approximately -0.65 V vs. Ag/AgCl at pH-values above 12. A stress test in a redox flow battery was applied with hold times at critical states of charge and at 32 °C as well as at 60 °C. Furthermore, the stability was investigated at the maximum concentration of the anolyte. All in all, the material showed the lowest decomposition rates at 60 °C reported so far for an organic anolyte in a redox flow battery.

Introduction

In the course of ongoing climate change, energy production has to switch from fossil fuels to renewable resources to dampen the effects of global warming.¹ But for the breakthrough of clean energy conversion, the introduction of green, environmentally friendly storage technologies is necessary to compensate for the inherent discontinuous power output of the main, solar- and wind-based, technologies. Nowadays, many possible approaches have been evaluated for this mammoth task.² Rechargeable batteries provide a broad range of applicable dimensions, which would enable the installation of a decentralized energy storage grid. However, market-ready products, like lithium batteries or vanadium redox flow batteries (RFB), suffer from expensive and dangerous electrolytes or raw materials that are mined under environmentally and socially harmful conditions.^{3–5} The recently emerging research field of RFB based on organic materials is capable of targeting these drawbacks.

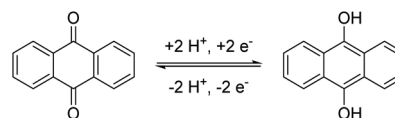
Numerous redox-active molecules, like ferrocenes,^{6,7} quinones,^{8,9} viologens,^{9–11} stable radicals,^{11–13} alloxazine,^{14,15} and flavine,¹⁶ have been subject to research showing the broad range of possible scaffolds of organic RFB (ORFB).

These molecules comprise earth-abundant elements targeting lower costs for battery electrolytes. Moreover, some materials, like TEMPO derivatives, do not require drastic electrolyte

pH-values or are even bioinspired, like flavines, which are based on vitamin B₂.¹⁶

Among these possible structures, quinones, in particular anthraquinones (AQ), are the best investigated anolyte materials.¹⁷ They combine a reversible redox chemistry involving two electrons per molecule (see Scheme 1) to result in a high specific capacity. Furthermore, their redox potential is highly depending on the pH-value of the electrolyte and the substitution pattern at the anthraquinone core resulting in a great potential for tailoring the molecule characteristic to the targeted application.¹⁸ They also show extraordinarily high stabilities during cycling and against side reactions,¹⁹ but this is also one of their major drawbacks. The high stability hinders derivatization reactions at the anthraquinone core and necessitates drastic or complex reaction conditions²⁰ resulting in the need of often cost-intensive starting materials. Nevertheless, these reactions are necessary to install linkers and solubility-promoting groups at the core to overcome the intrinsically low solubility of anthraquinone in water.

In this contribution, we report a fast, straight-forward one-step synthesis with high yields towards a highly water-soluble anthraquinone derivative. By utilizing cheap starting materials, reactants, solvents and simple reaction conditions, we report a new, economic anthraquinone active material based on 2,6-diaminoanthraquinone. The current literature lacks



Scheme 1 Schematic representation of the electrochemistry of anthraquinone.

^aLaboratory of Organic and Macromolecular Chemistry (IOMC), Friedrich Schiller University Jena, Humboldtstraße 10, 07743 Jena, Germany. E-mail: ulrich.schubert@uni-jena.de

^bCenter for Energy and Environmental Chemistry Jena (CEEC Jena), Friedrich Schiller University Jena, Philosophenweg 7a, 07743 Jena, Germany

† Electronic supplementary information (ESI) available. See DOI: 10.1039/d1ra05545c



examples where newly developed active materials are tested under more realistic conditions, like dwell times at high states of charge (SOC) as well as elevated temperatures. Nevertheless, these parameters are crucial, in particular for a future commercialization of the active material. Thus, we tested a 0.1 M solution of our new active material and included dwell times in combination with electrolyte temperatures of up to 60 °C in the cycling protocol. The molecules revealed a high stability during the hold times even when the temperature was increased. These findings were then confirmed by a long-term cycling test at maximum concentration.

Experimental

Chemicals and materials

All chemicals were bought with a purity of at least 95% and were used as received. Detailed information is provided in the ESI.† The ion-selective membrane (FKS-30, Fumatec GmbH, Germany) was cut into appropriate pieces and was prewetted in 1.5 M lithium chloride solution for at least 24 h prior to installation. GFA-6 (SGL SE, Germany) felts are used as porous electrodes.

Electrochemical analytics

Cyclic voltammetry. (CV) was performed on a VMP-3 (Bio-Logic, France) potentiostat/galvanostat using a standard three-electrode setup with an AgCl/Ag reference electrode (Ag wire in 3 M aq. potassium chloride solution), a platinum wire counter electrode and a glassy carbon working electrode (GCWE) with a diameter of 1.6 mm.

Battery experiments

All experiments were performed with the VMP-3 (Bio-Logic, France) potentiostat/galvanostat under an argon atmosphere in a glovebox (UNILab Plus Eco, MBraun, Germany, O₂ < 1 ppm, H₂O < 1 ppm, argon as protective gas). The electrolyte was pumped in the RFB through Norprene® A-60-G (θ_{inn} 1.6 mm, θ_{out} 4.8 mm, Saint-Gobain, France) with a pumping speed of approximately 25 mL min⁻¹ by a Hei-Flow Value 01 equipped with a C8 multi-channel pumping head (Heidolph, Germany). The RFB was designed by JenaBatteries GmbH (Germany) as a flat type cell with a membrane active area of 5 cm². A detailed overview of the components is provided in earlier publications of our group.¹¹ The standard temperature in the glovebox was 32 °C. For experiments at elevated temperatures, the capacity-limiting side was tempered in a sand bath (Hei-Tec, Heidolph, Germany), equipped with an external temperature sensor (PT 1000, Heidolph, Germany), at 60 °C. All tests were performed with an unbalanced, compositionally symmetric cell setup.

Electrolyte preparation. Appropriate amounts of lithium anthraquinone (LiAQs) were dissolved in 1 M aq. lithium chloride and 0.25 M lithium hydroxide solution and charged against an equally concentrated potassium ferrocyanide solution in the same supporting electrolyte. The applied current was set to 80 mA cm⁻² until a cell voltage of 1.45 V was reached. Afterwards, the battery was charged potentiostatically at 1.45 V

until the current density fell under 0.5 mA cm⁻². The received LiAQs solution was considered as fully charged, and it was mixed with the same amount of equally concentrated uncharged electrolyte. The obtained solution was considered to have a SOC of 50% and was split in two samples providing the capacity-limiting and -non-limiting side.

Current capacity test. The cell was charged and discharged with 10 mA cm⁻² between 0.45 V and -0.45 V. For charge tests the charging current was increased every six cycles by 10 mA cm⁻² until 80 mA cm⁻² was reached while the discharge current was kept at 10 mA cm⁻². The same protocol was used for discharge tests (with the discharge current being varied while the charge current being kept constant).

Cycling protocol – low concentration. Every cycle consisted of (1) a galvanostatic phase at 72 mA cm⁻² with an upper limiting voltage of 0.45 V, (2) a potentiostatic phase at 0.45 V with a lower limiting current of 2 mA cm⁻², (3) another galvanostatic phase at -72 mA cm⁻² with a lower limiting voltage of -0.45 V, and (4) another potentiostatic phase at -0.45 V with an upper limiting current of -2 mA cm⁻². After every 50th cycle, a hold time at the maximum SOC was applied. After 250 cycles at 32 °C, the protocol was repeated at 60 °C for 200 cycles.

Cycling protocol – high concentration. Every cycle consisted of (1) a galvanostatic phase at 80 mA cm⁻² with an upper limiting voltage of 0.60 V, (2) a potentiostatic phase at 0.60 V with a lower limiting current of 2 mA cm⁻², (3) another galvanostatic phase at -80 mA cm⁻² with a lower limiting voltage of -0.60 V, and (4) another potentiostatic phase at -0.60 V with an upper limiting current of -2 mA cm⁻².

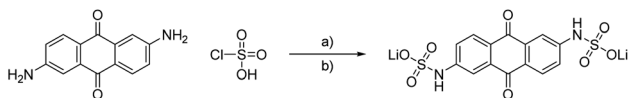
Results and discussion

Synthesis

The concept of using sulfamidic acids or sulfonamides as solubility enhancer in water represents a common strategy in the design process of new drugs.^{21–23} We used this approach to enhance the solubility of anthraquinones with amino side groups. On the one hand, the often applied 2,6-dihydroxy anthraquinone^{24,25} can be substituted by the one order of magnitude cheaper 2,6-diamino anthraquinone and, on the other hand, sulfonamides are highly stable and cleavage or rearrangement reactions need drastic conditions and long reaction times.²⁶ To further reduce the costs of the active material, we optimized the synthesis conditions by the usage of cheap reagents while maintaining high yields.

The first synthesis of sulfonamides from anthraquinones dates back to 1924, when different amino-AQ were transformed into their water-soluble derivatives by using chlorosulfuric acid, inert solvents like nitrobenzene, and organic nitrogen bases.²⁷ We adapted the conditions but changed to less dangerous solvents, and we receive high yields of above 87% (see Scheme 2). To increase the solubility of the active material, we applied a lithium chloride-based electrolyte to impose polarization effects similar to the lithium chloride/*N,N*-dimethylacetamide system for cellulose.²⁸ To prevent the formation of salts with different metal ions, lithium hydroxide was used for sulphate





Scheme 2 Schematic representation of the synthesis of LiAQS. (a) Dichloromethane, pyridine, 0 °C to room temperature, 16 h. (b) Water, lithium hydroxide, room temperature, 30 min, 87%.

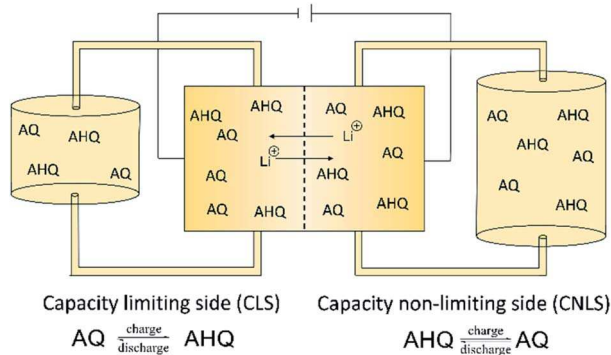


Fig. 1 Schematic representation of an unbalanced compositionally symmetric redox flow cell setup utilizing anthraquinone (AQ) as well as anthrahydroquinone (AHQ) and the representative half-cell reactions in the capacity limiting side (CLS) and non-limiting side (CNLS).

salt formation, despite the fact that, *e.g.*, sodium or potassium hydroxide would be much more cost effective.

Electrochemical analysis

The redox properties of the synthesized lithium anthraquinone 2,6-disulfamidic acid (LiAQS) were investigated *via* CV investigation. Since the redox chemistry of anthraquinones is known to be highly pH-dependent,¹⁸ firstly the redox reversibility of the material was studied. As expected, the reoxidation of the

hydroquinone to the quinone is hindered at pH values between 7 and 11 (see Fig. 2). At pH values of 13 and above, the AQ-typical redox pattern in the CV is visible.

The parameters of the redox reaction of the LiAQS was investigated by applying different scan speeds during the CV experiments at a pH-value of 14. While the reduction to the hydroquinone produces a sharp negative peak even at very fast scan speeds of 2000 mV s⁻¹, the peak of the reoxidation is broadened (see Fig. 2).

The reversibility of the redox reaction was investigated by plotting the peak current *vs.* the square root of the scan speed. The data points for the reduction and reoxidation can then be fitted linearly. The curves fit nicely to the datapoints, indicating reversible redox reactions of the LiAQS and a diffusion-controlled process.²⁹ Based on these findings we decided to use electrolytes with a pH-value between 13 and 14 for the following battery experiments. We thus used a lithium hydroxide concentration of 0.25 M for the battery electrolyte.

Battery experiments

In the recent years, anthraquinones have shown to be one of the most promising anolytes for redox flow batteries.¹⁷ Nevertheless, the need for high pH-values is one of their main drawbacks, limiting the selection of catholytes. The ferri-ferrocyanate has been established over the last years as the catholyte material of choice when using anthraquinones.^{18,19,24,25} However, we renounced full battery tests and focused our experiments on the investigation of the new LiAQS and its performance under unfavorable but realistic conditions. For this, we utilized the concept of an unbalanced, compositionally symmetric redox flow cell. The setup was firstly introduced by the group of Brushett³⁰ and further developed by Goulet and Aziz.³¹ It uses the same electrolyte in both half cells of the RFB, largely avoiding crossover artefacts (Fig. 1). Furthermore, we exposed our material to hold times in vulnerable SOCs and at

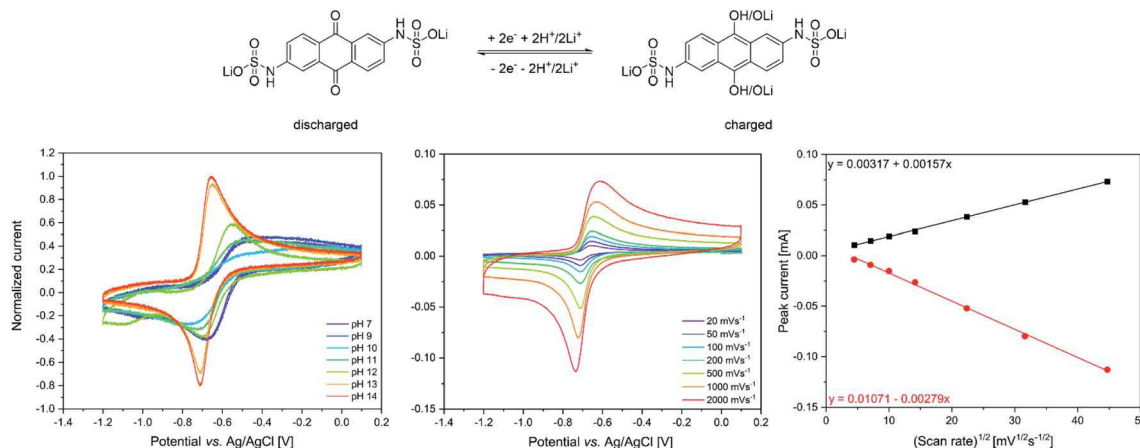


Fig. 2 Top: schematic representation of the redox chemistry of the LiAQS. Bottom: cyclic voltammetry of a 50 mM LiAQS in 0.1 M lithium chloride solution. Scan direction: 0 V to -1.2 V and back to 0 V. For each condition five scans were carried out and the third is shown. (left) pH-dependent investigation utilizing lithium hydroxide for adjusting the pH-value with a scan speed of 100 mVs⁻¹, (middle) CV at different scan speeds at a pH-value of 14, (right) plot of the peak current for the oxidation (black) and reduction process (red) *vs.* the square root of the scan speed at a pH-value of 14.



elevated temperatures to mimic more realistic conditions. The protocol includes 50 consecutive cycles with potentiostatic and galvanostatic parts (see Experimental details). This ensures that the cell reaches its maximum SOC. After 50 cycles, a hold time of 24 h at maximum SOC is applied. After 250 cycles, the protocol is repeated for 200 additional cycles at 60 °C.

The relatively low concentration of 0.1 M was used to keep the experiment's time in a manageable range and to highlight possible decomposition reactions.

The long-term test at low concentrations revealed an average decomposition rate of 0.4% d⁻¹ (see Fig. 3 upper left) during the cycling phases, which is low in comparison to other anthraquinone derivatives.¹⁷ Moreover, the decay rates during the hold times are barely visible, indicating a stable charged state, which is favorable regarding the integration of the battery in an electrical grid for long-term storage of energy. The high stability in high SOC's reduces the overall decay to 0.18% d⁻¹ (including hold times). Notably, the elevated temperatures in the glove box must be considered at this point since most of the published data are measured at room temperature, *i.e.* between 20 and 25 °C. The increase in temperature, although not extensive, might already trigger decomposition reactions. Nevertheless, in comparison to other quinone derivatives that feature the solubility-promoting group (SPG) directly attached to the

quinoidic core, the synthesized LiAQs is remarkably stable. The decay window ranging from 35% d⁻¹ for the 2,5-dimethoxy-3,6-dihydroxy-1,4-benzoquinone³² to 0.14% d⁻¹ for the 2,6-dihydroxyanthraquinone³³ in full battery setup and 70% d⁻¹ for tetramorpholinohydroquinone³⁴ and 0.08% d⁻¹ 2,7-anthraquinone disulfonic acid³³ in a symmetric cell set up. The topic of electrolyte lifetime in aqueous RFB is excellently summed up in the review of Kwabi *et al.*¹⁷

The Aziz group demonstrated that the introduction of a linker between AQ core and SPG can further increase the stability by one magnitude.^{8,19} However, for our system, this approach will be subject of future investigations.

Noteworthy, the 0.1 M LiAQs electrolyte reveals the same stability at 60 °C as at 32 °C, which is remarkable since increased temperatures usually promote decomposition reactions. The average decomposition rates during cycling phases and during hold times are nearly the same, resulting in an overall decay rate of 0.17% d⁻¹ (0.18% d⁻¹ at 32 °C). This is, to the best of our knowledge, the lowest ever measured value for an organic anolyte material at 60 °C. Furthermore, the coulombic efficiencies are not affected by the temperature change and is, with 99.95%, high. For an overview of all data of the low concentration long-term stability test see Table 1 in the ESI.† In the next step, the current capacity of the active material was

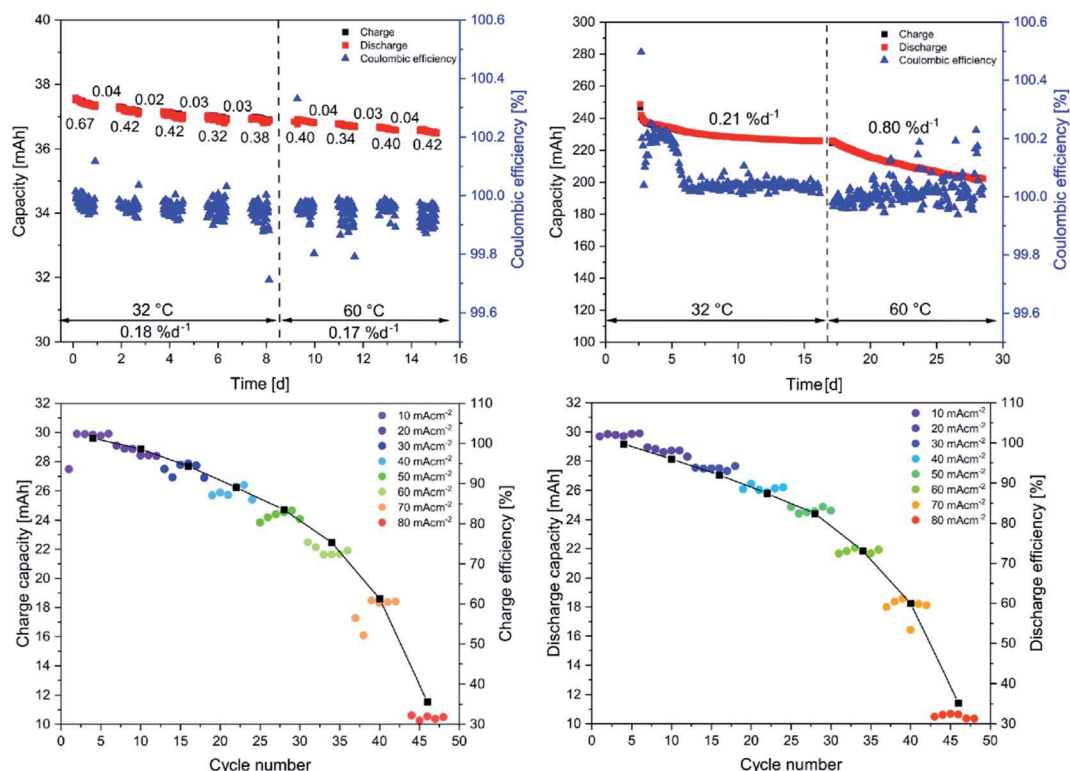


Fig. 3 (Top left) Long-term stability test using 15 mL of an aqueous 0.1 M LiAQs, 1 M LiCl and 0.25 M LiOH solution vs. 35 mL of the same solution. The values below the red and black squares indicate the decay rate during the representative 50 cycles in % d⁻¹. After every 50th cycle, the electrolyte is kept at maximum SOC for 24 h. The values above the squares represent the decay rates during this hold times. After 250 cycles, the temperature of the electrolyte is raised to 60 °C (indicated by the dashed line). The values below the temperature represent the decay rates over the whole temperature phases. (Top right) long-term test using 10 mL of a 0.75 M LiAQs, 1 M LiCl and 0.25 M LiOH solution vs. 25 mL of the same solution. Bottom: current capacity tests using 11.5 mL of a 0.1 M LiAQs, 1 M LiCl and 0.25 M LiOH solution vs. 35 mL of the same solution. Either the charge (left) or the discharge (right) current density is varied. The current density of the counter process is kept at 10 mA cm⁻².



investigated. Two experimental series were conducted, either with a changing charge or discharge current. The data reveals that a charge as well as a discharge current of 60 mA cm^{-2} can be applied until the achievable capacity drops below 80%, which is remarkably high for a 0.1 M solution (see Fig. 3).

In the last step, the behavior of the electrolyte at the maximal material concentration of 0.75 M was investigated in a long-term stability test. The electrolyte was charged potentiostatically and galvanostatically for 200 cycles at 32°C and 200 cycles at 60°C , like described for the low concentration test but without hold times. For an overview of all data of the high concentration long-term stability test see Table 2 in the ESI.† After an equilibration over ten cycles, during which the capacity strongly fades, the decay rate stabilizes over the next 190 cycles. Meanwhile, the coulombic efficiency (CE) rises until the 25th cycle and then slowly decreases until the 50th cycle. This might be caused by a longer equilibration time due to the maximal electrolyte concentration. In the 0.1 M LiAQs solution for comparison the CE is stable starting from the first cycle. After the equilibration, the CE of the 0.75 M solutions stabilizes above 99.95% and the capacity decay remains at around $0.2\% \text{ d}^{-1}$, confirming the findings for the 0.1 M solution. However, the subsequent 200 cycles at 60°C show a more pronounced fade of $0.8\% \text{ d}^{-1}$, indicating a temperature- and concentration-dependent decay mechanism. Nevertheless, the measured fade rates are the lowest obtained so far for anolytes at 60°C . In comparison to the experiments at 32°C , the CE fluctuates a bit more but is on average also above 99.95%.

Nevertheless, only approximately 50% of the theoretical capacity is addressable. We ascribe this behavior to the formation of quinhydrone complexes, formed from a fully charged, doubly reduced anthrahydroquinone and an uncharged anthraquinone, formally consisting of two half charged, singly reduced semiquinones.^{35–38} This process would be enhanced by an initial dimer formation, as shown for other 2,6-disubstituted anthraquinones,^{39,40} and hydrogen bonds formed by the sulfamic acid. The usage of lithium-based electrolytes might even enhance this behavior due to its oxophilicity and the possibility of complex formation based on lithium enolates.^{41–44}

Conclusion

A new active material was synthesized starting from an inexpensive 2,6-diamino anthraquinone. While the reaction conditions are mild and the reactants readily available, the yields are high, enabling the possibility for a further commercialization.

The RFB performance of the active material was investigated at low concentrations but under realistic stress conditions, like hold times in vulnerable SOC's or elevated temperatures. The LiAQs showed low decomposition rates of $0.2\% \text{ d}^{-1}$ at 32°C , which places it among the best performing AQ derivatives with the SPG directly linked to the AQ core. Furthermore, the stability at 60°C is comparable to that at 32°C . Based on this data, the LiAQs revealed, to the best of our knowledge, the highest stability of an organic anolyte at 60°C so far. With regard to a possible commercialization, we also determined the stability of the anolyte at the maximum concentration of 0.75 M.

The LiAQs showed similar decomposition rates at 32°C as at low concentration. However, the stability at 60°C is slightly decreased. Nevertheless, it is the best performing anolyte material under the used conditions so far.

A further increase in stability might be achieved by the introduction of a linker between the SPG and the anthraquinone core as the data by the group of Aziz suggests;^{8,19} this is the topic of ongoing investigations.

Author contributions

P. R. designed this project and wrote the manuscript. P. R. and K. S. carried out the experiments. M. D. H. and U. S. S. supervised the project. All authors provided critical feedback, discussed the results and commented on the manuscript.

Conflicts of interest

There are no conflicts to declare.

Acknowledgements

We acknowledge the Thuringian Ministry of Economic Affairs, Science and Digital Society (TMWWDG), the Thüringer Aufbaubank (TAB) and the European Regional Development Fund (ERDF), for financial support (2016 IZN 0009 and CEEC-01/2020). We further want to thank Dr Christian Friebe for his help and suggestions and Oliver Nolte for inspirations.

Notes and references

- 1 B. Obama, *Science*, 2017, **355**, 126–129.
- 2 I. Hadjipaschalis, A. Poullikkas and V. Efthimiou, *Renewable Sustainable Energy Rev.*, 2009, **13**, 1513–1522.
- 3 K. Liu, Y. Liu, D. Lin, A. Pei and Y. Cui, *Sci. Adv.*, 2018, **4**, eaas9820.
- 4 P. Alotto, M. Guarnieri and F. Moro, *Renewable Sustainable Energy Rev.*, 2014, **29**, 325–335.
- 5 C. Banza Lubaba Nkulu, L. Casas, V. Haufroid, T. De Putter, N. D. Saenen, T. Kayembe-Kitenge, P. Musa Obadia, D. Kyanika Wa Mukoma, J. M. Lunda Ilunga, T. S. Nawrot, O. Luboya Numbi, E. Smolders and B. Nemery, *Nat. Sustain.*, 2018, **1**, 495–504.
- 6 P. Navalpotro, E. Castillo-Martínez and J. Carretero-González, *Sustainable Energy Fuels*, 2021, **5**, 310–331.
- 7 P. S. Borchers, M. Strumpf, C. Friebe, I. Nischang, M. D. Hager, J. Elbert and U. S. Schubert, *Adv. Energy Mater.*, 2020, **10**, 2001825–2001833.
- 8 Y. L. Ji, M. A. Goulet, D. A. Pollack, D. G. Kwabi, S. Y. Jin, D. De Porcellinis, E. F. Kerr, R. G. Gordon and M. J. Aziz, *Adv. Energy Mater.*, 2019, **9**, 1900039–1900046.
- 9 S. J. Jin, Y. Jing, D. G. Kwabi, Y. L. Ji, L. C. Tong, D. De Porcellinis, M. A. Goulet, D. A. Pollack, R. G. Gordon and M. J. Aziz, *ACS Energy Lett.*, 2019, **4**, 1342–1348.
- 10 C. DeBruler, B. Hu, J. Moss, J. Luo and T. L. Liu, *ACS Energy Lett.*, 2018, **3**, 663–668.



- 11 T. Janoschka, N. Martin, M. D. Hager and U. S. Schubert, *Angew. Chem., Int. Ed.*, 2016, **55**, 14427–14430.
- 12 T. Janoschka, N. Martin, U. Martin, C. Friebe, S. Morgenstern, H. Hiller, M. D. Hager and U. S. Schubert, *Nature*, 2015, **527**, 78–81.
- 13 J. Winsberg, T. Janoschka, S. Morgenstern, T. Hagemann, S. Muench, G. Hauffman, J. F. Gohy, M. D. Hager and U. S. Schubert, *Adv. Mater.*, 2016, **28**, 2238–2243.
- 14 K. X. Lin, R. Gomez-Bombarelli, E. S. Beh, L. C. Tong, Q. Chen, A. Valle, A. Aspuru-Guzik, M. J. Aziz and R. G. Gordon, *Nat. Energy*, 2016, **1**, 1–8.
- 15 W. Lee, B. W. Kwon and Y. Kwon, *ACS Appl. Mater. Interfaces*, 2018, **10**, 36882–36891.
- 16 A. Orita, M. G. Verde, M. Sakai and Y. S. Meng, *Nat. Commun.*, 2016, **7**, 13230–13238.
- 17 D. G. Kwabi, Y. Ji and M. J. Aziz, *Chem. Rev.*, 2020, **120**, 6467–6489.
- 18 D. P. Tabor, R. Gomez-Bombarelli, L. C. Tong, R. G. Gordon, M. J. Aziz and A. Aspuru-Guzik, *J. Mater. Chem. A*, 2019, **7**, 12833–12841.
- 19 M. Wu, Y. Jing, A. A. Wong, E. M. Fell, S. J. Jin, Z. J. Tang, R. G. Gordon and M. J. Aziz, *Chem-US*, 2020, **6**, 1432–1442.
- 20 Y. Jing, M. Wu, A. A. Wong, E. M. Fell, S. Jin, D. A. Pollack, E. F. Kerr, R. G. Gordon and M. J. Aziz, *Green Chem.*, 2020, **22**, 6084–6092.
- 21 G. L. Perlovich, V. P. Kazachenko, N. N. Strakhova and O. A. Raevsky, *J. Chem. Eng. Data*, 2014, **59**, 4217–4226.
- 22 F. J. Bandelin and W. Malesh, *J. Am. Pharm. Assoc.*, 1959, **48**, 177–181.
- 23 F. Martínez and A. Gómez, *Phys. Chem. Liq.*, 2010, **40**, 411–420.
- 24 Z. J. Yang, L. C. Tong, D. P. Tabor, E. S. Beh, M. A. Goulet, D. De Porcellinis, A. Aspuru-Guzik, R. G. Gordon and M. J. Aziz, *Adv. Energy Mater.*, 2018, **8**, 1702056–1702065.
- 25 D. G. Kwabi, K. Lin, Y. Ji, E. F. Kerr, M.-A. Goulet, D. De Porcellinis, D. P. Tabor, D. A. Pollack, A. Aspuru-Guzik, R. G. Gordon and M. J. Aziz, *Joule*, 2018, **2**, 1894–1906.
- 26 S. Searles and S. Nukina, *Chem. Rev.*, 1959, **59**, 1077–1103.
- 27 F. Baumann, H. Walter, W. Hentrich and L. Zeh, IG Farbenindustrie AG, *Germany Pat.*, DE469564C, 1924.
- 28 C. L. McCormick, P. A. Callais and B. H. Hutchinson, *Macromolecules*, 1985, **18**, 2394–2401.
- 29 J. Winsberg, C. Stolze, A. Schwenke, S. Muench, M. D. Hager and U. S. Schubert, *ACS Energy Lett.*, 2017, **2**, 411–416.
- 30 J. D. Milshtein, J. L. Barton, R. M. Darling and F. R. Brushett, *J. Power Sources*, 2016, **327**, 151–159.
- 31 M. A. Goulet and M. J. Aziz, *J. Electrochem. Soc.*, 2018, **165**, A1466–A1477.
- 32 P. Sun, Y. Liu, Y. Li, M. A. Shehzad, Y. Liu, P. Zuo, Q. Chen, Z. Yang and T. Xu, *Ind. Eng. Chem. Res.*, 2019, **58**, 3994–3999.
- 33 M. A. Goulet, L. Tong, D. A. Pollack, D. P. Tabor, S. A. Odom, A. Aspuru-Guzik, E. E. Kwan, R. G. Gordon and M. J. Aziz, *J. Am. Chem. Soc.*, 2019, **141**, 8014–8019.
- 34 E. Drazevic, C. Szabo, D. Konya, T. Lund, K. Wedege and A. Bientien, *ACS Appl. Energy Mater.*, 2019, **2**, 4745–4754.
- 35 F. D'Souza, *J. Am. Chem. Soc.*, 1996, **118**, 923–924.
- 36 N. Hayashi, T. Yoshikawa, M. Kurakawa, T. Ohnuma, Y. Sugiyama and H. Higuchi, *Mol. Cryst. Liq. Cryst.*, 2006, **456**, 133–137.
- 37 K. Molčanov, C. Jelsch, B. Landeros, J. Hernández-Trujillo, E. Wenger, V. Stilinović, B. Kojić-Prodić and E. C. Escudero-Adán, *Cryst. Growth Des.*, 2018, **19**, 391–402.
- 38 S. Patai and Z. Rappoport, *The Quinonoid Compounds*, John Wiley & Sons Ltd., Hoboken, 1988, vol. 1.
- 39 T. J. Carney, S. J. Collins, J. S. Moore and F. R. Brushett, *Chem. Mater.*, 2017, **29**, 4801–4810.
- 40 C. Wiberg, T. J. Carney, F. Brushett, E. Ahlberg and E. G. Wang, *Electrochim. Acta*, 2019, **317**, 478–485.
- 41 D. Seebach, *Angew. Chem., Int. Ed.*, 1988, **27**, 1624–1654.
- 42 M. P. Sibi, *J. Am. Chem. Soc.*, 1998, **120**, 2991.
- 43 A. Streitwieser, *J. Mol. Model.*, 2006, **12**, 673–680.
- 44 A. Streitwieser, *J. Org. Chem.*, 2009, **74**, 4433–4446.



1 Supplemental Information

2 Anthraquinone-2,6-disulfamidic acid: An anolyte with low decomposition rates at elevated
3 temperatures

4 Philip Rohland^{a,b}, Kristin Schreyer^{a,b}, Martin D. Hager^{a,b}, Ulrich S. Schubert^{*,a,b}

5

6 * E-mail: ulrich.schubert@uni-jena.de

7 ^a Laboratory of Organic and Macromolecular Chemistry (IOMC), Friedrich Schiller University
8 Jena, Humboldtstrasse 10, 07743 Jena, Germany

9 ^b Center for Energy and Environmental Chemistry Jena (CEEC Jena), Friedrich Schiller
10 University Jena, Philosophenweg 7a, 07743 Jena, Germany

11

12

13

14

15

16

17 *General analytical instruments*

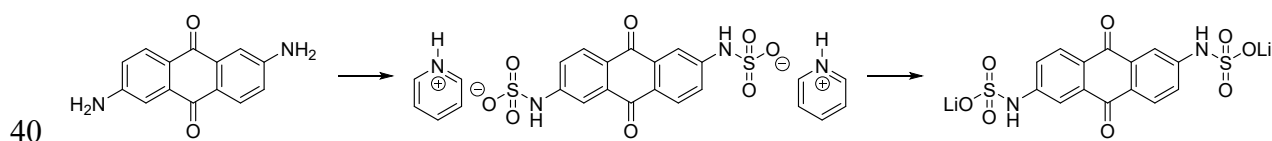
18 The NMR spectra were obtained utilizing an Avance I 300 MHz (Bruker, Germany) or
19 an Avance III 400 MHz (Bruker, Germany). The ESI-Q-TOF MS measurements were
20 performed applying a micrOTOF QII mass spectrometer (Bruker, Germany) with an
21 automatic syringe pump (KD Scientific, USA). An ESI source was used to generate ions
22 and the calibrated instrument measured in a m/z range between 50 and 3000. As
23 calibration standard, an ESI-L Low concentration tuning mix from Agilent was utilized.
24 The sample concentration ranged between 1 and 10 $\mu\text{g mL}^{-1}$. The samples were injected
25 in the instrument with a constant flow of 3 $\mu\text{L min}^{-1}$ (= 180 $\mu\text{L hr}^{-1}$). The data were
26 evaluated with the Bruker Data Analysis software version 4.2. For pH-measurements, a
27 Mettler Toledo FiveGO F2 equipped with a Mettler Toledo LF438 pH-electrode was
28 used. For the FT-IR spectroscopy investigations an Invenio S (Bruker, Germany) with a
29 Platinum ATR (Bruker, Germany) was used.

30 *Chemicals and materials*

31 If not noted otherwise, the solvents were purchased from standard suppliers and distilled prior
32 to usage. If solvents were used from a solvent purification system (SPS), they were obtained
33 from an MB-SPS-800 (MBraun Inertgas-Systeme GmbH, Germany) and stored under argon. If
34 water was used, deionized water was utilized. 2,6-Diaminoanthraquinone (Sigma-Aldrich,
35 Germany), lithium chloride (Sigma-Aldrich, Germany), pyridine (Fisher Scientific, Germany),
36 chlorosulfuric acid (Merk, Germany), potassium ferrocyanide trihydrate (Sigma-Aldrich,
37 Germany) were purchased by the corresponding suppliers and used as received.

38

39 *Synthesis of lithium anthraquinone 2,6-bis(sulfamate)*



41 30 g (126 mmol) of 2,6-diaminoanthraquinone was suspended in 600 mL of dichloromethane
 42 in a 1.5 L sulfonation flask equipped with a KPG (sealed precision glass) stirrer, a reflux con-
 43 denser, dropping funnel and a thermometer. The mixture was cooled to 0 °C in an ice bath.
 44 27.2 mL (44.04 g, 378 mmol) chlorosulfuric acid diluted with 60 mL dichloromethane was
 45 added to the mixture. During the addition, the suspension turned from brown-red to green-grey.
 46 Afterwards the reaction mixture was stirred for 30 min and, subsequently, 47.7 mL pyridine
 47 diluted with 60 mL dichloromethane was added slowly dropwise. The temperature of the
 48 mixture increased during the addition and the mixture turned to light brown. After complete
 49 addition, the mixture was allowed to heat to room temperature, was stirred for 16 h, and then
 50 stirred under reflux conditions for additional 2 h. After cooling to room temperature, the formed
 51 particulate was collected by filtration and washed with dichloromethane and acetone. The solid
 52 was added to 1.5 L of water, but did not completely dissolve. Lithium hydroxide was added
 53 until the pH value of the solution reached 12. The solid dissolved upon basification nearly
 54 completely and the mixture turned from light brown to dark red. Remaining solid was removed
 55 by filtration. The filtrate was concentrated by removing the solvent. The mixture was then added
 56 dropwise to 1.5 L of acetone and the precipitate was collected by filtration. The solid was
 57 washed with acetone to receive the desired product as red-brownish solid (42.2 g, 103 mmol,
 58 82%) ¹H NMR (D₂O, 300 MHz): δ [ppm] = 7.09 (2 H, m, C-CH-CN_H), 7.18 (2 H, d, J =
 59 2.26 Hz, CH-CH-CN_H), 7.51 (2 H, m, d, J = 8.48 Hz, CH-CH-CN_H), ¹³C NMR (D₂O,
 60 75 MHz): δ [ppm] = 113.65 (C₁₊₅), 120.98 (C₃₊₇), 124.92 (C₁₂₊₁₄), 129.02 (C₈₊₄),
 61 134.02 (C₁₃₊₁₁), 147.57 (C₂₊₆), 182.75 (C₉₊₁₀), (the additional peak at 168.06 ppm corresponds

62 to the C₉ and C₁₀ and is caused by tautomerism)^{1,2}. ⁷Li NMR (D₂O, 155 MHz): δ [ppm] = 0.02
63 (s), HR-MS (ESI m/z): calc. for [C₁₄H₈N₂O₈S₂]²⁻ 197.9867 found 197.9856.

64 *Solubility measurement*

65 An excess amount of 2,6-diamino anthraquinone (DAAQ) was placed into 1.5 mL pure water
66 or electrolyte (0.25 M LiOH and 1 M LiCl). After vortexing it for 6 hours the suspension was
67 filtered with a syringe filter (0.45 μm, Nylon 66, Applichrom, Germany) and adequate amounts
68 of solution were transferred into a HPLC vial and freeze dried. The solubility of the compound
69 was calculated by the mass differences with taking the electrolyte salt into account. The same
70 was done for the LiAQS in pure water.

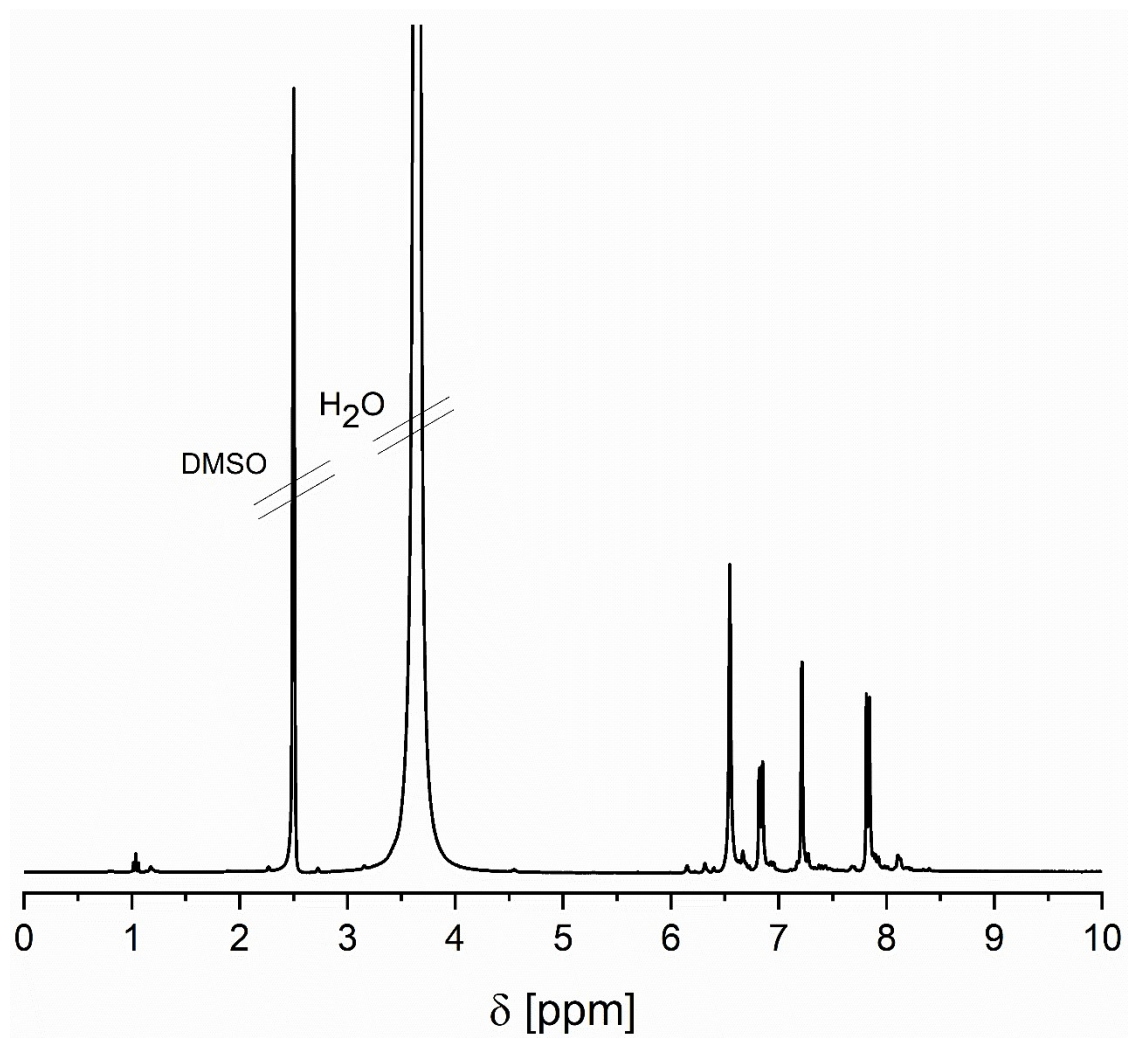
71 *Table 1: Maximum solubility of DAAQ and LiAQS.*

Compound	Solvent	Maximum concentration
DAAQ	pure water	0.051 M
DAAQ	electrolyte	0.081 M
LiAQS	pure water	0.373 M
LiAQS	electrolyte	0.750 M

72

73

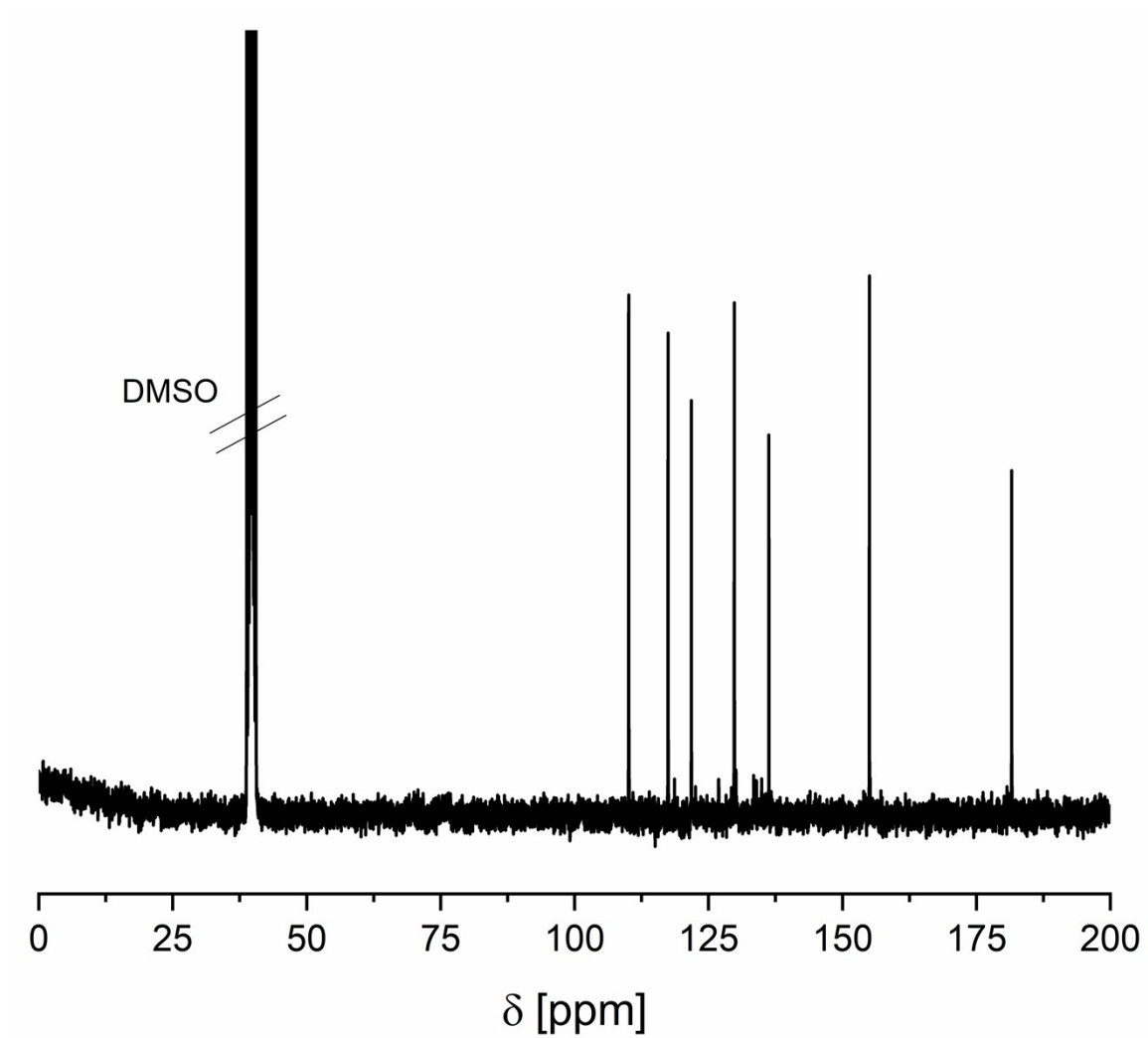
74



75

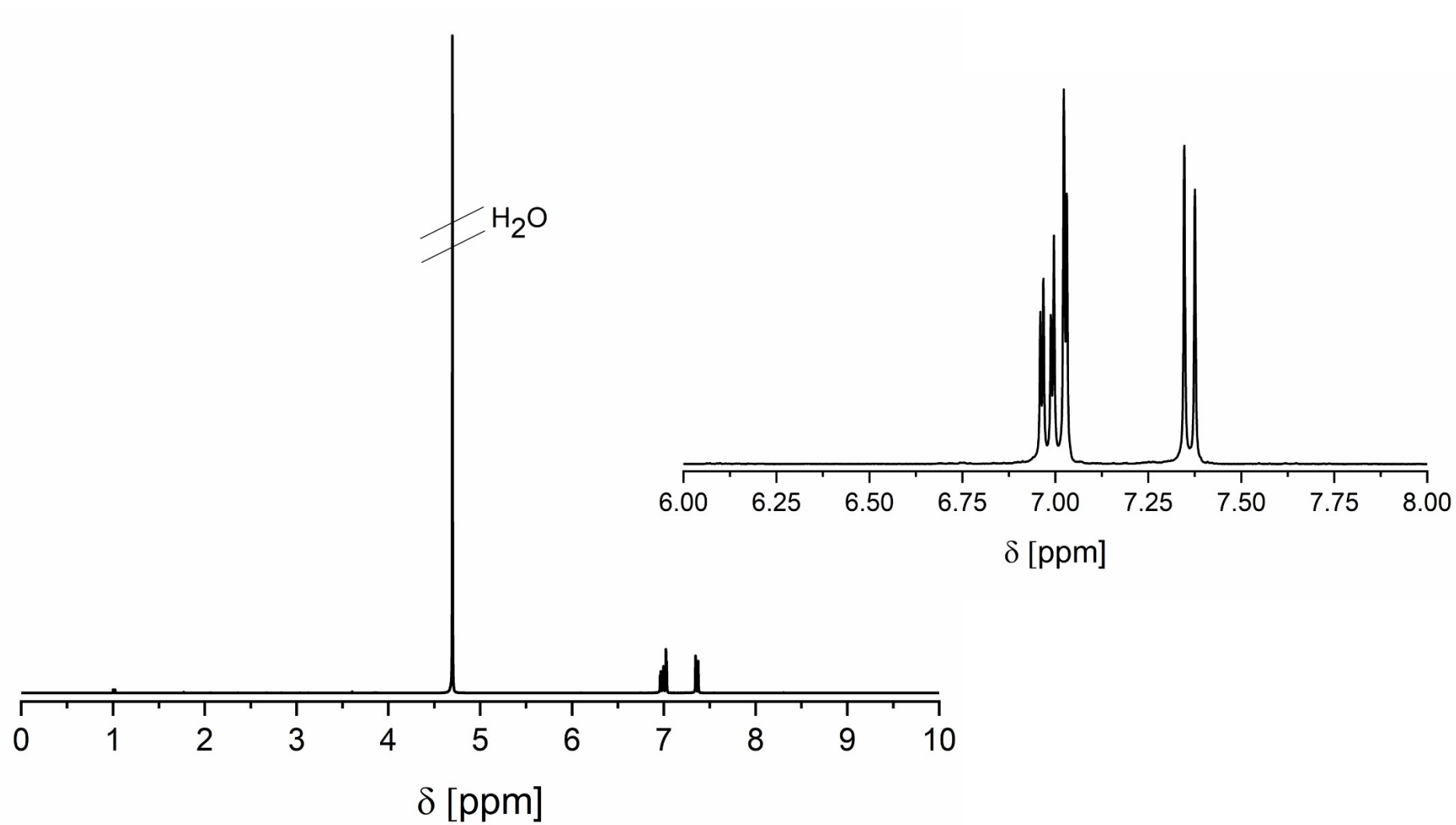
76 Figure 1: ¹H NMR spectrum of 2,6-diaminoanthraquinone (Sigma Aldrich) (300 MHz, DMSO-d₆).

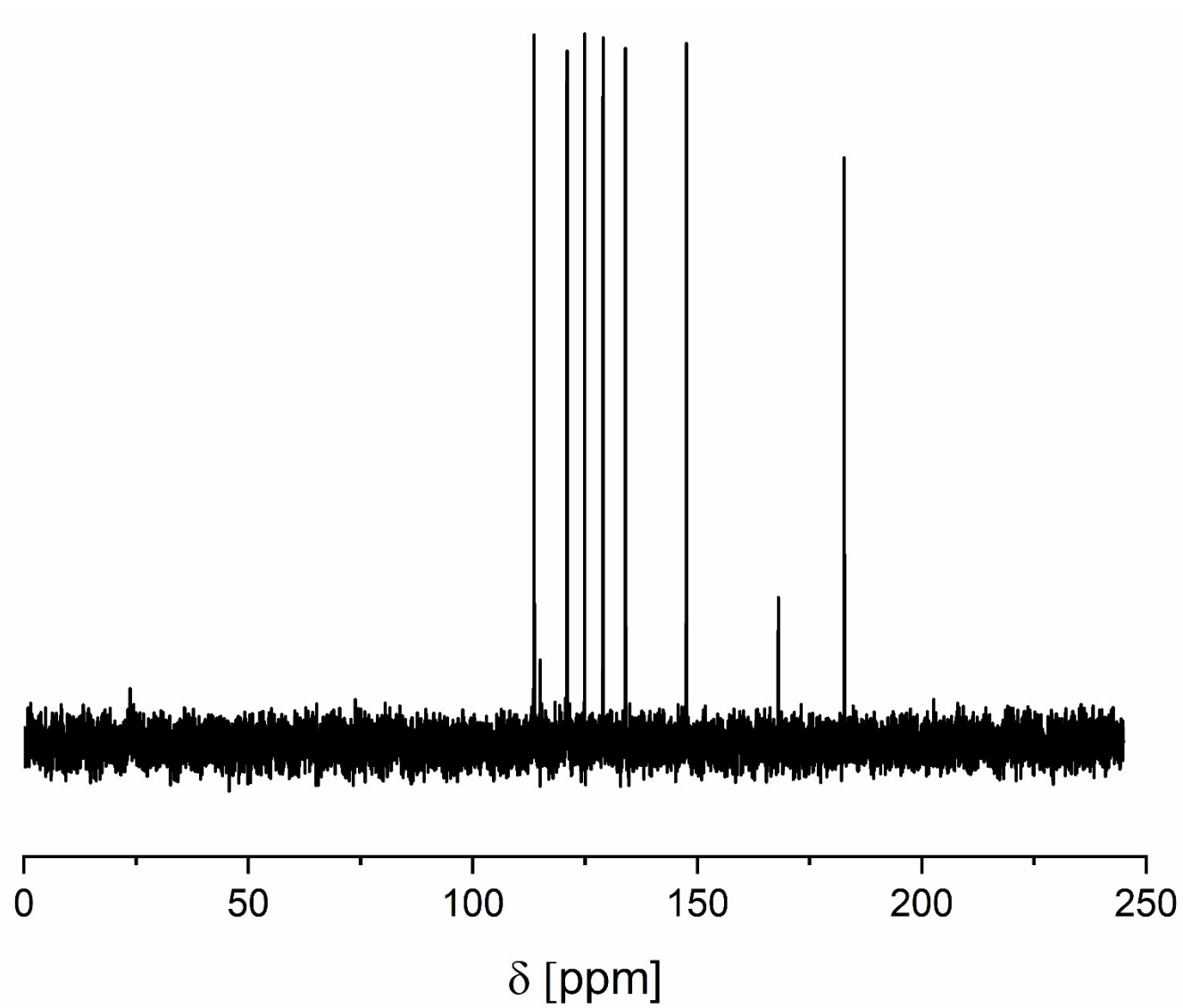
77



78

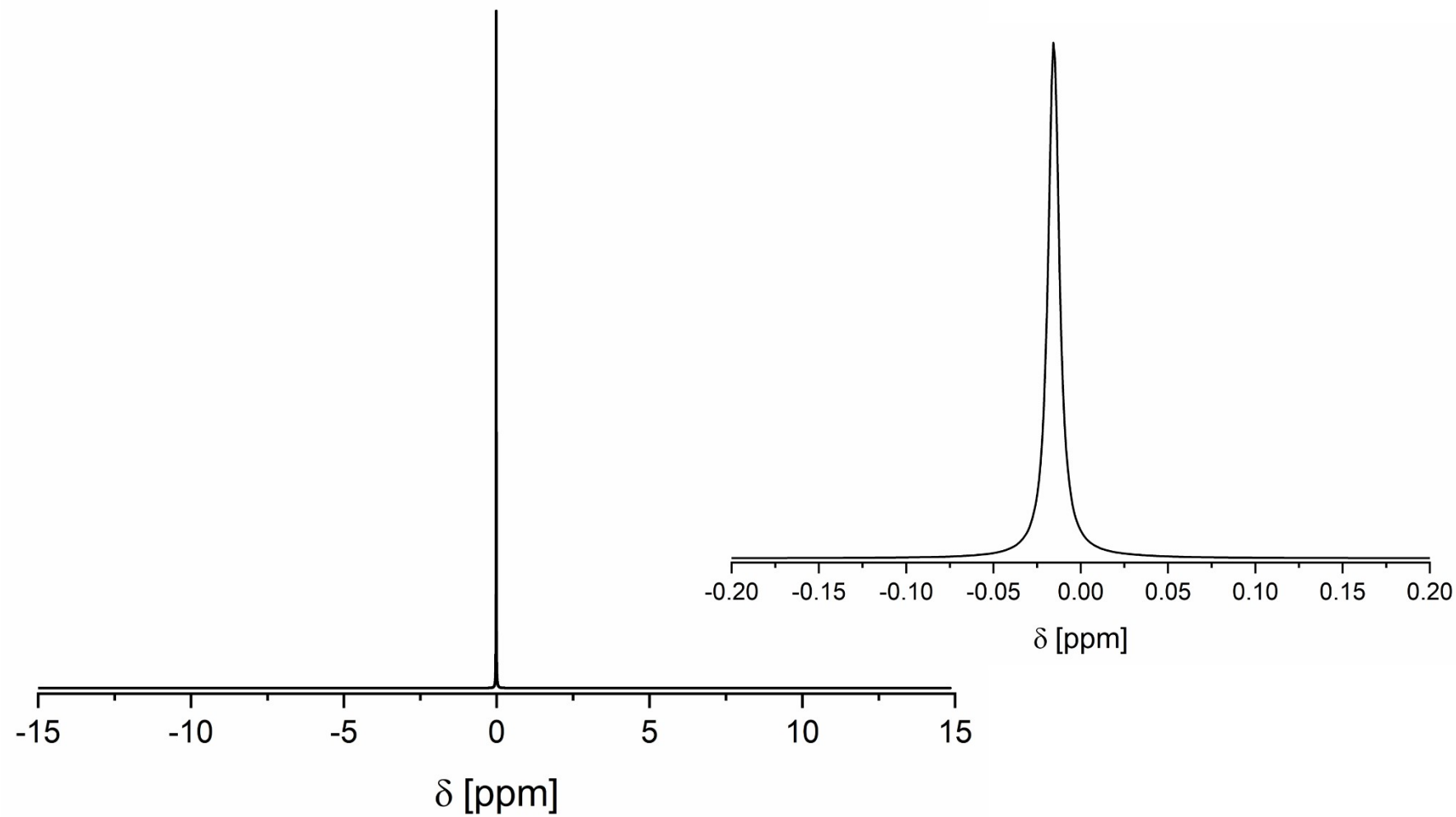
79 Figure 2: ^{13}C NMR spectrum of 2,6-diaminoanthraquinone (Sigma Aldrich) (300 MHz, $\text{DMSO-}d_6$).





83

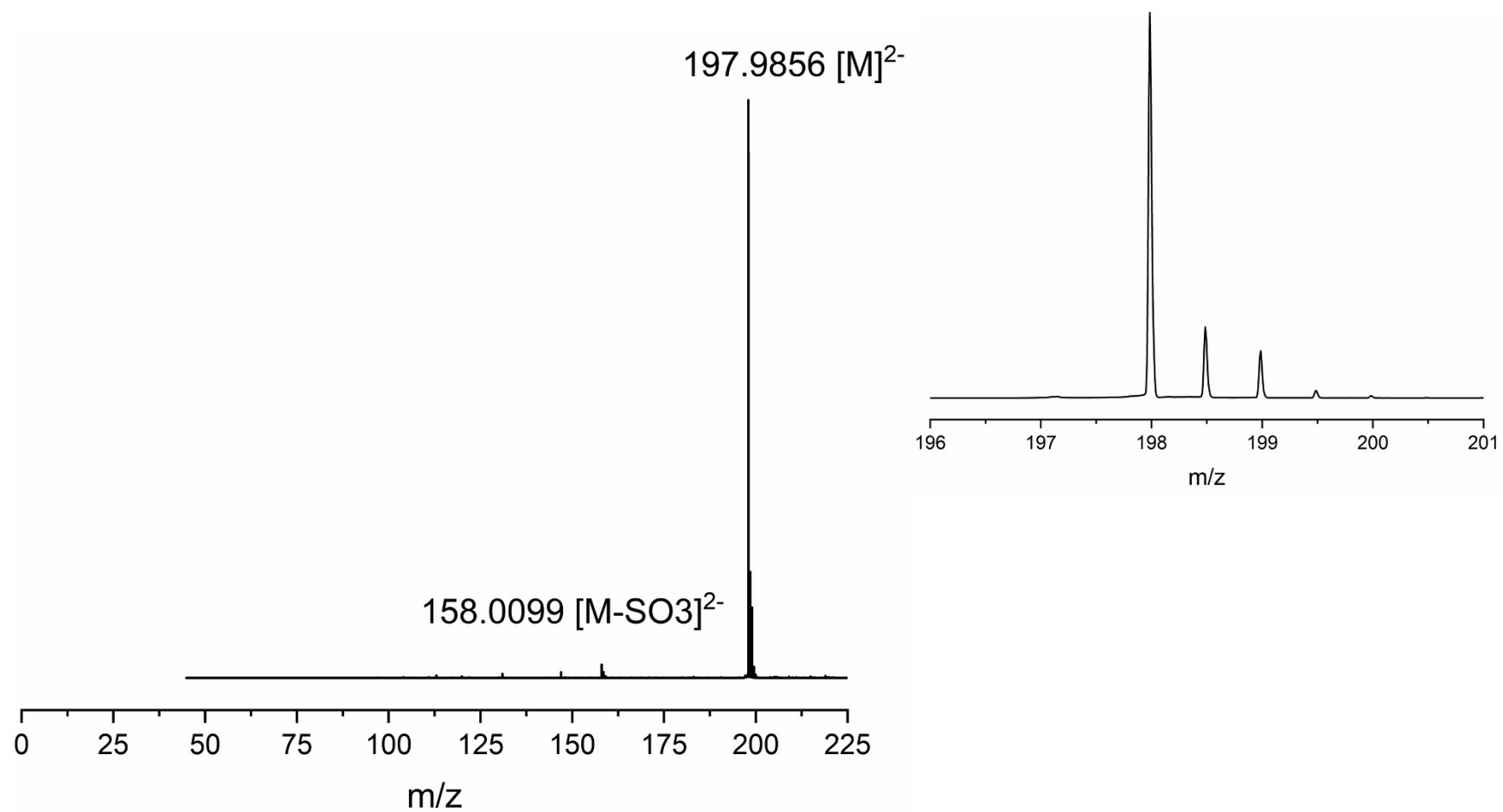
84 *Figure 4: ^{13}C NMR spectrum of lithium anthraquinone 2,6-bis(sulfamate) (75 MHz, deuterated water).*



85

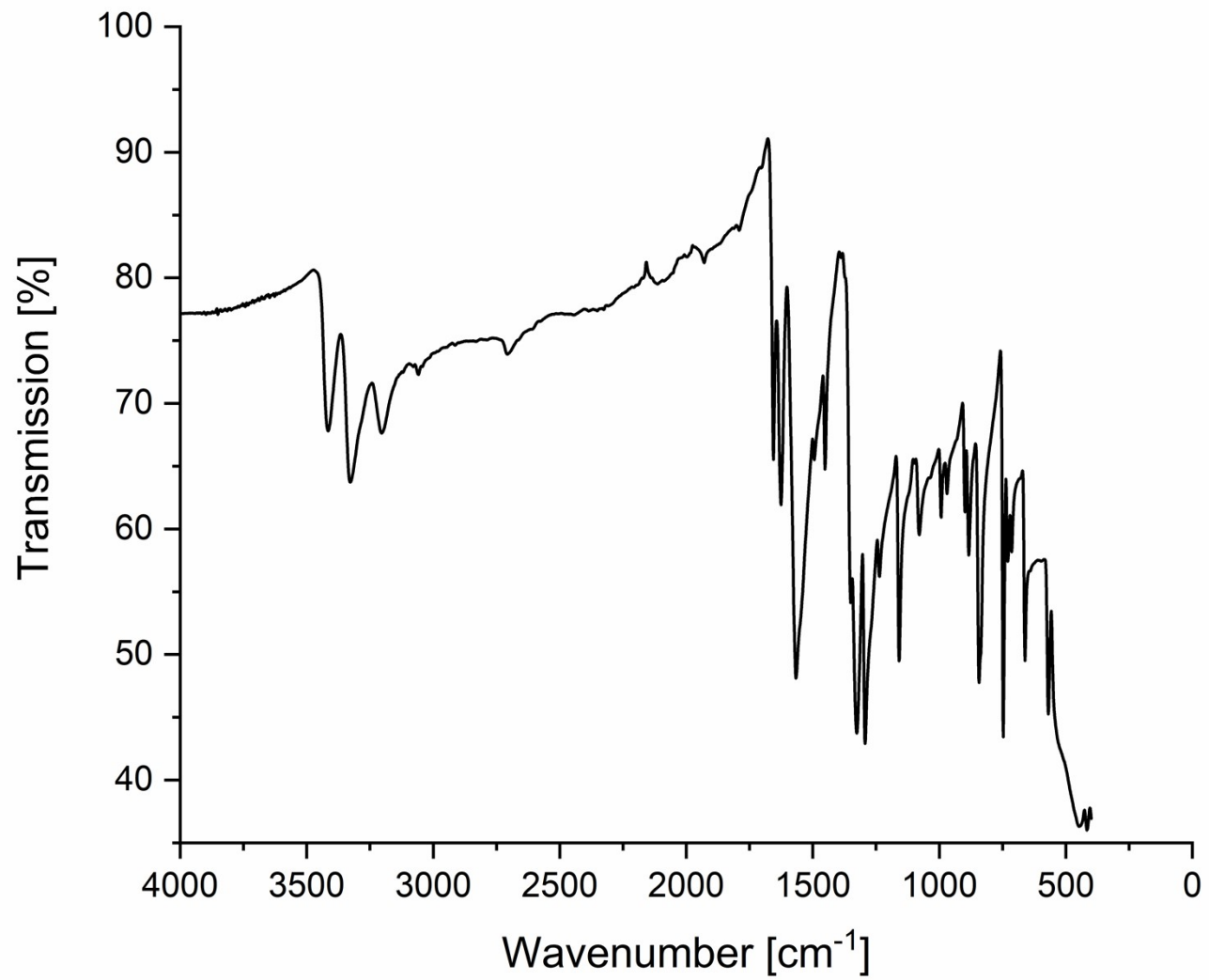
86 *Figure 5: ${}^7\text{Li}$ NMR spectrum of lithium anthraquinone 2,6-bis(sulfamate) (155 MHz, deuterated water). Inlet shows the zoomed spectrum between -0.20 and 0.20 ppm.*

87



88

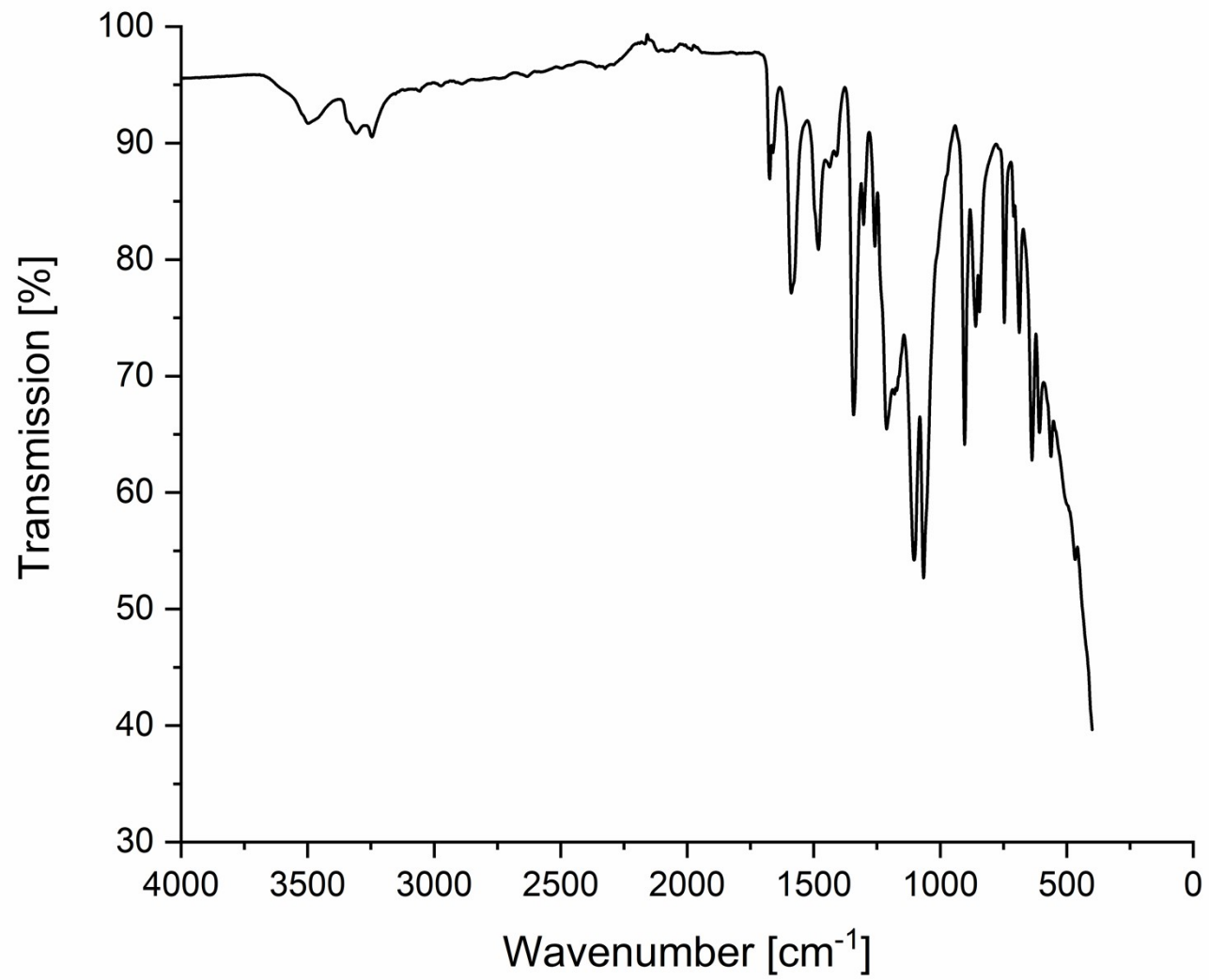
89 *Figure 6: HR-MS spectrum of anthraquinone 2,6-bis(sulfamate). The inset shows the isotopic pattern of the molecular ion peak.*



90

91 *Figure 7: FT-IR spectrum of 2,6-diaminoanthraquinone (Sigma Aldrich).*

92



93

94 *Figure 8: FT-IR spectrum of lithium anthraquinone 2,6-bis(sulfamate).*

95

96 Table 2: Summary of the data of the low concentration long term stability test.

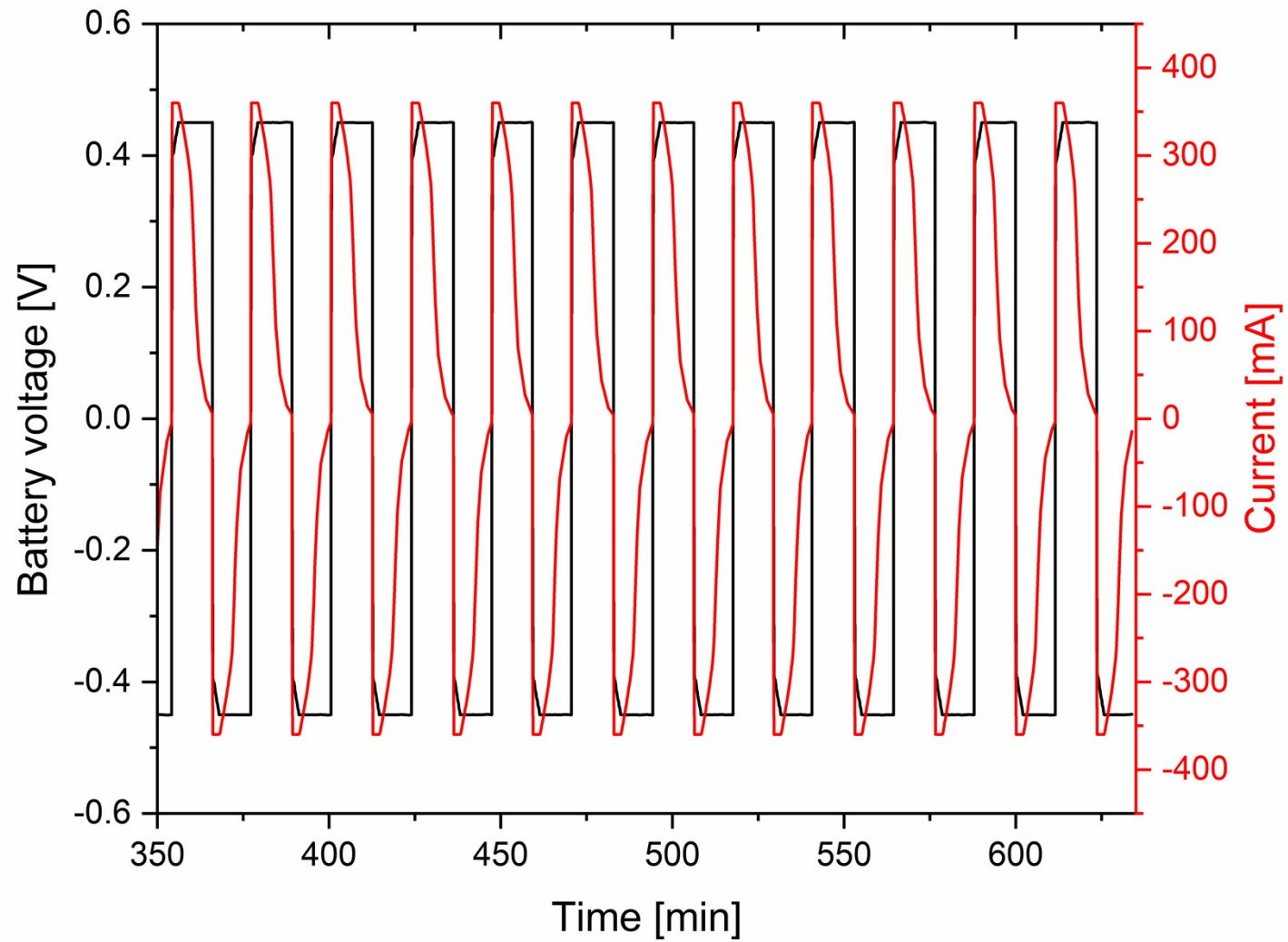
Active material concentration [mol L ⁻¹]	Volume CLS [mL]	Theoretical capacity CLS [mAh]	Electrolyte composition	Temperature [°C]	Cycle	Current density* [mA cm ⁻²]	Average coulombic efficiency [%]	Decay rate [%d ⁻¹]
0.1	15	80.2	0.1 M LiAQS 0.25 M LiOH 1 M LiCl	32	1-50	72 mA cm ⁻²	99.95	0.67
					50	Hold time	-	0.04
					50-100	72 mA cm ⁻²	99.95	0.42
					100	Hold time	-	0.02
					100-150	72 mA cm ⁻²	99.95	0.42
					150	Hold time	-	0.03
					150-200	72 mA cm ⁻²	99.95	0.32
					200	Hold time	-	0.03
200-250	72 mA cm ⁻²	99.95	0.38					
0.1	15	80.2	0.1 M LiAQS 0.25 M LiOH 1 M LiCl	60	1-50	72 mA cm ⁻²	99.95	0.40
					50	Hold time	-	0.04
					50-100	72 mA cm ⁻²	99.95	0.34
					100	Hold time	-	0.03
					100-150	72 mA cm ⁻²	99.95	0.40
					150	Hold time	-	0.04
					150-200	72 mA cm ⁻²	99.95	0.42

97 * Every cycle consisted of (1) a galvanostatic phase at 72 mAcm⁻² with an upper limiting voltage of 0.45 V, (2) a potentiostatic phase at 0.45 V with
98 a lower limiting current of 2 mAcm⁻², (3) another galvanostatic phase at -72 mAcm⁻² with a lower limiting voltage of -0.45 V, and (4) another
99 potentiostatic phase at -0.45 V with an upper limiting current of -2 mAcm⁻².

100 Table 3: Summary of the data of the high concentration long term stability test.

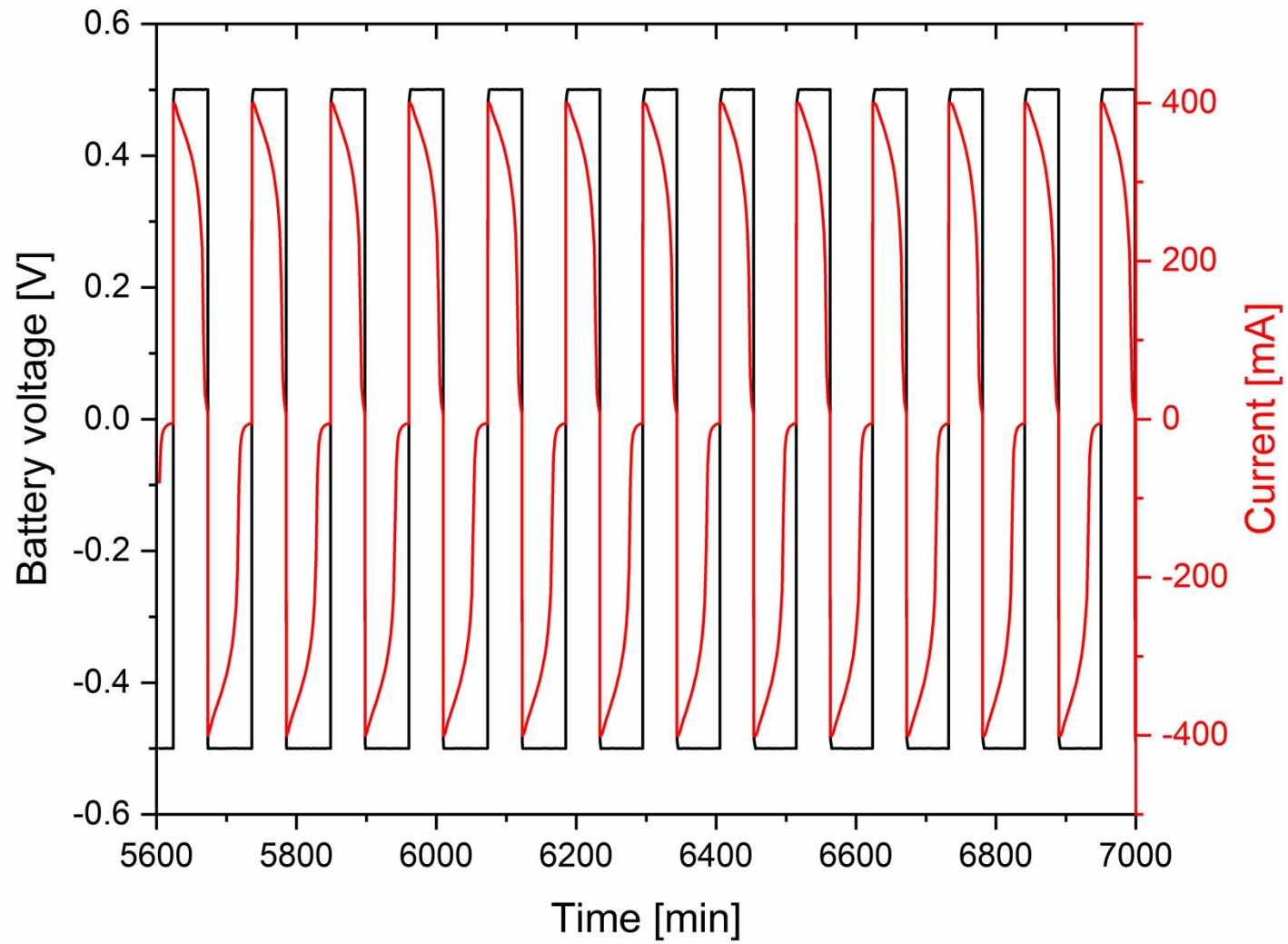
Active material concentration [mol L ⁻¹]	Volume CLS [mL]	Theoretical capacity CLS [mAh]	Electrolyte composition	Temperature [°C]	Cycle	Current density* [mA cm ⁻²]	Average coulombic efficiency [%]	Decay rate [%d ⁻¹]
0.75	10	402	0.75 M LiAQS 0.25 M LiOH 1 M LiCl	32	1-200	80 mA cm ⁻²	100	0.21
0.75	10	402	0.1 M LiAQS 0.25 M LiOH 1 M LiCl	60	1-200	80 mA cm ⁻²	100	0.80

101 * Every cycle consisted of (1) a galvanostatic phase at 80 mA cm⁻² with an upper limiting voltage of 0.60 V, (2) a potentiostatic phase at 0.60 V with
 102 a lower limiting current of 2 mA cm⁻², (3) another galvanostatic phase at -80 mA cm⁻² with a lower limiting voltage of -0.60 V, and (4) another
 103 potentiostatic phase at -0.60 V with an upper limiting current of -2 mA cm⁻².



104

105 *Figure 9: Voltage and current profile of the cycle 11 to 22 of the battery with a 0.1 M LiAQS electrolyte concentration.*



106

107 *Figure 10: Voltage and Current profile of the cycle 11 to 22 of the battery with a 0.75 M LiAQS electrolyte concentration.*

108 *Literature*

- 109 1. T. Kenny, S. M. Aly, D. Fortin and P. D. Harvey, *Chem. Commun.*, 2012, **48**, 11543-
110 11545.
- 111 2. V. Y. Fain, B. E. Zaitsev and M. A. Ryabov, *Russ. J. Gen. Chem.*, 2010, **80**, 550-550.
112

Publications P5

Liquid chromatography analysis of reactive oxoammonium cations.

P. Rohland, K. Schreyer, R. Burges, N. Fritz, M. D. Hager, U. S. Schubert

Abstract:

This study presents the first liquid chromatography method for the quantitative and qualitative analysis of highly reactive oxoammonium cations based on a simple derivatization reaction. Rapid 1,2-electrophilic addition reactions with olefins were used to transform these reactive species into analyzable derivatives. Three model substances were chosen to represent each of the main application fields of oxoammonium cations and to demonstrate the versatility of the method. The measuring protocol was validated according to the ICH and USP guidelines. The method revealed an excellent linearity ($R^2 = 0.9980\text{--}0.9990$) with a low limit of detection ($0.16\text{--}0.14\text{ mmol L}^{-1}$) and a low limit of quantification ($0.55\text{--}0.43\text{ mmol L}^{-1}$). The protocol was finally used to determine the oxoammonium cations in the presence of their corresponding radical, showing a robustness against impurity concentration of up to approx. 30%.



Liquid Chromatography Analysis of Reactive Oxoammonium Cations

Philip Rohland^{1,2} · Kristin Schreyer^{1,2} · Rene Burges^{1,2} · Nicole Fritz^{1,3} · Martin D. Hager^{1,2} · Ulrich S. Schubert^{1,2} 

Received: 11 March 2021 / Revised: 6 May 2021 / Accepted: 18 August 2021 / Published online: 7 September 2021
© The Author(s) 2021

Abstract

This study presents the first liquid chromatography method for the quantitative and qualitative analysis of highly reactive oxoammonium cations based on a simple derivatization reaction. Rapid 1,2-electrophilic addition reactions with olefins were used to transform these reactive species into analyzable derivatives. Three model substances were chosen to represent each of the main application fields of oxoammonium cations and to demonstrate the versatility of the method. The measuring protocol was validated according to the ICH and USP guidelines. The method revealed an excellent linearity ($R^2 = 0.9980\text{--}0.9990$) with a low limit of detection ($0.16\text{--}0.14\text{ mmol L}^{-1}$) and a low limit of quantification ($0.55\text{--}0.43\text{ mmol L}^{-1}$). The protocol was finally used to determine the oxoammonium cations in the presence of their corresponding radical, showing a robustness against impurity concentration of up to approx. 30%.

Keywords LC · LC–MS · Highly reactive analytes · Oxoammonium cations · Derivatization protocol

Introduction

Despite the fact that 2,2,6,6-tetramethylpiperidinyloxy (TEMPO)-based oxoammonium cations (OCs) play an important role in many current developments, like green oxidation chemistry or organic energy storage, they are fairly unheeded. Their most outstanding property is their stable and reversible redox behavior (Fig. 1) involving the oxoammonium cation **1** and the corresponding aminoxyl radical **2**. Another redox reaction, between the radical **2** and the hydroxylamine **3**, is possible but the pH-dependency of this step is limiting the application possibilities [1].

The reversible redox reactions of OCs are frequently used in organic synthesis to oxidize primary or secondary alcohols to the corresponding aldehydes/ketones or even carboxylic acids [2, 3]. The oxoammonium cation can act as

the oxidant itself or as oxidation catalyst in connection with cost-efficient inorganic oxidants like sodium hypochlorite or oxygen, offering a sustainable and green way to produce aldehydes, ketones, and carboxylic acids from alcohols [4–6]. Further fields of application are electrochemical energy storage, with the oxoammonium–aminoxyl redox couple as one of the best investigated systems with regard to organic batteries [7–9], and biological and pharmaceutical applications of the oxoammonium cation, *e.g.*, as antihypertensives or pro-oxidants [10–12].

Despite the broad application possibilities of OCs, the analytical methods for this species are rather limited. While many of their corresponding hydroxylamines and radicals can be identified and quantified using standard methods, like ESR, NMR, titration, or MS, even the qualitative analysis of the oxidized state is difficult [8, 13–15]. On the one hand, oxoammonium cations, in general, are prone to decomposition reactions and possess only a limited lifetime [16]. On the other hand, there are also method-specific drawbacks. Small amounts of radical disturb NMR measurements and ESR is neither sensitive nor sufficient accurate to quantify radical impurities to draw conclusions on cation purity [17, 18]. Furthermore, the IR or UV/Vis spectra of the radical and the oxoammonium cation are in many cases too similar for proper analysis [19–22]. A simple evaluation utilizing the increase or decrease of specific bands is thus often not suitable. However, more advanced techniques like near-infrared

✉ Ulrich S. Schubert
ulrich.schubert@uni-jena.de

¹ Laboratory of Organic and Macromolecular Chemistry (IOMC), Friedrich Schiller University Jena, Humboldtstraße 10, 07743 Jena, Germany

² Center for Energy and Environmental Chemistry Jena (CEEC Jena), Friedrich Schiller University Jena, Philosophenweg 7a, 07743 Jena, Germany

³ Jena Center for Soft Matter (JCSM), Friedrich Schiller University Jena, Philosophenweg 7, 07743 Jena, Germany

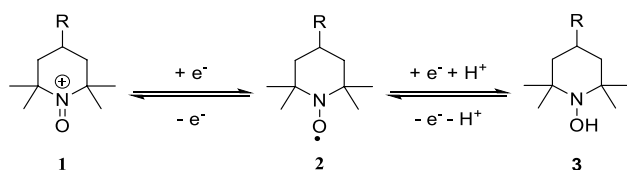


Fig. 1 Schematic representation of the redox chemistry of TEMPO-based molecules

spectroscopy in combination with chemometrics might overcome the problems [23–25]. MS techniques are suitable in terms of accuracy and sensitivity but the discrimination between the two redox species is not sufficient. Furthermore, the radical is oxidized to the corresponding oxoammonium cation under MS conditions [26] and the commonly used steel parts in HPLC and GC systems can reduce the oxoammonium cation to the radical form due to its high oxidation potential [8]. To circumvent the stated drawbacks, a derivatization reaction that transforms the oxoammonium cation into a less reactive and more distinguishable species is highly desirable.

In 1999, Takata and co-workers showed that oxoammonium cations can undergo fast 1,2-electrophilic additions with olefins under excellent yields [27]. But the derivatives were not stable, even at $-20\text{ }^{\circ}\text{C}$. We used the reaction introduced by Takata et al. as the starting point for our derivatization method (Fig. 2). We could improve the reaction conditions by optimization and could apply the new protocol to three different oxoammonium cations. Namely, the Bobbitt salt (*N*-(2,2,6,6-tetramethyl-1-oxopiperidin-1-ium-4-yl)acetamide tetrafluoroborate) (**4**), the TMA-TEMPO (2,2,6,6-tetramethyl-1-oxo-4-(trimethylammonium)piperidin-1-ium dichloride) OC (**5**), and the TEMPOL (4-hydroxy-2,2,6,6-tetramethyl-1-oxopiperidin-1-ium chloride) OC (**6**) were chosen as model substances for oxidation catalysts, organic radical batteries, and pharmaceutical applications, respectively, due to their wide spread in their respective fields (Fig. 2). We report that the standard solutions of the derivatives lose only approx. $0.5\% \text{ d}^{-1}$ over 12 days at $5\text{ }^{\circ}\text{C}$. We then demonstrated a valid derivatization-based liquid-chromatography method for separation, identification, and quantification of the oxoammonium cations, even in presence of the corresponding radical species.

Materials, Methods and Instruments

Chemicals and Reagents

Sodium chloride ($\geq 99.5\%$, Fisher Scientific Ltd., United Kingdom), TEMPOL (ABCR GmbH, Germany), 4-acetylamino-2,2,6,6-tetramethyl-1-piperidinoxy (TCI, Japan),

(*N*-(2,2,6,6-tetramethyl-1-oxopiperidin-1-ium-4-yl)acetamide tetrafluoroborate (TCI, Japan), tetramethyl urea (TMU) (TCI Chemicals, Japan), mesitylene (VWR International GmbH, Germany), acetonitrile (HiPerSolv CHROMANORM®, VWR International GmbH, Germany), water (HiPerSolv CHROMANORM®, VWR International GmbH, Germany), formic acid (HPLC LiChropur, Sigma Aldrich, USA), *N*-vinylcarbazole (Sigma Aldrich, USA) and ESI-L Low Concentration Tuning Mix (Agilent Technologies, USA) were purchased and used without further purification. TMA-TEMPO and methyl viologen were synthesized according to literature procedure [8].

Instrumentation

An UltiMate 3000 HPLC system equipped with a DAD (Thermo Scientific, USA) was used for separation, identification and quantification of the three derivatization products as well as the internal standard. For data processing the Chromeleon 7.2 software was used.

For assignment of the DAD signals, LC-MS measurements were performed utilizing a Series 1200 HPLC (Agilent Technologies, USA) equipped with a microTOF QII mass spectrometer (Bruker, Germany) and a DAD. Ions were generated using the electrospray ionization source (ESI) and a measurement range between m/z 280 and 3000 was used. The MS-data were evaluated with the Bruker Data Analysis software version 4.2 and the HPLC data were analyzed with the HyStar 3.2 software.

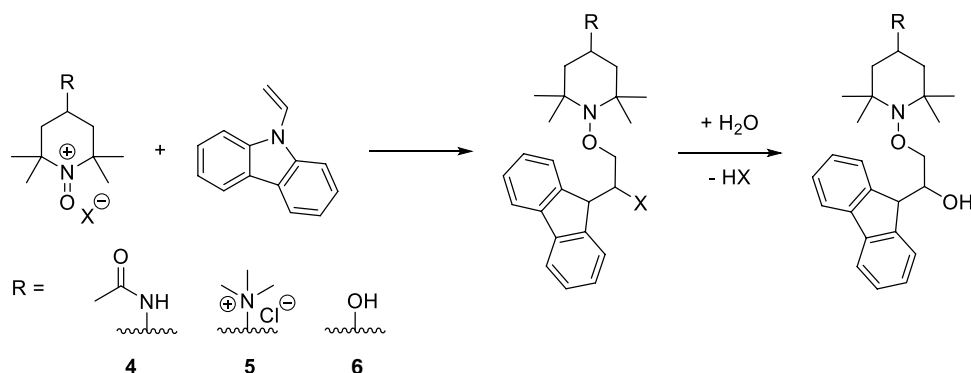
Weighing was done on an XS205 Dual Range balance (Mettler Toledo, USA).

Chromatographic Conditions

The HPLC separation was done with a C18 column (Kinetex EVO C18, $150\text{ mm} \times 4.6\text{ mm}$, $5\text{ }\mu\text{m}$, Phenomenex, Germany) using a gradient program with two mobile phases A and B. The mobile phase A is acetonitrile with $0.1\text{ vol.}\%$ formic acid and the mobile phase B is pure water with $0.1\text{ vol.}\%$ formic acid. The flow rate was set to 1.5 mL min^{-1} and the gradient was programmed as: Time (min)/B (%): $0.0/85.0$, $11.0/40.0$, $12.0/40.0$, $14.0/5.0$, $16.0/5.0$, $17.0/85.0$ and $22.0/85.0$. The column temperature was maintained at $40\text{ }^{\circ}\text{C}$ and the auto-sampler temperature was set to $5\text{ }^{\circ}\text{C}$. The injected volume of the sample solutions was $10\text{ }\mu\text{L}$. The absorbance was monitored using a DAD-detector.

The same conditions, mobile phase, injected volume and column was used for LC analytics with subsequent MS. The gradient program was extended to 27 min and programmed as: time (min)/B (%): $0.0/85.0$, $11.0/40.0$, $12.0/40.0$, $14.0/5.0$, $16.0/5.0$, $17.0/85.0$ and $27.0/85.0$ and

Fig. 2 Schematic representation of the derivatization reaction of the Bobbitt salt (4), TMA-TEMPO OC (5) and TEMPOL OC (6) to the corresponding analyzable derivatives



the auto-sampler temperature was room temperature. The split to the MS was measured as 1/3.

Derivatization Method and Sample Preparation

Stock Solution

Stock solutions of 0.1 M oxoammonium cations with 0.1 M sodium chloride in water were prepared. While the Bobbitt salt was used directly, for TEMPOL OC and TMA-TEMPO OC, the radicals were used and, subsequently, electrochemically oxidized in a redox flow battery (details in the supporting information). The stock solutions were stored at 4 °C until usage.

Sample Preparation for Stability Test

Samples of 1 mL for the stability tests were prepared from the oxoammonium stock solutions and a 0.1 M *N*-vinylcarbazole TMU solution, as well as 100 μL of a 83 mmol L⁻¹ (10 mg mL⁻¹) mesitylene solution in TMU as internal standard. The amounts of the components were chosen to fit the respective targeted OC concentration (*cf.* “Results and Discussion”), with a ratio of the derivatization reagent *N*-vinylcarbazole to the analyte of 2:1. The resulting mixture was diluted with TMU to 1 mL and injected into the chromatographic system.

Standard Sample Preparation

The samples were prepared as described for the stability tests, but they were homogenized for 3 min with a vortexer (Vortex Genie 2, Scientific Industries, USA) prior to injection into the chromatographic system.

Sample Preparation for LC–MS Measurements

The samples were prepared as described for the standard sample preparation. But before injection into the chromatographic system, the probes were diluted with TMU to 0.1 mg mL⁻¹ for the Bobbitt salt and TEMPOL OC and to 0.01 mg mL⁻¹ for the TMA-TEMPO OC sample.

Results and Discussion

Aminoxyl radicals can be oxidized to their corresponding oxoammonium cations either by utilizing oxidizing mineral acids, like perchloric acid [28] and sulfuric acid [29], or other strong oxidants like hypochlorites [30, 31]. But these procedures require additional purification steps to remove potentially disturbing side products. Furthermore, some of these techniques do not tolerate specific organic functional moieties, *e.g.*, the hydroxyl group of TEMPOL can react with sulfuric acid to form an ester [9]. Thus, we decided to use the mild electrochemical oxidation as analyte solution preparation procedure since the received oxoammonium cation solution can be directly used without further purification.

Stability of the Analyte

Takata et al. stated that the addition products of oxoammonium cations and olefins are rather unstable [27]. We thus wanted to investigate if the derivatization protocol of Takata et al. can be used for the named oxoammonium cations. For proper solubility, the utilized chloroform must be exchanged with a 1:3 (v:v) mixture of water and acetonitrile. The stability of the TMA-TEMPO derivative was subsequently investigated using ¹H NMR spectroscopy. Herein, freshly prepared analyte samples were placed inside the NMR spectrometer with a pre-tempered probe head (5, 10, 15, 25, 40 °C) for 480 min and every 5 min a spectrum was recorded (*cf.* SI for detailed analysis procedure and all data). The results revealed that the decomposition rates of

17.1% d⁻¹ at 5 °C and 99.9% d⁻¹ at 40 °C are much too high for HPLC analysis.

Consequently, we exchanged the used solvent mixture with tetramethyl urea (TMU). On the one hand, it is capable of dissolving even double-charged oxoammonium cations as well as the nonpolar internal standard mesitylene. On the other hand, TMU is not nucleophilic and can act as base and binds (possibly) formed acids, which would lead to analyte decomposition via carbazole cleavage. To investigate the impact of the solvent on the stability of the addition products, we prepared three different samples for each of three different concentrations (35, 28, 21 mmol L⁻¹) for each cation. The samples were kept in the auto-sampler at 5 °C for 12 days, and one measurement per day was carried out for each sample.

We wanted to eliminate variations due to sample preparation using the internal standard calibration method. While the ratios of the analyte and internal standard signals differ by up to 40% among the three samples for each concentration, they stay nearly constant over the time of the experiment showing a small trend of decrease. The high differences among the samples with the same concentration might be linked to difficulties during the preparation of the standard solution and possible problems during homogenization of the mixture. The challenge of changing concentrations because of diffusion and osmosis in the RFB is discussed below. The slow decrease of the analyte

signal over time can be correlated to the decomposition of the analyte. However, with approx. 0.5–1.0% d⁻¹ for the three different concentrations for the different oxoammonium cations, the decay is reduced to approx. one twentieth in comparison to initial derivatization procedure.

Analyte and Side Product Identification

The assignment of the DAD signals (Fig. 3) was done by mass spectrometry (see supporting information Figure S8–S10).

Method Transfer

For method transfer, the retention time of the analyte and the internal standard were determined on the LC–MS as well as on the LC system. The differences of around 0.6 min between the LC–MS and the LC are due to the increased path length in the chromatographic system of the LC–MS.

Method Validation

The developed method was validated according to ICH and USP Guide lines [32, 33]. This includes a system suitability test and the determination of validation parameters like specificity, linearity, accuracy, and precision.

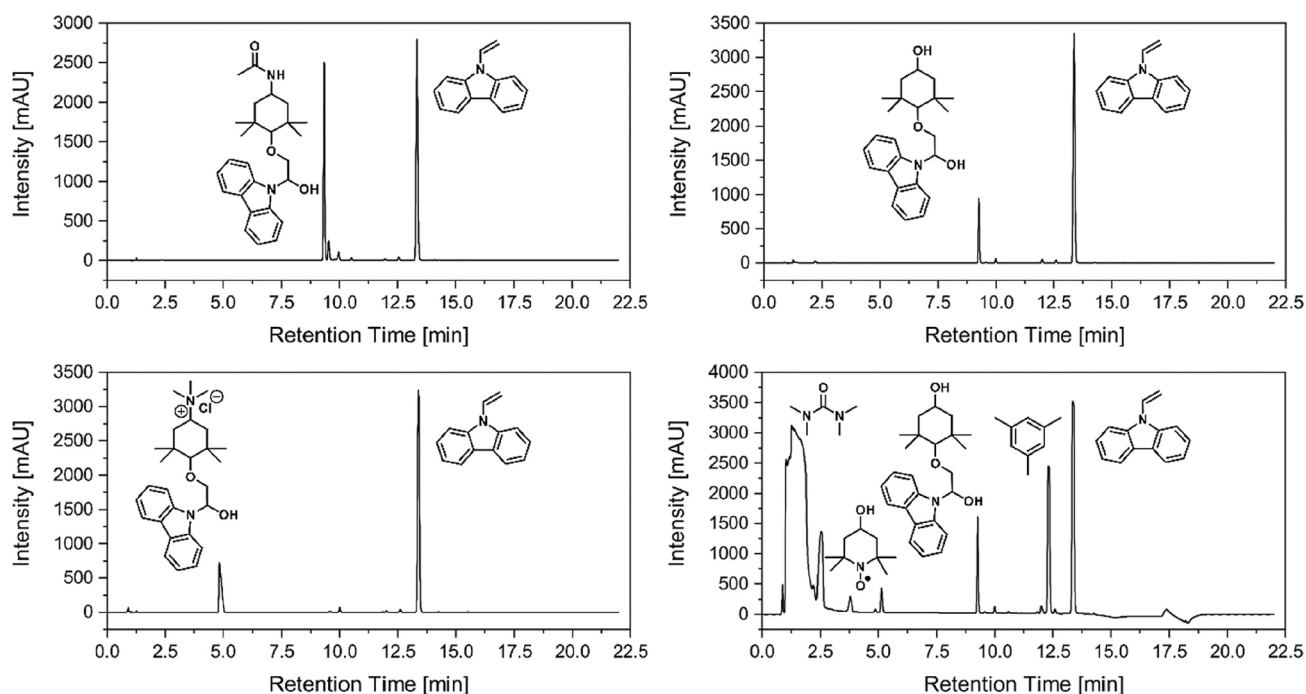


Fig. 3 Typical UV-chromatogram at 291 nm of the *N*-vinylcarbazole adducts of the Bobbitt salt (upper left), TEMPOL OC (upper right), TMA-TEMPO OC (lower left) and the UV-chromatogram at 209 nm of the adduct of the TEMPOL-OC (lower right)

System Suitability Test

After optimizing the sample preparation process (longer homogenization process), system suitability parameters were determined and compared to USP guidelines [34]. The parameters include resolution, plate count, capacity factor, tailing factor, and relative standard deviation (RSD) of the peak areas. To determine the parameters, the data from six replicate injections of solutions with a concentration of 30 mmol L⁻¹ were used. The parameters are summarized in Table 1. In general, the parameters fulfill the requirements of the guidelines. An exception is the resolution of the Bobbitt salt, which is a little bit too low with 1.87 (required to be higher than 2) but the peak overlap is so narrow that it is considered as not crucial. Furthermore, the tailing factor of the TMA-TEMPO OC is too high (should be ≤ 2), but it was considered acceptable because of the high resolution. Overall, the system suitability test was considered as successful.

Specificity

To determine the specificity of the method, the resolutions of the OC signals in a mixture with typical synthesis side products and decomposition products need to be investigated. For this purpose, the studied compounds were either commercially available synthesis-grade or self-synthesized chemicals. In both cases, the main side products and impurities are inherently included in the samples, rendering them suitable for specificity tests. The thus performed studies showed no

interferences of the OC signals and resolutions higher than 1.5 for all chromatograms (see Supporting Information).

Linearity and Range

The linearity was determined using calibration samples with analyte concentrations of 14, 21, 24, 28, and 35 mmol L⁻¹. For every concentration, six replicates were prepared and injected once per replicate. The received ratios of the peak areas of the analyte and the peak areas of the internal standard were plotted against the respective concentrations. The calibration curves were determined by the least-squares linear regression analysis and showed linear behavior in the whole studied range from 14 to 35 mmol L⁻¹ with a determination coefficient (R^2) of 0.9980 to 0.9990. The limits of detection (LOD) and the limits of quantification (LOQ) were calculated using the following formula [33]:

$$\text{LOD} = \frac{3.3\sigma}{S} \quad (1)$$

$$\text{LOQ} = \frac{10\sigma}{S} \quad (2)$$

σ = standard deviation of y-intercept of regression lines,
 S = slope of the calibration curve.

The results of the linearity studies are summarized in Table 2.

Table 1 Results of the system suitability test ($n=6$)

Parameter	Bobbitt salt	TMA-TEMPO OC	TEMPOL OC	Internal standard	Required according to USP
Resolution (R_s)	1.87	24.52	2.64	6.25	> 2
Plate count (N)	130,903	5773	127,494	64,575	> 2000
Capacity factor (k')	9.82	4.61	9.72	13.23	> 2
Tailing factor (T)	1.08	3.58	1.04	1.09	≤ 2
% RSD (peak area)	0.27	0.16	0.20	0.18	≤ 1

Table 2 Data of the linearity study

	Bobbitt salt	TMA-TEMPO OC	TEMPOL OC
Range (mmol L ⁻¹)	14–35	14–35	14–35
Determination coefficient (R^2)	0.9990	0.9985	0.9980
Slope of the calibration curve (S) mmol ⁻¹ L	175.5695	142.7708	68.4183
Intercept	-0.0068	-0.0973	-0.0299
Standard deviation of the slope (σ)	4.6347	3.1944	1.7834
Standard deviation of y-intercept (σ)	0.0075	0.0068	0.0037
LOD (mmol L ⁻¹)	0.13	0.14	0.16
LOQ (mmol L ⁻¹)	0.43	0.47	0.55

Accuracy and Precision

The accuracy and precision were evaluated using intraday and interday recovery experiments with three different samples with concentrations within the linearity range (18, 23 and 30 mmol L⁻¹). For each concentration, six replicates were prepared and injected, and the recovery and RSD were determined, representing the accuracy and precision, respectively. The procedure was repeated on two different days for interday testing (*cf.* SI for detailed analysis procedure and all data). The data are summarized in Table 3.

The precision tests of the method showed intraday RSD values of 6–7% for the Bobbitt salt and 6–8% for the TMA-TEMPO oxoammonium cation. Although the variations are rather high, they are acceptable for the analysis of highly reactive species with a completely newly developed method. We would link the high uncertainties to variations during the derivatization process and, although reduced, the still existing instability of the analytes. In comparison, the interday precision values of the Bobbitt salt (1–3%) and of the TMA-TEMPO oxoammonium cation (2–3%) are comparable to currently applied techniques for HPLC determination. The data for the TEMPOL oxoammonium cation revealed, in contrast, much higher variations of 16%, suggesting that the derivatization and analysis protocol is not suitable for this specific compound. A finding that is also confirmed by the recovery rates of 192–207% (intraday) and 165–175% (interday), with no clear correlation between concentration and deviation. This can be assigned to a possible oxidation of the hydroxy group in 4-position to the corresponding ketone, which can lead to the observed deviations [35].

The TMA-TEMPO oxoammonium cation also revealed high deviations of the recovery rates. In this case, an indirect linear dependency on the concentrations was found. Nevertheless, the received recovery values (121–142% intraday and 122–143% interday) are much too high. This might be caused by a demanding calibration because of the lack of commercially available reference substances. The consequent need of the preparation of the OC via electrochemical

oxidation of the TMA-TEMPO radical utilizing a redox flow cell suffers from technical problems like variable concentrations due to osmotic pressure differences [36–40]. To further optimize the method for the TMA-TEMPO system, these problems have to be overcome during future studies. However, the validation parameters suggest the possibility for quantitative analysis of TMA-TEMPO oxoammonium cation with this protocol.

In contrast, the results of the recovery study for the Bobbitt salt with 101–105% intraday- and 101–106% interday confirm the accuracy of the method for this analyte.

Sample Analysis

To further explore the applicability of the method, samples containing one type of OC and its corresponding radical were prepared and analyzed. For this purpose, 0.1 M solutions of the oxoammonium cation and 0.1 M solutions of the corresponding radical were used to produce samples with total concentrations of 35 mmol L⁻¹ and OC ratios of 80, 65, and 50%, respectively. The samples were prepared like described above. For each mixture, six samples were prepared and injected once in the HPLC-System. The recovery

Table 4 Data of the recovery studies for samples of the three different oxoammonium cations mixed with their corresponding radicals

	Concentration OC/radical [mmol L ⁻¹]	Recovery rate [%]	RSD [%]
Bobbitt salt	28/7	101.99	2.95
	22.75/12.25	109.50	2.54
	17.5/17.5	115.89	6.18
TMA-TEMPO OC	28/7	113.24	11.25
	22.75/12.25	140.82	4.83
	17.5/17.5	152.72	5.82
TEMPOL OC	28/7	202.93	2.97
	22.75/12.25	209.90	3.82
	17.5/17.5	225.15	1.79

Table 3 Data of the intraday (day one) and interday recovery experiments for accuracy and precision determination

	Concentration (mmol L ⁻¹)	Intraday		Interday	
		Recovery [%]	RSD [%]	Recovery [%]	RSD [%]
Bobbitt salt	30	101	6	101	3
	23	104	6	105	1
	18	105	7	106	2
TMA-TEMPO OC	30	121	8	122	2
	23	135	6	131	3
	18	142	8	143	3
TEMPOL OC	30	192	11	165	14
	23	206	4	175	16
	18	207	7	175	16

rates were determined using the calibration curve and are shown in Table 4.

The data revealed the same trend of deviations as described for the inter- and intraday recovery experiments but with slightly higher recovery rates for all three systems.

This suggests that an increasing amount of radicals interferes with the accuracy of the method, but the effect only becomes significant for radical concentrations higher than 30%. The problem of generally higher recovery rates of analyte in the presence of high radical amounts can be assigned to the possible reaction of the radical with allylic and benzylic substrates to alkoxyamines with similar structures to the analyte, in an NMP like manner [41, 42].

We concluded that the method can be in principle used for the quantitative analysis of oxoammonium cations even in the presence of a high amount of their corresponding radical, but the suitability for a certain substance has to be checked. The unsuitability of the method for the TEMPOL oxoammonium cation due to the possible oxidation of the 4-hydroxy group is confirmed [35].

Conclusion

We developed the first derivatization-based method for the HPLC determination of highly reactive oxoammonium cations. For this purpose, a 1,2-electropilic addition of oxoammonium cations to activated double bonds was used, as described by Takata et al. [27] Based on the latter, a determination protocol was developed and applied to three different cations, which act as model substances for oxidation catalysts, battery materials and pharmaceuticals. While the derivatized analytes are stable under auto-sampler conditions, with a very low decay rate of 0.5–1.0% d⁻¹, the method suffers from the lack of commercially available reference standards. Consequently, standards have to be self-synthesized utilizing electrochemical oxidation in redox flow cells. The consequent deviations in concentration due to osmotic processes makes the calibration error-prone. Nevertheless, the derivatization protocol and the HPLC determination method were validated according to the ICH and USP guidelines. Furthermore, we showed that the protocol can be used even for samples with high radical concentrations of up to 30%, rendering the method suitable for the qualitative and quantitative determination of a broad range of oxoammonium cations.

Supplementary Information The online version contains supplementary material available at <https://doi.org/10.1007/s10337-021-04084-1>.

Acknowledgements We want to thank Friederike Pielenz and Bärbel Rambach for the NMR measurements. Furthermore, we want to thank Dr. Christian Friebe for the helpful discussions and comments.

Author contributions PR and RB designed the study. KS, RB, NF and PR performed the experiments. The first draft of the manuscript was written by PR. MDH and USS supervised and acquired the financial support for the project. All authors discussed the results and contributed to the final manuscript.

Funding Open Access funding enabled and organized by Projekt DEAL. We acknowledge the Thüringer Aufbaubank (TAB), the European Social Fund (ESF), the Thuringian Ministry of Economic Affairs, Science and Digital Society (TMWWdG) for financial support. The study was co-financed by the state of Thuringia (2015 FGI 0021) with means of the EU in the framework of the EFRE program.

Availability of data and materials During the experiments are no other data produced which are not included in the text or supplementary information.

Code availability Not applicable.

Declarations

Conflict of interest The authors declare no conflict of interest.

Open Access This article is licensed under a Creative Commons Attribution 4.0 International License, which permits use, sharing, adaptation, distribution and reproduction in any medium or format, as long as you give appropriate credit to the original author(s) and the source, provide a link to the Creative Commons licence, and indicate if changes were made. The images or other third party material in this article are included in the article's Creative Commons licence, unless indicated otherwise in a credit line to the material. If material is not included in the article's Creative Commons licence and your intended use is not permitted by statutory regulation or exceeds the permitted use, you will need to obtain permission directly from the copyright holder. To view a copy of this licence, visit <http://creativecommons.org/licenses/by/4.0/>.

References

1. Finklea HO, Madhiri N (2008) Reorganization energies of TEMPO/TEMPO in water. *J Electroanal Chem* 621:129–133. <https://doi.org/10.1016/j.jelechem.2007.07.026>
2. Bobbitt JM, Brückner C, Merbouh N (2010) Oxoammonium- and nitroxide-catalyzed oxidations of alcohols. *Org React* 74:2777–2830. <https://doi.org/10.1002/0471264180.or074.02>
3. Beejapur HA, Zhang Q, Hu KC, Zhu L, Wang JL, Ye ZB (2019) TEMPO in chemical transformations: from homogeneous to heterogeneous. *ACS Catal* 9:2777–2830. <https://doi.org/10.1021/acscatal.8b05001>
4. Silva ABV, Silva ED, dos Santos AA, Princival JL (2020) A sustainable access to ynones through laccase/TEMPO-catalyzed metal- and halogen-free aerobic oxidation of propargylic alcohols in aqueous medium. *Catal Commun* 137:105946–105952. <https://doi.org/10.1016/j.catcom.2020.105946>
5. Denlinger KL, Carr P, Waddell DC, Mack J (2020) A recyclable, metal-free mechanochemical approach for the oxidation of alcohols to carboxylic acids. *Molecules* 25:364–374. <https://doi.org/10.3390/molecules25020364>
6. Pierre G, Punta C, Delattre C, Melone L, Dubessay P, Fiorati A, Pastori N, Galante YM, Michaud P (2017) TEMPO-mediated oxidation of polysaccharides: an ongoing story. *Carbohydr Polym* 165:71–85. <https://doi.org/10.1016/j.carbpol.2017.02.028>

7. Kwabi DG, Ji Y, Aziz MJ (2020) Electrolyte lifetime in aqueous organic redox flow batteries: a critical review. *Chem Rev* 120:6467–6489. <https://doi.org/10.1021/acs.chemrev.9b00599>
8. Janoschka T, Martin N, Hager MD, Schubert US (2016) An aqueous redox-flow battery with high capacity and power: the TEMPTMA/MV system. *Angew Chem Int Ed* 55:14427–14430. <https://doi.org/10.1002/anie.201606472>
9. Winsberg J, Stolze C, Schwenke A, Muench S, Hager MD, Schubert US (2017) Aqueous 2,2,6,6-tetramethylpiperidine-n-oxyl catholytes for a high-capacity and high current density oxygen-insensitive hybrid-flow battery. *ACS Energy Lett* 2:411–416. <https://doi.org/10.1021/acsenergylett.6b00655>
10. Wilcox CS, Pearlman A (2008) Chemistry and antihypertensive effects of tempol and other nitroxides. *Pharmacol Rev* 60:418–469. <https://doi.org/10.1124/pr.108.000240>
11. Zarling JA, Brunt VE, Vallerger AK, Li W, Tao A, Zarling DA, Minson CT (2015) Nitroxide pharmaceutical development for age-related degeneration and disease. *Front Genet* 6:325–334. <https://doi.org/10.3389/fgene.2015.00325>
12. Hall ED, Vaishnav RA, Mustafa AG (2010) Antioxidant therapies for traumatic brain injury. *Neurotherapeutics* 7:51–61. <https://doi.org/10.1016/j.nurt.2009.10.021>
13. Hagemann T, Strumpf M, Schröter E, Stolze C, Grube M, Nischang I, Hager MD, Schubert US (2019) (2,2,6,6-tetramethylpiperidin-1-yl)oxyl-containing zwitterionic polymer as catholyte species for high-capacity aqueous polymer redox flow batteries. *Chem Mater* 31:7987–7999. <https://doi.org/10.1021/acs.chemmater.9b02201>
14. Duan TT, Zhai TR, Liu HH, Yan ZL, Zhao Y, Feng L, Ma C (2016) One-pot three-component synthesis of quinazolines via a copper-catalysed oxidative amination reaction. *Org Biomol Chem* 14:6561–6567. <https://doi.org/10.1039/c6ob00625f>
15. Gong M, Kim JK, Zhao XL, Li YB, Zhang JY, Huang MM, Wu YJ (2019) Visible-light-induced alpha-oxyamination of 1,3-dicarbonyls with TEMPO via a photo(electro)catalytic process applying a DSSC anode or in a DSSC system. *Green Chem* 21:3615–3620. <https://doi.org/10.1039/c9gc01154d>
16. Ma Y, Loyns C, Price P, Chechik V (2011) Thermal decay of TEMPO in acidic media via an N-oxoammonium salt intermediate. *Org Biomol Chem* 9:5573–5578. <https://doi.org/10.1039/c1ob05475a>
17. Bobbitt JM, Eddy NA, Cady CX, Jin J, Gascon JA, Gelpi-Dominguez S, Zakrzewski J, Morton MD (2017) Preparation of some homologous TEMPO nitroxides and oxoammonium salts; notes on the NMR spectroscopy of nitroxide free radicals; observed radical nature of oxoammonium salt solutions containing trace amounts of corresponding nitroxides in an equilibrium relationship. *J Org Chem* 82:9279–9290. <https://doi.org/10.1021/acs.joc.7b00846>
18. Mazur M (2006) A dozen useful tips on how to minimise the influence of sources of error in quantitative electron paramagnetic resonance (EPR) spectroscopy—a review. *Anal Chim Acta* 561:1–15. <https://doi.org/10.1016/j.aca.2006.01.006>
19. Jiao Y, Tang B, Zhang Y, Xu JF, Wang Z, Zhang X (2018) Highly efficient supramolecular catalysis by endowing the reaction intermediate with adaptive reactivity. *Angew Chem Int Ed* 57:6077–6081. <https://doi.org/10.1002/anie.201713351>
20. Haidasz EA, Meng D, Amorati R, Baschieri A, Ingold KU, Valgimigli L, Pratt DA (2016) Acid is key to the radical-trapping antioxidant activity of nitroxides. *J Am Chem Soc* 138:5290–5298. <https://doi.org/10.1021/jacs.6b00677>
21. Grampp G, Rasmussen K (2002) Solvent dynamical effects on the electron self-exchange rate of the TEMPO/TEMPO+ couple (TEMPO = 2,2,6,6-tetramethyl-1-piperidinyloxy radical): Part I. ESR-linebroadening measurements at T = 298 K. *Phys Chem Chem Phys* 4:5546–5549. <https://doi.org/10.1039/b206313a>
22. Karimi B, Vahdati S, Vali H (2016) Synergistic catalysis within TEMPO-functionalized periodic mesoporous organosilica with bridge imidazolium groups in the aerobic oxidation of alcohols. *RSC Adv* 6:63717–63723. <https://doi.org/10.1039/c6ra15483b>
23. Vignaduzzo SE, Maggio RM, Olivieri AC (2020) Why should the pharmaceutical industry claim for the implementation of second-order chemometric models—A critical review. *J Pharm Biomed Anal* 179:112965. <https://doi.org/10.1016/j.jpba.2019.112965>
24. Singh I, Juneja P, Kaur B, Kumar P (2013) Pharmaceutical applications of chemometric techniques. *ISRN Anal Chem* 2013:1–13. <https://doi.org/10.1155/2013/795178>
25. Manley M (2014) Near-infrared spectroscopy and hyperspectral imaging: non-destructive analysis of biological materials. *Chem Soc Rev* 43:8200–8214. <https://doi.org/10.1039/c4cs00062e>
26. Smith CD, Bartley JP, Bottle SE, Micallef AS, Reid DA (2000) Electrospray ionization mass spectrometry of stable nitroxide free radicals and two isoindoline nitroxide dimers. *J Mass Spectrom* 35:607–611. [https://doi.org/10.1002/\(sici\)1096-9888\(200005\)35:5%3c607::Aid-jms967%3e3.0.Co;2-7](https://doi.org/10.1002/(sici)1096-9888(200005)35:5%3c607::Aid-jms967%3e3.0.Co;2-7)
27. Takata T, Tsujino Y, Nakanishi S, Nakamura K, Yoshida E, Endo T (1999) Electrophilic 1,2-addition of oxoammonium salts to olefins. *Chem Lett* 28:937–938. <https://doi.org/10.1246/cl.1999.937>
28. Bobbitt JM (1998) Oxoammonium salts. 6.14-acetylamino-2,2,6,6-tetramethylpiperidine-1-oxoammonium perchlorate: a stable and convenient reagent for the oxidation of alcohols. Silica gel catalysis. *J Org Chem* 63:9367–9374. <https://doi.org/10.1021/jo981322c>
29. Golubev VA, Zhdanov RI, Gida VM, Rozantsev EG (1971) Reaction of iminoxyl radicals with some mineral acids. *Bull Acad Sci USSR, Div Chem Sci* 20:768–770. <https://doi.org/10.1007/bf00853921>
30. Kelly CB, Mercadante MA, Hamlin TA, Fletcher MH, Leadbeater NE (2012) Oxidation of alpha-trifluoromethyl alcohols using a recyclable oxoammonium salt. *J Org Chem* 77:8131–8141. <https://doi.org/10.1021/jo301477s>
31. Bobbitt J, Tilley LJ, Murray S, Camire C, Eddy N (2012) A revised preparation of (4-acetamido-2,2,6,6-tetramethylpiperidin-1-yl)oxyl and 4-acetamido-2,2,6,6-tetramethyl-1-oxopiperidinium tetrafluoroborate: reagents for stoichiometric oxidations of alcohols. *Synthesis* 45:326–329. <https://doi.org/10.1055/s-0032-1317861>
32. Borman P, Elder D (2017) Q2(R1) validation of analytical procedures. In: Teasdale A, Elder D, Nims RW (eds) ICH quality guidelines: an implementation guide. Wiley, Hoboken, USA, pp 127–166. <https://doi.org/10.1002/9781118971147.ch5>
33. United States Pharmacopeia (2014) United States pharmacopeial convention. United States Pharmacopeia, Rockville
34. Evaluation CfD, Research a (1994) Reviewer guidance, validation of chromatographic methods
35. Marshall DL, Christian ML, Gryn'ova G, Coote ML, Barker PJ, Blanksby SJ (2011) Oxidation of 4-substituted TEMPO derivatives reveals modifications at the 1- and 4-positions. *Org Biomol Chem* 9:4936–4947. <https://doi.org/10.1039/c1ob05037k>
36. Hagemann T, Winsberg J, Grube M, Nischang I, Janoschka T, Martin N, Hager MD, Schubert US (2018) An aqueous all-organic redox-flow battery employing a (2,2,6,6-tetramethylpiperidin-1-yl)oxyl-containing polymer as catholyte and dimethyl viologen dichloride as anolyte. *J Power Sources* 378:546–554. <https://doi.org/10.1016/j.jpowsour.2017.09.007>
37. Yan L, Li D, Li S, Xu Z, Dong J, Jing W, Xing W (2016) Balancing osmotic pressure of electrolytes for nanoporous membrane vanadium redox flow battery with a draw solute. *ACS Appl Mater Interfaces* 8:35289–35297. <https://doi.org/10.1021/acsami.6b12068>
38. Prifti H, Parasuraman A, Winardi S, Lim TM, Skyllas-Kazacos M (2012) Membranes for redox flow battery applications.

- Membranes 2:275–306. <https://doi.org/10.3390/membranes2020275>
39. Li XF, Zhang HM, Mai ZS, Zhang HZ, Vankelecom I (2011) Ion exchange membranes for vanadium redox flow battery (VRB) applications. *Energ Environ Sci* 4:1147–1160. <https://doi.org/10.1039/c0ee00770f>
40. Feng T, Wang HN, Liu YY, Zhang J, Xiang Y, Lu SF (2019) A redox flow battery with high capacity retention using 12-phosphotungstic acid/iodine mixed solution as electrolytes. *J Power Sources*. <https://doi.org/10.1016/j.jpowsour.2019.226831>
41. Babiarz JE, Cunkle GT, DeBellis AD, Eveland D, Pastor SD, Shum SP (2002) The thermal reaction of sterically hindered nitroxyl radicals with allylic and benzylic substrates: experimental and computational evidence for divergent mechanisms. *J Org Chem* 67:6831–6834. <https://doi.org/10.1021/jo020426r>
42. Vogler T, Studer A (2008) Applications of TEMPO in synthesis. *Synthesis* 2008:1979–1993. <https://doi.org/10.1055/s-2008-1078445>

Publisher's Note Springer Nature remains neutral with regard to jurisdictional claims in published maps and institutional affiliations.

Supporting Information

Liquid chromatography analysis of reactive oxoammonium cations

Philip Rohland^{a,b}, Kristin. Schreyer^{a,b}, Rene. Burges^{a,b}, Nicole. Fritz^{a,c}, Martin D. Hager^{a,b},
Ulrich S. Schubert^{*,a,b}

^a Laboratory of Organic and Macromolecular Chemistry (IOMC), Friedrich Schiller University
Jena, Humboldtstraße 10, 07743 Jena, Germany

* E-mail: ulrich.schubert@uni-jena.de

^b Center for Energy and Environmental Chemistry Jena (CEEC Jena), Friedrich Schiller
University Jena, Philosophenweg 7a, 07743 Jena, Germany

^c Jena Center for Soft Matter (JCSM), Friedrich Schiller University Jena, Philosophenweg 7,
07743 Jena, Germany

Thursday, 9. March 2023

Materials

A FAA-3-50 (Fumasep GmbH, Germany) ion-exchange membrane was used for cell assembly. Prior to use, the membrane was cut in appropriate pieces and prewetted for at least 24 h in a 1.5 M aq. sodium chloride solution. GFA6 graphite felts (SGL SE, Germany) were used as porous electrodes. *N*-Vinylcarbazole (Sigma Aldrich, USA), acetonitrile- d_3 (Eurisotope, France), sodium chloride ($\geq 99.5\%$, Fisher Scientific Ltd., United Kingdom) and formic acid (for LC-MS, Honeywell Fluka, USA) were used without further purification. TMA-TEMPO and methyl viologen were synthesized according to literature procedure.[1]

Cell Assembly

The used redox flow cell was a flat type with an active area of 5 cm^2 (designed by JenaBatteries GmbH, Germany). A detailed overview of the used components is displayed in Figure S1.

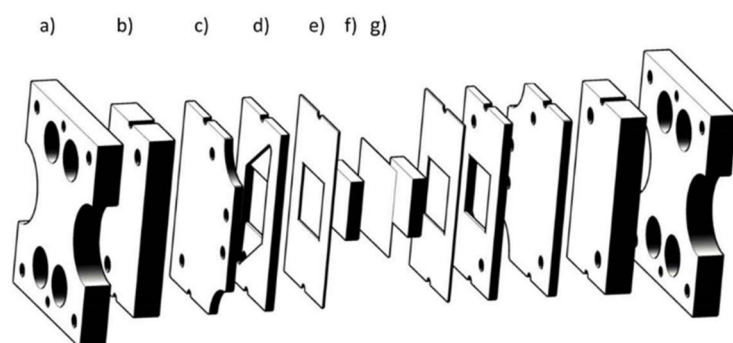


Figure S1: Schematic presentation of the electrochemical cell. One half cell consists of a metal frame (a), PTFE block with hose connections and rubber seal (b), graphite current collector (c), PTFE flow frame (d), rubber sealing (e), graphite felt (f). The half cells are separated by an ion-selective membrane (g).

Equipment and settings

Electrochemical charging was conducted using a VMP3 potentio-/galvanostat (BioLogic, France). A peristaltic pump (Hei-Flow Value 01 Multi with a multi-channel pumping head C8, Heidolph, Germany) and Tygon[®] A-60-G (\varnothing_{inn} 1.6 mm, \varnothing_{out} 4.8 mm, Saint-Gobain, France) peristaltic tubes were used for pumping, applying a flow rate of approx. 20 mL min^{-1} . All experiments were performed under ambient atmosphere. The NMR data were recorded with an Avance III 400 MHz (Bruker, Germany) at the indicated temperature. All stock solutions were prepared utilizing volumetric flasks (Duran, Germany). Weighing was done on an XS205 Dual Range balance (Mettler Toledo, USA).

Preparation of stock solutions (electrochemical oxidation)

10 mL of a 0.1 M radical solution with 0.1 M sodium chloride in water were prepared and charged against 20 mL of a 0.1 M aq. methyl viologen solution containing 0.1 M sodium chloride. A cell current of 80 mA cm⁻¹ was applied until the cell voltage reached 1.45 V, followed by potentiostatic charging until the current dropped below 0.5 mA cm⁻¹. At this point, the radical is considered as fully oxidized to the oxoammonium cation. The oxidized solutions were stored at 4 °C until the derivatization reaction was performed.

NMR Kinetic

Sample preparation: 0.125 mL of the TMA-TEMPO OC stock solution was mixed with 0.375 mL solution of 0.033 M *N*-vinylcarbazole dissolved acetonitrile-d₃. The sample was subsequently filtered through a 0.45 μm nylon filter (Macherey-Nagel GmbH & Co. KG, Germany). The 1:3 ratio of the solvents (water:acetonitrile) was selected due to the solubility of the compounds and to mimic solvent composition during HPLC measurements.

NMR kinetic settings: The probe head was precooled to the desired measuring temperature (5 °C, 10 °C, 15 °C, 25 °C and 40 °C). The time from mixing the solutions to measuring the first ¹H NMR spectrum was measured to approx. 5 min. Afterwards, a ¹H NMR spectrum was measured every 5 min. Additionally, a sample was measured at 5 °C with 0.1% formic acid added to further mimic the HPLC conditions.

NMR kinetic investigation: For kinetic studies, the change of the integral ratio of the *CH*-OH proton (Signal 5 in Figure S2) and the *C*_{aromat}*H* (Signal 1 in Figure S2) was analyzed. The underlying decomposition reaction[2] is shown in Figure S3. Since the data, in particular for 40 °C, suggest an exponential decrease, we fitted the following fit function to the received data:

$$y = A * e^{(-k*t)} \quad (1)$$

(A = starting value of the non-decomposed reaction product, set to 100 %, k = decomposition reaction constant, t = time).

The data are visualized in Figure S4 and the parameters of the fit functions are summarized in Table S1.

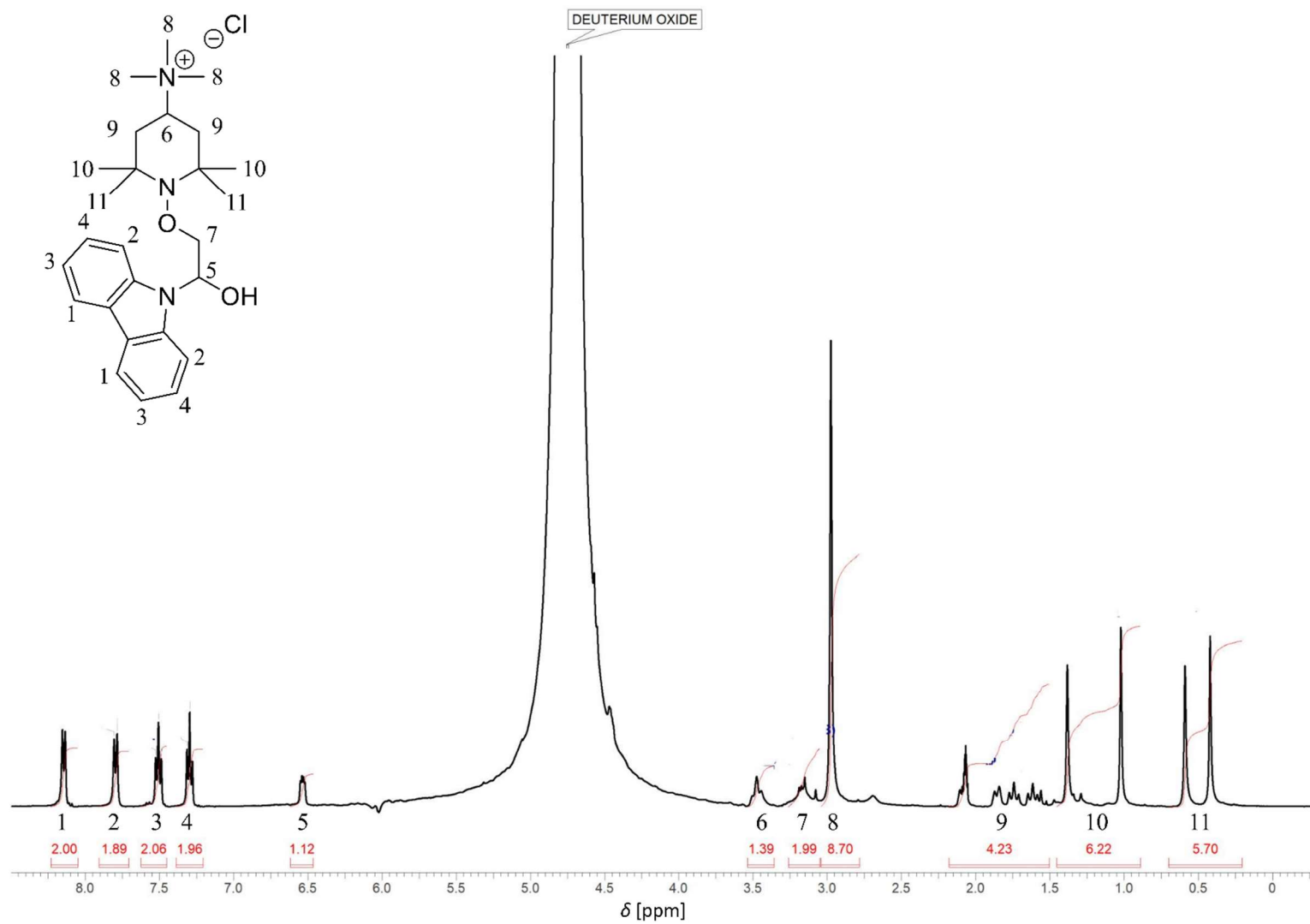


Figure S2: ^1H NMR spectrum of the TMA-TEMPO oxoammonium cation - N-vinylcarbazole reaction mixture at $t = 0$ min (D_2O , 400 MHz).

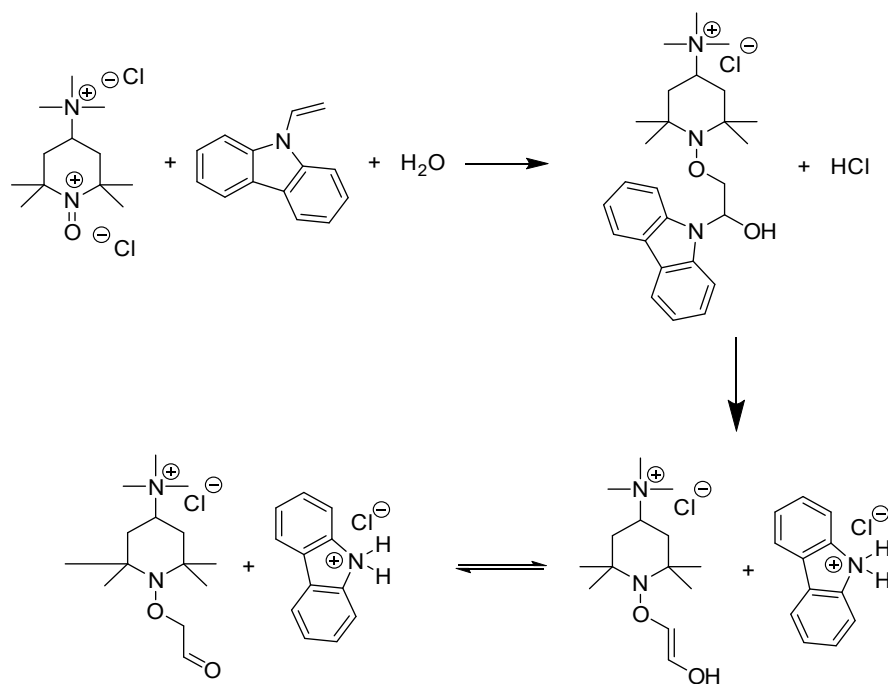


Figure S3: Schematic representation of the formation and decay reaction of the TMA-TEMPO oxoammonium cation *N*-vinylcarbazole addition product.

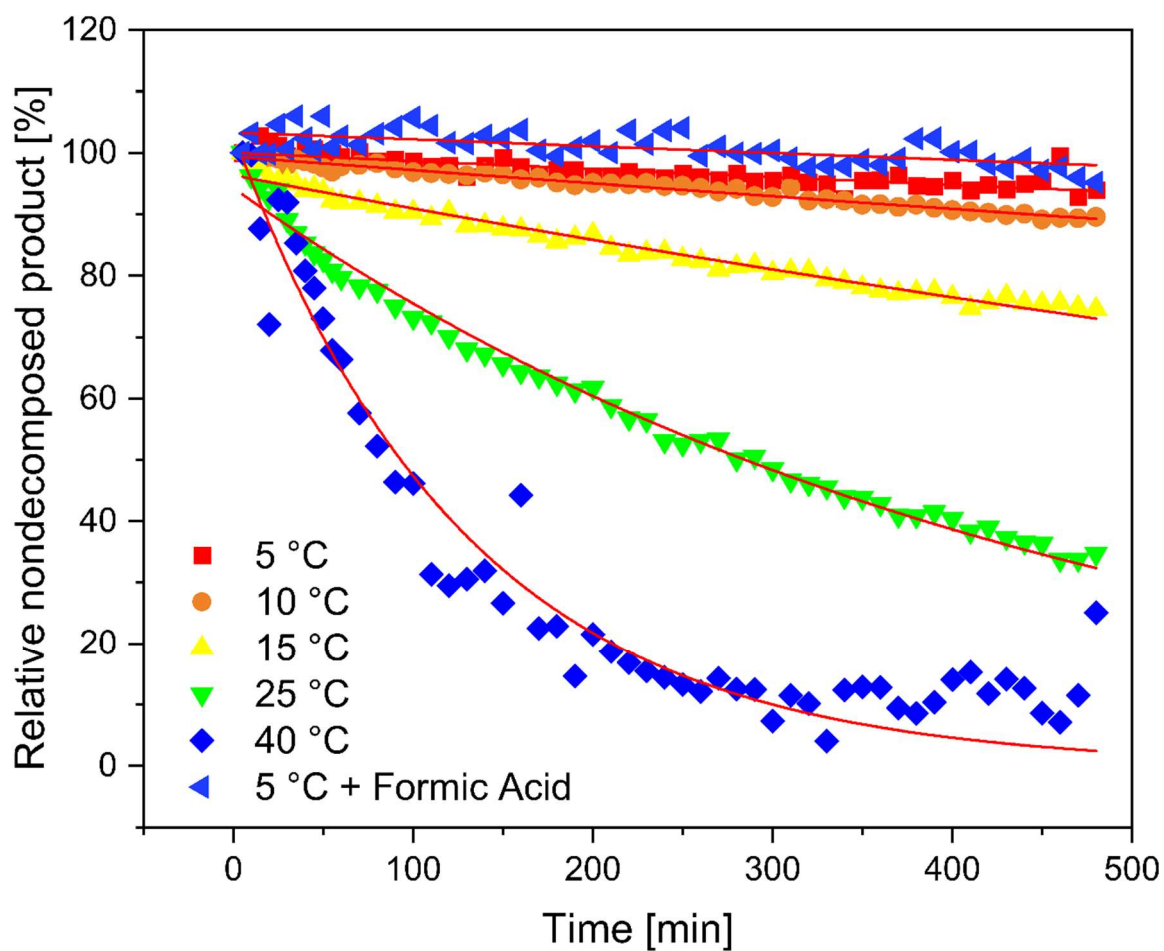


Figure S4: Decay of the TMA-TEMPO oxoammonium cation *N*-vinylcarbazole addition product at different temperatures.

Table S1: Summary of the fitting parameters of the exponential fit function (1).

Temperature [°C]	A [%]	Error of A [%]	k	Error of k	Decay after 24 h [%]
5	100.0	0.3	1.3×10^{-4}	1.2×10^{-5}	17.6
5 + formic acid	103.3	0.5	1.1×10^{-4}	1.7×10^{-5}	11.8
10	99.4	0.1	2.24×10^{-4}	4.5×10^{-6}	28.0
15	96.3	0.3	5.7×10^{-4}	1.2×10^{-5}	57.6
25	94.3	0.6	2.23×10^{-3}	3.4×10^{-5}	96.1
40	103.3	3.1	7.8×10^{-3}	4.0×10^{-4}	100.0

The wavy curve progression of the 5 °C and formic acid data set is mainly due to a difficult integration because of the increase of the solvent peak relative to the signal peaks due to the influence of the non-deuterated formic acid are the reason.

Stability measurement of the analytes

Stock solution: Oxoammonium cation was weighed in a volumetric flask (Duran, Germany) filled up with 0.1 M aqueous sodium chloride solution to produce a 0.1 M OC solution. For TEMPOL OC and TMA-TEMPO OC, the radicals were used and later oxidized electrochemically in a redox flow battery (for details see above). The stock solutions were stored at 4 °C until derivatization.

Sample preparation for stability test: Samples for the stability tests were prepared from the OC stock solutions, a 0.1 M *N*-vinylcarbazole TMU solution, as well as 100 µL of an 83 mmol L⁻¹ (10 mg mL⁻¹) mesitylene solution in TMU as internal standard. The amounts of the components were chosen to yield the respective targeted OC concentrations (21, 28 and 35 mmol L⁻¹), with a ratio of the derivatization reagent *N*-vinylcarbazole to the analyte of 2:1, in 1 mL of a TMU solution. The resulting mixture was injected into the chromatographic system. During the whole experiment the samples in the autosampler were kept at -5 °C.

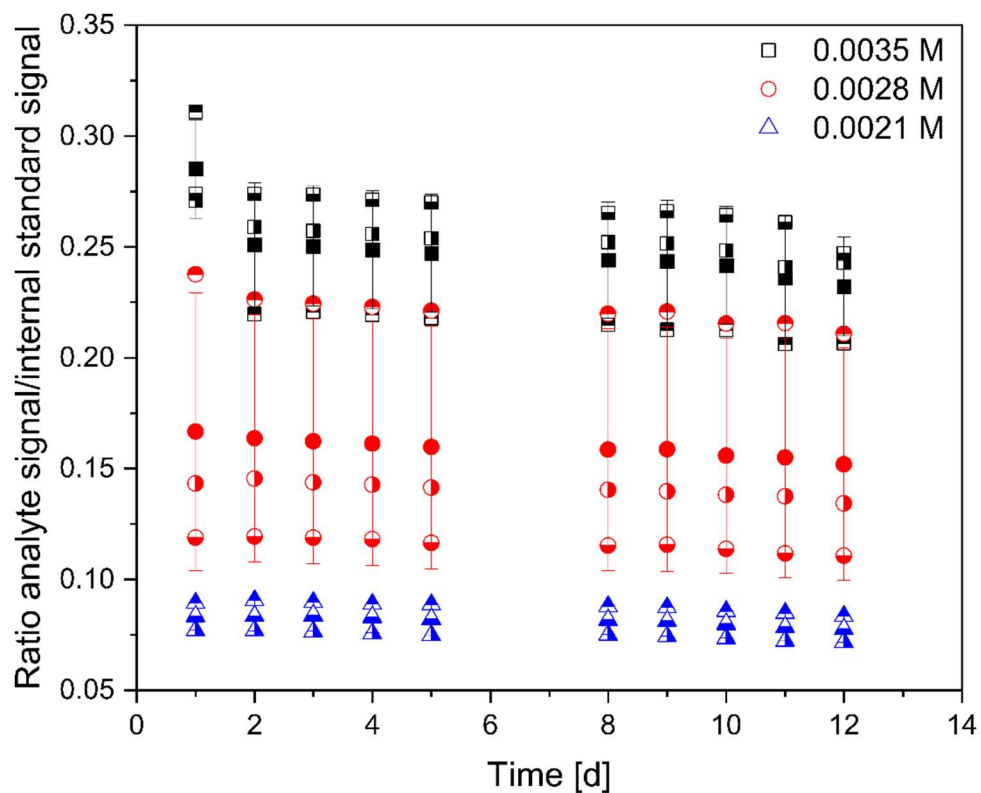


Figure S5: Stability data of the Bobbitt Salt. The fully filled symbols are the mean values with error bars of the individual values (partially filled).

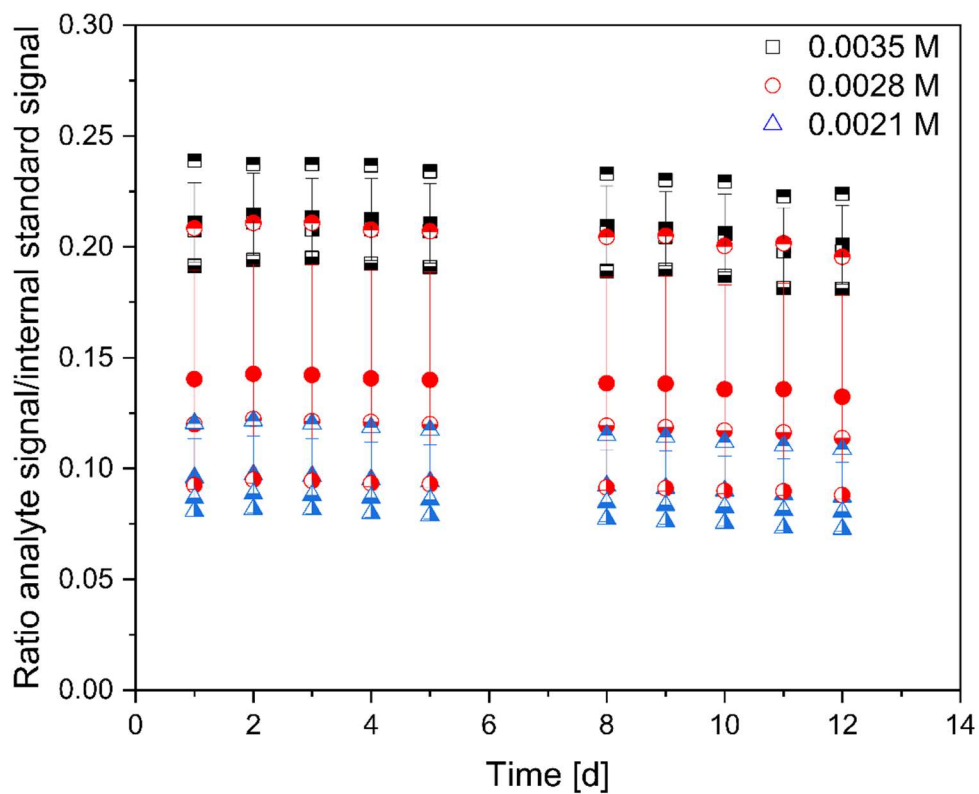


Figure S6: Stability data of the TMA-TEMPO oxoammonium cation. The fully filled symbols are the mean values with error bars of the individual values (partially filled).

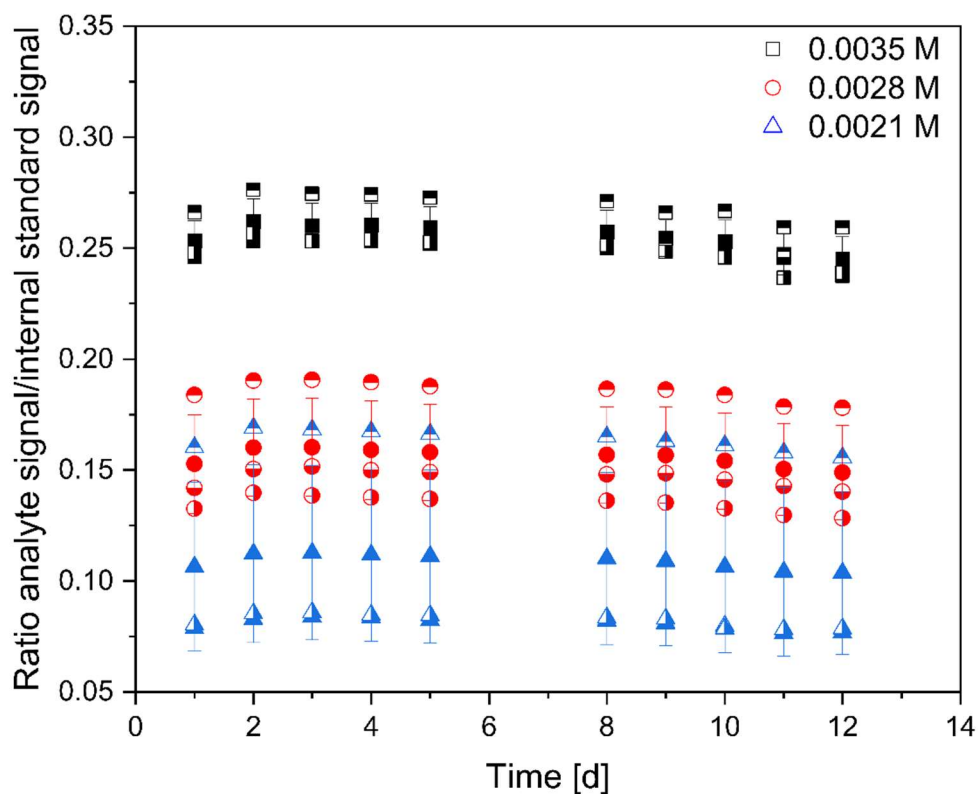


Figure S7: Stability data of the TEMPOL oxoammonium cation. The fully filled symbols are the mean values with error bars of the individual values (partially filled).

Linear calibration of the analytes

Sample preparation: The samples were prepared as described for the stability tests. Afterwards, they were homogenized for 3 minutes with a vortexer (Vortex Genie 2, Scientific Industries, USA) prior to injection into the chromatographic system. For each oxoammonium cation, six samples at five concentrations (14, 21, 24, 28 and 35 mmol L⁻¹) were prepared and injected once into the chromatographic system.

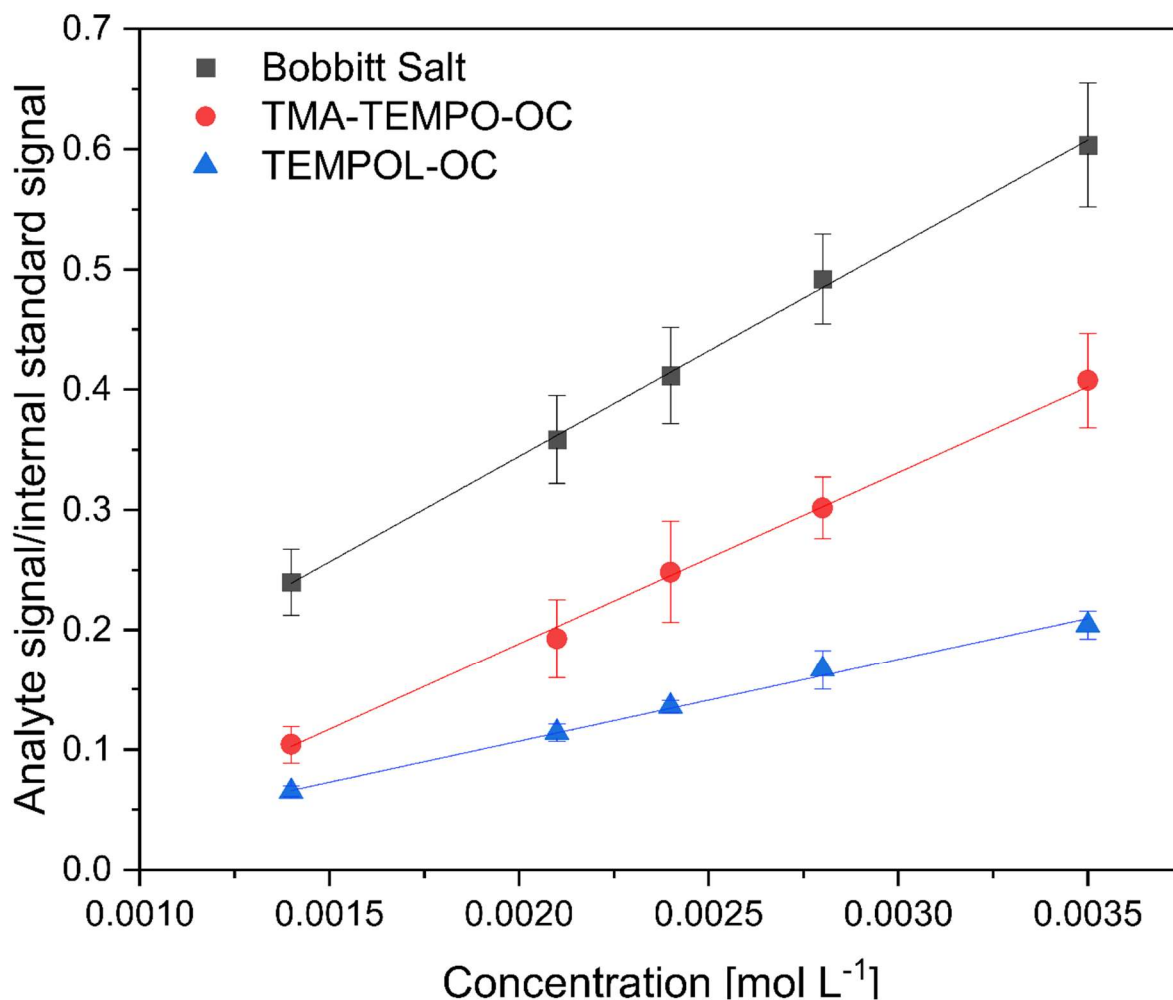


Figure S8: Linearity data of the three oxoammonium cations with error bars. The data points represent the mean values of the six individual measurements.

Analyte and side product identification

Sample preparation: The samples were prepared like described for the linear calibration. Before injection, the samples were diluted with TMU to 0.1 mg mL^{-1} for the Bobbitt salt and TEMPOL OC and to 0.01 mg mL^{-1} for the TMA-TEMPO OC sample. The measured chromatograms as well as the designated product MS spectra are shown in Figure S9 to Figure S11.

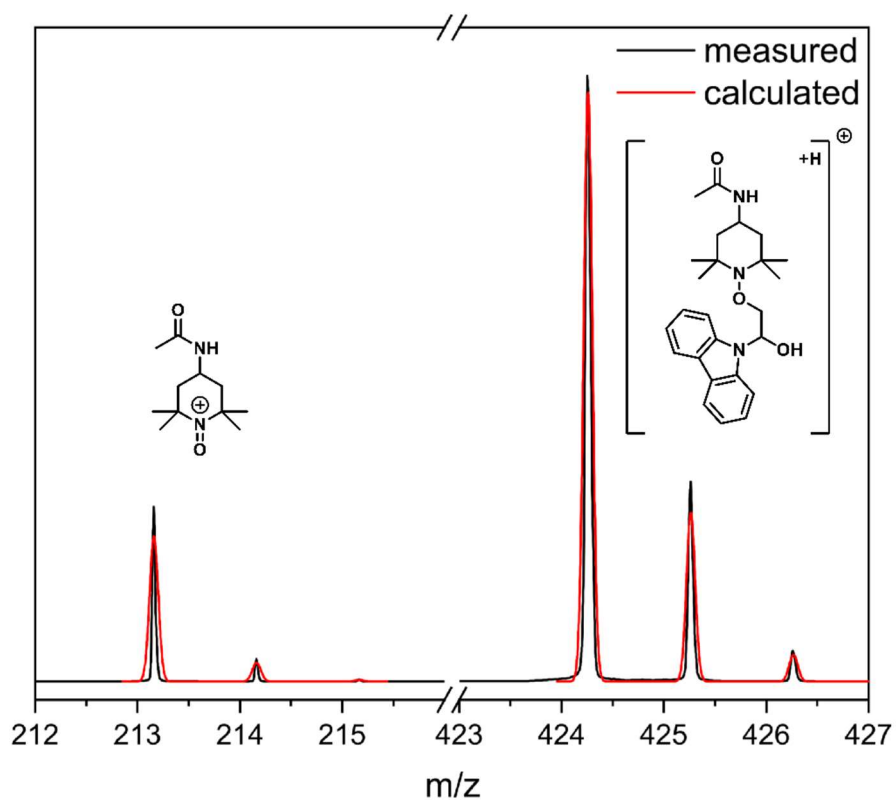
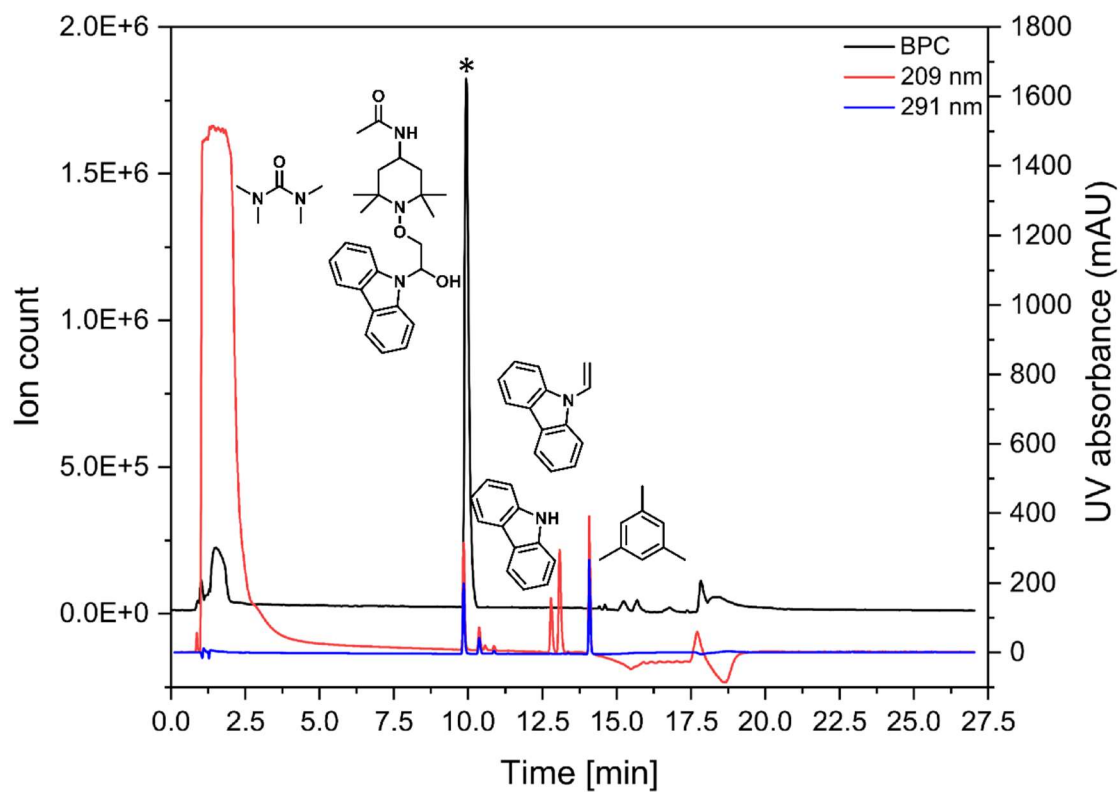


Figure S9: Top: LC-MS run of the Bobbitt Salt with the base peak chromatogram (BPC, black), the UV trace at 209 nm (red) and at 291 nm (blue). Bottom: Overlay of the measured (black) and calculated (red) isotopic pattern of the peak from 9.9 to 10.0 min (marked with *).

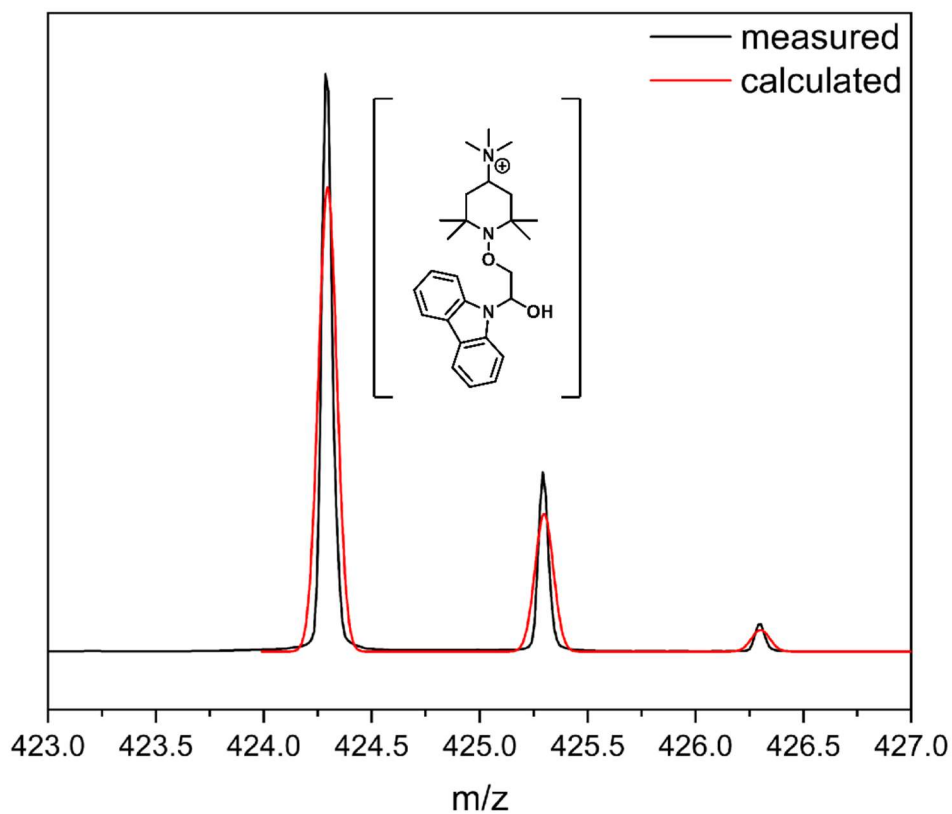
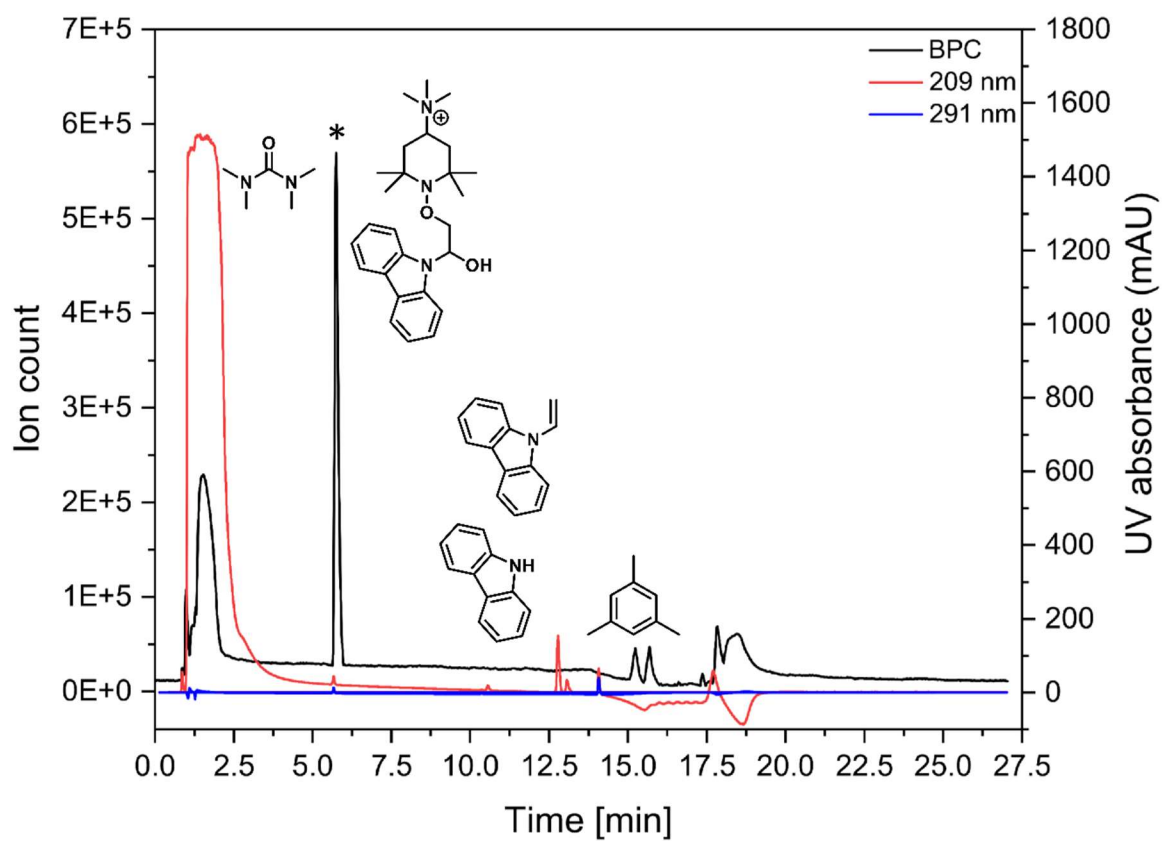


Figure S10: Top: LC-MS run of the TMA-TEMPO OC with the base peak chromatogram (BPC, black), the UV trace at 209 nm (red) and at 291 nm (blue). Low: Overlay of the measured (black) and calculated (red) isotopic pattern of the peak from 5.7 to 5.8 min (marked with *).

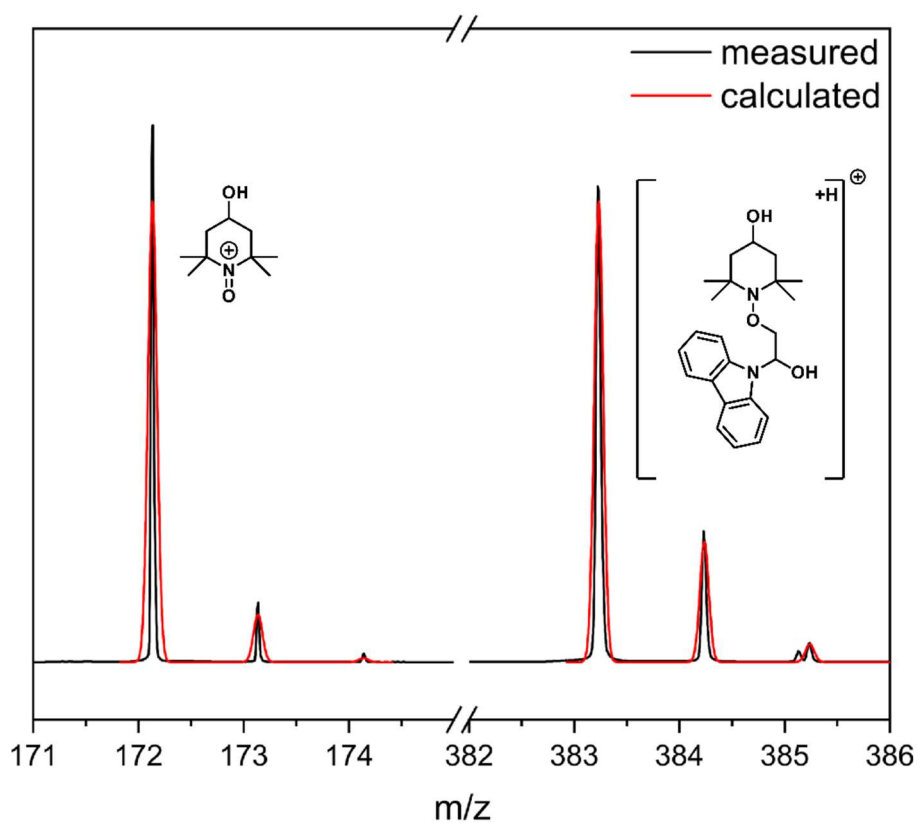
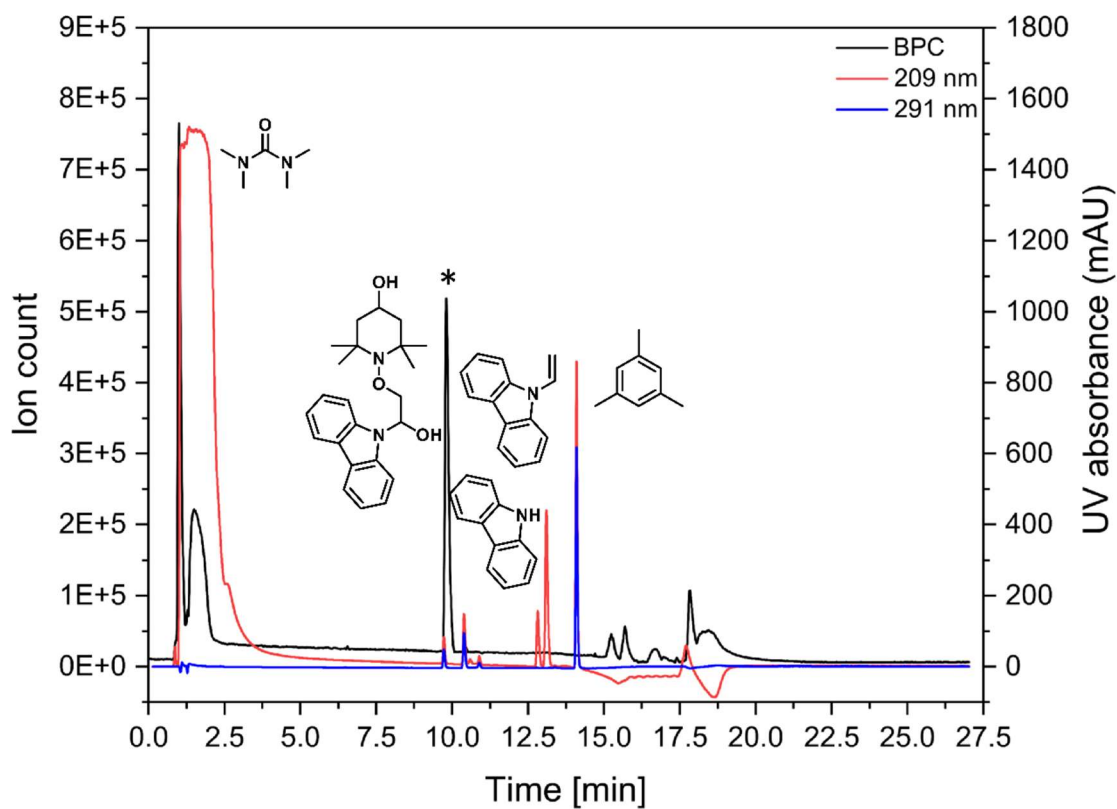


Figure S11: Top: LC-MS run of the TEMPOL CO with the base peak chromatogram (BPC, black), the UV trace at 209 nm (red) and at 291 nm (blue). Low: Overlay of the measured (black) and calculated (red) isotopic pattern of the peak from 9.8 to 9.9 min (marked with *).

Formulas[3]

Resolution (R_S):

$$R_S = \frac{2(t_{R2}-t_{R1})}{w_{b1}+w_{b2}} \quad (2)$$

t_{R1} retention time peak 1

t_{R2} retention time peak 1

w_{b1} bottom width peak 1

w_{b2} bottom width peak 2

with

$$w_b = 4\sigma \quad (3)$$

and

$$w_{hm} = 2.354\sigma \quad (4)$$

w_{hm} width at 50% height

$$R_S = \frac{4.708(t_{R2}-t_{R1})}{4(w_{hm1}+w_{hm2})} \quad (5)$$

Plate count (N):

$$N = 5.54 \left(\frac{t_R}{w_{hm}} \right)^2 \quad (6)$$

Capacity factor (k'):

$$k' = \frac{(t_R-t_M)}{t_M} \quad (7)$$

t_M hold-up time

Tailing factor (T):

$$T = \frac{w_{0.05}}{2f} \quad (8)$$

$w_{0.05}$ width at 5% height

f distance from the peak maximum to the leading edge of the peak at 5% height

Recovery rate (intraday) (RR_{intra}):

$$RR_{intra} = \frac{\bar{c}_{measured}}{c_{target}} * 100\% \quad (9)$$

$\bar{c}_{measured}$ average of the determined concentration of the analyte utilizing the calibration curve

c_{target} target concentration

Recovery rate (interday) (RR_{inter}):

$$RR_{inter} = \frac{\bar{\bar{c}}_{measured}}{c_{target}} * 100\% \quad (10)$$

$\bar{\bar{c}}_{measured}$ average of the average concentration of the analyte determined for the intraday recovery rate

c_{target} target concentration

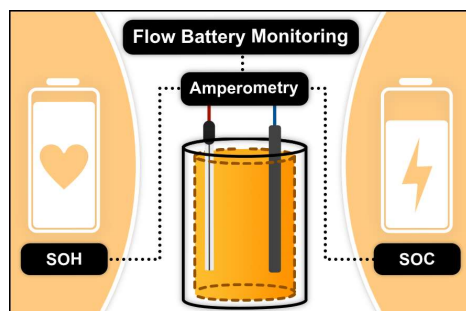
Literature

- [1] Janoschka T, Martin N, Hager MD, Schubert US (2016) An aqueous redox-flow battery with high capacity and power: The TEMPTMA/MV system. *Angew Chem Int Ed* 55:14427-14430. <https://doi.org/10.1002/anie.201606472>
- [2] Takata T, Tsujino Y, Nakanishi S, Nakamura K, Yoshida E, Endo T (1999) Electrophilic 1,2-addition of oxoammonium salts to olefins. *Chem Lett.* 28:937-938. <https://doi.org/10.1246/cl.1999.937>
- [3] United States Pharmacopeia (2014) United States Pharmacopeial Convention. United States Pharmacopeia, Rockville

Publications P6

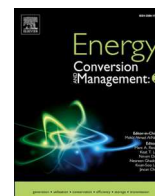
A low-cost amperometric sensor for the combined state-of-charge, capacity, and state-of-health monitoring of redox flow battery electrolytes.

C. Stolze, P. Rohland, K. Zub, O. Nolte, M. D. Hager, U S. Schubert



Abstract:

We recently introduced an amperometric, temperature-independent, and calibration-free method for the measurement of the state-of-charge (SOC) of redox flow battery (RFB) electrolytes. In the study at hand, the measurement accuracy of the method is re-evaluated and significantly improved. The absolute root-mean-square deviation (RMSD) is reduced from $\sim 5\%$ to below 0.5% over the complete SOC range. Based on this enhanced measurement accuracy, a new approach for the online co-estimation of an electrolyte's capacity and its state-of-health (SOH) is proposed and experimentally evaluated. In an operating RFB, relative RMSDs of 0.7 and 1.4% are obtained for the capacities of the catholyte and the anolyte, respectively. Utilizing this capacity measurement, SOH values with absolute RMSDs between 0.6 and 2.1% can be achieved. Furthermore, a low-cost microcontroller-based measurement unit (MMU) prototype was constructed and characterized. Based on the component prices and possible cost optimizations, total material costs of below 40 EUR (\$49) for two MMUs are calculated. In addition, a preliminary investigation of a low-cost bipolar, backfilled microelectrode (BBME) for material costs of below 2 EUR (\$2) is presented, its working principle demonstrated, and pathways for mitigating its stability issues are discussed. The methodological enhancements proposed in this study result in unprecedented measurement accuracies for the simultaneous SOC and SOH monitoring of both electrolytes in an operating RFB. The improved amperometric method stands out for its wide applicability, viable implementation costs, temperature as well as concentration independence, and excellent accuracy level. It, thus, has the potential to facilitate the RFB electrolyte development, improve the operational safety of RFBs, and optimize their operational performance.



A low-cost amperometric sensor for the combined state-of-charge, capacity, and state-of-health monitoring of redox flow battery electrolytes

Christian Stolze^{a,b}, Philip Rohland^{a,b}, Karina Zub^{a,c}, Oliver Nolte^{a,b}, Martin D. Hager^{a,b}, Ulrich S. Schubert^{a,b,c,*}

^a Laboratory of Organic and Macromolecular Chemistry (IOMC), Friedrich Schiller University Jena, Humboldtstraße 10, 07743 Jena, Germany

^b Center for Energy and Environmental Chemistry Jena (CEEC Jena), Friedrich Schiller University Jena, Philosophenweg 7a, 07743 Jena, Germany

^c Jena Center for Soft Matter (JCSM), Philosophenweg 7, 07743 Jena, Germany

ARTICLE INFO

Keywords:

Redox flow battery
State-of-charge
State-of-health
Monitoring
Sensor
Microelectrode

ABSTRACT

We recently introduced an amperometric, temperature-independent, and calibration-free method for the measurement of the state-of-charge (SOC) of redox flow battery (RFB) electrolytes. In the study at hand, the measurement accuracy of the method is re-evaluated and significantly improved. The absolute root-mean-square deviation (RMSD) is reduced from ~ 5% to below 0.5% over the complete SOC range. Based on this enhanced measurement accuracy, a new approach for the online co-estimation of an electrolyte's capacity and its state-of-health (SOH) is proposed and experimentally evaluated. In an operating RFB, relative RMSDs of 0.7 and 1.4% are obtained for the capacities of the catholyte and the anolyte, respectively. Utilizing this capacity measurement, SOH values with absolute RMSDs between 0.6 and 2.1% can be achieved. Furthermore, a low-cost microcontroller-based measurement unit (MMU) prototype was constructed and characterized. Based on the component prices and possible cost optimizations, total material costs of below 40 EUR (\$49) for two MMUs are calculated. In addition, a preliminary investigation of a low-cost bipolar, backfilled microelectrode (BBME) for material costs of below 2 EUR (\$2) is presented, its working principle demonstrated, and pathways for mitigating its stability issues are discussed. The methodological enhancements proposed in this study result in unprecedented measurement accuracies for the simultaneous SOC and SOH monitoring of both electrolytes in an operating RFB. The improved amperometric method stands out for its wide applicability, viable implementation costs, temperature as well as concentration independence, and excellent accuracy level. It, thus, has the potential to facilitate the RFB electrolyte development, improve the operational safety of RFBs, and optimize their operational performance.

1. Introduction

The development of reliable, safe, and long-term stable stationary energy storage systems for the storage of, e.g., wind and solar power has become one of the major challenges in the world-wide attempts to counteract climate change. The redox flow battery (RFB) represents one of the most promising technological approaches with respect to this. The continuous progress achieved in the development of suitable redox chemistries as well as the enhancement of electrochemical reactors (i.e., the flow cells) is remarkable.[1–8] While several RFB systems are approaching commercialization, the investigation of degradation mechanisms is getting more important and the demand for a cost-

efficient and reliable battery monitoring and management is increasing.[9–12] Due to the separation of the energy storage medium (electrolytes) and the energy conversion unit (flow cell), RFBs support a variety of different sensor interfaces and *in-situ* monitoring approaches in contrast to other battery technologies. Among the monitorable parameters, the electrolyte state-of-charge (SOC) and state-of-health (SOH) represent the most representative quantities for the overall battery state because of their impact on nearly all physicochemical parameters of the electrolytes. In addition, the monitoring of individual electrolyte SOC and SOHs is also of great interest for the investigation of electrolyte stabilities and half-cell imbalances, which have recently got a significantly increased attention in the organic RFB community.

* Corresponding author at: Laboratory of Organic and Macromolecular Chemistry (IOMC), Friedrich Schiller University Jena, Humboldtstraße 10, 07743 Jena, Germany.

E-mail address: ulrich.schubert@uni-jena.de (U.S. Schubert).

<https://doi.org/10.1016/j.ecmx.2022.100188>

Received 6 July 2021; Received in revised form 11 January 2022; Accepted 15 January 2022

Available online 22 January 2022

2590-1745/© 2022 The Authors. Published by Elsevier Ltd. This is an open access article under the CC BY-NC-ND license (<http://creativecommons.org/licenses/by-nc-nd/4.0/>).

[10–16] Due to the importance of the SOC and SOH measurements, a large variety of methods has been developed for their assessment in the past decade. For a detailed literature overview and comparison, which covers all available SOC and SOH measurement methods for RFBs, we would like to refer to our recent in-depth review.[11] While the literature standard method is based on open-circuit voltage (OCV) measurements,[17–20] more recent approaches are based on, e.g., measurements of the electrolyte viscosity,[17] the electrolyte density,[17,21,22] and infrared spectra.[23] Despite the demand for reliable SOC and SOH measurement methods, all existing techniques frequently require time-consuming calibration, are only applicable to specific electrolytes, are temperature or concentration dependent, require complex measurement hardware, are too expensive for standard applications, and/or only operate on the full-cell level and not on the half-cell level.[11,24] All this impedes the application and limits the accuracy of these existing methods and highlights the demand for more reliable and cost-efficient methods. With regard to this, amperometric measurement techniques are currently evolving into versatile and promising approaches for the assessment of electrolyte SOC[24,25] and electrolyte SOHs[14,26] in RFBs. In particular, we have recently proposed that the anodic and the cathodic mass-transfer-limited currents at basically any type of mass-transfer-limited electrode can be exploited to measure the state-of-charge in a large variety of RFB electrolytes (e.g., aqueous vanadium and aqueous organic electrolytes).[24] Disk-shaped microelectrodes have proven to be particularly suitable for this first calibration-free, temperature-independent, and concentration-independent SOC measurement technique.

Although this amperometric method exhibits the aforementioned advantages in contrast to conventional techniques, it only delivered absolute accuracies of 3 to 7% SOC. While this is on par with conventional SOC measurement methods, higher accuracies are generally required for thorough electrolyte investigations and performance optimizations in operating RFBs.[11] In addition, the original approach lacks the ability to provide electrolyte capacities and SOH values, which are equally important for RFB investigations and operation. With respect to this, Neyhouse *et al.* have recently utilized the mass-transfer-limited currents at disk microelectrodes for the evaluation of redox species concentrations and electrolyte SOH values both *ex-situ* and *in-situ*. [14,26] However, this approach was only demonstrated for comparably low redox species concentrations (≤ 0.1 M), requires a thorough calibration, and is temperature dependent as well as concentration dependent. It is, thus, not suited for industrial applications, where electrolyte composition and temperature vary over time.

As a consequence, the study at hand further explores the amperometric, temperature-independent, concentration-independent, and calibration-free SOC measurement approach to mitigate the remaining downsides of the original approach.[24] First, the method's accuracy is re-evaluated and improved, and its experimental setup is simplified. Subsequently, a microcontroller-based low-cost measurement hardware is utilized to demonstrate the method's cost efficiency and low hardware requirements. Furthermore, we theoretically motivate and experimentally verify an approach to achieve an online co-estimation of an electrolyte's capacity as well as its state-of-health (SOH) from the measured SOC values. This approach inherits the beneficial properties of the amperometric SOC measurement and, thus, overcomes the aforementioned issues of previous SOH and capacity measurement techniques. Finally, all improvements are evaluated in an *in-situ* measurement environment for both half-cells of an operating aqueous organic RFB under varying electrolyte concentrations and temperatures.

2. Theory

Prior to the presentation of the experimental results, this section briefly describes the general theoretical approach for the amperometric SOC measurement published earlier (section 2.1).[24] Subsequently, new equations and data analyses approaches are derived which enable a

more accurate SOC evaluation as well as an accurate electrolyte capacity and SOH co-estimation (sections 2.2 to 2.4).

2.1. Amperometric electrolyte state-of-charge measurement

We have recently proposed that the anodic and the cathodic mass-transfer-limited currents, $i_{l,a}$ and $i_{l,c}$, at disk-shaped microelectrodes can be exploited to measure the state-of-charge, SOC, in a large variety of RFB electrolytes.[24] These mass-transfer-limited currents can be predicted according to the following well-known equations:[24,27]

$$\begin{aligned} i_{l,a} &= 4nFrD_Rc_R = 4nFrD_Rc(1 - SOC) \text{ and} \\ i_{l,c} &= -4nFrD_Oc_O = -4nFrD_OcSOC, \end{aligned} \quad (1)$$

Here, F represents the Faraday's constant, n the number of transferred electrons, r the radius of the disk, $D_{O/R}$ the diffusion coefficients, $c_{O/R}$ the bulk concentrations of the oxidized and the reduced form of the redox couple, and $c = c_O + c_R$ its total concentration. The ratio of these currents enables the simple calculation of the electrolyte state-of-charge, $SOC \equiv c_Oc^{-1}$ or $\overline{SOC} \equiv c_Rc^{-1}$, according to:[24]

$$SOC = \frac{1}{1 - \frac{i_{l,a} D_O}{i_{l,c} D_R}} (\text{catholytes}) \text{ or } \overline{SOC} = \frac{1}{1 - \frac{i_{l,c} D_R}{i_{l,a} D_O}} (\text{anolytes}) \quad (2)$$

It can be assumed that $D_O D_R^{-1} \approx 1$ for a multitude of redox couples. [27] Alternatively, D_O and D_R can be measured separately by a variety of independent methods.

2.2. Amperometric electrolyte capacity co-estimation

The capacity of a RFB is a complex parameter, which changes during battery operation due to various capacity loss and degradation mechanisms such as cell component degradation, reactant cross-over, reactant decomposition, SOC imbalances, and electrolyte leakages.[11,16,28] The capacity changes on the battery level, however, are mainly connected to the individual changes in the electrolyte capacities. The development of methods for the online monitoring of the individual electrolyte capacities is, therefore, highly important. In this section, we derive a new mathematical approach that enables a simple electrolyte capacity co-estimation for basically any absolute electrolyte SOC measurement technique.

This co-estimation approach is based on the combination of the measured SOC values with the so-called coulomb counting technique. Traditionally, coulomb counting is used to estimate the SOC of any battery type by integrating the cell current, $i(t)$, during a charge or discharge process over the time, t : [17]

$$SOC(t_1) = SOC(t_0) + \frac{1}{Q_{max}} \int_{t_0}^{t_1} i(\tau) d\tau = SOC(t_0) + \frac{\Delta Q}{Q_{max}}. \quad (3)$$

While the transferred charge, ΔQ , is identical to the measurable current integral over time, the subsequent SOC estimation necessitates the *a priori* knowledge of the initial state-of-charge, $SOC(t_0)$, and the total capacity, Q_{max} . Both values, thus, need to be determined by additional methods. Furthermore, coulomb counting is commonly criticized for its significant error accumulation over time originating from small inaccuracies in the current measurements or even the lowest rates of side-reactions. Due to these downsides, it is usually not applied for SOC monitoring. However, it has been utilized to (re)calibrate other SOC monitoring methods during operation on a timescale of half-cycles. [11,17,22,29–31] On this timescale, the aforementioned error accumulation is negligible.

We propose in this study that coulomb counting is suited for a capacity co-estimation if combined with an accurate and independent SOC measurement. Rearrangement of equation (3) yields the total capacity:

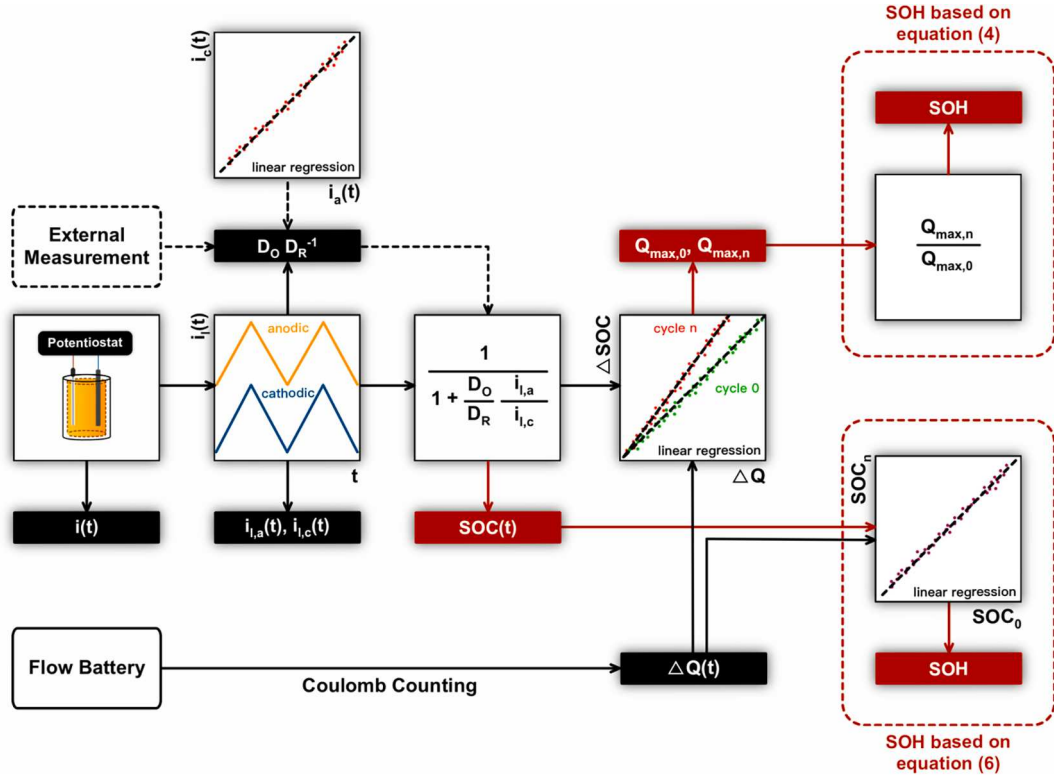


Fig. 1. Flowchart showing the evaluation steps used to calculate the electrolyte state-of-charge $SOC(t)$, the electrolyte capacity Q_{max} , and the electrolyte SOH from the mass-transfer-limited currents at a microelectrode ($i_{i,a}$ and $i_{i,c}$) and the charge transferred between the half-cells of an operating flow battery (ΔQ) measured over time.

$$Q_{max} = \underbrace{[SOC(t_1) - SOC(t_0)]^{-1}}_{\equiv \Delta SOC} \int_{t_0}^{t_1} i(\tau) d\tau = \frac{\Delta Q}{\Delta SOC}. \quad (4)$$

According to this equation, the simultaneous measurement of the charge transferred between the half-cells of an operating RFB (ΔQ) and the electrolyte SOC changes (ΔSOC) during an arbitrary time period ($\Delta t = t_1 - t_0$) enables a co-estimation of the individual electrolyte capacity (Q_{max}). Although remarkably simple, this approach has not been used, to the best of our knowledge, so far. This circumstance is most-likely due to the fact that previously reported SOC monitoring methods rely on coulomb counting for calibration or require the *a priori* knowledge of the electrolyte capacity for SOC evaluation.[11] Hence, the herein proposed capacity estimation is not applicable for many of the literature-known SOC measurement methods – including the open-circuit voltage cell techniques.

2.3. Amperometric electrolyte state-of-health co-estimation

An often-applied figure-of-merit for battery and electrolyte stability assessment is the state-of-health, which can be mathematically expressed as the ratio of the capacity in the n^{th} cycle (Q_{max}^n) to the initial or nominal capacity (Q_{max}^0). [11,16] The state-of-health in the n^{th} cycle is, thus, calculated by $SOH^n = \frac{Q_{max}^n}{Q_{max}^0} Q_{max}^0$. As a consequence, the electrolyte capacities obtained by equation (4) can be directly used to calculate the electrolyte SOH.

In addition, we suggest another evaluation approach for directly obtaining the SOH values from the SOC monitoring and coulomb counting, which can be mathematically derived as follows: Equation (3) may be formulated for two distinct cycles (e.g., the n^{th} and the first cycle) representing the relationship between the electrolyte SOC as a function of the transferred charge, ΔQ , in both cycles:

$$SOC^0 = SOC^0(t_0) + \frac{\Delta Q}{Q_{max}^0} \quad \text{and} \quad SOC^n = SOC^n(t_1) + \frac{\Delta Q}{Q_{max}^n}, \quad (5)$$

If the equation for the n^{th} cycle is rearranged for ΔQ (right equation) and inserted into the equation for the first cycle (left equation), one obtains a linear relationship between the SOC values of both cycles:

$$SOC^0(\Delta Q) = \underbrace{\frac{Q_{max}^n}{Q_{max}^0}}_{\equiv SOH^n} SOC^n(\Delta Q) + \frac{Q_{max}^n}{Q_{max}^0} SOC^n(t_1) + SOC^0(t_0). \quad (6)$$

The slope of this linear equation represents the SOH of the n^{th} cycle and, hence, can be obtained by a simple linear regression. Although this approach might be applicable to any electrolyte SOC measurement method, it is important to note that all methods that utilize coulomb counting for calibration purposes do not allow its application (e.g., most of the OCV cell methods).

2.4. Accuracy of amperometric SOC measurement

As a final step prior to the presentation of the experimental results, we would like to emphasize some important theoretical aspects for the accuracy evaluation of the proposed measurement techniques. The measurement uncertainties of the proposed electrolyte capacity and electrolyte SOH measurement methods are mainly dependent on the accuracy of the applied SOC measurement approach. For the amperometric method we observed absolute measurement uncertainties ranging from 3 to 7% in a previous study.[24] Although this accuracy is on par with the best SOC measurement methods reported so far,[11] it is desirable to increase the accuracy of this method further. For that, it is important to identify the main sources of the measurement errors.

In this study, the method's accuracy is assessed with samples prepared at defined reference SOC values (section 3.1). The measurement uncertainty according to equations (2) mainly depends on three factors:

Table 1

SOC measurement results for offline samples of different total concentrations of the ferri-/ferrocyanide redox couple in 0.5 M $\text{KCl}_{(\text{aq})}$ solutions as obtained with the Keithley 2400 SMU commercial potentiostat. $\Delta\text{SOC} \equiv \text{SOC} - \text{SOC}_{\text{ref}}$ represents the deviation of the measurement value from the true SOC of the sample.

$\text{SOC}_{\text{ref}} / \%$	400 mM ^[a]			200 mM ^[b]			100 mM ^[c]		
	$\Delta\text{SOC}^{[+]} / \%$	$\Delta\text{SOC}_c^{[\#]} / \%$	$\Delta\text{SOC}_L^{[3]} / \%$	$\Delta\text{SOC}^{[+]} / \%$	$\Delta\text{SOC}_c^{[\#]} / \%$	$\Delta\text{SOC}_L^{[3]} / \%$	$\Delta\text{SOC}^{[+]} / \%$	$\Delta\text{SOC}_c^{[\#]} / \%$	$\Delta\text{SOC}_L^{[3]} / \%$
1.01 ± 0.04	0.06 ± 0.04	0.04 ± 0.03	0.04 ± 0.01	0.30 ± 0.27	0.32 ± 0.27	0.22 ± 0.25	0.41 ± 0.13	0.28 ± 0.10	0.32 ± 0.12
5.03 ± 0.03	0.24 ± 0.08	0.15 ± 0.14	0.10 ± 0.06	0.37 ± 0.12	0.45 ± 0.08	0.09 ± 0.03	0.62 ± 0.08	0.11 ± 0.06	0.27 ± 0.07
25.02 ± 0.01	1.29 ± 1.15	1.03 ± 1.43	0.94 ± 1.67	1.11 ± 0.27	1.43 ± 0.13	0.19 ± 0.25	1.80 ± 0.09	0.19 ± 0.08	0.49 ± 0.09
50.00 ± 0.03	1.00 ± 0.12	0.60 ± 0.55	0.69 ± 0.12	1.48 ± 0.33	1.89 ± 0.25	0.30 ± 0.20	2.23 ± 0.26	0.26 ± 0.16	0.55 ± 0.26
74.98 ± 0.03	0.95 ± 0.20	0.61 ± 0.51	0.31 ± 0.20	1.46 ± 0.55	1.75 ± 0.71	0.38 ± 0.43	1.54 ± 0.10	0.30 ± 0.23	0.30 ± 0.10
95.00 ± 0.03	0.19 ± 0.07	0.14 ± 0.12	0.14 ± 0.07	0.26 ± 0.04	0.34 ± 0.02	0.05 ± 0.04	0.16 ± 0.02	0.32 ± 0.05	0.16 ± 0.02
98.99 ± 0.03	0.22 ± 0.19	0.25 ± 0.21	0.30 ± 0.21	0.03 ± 0.01	0.04 ± 0.01	0.04 ± 0.01	0.33 ± 0.08	0.47 ± 0.10	0.42 ± 0.08
RMSD	0.73	0.52	0.47	0.91	1.14	0.22	1.27	0.29	0.38

^[a] Average of three separately prepared sample batches and their standard deviations (batch 1 to 3).

^[b] Prepared by dilution of 400 mM sample (batch 3).

^[c] Prepared by dilution of 400 mM sample (batch 4).

^[+] Calculated from equation (2) using the assumption $D_O D_R^{-1} = 1$.

^[#] Calculated from equation (7) using the slope of the $i_{i,c}$ vs. $i_{i,a}$ regression line as estimate for $D_O D_R^{-1}$ in each repetition.

^[3] Calculated from equation (2) using the average literature value of $D_O D_R^{-1} = 1.07 \pm 0.07$ [32,33]

1. The error of the reference sample preparation (*i.e.*, the uncertainty of the reference SOC);
2. the error of the current measurement in the micro- to nanoampere range;
3. the error in the assumed or measured ratio of the diffusion coefficients, $D_O D_R^{-1}$.

While the measurement uncertainty introduced by (1) and (2) can be mitigated by using precise preparation procedures and measurement hardware for volume, mass, and current measurements (see [Supporting Information](#)), issue (3) has to be handled on the data analysis level: In our initial study, [24] the ratio of the diffusion coefficients was determined from the ratio of discrete current differences in the mass-transfer-limited currents at distinct SOC, $\Delta i_{i,c} \Delta i_{i,a}^{-1}$, or was assumed to be $D_O D_R^{-1} \approx 1$. Although approximately true for most redox couples, the latter assumption does not make use of the method's full accuracy. More accurate SOC values can be obtained, if $D_O D_R^{-1}$ is accurately known. This can either be achieved by separate experiments which directly measure D_O and D_R for a redox couple or with the following *in-situ* approach developed for the study at hand: The elimination of the SOC variable in equations (1) by rearranging and inserting one into the other yields a linear relationship between the mass-transfer-limited currents:

$$i_{i,c} = \frac{D_O}{D_R} i_{i,a} - 4nFrD_Oc. \quad (7)$$

A linear regression performed on a plot of $i_{i,c}$ vs. $i_{i,a}$ for samples of unknown but different SOC yields $D_O D_R^{-1}$ as the slope of this linear equation. It should be stressed, however, that equation (7) is valid only for sets of data points ($i_{i,c}$; $i_{i,a}$) for which the total concentration, c , and the microelectrode radius, r , remain constant and interference from convection is negligible. However, these conditions can be fulfilled by careful experimentation in both online and offline measurements as demonstrated later in this study. This approach theoretically provides $D_O D_R^{-1}$ without the explicit knowledge of the sample SOC.

3. Results and discussion

An extensive set of experiments has been performed to validate the proposed amperometric SOC, capacity, and SOH measurement. Their results are presented and discussed in the following section. For a brief overview, [Fig. 1](#) displays the experimental and analytical steps utilized for the evaluations as a flowchart.

3.1. Offline experiments

At first, offline experiments were performed to make use of the theoretical approaches for the accuracy improvements derived in section 2. Furthermore, microcontroller-based measurement hardware assembled from low-cost components was developed to demonstrate the anticipated cost efficiency of the approach. Prior to the offline (*ex-situ*) SOC measurements, however, we re-evaluated our sample preparation procedure to reduce the uncertainty of the reference SOC values utilized for the accuracy assessment of the amperometric SOC measurement method (see [Supporting Information](#)): Although not taken into account in our previous study, [24] the sample preparation procedure utilized therein caused absolute uncertainties of up to $\pm 1\%$ in the reference SOC. The improved sample preparation applied in the study at hand yielded a significantly lower absolute uncertainty of below $\pm 0.04\%$ for all offline samples. Due to this negligible uncertainty, we will also refer to the reference values as the “true” sample SOC in the remainder of this study.

3.1.1. Two-electrode setup and commercial potentiostat

To simplify the hardware requirements of the method, a simple two-electrode configuration with a gold microelectrode (diameter: 25 μm) as working electrode and a gold macroelectrode (diameter: 2 mm) as counter electrode was investigated as replacement for the more complicated closed, bipolar electrode setup utilized in the first study. [24] Due to the varying reference potential that arises from both a polarizable counter electrode and the significant overpotentials upon current flow at the electrode–electrolyte interface, care must be taken if a two-electrode setup without a reference electrode is utilized. Consequently, the surface areas of the counter electrodes in this study were at least four orders of magnitude larger than the surface areas of the working electrodes to mitigate the negative impacts of counter electrode polarization in the largest part of the investigated SOC ranges.

In a first offline experiment, different batches of the ferri-/ferrocyanide electrolytes at defined reference SOC of 1%, 5%, 25%, 50%, 75%, 95%, and 99% were measured three times utilizing the simplified two-electrode configuration. The raw measurement values for the currents, the obtained $D_O D_R^{-1}$ values, and the SOC of each of the batches and repetitions can be examined in [Tables S2 to S11](#) of the [Supporting Information](#). An average value of 1.03 ± 0.05 was obtained for $D_O D_R^{-1}$ over all samples as determined from the slopes of the linear regressions of the plots of $i_{i,c}$ vs. $i_{i,a}$. This value is close to the ratio of 1.09 ± 0.03 , which can be calculated from the average diffusion coefficients reported for 1 mM to 5 mM potassium ferri-/ferrocyanide in 0.1 M and 1 M KCl, respectively, by Konopka and McDuffie. [32] It also fits to the ratio of 1.05 ± 0.06 reported by Amatore *et al.* for 10 mM potassium ferri-/

Table 2

SOC measurement results for offline evaluation of samples with different total concentrations of the ferri-/ferrocyanide redox couple in 0.5 M KCl_(aq) solutions as obtained with the microcontroller-based measurement unit. $\Delta SOC \equiv SOC - SOC_{ref}$ represents the deviation of the measurement value from the true SOC of the sample (SOC_{ref}).

$SOC_{ref} / \%$	400 mM ^[a]			200 mM ^[b]			100 mM ^[c]		
	$\Delta SOC^{[+]} / \%$	$\Delta SOC_c^{[#]} / \%$	$\Delta SOC_L^{[§]} / \%$	$\Delta SOC^{[+]} / \%$	$\Delta SOC_c^{[#]} / \%$	$\Delta SOC_L^{[§]} / \%$	$\Delta SOC^{[+]} / \%$	$\Delta SOC_c^{[#]} / \%$	$\Delta SOC_L^{[§]} / \%$
1.01 ± 0.04	0.65 ± 0.61	0.65 ± 0.62	0.58 ± 0.55	0.41 ± 0.34	0.45 ± 0.36	0.35 ± 0.27	2.62 ± 2.00	2.45 ± 1.93	2.43 ± 1.81
5.03 ± 0.03	0.44 ± 0.32	0.44 ± 0.30	0.40 ± 0.40	0.66 ± 0.26	0.61 ± 0.25	0.51 ± 0.55	1.34 ± 1.32	1.37 ± 1.41	1.36 ± 1.45
25.02 ± 0.01	1.37 ± 1.18	1.15 ± 1.35	1.12 ± 1.59	1.15 ± 0.83	1.59 ± 1.29	0.57 ± 0.43	3.38 ± 1.37	2.19 ± 1.56	2.03 ± 1.33
50.00 ± 0.03	1.20 ± 0.32	0.90 ± 0.58	0.52 ± 0.27	0.90 ± 0.68	1.29 ± 0.60	0.96 ± 0.94	1.20 ± 1.57	1.17 ± 1.42	1.76 ± 0.49
74.98 ± 0.03	1.23 ± 0.29	1.01 ± 0.51	0.23 ± 0.18	1.68 ± 1.08	2.07 ± 1.52	0.71 ± 0.90	1.74 ± 1.53	1.68 ± 1.46	1.20 ± 0.86
95.00 ± 0.03	0.32 ± 0.26	0.33 ± 0.27	0.39 ± 0.21	0.44 ± 0.29	0.48 ± 0.42	0.58 ± 0.11	4.41 ± 1.94	4.77 ± 2.76	4.57 ± 2.42
98.99 ± 0.03	0.39 ± 0.21	0.40 ± 0.21	0.45 ± 0.24	0.06 ± 0.02	0.04 ± 0.01	0.13 ± 0.02	2.24 ± 1.35	2.38 ± 1.51	2.41 ± 1.52
RMSD	0.90	0.76	0.59	0.91	1.15	0.60	2.65	2.54	2.48

^[a] Average of three separately prepared sample batches and their standard deviations (batch 1 to 3).

^[b] Prepared by dilution of 400 mM sample (batch 3).

^[c] Prepared by dilution of 400 mM sample (batch 4).

^[+] Calculated from equation (2) using the assumption $D_O D_R^{-1} = 1$.

^[#] Calculated from equation (7) using the slope of the i_c vs. i_a regression line as estimate for $D_O D_R^{-1}$ in each repetition.

^[§] Calculated from equation (2) using the average literature value of $D_O D_R^{-1} = 1.07 \pm 0.07$ [32,33].

ferrocyanide in 1 M KCl.[33] The SOC values of the offline samples were evaluated from the mass-transfer-limited currents according to equation (2) with three different $D_O D_R^{-1}$ values: (i) Assuming equal diffusion coefficients (*i.e.*, $D_O D_R^{-1} \approx 1$), (ii) using $D_O D_R^{-1}$ as determined from the linear regression (equation (7)), and (iii) utilizing the average value of $D_O D_R^{-1} = 1.07 \pm 0.07$ as calculated from the two aforementioned literature reports. The results of this experiment are summarized in Table 1 for the total concentration range from 400 mM to 100 mM and the SOC range from 1 to 99%. Absolute RMSD values of between 0.3 and 1.3% SOC were obtained in average for all three evaluation approaches. Consequently, all offline results indicate a significantly higher accuracy for the amperometric SOC measurement than reported in our initial study where RMSDs between 2.2 and 6.5% were observed in offline experiments depending on the total concentration of the redox species and the applied $D_O D_R^{-1}$ value.[24] The remaining errors of the presented measurements can be attributed to statistical variations in the sample preparation (*i.e.*, weighed masses and mixed electrolyte volumes), measurement uncertainties for the low-current measurement, interferences from background currents which slightly distort the measurement of the diffusion-limited currents, and the measurement uncertainty of the $D_O D_R^{-1}$ values. The SOC values calculated using the literature value $D_O D_R^{-1} = 1.07 \pm 0.07$ exhibited the highest accuracy with absolute RMSDs of below 0.5% for all concentrations. However, the new regression approach for the online determination of $D_O D_R^{-1}$ delivered a significant accuracy improvement when compared to the previous study as well.

To further highlight this, we utilized the diffusion-limited currents reported by Kroner *et al.*[25] for 1.6 M vanadium electrolytes and calculated the SOC values using the $D_O D_R^{-1}$ determined with equation (7): A RMSD of 2.2% was obtained in contrast to the 6% calculated in our previous publication which utilized discrete current differences.[24] The higher error in comparison to the ferri-/ferrocyanide electrolyte can be attributed to the electrode type utilized by Kroner *et al.* and we are confident that microelectrodes would yield higher accuracies for VRFBs. Overall, the offline experiments demonstrate that the two-electrode setup represents a viable replacement for the more complicated and more expensive bipolar setup applied in our previous study. The improved sample preparation and the enhanced approach for the determination of $D_O D_R^{-1}$ revealed the benchmark-setting SOC measurement accuracy of the amperometric method.

3.1.2. Microcontroller-based measurement unit (MMU)

The amperometric SOC measurement necessitates in principle only a simple voltage source and an ammeter with sufficient accuracy and

precision. In order to demonstrate the cost efficiency, which results from these low hardware requirements, a low-cost microcontroller (Arduino nano) and commercially available integrated circuits were used to design a first prototype of a low-cost SOC measurement unit (Figure S1). The details of its construction are described in the Supporting Information. In order to investigate the accuracy of this microcontroller-based measurement unit (MMU), the experiments presented in the section 3.1.1 were repeated using this device instead of the commercial potentiostat.

The regression approach over the complete concentration range yielded a $D_O D_R^{-1}$ of 1.01 ± 0.05 , which is close to the value obtained with the commercial potentiostat. Table 2 summarizes the deviations of the measured SOC values from the true SOC of the samples. Again, absolute RMSDs of below 1% were observed for the practically more important higher concentrations (*i.e.*, 200 mM and 400 mM). The SOC accuracy for these concentrations was nearly identical to the ones obtained with the commercial potentiostat. However, at the lower concentration of 100 mM the RMSD differed significantly from the results obtained with the commercial potentiostat. This can be attributed to the larger statistical variations in the current measurements obtained by the microcontroller-based device at the lower concentration of the redox couple. This hypothesis is supported by the following findings: The ΔSOC and ΔSOC_c presented in Table 2 represent the average of the SOC values obtained from the repetitions of the measurement. On the other hand, Table S11 (Supporting Information) shows the results when the currents of the same repetitions are averaged prior to SOC calculation. Statistical variations of the current measurement are mitigated by the current averaging and, consequently, result in an 1% lower RMSD. This reveals the statistical nature of the higher measurement uncertainty at low concentrations.

3.2. Online monitoring

The simplified two-electrode setup (section 3.1.1), the presented methodological optimizations (section 3.1.1), and the MMUs (section 3.1.2) were subsequently applied for the online monitoring of an operating compositionally symmetric, unbalanced redox flow battery [10,13,34] utilizing a 1.30 ± 0.03 M *N,N,N*-2,2,6,6-heptamethylpiperidinyloxy-4-ammonium chloride (TEMPTMA) aqueous electrolyte. This section presents the experiments utilized to validate the accuracy improvements as well as the new approach for the electrolyte capacity and SOH measurement during RFB operation.

Both the capacity-limiting side (CLS, catholyte, 17.00 ± 0.02 mL) and the non-capacity-limiting side (NCLS, anolyte, 24.0 ± 0.03 mL) of the compositionally symmetric, unbalanced RFB were monitored with

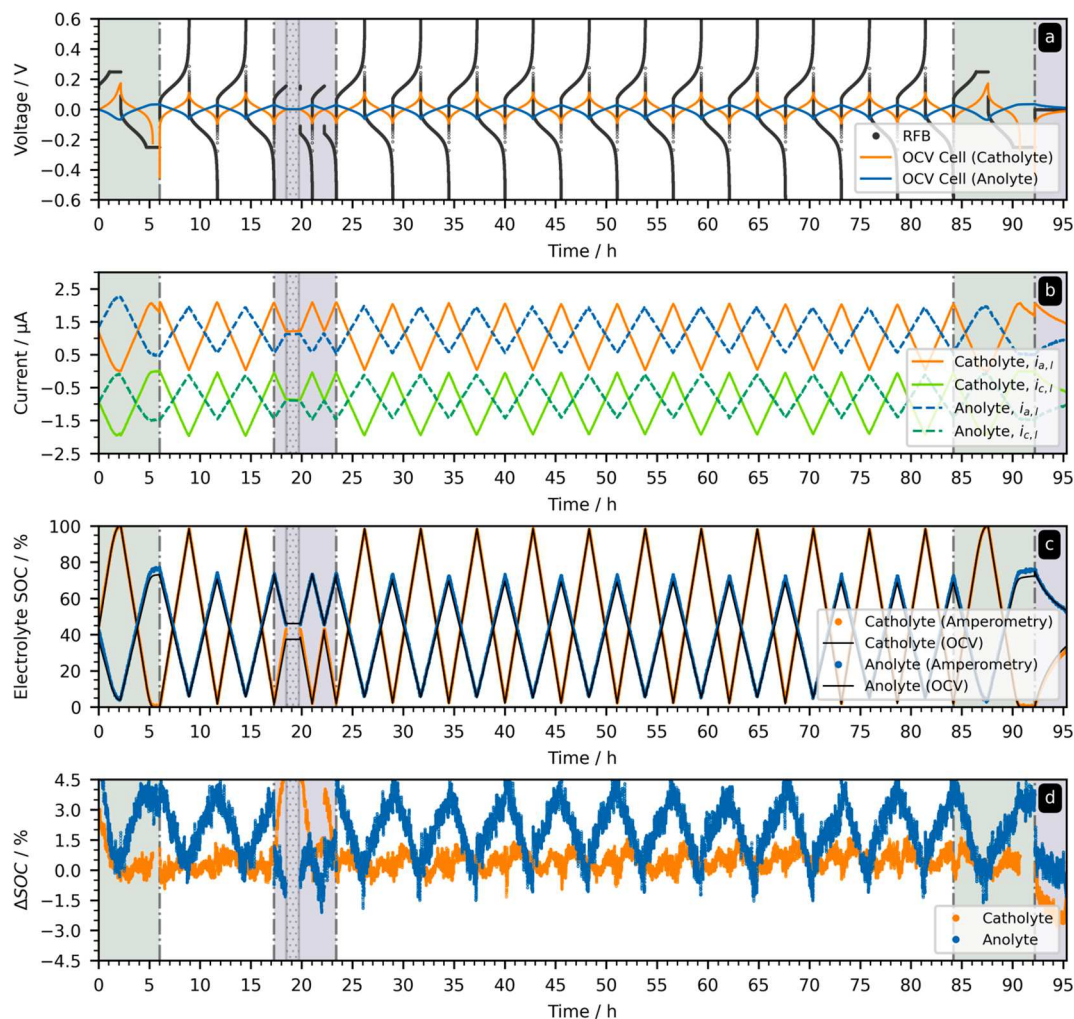


Fig. 2. Result of the online monitoring of both catholyte (17 mL) and anolyte (24 mL) in a compositionally symmetric, unbalanced aqueous RFB with 1.3 M TEMPTMA in three different cycling modes (green background: mixed galvanostatic and potentiostatic; blue background: incomplete galvanostatic cycling; white background: complete galvanostatic cycling): (a) Cell voltages of the RFB and the symmetric OCV cells used for measuring SOC reference values, (b) the mass-transfer-limited currents at the microelectrodes obtained *via* the microcontroller-based measurement units, (c) the SOC values obtained by both the OCV cell and the amperometric method, and (d) the absolute difference between the SOC values of both methods. In the time range from 18.5 to 19.8 h the experiment was paused to check the data on the MMU (hatched area). (For interpretation of the references to colour in this figure legend, the reader is referred to the web version of this article.)

regard to their SOC and capacity in two ways: (1) Applying the amperometric method using the MMUs for measurement and (2) applying the OCV cell method (with symmetric half-cells[29]) for validation against a widely accepted standard method. The OCV cells were (re)calibrated according to previously published procedures for each half-cycle.[17,22,29] This calibration method delivers an estimate for the electrolyte capacity from the OCV cell data as well. The online monitoring setup is schematically illustrated in Figure S3 of the Supporting Information. Due to the different locations of the two sensors in the RFB system, there was a detectable time delay between the electrolyte SOC sensed in the OCV cell and at the microelectrode, respectively. To obtain a fair comparison between the two methods, this difference was compensated by shifting the amperometric SOC data in time during data treatment (Figure S4, Supporting Information). For the calculation of the amperometric SOC, a $D_0D_R^{-1}$ of 0.9471 ± 0.0004 was applied for all experiments (Figure S5, Supporting Information).

In contrast to the purely galvanostatic cycling experiments performed in our previous study,[24] the RFB of this study was operated in three different cycling modes to unravel their impact on the methods' measurement accuracies: (1) Galvanostatic cycling with potentiostatic holding times at the voltage limits (cycles 0 and 16), (2) incomplete

galvanostatic cycles (cycles 3, 4, and 17), and (3) complete galvanostatic cycles (cycles 1 to 2 and cycles 5 to 15).

3.2.1. State-of-Charge monitoring

The voltage, current, and SOC data obtained for the 17.5 consecutive cycles of the compositionally symmetric, unbalanced TEMPTMA-based RFB are displayed in Fig. 2. For an unbiased comparison of the present results to the results of our previous study, a first evaluation of the obtained data takes only the complete, galvanostatic cycles of the capacity limiting side (catholyte) into consideration (cycles 1 to 2 and cycles 5 to 15, orange lines with white background in Fig. 2).

With an absolute RMSD of 0.6% (catholyte) between the amperometric and the OCV cell method, the SOC measurements in this experiment yielded a nearly three-fold lower average deviation between the methods when compared to the absolute RMSDs of 1.7 to 2.9% obtained previously.[24] Furthermore, while the analysis in the previous study revealed a statistical variation with a 1% percentile of -4.5 and a 99% percentile of 4.5% for the SOC deviations of the catholyte, the present experiments exhibited a 1% percentile of -0.4 and a 99% percentile of 1.3% . The 1% percentile expresses that 1% of all data points showed a Δ SOC lower than -0.4 and the 99% percentile expresses that 1% of all

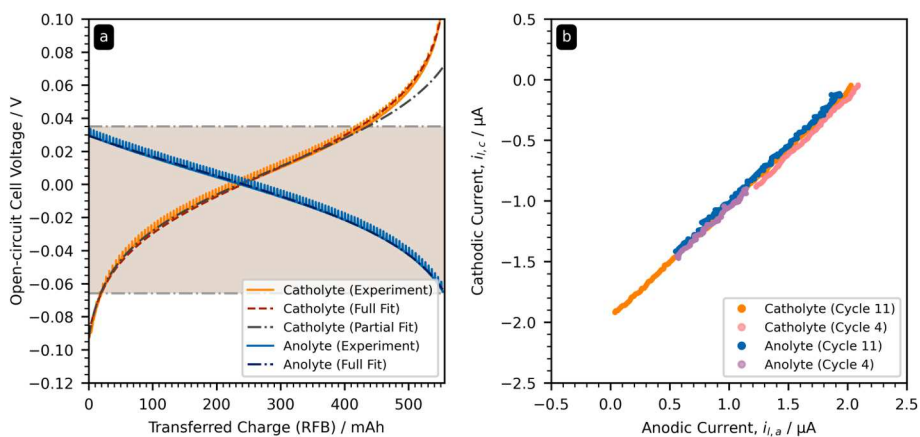


Fig. 3. (a) The open-circuit cell voltages obtained for catholyte and anolyte in the 11th charging half-cycle including the fit results for both data sets (complete galvanostatic cycling). The two fit curves for the catholyte represent the fit results when the complete data range is used (red dashed line) and when only the voltage range was also available for the anolyte (dashed black line). (b) The mass-transfer-limited currents obtained at the amperometric sensors in exemplary cycles representing complete (cycle 11) and incomplete (cycle 4) galvanostatic cycling. (For interpretation of the references to colour in this figure legend, the reader is referred to the web version of this article.)

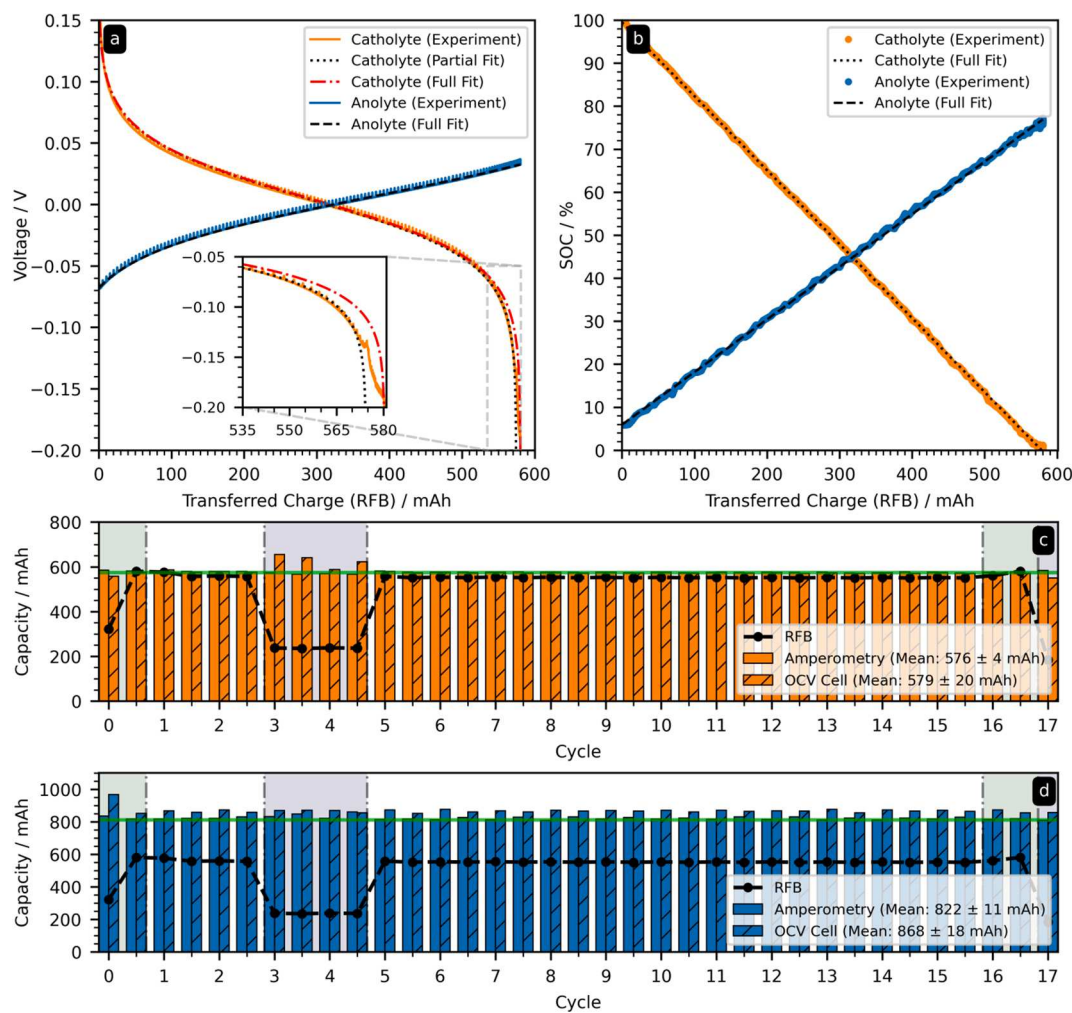


Fig. 4. Online electrolyte capacity monitoring for different cycling modes (background colors indicate: mixed galvanostatic and potentiostatic (green); incomplete galvanostatic cycling (blue); complete galvanostatic cycling (white)): (a) OCV cell voltage over transferred charge for exemplary half-cycle and corresponding fit curves (inset: deviation indicates a second species); (b) amperometric SOC over transferred charge for capacity measurement; (c) catholyte capacities per half-cycle (amperometric and OCV cell method); (d) anolyte capacities per half-cycle (amperometric and OCV cell method). Green lines in (c) and (d) represent the expected values (catholyte: 575 ± 12 mAh, anolyte: 812 ± 16 mAh). Numbers in the legends represent the average and the standard deviation of all cycles. Discharging half-cycles are indicated as non-integer values. (For interpretation of the references to colour in this figure legend, the reader is referred to the web version of this article.)

data points exhibited a Δ SOC higher than 1.3%. In other words, 98% of all SOC measurement values exhibited an absolute SOC deviation between the amperometric sensor and the OCV cell in the range from -0.4 to $+1.3\%$. That represents a three-fold lower statistical variation when

compared to the results of the previous study. The situation encountered for the monitoring of the anolyte is slightly different: A RMSD of 2.5% with a variation characterized by a 1% percentile of -0.8 and a 99% percentile of 4.3% was observed.

Despite the equal measurement procedures and the identical compositions of the catholyte and anolyte, the average uncertainty and variation of the SOC estimates is significantly larger for the anolyte.

In order to explain the observed difference, we would like to emphasize the following important aspect of this online experiment: The reference SOC provided by the OCV cell is not the true SOC of the electrolyte. In contrast to the presented RMSDs in the offline experiments of this study, the obtained online monitoring RMSD and statistical variations merely express the difference between the two methods. They do not represent the absolute accuracy of the method with respect to the true electrolyte SOC. Consequently, the cause for the higher average deviation and variation of the anolyte SOC values in comparison to the catholyte SOC values may be found in either (or both) of the methods.

However, it is more likely that the larger uncertainty is originating from the OCV cell based on the following reasoning: The major difference between the measurement data of catholyte and anolyte is the addressed SOC range. Both electrolytes had a similar starting SOC of approximately 42 to 44% (first cycle). The catholyte (the CLS) was subsequently cycled between approximately 0 and 100% SOC. In contrast to that, the anolyte (the NCLS) was cycled between approximately 5 and 75% SOC at the same time. In other words, the anolyte utilized only 70% of its available total capacity. The potential impact of a restricted SOC range on the calibration of the OCV cell data may be significant. Although the non-linear fit for the anolyte's OCV-capacity data exhibited an R^2 value of around 0.997, the missing data range is not necessarily extrapolated correctly by the regression algorithm. To illustrate this issue, the catholyte OCV data of an exemplary cycle was restricted to the same SOC range as the anolyte during the fitting procedure and compared to the full-range fit (Fig. 3a). As can be seen, the partial fit deviates significantly from the experimental data for those data ranges, which were not included for the non-linear regression (white background). This causes a more inaccurate result for the SOC (and the capacity) values obtained from the OCV cell. To further underline this, the restricted SOC range was applied for the non-linear regression in all cycles of the catholyte OCV data and the results are depicted in Figure S6 of the Supporting Information: A similar degree of SOC deviation and variation as observed for the anolyte data was evident (RMSD of 3.6%, a 1% percentile of -0.2% , and a 99% percentile of 7.6%). In contrast to that, the mass-transfer-limited currents displayed in Fig. 3b exhibited a nearly identical linear behavior for both electrolytes regardless of the utilized data range. The larger difference between the SOC data of amperometric and OCV cell method in the anolyte when compared to the catholyte in Fig. 2d can, hence, be fully attributed to the limitations of the OCV cell method. This additionally emphasizes that the quality of the fit and the comparison to coulomb counting as a reference SOC as utilized by Ressel *et al.* and Struckmann *et al.* [17,22] is no reliable accuracy indicator for the OCV cell method. This finding should be considered when re-calibrating the OCV cell during incomplete cycles.

The preceding discussion is equally relevant for the results obtained in other cycling modes: For the incomplete, galvanostatic cycling (cycles 3, 4, and 17; cycles with blue background in Fig. 2), where the catholyte was cycled in a SOC range from approximately 2.5 to 42% and the anolyte was cycled in a SOC range from about 44 to 73%, the deviations between both methods are apparently *vice versa*. As can be inferred from Fig. 2d, the catholyte data for these cycles exhibits a higher average deviation (RMSD: 2.3%) than the anolyte data (RMSD: 0.7%). On the other hand, both show a similar extend of variation around their RMSD (catholyte: 1% percentile: -0.3% , 99% percentile: 5.6% ; anolyte: 1% percentile: -1.4% , 99% percentile: 1.7%). We attribute these results again to the significantly smaller SOC ranges addressed during the incomplete cycles. It is mainly the OCV cell data, which causes the higher deviation and variation between the two methods. This conclusion is supported by the fact that the linearity of the mass-transfer-limited currents recorded in the incomplete cycles are basically identical to those currents recorded during the complete cycles (Fig. 3b).

Finally, a third cycling mode was applied and analyzed. For the mixed galvanostatic and potentiostatic cycling (cycles 0 and 16; cycles with green background in Fig. 2) two noteworthy anomalies were observed in the data sets of both methods:

1. For $SOC < 0.5\%$, the OCV cell data exhibited a deviation from the exponential slope (Fig. 4a).
2. For $SOC < 0.5\%$ and $SOC > 99.5\%$, the mass-transfer-limited currents on the catholyte side deviated from the expected linear behavior (Fig. 2b, orange line on green background).

The development of a second plateau in the open-circuit voltage range between -0.20 V and -0.15 V indicates the presence of a second redox species. In a recent study of our group, the existence of this second species was already reported and ascribed to the formation of a hydroxylamine species, which is a re-oxidizable side product of TEMPTMA degradation.[35] Since this second species influences a small fraction of the curve, the fit result is slightly off if these data points are included in the non-linear regression as illustrated in the inset of Fig. 4a.

With regard to the second observation, the decrease of the mass-transfer-limited currents for $SOC < 0.5\%$ and $SOC > 99.5\%$ is attributed to the natural shift of the counter electrode's equilibrium potential with changing SOC in the two-electrode setup as well as the increasing concentration overpotential for the reaction at the microelectrode. Both effects are discussed in detail in the Supporting Information and are in particular evident at extreme SOC values. Although this deviation in currents would distort a $D_oD_R^{-1}$ determination *via* the regression approach, we would like to stress that it represents no fundamental issue for the method. As evident from Fig. 2c, the SOC values estimated from these currents exhibited no significant deviations. If the online determination of $D_oD_R^{-1}$ is desired, one could either increase the applied voltage or simply exclude the distorted current values during the evaluation.

Consequently, the data points for $SOC < 0.5\%$ were excluded in the OCV cell data for the accuracy comparison of the methods in the mixed galvanostatic and potentiostatic cycling: A similar result for the SOC values as in the previous cycling modes was obtained. The average deviation and variation between both methods in the catholyte was characterized by a RMSD of 0.7%, a 1% percentile of -0.4% , and a 99% percentile of 2.4% , whereas the measurements in the anolyte resulted in a higher RMSD of 2.6%, a 1% percentile of -0.7% , and a 99% percentile of 5.4% . The higher RMSDs and statistical variations are once again caused by the issues of the OCV cell method with restricted SOC ranges.

3.2.2. Capacity measurement

After the validation of the highly accurate SOC measurement capabilities of the amperometric method, the new method for the capacity co-estimation derived in the theoretical section (section 2.2) of this manuscript was investigated. Independent capacity estimates were simultaneously measured *via* the OCV cell method for a direct comparison of the new method to a literature standard method. For additional validation, the absolute electrolyte capacities were also calculated from the volumetric capacity of the electrolyte (33.9 ± 0.7 mAh mL $^{-1}$) and the utilized volumes of the catholyte (17.00 ± 0.02 mL) and anolyte (24.0 ± 0.03 mL) in the RFB.

Fig. 4a exemplifies a plot of the charge transferred between the RFB half-cells, ΔQ , during the first mixed galvanostatic and potentiostatic discharging half-cycle *versus* the open-circuit cell voltages of both electrolytes as well as the corresponding non-linear regression. Fig. 4b displays the state-of-charge, SOC, as obtained by the amperometric sensors in both electrolytes over the transferred charge, ΔQ , for the same half-cycle. According to equation (4), the total capacity of the electrolyte, Q_{max} , can be obtained from the slopes of these ΔQ -SOC-curves. The two procedures were applied to all charging and discharging half-cycles of the 17.5 cycles of this experiment. The catholyte and anolyte capacities are displayed in Fig. 4c and Fig. 4d along with the battery capacity (*i.e.*,

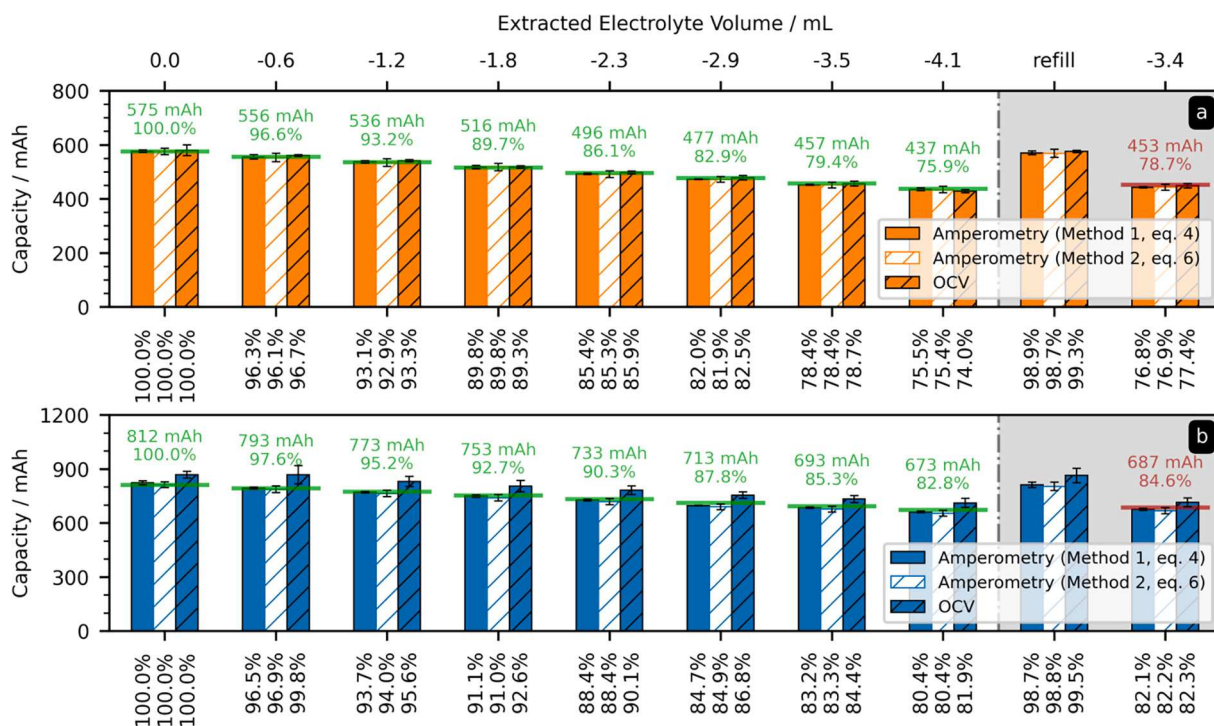


Fig. 5. Absolute capacity (left axes) and state-of-health values (bottom axes) of both electrolytes determined via the amperometric and the OCV cell method after extraction of defined electrolyte aliquots from each tank of the compositionally symmetric, unbalanced RFB (1.3 M TEMPTMA). The green values represent the expected values calculated from the measured aliquot masses, electrolyte density, and volumetric electrolyte capacity (see Table S15, Supporting Information). All experimental values represent the average of four consecutive cycles and the error bars represent their standard deviations. For the left bar group with grey background all aliquots were filled back to the tanks (no reference value given due to the unknown loss of some microliters of electrolyte during aliquot investigation and refilling). For the right bar group, 3.4 mL of electrolyte were extracted and exchanged with distilled water (red reference value is based on the average SOH values of the left bar group). (For interpretation of the references to colour in this figure legend, the reader is referred to the web version of this article.)

the transferred charge, ΔQ) as well as the calculated capacities (green lines) of the catholyte (575 ± 12 mAh) and anolyte (812 ± 16 mAh). As mentioned above, the calculated values were obtained from the known volumes and volumetric capacities of the catholyte and the anolyte.

The experimental results for the different cycling modes are as follows: With experimentally obtained average values of 576 ± 3 mAh (catholyte) and 820 ± 7 mAh (anolyte) for all half-cycles of the complete, galvanostatic cycles (cycles 1 to 2 and cycles 5 to 15), the amperometric capacity estimate is in excellent agreement with the theoretically expected capacity of both electrolytes (relative error: $< 1\%$). While it is also in agreement with the OCV cell capacity estimate for the catholyte (575 ± 4 mAh), the obtained OCV capacity for the anolyte (866 ± 6 mAh) deviates by approximately 6.7% from the expected value. Equal results are obtained for the mixed galvanostatic and potentiostatic cycling mode (cycles 0 and 16).

As discussed for the SOC analysis (section 3.2.2), the larger error of the OCV cell method is a result of the larger uncertainty in the non-linear regression originating from the comparably small SOC range covered by the anolyte. This is additionally confirmed by the capacity estimates obtained during the incomplete, galvanostatic cycles (cycles 3, 4, and 17). While the deviation from the expected value is slightly higher for the amperometric method as well, its relative error remains well below 1% for the catholyte capacity (572 ± 7 mAh) and around 3% for the anolyte capacity (834 ± 21 mAh). In contrast to that, the average error of the OCV cell capacity estimate of the catholyte increases to over 6% (611 ± 43 mAh) due to the restricted SOC range addressed during the incomplete charging/discharging and the corresponding value of the anolyte remains at over 6% (864 ± 8 mAh) for the same reason.

3.2.3. Detection of capacity degradation (State-of-Health)

As discussed in section 2.3, the amperometric capacity co-estimation

can be utilized to measure the electrolyte state-of-health. Based on the promising accuracy observed for the amperometric capacity co-estimation, experiments were performed to validate the method for the capacity loss and state-of-health detection in an operating RFB. The loss of capacity was emulated by extracting electrolyte aliquots of 587 ± 14 μ L from each tank in between consecutive cycling experiments (Table S13, Supporting Information). The theoretically expected decrease of the electrolyte SOH was calculated from the measured mass of the extracted electrolyte volume and the separately determined electrolyte density of 1.073 ± 0.009 g cm^{-3} (Table S12, Supporting Information). The SOH values were calculated for both the amperometric and the OCV cell method.

The capacity data obtained in the 17.5 cycles of the first experiment (Fig. 4c and Fig. 4d) were used as the 100% SOH reference level for either method. For the amperometry, two SOH values per aliquot extraction were determined which represent the two approaches for SOH calculation proposed in the theoretical section (section 2.2) of this study:

1. The explicit determination of the ratio of the electrolyte capacities obtained in the different cycles (equation (4)).
2. The calculation of the SOH directly from the slope of a linear regression of the SOC^0 vs. SOC^n plot (equation (6)).

The capacity values for method (2) were calculated by multiplying the measured SOH with the capacity of the 100% SOH sample. The SOH values for the OCV cell data were calculated from the capacity ratios according to method (1) for comparison as well. Fig. 5 summarizes the obtained results.

The amperometric measurement delivered capacity values which were in excellent agreement with the theoretical capacities. The relative

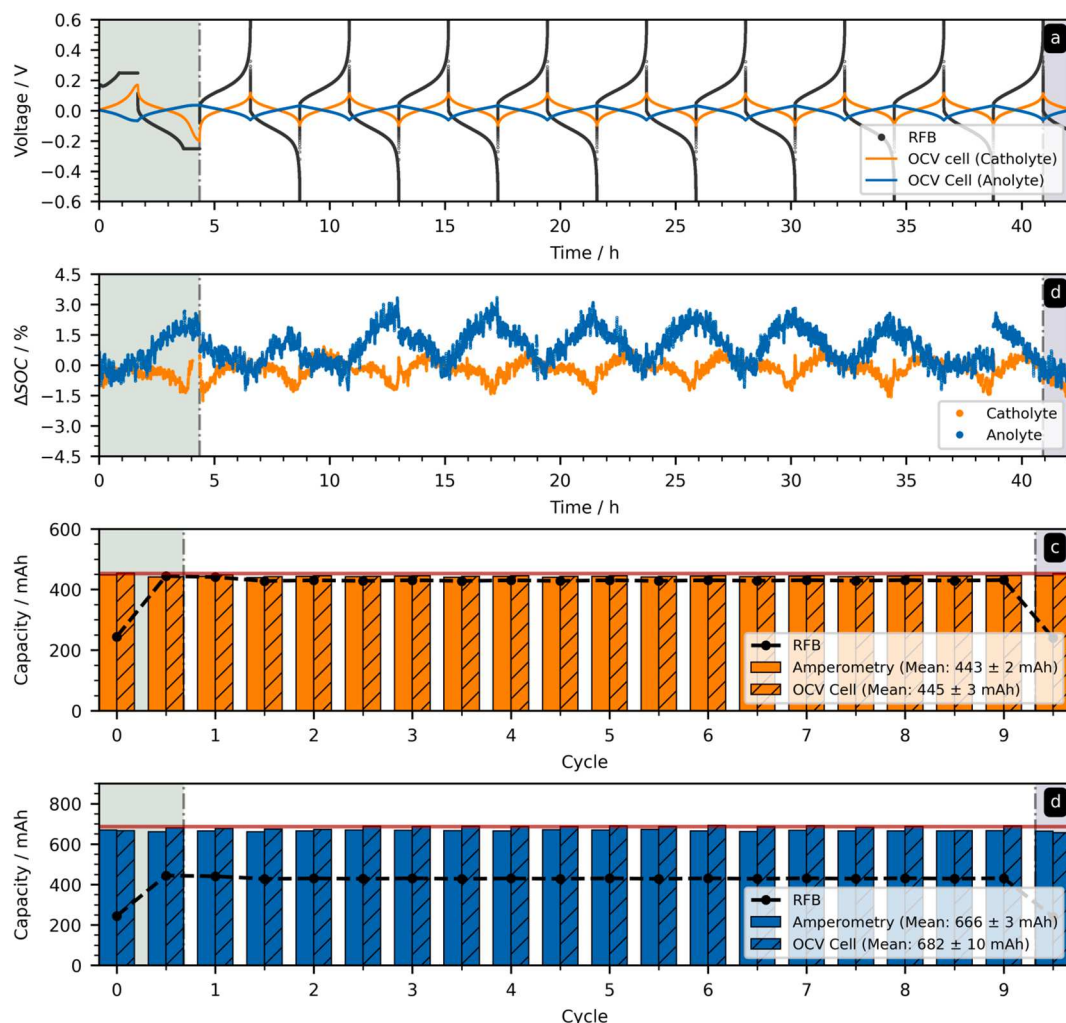


Fig. 6. Results of the online monitoring of the compositionally symmetric, unbalanced RFB (1.04 M and 1.1 M TEMPTMA) at an elevated electrolyte tank temperature of approximately 45 °C: (a) Voltages of the RFB and the OCV cells; (b) difference between the SOC measurement values of the amperometric and the OCV cell method for both electrolytes; (c) catholyte capacities in each half-cycle as obtained by the amperometric and the OCV cell method; (d) anolyte capacities in each half-cycle as obtained by the amperometric and the OCV cell method. (red line: expected capacity as obtained from the last bar group in Fig. 5). Non-integer half-cycles represent the discharging. (For interpretation of the references to colour in this figure legend, the reader is referred to the web version of this article.)

RMSD from the expected value was 0.7% for the catholyte and 1.4% for the anolyte in both method (1) and method (2). As in the previous experiment, the OCV cell capacity measurement was similarly accurate and precise for the catholyte (relative RMSD: 0.9%). The OCV cell based values for the anolyte were again overestimated in all cases (relative RMSD: 7.3%). With respect to the SOH measurement, all methods delivered absolute RMSDs from the expected SOH of below 0.8% for the catholyte. It is noteworthy that despite the higher inaccuracy observed for the capacity measurement of the OCV cell in the anolyte, its SOH estimates agreed well with the expected values.

Indeed, the absolute RMSD from the expected SOH values (1.1%) was 1% lower compared to the RMSD of the amperometric method (2.1%) in the anolyte, which indicates a constant relative error of the capacity estimation for the OCV cell in the investigated capacity range. However, the OCV cell method exhibited a significantly lower precision (*i.e.*, a higher variation of the SOH estimates from cycle to cycle) as can be inferred from the higher standard deviations of the measurement values (2.7 to 6.2%) when compared to the standard deviations of the amperometric values (0.6 to 1.4%). For the amperometric SOH, the

evaluation approaches (1) and (2) were equally accurate. However, the capacity-based method delivered a higher precision as evidenced by the lower standard deviations.

Subsequently, two final validation steps were performed (grey area in Fig. 5): All aliquots were filled back into their tanks. Approximately 99% SOH were regained. Hence, about 0.2 to 0.3 mL of electrolyte were lost for each half-cell during the experiment. Since it is impossible to calculate the theoretically expected loss of this step, no reference value is stated. In a last step, 3.4 mL of electrolyte were extracted from each tank and replaced by deionized water to confirm that not only SOH changes by volume loss but also SOH changes by concentration changes can be correctly assessed by the method. The dilution resulted in total concentrations of 1.04 M (catholyte) and 1.11 M (anolyte) of TEMPTMA. Hence, this experiment imitates a chemical decay of the redox molecule. The reference values for this step are based on the measured SOH values of the previous step and are, hence, not as reliable as the previous reference values. Consequently, the deviation of 2.6% observed between measured and expected values is higher than in the experimental steps before.

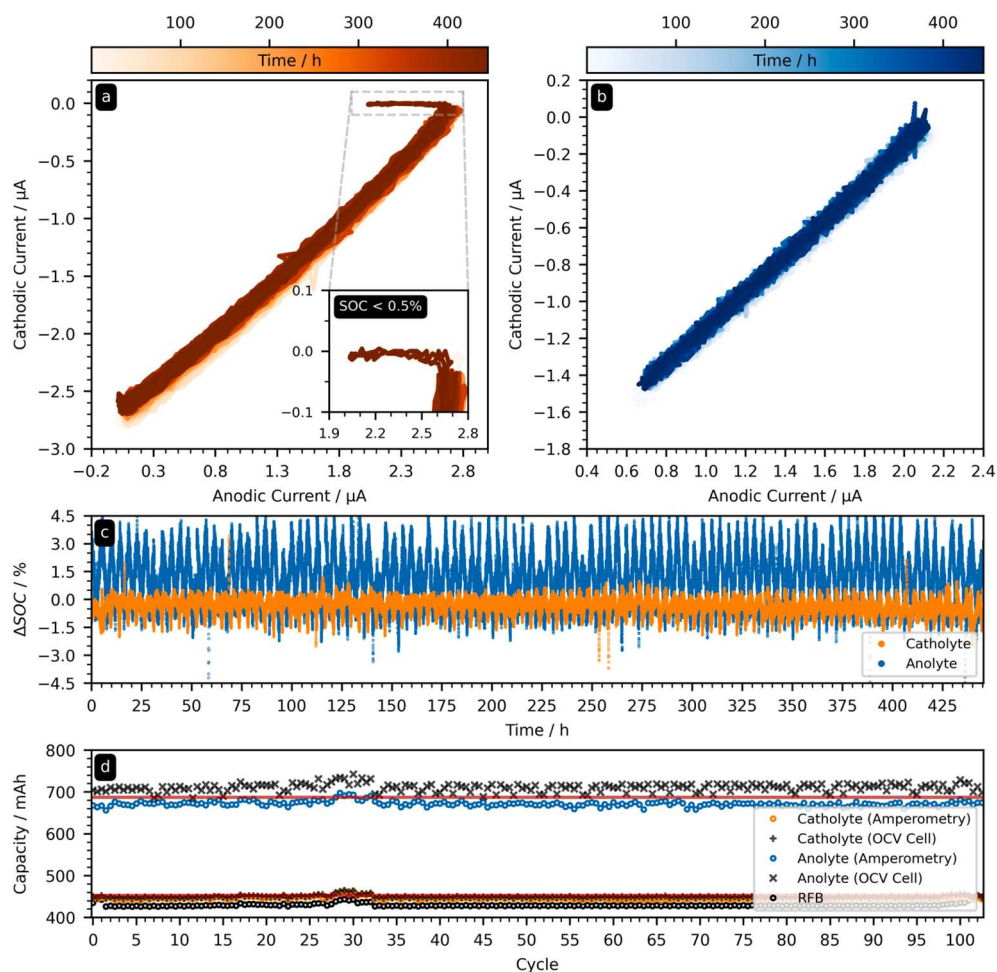


Fig. 7. Results of the long-term online monitoring of the compositionally symmetric, unbalanced RFB (1.3 M TEMPTMA) at room temperature: (a) mass-transfer-limited currents at the microelectrode in the catholyte tank over time; (b) mass-transfer-limited currents at the microelectrode in the anolyte tank over time; (c) difference between the SOC measurement values of the amperometric and the OCV cell method for both electrolytes; (d) capacity measurement values of the amperometric and the OCV cell method in both electrolytes as well as the transferred charge / capacity of the RFB (red line: expected capacity as obtained from the last bar group in Fig. 5). Non-integer half-cycles represent the discharging. (For interpretation of the references to colour in this figure legend, the reader is referred to the web version of this article.)

3.2.4. Monitoring at elevated temperature

The experiments performed under room temperature conditions were highly accurate. However, during the long-term operation of a RFB, temperatures can be expected to vary significantly. Monitoring methods, thus, need to be agnostic to such temperature changes in order to deliver accurate results even under elevated temperatures. Due to the inherent temperature independence of the amperometric SOC monitoring, no knowledge about the electrolyte temperature is required at all. This independence was already experimentally confirmed *via* offline experiments in our previous study.[24]

To investigate if the observed temperature independence also holds under operating conditions and for the co-estimation of capacity and SOH, both electrolyte compartments were placed in a heated oil bath. At an elevated temperature of 45 °C, the compositionally symmetric, unbalanced RFB was cycled for 10 cycles (Fig. 6a). SOC and capacity values for both methods were determined without using the known temperature value for the data analysis.

The SOC measurement results of both methods were comparable to the results obtained at room temperature: In the catholyte, a RMSD of 0.5% (1% percentile: -1.3%, 99% percentile: 0.6%) was observed, while for the anolyte again a slightly higher RMSD of 1.3% (1% percentile: -0.7%, 99% percentile: 2.7%) was obtained. The measured capacity and SOH values for both methods (Fig. 6c and Fig. 6d) were in agreement with each other and with the expected values as well. For the anolyte, a small difference of below 1.5% was observed in comparison to

the previous experiment (Fig. 5, last bar group). However, the results corresponded to the subsequent long-term experiment performed under room temperature (Fig. 7) directly after this experiment. We therefore ascribe this difference to a real loss of capacity due to electrolyte loss that has gone unnoticed during the adjustment of the experimental setup for this temperature experiment.

3.2.5. Long-term monitoring

All experiments in this and the previous study were only operated on time scales ranging from a few hours to a few days so far. However, for the industrial application of RFB sensors and the investigation of electrolyte long-term stabilities, the presented method needs to be reliable for weeks and months. In order to estimate the reliability of the amperometric method for a longer RFB operation, another online monitoring experiment was performed at room temperature using the symmetric RFB with the diluted electrolyte (Fig. 5, last bar group). This RFB was operated for approximately 19 days and performed 103 cycles during which both electrolytes were continuously monitored (Fig. 7).

The only recognizable change of measurement values over time was observed for the minimum values of the cathodic currents at the microelectrode in the catholyte (Fig. 7a and Fig. 7b), which changed from about -2.8 μ A to about -2.7 μ A (*i.e.*, < 4% relative change). Other than that, the experiment indicated no sign of degradation in both half-cells. The deviation of the catholyte current for SOC < 0.5% (Fig. 7a, inset) again originates from the large reference potential shift in the two-

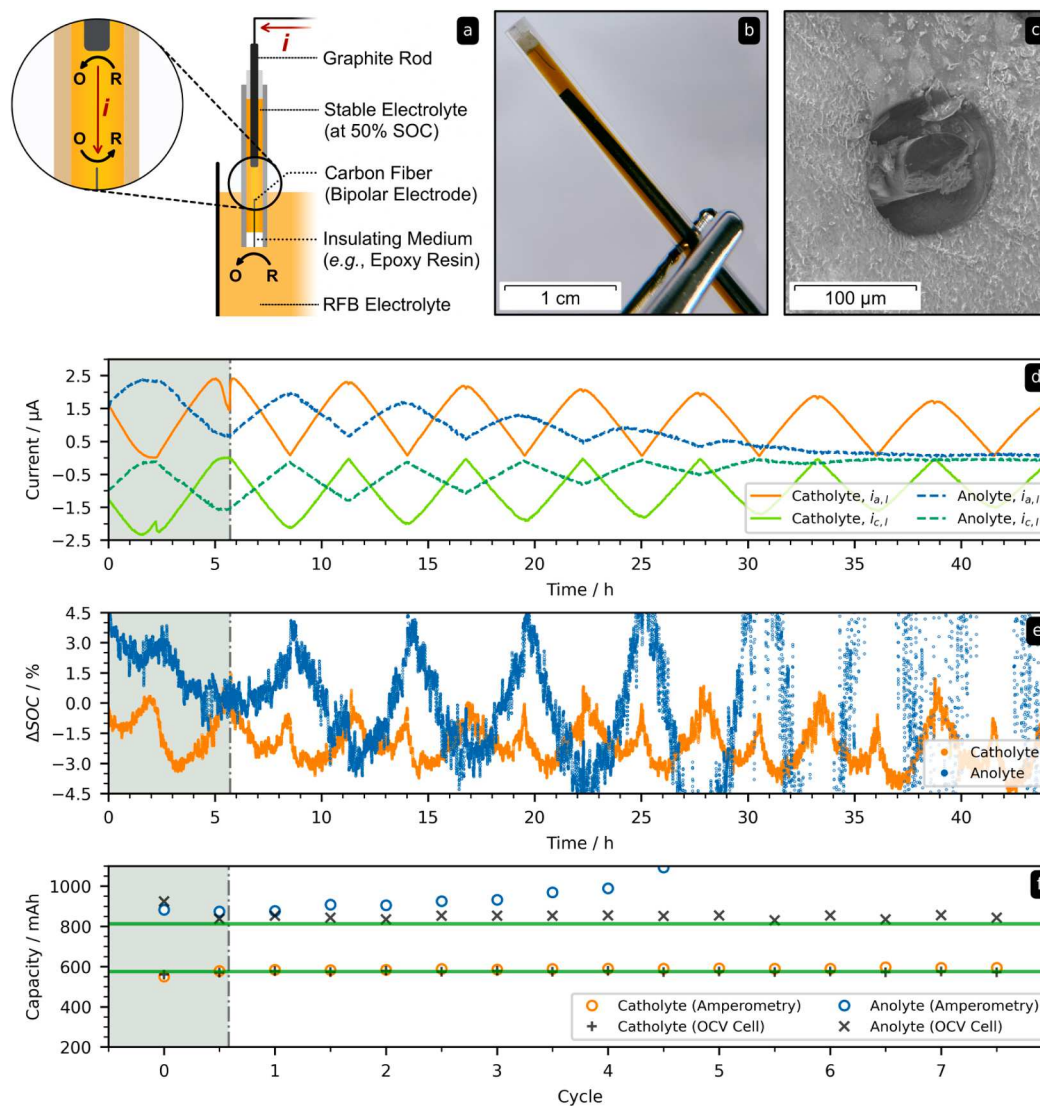


Fig. 8. (a) Schematical representation of a backfilled, bipolar microelectrode (BBME) illustrating the construction and the working principle; (b) photograph of a BBME with carbon fiber, graphite rod (1 mm), and 1.3 M TEMPTMA (42% SOC); (c) scanning electron micrograph of the BBME tip showing the carbon fiber surrounded by epoxy resin; (d) mass-transfer-limited currents of the BBMEs utilized for monitoring of the symmetric TEMPTMA RFB; (e) SOC difference between amperometric method and the OCV cell; (f) capacity estimates obtained from both methods (green line: expected values). (For interpretation of the references to colour in this figure legend, the reader is referred to the web version of this article.)

electrode setup at extreme SOC, which was discussed previously (Fig. 2).

The SOC, capacity, and SOH measurements remained highly reliable over the duration of nearly three weeks (Fig. 7c and Fig. 7d). For the catholyte, an absolute RMSD between amperometric and OCV cell method of 0.6% (1% percentile: -1.5% , 99% percentile: 0.4%) was observed over all 103 cycles. The anolyte monitoring was performed with an absolute RMSD of 2.1% (1% percentile: -1.2% , 99% percentile: 4.2%). Both results are basically identical to the results obtained in the preceding short-term experiments. Fig. 7d displays the capacity measurement values in both electrolytes along with the expected values (Fig. 5, last bar group) and the addressed RFB capacity (i.e., the transferred charge ΔQ). These results are in agreement with the previous results over the complete duration of the experiment as well for both the amperometric method (catholyte: 446 ± 3 mAh and $77.5 \pm 0.7\%$ SOH; anolyte: 672 ± 6 mAh and $81.7 \pm 1.3\%$ SOH) and the OCV cell method

(catholyte: 449 ± 3 mAh and $77.6 \pm 2.7\%$ SOH; anolyte: 710 ± 10 mAh and $81.8 \pm 2.0\%$ SOH). This experiment underlines the reliability of the amperometric method and highlights the degree of stability microelectrodes can deliver despite their small electrode surface.

3.2.6. Cost considerations

Finally, we would like to discuss some cost considerations for this amperometric method. As presented at the beginning of the experimental section (section 3.1), nearly all of the SOC measurements of this study were performed with a low-cost microcontroller-based measurement unit. In contrast to commercial potentiostats, which are designed to fulfill a variety of different and complex tasks, the presented MMU is custom-tailored to perform not more than the task of measuring the electrolyte SOC. This reduces the complexity of the required measurement hardware, the number of built-in components, and, thus, the overall material cost level. In order to illustrate this, Table S1 of the

Supporting Information lists all components of the MMU and the prices paid on initial purchase. Excluding the VAT, a single device was built for material costs of 56 EUR (or approximately \$68 at an exchange rate of 1.22 \$ / EUR (June 2021)). Indeed, 50% of those costs (28 EUR or \$34) were spent on the LCD display and breadboard, which would not be required in a commercial system due to the connection to a central battery management system (BMS) and the use of printed circuit boards and soldered components. Furthermore, this was only a first, unoptimized prototype to demonstrate the low hardware requirements of the amperometric SOC measurement; thus, it can be expected that the cost of a commercialized version of such a device will be significantly lower. For example, components like the real-time clock, the SD card reader, and the microSD card would not be utilized when the measurement unit was embedded into a commercial BMS. Consequently, the controller hardware for an amperometric sensor capable of monitoring both electrolytes of a commercial RFB system simultaneously can be expected to come at costs of well below 40 EUR / \$49.

3.3. Bipolar microelectrodes

As discussed in the previous section, the low cost of the required electronics is an advantage. However, the costs of the microelectrode and the counter electrode have been neglected in our reasoning so far. In the presented prototype, the electrode costs exceed the total costs of the MMU by more than one order of magnitude. Commercial counter electrodes can be replaced by graphite rods ($0.5 \text{ EUR cm}^{-1} / 0.6 \text{ \$ cm}^{-1}$) as was demonstrated during the experiments of this study. Consequently, the microelectrode becomes the cost-determining component of the measurement hardware. The commercial microelectrodes applied in this study are constructed from micrometer-sized wires or fibers. These are melted into a glass tube or capillary and are electrically connected to a cable for connection to an external circuit. Commercial microelectrodes of this type usually cost more than 300 EUR / \$366. Low-cost methods to produce microelectrodes are, therefore, required. Indeed, various approaches for microelectrode fabrication are already known from biosensor applications.[36,37] An alternative approach for the low-cost production of microelectrodes is investigated herein and is based on the principles of bipolar electrochemistry.[38–41]

3.3.1. Working principle

While the conventional microelectrodes for general electroanalytical purposes need to fulfill strong quality requirements such as a defined electrode diameter, the amperometric SOC measurement is rather robust against variations of, e.g., the electrode surface area. Although the electrode diameters influence the currents, the amperometric SOC value is independent of it (see equation (2)). Therefore, it is comparably uncomplicated to manufacture microelectrodes for this task. The arguably most difficult steps are the embedding of the microfiber in an electrically insulating medium and the establishment of a reliable electrical contact between the fiber and a cable for connection to the potentiostat. To circumvent the latter, a backfilled, bipolar microelectrode (BBME) was investigated for this study:[42]

Fig. 8 depicts a BBME as well as its working principle. The details of construction are described in the **Supporting Information**; however, in brief the BBME essentially represents a miniaturized version of the closed bipolar electrode setup described in our previous study.[24] If this electrode is immersed into an analyte solution with a counter electrode and if a voltage is applied between the graphite rod of the BBME and the counter electrode, then the overall current flow is limited by the microelectrode tip of the setup. Instead of directly conducting electrons from the microfiber to the graphite rod as it would be done in conventional microelectrodes, complementary electrochemical reactions at the longer end of the microfiber and at the graphite rod enable a passage of current (**Fig. 8a**). The BBME can be handled identically to

any conventional disk microelectrode. However, care must be taken that the part of the microwire protruding into the tube and the graphite rod have large surface areas compared to the microfiber or microwire tip. The latter is important to keep overpotentials inside the BBME as small as possible. For the study at hand, two electrodes of this kind were constructed from carbon fibers, graphite rods, and plastic tubes (**Fig. 8b**). They were backfilled with a 1.3 M TEMPTMA electrolyte at 42% SOC (see **Supporting Information**).

3.3.2. Characterization and costs

Both BBMEs were applied for the online monitoring of the electrolytes of the symmetric RFB utilized in the previous experiments before electrolyte dilution. **Fig. 8d** displays the mass-transfer-limited currents at the BBMEs, **Fig. 8e** the SOC differences between amperometric and OCV cell method, and **Fig. 8f** the measured capacities for eight consecutive cycles.

Although the BBMEs delivered accurate SOC values in the first four cycles with RMSDs of 1.9% (catholyte) and 2.2% (anolyte), the precision was significantly lower (catholyte: 1% percentile: -3.3% , 99% percentile: 0.8% ; anolyte: 1% percentile: -5.1% , 99% percentile: 4.6%) when compared to the commercial microelectrodes (see section 3.2). For the remaining cycles, the measurement error increases rapidly. With regard to the capacity measurement, the catholyte values (mean: $586 \pm 11 \text{ mAh}$) were in good agreement with the expected value. For the anolyte capacities, the values are off by more than 12% (mean: $909 \pm 33 \text{ mAh}$) during the first four cycles and increase further during the last four cycles.

The significantly inferior results of the BBME compared to the commercial microelectrode are related to the extreme decay of the mass-transfer-limited currents (**Fig. 8d**), which was particularly strong for the BBME on the anolyte side. This decay was reversible by electrode polishing, which indicates that surface changes during the electrochemical reactions at the utilized carbon fibers are the cause for the severe degradation observed in the experiment. However, EDX measurements of the pure carbon fibers were inconspicuous (**Figure S2, Supporting Information**) and EDX measurements at the BBME fiber tip revealed an interference by the surrounding epoxy resin which made a reliable evaluation impossible. It may also be that the epoxy resin caused some surface contamination of the fiber and/or exhibited unknown side reactions with the highly oxidative RFB electrolyte. While the exact cause for the observed current degradation remains unknown at this point and needs to be investigated in future studies, **Fig. 8c** emphasizes another issue: The carbon fiber was not tightly surrounded by the resin; hence, no planar and disk-shaped microelectrode surface was formed. This indicates a shrinkage of the epoxy resin during the hardening procedure indicating that the specific material combination is not ideal.

Although the presented results clearly demand further investigations and improvements, they also confirm two important things: (1) The bipolar electrochemical mechanisms for current conduction inside a BBME represents a viable replacement for establishing a direct electrical contact to the carbon fiber and (2) the BBME can deliver accurate SOC as well as capacity measurements as exemplified by the catholyte measurement results of the first cycles. The stability observed for commercial carbon fiber microelectrodes during the long-term experiments of this study (**Fig. 7**) justifies an optimistic perspective for the future optimization of the BBME stability.

Considering that the purchased 3 m of FEP tubing (36 EUR / \$44) and the 15 mL of two-component glue (6 EUR / \$7) can be used for the construction of at least 50 BBMEs and that the costs of a single carbon fiber are negligible, one BBME of the presented type can be constructed for material costs of not more than 2 EUR / \$2 in under 15 min by a trained person. Although the personnel costs, the energy costs, and alike cannot be estimated, the pure material cost of a BBME can be regarded as negligible.

4. Conclusion

In this study, a recently proposed amperometric method for the temperature-independent and concentration-independent state-of-charge (SOC) measurement of individual redox flow battery (RFB) electrolytes has been significantly enhanced and extended. The accuracy of the SOC measurement was increased by one order of magnitude to absolute root-mean-square deviations (RMSD) of below 0.5% from the true sample SOC. Furthermore, the method's diagnostic capabilities were extended for the online co-estimation of the individual electrolyte capacity and state-of-health (SOH). This approach was successfully applied for the simultaneous online monitoring of both anolyte and catholyte in an operating RFB. Relative RMSDs from the true sample capacity of 0.7 to 1.4% have been obtained with the amperometric method as well as absolute RMSDs of 0.6 to 2.1% in the SOH measurement. In a direct comparison, the amperometric method outperformed the simultaneously applied OCV cell method with regard to precision and accuracy in nearly all experiments. To the best of our knowledge, these results render the enhanced amperometric method the most accurate method available for the simultaneous SOC and capacity measurement on the electrolyte level to date.

Furthermore, the method's accuracy has proven to be largely independent from the investigated SOC range, temperature variations, concentration changes, the duration of the experiment, and the utilized redox couple (including vanadium RFB electrolytes). However, distinct studies investigating larger temperature ranges, redox couples with more complicated electrochemical properties (e.g., two-electron reactions, dimerization, polymers, etc.), and the impact of sensor position on the SOC measurement need to be performed to further unravel the full potential as well as the exact limitations of this method.

For the demonstration of the cost advantages, all amperometric SOC measurements were performed with the prototype of a microcontroller-based measurement unit (MMU) developed specifically for this method. Material cost calculations indicate that two MMUs can be manufactured for total material costs of well below 40 EUR (\$49). In addition, preliminary experiments with backfilled, bipolar microelectrodes (BBME) were performed to investigate an inexpensive pathway for the microelectrode fabrication on a laboratory scale. However, the BBME stability was insufficient most-likely due to incompatibilities between fiber and electrolyte with the sealing medium (epoxy). Upcoming studies will continue the investigation of inexpensive approaches for the preparation of microelectrodes and alternative, low-cost electrode types.

The ability to measure the electrolyte SOC, capacity, and SOH at the presented, benchmark-setting accuracy level enables the detailed

assessment of electrolyte stabilities and battery degradation mechanisms in operating RFBs. The remarkable diagnostic potential of the amperometric method in both offline/*ex-situ* and online/*in-situ* measurements can speed up the RFB development and will enable a safer and more reliable RFB operation at significantly lower costs.

CRedit authorship contribution statement

Christian Stolze: Conceptualization, Methodology, Software, Investigation, Data curation, Formal analysis, Writing – original draft. **Philip Rohland:** Investigation, Formal analysis, Writing – original draft, Writing – review & editing. **Karina Zub:** Investigation, Writing – review & editing. **Oliver Nolte:** Investigation, Writing – review & editing. **Martin D. Hager:** Supervision, Writing – review & editing. **Ulrich S. Schubert:** Supervision, Writing – review & editing, Funding acquisition.

Declaration of Competing Interest

The authors declare that they have no known competing financial interests or personal relationships that could have appeared to influence the work reported in this paper.

Acknowledgement

We gratefully acknowledge the financial support by the Thuringian Ministry for Economic Affairs, Science and Digital Society (TMWwG) (CEEC-01/2020), and the Thüringer Aufbaubank (TAB). The project on which these results are based was funded by the Free State of Thuringia under the number 2016 IZN 0009 and co-financed by funds from the European Union within the framework of the European Regional Development Fund (ERDF). The SEM facilities of the Jena Center for Soft Matter (JCSM) were established with a grant from the German Research Council (DFG).

Data Statement

The data that supports the findings of this study are available within the article and its [supplementary material](#). In addition, the original data files of this study are available from the corresponding author upon reasonable request.

Appendix: Abbreviations & Symbols

Table 3

Table 3
List of abbreviations used in this study.

Abbreviation	Description
BBME	Backfilled, bipolar microelectrode
BMS	Battery management system
CLS, NCLS	Capacity-limiting side, Non-capacity-limiting side
FB	Flow battery
MMU	Microcontroller-based measurement unit
OCV	Open-circuit voltage
RFB	Redox flow battery
RMSD	Root-mean-square deviation
SOC	State-of-charge
SOH	State-of-health
TEMPTMA	<i>N,N,N</i> -2,2,6,6-heptamethylpiperidinyloxy-4-ammonium chloride
<i>r</i>	Radius of disk microelectrode
$SOC^n(t)$	State-of-charge of an electrolyte as function of time in the n^{th} cycle
SOH^n	State-of-health of an electrolyte in the n^{th} cycle
<i>t</i>	Time
ΔQ	Total amount of charge transferred between RFB half-cells
Q_{max}	Total capacity of an electrolyte

Table 4

Table 4

List of mathematical symbols used in this study.

Symbol	Unit	Description
c_O, c_R	mol L^{-1}	Concentration of oxidized / reduced species
D_O, D_R	$\text{cm}^2 \text{s}^{-1}$	Diffusion coefficient of oxidized / reduced species
F	C mol^{-1}	Farraday constant
$i(t)$	A	Current flowing in the redox flow cell
$i_{t,a}, i_{t,c}$	A	Anodic / cathodic mass-transfer-limited current
n	1	Number of transferred electrons
r	m	Radius of disk microelectrode
$SOCh^n(t)$	%	State-of-charge of an electrolyte as function of time in the n^{th} cycle
SOH^n	%	State-of-health of an electrolyte in the n^{th} cycle
t	s	Time
$\Delta Q(t)$	Ah	Total amount of charge transferred between RFB half-cells
Q_{max}^n	Ah	Total capacity of an electrolyte (in the n^{th} cycle)

Appendix A. Supplementary data

Supplementary data to this article can be found online at <https://doi.org/10.1016/j.ecmx.2022.100188>.

References

- [1] Wei X, Pan W, Duan W, Hollas A, Yang Z, Li B, et al. ACS Energy Lett. 2017;2:2187.
- [2] Chen H, Cong G, Lu Y-C. J. Energy Chem. 2018;27:1304.
- [3] Dinesh A, Olivera S, Venkatesh K, Santosh MS, Priya MG, Inamuddin AM, et al. Environ. Chem. Lett. 2018;16:683.
- [4] Singh V, Kim S, Kang J, Byon HR. Nano Res. 2019. <https://doi.org/10.1007/s12274-019-2355-2>.
- [5] Li M, Rhodes Z, Cabrera-Pardo JR, Minter SD. Sustainable Energy Fuels 2020;4:4370.
- [6] Li Z, Lu YC. Adv. Mater. 2020;32:e2002132.
- [7] Sánchez-Díez E, Ventosa E, Guarnieri M, Trovò A, Flox C, Marcilla R, et al. J. Power Sources 2021;481:228804.
- [8] Arenas LF, Ponce de León C, Walsh FC. J. Energy Storage 2017;11:119.
- [9] Brushett FR, Aziz MJ, Rodby KE. ACS Energy Lett. 2020;5:879.
- [10] Kwabi DG, Ji Y, Aziz MJ. Chem Rev 2020;120:6467.
- [11] Nolte O, Volodin IA, Stolze C, Hager MD, Schubert US. Mater. Horiz. 2021;8:1866.
- [12] Yao YX, Lei JF, Shi Y, Ai F, Lu YC. Nat. Energy 2021. <https://doi.org/10.1038/s41560-020-00772-8>.
- [13] Goulet M-A, Aziz MJ. J. Electrochem. Soc. 2018;165:A1466.
- [14] Kowalski JA, Fenton AM, Neyhouse BJ, Brushett FR. J. Electrochem. Soc. 2020. <https://doi.org/10.1149/1945-7111/abb7e9>, 160513.
- [15] Jirabovornwisut T, Arpornwicheanop A. Int. J. Hydrogen Energy 2019;44:24485.
- [16] Perry ML, Saraidaridis JD, Darling RM. Curr. Opin. Electrochem. 2020;21:311.
- [17] Ressel S, Bill F, Holtz L, Janshen N, Chica A, Flower T, et al. J. Power Sources 2018;378:776.
- [18] Haisch T, Ji H, Weidlich C. Electrochim. Acta 2020;336.
- [19] Knehr KW, Kumbur EC. Electrochem. Commun. 2011;13:342.
- [20] Watt-Smith MJ, Ridley P, Wills RGA, Shah AA, Walsh FC. J. Chem. Technol. Biotechnol. 2013;88:126.
- [21] Li X, Xiong J, Tang A, Qin Y, Liu J, Yan C. Appl. Energy 2018;211:1050.
- [22] Struckmann T, Kuhn P, Ressel S. Electrochim. Acta 2020;362:137174.
- [23] Nolte O, Geitner R, Hager MD, Schubert US. Adv. Energy Mater. 2021;11.
- [24] Stolze C, Meurer JP, Hager MD, Schubert US. Chem. Mater. 2019;31:5363.
- [25] Kroner I, Becker M, Turek T. Batteries 2019;5:5.
- [26] B. Neyhouse, K. Tenny, Y.-M. Chiang and F. Brushett, DOI: 10.33774/chemrxiv-2021-snn5p (2021).
- [27] Bard AJ, Faulkner LR. Electrochemical methods : Fundamentals and applications. 2nd ed. USA: John Wiley & Sons Inc; 2001.
- [28] Yuan XZ, Song C, Platt A, Zhao N, Wang H, Li H, et al. Int. J. Energy Res. 2019;43:6599.
- [29] Stolze C, Hager MD, Schubert US. J. Power Sources 2019;423:60.
- [30] Wei Z, Bhattarai A, Zou C, Meng S, Lim TM, Skyllas-Kazacos M. J. Power Sources 2018;390:261.
- [31] Wei Z, Xiong R, Lim TM, Meng S, Skyllas-Kazacos M. J. Power Sources 2018;402:252.
- [32] Konopka SJ, McDuffie B. Anal. Chem. 1970;42:1741.
- [33] Amatore C, Szunerits S, Thouin L, Warkocz JS. Electrochem. Commun. 2000;2:353.
- [34] Darling RM, Perry ML. ECS Trans. 2013;53:31.
- [35] O. Nolte, P. Rohland, N. Ueberschaar, M. D. Hager and U. S. Schubert, J. Power Sources 2022, *accepted*, DOI: 10.1016/j.jpowsour.2022.230996.
- [36] Adly N, Weidlich S, Seyock S, Brings F, Yakushenko A, Offenhäusser A, et al. npj Flexible Electron. 2018. <https://doi.org/10.1038/s41528-018-0027-z>.
- [37] Schnitker J, Adly N, Seyock S, Bachmann B, Yakushenko A, Wolfrum B, et al. Adv. Biosyst. 2018;2:1700136.
- [38] Mavre F, Anand RK, Laws DR, Chow KF, Chang BY, Crooks JA, et al. Anal. Chem. 2010;82:8766.
- [39] Fosdick SE, Knust KN, Scida K, Crooks RM. Angew. Chem. Int. Ed. Engl. 2013;52:10438.
- [40] Sequeira CAC, Cardoso DSP, Gameiro MLF. Chem. Eng. Commun. 2016;203:1001.
- [41] Fakhrudin SMB, Inoue KY, Tsuga R, Matsue T. Electrochem. Commun. 2018;93:62.
- [42] Zhong P, Yu P, Wang K, Hao J, Fei J, Mao L. Analyst 2015;140:7154.

- Supporting Information -

A low-cost amperometric sensor for the combined state-of-charge, capacity, and state-of-health monitoring of redox flow battery electrolytes

Christian Stolze^{1,2}, Philip Rohland^{1,2}, Karina Zub^{1,3}, Oliver Nolte^{1,2}, Martin D. Hager^{1,2}, Ulrich S. Schubert^{1,2,3*}

¹ Laboratory of Organic and Macromolecular Chemistry (IOMC), Friedrich Schiller University Jena, Humboldtstraße 10, 07743 Jena, Germany.

² Center for Energy and Environmental Chemistry Jena (CEEC Jena), Friedrich Schiller University Jena, Philosophenweg 7a, 07743 Jena, Germany.

³ Jena Center for Soft Matter (JCSM), Philosophenweg 7, 07743 Jena, Germany.

Corresponding Author

*E-Mail: ulrich.schubert@uni-jena.de

CRedit author statement

Christian Stolze: Conceptualization, Methodology, Software, Investigation (equal), Formal analysis (lead), Data curation, Visualization, Writing – original draft (lead) • **Philip Rohland:** Investigation (equal), Formal analysis (supporting), Writing – original draft (supporting), Writing – review and editing: critical review (equal) • **Karina Zub:** Investigation (supporting), Writing – review and editing: critical review (equal) • **Oliver Nolte:** Investigation (supporting), Writing – review and editing: critical review (equal) • **Martin D. Hager:** Writing – review and editing: critical review (equal), Supervision of P.R. and O.N. (equal), Funding acquisition (equal) • **Ulrich S. Schubert:** Writing – review and editing: critical review (equal), Supervision of P.R., K.Z. and O.N. (equal), Funding acquisition (equal).

22 TABLE OF CONTENTS

Materials & Electrolyte Preparation	S3
Experimental Setups	S4
Experimental Methods: Accuracy of the Reference Sample Preparation	S10
Experimental Methods: Offline SOC Measurements & Data Treatment	S11
Experimental Methods: Online Monitoring Methods & Data Treatment	S17
The Impact of Sensor Position	S19
Determination of $D_O D_R^{-1}$ for Online Monitoring	S20
Accuracy of Analyte (NCLS) Data & Incomplete Cycles	S21
Limiting Currents at Extreme SOCs	S23
Capacity Loss & SOH Measurements	S24
Elevated Temperatures & Long-Term Experiments	S28
Measurement Uncertainties of SOC and SOH Measurements in Literature	S29

24 **Materials and Experimental Setups**

25 **Chemicals.** Potassium chloride (Fisher Scientific Ltd., United Kingdom), sodium chloride ($\geq 99.5\%$,
26 Fisher Scientific Ltd., United Kingdom), potassium ferricyanide (Sigma-Aldrich, USA), potassium
27 ferrocyanide trihydrate (Sigma-Aldrich, USA), *N,N,N*-2,2,6,6-heptamethylpiperidinyloxy-4-ammonium
28 chloride (TEMPTMA, **Figure S3a**) and *N,N'*-dimethyl-4,4-bipyridinium dichloride (methyl viologen,
29 MV) were used as received and diluted to the desired concentration with deionized water.

30 **Electrolyte preparation.** Appropriate amounts of potassium ferro- and ferricyanide were weight into
31 25 mL volumetric flask (A-Grade, ± 0.04 mL Schott AG, Germany) with a XS205 Dual Rand balance
32 (± 0.01 mg, Mettler Toledo, USA) to produce 0.4 M solutions with states-of-charge (SOC) of 1%, 5%,
33 25%, 50%, 75%, 95%, and 99%. Afterwards, the volumetric flasks were filled up with 0.5 M aq.
34 potassium chloride solution and shaken till the solids completely dissolved. For lower concentrated
35 solutions (0.2 M or 0.1 M), 10 mL potassium ferro- and ferricyanide solution (0.4 M or 0.2 M) were
36 diluted with 10 mL of 0.5 M aq. potassium chloride solution. For the volumetric measurement's 10 mL
37 volumetric pipettes (A-Grade, ± 0.02 mL, Schott AG, Germany) were used. For the online monitoring
38 experiments with the compositionally symmetric, unbalanced RFB, 25.0 ± 0.5 mL of the 1.3 M aq.
39 TEMPTMA solution were galvanostatically charged with 400 mA vs. 30 ± 1 mL of 1.3 M aq. MV
40 solution. After the limiting voltage of 1.45 V was reached, the cell was further charged potentiostatically
41 until the current decreased to 0.5 mA cm^{-2} . The electrolyte's volumetric capacity ($33.9 \pm 0.7 \text{ mAh mL}^{-1}$)
42 was calculated from the total charge of 846.1 mAh transferred during the charging process and the
43 electrolyte volume. The obtained electrolyte was mixed with 25 mL of the uncharged 1.3 M TEMPTMA
44 solution to obtain the starting solution for the symmetric RFB. For the volume measurements, 5 mL and
45 20 mL syringes (Injekt® Solo, 5 ± 0.1 mL, 20 ± 0.5 mL, M Braun Melsungen AG, Germany) were used.

46 **Microcontroller-based Measurement Unit (MMU).** The SOC measurement device was constructed
 47 from simple, commercially available electronic components (**Table S1**). A programmable Arduino Nano
 48 microcontroller was used as the control and computing unit.

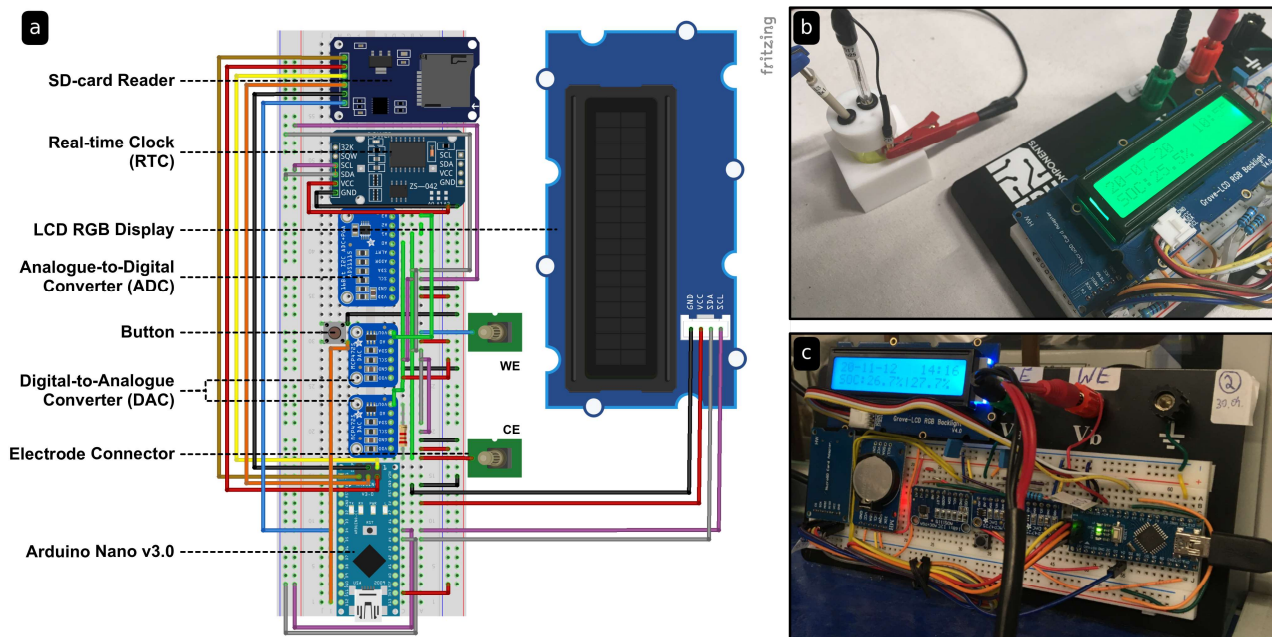
49 **Table S1.** Electronic components of the microcontroller-based measurement unit and their costs as paid on initial purchase.

Component	Supplier	Number / Amount	Total Cost ^[*]
Arduino Nano V3	az-delivery.de	5	€19.99
HTC TC-E250 incl. USB Cable	Amazon.de	5	€34.00
SEED Studio Grove RGB Display	conrad.de	5	€59.50
DS3231 RTC Real Time Clock	az-delivery.de	5	€12.49
Analogue-to-Digital Converter (ADS1115) with I2C-Interface	az-delivery.de	5	€19.99
Digital-to-Analogue Converter (MCP4725)	elmicro.com	5	€33.23
SPI Reader Micro SD Card Module	az-delivery.de	5	€6.99
SanDisk Ultra® microSDHC-Card 32 GB Class 10	conrad.de	5	€39.95
Tru Components EIC-102B Breadboard	conrad.de	5	€108.10
Ohmic Resistors (2.2 kOhm)	conrad.de	5	€0.24
Total costs (incl. German VAT, 19%):			€334.48
Total costs (excl. German VAT, 19%):			€281.08
Single Device Costs (excl. German VAT, 19%):^[#]			€56.22
Extrapolated Single Device Costs (excl. German VAT, 19%):^[§]			€19.07

50 ^[*] Costs of the given number of components, which represents the cost of the same component for five identical MMU
 51 prototypes (incl. German VAT of 19%).

52 ^[#] Cost of a single MMU, which can monitor a single electrolyte, as calculated from the total cost divided by five.

53 ^[§] Cost of a single MMU, if optimized for cost reduction by exchanging unnecessarily expensive components (i.e., the
 54 breadboard would be exchanged by inexpensive printed circuit board, LCD is not required as well if the MMU is integrated
 55 into a battery management system).



56

57 **Figure S1.** The microcontroller-based measurement unit for the amperometric SOC and capacity measurements represented
 58 as (a) the fritzing scheme of the electrical circuit, (b) a photograph with the offline measurement setup, and (c) a photograph
 59 during online measurements.

60 The fritzing scheme in **Figure S1a** illustrates the exact circuit layout used for the MMU prototype in this
 61 study. The device can be programmed to follow any kind of amperometric measurement procedure. For
 62 the SOC monitoring in this study, the device was programmed to periodically apply discrete cathodic
 63 and anodic voltage steps applied between the two electrodes followed by an equilibration period at zero
 64 volts. The mass-transfer limited currents were determined *via* the voltage drop measurement over the
 65 shunt resistor, to calculate the SOC using a $D_O D_R^{-1} = 1$ (or any other pre-defined value) and the voltages,
 66 currents, and SOC values were stored on a microSD card together with a timestamp from the RTC for
 67 optional data evaluation on a PC. The utilized breadboard and the RGB liquid crystal display for manual
 68 read-out represented in principle unnecessary components, which were utilized in this study for
 69 convenience purposes during experimentation only. An optimized MMU would utilize an inexpensive
 70 printed circuit board (PCB) instead of the expensive TRU component breadboard and a LCD would also

71 not be required, since the sensor data is recorded on a SD card or would be gathered by a central battery
72 management system in industrial applications. Consequently, **Table S1** lists both the true material costs
73 of the prototype (56.22 EUR) and the expected costs without the unnecessarily expensive components
74 (19.07 EUR). It can be expected that further optimizations of the MMU and economy of scale would
75 bring down the costs of a single sensor even more.

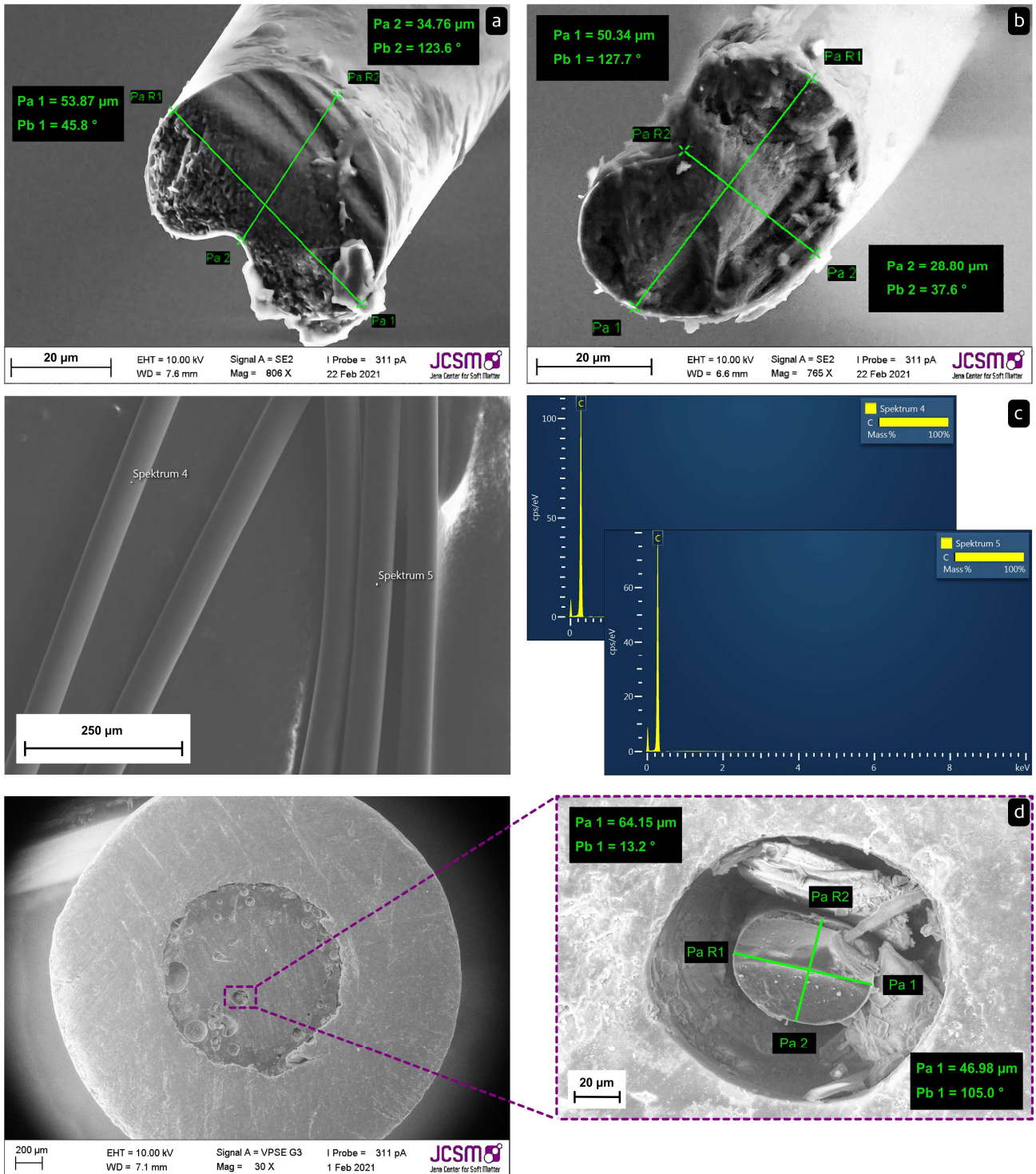
76 ***Symmetric Open-circuit Voltage (OCV) Cell.*** The OCV cells were used to measure electrolyte SOC
77 with a well-accepted monitoring method during online experiments with the compositionally symmetric,
78 unbalanced TEMPTMA RFB in both half-cells. The details of construction of those cells were described
79 in a previous study and the exact same procedure was used herein.¹ A 1.3 M aq. TEMPTMA solution at
80 approximately 50% SOC was used as reference electrolyte for the symmetric OCV cells.

81 ***Redox Flow Cell.*** A filter-press type redox flow cell (membrane active area: 5 cm², design: JenaBatteries
82 GmbH, Germany) was utilized. Prior to installation, a FAA-3-50 (Fumasep GmbH, Germany) ion-
83 selective membrane was cut into appropriate pieces and was pre-wetted for at least 24 h in 1.5 M sodium
84 chloride solution. GFA-6 (SGL SE, Germany) graphite felts were used as porous electrodes. The
85 electrolyte was pumped through the cell at 25 mL min⁻¹ using a membrane pump (Simdos 10, KNF
86 Neuberger, Germany). Tygon[®] A-60-G (inner diameter: 1.6 mm, outer diameter: 4.8 mm, Saint-Gobain,
87 France) tubes were utilized for the electrolyte flow. Detailed information about the cell design was
88 published in previous publications.²

89

90 **Backfilled, Bipolar Microelectrode (BBME).** Polyacrylonitrile (PAN) fibers (diameter: $\sim 70\ \mu\text{m}$; length:
91 $\sim 1\ \text{cm}$) were kindly provided by STW Schwarzwälder Textilwerke (Germany) and carbonized by SGL
92 Carbon. **Figure S2a** to **Figure S2c** shows scanning electron micrographs and EDX measurements for
93 the obtained carbon fibers. A carbon content of over 99.6% is evident and the fibers had an oval to
94 kidney-like shape with diameters varying between $50\ \text{to}\ 70\ \mu\text{m}$ (long axis) and $29\ \text{to}\ 35\ \mu\text{m}$ (short axis),
95 respectively. For the construction of a BBME, one of these carbon fibers was encapsulated at the tip of
96 a fluorinated ethylene propylene (FEP) tube (inner diameter: $1.6\ \text{mm}$, length: $6\ \text{cm}$, BGB Analytik
97 Vertrieb GmbH) using a two-component glue (epoxy resin, STANGER, Germany). At the one end, the
98 fiber tip forms a planar area with the resin (*i.e.*, this area is polished to form a planar disk microelectrode),
99 whereas the fiber freely protrudes into the FEP tube at the other side. The tube was subsequently filled
100 with a small portion of the RFB electrolyte at approximately 50% SOC and a graphite rod (diameter:
101 $1\ \text{mm}$, MERSEN GmbH) was inserted into this solution. Subsequently, the electrode was sealed at the
102 top using Parafilm[®]. **Figure S2d** displays SEM images of one of the BBMEs recorded after it was utilized
103 for the online monitoring.

104 **Offline SOC Measurement Setup.** Commercial gold disk microelectrodes (diameter: $25\ \mu\text{m}$), a gold
105 macroelectrode (diameter: $2\ \text{mm}$), and small volume voltammetry cells ($5\ \text{mL}$) with PTFE cap were
106 purchased from BioLogic, France. The amperometric offline SOC measurements were performed in a
107 two-electrode setup where the microelectrode was used as working electrode and the macroelectrode as
108 counter electrode. A Keithley 2400 Source Measure Unit (SMU) (Keithley Instruments, USA) or a self-
109 made MMU (**Figure S1b**) were used for application of the voltages between the two electrodes and for
110 the measurement of the current response. The measurement values were recorded manually.

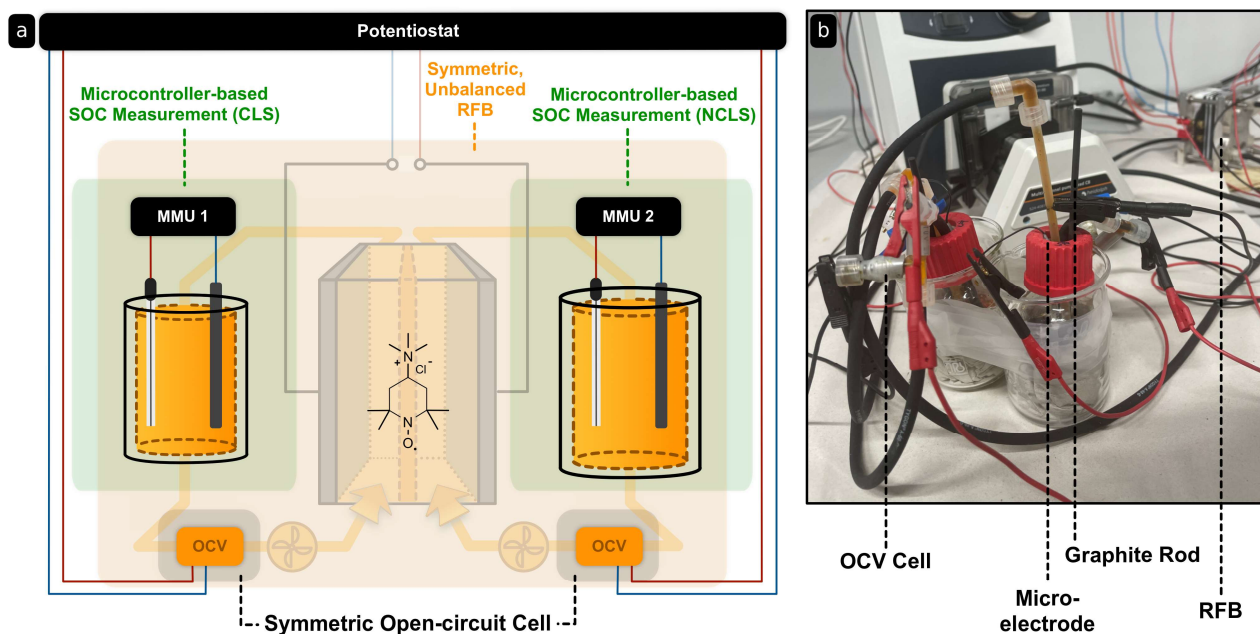


111

112 **Figure S2.** Scanning electron microscopy (SEM) of (a) a first carbonized PAN fiber and (b) a second carbonized PAN fiber;

113 (c) SEM and EDX of the carbonized fibers indicating a complete carbonization; (d) SEM of the assembled BBME tip after it

114 was used for online SOC monitoring. The fiber is glued into a FEP tube with epoxy resin.



115

116 **Figure S3.** (a) Schematic representation and (b) photograph of the setup used for the online monitoring experiments with
 117 the compositionally symmetric, unbalanced TEMPTMA/TEMPTMA RFB (orange background). For the CLS (catholyte) an
 118 electrolyte volume of 17.00 ± 0.04 mL was used, while the NCLS (anolyte) contained 24.00 ± 0.03 mL. Each tank contained
 119 either carbon-fiber microelectrode (diameter: $33 \mu\text{m}$) or a BBME as well as a graphite rod (diameter: 3 mm) connected to a
 120 microcontroller-based measurement unit (MMU, green background) for amperometric SOC monitoring. OCV cells (gray
 121 background) were added for reference SOC measurements.

122 **Online SOC and Capacity Monitoring Setup.** For the online/*in-situ* SOC monitoring a compositionally
 123 symmetric, unbalanced RFB was used with the previously prepared 1.3 M TEMPTMA electrolyte. The
 124 capacity-limiting side (CLS, catholyte) contained an electrolyte volume of 17.00 ± 0.04 mL whereas the
 125 non-capacity-limiting side (NCLS) contained 24.00 ± 0.03 mL of the same electrolyte. The electrolytes
 126 were filled into 25 mL glass bottles (Duran[®] GL45, Schott AG, Germany) using 5 mL and 10 mL
 127 volumetric pipettes (A-Grade: 5 ± 0.01 mL, 10 ± 0.02 mL, Schott AG, Germany) and piston pipettes
 128 (Transferpette[®] S 100 to 1000 μL , $1000 \pm 6 \mu\text{L}$, Brand GmbH & Co. KG, Germany). The bottles were
 129 sealed with a membrane screw cap (screw cap: BOLA PPS EX, GL45, borehole $\varnothing = 34$ mm, Bohlender

130 GmbH, Germany, membrane: silicon elastomer with PTFE coating, 3.3 mm thickness). A glassy carbon
131 microelectrode (diameter: 33 μm , BioLogic, France) and a graphite rod (diameter: 3 mm, Mersen GmbH,
132 Germany) was inserted into each of the two electrolyte tanks. The electrode pair of each tank was
133 connected to a MMU (**Figure S1**) for the amperometric SOC measurements. The electrolyte tubing inside
134 the tanks was placed as far away as possible from the electrodes and the tube feeding back the electrolyte
135 into the tank was placed in a way that caused the electrolyte to run down the inner wall of the bottle. The
136 latter was done to minimize the electrolyte convection in the tank. An open-circuit cell for each half-cell
137 was placed before the redox flow cell's electrolyte inlet. **Figure S3** displays the complete setup utilized
138 for all online monitoring experiments. The RFB as well as the OCV cells were controlled with a 16-
139 channel VMP3 potentiostat/galvanostat (BioLogic, France). For instrument control and data acquisition
140 the EC-LAB software version 11.26 was used.

141 **Experimental Methods**

142 *Accuracy of the Reference Sample Preparation.* In the previous study,³ ferri-/ferrocyanide solutions at
143 different SOCs were prepared by mixing potassium ferricyanide solutions with pure, separately prepared
144 potassium ferrocyanide solutions using a microbalance (± 0.01 mg uncertainty) and a 50 mL graduated
145 cylinder (± 0.5 mL uncertainty). Furthermore, the mixing procedure was conducted using 1 mL syringes
146 (± 0.01 mL uncertainty). While not properly taken into account in the initial study, this sample
147 preparation method caused an absolute uncertainty of up to $\pm 1\%$ in the reference SOC values according
148 to Gaussian error propagation. In other words, the uncertainty in the sample preparation already might
149 have constituted a significant part of the reported RMSDs of 4.3% (50 mM ferri-/ferrocyanide solutions)
150 and 2.2% (500 mM ferri-/ferrocyanide solutions) observed in the the offline SOC measurement. To rule
151 out errors originating from the inaccuracy of the reference SOC, the ferri-/ferrocyanide samples utilized
152 in the offline experiments of the present study were prepared by weighing and, subsequently, mixing the

153 dry substances. From these dry mixtures, the aqueous solutions of the corresponding reference SOC were
154 subsequently obtained. The performed mass measurements during repeated sample preparation were
155 accurate to approximately ± 1.2 mg resulting in an absolute uncertainty of the reference SOC value of
156 below $\pm 0.04\%$. For the study at hand, different total concentrations (100 mM, 200 mM, and 400 mM)
157 of ferri-/ferrocyanide solutions at defined SOC of 1%, 5%, 25%, 50%, 75%, 95%, and 99% were
158 prepared from the corresponding potassium salts in aqueous 0.5 M KCl solutions. The 400 mM samples
159 were prepared four times separately to assess statistical variations of the sample preparation, while the
160 lower concentrations were prepared by subsequent dilution of the 400 mM solutions of each SOC.

161 **Offline SOC Measurements.** The accuracy of the amperometric SOC measurement method was assessed
162 in ferri-/ferrocyanide solutions. All measurements were performed using the Keithley 2400 SMU and the
163 MMU, respectively, to evaluate the accuracy of the MMU as well. In all offline experiments, the mass-
164 transfer limited currents were recorded at the end of voltage steps to +0.5 V and -0.5 V with a step
165 duration of 30 s. Subsequent to each current measurement, the electrolyte was gently shaken and
166 equilibrated for 30 s. After both the anodic and the cathodic mass-transfer limited currents were recorded,
167 the electrodes were cleaned, polished, and dried to include the statistical variations arising from small
168 surface area changes at the microelectrode during electrode cleaning. For each sample, the measurement
169 was repeated three times. SOC were determined for each measurement separately. The average and the
170 standard deviation of all measurements performed in the same concentration and the same SOC were
171 calculated and are stated in **Table 1** (Keithley SMU) and **Table 2** (MMU) of the manuscript. All offline
172 experiments were performed at room temperature (294 K) without active temperature control. The results
173 of each single measurement (three measurements per batch) are stated in the following **Table S2** to **Table**
174 **S11**.

175 **Table S2.** Measurement results batch 1 of the 0.4 M ferri-/ferrocyanide solutions performed with the Keithley 2400 SMU
 176 potentiostat. ΔSOC and ΔSOC_R represent the deviation between the measured and the true sample SOC.

SOC_{true} %	$i_{l,a}$ nA			$i_{l,c}$ nA			$\bar{i}_{l,a}$ nA	$\bar{i}_{l,c}$ nA	$\Delta SOC^{[*]}$ %	$\Delta SOC_R^{[+]}$ %
	1 st	2 nd	3 rd	1 st	2 nd	3 rd	Mean	Mean	Mean	Mean
98.96	12.5	12.7	13.7	-1,225	-1,220.4	-1,214.2	13.0	-1,219.9	0.01	0.01
95.01	56.3	57.3	56.2	-1,154.2	-1,141.1	-1,138.3	56.6	-1,144.5	0.27	0.28
75.01	286.2	296.6	297.2	-919.2	-942.4	-946.6	293.3	-936.1	1.13	1.15
50.02	607.5	616.3	605.3	-631.4	-638.8	-635.0	609.7	-635.1	1.00	1.02
25.03	896.2	920.8	932.1	-315.9	-318.9	-320.7	916.4	-318.5	0.76	0.78
5.06	1,165.2	1,177.8	1,138.0	-64.1	-65.0	-64.8	1,160.3	-64.6	0.22	0.22
1.06	1,117.7	1,249.5	1,215.2	-13.3	-13.5	-13.3	1,194.1	-13.4	0.05	0.05
$D_O D_R^{-1}$	1.031	0.972	0.994					RMSD	0.65	0.66

177 ^[*] Calculated from the mean values of the currents and $D_O D_R^{-1} = 1$.

178 ^[+] Calculated from the mean values of the currents and the mean $D_O D_R^{-1} = 0.999$ determined by regression of $\bar{i}_{l,c}$ vs. $\bar{i}_{l,a}$.

179

180 **Table S3.** Measurement results batch 1 of the 0.4 M ferri-/ferrocyanide solutions performed with the microcontroller-based
 181 measurement unit (MMU). ΔSOC and ΔSOC_R represent the deviation between the measured and the true sample SOC.

SOC_{true} %	$i_{l,a}$ nA			$i_{l,c}$ nA			$\bar{i}_{l,a}$ nA	$\bar{i}_{l,c}$ nA	$\Delta SOC^{[*]}$ %	$\Delta SOC_R^{[+]}$ %
	1 st	2 nd	3 rd	1 st	2 nd	3 rd	Mean	Mean	Mean	Mean
98.96	11	14	21	-1,225	-1,220	-1,227	15	-1,226	0.19	0.19
95.01	61	61	50	-1,145	-1,145	-1,134	57	-1,141	0.20	0.22
75.01	282	300	289	-913	-945	-931	290	-929	1.20	1.26
50.02	610	614	606	-635	-649	-642	610	-642	1.26	1.35
25.03	895	920	913	-328	-303	-328	909	-319	0.98	1.05
5.06	1,167	1,174	1,145	-68	-50	-71	1,162	-63	0.08	0.10
1.06	1,156	1,238	1,213	-25	-25	-4	1,202	-18	0.42	0.42
$D_O D_R^{-1}$	1.007	0.986	0.996					RMSD	0.78	0.83

182 ^[*] Calculated from the mean values of the currents and $D_O D_R^{-1} = 1$.

183 ^[+] Calculated from the mean values of the currents and the mean $D_O D_R^{-1} = 0.996$ determined by regression of $\bar{i}_{l,c}$ vs. $\bar{i}_{l,a}$.

184 **Table S4.** Measurement results batch 2 of the 0.4 M ferri-/ferrocyanide solutions performed with the Keithley 2400 SMU
 185 potentiostat. ΔSOC and ΔSOC_R represent the deviation between the measured and the true sample SOC.

SOC_{true} %	$i_{l,a}$ nA			$i_{l,c}$ nA			$\bar{i}_{l,a}$ nA	$\bar{i}_{l,c}$ nA	$\Delta SOC^{[*]}$ %	$\Delta SOC_R^{[+]}$ %
	1 st	2 nd	3 rd	1 st	2 nd	3 rd	Mean	Mean	Mean	Mean
98.96	14.6	18.0	17.0	-1,227.6	-1,250.8	-1,253.2	16.5	-1,243.9	0.27	0.30
95.03	61.7	61.5	62.5	-1,216.2	-1,217.6	-1,230.6	61.9	-1,221.5	0.15	0.07
74.98	310.3	307.2	306.4	-966.5	-961.4	-955.4	308.0	-961.1	0.75	0.44
50.00	619.6	627.0	629.0	-645.4	-652.4	-653.4	625.4	-650.4	0.97	0.55
25.02	900.8	939.4	918.8	-236.1	-323.9	-322.8	919.7	-294.3	0.78	1.09
4.99	1,155.5	1,198.4	1,188.7	-65.7	-66.3	-66.1	1,180.9	-66.0	0.30	0.22
1.01	1,264.1	1,271.0	1,248.4	-13.3	-13.4	-13.4	1,261.2	-13.4	0.04	0.02
$D_O D_R^{-1}$	1.031	1.000	1.021					RMSD	0.57	0.51

186 ^[*] Calculated from the mean values of the currents and $D_O D_R^{-1} = 1$.

187 ^[+] Calculated from the mean values of the currents and the mean $D_O D_R^{-1} = 1.017$ determined by regression of $\bar{i}_{l,c}$ vs. $\bar{i}_{l,a}$.

188

189 **Table S5.** Measurement results batch 2 of the 0.4 M ferri-/ferrocyanide solutions performed with the microcontroller-based
 190 measurement unit (MMU). ΔSOC and ΔSOC_R represent the deviation between the measured and the true sample SOC.

SOC_{true} %	$i_{l,a}$ nA			$i_{l,c}$ nA			$\bar{i}_{l,a}$ nA	$\bar{i}_{l,c}$ nA	$\Delta SOC^{[*]}$ %	$\Delta SOC_R^{[+]}$ %
	1 st	2 nd	3 rd	1 st	2 nd	3 rd	Mean	Mean	Mean	Mean
98.96	07	021	18	-1,242	-1,242	-1,238	15	-1,241	0.18	0.20
95.03	61	061	68	-1,181	-1,213	-1,238	63	-1,211	0.00	0.05
74.98	300	293	303	-970	-970	-956	299	-965	1.39	1.19
50.00	614	628	621	-660	-653	-646	621	-653	1.25	0.98
25.02	906	920	920	-239	-314	-318	915	-290	0.94	1.14
4.99	1,177	1,119	1,167	-54	-68	-68	1,181	-63	0.10	0.04
1.01	1,259	1,266	1,245	-18	-39	-18	1,257	-25	0.94	0.92
$D_O D_R^{-1}$	1.016	0.991	1.027					RMSD	0.87	0.81

191 ^[*] Calculated from the mean values of the currents and $D_O D_R^{-1} = 1$.

192 ^[+] Calculated from the mean values of the currents and the mean $D_O D_R^{-1} = 1.011$ determined by regression of $\bar{i}_{l,c}$ vs. $\bar{i}_{l,a}$.

193 **Table S6.** Measurement results batch 3 of the 0.4 M ferri-/ferrocyanide solutions performed with the Keithley 2400 SMU
 194 potentiostat. ΔSOC and ΔSOC_R represent the deviation between the measured and the true sample SOC.

SOC_{true} %	$i_{l,a}$ nA			$i_{l,c}$ nA			$\bar{i}_{l,a}$ nA	$\bar{i}_{l,c}$ nA	$\Delta SOC^{[*]}$ %	$\Delta SOC_R^{[+]}$ %
	1 st	2 nd	3 rd	1 st	2 nd	3 rd	Mean	Mean	Mean	Mean
99.01	14.1	18.3	17.7	-1,251.9	-1,226.9	-1,196.5	16.7	-1,225.1	0.35	0.41
94.98	59.4	61.1	61.6	-1,155.1	-1,194.9	-1,196.6	60.7	-1,182.2	0.13	0.08
74.94	297.7	302.7	295.9	-932.5	-949.1	-943.0	298.8	-941.5	0.97	0.15
49.97	601.3	609.1	618.9	-627.2	-636.9	-639.1	609.8	-634.4	1.02	0.09
25.02	892.7	880.7	877.0	-310.2	-315.0	-314.4	883.7	-313.2	1.15	0.30
5.04	1,155.3	1,130.7	1,155.2	-63.4	-63.2	-64.3	1,147.1	-63.6	0.21	0.00
1.00	1,172.1	1,181.3	1,148.8	-12.5	-13.2	-13.0	1,167.4	-12.9	0.09	0.05
$D_O D_R^{-1}$	1.037	1.056	1.044					RMSD	0.57	0.51

195 ^[*] Calculated from the mean values of the currents and $D_O D_R^{-1} = 1$.

196 ^[+] Calculated from the mean values of the currents and the mean $D_O D_R^{-1} = 1.045$ determined by regression of $\bar{i}_{l,c}$ vs. $\bar{i}_{l,a}$.

197

198 **Table S7.** Measurement results batch 3 of the 0.4 M ferri-/ferrocyanide solutions performed with the microcontroller-based
 199 measurement unit (MMU). ΔSOC and ΔSOC_R represent the deviation between the measured and the true sample SOC.

SOC_{true} %	$i_{l,a}$ nA			$i_{l,c}$ nA			$\bar{i}_{l,a}$ nA	$\bar{i}_{l,c}$ nA	$\Delta SOC^{[*]}$ %	$\Delta SOC_R^{[+]}$ %
	1 st	2 nd	3 rd	1 st	2 nd	3 rd	Mean	Mean	Mean	Mean
99.01	18	14	18	-1,245	-1,206	-1,184	17	-1,212	0.36	0.40
94.98	54	68	57	-1,163	-1,177	-1,202	60	-1,181	0.21	0.07
74.98	293	296	296	-924	-942	-945	295	-937	1.11	0.59
49.97	606	621	617	-639	-649	-635	615	-641	1.08	0.36
25.02	892	895	888	-328	-314	-310	892	-317	1.23	0.68
5.04	1,156	1,138	1,152	-61	-61	-64	1,149	-62	0.08	0.06
1.00	1,167	1,184	1,195	-11	-14	-11	1,182	-12	0.01	0.02
$D_O D_R^{-1}$	1.033	1.031	1.023					RMSD	0.76	0.40

200 ^[*] Calculated from the mean values of the currents and $D_O D_R^{-1} = 1$.

201 ^[+] Calculated from the mean values of the currents and the mean $D_O D_R^{-1} = 1.029$ determined by regression of $\bar{i}_{l,c}$ vs. $\bar{i}_{l,a}$.

202 **Table S8.** Measurement results of the 0.2 M ferri-/ferrocyanide solutions performed with the Keithley 2400 SMU potentiostat.
 203 ΔSOC and ΔSOC_R represent the deviation between the measured and the true sample SOC.

SOC_{true} %	$i_{l,a}$ nA			$i_{l,c}$ nA			$\bar{i}_{l,a}$ nA	$\bar{i}_{l,c}$ nA	$\Delta SOC^{[*]}$ %	$\Delta SOC_R^{[+]}$ %
	1 st	2 nd	3 rd	1 st	2 nd	3 rd	Mean	Mean	Mean	Mean
99.01	6.5	6.5	6.4	-660.6	-659.8	-659.2	6.4	-659.8	0.03	0.04
94.98	32.2	31.8	033.2	-647.7	-640.8	-657.9	32.4	-648.8	0.26	0.34
74.94	169.3	160.9	148.7	-534.7	-516.0	-498.4	159.6	-516.4	1.44	1.74
49.97	341.4	328.1	338.8	-361.4	-352.5	-354.6	336.1	-356.2	1.48	1.89
25.02	515.2	503.4	516.9	-183.2	-179.9	-179.9	511.8	-181.0	1.11	1.43
5.04	624.1	625.2	648.4	-36.4	-36.0	-36.1	632.5	-36.2	0.36	0.45
1.00	689.7	680.5	674.1	-8.5	-11.1	-7.4	681.4	-9.0	0.30	0.33
$D_O D_R^{-1}$	0.991	0.986	0.974					RMSD	0.91	1.14

204 ^[*] Calculated from the mean values of the currents and $D_O D_R^{-1} = 1$.

205 ^[+] Calculated from the mean values of the currents and the mean $D_O D_R^{-1} = 0.984$ determined by regression of $\bar{i}_{l,c}$ vs. $\bar{i}_{l,a}$.

206

207 **Table S9.** Measurement results of the 0.2 M ferri-/ferrocyanide solutions performed with the microcontroller-based
 208 measurement unit (MMU). ΔSOC and ΔSOC_R represent the deviation between the measured and the true sample SOC.

SOC_{true} %	$i_{l,a}$ nA			$i_{l,c}$ nA			$\bar{i}_{l,a}$ nA	$\bar{i}_{l,c}$ nA	$\Delta SOC^{[*]}$ %	$\Delta SOC_R^{[+]}$ %
	1 st	2 nd	3 rd	1 st	2 nd	3 rd	Mean	Mean	Mean	Mean
99.01	7	7	7	-664	-667	-646	7	-659	0.06	0.04
94.98	36	36	29	-653	-635	-653	34	-647	0.07	0.17
74.98	168	161	139	-535	-507	-489	156	-510	1.65	2.04
49.97	339	335	346	-350	-357	-342	340	-350	0.73	1.29
25.02	528	503	510	-178	-182	-186	513	-182	1.14	1.57
5.04	631	631	660	-36	-39	-29	640	-35	0.09	0.20
1.00	678	678	671	-11	-7	-11	675	-10	0.41	0.44
$D_O D_R^{-1}$	0.999	0.986	0.949					RMSD	0.82	1.11

209 ^[*] Calculated from the mean values of the currents and $D_O D_R^{-1} = 1$.

210 ^[+] Calculated from the mean values of the currents and the mean $D_O D_R^{-1} = 0.978$ determined by regression of $\bar{i}_{l,c}$ vs. $\bar{i}_{l,a}$.

211 **Table S10.** Measurement results of the 0.1 M ferri-/ferrocyanide solutions performed with the Keithley 2400 SMU
 212 potentiostat. ΔSOC and ΔSOC_R represent the deviation between the measured and the true sample SOC.

SOC_{true} %	$i_{l,a}$ nA			$i_{l,c}$ nA			$\bar{i}_{l,a}$ nA	$\bar{i}_{l,c}$ nA	$\Delta SOC^{[*]}$ %	$\Delta SOC_R^{[+]}$ %
	1 st	2 nd	3 rd	1 st	2 nd	3 rd	Mean	Mean	Mean	Mean
99.02	4.28	4.4	4.8	-339.7	-339.0	-341.1	4.5	-339.9	0.33	0.47
94.96	17.1	17.1	16.9	-333.7	-332.2	-329.9	17.0	-331.9	0.16	0.32
74.98	80.8	81.9	81.4	-265.0	-265.6	-264.7	81.4	-265.1	1.54	0.30
50.03	165.8	164.0	161.7	-180.1	-178.8	-179.1	163.8	-179.4	2.23	0.26
25.02	244.1	244.2	242.6	-89.0	-89.6	-89.2	243.6	-89.3	1.80	0.11
5.04	312.0	314.3	302.4	-18.9	-89.6	-18.2	309.6	-18.5	0.62	0.11
0.97	293.5	297.7	29.5	-4.1	-3.8	-4.5	295.5	-4.1	0.41	0.28
$D_O D_R^{-1}$	1.103	1.093	1.118					RMSD	1.27	0.29

213 ^[*] Calculated from the mean values of the currents and $D_O D_R^{-1} = 1$.

214 ^[+] Calculated from the mean values of the currents and the mean $D_O D_R^{-1} = 1.105$ determined by regression of $\bar{i}_{l,c}$ vs. $\bar{i}_{l,a}$.

215

216 **Table S11.** Measurement results of the 0.1 M ferri-/ferrocyanide solutions performed with the microcontroller-based
 217 measurement unit (MMU). ΔSOC and ΔSOC_R represent the deviation between the measured and the true sample SOC.

SOC_{true} %	$i_{l,a}$ nA			$i_{l,c}$ nA			$\bar{i}_{l,a}$ nA	$\bar{i}_{l,c}$ nA	$\Delta SOC^{[*]}$ %	$\Delta SOC_R^{[+]}$ %
	1 st	2 nd	3 rd	1 st	2 nd	3 rd	Mean	Mean	Mean	Mean
99.02	14	14	1	-334	-338	-334	10	-335	1.82	2.05
94.96	4	7	43	-317	-313	-327	18	-319	0.30	0.72
74.98	71	78	82	-256	-256	-249	77	-254	1.74	0.29
50.03	167	185	164	-167	-181	-185	172	-178	0.78	1.20
25.02	238	206	232	-98	-85	-85	225	-89	3.37	1.79
5.04	317	302	299	-7	-18	-14	306	-13	0.94	1.24
0.97	303	299	299	-18	-1	-11	300	-10	2.25	2.01
$D_O D_R^{-1}$	1.026	1.092	1.130					RMSD	1.87	1.47

218 ^[*] Calculated from the mean values of the currents and $D_O D_R^{-1} = 1$.

219 ^[+] Calculated from the mean values of the currents and the mean $D_O D_R^{-1} = 1.083$ determined by regression of $\bar{i}_{l,c}$ vs. $\bar{i}_{l,a}$.

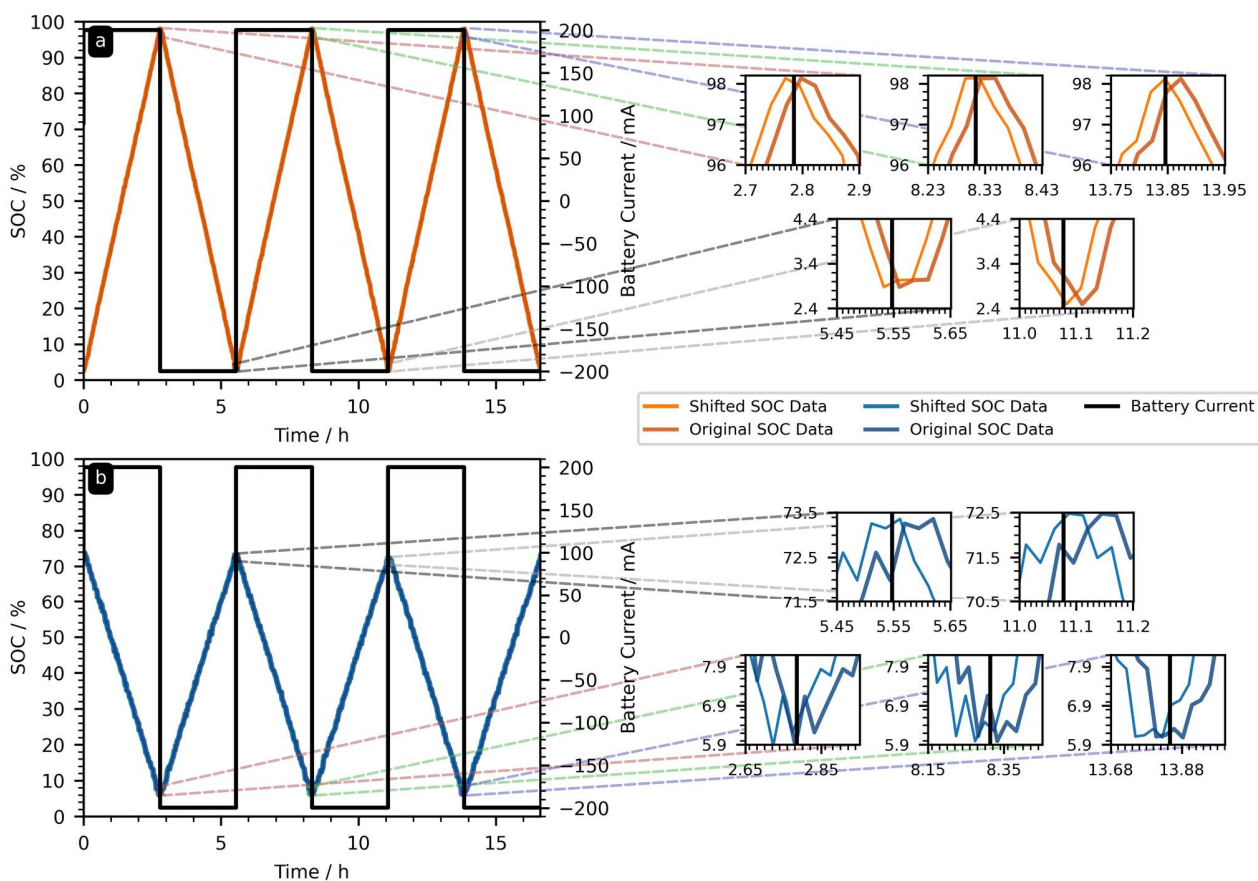
220 **Online Monitoring Methods.** Three channels of the VMP3 potentiostat were synchronized to operate the
 221 RFB and OCV cells simultaneously. For the RFB charging and discharging, three different cycling
 222 modes were applied: (1) Mixed galvanostatic and potentiostatic cycling in which the RFB was
 223 galvanostatically charged/discharged at ± 200 mA to the cell voltage limits of ± 0.6 V directly followed
 224 by a potentiostatic hold time till the cell current decreased to 0.5 mA cm^{-2} ; (2) complete, galvanostatic
 225 charging at currents of ± 200 mA with cell voltage limits of ± 0.6 V; (3) incomplete galvanostatic cycles
 226 at currents of ± 200 mA starting from a completely charged or discharged state until the RFB's open-
 227 circuit voltage reached 0 V (*i.e.*, equal electrolyte SOC_s in both half-cells). The voltage of the OCV cells
 228 used for SOC monitoring was recorded by the other two VMP3 channels in 5 s intervals. The OCV cells
 229 were re-calibrated during data treatment in each half-cycle by using the method introduced by Ressel *et*
 230 *al.* recently.^{4,5} A non-linear regression was performed on the measured OCV-capacity data based on a
 231 combination of coulomb counting and the Nernst equation:

$$E_{OCV} = E_{ref} \pm \frac{RT}{nF} \ln \left(\frac{\Delta Q + Q_0}{Q_{max} - \Delta Q - Q_0} \right). \quad (1)$$

232 Herein, E_{ref} is the reference potential of the OCV cell, R is the gas constant, T is the electrolyte
 233 temperature, F is the Faraday's constant, ΔQ is the charge transferred during (dis)charging, Q_{max} is the
 234 electrolyte capacity, and Q_0 represents the initial charge stored in the electrolyte. E_{ref} , Q_{max} , and Q_0 are
 235 the calibration parameters obtained from the non-linear regression. To calculate the SOC for the OCV
 236 cells in all experiments of this study, the resulting fit curve was utilized. The obtained voltage values of
 237 this curve were used to calculate the SOC according to the rearranged Nernst equation:

$$SOC_{OCV} = \frac{1}{1 + \exp \left[\mp \frac{nF}{RT} (E_{OCV} - E_{ref}) \right]}. \quad (2)$$

238 These SOC values were applied as reference values for comparison with the SOC values obtained from
 239 the amperometric method. Furthermore, the electrolyte capacities Q_{max} which resulted from the non-
 240 linear regression during each half-cell represent the capacity values stated for the OCV cells throughout
 241 this study. The signs in both equations have to be chosen accordingly depending on the electrolyte type
 242 (catholyte, anolyte) and whether a charging or discharging process was performed. For the amperometric
 243 SOC measurement with the MMU, voltage steps of ± 0.25 V were applied for 30 s between the electrodes
 244 and the mass-transfer limited currents were recorded at the end of the step.



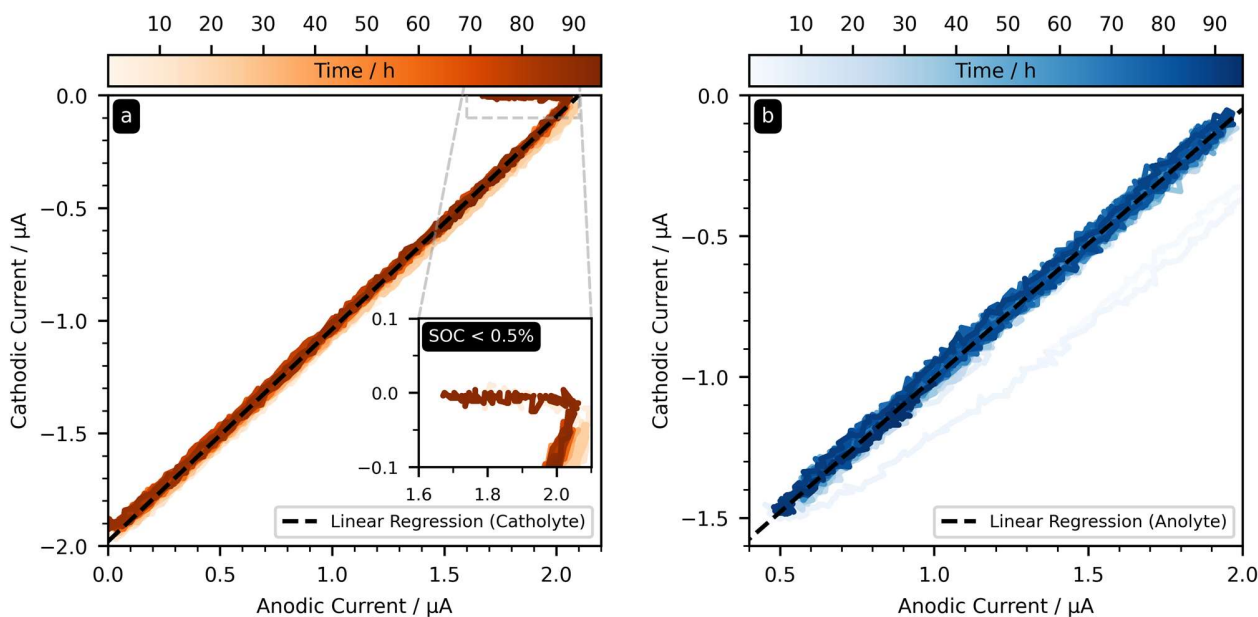
245
 246 **Figure S4.** Amperometric SOC and current data for (a) the catholyte (CLS) and the anolyte (NCLS) for exemplary cycles of
 247 the compositionally symmetric, unbalanced 1.3 M TEMPTMA/TEMPTMA RFB. The zoom insets illustrate how the original
 248 data was shifted in time to correct for the experimental time differences.

249 A 30 s rest period at 0 V was performed for equilibration between the anodic and cathodic voltage steps.
250 The procedure yielded one SOC value every 90 s. Differences in the SOC measurement values between
251 the OCV cell method and the amperometric method, ΔSOC_i , were calculated for all N data points of each
252 experiment. Root-mean-square deviations (RMSD) were calculated from the ΔSOC_i according to
253 $\sqrt{N^{-1} \sum_i^N \Delta SOC_i^2}$. The measurements of the VMP3 and the MMU were started simultaneously. Time
254 differences between the OCV cell and amperometric SOC data were compensated during data treatment
255 and a constant value of $D_O D_R^{-1} = 0.9471 \pm 0.0004$ was utilized for the amperometric SOC evaluation.
256 The procedures to determine the time difference as well as the $D_O D_R^{-1}$ value are detailed in the following
257 two sections.

258 ***The Impact of Sensor Position.*** The position of any SOC sensor in a RFB system has a significant impact
259 on the measurement because it only reflects the local electrolyte environment of the sensor. SOC changes
260 in the electrolyte require time to take effect at the sensor location even during pumped RFB operation.
261 The comparison of the amperometric and OCV cell sensors in the present study is, therefore, complicated
262 by this circumstance. As illustrated in **Figure S3**, the amperometric sensors were positioned in the tanks,
263 whereas the OCV cells were placed at the tank outlet. Due to the delay in electrolyte mixing, there is an
264 expected time difference between the SOC signal of the OCV cell and the amperometric sensor. In
265 addition to that, the MMU operated with independent RTCs which were not ideally synchronized with
266 the PC controlling the potentiostat. As a consequence, time differences between the SOC signals of both
267 sensors varied from a few seconds to up to four minutes depending on the position of the microelectrode
268 and the electrolyte in- and outlets within the tank. During the data treatment of each online experiment,
269 these time differences were compensated by shifting the complete amperometric data by a constant value,
270 Δt_{corr} , in time for all data points of the experiment. The Δt_{corr} was determined by the difference between

271 the SOC signal extrema to the time of current inversion (**Figure S4**). While this procedure represents a
272 simple way to ensure a fair comparison of the two sensors, the impact of sensor positions in RFBs
273 necessitates increased research efforts in general.⁶

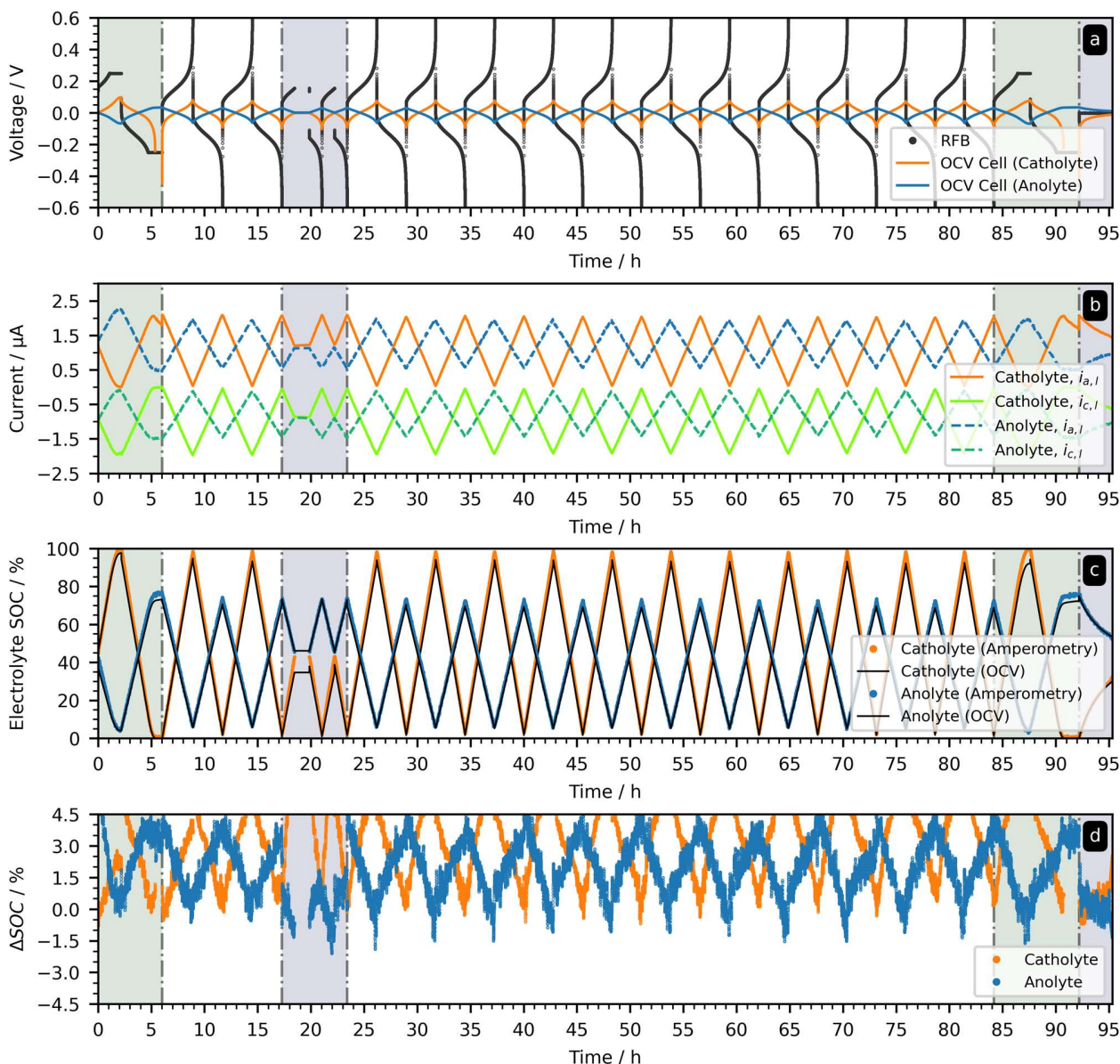
274 **Determination of $D_O D_R^{-1}$ for Online Monitoring.** The capability to perform an online determination of
275 $D_O D_R^{-1}$ without the knowledge of the electrolyte's SOC represents an interesting property of the
276 amperometric method. However, all investigations performed by the authors of this study with this
277 method so far indicate that the value of $D_O D_R^{-1}$ is independent from relevant RFB parameters such as the
278 electrolyte SOC, the total concentration of the redox species, the electrolyte SOH, and the electrolyte
279 temperature for a specific RFB electrolyte. From this perspective, it seems to be more reasonable to
280 determine the $D_O D_R^{-1}$ value once and use it consistently for a specific redox couple. As demonstrated
281 with the results of the offline experiments with ferri-/ferrocyanide (**Table 1** and **Table 2**), the utilization
282 of an *ex-situ*/offline determined value of $D_O D_R^{-1}$ can even be beneficial for the accuracy of the SOC
283 measurement. Furthermore, this approach comes at lower computational costs, simplifies data treatment,
284 and significantly decreases the probability for a convective distortion which can disturb the $D_O D_R^{-1}$ online
285 estimation. As a consequence, no online determination of $D_O D_R^{-1}$ was performed in the online
286 experiments of this study. Instead, a constant value of $D_O D_R^{-1} = 0.9471 \pm 0.0004$ was applied for the
287 amperometric SOC calculation, which represents the average of the $D_O D_R^{-1}$ values obtained for catholyte
288 ($D_O D_R^{-1} = 0.9404 \pm 0.0003$) and anolyte ($D_O D_R^{-1} = 0.9537 \pm 0.0003$) *via* the linear regression of
289 cathodic *vs.* anodic diffusion-limited currents in the first experiment (**Figure S5**). The given uncertainties
290 of the electrolyte specific values represent the standard errors of the estimated regression slope. The
291 uncertainty of the average value is the result of a Gaussian error propagation. Although all experiments
292 indicate a wide-spread invariability of $D_O D_R^{-1}$ so far, we would like to stress that it cannot be taken for
293 granted at this point of research and should be verified for each new electrolyte.



294

295 **Figure S5.** Amperometric current data for (a) the catholyte (CLS) and the anolyte (NCLS) of all cycles of the symmetric,
 296 unbalanced 1.3 M TEMPTMA RFB. The regressions yielded slopes of 0.9404 ± 0.0003 (catholyte) and 0.9537 ± 0.0003
 297 (anolyte). The deviating data points for the catholyte are the result of the high overpotentials expected for extreme SOCs at
 298 the utilized two-electrode setup. The light blue data points in the anolyte graph exemplify the impact of electrolyte convection
 299 on the current data (first cycle). The first cycle was, therefore, not included in the linear regressions.

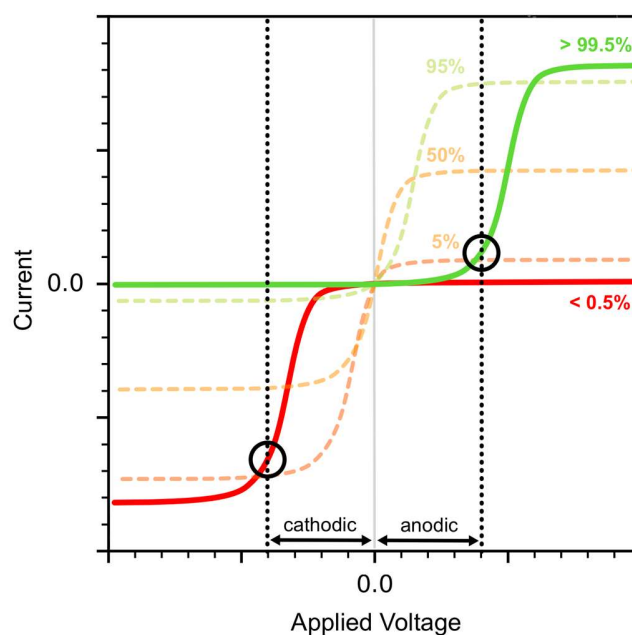
300 **Accuracy of Anolyte (NCLS) Data & Incomplete Cycles.** During all online monitoring experiments, the
 301 anolyte (*i.e.*, the NCLS of the RFB) exhibited significantly higher deviations and variations between the
 302 SOC values obtained by the amperometric and OCV cell method. As discussed in the main text of our
 303 study, this is a result of the limitation of the OCV cell method when using OCV-capacity data of
 304 incomplete cycles for (re-)calibration. To underline this conclusion, **Figure S6** displays the same data
 305 provided in **Figure 2** of the manuscript with only one difference: Instead of using the full OCV-capacity
 306 data measured in the catholyte, the data range was restricted to the same voltage range that was available
 307 for the anolyte during the non-linear regression. As a consequence, the SOC deviation measured for the
 308 catholyte increased to the same level observed for the anolyte (**Figure S6d**).



309

310 **Figure S6.** Same data as **Figure 2** of the manuscript with one difference: For the non-linear regression performed for re-
 311 calibration of the OCV cell, the catholyte data range was restricted to the same range available for the anolyte (*i.e.*,
 312 approximately 5 to 75% SOC). This results in higher systematic measurement errors for the SOC values of the OCV cell and,
 313 subsequently, in a higher deviation between the amperometric and the OCV cell method as evident from (d). In the time range
 314 from 18 h to 20 h the experiment was paused to check the data on the MMU (no data points were recorded in that time range
 315 and the RFB was in open-circuit mode).

316 **Limiting Currents at Extreme SOC_s.** As evident from **Figure S6b** the mass-transfer limited currents at
 317 the microelectrode decreased during potentiostatic hold-times for the catholyte (orange line, green
 318 background) at extreme SOC_s (*i.e.*, for SOC < 0.5% and SOC > 99.5%). This can be explained as follows:
 319 Due to the change of the electrolyte's equilibrium potential with a changing electrolyte SOC, the
 320 reference potential provided by the counter electrode in the applied two-electrode setup also shifts during
 321 the online monitoring. This results in a shift of the sigmoidal current signal in the current-voltage diagram
 322 into a more anodic or more cathodic direction (depending on the SOC). This is illustrated schematically
 323 in **Figure S7**. Due to the described shift of the microelectrode's current response, the applied voltage
 324 (either of the two dotted lines) difference may not be sufficient to attain mass-transfer limiting conditions
 325 at the microelectrode under extreme SOC conditions.



326
 327 **Figure S7.** Schematic representation of the current response of the amperometric two-electrode setup. Dotted vertical lines
 328 represent the fixed voltage values that were applied. Dashed lines represent electrolytes with moderate SOC_s, and solid lines
 329 represent electrolytes at extreme SOC_s. The black circles mark the failed measurement of the mass-transfer limited current at
 330 extreme SOC_s, because it is not the limiting current that is measured but a current in the rising portion of the voltammogram.
 331 For moderate SOC_s the applied voltage is always sufficient to measure the limiting current.

332 Consequently, the current measured at a fixed voltage value over the complete SOC range not always
333 represents the plateau current at extreme SOC. Instead, it could represent an arbitrary value in the rising
334 portion of the voltammogram, if the voltage is too small. This explains why the measured current for the
335 catholyte continuously decreased above a specific SOC during continued potentiostatic charging.
336 However, if on the other hand the voltage would be too large, the solvent could decompose in an
337 unwanted electrochemical side reaction. In addition to the aforementioned reference potential shift, the
338 increasing concentration overpotential at the electrodes at extreme SOC can cause an additional shift of
339 the reaction to a more anodic (for $SOC < 0.5\%$) or more cathodic (for $SOC > 99.5\%$) potential.

340 **Capacity Loss & SOH Measurements.** To investigate the accuracy of the amperometric and OCV cell
341 method in measuring the capacity loss and state-of-health of the electrolytes during RFB operation,
342 electrolyte aliquots of 0.5 ± 0.05 mL were extracted seven times from both tanks with 1 mL syringes
343 (Injekt[®] Solo, 0.5 ± 0.05 mL, B. Braun Melsungen AG, Germany) equipped with injection needles
344 (Sterican[®], \varnothing_{out} 0.8 mm, length: 120 mm, B. Braun Melsungen AG, Germany). A syringe was used
345 instead of a more accurate pipette, because it allowed to extract the electrolyte without opening the tanks.
346 Each aliquot was stored in a separate GC-vial (2 mL WO Screw Vials + ND9 Screw Cap with PTFE
347 septa, AppliChrom, Germany). After each extraction, the RFB was cycled in at least four cycles (one
348 mixed galvanostatic and potentiostatic cycle and three complete galvanostatic cycles) and the capacity
349 of each electrolyte was determined both amperometrically and with the OCV cells. In order to obtain a
350 reliable reference capacity and SOH, the aliquot volumes were determined with a mass and density
351 measurement. For the density measurement, the mass of five separate aliquots with a volume of
352 approximately 500 ± 4 μ L (Transferpette[®] S 100 to 1000 μ L, Brand GmbH & Co. KG, Germany) was
353 measured using a Mettler Toledo XS205 (USA). These aliquots were taken from a separate 1.3 M aq.
354 TEMPTMA electrolyte at 50% SOC.

355 **Table S12.** Masses measured for five separate 500 μL aliquots of a 1.3 M aq. TEMPTMA electrolyte at 50% SOC. An average
356 electrolyte density of $1.073 \pm 0.009 \text{ g cm}^{-3}$ was calculated from the average mass and volume of the five samples and its
357 measurement uncertainty was calculated *via* Gaussian error propagation.

Aliquot	Volume μL	Mass mg
1	500 ± 4	536.83 ± 0.01
2	500 ± 4	535.29 ± 0.01
3	500 ± 4	535.79 ± 0.01
4	500 ± 4	535.59 ± 0.01
5	500 ± 4	537.10 ± 0.01
Average:	500 ± 4	536.32 ± 0.01

358 The average electrolyte density calculated from the measured aliquot masses and volumes of the five
359 aliquots was $1.073 \pm 0.009 \text{ g cm}^{-3}$ (**Table S12**). Subsequently, the masses of the electrolyte aliquots taken
360 from the RFB tanks were determined with a Mettler Toledo XS205 (USA) by weighing the empty GC-
361 vials and the filled GC-vials. The volume of each electrolyte aliquot was then calculated from the
362 measured masses and the previously determined electrolyte density (**Table S13**). As an additional cross-
363 validation of the described electrolyte volume measurement, the accuracy of the 1 mL syringes was
364 assessed in a similar way: A volume of 0.5 mL of distilled water was measured with the syringe and its
365 mass was subsequently measured (Mettler Toledo XS205, USA). The water volume was then calculated
366 from density of water at 20 °C ($0.99823 \text{ g cm}^{-3}$). This procedure was repeated for five syringes five times
367 per syringe and yielded an average volume of $570 \pm 15 \mu\text{L}$ (**Table S14**). Consequently, a real volume of
368 $570 \pm 15 \mu\text{L}$ is extracted with the utilized 1 mL syringes if a volume of 0.5 mL is targeted based on the
369 syringe scale. This is in agreement with the determined average volume of the electrolyte aliquots
370 ($587 \pm 14 \mu\text{L}$), which were extracted with the same type of syringe. This confirms that the determined
371 density of the TEMPTMA electrolyte represents a reliable value.

372 **Table S13.** Masses measured for the electrolyte aliquots which were extracted from the catholyte and anolyte tanks for
 373 simulation of a capacity loss. Mass of empty and full vials have a measurement uncertainty of 0.01 mg and, thus, the aliquot
 374 masses come with an uncertainty of 0.02 mg. As calculated from Gaussian error propagation, the measured aliquot volumes
 375 thus have a measurement uncertainty of 5 μL .

Aliquot	Mass (full vial)		Mass (empty vial)		Aliquot Mass		Aliquot Volume	
	mg		mg		mg		μL	
	Anolyte	Catholyte	Anolyte	Catholyte	Anolyte	Catholyte	Anolyte	Catholyte
1 ^[*]							579	578
2 ^[*]	3872.66	3863.18	2630.45	2622.66	1242.21	1240.52	579	578
3	3239.20	3262.67	3606.74	2625.10	632.46	637.57	589	594
4	3260.33	3298.00	2628.54	2644.85	631.79	653.15	589	608
5	3277.10	3212.32	2633.51	2617.13	643.59	595.19	600	554
6	3256.65	3257.63	2629.97	2629.94	626.68	627.69	584	585
7	3267.67	3242.75	2618.70	2603.70	648.97	639.05	605	595

376 ^[*] The first two samples were accidentally filled into one vial and, therefore, only the combined volume was determined. For
 377 further data treatment an equal volume of both aliquots was assumed.

378
 379 **Table S14.** Experimental results for the determination of the volume error of the 1 mL syringes utilized for the extraction of
 380 the electrolyte aliquots from the RFB tanks. The masses of five water aliquots (volume: 0.5 mL) were determined for five
 381 syringes. An average mass of 569 ± 15 mg was obtained which corresponds to an average volume of 570 ± 15 μL as calculated
 382 from the average mass and the density of water at 20 °C (0.99823 g cm^{-3}).

	Mass mg		Mass mg		Mass mg		Mass mg		Mass mg
	600.70		548.26		551.72		549.61		571.11
Syringe 1	592.85	Syringe 2	554.04	Syringe 3	562.72	Syringe 4	566.80	Syringe 5	577.21
	593.73		556.48		565.51		568.61		574.33
	583.08		559.34		564.82		556.12		578.55
	590.72		555.30		553.16		571.45		585.48
	Average: 569 ± 15 mg (570 ± 15 μL)								

383 Finally, the seven measured electrolyte aliquot volumes and the volumetric capacity of the electrolyte
 384 ($33.9 \pm 0.7 \text{ mAh mL}^{-1}$) were used to calculate the corresponding theoretical capacity of each half-cell
 385 after the aliquot extraction (**Table S15**). Additionally, the SOH loss was directly calculated from the
 386 initial volume of the electrolyte in the tank and the measured extracted volume of the electrolyte aliquots.
 387 These values were used as reliable reference values and compared with the measured capacities and SOH
 388 values obtained by the amperometric and OCV cell method for accuracy assessment of the methods
 389 (**Figure 5** of the manuscript).

390 **Table S15.** Reference values for electrolyte capacity and SOH of each half-cell of the RFB after extraction of the electrolyte
 391 aliquots. The amperometric and OCV cell estimates for each electrolyte were compared against these values.

Aliquot	Aliquot Volume		Tank Volume		Electrolyte SOH ^[*]		Electrolyte Capacity ^[#]	
	μL		mL		$\%$		mAh	
	Catholyte (CLS)	Anolyte (NCLS)	Catholyte (CLS)	Anolyte (NCLS)	Catholyte (CLS)	Anolyte (NCLS)	Catholyte (CLS)	Anolyte (NCLS)
Initial ^[+]	-	-	17.00 ± 0.02	24.00 ± 0.03	100	100	575 ± 12	812 ± 16
1	579 ± 5	578 ± 5	16.42 ± 0.02	23.42 ± 0.03	96.6 ± 0.2	97.6 ± 0.2	556 ± 11	793 ± 16
2	579 ± 5	578 ± 5	15.84 ± 0.02	22.84 ± 0.03	93.2 ± 0.2	95.2 ± 0.2	536 ± 11	773 ± 16
3	589 ± 5	594 ± 5	15.25 ± 0.03	22.25 ± 0.03	89.7 ± 0.2	92.7 ± 0.2	516 ± 10	753 ± 15
4	589 ± 5	608 ± 5	14.64 ± 0.03	21.66 ± 0.03	86.1 ± 0.2	90.3 ± 0.2	496 ± 10	733 ± 15
5	600 ± 5	554 ± 5	14.09 ± 0.03	21.06 ± 0.03	82.9 ± 0.2	87.8 ± 0.2	477 ± 10	713 ± 14
6	584 ± 5	585 ± 5	13.50 ± 0.03	20.48 ± 0.03	79.4 ± 0.2	85.3 ± 0.2	457 ± 9	693 ± 14
7	605 ± 5	595 ± 5	12.91 ± 0.03	19.88 ± 0.03	75.9 ± 0.2	82.8 ± 0.2	437 ± 9	673 ± 14
Refill ^[§]	-	-	16.8 ± 0.2	23.7 ± 0.5	98.9 ± 1.4	98.7 ± 2.3	569 ± 14	802 ± 24
Dilute ^[*] J	3403 ± 29	3418 ± 29	13.4 ± 0.2	20.3 ± 0.5	78.9 ± 1.4	84.5 ± 2.3	454 ± 12	686 ± 23

392 ^[+] Initial values are taken from the results of the setup procedure and the results of first experiment (17 cycles).

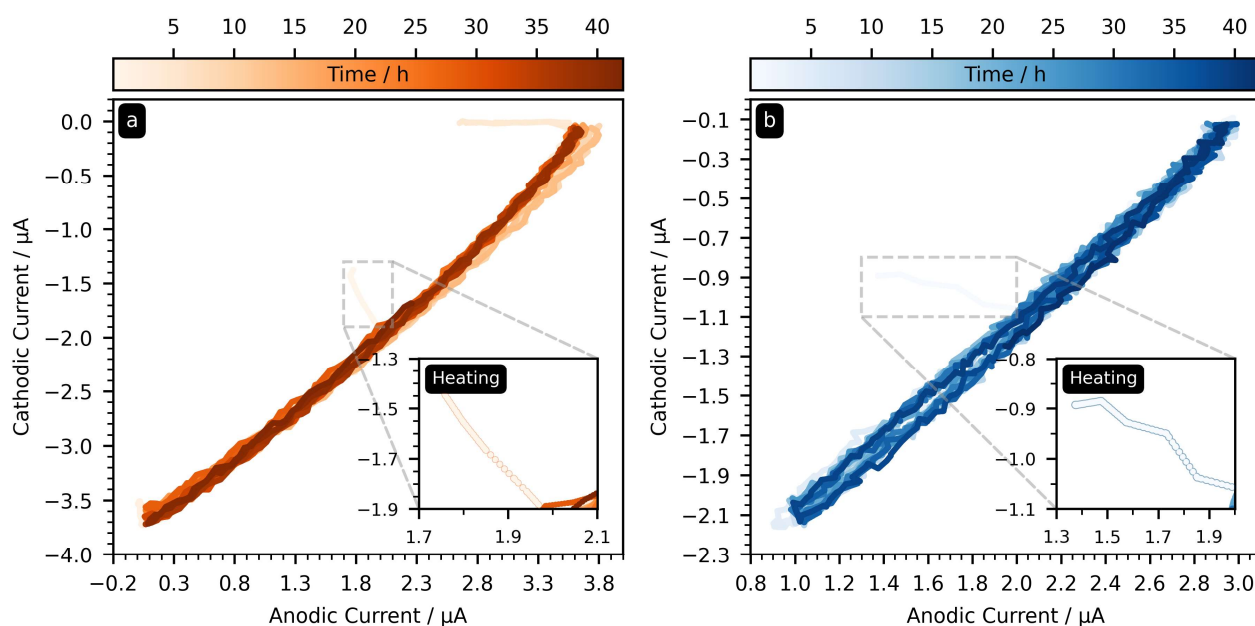
393 ^[*] Determined directly from the ratio of the new volume after aliquot extraction and the initial volume.

394 ^[#] Determined from the calculated reference SOH and the initial capacity.

395 ^[§] All aliquots were reinjected into the tanks. Tank volume, SOH, and capacity values were calculated from the
 396 amperometric SOH measurement and the initial tank volume due to the unknown and inevitable electrolyte losses during
 397 experimentation with and refilling of the aliquots.

398 ^[*] After the refilling, again 3.4 mL of electrolyte were extracted from both tanks and the same amount of water was
 399 reinjected for dilution of the electrolytes. Tank volume was calculated from the extracted aliquot volume and the estimated
 400 tank volume of the previous step. SOH and capacity values were calculated in the same way as for the aliquots 1 to 7.

401 **Online Monitoring at Elevated Temperature.** Both tanks of the RFB were placed inside an oil bath,
402 which was heated to 45 °C during the first charging cycle. The battery was then consecutively cycled for
403 42 h and a number of 10 cycles (cycling modes: 1 mixed galvanostatic and potentiostatic, 8.5 complete
404 galvanostatic, 0.5 incomplete galvanostatic). **Figure S8** displays the mass-transfer limited currents
405 measured at the microelectrodes, which are significantly higher than those currents obtained at room
406 temperature (compare to, *e.g.*, **Figure S5**). This is a result of the increased diffusivity of the redox-active
407 molecules, which facilitates the mass transfer to the electrode surface and, consequently, also increases
408 the current response of the microelectrode. The currents behaved less linear than in the previous
409 experiments as a result of the repositioning of the microelectrodes during transfer of the tanks into the
410 oil bath, which increased the impact of convection at the microelectrode. However, this was no issue for
411 the SOC and capacity measurement (**Figure 6**, main manuscript).



412
413 **Figure S8.** Amperometric current data for the 10 cycles operated at an elevated temperature of 45 °C for (a) the catholyte
414 (CLS) and (b) the anolyte (NCLS) of all cycles of the symmetric, unbalanced TEMPTMA RFB. The insets show the current
415 behaviors observed during the heating of the electrolytes until a stable temperature level was reached.

416 **Long-term Monitoring.** For the monitoring of the RFB for a longer period of time (19 days), the same
 417 oil bath was turned off so that the electrolytes cooled down. Other than that, the setup remained
 418 untouched after the experiment at elevated temperature and over the course of the complete long-term
 419 experiment.

420 **Measurement Uncertainties of SOC and SOH Measurements in Literature**

421 In a recent review on electrolyte characterization and monitoring techniques, we have surveyed all SOC
 422 and SOH measurement methods found in the scientific literature.⁶

423 **Table S16.** Literature values for the measurement uncertainties presented in literature for some of the most important methods
 424 capable of evaluating electrolyte SOC and SOH.⁶ It should be noted that the values must be carefully evaluated before
 425 comparing them among each other due to the highly distinct experimental conditions and their different origin (see footnotes).

Measurement Method	Absolute Uncertainty	
	SOC	SOH
Titration	~5%	~5%
Open-circuit potential / voltage (OCP/OCV)	3 to 5%	1 to 5%
Spectroscopy and photometry	1 to 3%	-
Electrolyte Conductivity	~1%	-
Electrolyte viscosity and density	~4%	1 to 3%
Acoustic properties	~5%	-
Amperometry (present study)	~0.5% ^[a]	0.6 to 2.1% ^[b]

426 ^[a] Absolute RMSD from true SOC (*ex-situ*, using concentration based SOC (uncertainty: $\pm 0.04\%$)).

427 ^[b] Absolute RMSD from true SOH (*in-situ*, using SOH values known from electrolyte volume extraction)

428 This review contains a detailed discussion and a summarizing table on all these methods, their specific
 429 properties, their measurement accuracies, and a reference to the original studies they were reported in.

430 While we highly recommend reading the full review to understand all details about the existing

431 electrolyte SOC and SOH measurement methods, **Table S16** provides a quick comparison of
432 measurement uncertainties reported in the scientific literature (we refer to the Table 6 of the review for
433 a more detailed version with references). However, directly comparing these values without considering
434 the context they were measured in can be highly ambiguous. This is due to the distinct experimental
435 conditions under which the values were obtained, and the different nature of uncertainties stated in the
436 different studies (e.g., precisions, accuracies, deviations from a validation method with known or
437 unknown accuracy, etc.). Because of this ambiguity, this comparison to literature values is only found in
438 the supporting information of the study at hand. As a more reliable accuracy assessment method, we
439 decided to utilize a two-fold validation in the main text since: (1) the concentration-based *ex-situ*
440 validation (section 3.1) and (2) the direct *in-situ* comparison with OCV cell (section 3.2).

441 We believe that the SOC and SOH method development in the RFB literature currently lags a consistent
442 protocol for the accuracy assessment of newly developed measurement methods.⁶ It is an inherent issue
443 that the *in-situ* value of the measurement variable (*i.e.*, SOC or SOH) is usually unknown and can only
444 be assessed by other methods, which themselves come with absolute measurement uncertainties in the
445 range of 3 to 5%. In addition, the different methods are often evaluated under very distinct experimental
446 conditions and with different redox species. This renders the direct comparison of error values reported
447 in the different studies highly ambiguous.⁶ Many studies in the RFB literature present “measurement
448 errors” or “measurement accuracies” by repeating the SOC and/or SOH measurement and stating
449 standard deviations. However, this approach evaluates the precision (*i.e.*, the reproducibility of
450 measurement values) rather than the accuracy (*i.e.*, the deviation from the true value) of the method.
451 Some studies utilize redox titrations to obtain *ex-situ* reference values for the sample SOC and SOH of a
452 RFB electrolyte.^{7, 8} However, titration-based SOC and SOH measurement itself comes with relative
453 measurement uncertainties of 5%,⁸ which makes it impossible to use titration to assess the accuracy of

454 more accurate SOC measurement methods. Other studies utilize (galvanostatic) coulomb counting as an
455 internal reference value to assess the measurement accuracy,^{4, 5} which can introduce unknown
456 measurement errors by undesired mass-transfer limitations, overpotentials, and side reactions. As already
457 highlighted in our recent review,⁶ it would be desirable to establish a standardized evaluation protocol
458 for the SOC and SOH method development in this field in general.

459 REFERENCES

- 460 ¹ C. Stolze, M. D. Hager and U. S. Schubert, *J. Power Sources* **423**, 60 (2019).
- 461 ² T. Janoschka, N. Martin, U. Martin, C. Friebe, S. Morgenstern, H. Hiller, M. D. Hager and U. S.
462 Schubert, *Nature* **527**, 78 (2015).
- 463 ³ C. Stolze, J. P. Meurer, M. D. Hager and U. S. Schubert, *Chem. Mater.* **31**, 5363 (2019).
- 464 ⁴ S. Ressel, F. Bill, L. Holtz, N. Janshen, A. Chica, T. Flower, C. Weidlich and T. Struckmann, *J.*
465 *Power Sources* **378**, 776 (2018).
- 466 ⁵ T. Struckmann, P. Kuhn and S. Ressel, *Electrochim. Acta* **362**, 137174 (2020).
- 467 ⁶ O. Nolte, I. A. Volodin, C. Stolze, M. D. Hager and U. S. Schubert, *Mater. Horiz.* **8**, 1866 (2021).
- 468 ⁷ I. Kroner, M. Becker and T. Turek, *Batteries* **5**, 5 (2019).
- 469 ⁸ M. Skyllas-Kazacos and M. Kazacos, *J. Power Sources* **196**, 8822 (2011).

470

Publications P7

Inkjet-printed microband electrodes for a cost-efficient state-of-charge monitoring in redox flow batteries.

Karina Zub, Christian Stolze, Philip Rohland, Steffi Stumpf, Stephanie Hoeppener, Martin D. Hager, Ulrich S. Schubert

Abstract:

A readily available prototyping process for the fabrication of low-cost microband electrodes is introduced which are applicable for the accurate amperometric state-of-charge (SOC) measurement in redox flow battery (RFB) electrolytes. For this purpose, an inexpensive and straightforward inkjet printing of conductive platinum-based and insulating polymer-based inks was investigated. The general electrochemical sensing capabilities and the electrode's performance when applied for the recently reported amperometric SOC measurement method was compared to sputter-coated as well as to commercial microelectrodes in ferri-/ferrocyanide electrolytes. Absolute root-mean-square deviations (RMSD) were found to be below 1% SOC for the printed microband electrodes. The low material costs of about €2.52 (\$2.93) for the presented prototype and the simplicity of the fabrication process could facilitate a widespread application of the promising amperometric SOC measurement in RFBs.



Inkjet-printed microband electrodes for a cost-efficient state-of-charge monitoring in redox flow batteries

Karina Zub^{a,b}, Christian Stolze^{a,c}, Philip Rohland^{a,c}, Steffi Stumpf^{a,b}, Stephanie Hoepfner^{a,b}, Martin D. Hager^{a,b,c}, Ulrich S. Schubert^{a,b,c,*}

^a Laboratory for Organic and Macromolecular Chemistry (IOMC), Friedrich Schiller University Jena, Humboldtstr. 10, 07743 Jena, Germany

^b Jena Center for Soft Matter (JCSM), Friedrich Schiller University Jena, Philosophenweg 7, 07743 Jena, Germany

^c Center for Energy and Environmental Chemistry Jena (CEEC), Friedrich Schiller University Jena, Philosophenweg 7a, 07743 Jena, Germany

ARTICLE INFO

Keywords:
Microelectrode
Microband
State-of-charge
Inkjet
Sputtering
Battery

ABSTRACT

A readily available prototyping process for the fabrication of low-cost microband electrodes is introduced, which are applicable for the accurate amperometric state-of-charge (SOC) measurement in redox flow battery (RFB) electrolytes. For this purpose, an inexpensive and straightforward inkjet printing of conductive platinum-based and insulating polymer-based inks was investigated. The overall inkjet-printed microband electrode performance in 0.4 M ferri-/ferrocyanide with 0.5 M KCl as supporting electrolyte were compared to sputter-coated microband electrodes and commercial disk microelectrodes using an SOC measurement method based on steady-state amperometry. Absolute root-mean-square deviations (RMSD) are below 1.04% SOC for the printed microband electrodes. The low material costs of about €2.52 (USD2.86) for the presented prototype and the simplicity of the fabrication process could facilitate a widespread application of the amperometric SOC measurement in RFBs.

1. Introduction

The redox flow battery (RFB) technology has increasingly gained attention in both industry and academia over the past two decades and continues to do so [1–5]. This is due to the urgent demand for safe and reliable electricity storage solutions, which are suitable for buffering large amounts of energy from volatile, renewable energy sources such as wind or solar power. With regard to this, RFBs represent promising candidates for stationary energy storage because of their independent scalability of power and capacity, which is unique among the different types of battery technologies. This independent scalability originates from the separation of the electrochemical reactor (*i.e.*, the flow cell) and the storage material (*i.e.*, two separate electrolytes containing dissolved redox couples which are pumped through the flow cell). The electrolytes in the positive and negative half-cell of a RFB are usually referred to as catholyte and anolyte, respectively. For a reliable investigation and an efficient, safe operation of any type of large-scale battery, it is mandatory to monitor and to control technical and operational parameters during the charging and discharging processes of RFBs. In particular, the state-of-charge (SOC) and the state-of-health (SOH) of

the two electrolytes in a RFB represent important monitoring parameters due to their strong impact on the majority of physicochemical parameters of any RFB electrolyte as we have highlighted and discussed in detail recently [6]. In general, the SOC expresses the degree of charge that has been stored in a battery or half-cell with reference to its total capacity, whereas the SOH describes the remaining capacity after a number of cycles as a fraction of the initial or nominal capacity of the battery or half-cell. The state-of-charge of a catholyte (SOC) or an anolyte (\overline{SOC}) is defined *via* the concentration of the oxidized (c_O, \overline{c}_O) and the reduced (c_R, \overline{c}_R) form of a redox couple in solution within the study at hand:

$$SOC = \frac{c_O}{c_O + c_R} \quad \text{and} \quad \overline{SOC} = \frac{\overline{c}_R}{\overline{c}_O + \overline{c}_R} \quad (1)$$

In recent studies by our group, it was demonstrated that steady-state amperometry at disk microelectrodes can provide highly accurate values for the electrolyte SOC with absolute RMSDs of less than 0.5% in *ex-situ* and *in-situ* measurements [7,8]. In addition, the same method is capable of an accurate online electrolyte capacity (and thus also SOH) measurement with RMSDs below 2% [8]. This state-of-charge measurement approach is applicable to RFBs employing different redox chemistries (*e.*

* Corresponding author at: Laboratory for Organic and Macromolecular Chemistry (IOMC), Friedrich Schiller University Jena, Humboldtstr. 10, 07743 Jena, Germany.

E-mail address: ulrich.schubert@uni-jena.de (U.S. Schubert).

<https://doi.org/10.1016/j.snb.2022.132291>

Received 8 February 2022; Received in revised form 24 June 2022; Accepted 27 June 2022

Available online 29 June 2022

0925-4005/© 2022 The Author(s). Published by Elsevier B.V. This is an open access article under the CC BY license (<http://creativecommons.org/licenses/by/4.0/>).

g., based on vanadium or (2,2,6,6-tetramethylpiperidin-1-yl)oxyl (TEMPO)), is calibration-free, highly accurate, and temperature as well as concentration independent; as a consequence, it is highly suitable for the online monitoring of electrolyte SOCs in RFB. Furthermore, the required measurement electronics for these sensors can be realized with commercially available low-cost components [8]. However, the costs of commercial microelectrodes, which are typically higher than €350 (USD398), are at least one order of magnitude more costly than that of the measurement electronics.

Consequently, alternative methods for the cost-efficient fabrication of suitable types of microelectrodes must be developed. In addition to the cost issue, carbon fiber and metal wire based disk microelectrodes utilized for the amperometric electrolyte monitoring so far provide only comparably small currents, which require more efforts for a reliable and accurate detection [7,9]. These small currents are a result of the micrometer-sized electrode surface diameters of the utilized disk microelectrodes. Although several alternative microelectrode types with a larger electrode surface area than disk microelectrodes exist [10–13], we believe that in particular microband electrodes have the potential to mitigate the aforementioned issues [10]. The general layout of such microband electrodes requires a thin conductive structure embedded between two insulating layers. Only a line-like cross-sectional surface of the conductive structure (*i.e.*, the microband) is exposed to the electrolyte as the electrode surface. This microband is characterized by a micro- or nanometer size in one dimension but a macroscopic size in the second dimension. In the remainder of the study, we will refer to the microscopic dimension of the microelectrode structure as “width” and to the macroscopic dimension as “length”, irrespective of the exact geometrical layout. Common microelectrode layouts are summarized in Fig. 1. When compared to disk microelectrodes (Fig. 1a), the significantly larger electrode surface area of microband electrodes (Fig. 1b,c) resulting from its macroscopic length causes a significantly increased current response in electrochemical measurements. On the other hand, microband electrodes still exhibit (quasi-)stationary current signals due to their microscopic width and are, thus, suited for amperometric SOC measurements. One common way to fabricate microband electrodes is to sandwich a conductive layer between two layers of insulating and inert materials, so that only a defined edge is exposed to the electrolyte. This can be achieved by, for example, sealing a platinum or gold foil in epoxy resin (Fig. 1b) [14], sandwiching sputter-coated platinum films between two glass plates [15] (Fig. 1b), and by screen printing carbon-based inks as thin lines [16–18] (Fig. 1c).

With regard to the electrode material, gold and platinum exhibit beneficial properties such as an excellent electrochemical stability in a wide range of electrolytes; however, the costs of these materials are comparatively high and, therefore, its economic use is required. In the conventional production of, *e.g.*, platinum-based electrochemical sensors, fabrication methods such as electron-beam lithography [19,20],

ion-beam lithography [21], and photolithography [22] have been used. While these methods make it possible to form sensors with defined electrode structures and high performance, their costs are relatively high, due to the technological peculiarities of production, *i.e.*, the requirement of clean rooms and special instrumentation. For these reasons, alternative production methods like screen and inkjet printing are in the focus of research efforts.

Inkjet printing deposition has been demonstrated as a straightforward approach to fabricate conductive (micro)structures with low experimental requirements including, for example, the utilization of conventional office printers [23,24]. In general, this method utilizes the accurate dosing of small amounts of an ink onto a surface by means of a printing nozzle. Due to the high accuracy of the ink deposition process, it is a non-contact, mask-less approach which allows the fabrication of structural features with micrometer resolution in the horizontal and nanometer resolution in the vertical direction. One of the most attractive features of the inkjet printing technology is the availability of different inks (*e.g.*, comprising colloidal suspensions, nanoparticles, carbon nanotubes, and polymers) which can be deposited in different multilayer structures to fabricate even complex device layouts. As such, inkjet printing is regarded as a promising technology for the economic and customized design of a wide range of different structures. Due to these advantages, inkjet printing was utilized already for the fabrication of microelectrodes in pH sensors [25,26], gas sensors [27,28], temperature sensors [29–31], humidity sensors [32,33], and biosensors [34–36]. Although inkjet printing cannot be considered a replacement for conventional manufacturing approaches, this method can simplify the fabrication process and can reduce costs significantly. The extremely low material consumption makes this approach attractive when handling expensive materials such as the platinum ink used in this work. The freedom to choose almost any substrate for the microelectrode – depending on the environment of use – as well as the ability to customize the microelectrode pattern simply by changing the print layout in a graphical editing software, renders inkjet printing a convenient method for the prototyping of sensors in research laboratories and for the production of low-cost sensors in industry. Since redox flow batteries keep evolving into one of the relevant future energy storage technologies, the demand for cost-efficient sensors to monitor different physicochemical properties increases in both laboratory installations for basic investigations and in the industry for their large-scale operation. Up to now, no studies on the application of inkjet printing for the inexpensive prototyping of RFB sensors have been reported. However, this technique represents an interesting and promising approach considering the aforementioned examples of printed sensors in other fields of research and the recent methodological advances for the RFB electrolyte analyses and monitoring [7–9,37], which require cost-efficient and easily accessible microelectrodes. In this study, we therefore investigated an inkjet printing approach for the fast and cost-efficient fabrication of

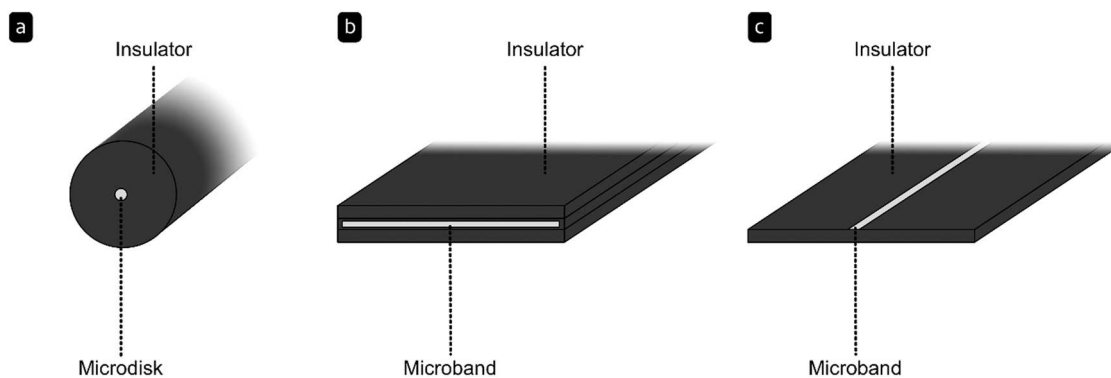


Fig. 1. Schematic representations of (a) a conventional disk microelectrode where two dimensions are microscopic, and (b, c) microband electrodes with one microscopic dimension (“width”) and one macroscopic dimension (“length”) in two different layouts. The layout displayed in (b) was applied in the experiments of this study.

microband electrodes, which can be used for the state-of-charge monitoring in redox flow batteries.

The remainder of this study is organized as follows: Section 2 provides some general theoretical background information on steady-state amperometry with microelectrodes and a short mathematical derivation of the equations required for the SOC measurement with microband electrodes in particular. In Section 3, the manufacturing procedure for the inkjet-printed and sputtered microband electrodes prepared in this study is detailed. Finally, Section 4 presents the experimental results obtained in this study which include: (1) The characterization of the electrodes with regard to their electrochemical performance for SOC measurements in RFB electrolytes, (2) an experimental performance comparison to microband electrodes fabricated by electron-beam (e-beam) metal sputtering as well as to commercial disk microelectrodes utilized in previous studies of our group [7,8], and (3) a material cost estimation for the inkjet-printed electrode prototypes. The latter highlights the economic advantages of printed microband electrodes compared to commercial disk microelectrodes in particular for laboratory-scale applications and rapid prototyping of SOC sensors based on steady-state amperometry.

2. Theory

2.1. Steady-state amperometry for SOC measurements

The microband electrodes investigated in this study are specifically designed for the application as low-cost microelectrodes for SOC sensors in RFB electrolytes. In general, the current at an electrode in an electrochemical experiment is usually related to the concentration of the redox couples in the electrolyte. It is well-known that the currents at microelectrodes of various types yield a steady state (for disk, spherical, and hemispherical microelectrodes) or a quasi-steady state (for cylinder and band microelectrodes) for long times [10]. At sufficiently high overpotential, the mass-transfer limited currents at a microelectrode of arbitrary type can be mathematically described by [10]:

$$i_{l,a} = zFAm_Rc_R \quad \text{and} \quad i_{l,c} = -zFAm_Oc_O. \quad (2)$$

Here, $i_{l,a}$ represents the anodic mass-transfer limited current, $i_{l,c}$ the cathodic mass-transfer limited current, z the number of transferred electrons, F the Faraday's constant, A the electrode surface, $m_{O/R}$ the mass-transfer coefficient of the redox species, c the concentration of the redox species, and subscripts O and R denote the oxidized and reduced form of the investigated redox species in solution, respectively. Depending on whether a positive or negative overpotential (η) is applied, the current i observed at the microelectrode depends on the mass-transfer and concentration of the oxidized ($\eta \ll 0$, $i \equiv i_{l,c}$) or reduced ($\eta \gg 0$, $i \equiv i_{l,a}$) form of the redox couple in solution. Notably, these equations are derived without any assumption about the nature of the electrode reaction. In particular, they are thus independent from any kinetic complications, which is part of their remarkable utility for electrochemical analyses. As we have recently demonstrated, the two currents (Eq. (2)) and the definition of the state-of-charge (Eq. (1)) can be exploited to determine the state-of-charge of a catholyte (SOC) or an anolyte (\overline{SOC}) according to [7]:

$$SOC = \left[1 - \frac{i_{l,a} m_O}{i_{l,c} m_R} \right]^{-1} \quad \text{and} \quad (3)$$

$$\overline{SOC} = \left[1 - \frac{i_{l,c} m_R}{i_{l,a} m_O} \right]^{-1}.$$

While we have experimentally demonstrated the viability of this approach only for disk microelectrodes in previous studies so far, it is theoretically valid for other types of microelectrodes like, e.g., the microband electrode, as well.

2.2. State-of-charge measurements with microband electrodes

For microbands, the mass-transfer coefficients m_O and m_R can be calculated by [10].

$$m_{O/R} = \frac{2\pi D_{O/R}}{w \ln(64D_{O/R}tw^{-2})} \quad (4)$$

where w denotes the microband width and t the measurement time. Because $m_{O/R}$ is time-dependent but changes only slightly at long times, one usually refers to a "quasi"-steady state current. Using Eq. (4), the SOC of a RFB catholyte containing both O and R can be calculated from the quasi-steady state currents at the microband electrode according to:

$$SOC = \left[1 - \frac{i_{l,a} m_O}{i_{l,c} m_R} \right]^{-1} = \left[1 - \frac{i_{l,a} D_O \ln(64D_R tw^{-2})}{i_{l,c} D_R \underbrace{\ln(64D_O tw^{-2})}_{\approx 1}} \right]^{-1} \quad (5)$$

$$\approx \left[1 - \frac{i_{l,a} D_O}{i_{l,c} D_R} \right]^{-1}$$

The relative error of the approximation in this equation can be evaluated by comparing the SOC values obtained with and without the approximation: For most redox species (where $0.8 < D_O D_R^{-1} < 1.2$) and for reasonable experimental parameters ($w < 1 \mu\text{m}$; $t > 1 \text{s}$), the approximation is theoretically accurate to within $\pm 1\%$ (relative error) with $D_O D_R^{-1} \rightarrow 1$, $w \rightarrow 0$, and/or $t \rightarrow \infty$ yielding theoretically identical values. Hence, the same equation previously demonstrated to be valid and highly accurate for disk microelectrodes [7,8] can theoretically be applied for microband electrodes as well. In addition, as a result of the approximation and the fact that both mass-transfer limited currents are directly proportional to the electrode surface A (see Eq. (2)), changes in the surface area cancel out during the SOC evaluation according to Eq. (5). In other words, the SOC measurement is independent from changes in the electrode surface that may occur during the measurement. The only requirement is that the ratio of the diffusion coefficients, $D_O D_R^{-1}$, is known accurately. This can be determined via various approaches:

- using disk microelectrodes of known diameter in solutions of known concentration of O and R to determine D_O and D_R separately
- using other electrochemical or physical methods (e.g., cyclic voltammetry, rotating-disk electrode measurements, diffusion nuclear magnetic resonance spectroscopy (DOSY), etc.) to determine D_O and D_R separately
- using the implicit approach for the direct determination of $D_O D_R^{-1}$ via microelectrode amperometry in samples of unknown but different SOC we have suggested earlier [8]

3. Materials and methods

3.1. Materials

Flexible Kapton® HN foils of 125- μm thickness were purchased from DuPont. Platinum nano-ink with polyvinylpyrrolidone as a stabilizer in ethylene glycol was obtained from AkkoLab (Russia). A UV curable ink (SunTronic®) was purchased from Sigma Aldrich, USA. Both ink formulations, potassium ferricyanide (Sigma-Aldrich, USA), potassium ferrocyanide trihydrate (Sigma-Aldrich, USA), and potassium chloride (Fisher Scientific Ltd., United Kingdom) were used as received.

3.2. Microband electrode fabrication

All microband electrodes in this study were designed in a double-layer configuration resembling the layout depicted in Fig. 1b and were fabricated on a flexible polyamide substrate (Kapton foil, thickness:

125 μm) under ambient conditions. The rectangular shape chosen for the platinum layers featured a dimension of $2.5 \times 20 \text{ mm}$. The individual processing steps of the device fabrication are illustrated in Fig. 2. Kapton foil was initially thoroughly cleaned with acetone and isopropanol prior to treatment with argon plasma (Diener Electronics) for 3 min to remove contamination from the surface and to increase the surface hydrophilicity.

Pt nano-ink was printed using a commercial lab-scale inkjet-printer (Dimatix DMP-2800) equipped with a cartridge capable of ejecting 10 pL of droplet volume. The use of a standard waveform and a firing voltage of $23 \pm 1 \text{ V}$ resulted in a stable droplet formation. To ensure fast evaporation of the solvents, the temperature of the print bed of the printer was set to $60 \text{ }^\circ\text{C}$. Since the commercially available Pt nano-ink contained only a relatively low amount of Pt nanoparticles (5–6 wt-%), it was necessary to print two layers with a drop spacing of $15 \mu\text{m}$ in order to reduce the electrical resistance of the resulting film. Subsequently, the sample was annealed on a hot plate with a temperature of $300 \text{ }^\circ\text{C}$ for 5 min.

As displayed in route B of Fig. 2, the fabrication of sputtered microband electrodes used to evaluate the quality of the printed electrodes required the utilization of a suitable mask. This was realized by simply applying a sticky tape template on a cleaned Kapton foil. Platinum was deposited using a laboratory sputtering system (CCU-010-HV Safematic, Switzerland) equipped with a platinum target. Platinum layers with a thickness of 40 and 100 nm were sputter-coated on the Kapton foil utilizing a calibrated quartz sensor system to control the resulting film thickness.

Subsequently, an UV-curable, insulating ink was deposited on top of both conductive layer types by means of inkjet printing to seal the conducting layer. The upper $\sim 30\%$ of the layer was not covered to allow an electrical contact between the conductive layer and a potentiostat. For the printing of the insulating layer, the printer settings were adjusted as follows: The drop space was adjusted to $30 \mu\text{m}$, the nozzle temperature was kept at $50 \text{ }^\circ\text{C}$, the firing voltage was set to 23 V , and the print bed of the inkjet printer was kept at room temperature. Five layers were printed consecutively on top of each other to ensure a good sealing. Finally, the samples were exposed to UV light for 3 min in order to obtain the solid insulating layer.

Microband electrodes were finally obtained from the sealed, printed and the sealed, sputter-coated Pt layers, respectively, by cutting off the bottom tip of the electrode to obtain a clean microband electrode surface.

3.3. Scanning Electron Microscopy (SEM)

A Sigma VP field emission scanning electron microscope (Carl-Zeiss AG, Germany) was used to image the inkjet printed Pt nanoparticles layer. Measurements were done using the InLens detector with an acceleration voltage of 3 kV .

3.4. Electrolyte preparation

Several 0.4 M solutions of ferri-/ferrocyanide with defined SOC of 1%, 5%, 25%, 50%, 75%, 95%, and 99%, respectively, were prepared by weighing appropriate amounts of potassium ferro- and ferricyanide with a XS205 Dual Rand balance (Mettler Toledo, USA). The solid mixtures of both materials were filled into volumetric flasks (25 mL, A-Grade, $\pm 0.04 \text{ mL}$ Schott AG, Germany). Subsequently, the volumetric flasks were filled up with 0.5 M aq. potassium chloride solution and shaken until the solids were completely dissolved.

3.5. Electrochemical measurements

For the cyclic voltammetry and the amperometric SOC measurements, a small-volume cell setup (5 mL, BioLogic, France) was utilized in a two-electrode configuration with the microband electrode as the working electrode and a graphite rod (diameter: 3 mm, Mersen SA, France) as counter electrode with a significantly larger surface area than the working electrode. The experiment was performed utilizing a computer-controlled 16-channel VMP3 potentiostat/galvanostat (Bio-Logic, France). For instrument control and data acquisition the EC-Lab 11.26 software was used.

3.6. Steady-state amperometry for SOC measurements

State-of-charge measurements by steady-state amperometry were performed similar to the *ex-situ* experiments with commercial disk microelectrodes detailed in a previous study: [8] Briefly, the current responses of the microband electrodes were measured in consecutive potential step experiments at 0.4 V (anodic step) and -0.4 V (cathodic step) versus the counter electrode with a step duration of 60 s. The mass-transfer limited currents for calculation of the SOC were recorded at the end of each step. Between the anodic and cathodic step, the electrolyte was gently shaken and equilibrated for 120 s. Before transfer of each electrode to the next electrolyte sample, it was cleaned by rinsing

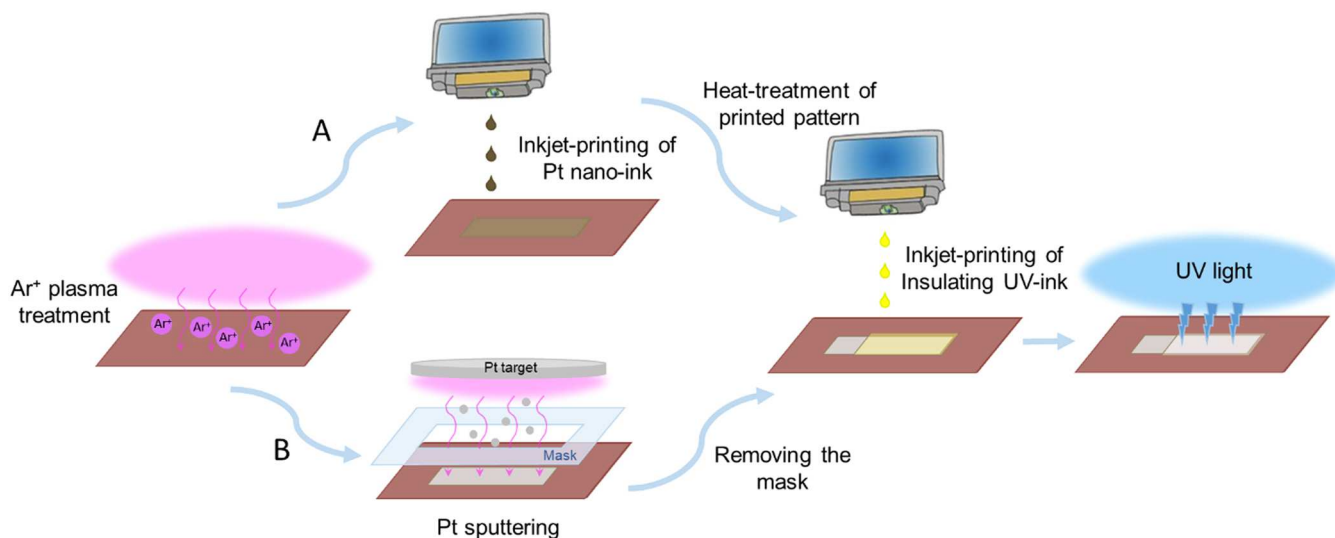


Fig. 2. Schematic representation of the fabrication process of the microband electrode by (A) inkjet printing and (B) sputter coating. The conductive Pt layers are coated with an insulating layer of UV curable ink. The obtained samples are subsequently cut to obtain a cross-section of the platinum layer – the microelectrode (Fig. 1b).

with distilled water and subsequently dried with a tissue. For each electrolyte sample, three different microband electrodes were used and values were recorded once per electrode. The experiment was performed at room temperature (~ 294 K).

4. Results and discussion

4.1. Microband electrode characterization

The general layout of the microband electrodes requires the printing of conductive layers with dimensions of 2.5×20 mm. The layout is schematically shown in Fig. 3a. To fabricate robust microband electrodes with high conductivity, two layers of the Pt ink were printed. However, the printed structures are initially non-conductive and, thus, a subsequent annealing process at 300°C for 5 min was required to reduce the area-specific resistance. During this annealing process, the Pt nanoparticles formed a dense layer of coagulated Pt grains (Fig. 3b) and the polyvinylpyrrolidone as well as the ethylene glycol residuals were removed. Cross-sectional SEM investigations revealed a thickness of 250–290 nm of the printed layers after annealing. Occasionally, slight delamination of the Pt layer from the Kapton surface was observed which was ascribed to the mechanical stress exerted on the structure during sample preparation for the SEM measurement (*i.e.*, cutting to obtain cross-sectional views).

Afterwards, the Pt layers were coated with an insulating layer of UV-curable ink, which shielded the Pt layer from the electrolyte during the electrochemical investigations. Only the top part of the structure was left uncovered to serve as a connector to the measurement electronics. The microband electrode was finally obtained by cutting off the front edge of the sample to expose the cross-section (Fig. 3c) which resulted in the desired Pt microband (Fig. 3a).

In order to evaluate the quality of the printed microband electrodes, two sets of additional Pt microband electrodes were prepared by e-beam sputter-coating in a similar process (Fig. 2). The thicknesses of the sputtered Pt layers were 40 and 100 nm, respectively. The microband electrodes obtained from this process served as a reference system to verify the quality of the annealed inkjet-printed microband electrodes.

To verify that the proposed fabrication procedure leads to microband electrodes which are suitable for the amperometric SOC monitoring, cyclic voltammetry experiments were performed first. Fig. 4a displays representative, normalized cyclic voltammograms recorded in a 0.4 M ferri-/ferrocyanide electrolyte (0.5 M $\text{KCl}_{(\text{aq})}$, 25% SOC) using the inkjet-printed and the two sputter-coated microband electrodes. For comparison, the measurement was additionally performed with a commercial Pt disk microelectrode (diameter: $25\ \mu\text{m}$). All electrodes exhibited the expected behavior with the characteristic sigmoidal shape in the corresponding current-voltage diagram, which is a result of the (quasi)-stationary concentration profiles formed at the microelectrode

surface upon oxidation or reduction of the electroactive species. All electrodes fabricated by e-beam sputtering exhibited slightly distorted voltammograms with less defined current plateaus in contrast to the commercial and the inkjet-printed electrodes. Fig. 4b shows the corresponding cyclic voltammograms obtained at the same inkjet-printed microband electrode after three sequential cuts of the electrode to obtain fresh electrode surfaces, while Fig. 4c displays the corresponding voltammograms for the commercial microelectrode after polishing. As expected, the microband electrodes exhibited mass-transfer limited currents which are by at least one order of magnitude larger than that at the disk microelectrode. While reproducible current values were obtained for the commercial microelectrode after polishing (Fig. 4c), the absolute currents of a single inkjet-printed microband electrode varied by $\sim 400\%$ from cut 1 to cut 3 as can be observed in Fig. 4b. Due to the relationship between current and electrode surface area, this variation can be attributed to the change of the electrode surface area upon cutting. The reproducibility of the current values, consequently, depends on how reproducible the cutting is performed. While this should be no issue for an industrial electrode production, it is more challenging on the laboratory scale.

However, with regard to the application as part of an RFB electrolyte state-of-charge sensor, for which these microband electrodes were specifically designed, the observed variation in the electrode surface area is no issue: Eq. (5) is independent from the electrode surface area. Although the latter is implicitly contained in both $i_{l,a}$ and $i_{l,c}$, it cancels out since the ratio of both currents is calculated. Finally, we would like to highlight that the voltammograms were only investigated qualitatively, not quantitatively, to demonstrate the general applicability of the manufactured microband electrodes. For the desired amperometric SOC measurement, only the mass-transfer limited currents (*i.e.*, the plateaus in the voltammograms) are required. This has the benefit that any kinetic factors of the electrode reaction that may prevail for low overpotentials (*i.e.*, between the plateau regions) and any electrode surface changes do not have an impact on the evaluation of the SOC via amperometric methods [7,10].

4.2. Amperometric SOC measurement

After verification of the expected electrochemical behavior in the cyclic voltammetric experiments, the microband electrodes were applied to the SOC measurement in 0.4 M ferri-/ferrocyanide solutions of defined SOC to assess their suitability for the application as part of amperometric sensors. The SOC of each electrolyte sample was calculated using the approximation in Eq. (5). The $D_{\text{O}}D_{\text{R}}^{-1}$ of the ferricyanide and ferrocyanide species was either assumed to be unity or was determined from literature values. Konopka and McDuffie reported diffusion coefficients for both species in 1–5 mM potassium ferri-/ferrocyanide in 0.1 M and 1 M KCl, respectively, which yield an average ratio

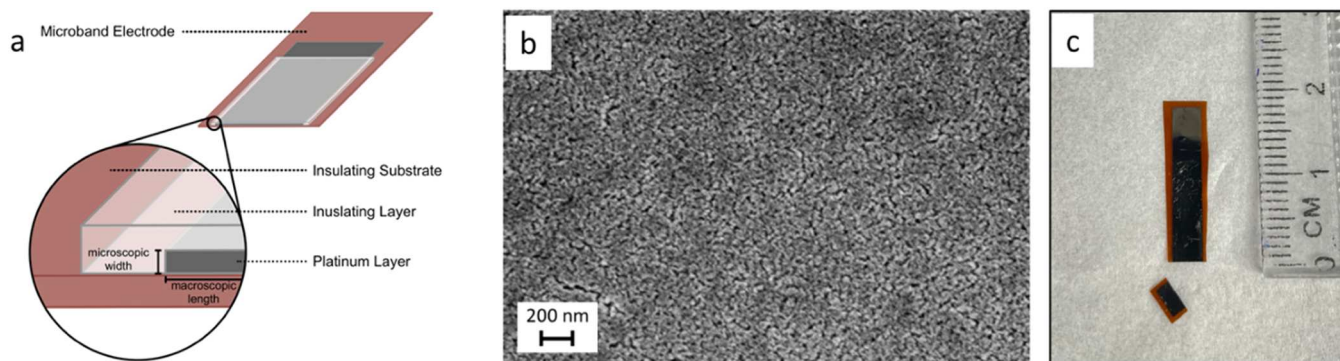


Fig. 3. a) Schematic representation of the microband electrode layout. b) SEM micrograph of the annealed inkjet-printed Pt layer indicating the formation of a dense layer of coagulated Pt nanoparticles after annealing at 300°C for 5 min. c) Final microband electrodes fabricated by inkjet printing. The bottom part of the microband electrode is cut off to expose the Pt layer in a line-like structure which represents the actual microband electrode.

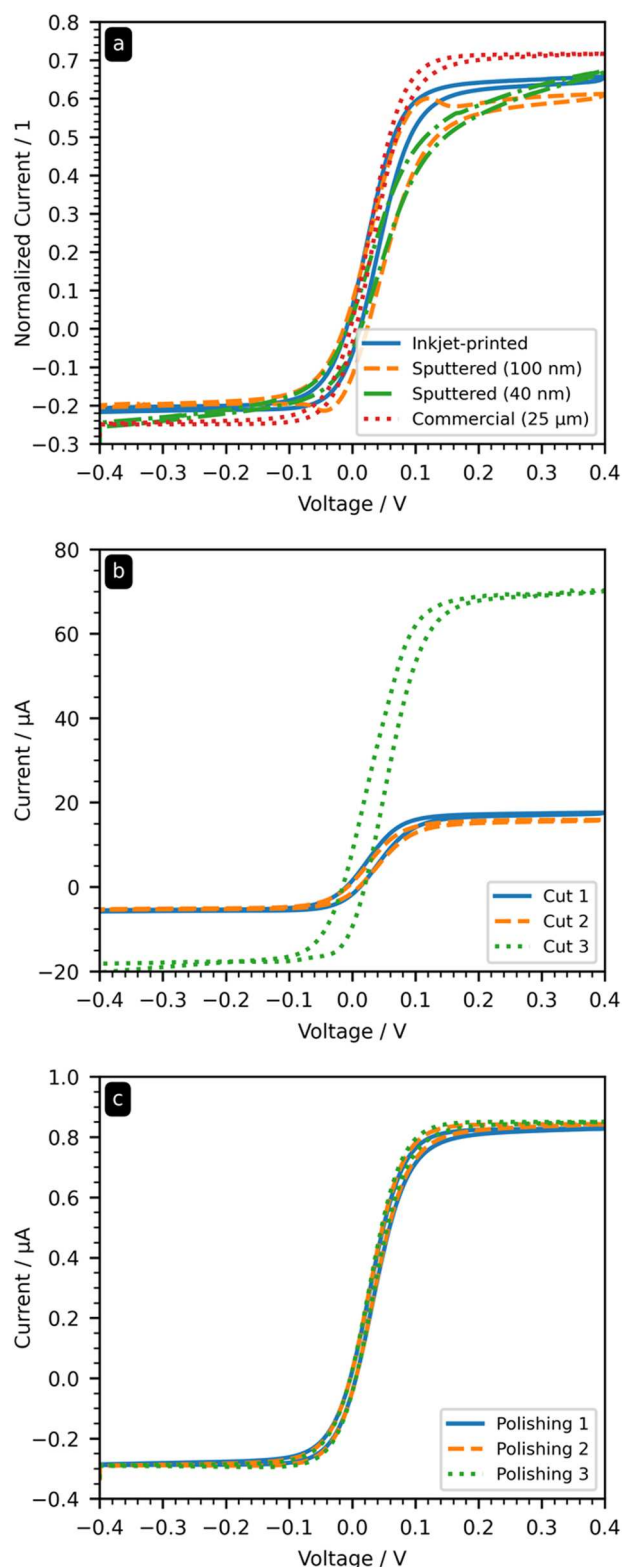


Fig. 4. Cyclic voltammograms of 0.4 M ferri-/ferrocyanide solutions (25% SOC) recorded at 5 mV s⁻¹ for (a) different microband electrodes and the commercial microelectrode with currents normalized to the sum of the absolute plateau currents; (b) inkjet-printed microelectrodes with significantly varying currents after cutting the electrode tip to obtain a clean electrode surface; (c) a commercial Pt wire microelectrode (diameter: 25 μm) after polishing to obtain a clean electrode surface.

(± standard deviation) of $D_O D_R^{-1} = 1.09 \pm 0.03$ [38]. Similarly, Amatore et al. reported average values (± standard deviation) for 10 mM potassium ferri-/ferrocyanide corresponding to a $D_O D_R^{-1}$ of 1.05 ± 0.06 [39]. The ratio utilized for the SOC calculation in this study is the average (± standard deviation) of these two literature values, that is $D_O D_R^{-1} = 1.07 \pm 0.07$. Table 1 summarizes the results of the SOC measurements in form of the average and standard deviation for SOC values obtained for three electrodes of each type.

Regardless of the $D_O D_R^{-1}$ utilized for the evaluation, the results obtained with the sputtered electrodes of 100 nm thickness and with the inkjet-printed electrodes are in excellent agreement with the true electrolyte SOC values (SOC_{ref}). The absolute root-mean-square deviations (RMSD) of the SOC values obtained with these electrodes are not larger than 1.04%. This is comparable to the achievable accuracy (absolute RMSD below 0.5%) reported for commercial gold disk microelectrodes (diameter: 25 μm) in a similar experiment of our previous study [8]. In contrast to that, the sputtered electrodes with a thickness of 40 nm exhibited higher absolute RMSDs of around 3%. This can most-likely be attributed to the increasing electrical resistance caused by the lower thickness of the sputtered 40 nm samples. Despite the observed difference, a deviation of 3% over the full SOC range still represents an accuracy which is on par with conventional SOC measurement techniques (e.g., the open-circuit voltage (OCV) cell and the spectroscopic methods) [6]. While a long-term stability assessment of the electrodes was not within the scope of this study, no signs of electrode degradation were observed during the course of the experiments.

4.3. Material cost estimation for prototype

While the inkjet printing approach provides microband electrodes with an excellent measurement accuracy, their fabrication costs are of particular interest for a wide application in the monitoring of the RFB electrolyte SOC. Thus, the material costs for the prototyping of the inkjet-printed microband electrodes of this study were estimated on the basis of the individual component costs for the consumables and the amount of microband electrodes printed in this study (Table 2). An approximate total material cost of €2.52 (USD2.86, based on exchange course in January 2022) was determined. The main items in this cost estimation clearly are the cartridge and the platinum ink. However, cartridges with a small filling volume of 1.5 mL were utilized for the prototyping in this study and in future applications either larger cartridges or a continuous ink feeding procedure would further reduce the cost impact of the cartridge. A reduction of the required platinum ink amounts can be achieved by optimizing the layer thickness, the electrode dimensions, and the electrode layout. Furthermore, graphite inks could be an alternative basis for the microband electrode.

Although it should be noted that an estimation of, e.g., the personnel and energy costs cannot be included at this point, the total production costs for the presented printed electrodes can be expected to be in a similar order of magnitude discussed here because printing procedures in general are highly automatable as well as scalable. Despite the satisfying operational stability observed over the course of the measurements in this study, dedicated long-term investigations for the manufactured microband electrodes are pending and should be considered during future in-depth cost analyses. Although it is difficult to approximate the real cost advantage of printed microband electrodes compared to commercial microelectrodes at this research state, we would like to emphasize for comparison that commercial disk microelectrodes usually come at costs over €350 (USD398). Since these are significantly more difficult to assemble than the printed microband electrodes presented in this study and their production is less automatable, we expect a significant cost-advantage for the printed microband electrodes. While further investigations are required to provide a reliable cost estimation for the industrial scale, we believe that laboratories requiring easily accessible, low-cost microelectrodes can already benefit

Table 1

SOC measurement results for samples of different SOC values of the 0.4 M ferri-/ferrocyanide in 0.5 M KCl(aq) solutions as obtained from the mass-transfer limited currents at the sputtered and inkjet-printed microband electrodes. $\Delta SOC \equiv SOC - SOC_{ref}$ represents the absolute deviation of the measurement value from the true SOC of the sample. The stated ΔSOC values are the average of measurements with three electrodes of the same type and the corresponding standard deviation.

SOC _{ref} ^[a]	Sputtered, 100 nm		Sputtered, 40 nm		Inkjet-printed	
	ΔSOC_1 ^[b]	$\Delta SOC_{1.07}$ ^[c]	ΔSOC_1 ^[b]	$\Delta SOC_{1.07}$ ^[c]	ΔSOC_1 ^[b]	$\Delta SOC_{1.07}$ ^[c]
%	%	%	%	%	%	%
99.01	0.52 ± 0.12	0.62 ± 0.13	0.28 ± 0.12	0.37 ± 0.15	0.36 ± 0.37	0.45 ± 0.39
95.00	0.51 ± 0.61	0.88 ± 0.65	0.46 ± 0.61	0.38 ± 0.09	0.29 ± 0.15	0.11 ± 0.07
75.02	0.90 ± 0.20	1.72 ± 1.03	2.84 ± 0.20	1.65 ± 1.19	0.44 ± 0.61	0.84 ± 0.63
50.00	1.16 ± 0.42	0.53 ± 0.42	4.40 ± 1.20	2.72 ± 1.21	1.48 ± 1.44	1.15 ± 0.42
25.00	0.70 ± 0.40	0.83 ± 0.76	5.60 ± 3.54	5.02 ± 2.20	0.88 ± 0.48	2.09 ± 0.46
5.02	0.66 ± 0.62	0.51 ± 0.30	2.16 ± 0.97	1.93 ± 0.68	0.25 ± 0.17	0.24 ± 0.18
1.02	0.79 ± 0.28	0.68 ± 0.26	0.92 ± 0.79	0.84 ± 0.67	1.04 ± 1.16	0.91 ± 1.09
RMSD	0.78	0.91	3.04	2.39	0.80	1.04

^[a] Reference value calculated from the known molar masses and measured weights of the dry substances. Absolute uncertainties of the reference values are below 0.0003% according to Gaussian error propagation.

^[b] Calculated from Eq. (5) using $D_O D_R^{-1} = 1$.

^[c] Calculated from Eq. (5) using $D_O D_R^{-1} = 1.07 \pm 0.07$ as obtained from literature values. [38,39]

Table 2

Material costs estimated for the fabrication of a single inkjet-printed microband electrode based on the maximum filling volume of one cartridge (1.5 mL).

Component	Purchased Amount ^[a]	Total Costs ^[a]	Number of electrodes ^[b]	Cost per Electrode ^[c]
Pt Ink	1 mL	€55	50	€1.10
Suntronic ink	250 mL	€199	4200	€0.05
Kapton foil	625 cm ² (DIN A4)	€20	500	€0.04
Dimatix cartridge	2	€200	150	€1.33
Material cost for a single inkjet-printed microband electrode				€2.52 (USD2.86)

^[a] Numbers based on the purchased amounts of the corresponding component.

^[b] Approximate number of electrodes that can be produced with the purchased component amount (based on our experience from the experiments), assuming electrodes with a Pt layer dimension of 0.25 × 2 cm printed on a substrate piece with a dimension of 0.5 × 2.5 cm.

^[c] Costs for a single electrode based on the number of electrodes that can be fabricated with the given amount (based on our experience from the presented experiments).

from the presented approach to obtain microelectrodes for the efficient amperometric SOC measurement in RFB electrolytes. The latter may be further facilitated, if future research focuses on the application of office inkjet printers [23] or other printing techniques [16] for the fabrication of microband electrodes for the state-of-charge monitoring in redox flow battery electrolytes.

5. Conclusions

We investigated the fabrication of inexpensive and mechanically flexible microband electrodes using inkjet printing for the prototyping of state-of-charge (SOC) sensors in redox flow batteries (RFB). The printed microband electrodes exhibited a good electrochemical performance and provided highly accurate results for the SOC measurement in ferri-/ferrocyanide electrolytes as model systems. Absolute RMSDs below 1% were obtained during measurements over the complete SOC range, which is on par with results we recently obtained with commercial microelectrodes in similar measurements. Due to the geometrical benefits of microband electrodes compared to disk microelectrodes, higher absolute current values are obtained which are less demanding for the measurement hardware. The processes applied to design and produce the electrodes relied on readily available materials and simple, automatable manufacturing steps. Compared to commercial disk microelectrodes, the investigated inkjet-printed microband electrodes can be

designed in virtually any layout, providing a high flexibility for the overall sensor design. According to our cost approximations, a single printed microband electrode comes at a material cost of €2.52 (USD2.86) making it highly attractive for laboratory prototyping and for the future application as SOC sensors in RFB electrolytes. Although the ferri-/ferrocyanide redox couple has been used in this study due to the ease of preparation of samples with defined SOC values, the measurement principle is applicable to a wide range of organic and inorganic RFB electrolytes as has been already demonstrated with disk microelectrodes in previous studies. Further cost optimization can be expected by the reduction of the utilized material amounts and by improving the layout of the microband electrodes in future studies.

CRedit authorship contribution statement

Karina Zub: Methodology (lead), Investigation (lead), Formal analysis (equal), Visualization (lead), Writing – original draft (equal), Writing – review and editing: critical review (equal). **Christian Stolze:** Conceptualization, Methodology (supporting), Investigation (supporting), Formal analysis (equal), Visualization (equal), Writing – original draft (equal), Writing – review and editing: critical review (equal). **Philip Rohland:** Investigation (supporting), Formal analysis (equal), Writing – original draft (supporting), Writing – review and editing: critical review (equal). **Steffi Stumpf:** Investigation (supporting), Writing – review and editing: critical review (equal). **Stephanie Hoepfener:** Writing – review and editing: critical review (equal), Supervision of K.Z. (equal), Funding acquisition (equal). **Martin D. Hager:** Writing – review and editing: critical review (equal), Supervision of P.R. (equal), Funding acquisition (equal). **Ulrich S. Schubert:** Writing – review and editing: critical review (equal), Supervision of P.R. and K.Z. (equal), Funding acquisition (equal).

Declaration of Competing Interest

The authors declare that they have no known competing financial interests or personal relationships that could have appeared to influence the work reported in this paper.

Acknowledgment

We gratefully acknowledge the financial support by Thuringian Ministry for Economic Affairs/Thuringian Ministry, Science and Digital Society (TMWwG) (CEEC-01/2020) and the Thüringer Aufbaubank (TAB). The project on which these results are based was funded by the Free State of Thuringia under number 2016 IZN 0009 and co-financed

by funds from the European Union within the framework of the European Regional Development Fund (ERFE). SEM facilities of the Jena Center for Soft Matter (JCSM) were established with a grant from the Deutsche Forschungsgemeinschaft (DFG) (INST 275/307-1 FUGG).

References

- [1] L.F. Arenas, C. Ponce de León, F.C. Walsh, Engineering aspects of the design, construction and performance of modular redox flow batteries for energy storage, *J. Energy Storage* 11 (2017) 119–153.
- [2] M. Li, Z. Rhodes, J.R. Cabrera-Pardo, S.D. Minter, Recent advancements in rational design of non-aqueous organic redox flow batteries, *Sustain. Energy Fuels* 4 (9) (2020) 4370–4389.
- [3] Z. Li, Y.C. Lu, Material design of aqueous redox flow batteries: fundamental challenges and mitigation strategies, *Adv. Mater.* 32 (47) (2020), e2002132.
- [4] E. Sánchez-Díez, E. Ventosa, M. Guarnieri, A. Trovò, C. Flox, R. Marcilla, F. Soavi, P. Mazur, E. Aranzabe, R. Ferret, Redox flow batteries: status and perspective towards sustainable stationary energy storage, *J. Power Sources* 481 (2021) 228804–228827.
- [5] R.K. Emmett, M.E. Roberts, Recent developments in alternative aqueous redox flow batteries for grid-scale energy storage, *J. Power Sources* (2021) 506.
- [6] O. Nolte, I.A. Volodin, C. Stolze, M.D. Hager, U.S. Schubert, Trust is good, control is better: a review on monitoring and characterization techniques for flow battery electrolytes, *Mater. Horiz.* 8 (7) (2021) 1866–1925.
- [7] C. Stolze, J.P. Meurer, M.D. Hager, U.S. Schubert, An amperometric, temperature-independent, and calibration-free method for the real-time state-of-charge monitoring of redox flow battery electrolytes, *Chem. Mater.* 31 (15) (2019) 5363–5369.
- [8] C. Stolze, P. Rohland, K. Zub, O. Nolte, M.D. Hager, U.S. Schubert, A low-cost amperometric sensor for the combined state-of-charge, capacity, and state-of-health monitoring of redox flow battery electrolytes, *Energy Convers. Manag.* X 14 (2022), 100188.
- [9] J.A. Kowalski, A.M. Fenton, B.J. Neyhouse, F.R. Brushett, A method for evaluating soluble redox couple stability using microelectrode voltammetry, *J. Electrochem. Soc.* 167 (2020) 16.
- [10] Bard, A.J.; Faulkner, L.R., *Electrochemical methods: fundamentals and applications*. 2nd ed.; John Wiley & Sons, Inc.: USA, 2001.
- [11] S. Siraj, C.R. McRae, D.K.Y. Wong, Effective activation of physically small carbon electrodes by n-butylsilane reduction, *Electrochem Commun.* 64 (2016) 35–41.
- [12] S. Siraj, C.R. McRae, D.K.Y. Wong, Hydrogenating carbon electrodes by n-butylsilane reduction to achieve an antifouling surface for selective dopamine detection, *Sens. Actuators B Chem.* (2021) 327.
- [13] M. McNally, D.K. Wong, An in vivo probe based on mechanically strong but structurally small carbon electrodes with an appreciable surface area, *Anal. Chem.* 73 (20) (2001), 4793–800.
- [14] K. Aoki, K. Tokuda, H. Matsuda, Derivation of an approximate equation for chronoamperometric curves at microband electrodes and its experimental verification, *J. Electroanal. Chem. Interfacial Electrochem.* 230 (1–2) (1987) 61–67.
- [15] T.V. Shea, A.J. Bard, Digital simulation of homogeneous chemical reactions coupled to heterogeneous electron transfer and applications at platinum/mica/platinum ultramicroband electrodes, *Anal. Chem.* 59 (17) (2002) 2101–2111.
- [16] M.Y. Vagin, A.N. Sekretaryova, R.S. Reategui, I. Lundstrom, F. Winquist, M. Eriksson, Arrays of screen-printed graphite microband electrodes as a versatile electroanalysis platform, *ChemElectroChem* 1 (4) (2014) 755–762.
- [17] F.J. Rawson, W.M. Purcell, J. Xu, R.M. Pemberton, P.R. Fielden, N. Biddle, J. P. Hart, A microband lactate biosensor fabricated using a water-based screen-printed carbon ink, *Talanta* 77 (3) (2009), 1149–54.
- [18] L. Authier, C. Grossiord, P. Brossier, Gold nanoparticle-based quantitative electrochemical detection of amplified human cytomegalovirus DNA using disposable microband electrodes, *Anal. Chem.* 73 (18) (2001), 4450–6.
- [19] S.Y. Cha, H.C. Lee, W.J. Lee, H.G. Kim, Platinum bottom electrodes formed by electron-beam evaporation for high-dielectric thin films, *Jpn. J. Appl. Phys.* 34 (Part 1, No. 9B) (1995) 5220–5223.
- [20] F. Virgilio, M. Prasciolu, P. Ugo, M. Tormen, Development of electrochemical biosensors by e-beam lithography for medical diagnostics, *Microelectron. Eng.* 111 (2013) 320–324.
- [21] V.V. Poplavskii, A.V. Dorozhko, Microstructure and composition of catalytic layers formed by the ion-beam-assisted deposition of platinum onto carbon substrates, *J. Surf. Investig.* 7 (2) (2013) 303–309. X-ray, Synchrotron and Neutron Techniques.
- [22] P.K. Kannan, C. Hu, H. Morgan, S.A. Moshkalev, C.S. Rout, Electrochemical sensing of bisphenol using a multilayer graphene nanobelt modified photolithography patterned platinum electrode, *Nanotechnology* 27 (37) (2016), 375504.
- [23] E.T.S.G. da Silva, T.M.R. Alves, L.T. Kubota, Direct toner printing: a versatile technology for easy fabrication of flexible miniaturized electrodes, *Electroanalysis* 30 (2) (2018) 345–352.
- [24] K. Zub, J. Winsberg, U.S. Schubert, S. Hoepfner, Inkjet-printing of supercapacitors, *ChemistrySelect* 5 (36) (2020) 11322–11330.
- [25] Y. Qin, H.-J. Kwon, A. Subrahmanyam, M.M. Howlader, P.R. Selvaganapathy, A. Adronov, M.J. Deen, Inkjet-printed bifunctional carbon nanotubes for pH sensing, *Mater. Lett.* 176 (2016) 68–70.
- [26] M.J. Kangas, R. Lukowicz, J. Atwater, A. Pliego, Y. Al-Shdifat, S. Havenridge, R. Burks, B. Garver, M. Mayer, A.E. Holmes, Printed colorimetric arrays for the identification and quantification of acids and bases, *Anal. Chem.* 90 (16) (2018) 9990–9996.
- [27] O. Kassem, M. Saadaoui, M. Rieu, J.-P. Viricelle, A novel approach to a fully inkjet printed SnO₂-based gas sensor on a flexible foil, *J. Mater. Chem. C* 7 (39) (2019) 12343–12353.
- [28] A.S. Alshammari, M.R. Alenezi, K.T. Lai, S.R.P. Silva, Inkjet printing of polymer functionalized CNT gas sensor with enhanced sensing properties, *Mater. Lett.* 189 (2017) 299–302.
- [29] S. Ali, S. Khan, A. Bermak, Inkjet-printed human body temperature sensor for wearable electronics, *IEEE Access* 7 (2019) 163981–163987.
- [30] Barmpakos, D.; Segkos, A.; Tsamis, C.; Kaltsas, G., A Disposable Inkjet-Printed Humidity and Temperature Sensor Fabricated on Paper. *Proceedings* 2018, 2, (13).
- [31] Y.-F. Wang, T. Sekine, Y. Takeda, K. Yokosawa, H. Matsui, D. Kumaki, T. Shiba, T. Nishikawa, S. Tokito, Fully printed PEDOT: PSS-based temperature sensor with high humidity stability for wireless healthcare monitoring, *Sci. Rep.* 10 (1) (2020) 1–8.
- [32] C.-H. Su, H.-L. Chiu, Y.-C. Chen, M. Yesilmen, F. Schulz, B. Ketelsen, T. Vossmeier, Y.-C. Liao, Highly responsive PEG/Gold nanoparticle thin-film humidity sensor via inkjet printing technology, *Langmuir* 35 (9) (2019) 3256–3264.
- [33] Sulaiman, S.; Rashid, N.A.; Aziz, A.S.A.; Jun, L.Q.; Jaafar, S.M.H.S.M. In Inkjet-Printed Graphene-based Flexible Humidity Sensor for Environmental Applications, 2020 IEEE International Conference on Semiconductor Electronics (ICSE), 28–29 July 2020, 2020; pp 148–151.
- [34] B. Bachmann, N.Y. Adly, J. Schnitker, A. Yakushenko, P. Rinklin, A. Offenhäusser, B. Wolfrum, All-inkjet-printed gold microelectrode arrays for extracellular recording of action potentials, *Flex. Print. Electron.* 2 (3) (2017), 035003.
- [35] L.D. Garma, L.M. Ferrari, P. Scognamiglio, F. Greco, F. Santoro, Inkjet-printed PEDOT: PSS multi-electrode arrays for low-cost in vitro electrophysiology, *Lab Chip* 19 (22) (2019) 3776–3786.
- [36] J. Schnitker, N. Adly, S. Seyock, B. Bachmann, A. Yakushenko, B. Wolfrum, A. Offenhäusser, Rapid prototyping of ultralow-cost, inkjet-printed carbon microelectrodes for flexible bioelectronic devices, *Adv. Biosyst.* 2 (3) (2018) 1700136.
- [37] Neyhouse, B.; Tenny, K.; Chiang, Y.-M.; Brushett, F., A microelectrode-based sensor for measuring operando active species concentrations in redox flow cells. In 2021.
- [38] S.J. Konopka, B. McDuffie, Diffusion coefficients of ferri- and ferrocyanide ions in aqueous media, using twin-electrode thin-layer electrochemistry, *Anal. Chem.* 42 (14) (1970) 1741–1746.
- [39] C. Amatore, S. Zsuzsnerits, L. Thouin, J.S. Warkocz, Mapping concentration profiles within the diffusion layer of an electrode Part III. Steady-state and time-dependent profiles via amperometric measurements with an ultramicroelectrode probe, *Electrochem Commun.* 2 (5) (2000) 353–358.

Karina Zub. was born in Omsk, Russia, in 1992. She studied chemistry and photosensitive materials at the Saint-Petersburg State University of Film and Television. After obtaining her Diploma degree she started working as a research engineer for holographic materials at the National Research Center „Kurchatov Institute“ in Saint-Petersburg. After two years of research work, she joined Prof. U. S. Schubert’s group at the Friedrich Schiller University Jena, Germany. Her current work focus is on inkjet printing of functional materials and devices.

Christian Stolze. Christian Stolze studied physics at the Friedrich Schiller University Jena, Germany, graduating with a diploma in the group of Prof. Dr Ulrich S. Schubert in 2020, where he specialized in the characterization and optimization of organic radical batteries and flow batteries. His current research interests are focused on the development of state-of-charge and state-of-health measurement techniques for flow battery electrolytes as well as the investigation of electrochemical approaches for increasing the energy density of flow batteries.

Philip Rohland. Philip Rohland studied Chemistry at the Friedrich Schiller University Jena, Germany and finished his Master’s degree in the field of functional dyes. In 2017, he joined the group of Prof. Schubert as a PhD student, where he synthesizes organic active materials for redox flow batteries and evaluates new investigation possibilities of internal processes.

Steffi Stumpf. Steffi Stumpf studied at the Friedrich Schiller University (FSU) in Jena, Germany, graduating with a diploma in 2005. She has experience in a variety of research fields related to virology and immunopathology. Since 2012 she is related to the Electron Microscopy Group of the Jena Center for Soft Matter (JCSM). Her work particularly focuses on Scanning Electron Microscopy (SEM) of a variety of materials from the life- and energy-sciences.

Stephanie Hoepfner. Stephanie Hoepfner studied physics at the Westfälische Wilhelms-University Münster, Germany, where she earned her PhD degree in 2001 under the supervision of Prof. H. Fuchs and Prof. L. F. Chi. Thereafter, she joined the group of Prof. J. Sagiv at the Weizmann Institute of Science, Israel, as a Minerva fellow. In 2003 she moved to the group of Prof. U. S. Schubert, Eindhoven University of Technology, The Netherlands. Since 2009, she has been the project leader for Nanolithography and Surface Functionalization, and is responsible for electron microscopy in the Jena Center for Soft Matter at the Friedrich Schiller University Jena, Germany.

Martin D. Hager. Martin D. Hager completed his PhD in 2007 at the Friedrich Schiller University Jena. After postdoctoral research at the TU Eindhoven, in 2008 he became a

group leader in the group of Prof. Dr. Ulrich S. Schubert at the FSU Jena. His research interests include reversible polymer systems for self-healing applications, conjugated polymers for solar cells, as well as redox-active polymers for batteries (from small printable devices to large redox-flow-batteries).

Ulrich S. Schubert. Ulrich S. Schubert performed his PhD studies at the Universities of Bayreuth and South Florida. After a postdoctoral training at the University of Strasbourg

with Prof. Lehn (Nobel Prize 1987), he moved to the TU Munich and obtained his Habilitation in 1999. In 1999–2000 he was Professor at the University of Munich, and during 2000–2007 Full-Professor at the TU Eindhoven. Since 2007, he is a Full-Professor at the Friedrich Schiller University Jena, Germany. He is founding director of the Center for Energy and Environmental Chemistry Jena (CEEC Jena) and coordinator of the DFG priority program “Polymer-based Batteries” (SPP 2248) and the EU ITN “POLYSTORAGE” (GA 860403).